Ion complexation modelling of ferrihydrite:

From fundamentals of metal (hydr)oxide nanoparticles to applications in soil systems

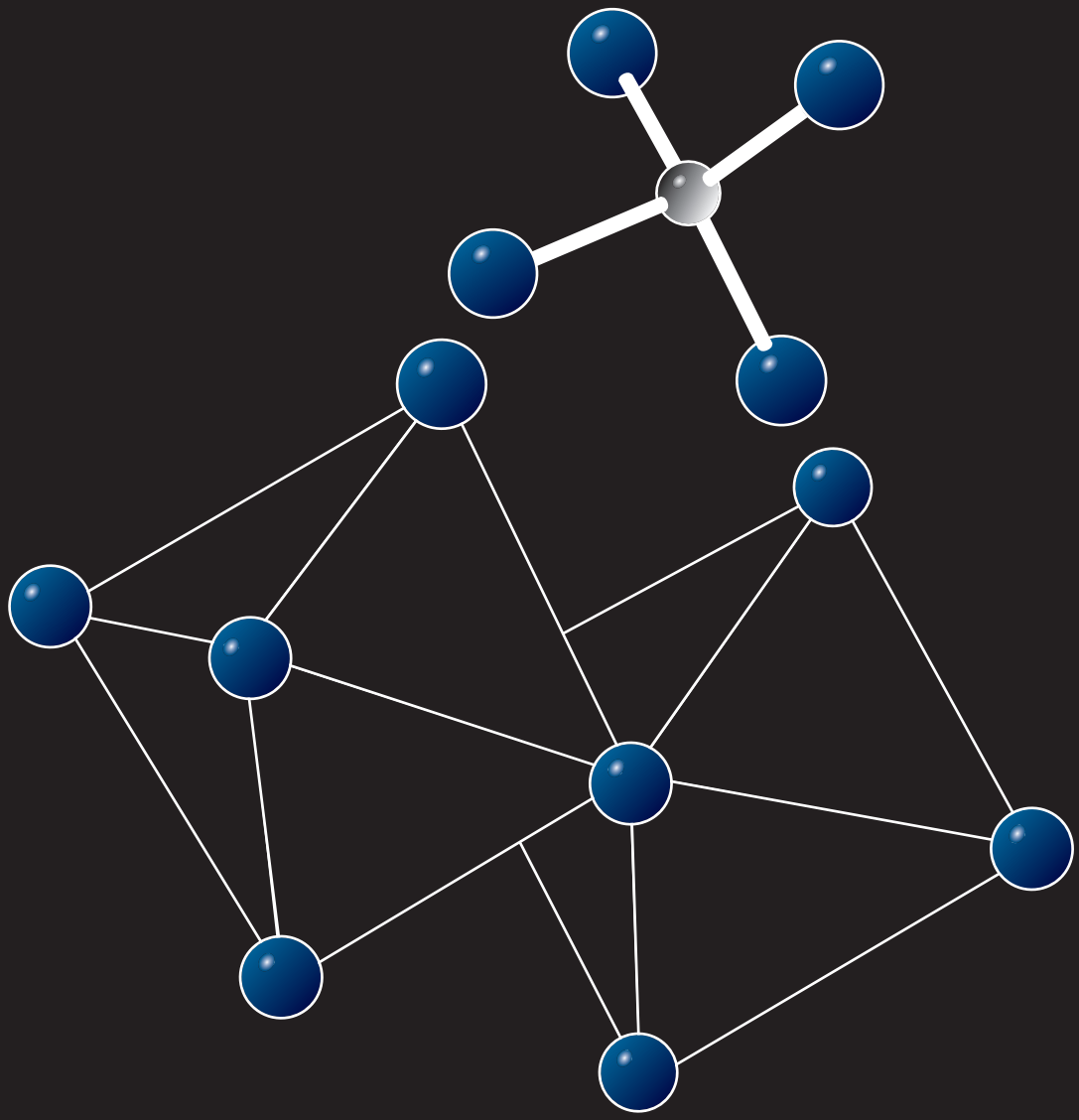

Juan Carlos Mendez Fernandez

Ion complexation modelling of ferrihydrite: From fundamentals of metal (hydr)oxide nanoparticles to applications in soils systems

Juan Carlos Mendez Fernandez

Thesis committee

Promotor
Prof. Dr R.N.J. Comans
Professor of Soil Chemistry and Chemical Soil Quality
Wageningen University & Research

Co-promotor
Dr T. Hiemstra
Assistant professor, Soil Chemistry and Chemical Soil Quality
Wageningen University & Research

Other members
Prof. Dr H.H.M. Rijnaarts, Wageningen University & Research
Prof. Dr C.P. Slomp, Utrecht University
Dr M.L. Machesky, University of Illinois, Champaign IL, USA
Prof. Dr J.P. Gustafsson, Swedish University of Agricultural Sciences, Uppsala, Sweden

This research was conducted under the auspices of the Graduate School for Socio-Economic and Natural Sciences of the Environment (SENSE)

Ion complexation modelling of ferrihydrite: From fundamentals of metal (hydr)oxide nanoparticles to applications in soils systems

Juan Carlos Mendez Fernandez

Thesis
submitted in fulfilment of the requirements for the degree of doctor
at Wageningen University
by the authority of the Rector Magnificus,
Prof. Dr A.P.J. Mol,
in the presence of the
Thesis Committee appointed by the Academic Board
to be defended in public
on Thursday 27 August 2020
at 11 a.m. in the Aula.

Juan Carlos Mendez Fernandez
Ion complexation modelling of ferrihydrite: From fundamentals of metal (hydr)oxide nanoparticles to applications in soils systems,
306 pages.

PhD thesis, Wageningen University, Wageningen, the Netherlands (2020)
With references, with summaries in English and Spanish

ISBN: 978-94-6395-445-7
DOI: doi.org/10.18174/525623

Abstract

Ferrihydrite (Fh) is the most important iron (hydr)oxide nanoparticle in nature. Due to its large surface reactivity, Fh influences the cycling, availability, and mobility of nutrients and pollutants in soils and water bodies, largely *via* adsorption processes. Ferrihydrite also forms stable complexes with natural organic matter (NOM), contributing to the long-term stabilization of organic carbon in soils. In the context of surface complexation modeling (SCM), studying the surface reactivity of Fh is important because this nanomaterial is envisioned as a good proxy for describing the reactivity of the natural metal (hydr)oxide fraction in soils. However, despite the recognized importance of Fh as a highly reactive material, many fundamental aspects of its surface reactivity have remained poorly understood. This thesis aimed to gain new insights into the surface reactivity of Fh, focusing on the analysis of ion adsorption mechanisms and on the development of a SCM framework for describing the adsorption of a suite of relevant cat- and anions to Fh in a realistic physical-chemical manner. In this thesis, a special emphasis is given to the adsorption of phosphate (PO_4) and its interfacial interactions with other ions (*i.e.* Ca, Mg, CO_3) that are relevant in nature and from the perspective of soil chemical analysis. Phosphate has been chosen as a model oxyanion due to its ubiquity in the environment and its high affinity for binding Fe (hydr)oxide surfaces. Moreover, the adsorption of Ca and Mg to Fh has been also studied in single-ion systems due to the abundance of these ions in the environment and their effect on the adsorption behavior of other ions, such as PO_4.

The approaches implemented in this thesis comprise adsorption experiments with freshly-prepared Fh nanoparticles and data interpretation using an advanced SCM (*i.e.* CD-MUSIC model) as well as molecular orbital (MO) calculations that allow to derive independently the charge distribution (CD) coefficients of the surface complexes considered in the modeling. The consistent treatment of the size dependency of the Fh properties is an essential aspect of this thesis. For this, a novel methodology has been proposed to evaluate the specific surface area (SSA) of Fh nanoparticles in suspension and to derive a coherent set of size-dependent values for the molar mass, mass density, and Stern Layer capacitance(s) of Fh, which are all of major importance for scaling and modeling the collected ion adsorption data. The combination of the above approaches allowed the development of a self-consistent thermodynamic database for describing ion adsorption to Fh. The insights obtained from the model systems, using synthetic Fh suspensions, have been applied to assess the reactive surface area (RSA) of the metal (hydr)oxide fraction in a series of agricultural Dutch top-soils and weathered tropical top-soils. Ferrihydrite is found to be a better proxy than well-crystallized goethite for describing the reactivity of the metal (hydr)oxide fraction in both soil series, despite the contrasting differences in the ratio of crystalline and nanocrystalline metal (hydr)oxides in these two soil series. The reactive metal (hydr)oxide fraction in these soils is dominated by nano-sized particles (~1.5 – 5.0 nm) with a variable specific surface area (SSA ~350 – 1700 $m^2\ g^{-1}$). The interaction between metal (hydr)oxide nanoparticles and NOM has been evaluated in these soil series and a structural model has been formulated for the nanoscale arrangement of the organo-mineral associations in soils. Overall, the results of this thesis are relevant from both a fundamental and a practical perspective. They contribute to increase our understanding of molecular-scale ion adsorption processes occurring at the solid-solution interface of Fh, which is important to develop more accurate predictions of the behavior and availability of ions at the macroscopic level, studied at the laboratory and field scale.

Table of contents

CHAPTER 1

General Introduction

Juan C. Mendez

1.1. Relevance of the study

1.1.1. Global iron cycling

Ferrihydrite (Fh) is an important iron (hydr)oxide nanoparticle ($Fe_{ox}NP$) present in most natural environments. It is a key component of the global biogeochemical cycle of iron (Fe). Ferrihydrite is the first solid (hydr)oxide phase formed at precipitation of Fe(III) ions and it works as a precursor for the formation of other, more crystalline, Fe (hydr)oxides (*e.g.* hematite, goethite).[1,2] Fh can be formed by forced hydrolysis of Fe(III) in solution or by the oxidation of Fe(II) species.[2] In nature, Fh particles may be surrounded by organic matter molecules[3,4] or associated with other minerals such as phyllosilicate clays or well-crystallized metal (hydr)oxides.[2,5] Fh nanoparticles are thermodynamically unstable and have a rather high solubility that leads to particle growth and transformation into other Fe (hydr)oxides with a higher intrinsic stability.[6] Because of its high solubility, Fh often controls the availability of Fe for plant uptake[7,8] *via* dissolution processes, especially under oxic soil conditions. The transport of $Fe_{ox}NPs$ (*i.e.* Fh-like particles) from the continent to the ocean represents a significant input of Fe into marine environments.[9] These $Fe_{ox}NPs$ regulate the availability of Fe in the oceans, affecting their primary productivity and consequently, the global concentrations of atmospheric CO_2 by altering the rates of carbon sequestration in oceans.[10–12] Moreover, these $Fe_{ox}NPs$ may transport adsorbed metal ions and anions in the environment from one location to another.

1.1.2. Nutrients availability in soils: assessment of phosphate availability

In soil environments, Fh is one of the most reactive mineral phases due to the ultra-small size of the primary particles (~2–5 nm) and corresponding large specific surface areas (SSA ~300 – 850 $m^2\ g^{-1}$),[3,13] even if present in low mass-based concentrations. For instance, in one cubic meter of soil (*i.e.* 1 m depth × 1 m^2 surface) with a bulk density of ρ_{soil} ~ 1500 kg m^{-3} and only (!) 1% w/w of Fh, the corresponding contribution of Fh in terms of surface area is in the order of ~10^7 m^2 (ten million!). Thereby, Fh can greatly regulate the bioavailability and mobility of nutrients and pollutants in the environment, especially those of oxyanions with high affinity for metal (hydr)oxide surfaces, such as phosphate (PO_4).

The adsorption of PO_4 to the natural fraction of $Fe_{ox}NPs$ is a relevant process in soils of natural and agricultural systems because it often leads to PO_4 solution concentrations (*e.g.* < 10 µM in non-fertilized soils) that are much lower than the required optimum for plant growth.[14,15] The adsorption of PO_4 to the nano-meter sized oxide fraction is a rather complex phenomenon, as it depends not only on the physical-chemical properties of the surfaces of the adsorbent, but also on the overall chemical composition of the solution phase (*i.e.* pH, type and concentration of coexisting ions), as well as on the presence of organic matter.[16,17] Hence, a comprehensive understanding of all the individual factors affecting the overall adsorption process of PO_4 is required for predicting the chemical behavior of this essential nutrient in the environment.

The availability of P in arable lands and pastures is traditionally assessed with routine analysis in laboratories using a variety of methods that differ in their mechanisms of PO_4 extraction.[18–20] The amount of extracted PO_4 can greatly vary from one method to another, which might lead to contradicting conclusions about the soil P status when different methods are used for the same soil sample.[21,22] The inability of some soil P analyses to predict accurately the soil P status can be partly attributed to a poor mechanistic understanding of the chemical processes affecting the extractability of PO_4.[23] Thus, there is a need for better understanding the chemical factors affecting the PO_4 release from the natural fraction

of Fe (hydr)oxides, which would help to achieve more mechanistic interpretations of the outcome of soil P analyses.

1.1.3. Soil organic carbon stabilization

In natural environments, Fh nanoparticles may precipitate in the presence of soil organic carbon (SOC), forming chemically (meta) stable organo-mineral complexes.[24–29] The formation of these organo-mineral complexes is related to the physical-chemical surface properties of the naturally formed Fh nanoparticles. Moreover, the interaction with ubiquitously present inorganic ions also affect the formation and stability of these organo-mineral complexes. For instance, oxyanions such as PO_4 and AsO_4 compete with SOC for the binding sites at the Fh surfaces, which will lead to less and weaker interactions between SOC and Fh.[16,30,31] Inverse relationships have been found between the loadings of SOC and PO_4 in the surfaces of metal (hydr)oxides of soils.[32,33] On the other hand, divalent cations such as calcium (Ca) may enhance the binding of SOC to the Fh surfaces due to the combined effect of stronger electrostatic interactions and formation of ternary Fe-SOC-Ca complexes.[34,35] Therefore, studying the surface reactivity of Fh is also important from the perspective of a long-term stabilization of organic carbon in soils and sediments, which consequently contributes to mitigating the effects of increasing CO_2 emissions on the global climate.[36–38]

1.1.4. Environmental and remediation technologies

Lastly, studying the mechanisms of ion adsorption to Fh is relevant from the practical perspective of environmental engineering and remediation technologies. Promising results have been obtained from the use of engineered Fe_{ox}NPs for removing contaminants from drinking- and wastewater.[39,40] For instance, the removal of PO_4 from municipal and industrial wastewater, agricultural drainage, and household sources is critical for preventing environmental problems such as eutrophication of water bodies.[41] For this, Fe_{ox}NPs are envisioned as good cost-effect materials.[40,42] Field applications of Fh nanoparticles have been proposed to amend P-enriched soils and reduce the potential runoff of P to the groundwater.[43] Recently, Koopmans et al.[44] applied a Fe oxide sludge, containing mainly siliceous Fh, to increase the reactive surface area of a non-calcareous sandy soil and effectively reduce the concentration of PO_4 in the soil solution.

Despite the encouraging results, some critical aspects that reduce the efficiency of contaminant removal by Fe_{ox}NPs still need to be addressed[40] (*e.g.* particle aggregation, reduction of reactive surface area, and competitive adsorption of coexisting ions). These challenges underline the importance of this thesis, which contributes to improve our understanding of the surface reactivity of Fe_{ox}NPs and their mechanisms of ion adsorption.

1.2. Ferrihydrite: a brief retrospection of literature

The aim of this literature retrospection is to frame the contributions of this PhD thesis within the vast amount of research performed about Fh over the years. Together with Sections 1.3 and 1.4, this section is intended to provide an overview of important studies that have contributed to the state-of-the-art knowledge about Fh reactivity at the moment of starting this thesis.

1.2.1. Ferrihydrite identification

Nowadays, the ubiquity of Fh as a naturally occurring nanomineral in soils, sediments, and water environments is well-recognized.[2,45] However, the name "ferrihydrite" and its recognition as a distinct mineral phase is relatively new in the scientific literature, if compared to other Fe (hydr)oxides (*e.g.* goethite, hematite). It has been "only" 50 years since Chukhrov et al.[46] in 1972 firstly introduced this name for referring to a Fe (hydr)oxide precipitate, formed on the walls of an old mine deposit. By 1974, the name ferrihydrite had been formally approved by the nomenclature commission of the International Mineralogical Association,[47] and it started soon to be adopted by other researchers[48] for referring to the "amorphous" solid phases of ferric oxides, until then known as "hydrous ferric oxide" (HFO). Nowadays, the names "two-line" and "six-line" Fh are commonly assigned to the end members of a range of Fh materials according to the number of reflection peaks distinguishable in the X-ray diffraction patterns. The particle size of these end-members vary from ~2 nm for 2LFh to ~6 nm for 6LFh.[2]

The natural Fh material described by Chukhrov et al.[46,47] has X-ray diffraction patterns that are consistent with those reported previously by Towe and Bradley[49] in 1967 for a synthetic Fe (hydr)oxide precipitate obtained by forced hydrolysis of a ferric nitrate solution. In addition, Towe and Bradley[49] reported similar X-ray diffraction patterns for a Fe micelle extracted from ferritin, a biological Fe storage protein. The studies of Chukhrov et al.[46,47] and Towe and Bradley[49] greatly contributed to finish a long scientific controversy about the existence of a naturally formed Fe(III) precipitate, analogous to the synthetic "amorphous" oxide freshly precipitated in the laboratory from hydrolyzed Fe(III) solutions. The direct identification of Fh in soils using X-ray diffraction is rather challenging because of the weak and broad diffraction peaks observed for this material.[50] It was approximately 10 years after the work of Chukhrov et al.[46] that a direct identification of Fh was reported for the first time in the groundwater of soils, using X-ray diffraction and Mössbauer spectroscopy.[2,51]

1.2.2. Ion adsorption studies

Despite the relatively recent recognition of Fh as a distinctive mineral phase, the extraordinarily high ion binding capacity of this material had been acknowledged long before. For instance, in 1837 Bunsen and Berthold[52] already documented the capacity of freshly precipitated Fe (hydr)oxides to effectively remove arsenite from solution. However, the authors postulated the formation of basic ferric arsenite salts as the mechanism explaining such observations. Almost a century later, different research groups recognized this observation as an ion adsorption process that is influenced by specific experimental conditions.[53,54] In other early studies, the relevance of freshly-precipitated Fe (hydr)oxides for adsorbing organic compounds and radionuclides was also recognized, as it can be noted respectively in the works of Grbttie and Williams[55] in 1928 and Kurvatov[56] in 1932.

Since then, synthetic Fh suspensions have been extensively used for studying the adsorption of both metal cations[57–60] and oxyanions.[61,62] The ion adsorption studies prior to 1990 have been critically evaluated and compiled by Dzombak and Morel[63] in the context of Surface Complexation Modeling (SCM) development. Cornell and Schwertmann[2] present an overview of the ion adsorption studies found in the literature until early 2000's. More recently, ion adsorption studies using synthetic Fh as a model (hydr)oxide nanomaterial have continued, many of these focusing on providing a more realistic physical-chemical picture of the ion adsorption processes, using SCM, advance spectroscopic techniques, and/or quantum chemical computations (*e.g.* see references [64–78]).

Despite the substantial number of studies, most of the ion adsorption data collected for fresh Fh materials have been measured in single-ion systems, whereas for geochemical and soil chemical

applications the interactions between multiple adsorbing ions is important. However, adsorption studies in multi-component systems have received considerably less attention. To date, the interfacial interaction of PO_4 with major ions has not been systematically tested for systems with freshly-prepared Fh, while this is key for understanding the adsorption behavior of this oxyanion in more complex media, for instance in the extraction solution of common soil tests for P availability. For instance, cooperative adsorption interactions with metal ions such as Ca and Mg, and competitive adsorption interactions with CO_3 ions need to be analyzed if the aim is to develop a robust modeling approach applicable for describing PO_4 adsorption in a wide range of environmental and analytical conditions. Moreover, as I will show in this thesis, analyzing ion adsorption in multicomponent systems allows the elucidation of additional adsorption mechanisms that otherwise cannot be identified by only studying ion adsorption in single-ion systems.

In addition, a consistent interpretation and modeling of ion adsorption data collected in literature for different Fh suspensions is a challenging task, because the surface area of Fh may vary substantially depending on the preparation protocol and aging conditions.[63,79,80] For fresh Fh suspensions, this variation cannot be assessed as it is conventionally done for crystallized metal (hydr)oxides, using for instance gas adsorption analysis.[81,82] In the present thesis, a self-consistent scaling and modeling approach of data has been made possible, thanks to the development and implementation of a novel probe-ion approach for assessing the specific surface area (SSA) of fresh Fh in suspension. In this approach, the adsorption of PO_4 is measured in single-ion Fh systems and the data are interpreted with the charge distribution (CD) model, defining the SSA as the only adjustable parameter. The above issue will be further explained in Section 1.4.

1.3. Mineral and surface structure of ferrihydrite

Detailed knowledge about how atoms are arranged in the core (*i.e.* crystal structure) and surface of metal (hydr)oxides is essential to understand their thermodynamic behavior, magnetic properties, and surface reactivity.[83–85] The latter aspect is especially important for studying and elucidating mechanisms of ion adsorption. However, the mineral and surface structure of Fh have remained rather enigmatic for many years. This has hampered the development of a mechanistic SCM that incorporates a realistic molecular representation of the adsorption processes at the surfaces of this important nanomaterial. The study of ion adsorption in relation to the mineral and surface composition of Fh constitutes a central aspect in the interpretation and modeling of the adsorption data collected in this thesis. In this section, an overview is provided about the developments that have contributed to the state-of-the-art knowledge on the mineral and surface structure of Fh.

1.3.1. Mineral structure

In the pioneering work of Towe and Bradley[49] in 1967, a crystal model with a chemical composition of $Fe_5HO_8 \cdot 4H_2O$ was proposed for Fh. In this model, the mineral structure of Fh was related to that of hematite but with a larger number of vacant Fe(III) sites, *i.e.* Fh was proposed to be a defective type of hematite. Contemporaneous to the work of Towe and Bradley,[49] Harrison et al.[86] proposed an atomic structure for the Fe (hydr)oxide core of ferritin, a Fh-like iron storage protein, with a corresponding chemical composition of FeOOH. In Harrison's model the Fe(III) atoms are randomly present in octahedral and tetrahedral coordination. Since then, several models have been proposed for the mineral structure of Fh. An overview of the "classical" structural models proposed for Fh is discussed in the literature review of Jambor and Dutrizac.[45] Amongst these, the models proposed by Eggleton and

Fitzpatrick[87] in 1988 and by Drits et al.[88] in 1993 have received wide attention in the literature. In the former model,[87] two sheets of Fe(III) octahedra are linked by two sheets of mixed Fe(III) in tetrahedral and octahedral coordination, with a stoichiometry of FeOOH for the bulk mineral, and an overall chemical composition that varies between $Fe_4(OH)_{12}$ and $Fe_5O_3(OH)_9$ due to the high and variable water content. On the other hand, in the model of Drits et al.[88] the structure of Fh is seen as a *multiphase* system that consists of both defected and defect-free phases, including variable amounts of nanocrystalline hematite, maghemite/magnetite, and/or a highly defective material. One fundamental difference between the model of Eggleton and Fitzpatrick[87] and that of Drits et al.[88] is the presence and absence, respectively, of Fe(III) in tetrahedral coordination. Since then, two types of "competing" structural models existed in the literature in which the existence or absence of tetrahedral Fe(III) in the crystal structure of Fh was a central point of debate.[89]

More recently, Michel et al.[90,91] proposed a new structural model for Fh based on the analysis of the pair distribution function (PDF) of data collected with High-Energy X-ray Total Scattering (HEXS). According to Michel's model, the mineral structure of Fh is a periodic *single-phase* containing three types of Fe(III) atoms, namely Fe1, Fe2, and Fe3. The Fe1 and Fe2 atoms represent, in an ideal structure, respectively 60% and 20% of total Fe(III) in the mineral and have an octahedral coordination, whereas the Fe3 atoms (20%) are present in tetrahedral coordination. In the mineral structure of Fh, Fe_{13} units (*i.e.* δ-Keggin like structures, see references [92,93] for further explanation) can be recognized in which 12 Fe octahedra (Fe1 and Fe2) are surrounding one central Fe3 tetrahedron (Figure 1.1a). For Fh with an ideal structure, the chemical composition is $FeO_{1.6}H_{0.2}$, which interestingly is in close agreement with the composition that Towe and Bradley[49] had proposed ~40 years before.

In recent studies, using advanced spectroscopic techniques such as high resolution EXAFS[83] and XANES,[89] conclusive evidence has been found for the presence of tetrahedral Fe(III) in the mineral core of Fh, setting an end to a long-term dispute. In addition, the structural model of Michel et al.[90,91] has been supported by further evidence, as found by Pinney et al.,[94] Peak and Regier,[89] Xu et al.,[95] Maillot et al.,[83] Mikutta,[96] and Harrington et al.[97] Although the debate about a ultimate crystal model for Fh is maybe not yet fully settled,[98–100] the Michel's model has gained wide acceptance in the current scientific literature.

Important to note is the fact that Michel et al.[91] reported systematic discrepancies between model and experimental data. These differences were attributed to the presence of randomly distributed vacancies of Fe(III) positions in the mineral structure that gradually disappeared with Fh aging, ultimately leading to a defect-free material called "ferrifh". However, according to Hiemstra,[84] this phenomenon is not related to vacancies of Fe(III) in the mineral bulk structure, but it is due to a surface contribution, thereby advocating a core-surface model. This notion has led to the development of a model for the surface structure of Fh, which is described in the next section.

1.3.2. Surface structure

At the surface, the repetitive arrangement of metal ions of the mineral core is interrupted, changing the coordination environment of the metal ions present at the mineral-solution interfaces. The metal ions present at the surfaces will have different physical-chemical properties in comparison to those present in the mineral core. The relatively high fraction of surface metal ions, in relation to the number of ions in the bulk mineral, makes the surface structure a crucial factor determining the overall stability and reactivity of nanoparticles.[6,101,102] Therefore, analyzing the surface structure of Fh is essential for understanding the overall behavior of this nanomaterial.

According to the surface depletion (SD) model proposed by Hiemstra,[84] the surface of Fh forms an "inter-phase" with a distinct chemical and polyhedral composition that differ from those of the mineral core. In general, Fh can be seen as the combination of a mineral core that is defect-free and hydrogen poor, and a surface layer that is water-rich due to the large contribution of -OH and -OH_2 surface groups.[84] The presence of a distinct surface layer with a polyhedral composition that differs from the mineral core of Fh, as proposed in the SD model, is supported by recent studies using Mössbauer spectroscopy[103] and *in-situ* collected small-angle X-ray scattering (SAXS) data.[93]

More specifically, the fundamental difference between the core and surface composition of Fh results from the surface depletion of part of the Fe2 octahedra and Fe3 tetrahedra. At the surfaces of Fh, part of the Fe2 and Fe3 polyhedra are less stable than the Fe1 octahedra. The Fe3 polyhedra have intrinsically a lower stability as the ionic radius of the Fe^{3+} cation is rather large and fits less well in a tetrahedral coordination. The lower stability of the Fe2 octahedra at the Fh surface may arise from the large asymmetry in the coordination sphere of the central Fe^{3+} cation in the Fh structure.[84] Fe2 and Fe3 polyhedra are only stable at the surface if the ligands coordinate simultaneously to another Fe of the surface. Consequently, only Fe1 octahedra form singly coordinated groups (≡$FeOH^{-0.5}$) at the surfaces of Fh, and these groups are involved in adsorption processes of ions *via* ligand exchange reactions. Figure 1.1b shows the polyhedral representation of an idealized Fh particle in which parallel sheets of edge-sharing Fe1 octahedra (blue colored) are linked together by Fe2 (orange colored) and Fe3 (red colored) ions.

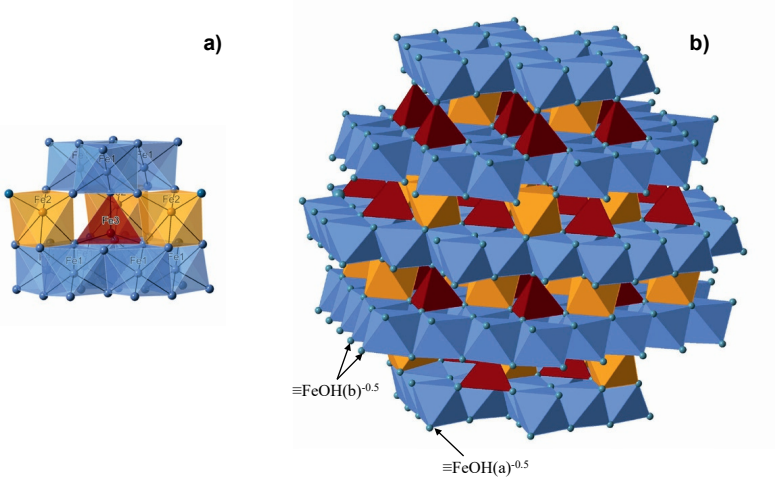

Figure 1.1. **a)** Representation of a Fe_{13} unit (Keggin structure) as can be distinguished in the mineral core of ferrihydrite particles. A Keggin unit consists of a central Fe3 tetrahedron (red colored) surrounded by Fe2 (orange colored) and Fe1 octahedra (blue colored). Note the asymmetrical position of Fe2 in the polyhedron. The blue spheres are the oxygen ions. The protons are not shown. **b)** Representation of a ferrihydrite particle with a size of ~ 2.5 nm and chemical composition equivalent to $FeO_{1.4}(OH)_{0.2}\cdot nH_2O$ with n = 1.5. Sheets of Fe1 octahedra (blue color) are connected by Fe2 (orange colored) and Fe3 polyhedra (red colored). Oxygen atoms are given as blue spheres. The protons are not shown. The constructed Fh particle is surface depleted by Fe2 octahedra and Fe3 tetrahedra because part of these polyhedra become unstable at the surface when forming singly coordinated surface groups. Figure is adapted from Hiemstra.[84] In the surface of Fh, only singly-coordinated (≡$FeOH^{-0.5}$) groups reacts with ions *via* a ligand exchange processes. Structurally, two types of singly coordinated groups are distinguished: ≡$FeOH(a)^{-0.5}$ and ≡$FeOH(b)^{-0.5}$, which can form either single edge (^{1}E) or double corner (^{2}C) bidentate surface complexes, respectively. Both types of groups can form monodentate complexes. Examples of these types of groups are pointed out in panel b.

With the SD model, a suite of size-dependent properties of Fh can be explained quantitatively.[80,84] According to this model, the overall chemical composition of Fh is $FeO_{1.4}(OH)_{0.2}{\cdot}nH_2O$, where $FeO_{1.4}(OH)_{0.2}$ is the composition of the mineral core, and nH_2O is the variable molar amount of chemisorbed water completing the coordination spheres of the Fe^{3+} ions present at the surface. As the particle size decreases, the fraction of Fe^{3+} ions forming surface groups becomes larger, leading to increasing values of nH_2O. Consequently, the molar mass of Fh (M_{nano}) increases with decreasing particle size, whereas the value of mass density (ρ_{nano}) decreases because the surface groups ($-OH_2$ and –OH) will contribute more to the particle volume than to the mass. This changes the relationship between the specific surface area SSA ($m^2\ g^{-1}$) and the mean particle diameter. Moreover, the SD model also explains other physical-chemical properties of Fh such as the size-dependent ratio of edge and corner sharing of the Fe polyhedra of Fh[80], the size-dependency of magnetic properties,[104] and the size-dependent solubility of Fh.[6]

1.4. Surface area assessment

The specific surface area (SSA in $m^2\ g^{-1}$ oxide) is a key property of Fh because it determines the high adsorption capacity of this nanomaterial. In systems with a given solid concentration (kg L^{-1}) and surface site density, the number of sites available for ion binding is defined by the SSA value. For Fh nanoparticles (d ~2–5 nm), the SSA is up to ~10–15 times larger compared to well-crystallized Fe (hydr)oxides having a larger particle size (*e.g.* goethite, hematite). The SSA is also important because it defines a number of size-dependent properties of Fh nanoparticles, comprising chemical composition, molar mass (M_{nano}) and mass density (ρ_{nano}),[84,105] as well as the thermodynamic stability and solubility of Fh.[6] The SSA of Fh is required for scaling ion adsorption data to the unit mol m^{-2}, because these data are often collected on a mass or molar basis (*e.g.* mol g^{-1} or mol mol^{-1} Fe). Scaling to surface area is particularly important for interpretation of adsorption data with SCM because the metal (hydr)oxides usually have a (variable!) surface charge, radiating an electrostatic field that is related to the surface charge density (in C m^{-2}). This charge density is used to calculate the variable electrostatic energy contribution involved in the binding process of ions, using an electrical double layer model (EDL).

The SSA of freshly-prepared Fh in suspension depends on the precipitation conditions. Slight variations in the preparation protocol of Fh might lead to significant differences in its value of SSA. In addition, the SSA of Fh decreases over time (Figure 1.2) because Fh nanoparticles are thermodynamically unstable and tend to grow spontaneously, by for instance Ostwald ripening. The rate of particle growth and correspondingly, the rate of SSA decrease, depends on the aging conditions of the Fh suspensions, as it will be shown in this thesis. Therefore, a precise and consistent assessment of the SSA is essential for comparing the results of ion adsorption studies performed with Fh suspensions that have been produced with different protocols and/or have a different aging history. This is required for developing a consistent thermodynamic database for applications of SCM using Fh as a reference oxide material.

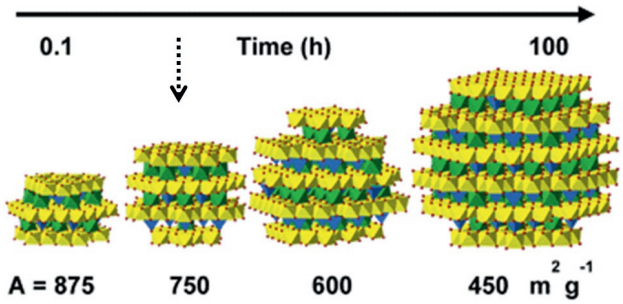

Figure 1.2. Representation of the growth of a ferrihydrite nanoparticle as a function of time (h) and the corresponding change in specific surface area A (m^2 g^{-1}). The dotted arrow gives the time of ~4 hours, which corresponds to the aging time of ferrihydrite suspensions as commonly used in batch adsorption experiments. Figure taken from the online publication corresponding to Chapter 3 of this thesis.[106]

The gas adsorption analysis (*e.g.* N_2, Ar) and interpretation with the BET equation is by far the most common method for assessing the SSA (A_{BET}) of regular metal (hydr)oxides.[2] However, when applied to oxide nanomaterials such as Fh, this technique presents a number of drawbacks. A major limitation of the gas adsorption analysis is that it requires sample drying and outgassing, which leads to a partially irreversible aggregation of the primary Fh nanoparticles and a significant reduction of the SSA.[60,81,82,107] The reduction in SSA due to particle aggregation can be as large as 50% in comparison to the SSA of Fh kept in the wet state (Chapter 2) and, as I will discuss in this thesis, this aggregation may be not entirely reversible making freeze-dried Fh a less suitable candidate for ion adsorption studies. In literature, other methods have been proposed to assess the SSA of Fh,[87,108,109] some of them based on probing the surface with reactive ions that specifically adsorb to Fh in suspension.[60,110] However, despite the extensive efforts, a consistent and unambiguous assessment of the SSA of Fh in suspension has remained challenging. Moreover, testing consistency between different methods applied to the same sample is rarely found in the literature.[2,87,108]

Considering the above issues, in this thesis I propose a novel approach to assess the SSA of Fh in suspension, in a way that is consistent with the description of the primary surface charge and specific adsorption of ions. The inferred methodology has been implemented in all adsorption experiments performed in this thesis, allowing the development of an internally consistent thermodynamic database for describing the adsorption of major ions relevant in the natural environment (*e.g.* PO_4, CO_3, Ca, Mg, and others).

1.5. Surface complexation modeling

As mentioned before, the adsorption of ions to the mineral surfaces of metal (hydr)oxides is a rather complex phenomenon influenced by a large number of factors such as the chemical composition of the solution phase (*e.g.* pH, ionic strength, and coexisting cations) and the various properties of the surface. As adsorption reactions proceed, the physical-chemical properties of the solid-solution interface change due to the influence of an electrostatic field, originated from the presence and development of surface charge. Surface complexation models (SCMs) are a key tool for deriving mechanistic-based descriptions of how these multiple factors interact and affect the overall adsorption of ionic species.

Over the years, several SCMs have been proposed for describing ion adsorption to metal (hydr)oxides, *e.g.* the constant capacitance model,[111] the triple-layer model,[60,112] the generalized two-layer model,[63] and the CD-MUSIC model.[113,114] Common characteristics of these SCMs is the use of equilibrium thermodynamic approaches formulating ion adsorption reactions, the use of mass and charge balance equations, and corrections of the intrinsic adsorption energy for electrostatics effects due to surface charging.[63,115,116] However, these SCMs differ in their representation of the solid-solution interface, and as a result, in their calculation of the electrostatic energy involved in the ion adsorption. Moreover, traditional models generally use a hypothetical single site approach to describe ion binding without a proper relation to the surface structure, while metal (hydr)oxides generally have various types of reactive sites. These single site approaches contrast with a model framework, known as the Multi-Site Ion Complexation model (MUSIC), in which different types of charged binding sites are defined with site densities that are based on surface structural information

The CD-MUSIC model is presently one of the most advanced SCM for describing the adsorption of ions to the surfaces of metal (hydr)oxides.[115,117,118] This approach actually consists of two components: a structural approach for describing interfacial charge distribution (CD) of the adsorbed surface complexes, and a structural treatment of the mineral surface defining a suite of reactive sites (MUSIC model). The CD-MUSIC model provides a realistic physical-chemical framework for describing various ion adsorption phenomena and surface speciation, allowing to link measurable processes occurring at the nanoscale to observations observed at the macroscopic scale. The key features of the CD and MUSIC models, in combination extensively applied in this thesis, are introduced below.

1.5.1. Charge distribution (CD) model

In the CD model, specifically adsorbed ions, *i.e.* inner-sphere complexes, are not treated as point charges but instead, their charge is distributed over two different electrostatic planes.[113] This interfacial distribution of charge is the main feature distinguishing the CD model from other SCMs. The rationale for the charge distribution concept is that, at the compact part of the double layer, the electrostatic potential changes drastically. Therefore, the ligands of the adsorbed ions common with the metal ions in the surface will experience the effect of the surface potential, whereas other ligands of the adsorbed moiety will experience a different potential. In the model, the interfacial charge distribution is defined by means of the CD coefficients (*i.e.* Δz_0, Δz_1, Δz_2).

In its most updated version, the CD model has been combined with an extended Stern layer approach to describe the compact part of the electrical double layer (EDL).[119] This electrostatic representation of the solid-solution interface is illustrated and explained in Figure 1.3.

The charge distribution coefficients are used to calculate the electrostatic contribution to the overall adsorption energy. For instance, one may formulate the adsorption reaction of a phosphate ion (PO_4^{3-}) *via* ligand exchange with two negatively charged singly coordinated groups ($\equiv FeOH^{-1/2}$) at the surface of a Fe (hydr)oxide as:

$$2{\equiv}FeOH^{-1/2} + PO_4^{3-}(aq) + 2H^+(aq) \leftrightarrow {\equiv}(FeO)_2^{-1+\Delta z0}PO_2^{\Delta z1} + 2H_2O(l); \quad \log K_{(ads)} \qquad \text{(Equation 1.1)}$$

where Δz_0 and Δz_1 represent the change of charge introduced in the 0- and 1- plane respectively upon adsorption of 1 PO_4^{3-} and 2 H^+, and the overall change in charge is $\Delta z = \Delta z_0 + \Delta z_1 = -1$.

In Equation 1.1, the $\log K_{(ads)}$ value is related to the total change in Gibbs free energy (ΔG_{ads}, in kJ mol^{-1}), according to the expression $\log K_{(ads)} = -\Delta G_{ads} / 2.3RT$, with R being the ideal gas constant (in J mol^{-1} K^{-1}) and T the absolute temperature (in K). The ΔG_{ads} is a combination of two energy contributions:

$$\Delta G_{ads} = \Delta G_{chem} + \Delta G_{elec} \quad \text{(Equation 1.2)}$$

where ΔG_{chem} is the intrinsic adsorption energy due to the formation of chemical bonds, and ΔG_{elec} is the (variable) electrostatic energy contribution. In the CD model approach, the ΔG_{elec} is defined as:

$$\Delta G_{elec} = \Delta z_0 F \Psi_0 + \Delta z_1 F \Psi_1 \quad \text{(Equation 1.3)}$$

where Ψ_0 and Ψ_1 are respectively the electrostatic potentials (in V) at the 0- and 1-planes.

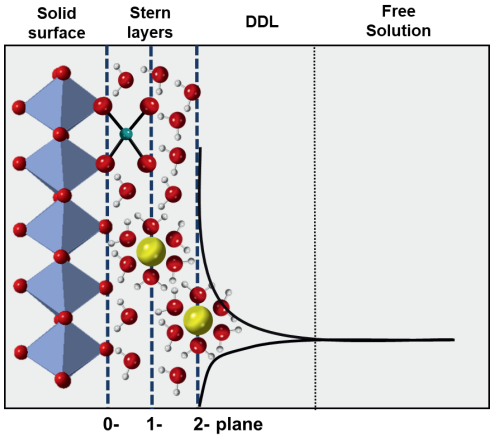

Figure 1.3. Schematic representation of the ferrihydrite-solution interface according to the extended Stern layer model as described by Hiemstra and Van Riemsdijk.[119] The blue polyhedra represent the Fe1 octahedra at the surface of Fh forming singly coordinated groups that react with protons and other ions such a PO_4. The red spheres in the Fe1 octahedra are oxygen atoms, which can be either singly (–OH) or doubly ($–OH_2$) protonated when present at the surfaces of Fh. For simplification, the protons have been omitted from the surface –O ligands. At the interface, three electrostatic planes are defined, namely the 0- (or surface-) plane, the 1- plane, and the 2- (or d-) plane. These planes define an inner and an outer Stern layer, each one with a corresponding capacitance value, C_1 and C_2. The inner Stern layer represents the space between the distance of minimum approach of hydrated electrolyte ions (1- plane) and the metal (hydr)oxide surface (0- plane), whereas the outer Stern layer represents the charge separation existing between the 1- plane and the head end of the diffuse double layer (DDL). Water molecules (red spheres are oxygen with bound protons given as white spheres) are present in the Stern layers. Structurally, these water molecules are differently organized than the "free" water molecules in the solution phase, due to H-bonding with surface groups, orientation on adsorbed ions, and the charged surface groups. In the scheme, a phosphate ion (turquoise sphere) is adsorbed as inner-sphere bidentate complex, sharing two ligands with the surface of Fh whereas two other ligands are located at the 1-plane. This distinction in the position of the ion ligands leads to the concept of charge distribution. The yellow spheres represent hydrated ions. These ions form outer-sphere complexes when they reach their minimum distance of approach. In such a case, the charge of these ions is fully attributed to the 1-plane in the CD model.

As it can be inferred from Equation 1.3, the contribution of the electrostatic component to the total adsorption energy depends on the distribution of the total change of charge Δz over two electrostatic

positions ($\Delta z = \Delta z_0 + \Delta z_1$). The values of these CD coefficients are related to the structure of an adsorbed complex in the interface. For instance, for a PO_4^{3-} ion forming an inner-sphere monodentate complex (*i.e.* sharing one common ligand with the surface) about ~ ¼ and ~ ¾ of the ion charge are located at the surface and 1- plane respectively; whereas for the formation of a bidentate PO_4^{3-} complex (*i.e.* two common ligands with the surface) the corresponding distribution of ligand charge is ~ ½ for both the surface and the 1- plane. Therefore, molecular scale information about the binding mechanisms is a key aspect in the CD model. In this respect, advances in *in-situ* spectroscopic techniques and in quantum chemical calculations have contributed to constrain the CD model with adsorption mechanisms that are realistic from a physical perspective. *Vice-versa*, the CD model may also be useful in certain cases to reveal the main binding mode of surface species, based on the values of the charge distribution needed for describing adsorption phenomena.[120]

In the original approach,[113] the CD coefficients were estimated applying the Pauling bond valence concept. The assumption is a symmetrical distribution of the charge of the central ion over the coordinating ligands. However, the bond length between the central ion and the various coordinating ligands often differs, leading to an asymmetrical charge distribution. These differences in bond lengths can be interpreted with the Brown bond valence concept, using bond lengths calculated from the optimized geometry of the adsorption complexes, found with molecular orbital (MO) calculations.[119] In this thesis, I have implemented this approach using optimized geometries for the different adsorbed complexes, which have been obtained using a common template composed by two linked Fe(III) octahedra that represent the surface groups of Fh (see ref [121] for details on the template). In addition, the interfacial charge distribution is affected by a change in dipole orientation of interfacial water molecules upon adsorption. This will be included in the present CD modeling.[119]

1.5.2. Multi-Site Ion Complexation (MUSIC) approach for ferrihydrite

The rational of the MUSIC approach is that at the mineral-solution interfaces of metal (hydr)oxides various types of surface groups exist (*i.e.* surface heterogeneity) and these groups may have a different affinity for binding protons.[114] In this approach, the charge undersaturation of the surface -O(H) ligands is used to estimate the intrinsic proton affinity (*i.e.* $\log K_H$) of the different types of surface groups. This charge undersaturation is linked to the coordination number of the ligands with metal ion(s) of the solid, which was originally calculated with the Pauling bond valence. In a later model refinement,[122] the charge undersaturation of the surface -O(H) ligands was calculated on the basis of the Brown bond valence, which accounts for asymmetrical distribution of charge in the coordination environment of the central metal ion(s) of the complex. This refined approach also accounts for the contribution of H bonds to charge neutralization of the surface ligands.[122] The MUSIC approach has been applied to describe the relationship between the surface charge (σ) and the pH in solution for various metal (hydr)oxides, including goethite (α-FeOOH),[122] gibbsite (α-$Al(OH)_3$),[123] rutile (α-TiO_2),[124,125] and cassiterite (α-SnO_2).[126]

From the above, a crucial aspect of the MUSIC model is the detailed analysis of the surface structure of the metal (hydr)oxide involved. For Fh, this information was unknown until not long ago, and this had impeded the development of a mechanistic ion adsorption model for this nanomaterial. Therefore, Hiemstra and van Riemsdijk[105] firstly attempted in 2009 to develop an ion complexation model for Fh using the structure of goethite as a starting point. Although the model has a disputable origin, the type of surface groups used, and corresponding site densities, have a strong resemblance with a more recent approach that is firmly based on the newest insights into the mineral and surface structure of Fh.[72] In their early work, Hiemstra and van Riemsdijk[105] also formulated a set of mathematical relationships that

describe the size-dependency of the molar mass and mass density of nanoparticles in general, which will be applied in the present work.

After unravelling the surface structure of Fh,[84] Hiemstra and Zhao[72] have developed an appropriate MUSIC approach for Fh, in which the types of sites and corresponding densities have been derived independently from the surface analysis of Fh, based on the structural insights described in Section 1.3. For Fh, three types of surface groups can be identified according to the coordination number with Fe, namely singly ($\equiv FeOH^{-0.5}$), doubly ($\equiv Fe_2OH^0$), and triply ($\equiv Fe_3O^{-0.5}$) coordinated groups. The singly coordinated groups bind protons and react with ions *via* ligand exchange reactions. Structurally, two types of singly coordinated groups are distinguished: $\equiv FeOH(a)^{-0.5}$ and $\equiv FeOH(b)^{-0.5}$, which can form either single edge (^1E) or double corner (^2C) bidentate surface complexes, respectively. The corresponding site densities of these groups are $N_s(a) = 3.0 \pm 0.6$ nm^{-2} and $N_s(b) = 2.8 \pm 0.6$ nm^{-2}. Both types of $\equiv FeOH^{-0.5}$ groups (a and b) may also form single corner (^1C) monodentate surface complexes with for instance oxyanions. For illustration, examples of these two types of singly coordinated groups are pointed out in Figure 1.1b. The doubly coordinated groups are uncharged and do not react with protons or ions under common pH conditions. Various types of triply coordinated groups exist at the surface of Fh. These $\equiv Fe_3O^{-0.5}$ groups have very different proton affinities, leading partially to an internal charge compensation. Overall, the suite of triply coordinated groups is represented by a single type of site with a net surface density of $N_s(T) = 1.4 \pm 0.5$ nm^{-2}, which has been established by fitting PO_4 adsorption data. The triply coordinated surface groups do not take part in ligand exchange reactions but contribute to the development of primary surface charge.

The above MUSIC approach for Fh has been applied to describe the adsorption of oxyanions such as PO_4, AsO_4, $As(OH)_3$,[72] $Si(OH)_4$[80]. In the present thesis, this modeling framework will also be applied to describe the interfacial interactions of PO_4 with other important anions as well as metal cations. For the metal cations, this will be done by introducing the concept of high and low affinity sites, which will be rationalized based on an analysis of the surface structure of Fh.

1.6. Ferrihydrite as a proxy for natural soils' oxides

The availability and mobility of ions in soils is largely controlled by sorption processes with natural organic matter, clays, and metal (hydr)oxides. The latter are particularly important for the binding of oxyanions such as PO_4 and AsO_4.[17] The edges of clay minerals with oxidic properties may also contribute to the adsorption of oxyanions,[127] particularly in clay soils. The natural metal (hydr)oxide fraction in soils comprises a range of materials with a variable chemical composition and crystallinity. In addition to information about the interaction of metal (hydr)oxide particles and soil organic matter, implementation of SCM for describing ion adsorption to the natural oxide fraction of soils also requires *i*) information about the reactive surface area of metal (hydr)oxide fraction in the soil samples (RSA in m^2 kg^{-1} soil), and *ii*) the choice of a proper reference material representing the mineral oxide fraction of these soils. The latter aspect is important because, as I will show in this thesis, different reference oxide materials might have different adsorption properties, which would affect consequently the outcome of the model descriptions.

Previously, a novel approach has been developed for assessing the effective RSA of the metal (hydr)oxide fraction in soils, which uses native soil PO_4 as probe-ion.[3] This methodology also provides an estimation of the total pool of PO_4 associated to this metal (hydr)oxide fraction. In the approach, soil samples are equilibrated with 0.5 M $NaHCO_3$ at different solution-to-solid ratios (SSR) and the

adsorption interaction PO_4–CO_3 was interpreted by CD modeling, using well-crystallized goethite as a reference (hydr)oxide material. This material was chosen because of the existence of an internally consistent thermodynamic database with intrinsic adsorption constants for a range of relevant ions. However, application of this probe-ion methodology to a series of agricultural top-soils from the Netherlands revealed that the reactive metal (hydr)oxide fraction is dominated by nanoparticles (d ~ 2 – 6 nm) with a high specific surface area (SSA ~200 – 1200 m^2 g^{-1}).[3] In literature, other studies have also provided evidence for the presence of nanoparticles as the dominant reactive fraction of metal (hydr)oxides in soils.[13,44,128]

The results of these studies advocate the use of Fh nanoparticles as a proxy for the natural fraction of metal (hydr)oxides for assessing the RSA of soils with SCM. Using the thermodynamic database developed in this thesis for ion adsorption to Fh, a subsequent aim is to test whether Fh is a better proxy than goethite for describing with SCM the surface reactivity of the metal (hydr)oxide fraction in field top-soils from both temperate and tropical regions. In the latter soils, the crystalline metal (hydr)oxides (*e.g.* goethite, hematite, and gibbsite) often dominate the (hydr)oxide fraction on a mass basis,[129,130] while the contribution of the fraction containing nano-sized oxides (*e.g.* Fh-like materials) may be relatively small on a mass basis. Nonetheless, due to their high surface area and high surface site density of reactive groups, Fe and Al (hydr)oxide nanoparticles may greatly contribute to the total PO_4 adsorption even at very low concentrations,[50] which I propose in this study as a hypothesis. To the best of my knowledge, the most recent insights into the mineral and surface structure of Fh have not been implemented yet in SCM studies to describe the PO_4 adsorption to the reactive fraction of oxides in soils.

1.7. Objectives and thesis outline

Considering all the above, a **first objective** of this thesis is to develop a systematic approach for assessing the SSA of Fh in suspensions by using either the H^+ or PO_4 as probe-ions and by interpreting the primary adsorption results with a consistent modeling approach that accounts for the size-dependency of a number of important Fh properties such as the molar mass (M_{nano}) and the mass density (ρ_{nano}). Applied to freshly precipitated Fh, this method will provide insights into the mechanisms and rate of particle growth of Fh at aging. In addition, the use of this approach for assessing SSA of Fh in all adsorption experiments allowed me to compile an internally consistent thermodynamic database with intrinsic ion affinity constants (log$K$) for Fh.

A **second objective** of this thesis is to gain mechanistic insights into the surface reactivity of Fh in relation to ion adsorption phenomena, and to develop a consistent modeling approach for describing simultaneously, in a realistic physical-chemical manner, the adsorption of a series of relevant cat- and anions to Fh. This modeling approach incorporates state-of-the-art knowledge about the mineral and surface structure of Fh. In this thesis, special emphasis is given to the adsorption of PO_4 to Fh and to the interfacial interactions of this oxyanion with other major ions of relevance in nature and from the perspective of soil chemical analysis for assessing P availability. Therefore, for PO_4, its synergistic adsorption interaction with the divalent cations Ca and Mg, as well as its competitive adsorption interaction with CO_3 ions will be extensively analyzed in this thesis. Moreover, the adsorption of the alkaline-earth metal ions will be studied in single-ion systems with Fh since these ions are generally abundant in the environment and might affect the chemical behavior of important nutrients and pollutants, *e.g.* PO_4 and AsO_4. From a more fundamental perspective, analyzing the adsorption of these

cations will enable the study of the surface site heterogeneity for the binding of cations (*i.e.* occurrence of high and low affinity sites), in consistency with the structural surface model of Fh.[84]

A **third objective** of this thesis is to quantify the reactive surface area of field soil samples and to describe the extractability of phosphate in a series of agricultural top-soils from temperate and tropical regions, which is important, for instance, to enable mechanistic interpretations of the results of different soil extraction methods, commonly used to asses PO_4-availability For this, the thermodynamic database developed in this thesis for Fh will be implemented in the SCM of the selected soil samples. The hypothesis is that Fh is a better proxy for the natural fraction of metal (hydr)oxides in agricultural top-soils, rather than well-crystallized goethite. In this thesis, the analysis of the surface reactivity of the metal (hydr)oxide in soils will also enable to study the nano-scale interactions between this reactive mineral (hydr)oxide fraction and SOM.

This thesis consists of nine chapters, including the present introduction (**Chapter 1**), seven experimental and modeling chapters (**Chapters 2 – 8**), and a synthesis and discussion chapter (**Chapter 9**). The experimental and modeling chapters can be organized, according to their main goal/subject, into three sections as shown in Table 1.1.

Table 1.1. Summary of the experimental chapters of this thesis, which have been organized in three different sections according to their main subject.

Section	Chapter	Main topic
1. Basic insights into the surface reactivity of Fh	2	Develop a systematic approach for probing the surface area of Fh with phosphate, consistently with the description of primary charge
	3	Study of the dynamic change of the specific surface area of Fh: Modeling and mechanisms
2. Parametrization of the ion adsorption model	4	Adsorption of alkaline-earth ions to Fh: high and low affinity sites
	5	Cooperative interaction of phosphate with Ca and Mg ions for the binding to ferrihydrite
	6	Competitive interaction of phosphate with (bi)carbonate ions for the binding to ferrihydrite
3. Application of the developed SCM to soils	7	Assessing the reactive surface area of Dutch top-soils using Fh as a proxy for the natural metal (hydr)oxide nanoparticles
	8	Surface reactivity of the natural metal (hydr)oxide fraction in weathered tropical soils

In **Chapter 2**, a novel approach is proposed for assessing the SSA of Fh preparations kept in the wet state, using H^+ as a probe ion. For this study, the pH-dependent primary charge of Fh has been measured in solutions with a series of different types of electrolyte ions. For data interpretation and modeling, the capacitance of the electrical double layer of well-crystallized goethite is used as a reference and translated in a consistent and systematic manner into the capacitance of Fh, using the molar mass (M_{nano}), the mass density (ρ_{nano}), and the surface curvature. The results show full consistency between the values of SSA of Fh derived with the present H^+ probing methodology and an approach that uses PO_4 as probe ion. However, probing the surface of Fh with PO_4 is preferred because measuring the primary charge is

more time-consuming and less sensitive than measuring the PO_4 adsorption. The validated probe ion methodology with PO_4 can be considered as an excellent and practical alternative to overcome the severe limitations of the traditional BET technique for assessing the SSA of metal (hydr)oxide nanoparticles, as well as the limitations of approaches that use transmission electron microscopy (TEM).

The probe-ion method with PO_4 has been applied in **Chapter 3** to trace the changes in the SSA of Fh produced by ultra-fast neutralization with NaOH of an acid $Fe(NO_3)_3$ solution. This allowed to reveal the major factors (*i.e.* time, pH, temperature, and organic molecules) controlling the change in SSA of Fh. The data provided insights into the mechanisms and rate of particle growth of Fh by Ostwald ripening, which allowed the development of a dynamic model that predicts the initial size of Fh nanoparticles and their change in diameter and corresponding SSA. The dynamic model has also been applied to describe the pH-dependent aging of Fh suspensions synthesized by standard procedures. The insights gained allow the preparation of Fh suspensions with a well-targeted surface reactivity, which contributes to high-quality measurements of the ion adsorption in different Fh batches.

In **Chapter 4,** the adsorption of Ca and Mg ions (M^{2+}) to Fh has been comprehensively studied in single-ion systems over a wide range of pH values, ionic strengths, and total molar M^{2+}/Fe ratios. The adsorption data were consistently scaled to the surface area using the ion probing methodology developed in Chapter 2. To describe the results, the surface complexation model, initially developed for describing the adsorption of oxyanions to Fh, has been further developed in this chapter by distinguishing reactive surface sites with high and low affinities for the binding of metal ions. For the first time, an attempt is made to identify and quantify the plausible surface configurations that are possibly related to the observed differences in the binding affinity of metal ions. The mechanistic insights developed in this chapter have been generalized for describing, in a self-consistent manner, the binding of the entire series of alkaline-earth ions, which comprises Be^{2+}, Mg^{2+}, Ca^{2+}, Sr^{2+}, Ba^{2+}, and Ra^{2+}.

In **Chapter 5**, the interfacial interaction of PO_4 with Ca and Mg ions (M^{2+}) has been extensively analyzed in binary adsorption systems with Fh, covering a broad range of pH values, M^{2+}/PO_4 ratios, and ion loadings. The adsorption data were scaled to the surface area determined with the PO_4 probe-ion method (Chapters 2 and 3) and the results were interpreted with the extended structural surface model for ferrihydrite (Chapter 4). The PO_4–M^{2+} interaction is a typical example of the cooperative binding of cat- and anions. The adsorption of PO_4 and M^{2+} is mutually enhanced when these ions are simultaneously present in the system. For Fh systems, this synergistic adsorption is largely explained by the formation of anion-bridged (*i.e.* ≡Fe–PO_4–M^{2+}) ternary complexes, which has been revealed by CD modeling of the collected adsorption data. The results of this chapter enable the evaluation of the difference in the pH-dependent cooperative adsorption of Ca and PO_4 between Fh and goethite systems.

In Chapter 6, the interaction between CO_3 and PO_4 was studied in closed systems with Fh, using a range of total added CO_3 concentrations that are relevant for environmental systems (*e.g.* groundwater) and for interpretation of soil chemical analysis data (*e.g.* 0.5 M $NaHCO_3$ soil extractions). In the applied approach, the binding modes of CO_3 to Fh and the corresponding affinity constants have been derived by only measuring the competitive effect of this ion on the adsorption of PO_4. The thus-calibrated model describes well the CO_3 interaction with Fh measured in single-ion systems, showing the validity of the implemented approach for describing CO_3 adsorption in a wide range of conditions. Differences in the competitive CO_3-PO_4 interaction between ferrihydrite and goethite systems are discussed in this chapter. The CD model parameters derived in this work for the CO_3-PO_4 interaction have been applied in Chapters 7 and 8 for assessing the reactive surface area of agricultural top-soils.

In **Chapter 7**, the model parameters for the competitive interaction CO_3–PO_4 in Fh systems (Chapter 6) have been used to describe, for a series of Dutch agricultural top-soils, the results obtained from a probe-ion method that consists of a series of soil extractions with 0.5 M $NaHCO_3$ at different solution-to-solid ratios. This approach reveals simultaneously the fraction of reversibly adsorbed PO_4 (R-PO_4) and the reactive surface area of soils (RSA). The latter is an essential parameter for describing ion adsorption phenomena in soils using SCM. The results show that the natural fraction of (hydr)oxides of these top-soils is dominated by nano-sized particles (d ~1.5–5.0 nm). It is also shown that Fh is a better proxy than goethite for assessing the RSA of these Dutch top-soils with the ion-probing methodology and for predicting the availability of PO_4 using SCM. Combining modeling and experimental results, a structural model is proposed for explaining the observed remarkable relationships of the soil organic carbon content with the derived RSA, as well as with the specific surface area and mean particle size of the metal (hydr)oxide fraction of these soils.

In **Chapter 8**, the probe-ion method, initially developed and tested for soils from regions with a temperate climate, has been applied for assessing the RSA of a series of tropical soils used for agriculture. In general, these highly weathered soils have a higher content of Fe and Al (hydr)oxides and a lower content of P, as compared to the set of top-soils from the Netherlands studied in Chapter 7. The results show that the probe-ion method can also be effectively used in this set of low-P soils without major adaptations. Similar to the observations for Dutch top-soils, Fh is shown to be a better proxy than goethite for describing the surface reactivity of the metal (hydr)oxide fraction in these tropical soil samples, even though the crystalline Fe and Al (hydr)oxides are, on a mass basis, the dominant fraction of metal (hydr)oxides in these soils. Combining experimental and modeling results, a conceptual model is formulated for the structural arrangement of the organo-mineral associations in these oxide-rich soils. Similarities and differences are established with the structural model proposed in Chapter 7 for the studied soils from a temperate region.

Finally, in **Chapter 9**, I will summarize the major findings of my PhD thesis and will critically discuss a number of results and concepts that, from my perspective, deserve further analysis in the overall context of this thesis. In addition, I will frame in a broader context the implications of my findings, and when opportune, I will propose future research opportunities in light of the results obtained in this thesis.

References

(1) Guo, H.; Barnard, A. S. Naturally Occurring Iron Oxide Nanoparticles: Morphology, Surface Chemistry and Environmental Stability. *J. Mater. Chem. A* **2013**, *1* (1), 27–42.

(2) Cornell, R. M.; Schwertmann, U. *The Iron Oxides: Structure, Properties, Reactions, Ocurrence and Uses*, Second Edi.; WILEY-VCH, Germany, 2003.

(3) Hiemstra, T.; Antelo, J.; Rahnemaie, R.; van Riemsdijk, W. H. Nanoparticles in Natural Systems I: The Effective Reactive Surface Area of the Natural Oxide Fraction in Field Samples. *Geochim. Cosmochim. Acta* **2010**, *74* (1), 41–58.

(4) Perret, D.; Gaillard, J. F.; Dominik, J.; Atteia, O. The Diversity of Natural Hydrous Iron Oxides. *Environ. Sci. Technol.* **2000**, *34* (17), 3540–3546.

(5) Wei, S. Y.; Liu, F.; Feng, X. H.; Tan, W. F.; Koopal, L. K. Formation and Transformation of Iron Oxide-Kaolinite Associations in the Presence of Iron(II). *Soil Sci. Soc. Am. J.* **2011**, *75* (1), 45–55.

(6) Hiemstra, T. Formation, Stability, and Solubility of Metal Oxide Nanoparticles: Surface Entropy, Enthalpy, and Free Energy of Ferrihydrite. *Geochim. Cosmochim. Acta* **2015**, *158*, 179–198.

(7) Schwertmann, U. Solubility and Dissolution of Iron Oxides. *Plant Soil* **1991**, *130* (1/2), 1–25.

(8) Li, F.; Koopal, L.; Tan, W. Roles of Different Types of Oxalate Surface Complexes in Dissolution Process of Ferrihydrite Aggregates. *Sci. Rep.* **2018**, *8* (1), 2060.

(9) Hochella, M. F.; Lower, S. K.; Maurice, P. A.; Penn, R. L.; Sahai, N.; Sparks, D. L.; Twining, B. S. Nanominerals, Mineral Nanoparticles, and Earth Systems. *Science (80-.).* **2008**, *319* (5870), 1631–1635.

(10) Boyd, P. W.; Watson, A. J.; Law, C. S.; Abraham, E. R.; Trull, T.; Murdoch, R.; Bakker, D. C. E.; Bowie, A. R.; Buesseler, K. O.; Chang, H.; et al. A Mesoscale Phytoplankton Bloom in the Polar Southern Ocean Stimulated by Iron Fertilization. *Nature* **2000**, *407* (6805), 695–702.

(11) Tagliabue, A.; Bowie, A. R.; Boyd, P. W.; Buck, K. N.; Johnson, K. S.; Saito, M. A. The Integral Role of Iron in Ocean Biogeochemistry. *Nature*. Nature Publishing Group March 1, 2017, pp 51–59.

(12) Wu, J.; Boyle, E.; Sunda, W.; Wen, L. S. Soluble and Colloidal Iron in the Oligotrophic North Atlantic and North Pacific. *Science (80-.).* **2001**, *293* (5531), 847–849.

(13) Eusterhues, K.; Rumpel, C.; Kögel-Knabner, I. Organo-Mineral Associations in Sandy Acid Forest Soils: Importance of Specific Surface Area, Iron Oxides and Micropores. *Eur. J. Soil Sci.* **2005**, *56* (6), 753–763.

(14) Gerke, J. The Acquisition of Phosphate by Higher Plants: Effect of Carboxylate Release by the Roots. A Critical Review. *Journal of Plant Nutrition and Soil Science*. Wiley-VCH Verlag June 1, 2015, pp 351–364.

(15) Hinsinger, P. Bioavailability of Soil Inorganic P in the Rhizosphere as Affected by Root-Induced Chemical Changes: A Review. *Plant Soil* **2001**, *237* (2), 173–195.

(16) Gustafsson, J. P. Arsenate Adsorption to Soils: Modelling the Competition from Humic Substances. *Geoderma* **2006**, *136* (1–2), 320–330.

(17) Weng, L.; van Riemsdijk, W. H.; Hiemstra, T. Factors Controlling Phosphate Interaction with Iron Oxides. *J. Environ. Qual.* **2012**, *41* (3), 628–635.

(18) Sánchez-Alcalá, I.; del Campillo, M. C.; Torrent, J. Critical Olsen P and CaCl 2 -P Levels as Related to Soil Properties: Results from Micropot Experiments. *Soil Use Manag.* **2015**, *31* (2), 233–240.

(19) McDowell, R. .; Sharpley, A. . Phosphorus Solubility and Release Kinetics as a Function of Soil Test P Concentration. *Geoderma* **2003**, *112* (1–2), 143–154.

(20) van Rotterdam, A. M. D.; Bussink, D. W.; Temminghoff, E. J. M.; van Riemsdijk, W. H. Predicting the Potential of Soils to Supply Phosphorus by Integrating Soil Chemical Processes and Standard Soil Tests. *Geoderma* **2012**, *189–190*, 617–626.

(21) Sánchez-Alcalá, I.; del Campillo, M. C.; Torrent, J. Extraction with 0.01 m CaCl 2 Underestimates the Concentration of Phosphorus in the Soil Solution. *Soil Use Manag.* **2014**, n/a-n/a.

(22) Koopmans, G. F.; Chardon, W. J.; Dekker, P. H. M.; Römkens, P. F. A. M.; Schoumans, O. F. Comparing Different Extraction Methods for Estimating Phosphorus Solubility in Various Soil Types. *Soil Sci.* **2006**, *171* (2), 103–116.

(23) Morel, C.; Tunney, H.; Plénet, D.; Pellerin, S. Transfer of Phosphate Ions between Soil and Solution: Perspectives in Soil Testing. In *Journal of Environmental Quality*; American Soc of Agronomy Inc, 2000; Vol. 29, pp 50–59.

(24) Kleber, M.; Eusterhues, K.; Keiluweit, M.; Mikutta, C.; Mikutta, R.; Nico, P. S. Mineral-Organic Associations: Formation, Properties, and Relevance in Soil Environments. *Adv. Agron.* **2015**, *130*, 1–140.

(25) Wagai, R.; Mayer, L. M. Sorptive Stabilization of Organic Matter in Soils by Hydrous Iron Oxides. *Geochim. Cosmochim. Acta* **2007**, *71* (1), 25–35.

(26) Mikutta, R.; Kleber, M.; Torn, M. S.; Jahn, R. Stabilization of Soil Organic Matter: Association with Minerals or Chemical Recalcitrance? *Biogeochemistry* **2006**, *77* (1), 25–56.

(27) Wiesmeier, M.; Urbanski, L.; Hobley, E.; Lang, B.; von Lützow, M.; Marin-Spiotta, E.; van Wesemael, B.; Rabot, E.; Ließ, M.; Garcia-Franco, N.; et al. Soil Organic Carbon Storage as a Key Function of Soils - A Review of Drivers and Indicators at Various Scales. *Geoderma*. Elsevier B.V. January 1, 2019, pp 149–162.

(28) Wiseman, C. L. S.; Püttmann, W. Interactions between Mineral Phases in the Preservation of Soil Organic Matter. *Geoderma* **2006**, *134* (1–2), 109–118.

(29) Kleber, M.; Mikutta, R.; Torn, M. S.; Jahn, R. Poorly Crystalline Mineral Phases Protect Organic Matter in Acid Subsoil Horizons. *Eur. J. Soil Sci.* **2005**, *56* (6), 717–725.

(30) Weng, L.; van Riemsdijk, W. H.; Hiemstra, T. Humic Nanoparticles at the Oxide−Water Interface: Interactions with Phosphate Ion Adsorption. *Environ. Sci. Technol.* **2008**, *42* (23), 8747–8752.

(31) Xue, Q.; Ran, Y.; Tan, Y.; Peacock, C. L.; Du, H. Arsenite and Arsenate Binding to Ferrihydrite Organo-Mineral Coprecipitate: Implications for Arsenic Mobility and Fate in Natural Environments. *Chemosphere* **2019**, *224*, 103–110.

(32) Hiemstra, T.; Antelo, J.; van Rotterdam, A. M. D.; van Riemsdijk, W. H. Nanoparticles in Natural Systems II: The

Natural Oxide Fraction at Interaction with Natural Organic Matter and Phosphate. *Geochim. Cosmochim. Acta* **2010**, *74* (1), 59–69.

(33) Regelink, I. C.; Weng, L.; Lair, G. J.; Comans, R. N. J. Adsorption of Phosphate and Organic Matter on Metal (Hydr)Oxides in Arable and Forest Soil: A Mechanistic Modelling Study. *Eur. J. Soil Sci.* **2015**, *66* (5), 867–875.

(34) Adhikari, D.; Sowers, T.; Stuckey, J. W.; Wang, X.; Sparks, D. L.; Yang, Y. Formation and Redox Reactivity of Ferrihydrite-Organic Carbon-Calcium Co-Precipitates. *Geochim. Cosmochim. Acta* **2019**, *244*, 86–98.

(35) Weng, L. P.; Koopal, L. K.; Hiemstra, T.; Meeussen, J. C. L.; Van Riemsdijk, W. H. Interactions of Calcium and Fulvic Acid at the Goethite-Water Interface. *Geochim. Cosmochim. Acta* **2005**, *69* (2), 325–339.

(36) Lal, R. Soil Carbon Sequestration Impacts on Global Climate Change and Food Security. *Science*. American Association for the Advancement of Science June 11, 2004, pp 1623–1627.

(37) Cotrufo, M. F.; Ranalli, M. G.; Haddix, M. L.; Six, J.; Lugato, E. Soil Carbon Storage Informed by Particulate and Mineral-Associated Organic Matter. *Nat. Geosci.* **2019**.

(38) Yang, Y.; Tilman, D.; Furey, G.; Lehman, C. Soil Carbon Sequestration Accelerated by Restoration of Grassland Biodiversity. *Nat. Commun.* **2019**, *10* (1).

(39) Zhang, Y.; Wu, B.; Xu, H.; Liu, H.; Wang, M.; He, Y.; Pan, B. Nanomaterials-Enabled Water and Wastewater Treatment. *NanoImpact* **2016**, *3–4*, 22–39.

(40) Xu, P.; Zeng, G. M.; Huang, D. L.; Feng, C. L.; Hu, S.; Zhao, M. H.; Lai, C.; Wei, Z.; Huang, C.; Xie, G. X.; et al. Use of Iron Oxide Nanomaterials in Wastewater Treatment: A Review. *Sci. Total Environ.* **2012**, *424*, 1–10.

(41) Wu, B.; Wan, J.; Zhang, Y.; Pan, B.; Lo, I. M. C. Selective Phosphate Removal from Water and Wastewater Using Sorption: Process Fundamentals and Removal Mechanisms. *Environ. Sci. Technol.* **2020**, *54* (1), 50–66.

(42) Wu, B.; Wan, J.; Zhang, Y.; Pan, B.; Lo, I. M. C. Selective Phosphate Removal from Water and Wastewater Using Sorption: Process Fundamentals and Removal Mechanisms. *Environ. Sci. Technol.* **2020**, *54* (1), 50–66.

(43) Rhoton, F. E.; Bigham, J. M. Phosphate Adsorption by Ferrihydrite-Amended Soils. *J. Environ. Qual.* **2005**, *34* (3), 890–896.

(44) Koopmans, G. F. F.; Hiemstra, T.; Vaseur, C.; Chardon, W. J. J.; Voegelin, A.; Groenenberg, J. E. E. Use of Iron Oxide Nanoparticles for Immobilizing Phosphorus In-Situ: Increase in Soil Reactive Surface Area and Effect on Soluble Phosphorus. *Sci. Total Environ.* **2020**, *711*, 135220.

(45) Jambor, J. L.; Dutrizac, J. E. Occurrence and Constitution of Natural and Synthetic Ferrihydrite, a Widespread Iron Oxyhydroxide. *Chem. Rev.* **1998**, *98* (7), 2549–2586.

(46) Chukhrov, F. V.; Zvyagin, B. B.; Ermilova, L. P.; Gorshkov, A. I. New Data on Iron Oxides in the Weathering Zone. In *Proc. Int. Clay Conf*; Consejo Superior de Investigaciones Científicas, División de Ciencias: Madrid, 1972; pp 397–404.

(47) Chukhrov, F. V.; Zvyagin, B. B.; Gorshkov, A. I.; Yermilova, L. P.; Balashova, V. V. Ferrihydrite. *Int. Geol. Rev.* **1974**, *16* (10), 1131–1143.

(48) Schwertmann, U.; Fischer, W. R. Natural "Amorphous" Ferric Hydroxide. *Geoderma* **1973**, *10* (3), 237–247.

(49) Towe, K. M.; Bradley, W. F. Mineralogical Constitution of Colloidal "Hydrous Ferric Oxides." *J. Colloid Interface Sci.* **1967**, *24* (3), 384–392.

(50) Childs, C. W. Ferrihydrite: A Review of Structure, Properties and Occurrence in Relation to Soils. *Zeitschrift für Pflanzenernährung und Bodenkd.* **1992**, *155* (5), 441–448.

(51) Schwertmann, U.; Schulze, D. G.; Murad, E. Identification of Ferrihydrite in Soils by Dissolution Kinetics, Differential X-Ray Diffraction, and Mössbauer Spectroscopy1. *Soil Sci. Soc. Am. J.* **1982**, *46* (4), 869–875.

(52) Bunsen, R. W.; Berthold, A. A. Eisenoxydhydrat, Das Gegengift Des Weissen Arseniks Oder Der Arsenigen Säure (In German). Dieterich: Göttingen 1837.

(53) Yoe, J. H. The Adsorption of Arsenious Acid by Hydrous Ferric Oxide. *J. Am. Chem. Soc.* **1930**, *52* (7), 2785–2790.

(54) Boswell, M. C.; Dickson, J. V. The Adsorption of Arsenious Acid by Ferric Hydroxide. *J. Am. Chem. Soc.* **1918**, *40* (12), 1793–1801.

(55) Grbttie, D. P.; Williams, R. J. The Adsorption of Organic Compounds on Hydrous Oxides and Fuller's Earth. *J. Am. Chem. Soc.* **1928**, *50* (3), 668–672.

(56) Kurbatow, I. W. Adsorption of Thorium X by Ferric Hydroxide at Different PH. *J. Phys. Chem.* **1932**, *36* (4), 1241–1247.

(57) Benjamin, M. M.; Leckie, J. O. Multiple-Site Adsorption of Cd, Cu, Zn, and Pb on Amorphous Iron Oxyhydroxide. *J. Colloid Interface Sci.* **1981**, *79* (1), 209–221.

(58) Kinniburgh, D. G.; Jackson, M. L.; Syers, J. K. Adsorption of Alkaline Earth, Transition, and Heavy Metal Cations by Hydrous Oxide Gels of Iron and Aluminum1. *Soil Sci. Soc. Am. J.* **1976**, *40* (5), 796.

(59) Kinniburgh, D. G.; Jackson, M. L. Concentration and PH Dependence of Calcium and Zinc Adsorption by Iron Hydrous Oxide Gel. *Soil Sci. Soc. Am. J.* **1982**, *46* (1), 56–61.

(60) Davis, J. A.; Leckie, J. O. Surface Ionization and Complexation at the Oxide/Water Interface II. Surface Properties of Amorphous Iron Oxyhydroxide and Adsorption of Metal Ions. *J. Colloid Interface Sci.* **1978**, *67* (1), 90–107.

(61) Davis, J. A.; Leckie, J. O. Surface Ionization and Complexation at the Oxide/Water Interface. 3. Adsorption of Anions. *J. Colloid Interface Sci.* **1980**, *74* (1), 32–43.

(62) Zachara, J. M.; Girvin, D. C.; Schmidt, R. L.; Resch, C. T. Chromate Adsorption on Amorphous Iron Oxyhydroxide in the Presence of Major Groundwater Ions. *Environ. Sci. Technol.* **1987**, *21* (6), 589–594.

(63) Dzombak, D. A.; Morel, F. M. M. *Surface Complexation Modeling: Hydrous Ferric Oxide*; John Wiley & Sons, Inc.: New York, 1990.

(64) Hu, S.; Lu, Y.; Peng, L.; Wang, P.; Zhu, M.; Dohnalkova, A. C.; Chen, H.; Lin, Z.; Dang, Z.; Shi, Z. Coupled Kinetics of Ferrihydrite Transformation and As(V) Sequestration under the Effect of Humic Acids: A Mechanistic and Quantitative Study. *Environ. Sci. Technol.* **2018**, *52* (20), 11632–11641.

(65) Johnston, C. P.; Chrysochoou, M. Mechanisms of Chromate, Selenate, and Sulfate Adsorption on Al-Substituted Ferrihydrite: Implications for Ferrihydrite Surface Structure and Reactivity. *Environ. Sci. Technol.* **2016**, *50* (7), 3589–3596.

(66) Wang, X.; Kubicki, J. D.; Boily, J. F.; Waychunas, G. A.; Hu, Y.; Feng, X.; Zhu, M. Binding Geometries of Silicate Species on Ferrihydrite Surfaces. *ACS Earth Sp. Chem.* **2018**, *2* (2), 125–134.

(67) Swedlund, P. J.; Holtkamp, H.; Song, Y.; Daughney, C. J. Arsenate-Ferrihydrite Systems from Minutes to Months: A Macroscopic and IR Spectroscopic Study of an Elusive Equilibrium. *Environ. Sci. Technol.* **2014**, *48* (5), 2759–2765.

(68) Wang, X.; Hu, Y.; Tang, Y.; Yang, P.; Feng, X.; Xu, W.; Zhu, M. Phosphate and Phytate Adsorption and Precipitation on Ferrihydrite Surfaces. *Environ. Sci. Nano* **2017**, *4* (11), 2193–2204.

(69) Tian, L.; Shi, Z.; Lu, Y.; Dohnalkova, A. C.; Lin, Z.; Dang, Z. Kinetics of Cation and Oxyanion Adsorption and Desorption on Ferrihydrite: Roles of Ferrihydrite Binding Sites and a Unified Model. *Environ. Sci. Technol.* **2017**, *51* (18), 10605–10614.

(70) Sowers, T. D.; Stuckey, J. W.; Sparks, D. L. The Synergistic Effect of Calcium on Organic Carbon Sequestration to Ferrihydrite. *Geochem. Trans.* **2018**, *19* (1), 4.

(71) Tiberg, C.; Gustafsson, J. P. Phosphate Effects on Cadmium(II) Sorption to Ferrihydrite. *J. Colloid Interface Sci.* **2016**, *471*, 103–111.

(72) Hiemstra, T.; Zhao, W. Reactivity of Ferrihydrite and Ferritin in Relation to Surface Structure, Size, and Nanoparticle Formation Studied for Phosphate and Arsenate. *Environ. Sci. Nano* **2016**, *3*, 1265–1279.

(73) Liu, J.; Zhu, R.; Liang, X.; Ma, L.; Lin, X.; Zhu, J.; He, H.; Parker, S. C.; Molinari, M. Synergistic Adsorption of Cd(II) with Sulfate/Phosphate on Ferrihydrite: An in Situ ATR-FTIR/2D-COS Study. *Chem. Geol.* **2018**, *477*, 12–21.

(74) Swedlund, P. J.; Miskelly, G. M.; McQuillan, A. J. Silicic Acid Adsorption and Oligomerization at the Ferrihydrite - Water Interface: Interpretation of ATR-IR Spectra Based on a Model Surface Structure. *Langmuir* **2010**, *26* (5), 3394–3401.

(75) Antelo, J.; Arce, F.; Fiol, S. Arsenate and Phosphate Adsorption on Ferrihydrite Nanoparticles. Synergetic Interaction with Calcium Ions. *Chem. Geol.* **2015**, *410*, 53–62.

(76) Bompoti, N. M.; Chrysochoou, M.; Machesky, M. L. A Unified Surface Complexation Modeling Approach for Chromate Adsorption on Iron Oxides. *Environ. Sci. Technol.* **2019**, *53* (11), 6352–6361.

(77) Rossberg, A.; Ulrich, K.-U.; Weiss, S.; Tsushima, S.; Hiemstra, T.; Scheinost, A. C. Identification of Uranyl Surface Complexes on Ferrihydrite: Advanced EXAFS Data Analysis and CD-MUSIC Modeling. *Environ. Sci. Technol.* **2009**, *43* (5), 1400–1406.

(78) Larsson, M. A.; Persson, I.; Sjöstedt, C.; Gustafsson, J. P. Vanadate Complexation to Ferrihydrite: X-Ray Absorption Spectroscopy and CD-MUSIC Modelling. *Environ. Chem.* **2017**, *14* (3), 141–150.

(79) Bompoti, N.; Chrysochoou, M.; Machesky, M. Surface Structure of Ferrihydrite: Insights from Modeling Surface Charge. *Chem. Geol.* **2017**, *464*, 34–45.

(80) Hiemstra, T. Ferrihydrite Interaction with Silicate and Competing Oxyanions: Geometry and Hydrogen Bonding of Surface Species. *Geochim. Cosmochim. Acta* **2018**, *238*, 453–476.

(81) Weidler, P. G. BET Sample Pretreatment of Synthetic Ferrihydrite and Its Influence on the Determination of Surface Area and Porosity. *J. Porous Mater.* **1997**, *4* (3), 165–169.

(82) Yates, D. E.; Grieser, F.; Cooper, R.; Healy, T. W. Tritium Exchange Studies on Metal Oxide Colloidal Dispersions. *Aust. J. Chem.* **1977**, *30* (8), 1655–1660.

(83) Maillot, F.; Morin, G.; Wang, Y.; Bonnin, D.; Ildefonse, P.; Chaneac, C.; Calas, G. New Insight into the Structure of Nanocrystalline Ferrihydrite: EXAFS Evidence for Tetrahedrally Coordinated Iron(III). *Geochim. Cosmochim. Acta* **2011**, *75* (10), 2708–2720.

(84) Hiemstra, T. Surface and Mineral Structure of Ferrihydrite. *Geochim. Cosmochim. Acta* **2013**, *105*, 316–325.

(85) Navrotsky, A.; Mazeina, L.; Majzlan, J. Size-Driven Structural Thermodynamic Complexity in Iron Oxides. *Science (80-.).* **2008**, *319* (March), 1635–1639.

(86) Harrison, P. M.; Fischbach, F. A.; Hoy, T. G.; Haggis, G. H. Ferric Oxyhydroxide Core of Ferritin. *Nature* **1967**, *216* (5121), 1188–1190.

(87) Eggleton, R. A.; Fitzpatrick, R. W. New Data and a Revised Structural Model for Ferrihydrite. *Clays Clay Miner.* **1988**, *36* (2), 111–124.

(88) Drits, V. A.; Sakharov, B. A.; Salyn, A. L.; Manceau, A. Structural Model for Ferrihydrite. *Clay Miner.* **1993**, *28* (2), 185–207.

(89) Peak, D.; Regier, T. Direct Observation of Tetrahedrally Coordinated Fe(III) in Ferrihydrite. *Environ. Sci. Technol.* **2012**, *46* (6), 3163–3168.

(90) Michel, F. M.; Ehm, L.; Antao, S. M.; Lee, P. L.; Chupas, P. J.; Liu, G.; Strongin, D. R.; Schoonen, M. A. A.; Phillips, B. L.; Parise, J. B. The Structure of Ferrihydrite, a Nanocrystalline Material. *Science* **2007**, *316* (5832), 1726–1729.

(91) Michel, F. M.; Barron, V.; Torrent, J.; Morales, M. P.; Serna, C. J.; Boily, J.-F.; Liu, Q.; Ambrosini, A.; Cismasu, A. C.; Brown, G. E. Ordered Ferrimagnetic Form of Ferrihydrite Reveals Links among Structure, Composition, and Magnetism. *Proc. Natl. Acad. Sci.* **2010**, *107* (7), 2787–2792.

(92) Casey, W. H. Large Aqueous Aluminum Hydroxide Molecules. *Chem. Rev.* **2006**, *106* (1), 1–16.

(93) Weatherill, J. S.; Morris, K.; Bots, P.; Stawski, T. M.; Janssen, A.; Abrahamsen, L.; Blackham, R.; Shaw, S. Ferrihydrite Formation: The Role of Fe13 Keggin Clusters. *Environ. Sci. Technol.* **2016**, *50* (17), 9333–9342.

(94) Pinney, N.; Kubicki, J. D.; Middlemiss, D. S.; Grey, C. P.; Morgan, D. Density Functional Theory Study of Ferrihydrite and Related Fe-Oxyhydroxides. *Chem. Mater.* **2009**, *21* (24), 5727–5742.

(95) Xu, W.; Hausner, D. B.; Harrington, R.; Lee, P. L.; Strongin, D. R.; Parise, J. B. Structural Water in Ferrihydrite and Constraints This Provides on Possible Structure Models. *Am. Mineral.* **2011**, *96* (4), 513–520.

(96) Mikutta, C. X-Ray Absorption Spectroscopy Study on the Effect of Hydroxybenzoic Acids on the Formation and Structure of Ferrihydrite. *Geochim. Cosmochim. Acta* **2011**, *75* (18), 5122–5139.

(97) Harrington, R.; Hausner, D. B.; Xu, W.; Bhandari, N.; Michel, F. M.; Brown, G. E.; Strongin, D. R.; Parise, J. B. Neutron Pair Distribution Function Study of Two-Line Ferrihydrite. *Environ. Sci. Technol.* **2011**, *45* (23), 9883–9890.

(98) Rancourt, D. G.; Meunier, J. F. Constraints on Structural Models of Ferrihydrite as a Nanocrystalline Material. *Am. Mineral.* **2008**, *93* (8–9), 1412–1417.

(99) Manceau, A. PDF Analysis of Ferrihydrite and the Violation of Pauling's Principia. *Clay Miner.* **2010**, *45* (2), 225–228.

(100) Manceau, A. Critical Evaluation of the Revised Akdalaite Model for Ferrihydrite. *Am. Mineral.* **2011**, *96* (4), 521–533.

(101) Hochella, M. F.; Mogk, D. W.; Ranville, J.; Allen, I. C.; Luther, G. W.; Marr, L. C.; McGrail, B. P.; Murayama, M.; Qafoku, N. P.; Rosso, K. M.; et al. Natural, Incidental, and Engineered Nanomaterials and Their Impacts on the Earth System. *Science*. American Association for the Advancement of Science 2019.

(102) Grassian, V. H. When Size Really Matters: Size-Dependent Properties and Surface Chemistry of Metal and Metal Oxide Nanoparticles in Gas and Liquid Phase Environments. *J. Phys. Chem. C* **2008**, *112* (47), 18303–18313.

(103) Wang, X.; Zhu, M.; Koopal, L. K.; Li, W.; Xu, W.; Liu, F.; Zhang, J.; Liu, Q.; Feng, X.; Sparks, D. L. Effects of Crystallite Size on the Structure and Magnetism of Ferrihydrite. *Environ. Sci. Nano* **2016**, *3* (1), 190–202.

(104) Hiemstra, T. Surface Structure Controlling Nanoparticle Behavior: Magnetism of Ferrihydrite, Magnetite, and Maghemite. *Environ. Sci. Nano* **2018**, *5* (3), 752–764.

(105) Hiemstra, T.; Van Riemsdijk, W. H. A Surface Structural Model for Ferrihydrite I: Sites Related to Primary Charge, Molar Mass, and Mass Density. *Geochim. Cosmochim. Acta* **2009**, *73* (15), 4423–4436.

(106) Hiemstra, T.; Mendez, J. C.; Li, J. Evolution of the Reactive Surface Area of Ferrihydrite: Time, pH, and Temperature Dependency of Growth by Ostwald Ripening. *Environ. Sci. Nano* **2019**, *6* (3), 820–833.

(107) Strehlau, J. H.; Toner, B. M.; Arnold, W. A.; Penn, R. L. Accessible Reactive Surface Area and Abiotic Redox Reactivity of Iron Oxyhydroxides in Acidic Brines. *Geochim. Cosmochim. Acta* **2017**, *197*, 345–355.

(108) Pyman, M. A. F.; Posner, A. M. The Surface Areas of Amorphous Mixed Oxides and Their Relation to Potentiometric Titration. *J. Colloid Interface Sci.* **1978**, *66* (1), 85–94.

(109) Burleson, D. J.; Penn, R. L. Two-Step Growth of Goethite from Ferrihydrite. *Langmuir* **2006**, *22* (1), 402–409.

(110) Anderson, M. A.; Malotky, D. T. The Adsorption of Protolyzable Anions on Hydrous Oxides at the Isoelectric PH. *J. Colloid Interface Sci.* **1979**, *72* (3), 413–427.

(111) Sigg, L.; Stumm, W. The Interaction of Anions and Weak Acids with the Hydrous Goethite (α-FeOOH) Surface. *Colloids and Surfaces* **1981**, *2* (2), 101–117.

(112) Davis, J. A.; James, R. O.; Leckie, J. O. Surface Ionization and Complexation at the Oxide/Water Interface: I. Computation of Electrical Double Layer Properties in Simple Electrolytes. *J. Colloid Interface Sci.* **1978**, *63* (3), 480–499.

(113) Hiemstra, T.; Van Riemsdijk, W. H. A Surface Structural Approach to Ion Adsorption: The Charge Distribution (CD) Model. *J. Colloid Interface Sci.* **1996**, *179* (2), 488–508.

(114) Hiemstra, T.; Van Riemsdijk, W. H.; Bolt, G. H. Multisite Proton Adsorption Modeling at the Solid/Solution Interface of (Hydr)Oxides: A New Approach. I. Model Description and Evaluation of Intrinsic Reaction Constants. *J. Colloid Interface Sci.* **1989**, *133* (1), 91–104.

(115) Groenenberg, J. E.; Lofts, S. The Use of Assemblage Models to Describe Trace Element Partitioning, Speciation, and Fate: A Review. *Environ. Toxicol. Chem.* **2014**, *33* (10), 2181–2196.

(116) Goldberg, S. Application of Surface Complexation Models to Anion Adsorption by Natural Materials. *Environ. Toxicol. Chem.* **2014**, *33* (10), 2172–2180.

(117) Komárek, M.; Antelo, J.; Králová, M.; Veselská, V.; Číhalová, S.; Chrastný, V.; Ettler, V.; Filip, J.; Yu, Q.; Fein, J. B.; et al. Revisiting Models of Cd, Cu, Pb and Zn Adsorption onto Fe(III) Oxides. *Chem. Geol.* **2018**, *493*, 189–198.

(118) Koopal, L.; Tan, W.; Avena, M. Equilibrium Mono- and Multicomponent Adsorption Models: From Homogeneous Ideal to Heterogeneous Non-Ideal Binding. *Adv. Colloid Interface Sci.* **2020**, 102138.

(119) Hiemstra, T.; Van Riemsdijk, W. H. On the Relationship between Charge Distribution, Surface Hydration, and the Structure of the Interface of Metal Hydroxides. *J. Colloid Interface Sci.* **2006**, *301* (1), 1–18.

(120) Rietra, R. P. J. J.; Hiemstra, T.; Van Riemsdijk, W. H. The Relationship between Molecular Structure and Ion Adsorption on Variable Charge Minerals. *Geochim. Cosmochim. Acta* **1999**, *63* (19–20), 3009–3015.

(121) Rahnemaie, R.; Hiemstra, T.; Van Riemsdijk, W. H. Geometry, Charge Distribution, and Surface Speciation of Phosphate on Goethite. *Langmuir* **2007**, *23* (7), 3680–3689.

(122) Hiemstra, T.; Venema, P.; Van Riemsdijk, W. H. Intrinsic Proton Affinity of Reactive Surface Groups of Metal (Hydr)Oxides: The Bond Valence Principle. *J. Colloid Interface Sci.* **1996**, *184* (2), 680–692.

(123) Hiemstra, T.; Yong, H.; Van Riemsdijk, W. H. Interfacial Charging Phenomena of Aluminum (Hydr)Oxides. *Langmuir* **1999**, *15* (18), 5942–5955.

(124) Machesky, M. L.; Předota, M.; Wesolowski, D. J.; Vlcek, L.; Cummings, P. T.; Rosenqvist, J.; Ridley, M. K.; Kubicki, J. D.; Bandura, A. V.; Kumar, N.; et al. Surface Protonation at the Rutile (110) Interface: Explicit Incorporation of Solvation Structure within the Refined MUSIC Model Framework. *Langmuir* **2008**, *24* (21), 12331–12339.

(125) Ridley, M. K.; Hiemstra, T.; van Riemsdijk, W. H.; Machesky, M. L. Inner-Sphere Complexation of Cations at the Rutile-Water Interface: A Concise Surface Structural Interpretation with the CD and MUSIC Model. *Geochim. Cosmochim. Acta* **2009**, *73* (7), 1841–1856.

(126) Rosenqvist, J.; Machesky, M. L.; Vlcek, L.; Cummings, P. T.; Wesolowski, D. J. Charging Properties of Cassiterite (α-SnO2) Surfaces in NaCl and RbCl Ionic Media. *Langmuir* **2009**, *25* (18), 10852–10862.

(127) Gérard, F. Clay Minerals, Iron/Aluminum Oxides, and Their Contribution to Phosphate Sorption in Soils — A Myth Revisited. *Geoderma* **2016**, *262*, 213–226.

(128) Regelink, I. C.; Weng, L.; Koopmans, G. F.; van Riemsdijk, W. H. Asymmetric Flow Field-Flow Fractionation as a New Approach to Analyse Iron-(Hydr)Oxide Nanoparticles in Soil Extracts. *Geoderma* **2013**, *202–203*, 134–141.

(129) Kämpf, N.; Scheinost, A.; Schulze, D. Oxide Minerals in Soils. In *Handbook of Soil Sciences*; Handbook of Soil Science; CRC Press, 2011; pp 1–34.

(130) Xu, R. K.; Qafoku, N. P.; Van Ranst, E.; Li, J. Y.; Jiang, J. Adsorption Properties of Subtropical and Tropical Variable Charge Soils: Implications from Climate Change and Biochar Amendment. In *Advances in Agronomy*; 2016; Vol. 135, pp 1–58.

CHAPTER 2

Surface area of ferrihydrite consistently related to primary surface charge, ion pair formation, and specific ion adsorption

Juan C. Mendez, Tjisse Hiemstra

Published as:

Mendez, J.C., Hiemstra, T. 2020. Surface area of ferrihydrite consistently related to primary surface charge, ion pair formation, and specific ion adsorption. *Chem. Geol.* 532, 119304. doi.org/10.1016/j.chemgeo.2019.119304

Abstract

The specific surface area (SSA) of metal oxides is pivotal for the scaling of surface phenomena. For ferrihydrite (Fh), the SSA can be assessed by probing the surface with ions that specifically adsorb (*e.g.* protons or phosphate). In the approach, an appropriate material with a known surface chemical behavior is used as reference, accounting for differences in *e.g.* surface sites and structure. As Fh is a nanomaterial, the size-dependency of many of its properties requires a consistent implementation for data analysis and modeling. In the present study, the proton adsorption of Fh was measured in $NaNO_3$, NaCl, and $NaClO_4$ solutions using a potentiometric titration methodology that leads to an internally consistent primary data set (H^+/Fe). For data interpretation, we employed a size-dependent molar mass, mass density, and chemical composition ($FeO_{1.4}(OH)_{0.2}\cdot nH_2O$), as well as a size-dependent surface curvature since the latter increases the value of the Stern layer capacitance. Using well-crystallized goethite as a reference, state-of-the-art multisite complexation modeling discloses the underlying SSA of Fh. Similar to goethite, a significant variation in electrolyte affinity constants (log*K*) is found for Fh. This largely explains the differences in pH_{PZC} reported in literature when using *e.g.* KNO_3 or NaCl rather than $NaNO_3$ as electrolyte solution. Our data collection was done for Fh materials with a known aging history. The same Fh samples were also probed with phosphate ions and the collected primary data (PO_4/Fe) were interpreted with the CD model. This methodology yields SSA values that are consistent with those found by probing the surface of Fh with protons. As ion probing with phosphate is rapid and sensitive, it is recommended as a tool to determine the SSA of Fh materials. This enables the development of a consistent thermodynamic database for application of surface complexation modeling in natural systems.

Keywords: iron nanoparticles, potentiometric titrations, probe ions, surface reactivity, electrolyte ions, CD model

2.1. Introduction

Ferrihydrite (Fh) is a highly reactive Fe(III)-oxide nanomaterial. It is omnipresent in nature where it strongly contributes to regulating the geochemical cycling of numerous elements, particularly *via* adsorption processes.[1–3] Since Fh has a high adsorption capacity, it is also a promising material for environmental engineering and remediation. Due to its relevance, Fh nanoparticles are often synthesized in the laboratory to study the binding of metal ions,[4–7] oxyanions,[8–11] and organic compounds,[12–14] applying a range of *in-situ* spectroscopic techniques as well as surface complexation modeling (SCM). Understanding the surface reactivity of Fh is also interesting from a scientific perspective in general.

The surface area is a key characteristic of Fh, as it determines the extraordinary ion adsorption capacity of Fh as well as a large number of the size-dependent properties of this nanomineral, such as the chemical composition, the corresponding molar mass (M_{nano}, g mol^{-1} Fe) and the mass density (ρ_{nano}, g m^{-3}).[8,15] For the interpretation of experimental ion adsorption data, which are often expressed on a mass basis (mol g^{-1}), scaling to the specific surface area (SSA) is required to account for the variation in the number of surface sites available in the system. In addition, the SSA is important in model interpretation because it is involved in the contribution of the electrostatic field to the overall adsorption energy of ions. Moreover, Fh has a strong surface curvature that changes this electrostatic contribution in comparison to a linear field at a planar crystal face. This will lead to an increase in the surface charge density, which consequently will depend on the particle size[16,17] and corresponding SSA.

The SSA often varies between Fh preparations, as it is well documented in various studies.[18–20] Slight variations in the conditions of Fe(III) precipitation lead to the formation of Fh particles with different size, which hampers a reproducible synthesis of this nanomaterial. In addition, the SSA of Fh changes over time because Fh nanoparticles are thermodynamically metastable and grow spontaneously.[21–23] Therefore, data of different ion adsorption studies can only be compared when consistently scaled to the SSA. Only then, a consistent set of thermodynamic affinity constants (log$K$) for ions can be derived, which can be used in applications of SCM.

Over the past decades, a large variety of methods have been used to assess the SSA of Fh,[18,19] which comprises multilayer adsorption of gases,[24,25] monolayer adsorption of organic molecules,[26] phosphate (PO_4) ions[27] and water,[28] as well as cation exclusion at low pH or proton binding.[29] Despite the extensive efforts, a consistent and unambiguous assessment of the SSA of Fh in suspension remains challenging. In addition, assessment of the SSA with different methods applied to the same sample is rare in literature.[19,26,28]

Gas adsorption analysis (*e.g.* N_2, Ar) applying the BET equation[30] is traditionally used to measure the SSA (A_{BET}) of regular metal (hydr)oxides[19] and silica particles.[31] With adaptations, the approach can also be applied to microporous metal-organic frameworks.[32–34] The gas adsorption analysis requires sample drying and outgassing,[25,29,35,36] which causes in the case of Fh an irreversible aggregation of the primary nanoparticles and a reduction of the SSA that no longer reflects the reactive surface area of Fh kept in the wet state.

Transmission Electron Microscopy (TEM) can provide a first estimate of the SSA of Fh (A_{TEM}),[21,36,37] but A_{TEM} measurements are often associated with significant uncertainties related to methodological artefacts, statistical problems, and interpretation of data.[38] In the approach, the experimental particle diameter based on an idealized spherical shape is translated into a SSA, assuming a certain mass density. A more precise assessment of A_{TEM} requires additional information such as the

particle size distribution, the aspect ratio of the particles, particle porosity, and surface roughness, reducing the precision and accuracy of the TEM approach.[10]

Because of the above multiple challenges, methods that are based on probing the surface of Fh with reactive ions, rather than with gas molecules, have been proposed. In their pioneering work, Davis and Leckie[29] have used the adsorption of protons as a tool (H^+ surface probing). Probing the surface can also be done with PO_4.[27] From an analytical perspective, the use of PO_4 has the advantage that it can be measured accurately and because of its high adsorption affinity, PO_4 is less sensitive to interference of ions such as carbonate.[39] Previously, linearization of the Langmuir adsorption isotherm of PO_4 was used to estimate the monolayer coverage of Fh by this anion.[27] More recently, the SSA of Fh in suspension has been assessed with CD modeling.[23] With the latter approach, the SSA of Fh preparations can be derived with precision. To date, the calibration of this probing method with PO_4 is based on an estimate of the SSA of the used Fh material,[8] making the accuracy of the method uncertain. Consistency with other methods of ion surface probing, particularly with protons, has not been established yet.

Based on the above, our first objective is to develop a methodology for systematically deriving the SSA of Fh in suspension using H^+ as probe ion and evaluate the consistency when probing the surface of Fh with PO_4. Since the surface area of Fh changes continuously due to particle growth, the adsorption of both ions will be measured simultaneously for Fh in a suspension that is regularly sampled during aging. The central question is whether we can consistently describe the adsorption of H and PO_4 within a common modeling framework using a consistent set of parameters that allow the calculation of unique set of values for the SSA.

One of the many key aspects in the interpretation of the H^+ adsorption data is the affinity of the background electrolyte ions. In literature, the pH-dependent surface charge of Fh has been studied extensively in different types of background electrolyte solutions.[24,40–45] However, the variation in ion pair affinity is difficult to resolve from literature studies because of the use of Fh materials prepared by different methods. To the best of our knowledge, no previous study has measured the variation in electrolyte ion affinity for Fh in a consistent manner, based on a common reference state of the material studied. As this is a challenge, it will be an additional objective of the present study. For this, we will collect sets of H^+ adsorption data in various electrolyte solutions using a methodology that leads to an internally consistent data set, as previously developed for goethite.[46]

Interpretation of ion adsorption data requires detailed insights into the mineral and surface structure of Fh. Over the years, many research groups have contributed to elucidate the mineral structure of this nanomaterial.[26,47–56] This information has been used to formulate a structural surface model for Fh,[57] allowing the development of a mechanistic ion complexation model for Fh that uses these state-of-the-art insights to reveal a set of reactive surface site densities.[8] Presently, we will apply this multisite ion complexation model for interpreting the collected H^+ and PO_4 adsorption data.

Since Fh particles are nano-sized, scaling of the primary adsorption data requires more attention than usual before such data can be interpreted with any SCM. This crucial aspect in the primary data processing will be comprehensively addressed in the present study. We will introduce a systematic approach for scaling of the primary ion adsorption data, which can consistently account for the above-mentioned size-dependent factors, comprising the chemical composition and the corresponding molar mass M_{nano} and mass density ρ_{nano}. The latter parameter will be relevant as it defines the relationship between the surface area A and the particle diameter d which is a measure for the surface curvature and determines the capacitance of the Stern layer.[15] The sensitivity of the assessment of the SSA to these factors will be evaluated in the discussion of our work.

2.2. Experimental

Pre-boiled ultrapure water (18.2 MΩcm at 25 °C, <1 ppb TOC) and chemical reactants of analytical grade were used to prepare all the stock solutions and Fh suspensions. Contact between solutions and air was minimized to prevent the intrusion of atmospheric CO_2(g). The stock suspensions of Fh were purged with moist N_2(g) for at least 20 h to remove CO_2(g). The N_2(g) was purified by passing it through sequential traps with 1.0 M H_2SO_4, 1.0 M NaOH, and ultrapure water.

2.2.1. Ferrihydrite synthesis

Three different batches of Fh suspensions (Fh_1, Fh_2, and Fh_3) were prepared following a methodology described previously.[23,39] Briefly, solutions containing about 3.7 mM $Fe(NO_3)_3 \cdot 9H_2O$, dissolved in 0.01 M HNO_3, were titrated by adding in steps a freshly-prepared solution of 0.02 M NaOH. The final pH was either 6.0 (Fh_1 and Fh_2) or 8.2 (Fh_3). The Fh suspensions were centrifuged at 3500*g* for 45 min. Next, the supernatant was carefully removed, and the precipitated Fh particles were re-suspended in a 0.01 M $NaNO_3$ background electrolyte solution.

Prior to any use, each preparation was first aged at 20 ºC during 4 h after neutralization. The subsequent treatments were different. Fh_1 was acidified to pH 5.1 and stored at 4 ºC for 72 h. Next, the temperature was brought back to 20 ºC and the suspension was continuously purged with moist N_2(g) for 20 to 68 h, depending on the final aging period. This Fh preparation was used in a series of experiments at 96, 120, and 144 h since precipitation. The Fh_2 and Fh_3 suspensions were first stored in closed bottles at the pH of preparation (pH 6.0 and pH 8.2 respectively) for 4 h, and then were purged with N_2(g) until the start of the acid-base titrations and PO_4 adsorption experiments (*i.e.* 24 h since precipitation). The total Fe concentration of the suspensions was 20.1 ± 1.3 mM, as measured by inductively coupled plasma - optical emission spectrometry (ICP-OES) in a matrix of 0.8 M H_2SO_4. The recovery efficiency of Fe with respect to the total Fe added initially was ~100 % for Fh_1 and Fh_3, whereas for Fh_2 this value was 93 %. This poor recovery efficiency of Fe for Fh_2 may lead to lower values of SSA for the Fh suspension, as it will be discussed later in Section 2.3.3.

2.2.2. Potentiometric titrations

Two types of potentiometric titration experiments were performed. For all suspensions, classical forward and backward acid-base titrations were done, using $NaNO_3$ as background electrolyte solution at different levels: 0.05, 0.20, and/or 1.0 M. For Fh_1, we applied additionally a methodology with internally consistent one-way (base) titrations in three types of background solutions (*i.e.* $NaNO_3$, NaCl, and $NaClO_4$) at two different concentrations (0.20 and 0.50 M). These background solutions were selected based on the expected differences in affinity of the accompanying anions for Fh. All data collected for each of the different electrolyte ions were scaled relatively to the charge of Fh in a common stock suspension (Fh_1 at pH 5.11 ± 0.01 in 0.01 M $NaNO_3$) from which the sub samples were taken for various titrations in different electrolyte solutions, similarly as done previously for goethite suspensions.[46,58] Aliquots of 40, 50, and 75 mL of Fh stock suspensions were used to conduct the titrations with Fh_1, Fh_2, and Fh_3 respectively. Details about the specific conditions of each titration experiment are summarized in Table S2.1 in the Supplementary Information.

Standardized CO_2-free 0.100 M HNO_3 and NaOH solutions were used as acid and base titrants respectively. The titrations were performed at 20 ºC in sealed reaction vessels of 50 or 100 mL, equipped with a combined glass electrode, a magnetic stirrer, and two inlets to allow the addition of titrants and the injection of moist purified N_2(g). The glass electrode was calibrated with standard buffer solutions

(Merck KGaA, Germany) ranging from pH 4.00 to 9.00. First, the ionic strength of each system was adjusted to the target value by adding appropriate volumes of the stock solutions with background electrolyte. For Fh_2 and Fh_3, the pH of the suspension was adjusted to pH ~4.7 using the same acid titrant solution, whereas for Fh_1 the pH was kept constant at a value of 5.11± 0.01 as mentioned above.

Before starting the titrations, the above Fh suspensions were equilibrated under a continuous flow of N_2(g) for ~1 h. Change of less than 0.01 pH unit min^{-1} was defined as the equilibrium criterion, which was typically achieved within 2–3 min after each addition of the titrant. Titrations with base solution continued until a pH of ~9.5 was reached. Then, the addition of acid titrant started in the case of the forward-backward titrations. The addition of stock background electrolyte solutions to adjust the ionic strength was performed in the acid pH range. The duration of the forward-backward titrations at each ionic strength was ~1–1.5 h. This time is short if compared with the aging period (96 h) of the Fh_1 before starting the experiments. For the one-way titrations, we used individual aliquots of the Fh_1 suspension that served as common reference state.

The excess H^+ adsorption to Fh (mmol H^+ mol^{-1} Fe) was calculated from the raw potentiometric titration data (*i.e.* pH vs mL added acid/base) as explained elsewhere.[59] The classical Davies equation (with D = 0.2) was used to calculate the activity coefficients. Further scaling of the primary data was done as described in Section 2.3.1.

2.2.3. Phosphate adsorption

For all the Fh suspensions, previously purged with N_2(g), batch adsorption experiments with PO_4 were performed in parallel to the potentiometric titrations. Each individual system was prepared in 50 mL polypropylene tubes, using a total solution volume of 40 mL. First, a proper volume of background electrolyte solution was added (0.010 M $NaNO_3$), followed by the addition of 4.0 mL of stock solution of Fh re-suspended in 0.010 M $NaNO_3$. This led to total Fe concentrations of ~2.0 mM in the adsorption systems. Next, volumes of 1.0–1.7 mL of 0.010 M HNO_3 or NaOH were added to adjust the pH to the desired range. Finally, 2.00 mL of a 0.010 M NaH_2PO_4 stock solution was added to the systems, which yielded a total initial PO_4 concentration of ~0.50 mM. Each adsorption series was composed of 4 evaluation points within a pH range of ~4.5 to 8.0.

The PO_4 adsorption systems were continuously shaken (120 strokes min^{-1}) at 20 °C, and after 20 h of equilibration, the suspensions were centrifuged at 3500*g* for 15 min. For each system, an aliquot of the supernatant was passed through a 0.45 µm filter and acidified with HNO_3 to analyze the total concentration of P in solution by ICP-OES. The equilibrium pH in the remaining solution was measured with a glass electrode after re-suspending the Fh particles. The adsorption of PO_4 was estimated from the difference between the total added and final concentrations of PO_4 in the equilibrium solution. These surface probing data were consistently interpreted with charge distribution (CD) model, resulting in a specific surface area (A_{PO_4}). The PO_4 adsorption envelopes of each Fh suspension are presented in Figure S2.4, together with the modeled PO_4 adsorption and surface speciation of this oxyanion.

2.2.4. Data analysis and modeling

The CD model[60] was applied, in combination with a recent multisite ion complexation model (MUSIC) for Fh,[8] to interpret the results of both the potentiometric titrations and the PO_4 adsorption experiments. In the structural model of Fh, the site densities (N_s) of the singly (N_s = 5.8 nm^{-2}) and triply (N_s = 1.4 nm^{-2}) coordinated groups were derived from an independent analysis of the surface structure.[8] The electrical double layer (EDL) was described with the extended Stern Layer approach[61] and spherical

double layer theory was applied to the compact part of the EDL to calculate the size-dependent capacitance values ($C_{nano,1}$ and $C_{nano,2}$) of the Fh particles.[15] Modeling was performed with the software ECOSAT (version 4.9)[62] and the parameters optimization was done with the FIT program (version 2.581).[63]

2.3. Results and discussion

2.3.1. Primary surface charge

2.3.1.1. Data processing

Figure 2.1 shows the excess H^+ adsorption of Fh at different scales. The excess adsorption depends on the pH and ionic strength, as it is typically found for fresh Fh suspensions[10,24,42,44] and metal (hydr)oxides in general. For nanoparticles, and particularly for freshly-prepared Fh, the scaling of the primary H^+ adsorption data, as well as its interpretation in terms of surface charge, differs in a number of crucial points from the traditional approach that can be followed for most other metal (hydr)oxides. The reason is that the chemical composition and the related molar mass M_{nano} (g Fh mol^{-1} Fe) of Fh, as well as its surface area A (m^2 g^{-1}) and mass density ρ_{nano} (g cm^{-3}), are not known beforehand. All these properties are particle size-dependent, which requires a consistent scaling approach as described next.

The excess H^+ adsorption, expressed per mole Fe present in the system as Fh (H/Fe), is one of the most basic and indisputable forms of representing titration data. For Fh_1, this molar excess ratio is given at the left y-axis of Figure 2.1a. The H/Fe excess ratio is still relative to the starting point of the titration (red point in Figure 2.1a). It can be changed into an absolute scale, using the common intersection point (pH_{CIP}) of the titration curves measured at three different concentrations of background electrolyte (black arrow in Figure 2.1a). This scaling has been widely used in literature,[59,64,65] however, it is only valid if the background ions have a (nearly) equal affinity for the surface groups of the studied metal oxide. As we will discuss later, $NaNO_3$ seems the most suitable background solution for scaling H^+ adsorption data of Fh. The thus-scaled excess adsorption (ΔH/Fe) is given at the right y-axis of Figure 2.1a.

A next step in the translation of the basic H/Fe ratio to surface charge is expressing the excess H^+ adsorption per unit mass. This requires information about the chemical composition of Fh, which can be given as $FeO_{1.4}(OH)_{0.2}{\cdot}nH_2O$. The first part of the equation ($FeO_{1.4}(OH)_{0.2}$) refers to the composition of the mineral core of Fh,[52] whereas the second part (nH_2O) gives the amount of chemisorbed water that is involved in the formation of surface groups upon saturation of the coordination spheres of the Fe ions present at the surface.[23] In the past, due to the lack of detailed insights into the mineral and surface structure of Fh, the chemical composition of Fh has been often simplified to FeOOH (or $FeO_{1.5}{\cdot}½\ H_2O$) and this value was used for the translation of H^+ adsorption per mass unit. More recently, the chemical composition $FeO_{1.4}(OH)_{0.2}$ was applied.[45] However, the use of the latter formula ignores the formation of additional surface groups (nH_2O). It will lead to a higher value for the surface charge if expressed per unit mass, and this will increase the SSA when interpreted with modeling, or it will lead to relatively high capacitance values if the SSA is fixed to a standard value as found by Bompoti et al.[20]

Based on the chemical composition of Fh, one can calculate its molar mass. For $FeO_{1.4}(OH)_{0.2}$ as the bulk material, the molar mass is M_{core} = 81.65 g mol^{-1} Fe, while for $FeO_{1.5}{\cdot}½H_2O$ the molar mass is M = 89 g mol^{-1} Fe. The excess water content can be measured by removing the physisorbed water at 125

°C,[49,54] showing that the actual molar mass of Fh is particle size dependent.[57] For Fh, the value of nH$_2$O varies between ~0.25 – 1.1 as a function of the particle size (~2 – 6 nm).[23] In principle, the experimental chemical composition of Fh, *i.e.* its water content nH$_2$O, can be used to derive the SSA, as the amount of chemisorbed water and A_{TEM} are related as follows from the data of Michel et al.[49] (Figure S2.10). A crucial aspect in this method is the temperature used in the interpretation of the thermogravimetric analysis (TGA) to distinguish chemisorbed and physisorbed water.[54]

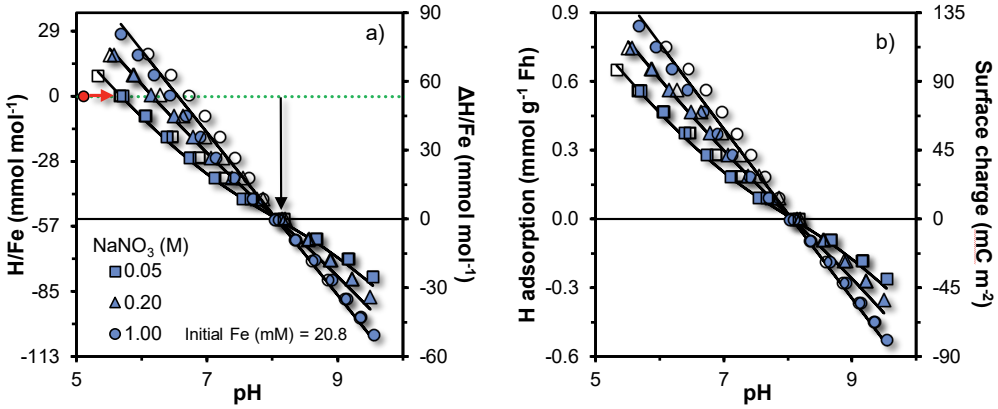

Figure 2.1. **Panel a**: Molar ratio (H/Fe) of the pH-dependent excess H$^+$ adsorption to Fh (symbols), expressed in a relative (left y-axis) and an absolute scale (right y-axis). Transformation of values from the left into right y-axis was done by defining pH$_{CIP}$ = pH$_{PZC}$. The red point represents the initial condition of the Fh$_1$ stock solution, which is used as preliminary reference value. Addition of electrolyte solution before the start of the titrations increases the pH (red arrow) and correspondingly the surface charge, although the latter change is little in this experiment. **Panel b**: Excess H$^+$ adsorption expressed per mass unit of Fh (left y-axis) and surface charge density (mC m^{-2}). Titrations are for the Fh$_1$ suspension, produced at pH 6.00 and aged for 96 hours (stored at 4 °C for 72 h). Forward (closed symbols) and backward (open symbols) titrations were performed using a CO$_2$-free 0.10 M solutions of NaOH and HNO$_3$ respectively. NaNO$_3$ solution was used as background electrolyte. The lines are CD-MUSIC model simulations, using the ion pair formation constants for Na$^+$ and NO$_3^-$ presented in Table 2.1. The initial total Fe concentration was 20.8 mM. A specific surface area of A_H = 642 ± 10 m^2 g^{-1} at a corresponding molar mass of M_{nano}= 95.6 g Fh mol^{-1} Fe was used to calculate the H$^+$ adsorption and charge density presented in panel b. This value was iteratively found by modeling, see text.

The chemical composition (nH$_2$O) and molar mass (M_{nano}) of Fh can also be found by calculation using a self-consistent set of mathematical expressions[10,23] with the SSA as input. This implies that the scaling of the excess proton ratio (ΔH/Fe) of Figure 2.1a to the proton adsorption per unit mass (mmol g^{-1} Fh) of Figure 2.1b requires the value of the yet unknown SSA or particle size. In theory, the value of the SSA of Fh can be derived by interpreting the experimental ion adsorption data with a parameterized surface complexation model (SCM). However, the model parametrization can only be done if the adsorption data (mol g^{-1}) are scaled to the SSA (m^2 g^{-1}). For traditional metal oxides, the BET surface area is used for scaling, but as we mentioned before, this is not appropriate for Fh. This obstructs for Fh an independent calibration of the parameters of the SCM because the determination of the affinity constants is inversely correlated with the SSA[66,67] Therefore, another route will be used. The parametrized behavior of well-crystalized goethite will be used as a reference.

In our modeling approach, the Stern capacitances values of Fh are not treated as fitting parameters but will be calculated independently accounting for the surface curvature of the material involved. The size-dependency of the capacitance will be explicitly considered using as reference a set of representative values for the capacitance values of an inner (C_1) and outer (C_2) Stern layer with zero

curvature. This approach also provides consistency in the treatment of Fh suspensions with different particle sizes, as the Stern layer capacitances can be adapted correspondingly. In the present study, we will use as reference a set of capacitance values (C_1 = 0.90 F m^{-2} and C_2 = 0.74 F m^{-2}) representative for well-crystalized goethite as derived by Hiemstra and Van Riemsdijk.[15] In Section 2.3.2.3 we will discuss the sensitivity of our approach if the influence of surface curvature on the capacitance values is not considered in the modeling.

In the calculations, the particle size (d) of Fh is consistently linked to its surface area (A_H) by using the corresponding value of the mass density ρ_{nano}. As mentioned above, the latter value is not a constant, because the coordinated water in excess (nH$_2$O) contributes more to the particle volume than to the particle mass.[15,23] From the above, it is obvious that both data scaling and interpretation requires a consistent set of parameter values comprising the molar mass (M_{nano}), mass density (ρ_{nano}), particle size (d), and Stern layer capacitances (C_{nano}). Having as the starting point a given A value, the consistent set of parameters can be derived with the following equations:

$$M_{\mathrm{nano}} = \frac{M_{\mathrm{core}}}{1 - A\, N_{\mathrm{H_2O}}\, M_{\mathrm{H_2O}}} \qquad \text{(Equation 2.1)}$$

$$\rho_{\mathrm{nano}} = \frac{M_{\mathrm{core}}}{V_{\mathrm{O}}\,[n_{\mathrm{O}} - (n_{\mathrm{O}} - M_{\mathrm{core}}/M_{\mathrm{H_2O}})\, A\, N_{\mathrm{H_2O}}\, M_{\mathrm{H_2O}}]} \qquad \text{(Equation 2.2)}$$

$$d = \frac{6}{\rho_{\mathrm{nano}}\, A} \qquad \text{(Equation 2.3)}$$

in which M_{core} is the molar mass of the mineral core (81.65 g mol^{-1} Fe), M_{H_2O} is the molar mass of water (18 g mol^{-1}), N_{H_2O} is the excess surface water density of Fh (12.6 10^{-6} mol m^{-2}),[68] V_O is the volume of the lattice expressed per mole oxygen ions (10.7 10^{-6} m^3 mol^{-1} O), n_O is the mean number of oxygen ions per metal ion in the core (n_O = 1.6 for $FeO_{1.4}(OH)_{0.2}$), and A (m^2 g^{-1}) is the yet unknown specific surface area. The mean particle diameter calculated with Equation 2.3 can be used to calculate the size-dependency of the capacitance values ($C_{nano,1}$ and $C_{nano,2}$) of Fh, according to:

$$C_{\mathrm{nano},1} = \frac{d + \Delta d_1}{d}\, C_1 \qquad \text{(Equation 2.4.1)}$$

$$C_{\mathrm{nano},2} = \frac{d + \Delta d_1 + \Delta d_2}{d + \Delta d_1}\, C_2 \qquad \text{(Equation 2.4.2)}$$

where Δd_1 (2 × 0.35 nm) and Δd_2 (2 × 0.35 nm) are twice the thickness of the inner and outer Stern layers respectively, and C_1 (0.90 F m^{-2}) and C_2 (0.74 F m^{-2}) are the capacitances of the reference surface with zero curvature.[61]

With the above approach, we derived by iterative CD-MUSIC modeling for the Fh_1 preparation a mean particle diameter of d = ~2.48 nm, a specific surface area (SSA) of A_H = 642 ± 10 m^2 g^{-1}, n = 0.77, and the corresponding molar mass is M_{nano} = 81.65 + (0.77×18) = 95.6 g mol^{-1}. In this modeling, we relied on the ion pair formation constants of the goethite material that was used as reference.[61] The scaling of Figure 2.1b is based on these values.

2.3.1.2. Interaction with electrolyte ions

The scaling of the H^+ adsorption of Fh materials measured in various types of electrolyte solution (*e.g.* NaCl, $NaClO_4$, or $NaNO_3$) is rather uncertain as it is difficult to find the absolute value of the zero–charge condition, even for data set collected for the same material. The reason is that common intersection points (cip) do not exist by definition if the affinity of electrolyte ions is rather asymmetrical. This hinders a reliable translation of the basic data on the relative scale (H/Fe) to the absolute scale (ΔH/Fe). For this reason, Rietra et al.[58] have suggested to perform connected potentiometric titrations in systems prepared from the same stock that is kept under well-defined conditions. The surface charge of the material in this stock suspension is used as common reference.

The above concept of a common stock used as a reference has been implemented by Rahnemaie et al.[46] to study the variation in ion pair formation constants for goethite. This creates a self-consistent set of H^+ adsorption data. For fresh Fh suspensions, however, obtaining a self-consistent set of H^+ titrations is more challenging from an experimental perspective. A major problem is that Fh is chemically less stable in comparison with well-crystalized Fe-(hydr)oxides, such as goethite or hematite.[69] The SSA of Fh will change continuously with time as a function of the aging conditions.[23,49] When using the same stock suspension as a reference for a large number of experiments, one should ideally correct for intervening changes in SSA due to the aging of the Fh batch. This is particularly relevant if the experiments are performed in time intervals and under aging conditions[21,23] that promote a rapid change in SSA.

In the present study, a set of acid-base titrations is reported for three different electrolytes at a single salt level and a fixed moment of aging. The collected data at the 0.20 M level are shown in Figure 2.2a for Fh_1 after an aging time of t = 120 h. The experiment was repeated for the 0.50 M level (Figure 2.2b) using the same Fh_1 suspension but with one more day of aging (t = 144 h). The same batch with Fh_1 has also been used to measure the proton adsorption by varying the electrolyte level of a single salt ($NaNO_3$). The latter data have already been given in Figure 2.1 and were collected at an aging time of t = 96 h. In Figures 2.1a and 2.2, the red symbol represents the common reference condition of the Fh_1 stock suspension in 0.01 M $NaNO_3$. The pH of this stock suspension remained unchanged within the uncertainty (5.11 ± 0.01) during the whole period of aging. Figure 2.2 shows that, upon the addition of the different types of electrolyte solutions, the pH of the Fh_1 suspension increased by ~0.7–1.4. The corresponding increase of the surface charge is almost negligible and not visible at the y-scale for the given experimental conditions.

Figure 2.2 shows that the effect of the different types of electrolyte anions on the H adsorption is most evident below the pH of point of zero charge (pH_{PZC}). At a given pH, the highest positive surface charge is developed in the presence of Cl^- and the lowest is for ClO_4^-. The variation is due to a different degree of interaction of the counter-anions with the surface of Fh. The stronger interaction of Cl^- ions, relatively to that of ClO_4^-, has been attributed to a larger charge-to-size ratio of Cl^- ions.[70] Ions of smaller size are closer to the surface and therefore, may have a stronger interaction with the surface groups.[71] Additionally, specific interactions between anions and mineral surfaces may also contribute to these differences.[16,46] Our data show that for Fh, the interaction of electrolyte anions increases in the order of $ClO_4^- < NO_3^- < Cl^-$. The same trend in anion affinity has been previously reported for other iron (hydr)oxides such as goethite[46,58,72,73] and lepidocrocite.[70]

As suggested by our data (Figure 2.2), the differences in electrolyte affinity results in a shift of the pH_{PZC} with the type of electrolyte solution. Only if the electrolyte cation and anion have the same affinity, the pH_{PZC} can be found indisputable from the pH_{CIP} of acid-base titrations at different salt levels.

In the present approach, we have used pH_{CIP} derived by acid-base titrations in $NaNO_3$ (Figure 2.1a), because both electrolyte ions have a very similar affinity constant.[58,61,73] In that case, the corresponding pH_{CIP} also represents the pristine point of zero charge, which is pH_{PPZC} = ~8.1 for Fh.

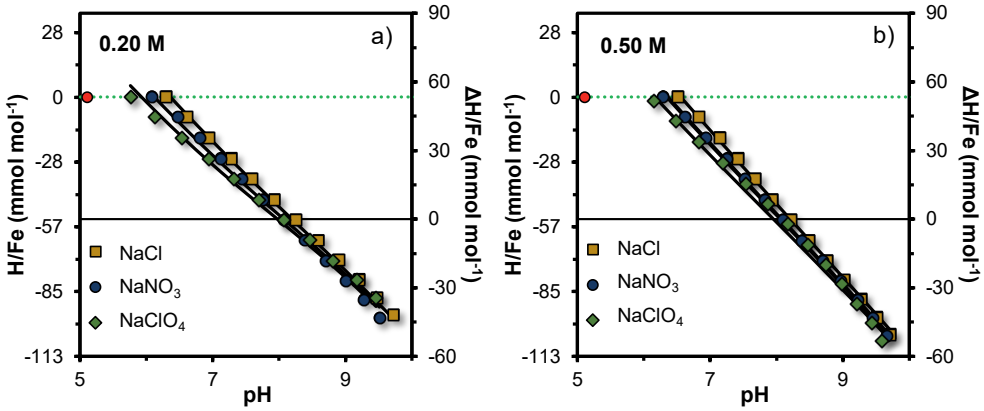

Figure 2.2. pH dependency of the excess H adsorption of Fh_1 presented on a relative (H/Fe) and absolute (ΔH/Fe) scale for systems with $NaNO_3$, NaCl, or $NaClO_4$ background electrolyte solutions at a concentration of either 0.20 M (a) or 0.50 M (b). The corresponding time of aging of the Fh suspension was t = 120 h (a) and t = 144 h (b). The red point represents the initial reference condition of the Fh_1 stock solution. The lines have been calculated with the CD-MUSIC model using the parameters of Table 2.1. The values of the SSA are A_H = 638 ± 12 m^2 g^{-1} (a) and A_H = 613 ± 16 m^2 g^{-1} (b) with corresponding M_{nano} values of 95.5 and 94.8 g mol^{-1} Fe respectively. These values were calculated consistently using the H^+ adsorption data measured in $NaNO_3$ (for explanation, see text).

2.3.1.3. Time dependency of surface reactivity

Recently, the evolution of the surface area of Fh has been studied as a function of time, pH, and temperature of aging. In this approach, the PO_4 ion was used to probe the changes in the specific surface area (A_{PO_4}) of Fh. The collected PO_4 adsorption data were also used to gain insights into the mechanisms and rate of growth of Fh (see Hiemstra et al.[23] for more information about the aging mechanisms of Fh). The interpretation of the PO_4 adsorption was done with the charge distribution and multisite ion complexation model for Fh using the parameter set of Hiemstra and Zhao.[8] This parameter set has been derived by scaling the PO_4 adsorption to a SSA (m^2 mol^{-1} Fe), suggested by Hiemstra and Van Riemsdijk[15] as representative for freshly-prepared Fh within the 1-pK framework. This best guess of the SSA based on literature data was derived using well-crystallized goethite as a reference with respect to the ion pair formation constants for Na^+ and NO_3^-, and the reference Stern layer capacitances.

Based on the PO_4 adsorption measured at each reaction time, the corresponding SSA has been calculated for the various materials studied here, applying the parameter set of Table 2.1. A detailed description of the approach used to assess A_{PO_4} is presented in Appendix D of the Supplementary Information. Figure 2.3 shows the time dependency of the SSA of Fh_1 measured with PO_4 as probe ion (green diamonds). The preparation and initial aging (t = 4 h) of Fh_1 was at pH = 6.0 and 20 °C, followed by acidification to pH 5.11 and storage of 72 hours at 4 °C, before returning back to 20 °C, as described in the Experimental Section. For comparison, we also give for a similar Fh preparation[23] the evolution of the SSA at pH 6.0 and constant 20 °C (blue spheres). The lines in Figure 2.3 have been calculated

with a model recently developed for the particle growth of Fh by Ostwald ripening,[23] in which the growth-rate is related to the particle-size dependent solubility of Fh, calculated with the Ostwald-Freundlich theory.[68] The initial particle size predicted with this dynamic model is in line with the mean particle size (2.0 ± 0.3 nm) found by TEM for fresh Fh precipitates.[49,74]

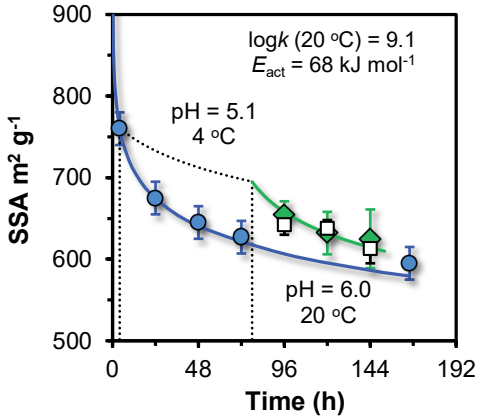

Figure 2.3. Change in the specific surface area ($m^2\ g^{-1}$) of Fh_1 measured using either H^+ (open squares) or PO_4 (green diamonds) as probe ions. The lines have been calculated with a dynamic model [23] and show the aging history of the Fh_1 suspension: i) synthesis and aging at pH 6.00 and 20 °C for 4 h, ii) aging at pH 5.11 and 4 °C for 72 h (dotted line), and iii) subsequent aging at pH 5.11 and 20 °C under a purified N_2 atmosphere (green line). As reference, we also included the experimental (blue symbols) and modeled (blue line) evolution of the SSA of a different Fh suspension, aged at constant pH 6.00 at 20 °C. The rate constant log*k* of the Fh particles growth is 9.1 at 20 °C and its pH dependency of log*k* is -0.11 ΔpH. The temperature dependency of the log*k* value is described using an activation energy of E_{act} = 68 kJ mol^{-1}.

The experimental time dependency of the SSA of Fh_1 can also be obtained by interpreting the acid-base titration data in $NaNO_3$ (Figures 2.1 and 2.2) with surface complexation modeling. For our analysis, we applied the parameter set of Table 2.1. The obtained A_H values for Fh_1 are shown in Figure 2.3 as open squares. Within the uncertainties, the SSAs obtained with H^+ titrations in $NaNO_3$ are equal to the values found by surface probing with PO_4. As mentioned before, the parametrization of the model for the PO_4 adsorption has been based so far on the best guess for the SSA of Fh proposed by Hiemstra and Van Riemsdijk,[15] without any explicit test for consistency with surface charge. The present results show that the primary surface charge of Fh in $NaNO_3$ solutions is consistent with the scaling of PO_4 adsorption per unit surface area and *vice versa*. Figure 2.3 also shows that the time-dependent variation of our data collected for Fh_1 can be well understood with the dynamic model for aging of Fh (lines) that we recently developed.[23] It must be noted that the accuracy in the predictions of the dynamic model is conditioned by the reproducibility of the preparation method of Fh, as we will discuss it in Section 2.3.3.

In the present study, we have calculated the reactive surface area A_H for a large number of Fh preparations using the H^+ adsorption data reported in literature. The set of A_H values given in Appendix F is an extension of previous work[10] that has been reinterpreted, where needed. The overview shows that the surface area of Fh in the wet state, prepared by a variety of methods and aged for short periods at different conditions, ranges from 530–720 $m^2\ g^{-1}$ having corresponding molar masses of 92.8–97.6 g mol Fe^{-1}, *i.e.* A = 49–70 10^3 m^2 mol^{-1} Fe.

Table 2.1. Surface reactions, charge distribution coefficients and log*K* values for the primary surface charge reactions and for the adsorption of phosphate to Fh. The proton and electrolyte affinity constants have been set equal for the singly ($\equiv FeOH^{-0.5}$) and triply ($\equiv Fe_3O^{-0.5}$) coordinated surface groups. The surface sites densities, respectively N_s=5.8 and N_s=1.4 nm^{-2}, are taken from Hiemstra and Zhao.[8] The size-dependency of the Stern capacitance values of the inner and outer Stern is accounted for by applying spherical double layer theory (Equation 2.4), using the reference values of C_1 = 0.90 F m^{-2} and C_2 = 0.74 F m^{-2} for a surface with zero curvature (see text).

Reaction		Δz_0	Δz_1	Δz_2	log*K*	Eq.
Primary charge						
$\equiv FeOH^{-0.5} + H^+ \leftrightarrow \equiv FeOH_2^{+0.5}$	(a/b)*	1	0	0	8.10*	(2.5.1)
$\equiv Fe_3O^{-0.5} + H^+ \leftrightarrow \equiv Fe_3OH^{+0.5}$		1	0	0	8.10*	(2.5.2)
$\equiv FeOH^{-0.5} + Na^+ \leftrightarrow \equiv FeOH^{-0.5}\text{--}Na^+$	(a/b)*	0	1	0	-0.60 ± 0.02**	(2.6.1)
$\equiv Fe_3O^{-0.5} + Na^+ \leftrightarrow \equiv Fe_3O^{-0.5}\text{--}Na^+$		0	1	0	-0.60 ± 0.02**	(2.6.2)
$\equiv FeOH^{-0.5} + Na^+ \leftrightarrow \equiv FeOH^{-0.5}\text{--}K^+$	(a/b)*	0	1	0	-1.61 ± 0.13**/#	(2.7.1)
$\equiv Fe_3O^{-0.5} + Na^+ \leftrightarrow \equiv Fe_3O^{-0.5}\text{--}K^+$		0	1	0	-1.61 ± 0.13**/#	(2.7.2)
$\equiv FeOH^{-0.5} + Na^+ \leftrightarrow \equiv FeOH^{-0.5}\text{--}Li^+$	(a/b)*	0	1	0	0.10 ± 0.02**/#	(2.8.1)
$\equiv Fe_3O^{-0.5} + Na^+ \leftrightarrow \equiv Fe_3O^{-0.5}\text{--}Li^+$		0	1	0	0.10 ± 0.02**/#	(2.8.2)
$\equiv FeOH^{-0.5} + H^+ + NO_3^- \leftrightarrow \equiv FeOH_2^{+0.5}\text{--}NO_3^-$	(a/b)*	1	-1	0	8.10 - 0.68 ± 0.02**	(2.9.1)
$\equiv Fe_3O^{-0.5} + H^+ + NO_3^- \leftrightarrow \equiv Fe_3OH^{+0.5}\text{--}NO_3^-$		1	-1	0	8.10 - 0.68 ± 0.02**	(2.9.2)
$\equiv FeOH^{-0.5} + H^+ + Cl^- \leftrightarrow \equiv FeOH_2^{+0.5}\text{--}Cl^-$	(a/b)*	1	-1	0	8.10 - 0.36 ± 0.04***	(2.10.1)
$\equiv Fe_3O^{-0.5} + H^+ + Cl^- \leftrightarrow \equiv Fe_3OH^{+0.5}\text{--}Cl^-$		1	-1	0	8.10 - 0.36 ± 0.04***	(2.10.2)
$\equiv FeOH^{-0.5} + H^+ + ClO_4^- \leftrightarrow \equiv FeOH_2^{+0.5}\text{--}ClO_4^-$	(a/b)*	1	-1	0	8.10 - 0.97 ± 0.04***	(2.11.1)
$\equiv Fe_3O^{-0.5} + H^+ + ClO_4^- \leftrightarrow \equiv Fe_3OH^{+0.5}\text{--}ClO_4^-$		1	-1	0	8.10 - 0.97 ± 0.04***	(2.11.2)
Phosphate adsorption						
$\equiv FeOH^{-0.5} + PO_4^{3-} + 2H^+ \leftrightarrow \equiv FeO^{-0.22}PO_2OH^{-1.28} + H_2O$	(a/b)*	0.28	-1.28	0	26.36 ± 0.20*	(2.12)
$\equiv FeOH^{-0.5} + PO_4^{3-} + 3H^+ \leftrightarrow \equiv FeO^{-0.17}PO(OH)_2^{-0.33} + H_2O$	(a/b)*	0.33	-0.33	0	29.84 ± 0.23*	(2.13)
$2\equiv FeOH^{-0.5} + PO_4^{3-} + 2H^+ \leftrightarrow \equiv(FeO)_2^{-0.54}PO_2^{-1.46} + 2H_2O$	(b)*	0.46	-1.46	0	28.31 ± 0.04*	(2.14)
$2\equiv FeOH^{-0.5} + PO_4^{3-} + 3H^+ \leftrightarrow \equiv(FeO)_2^{-0.35}POOH^{-0.65} + 2H_2O$	(b)*	0.65	-0.65	0	33.52 ± 0.13*	(2.15)

* (a/b) refers to monodentate reactions that occur with singly coordinate groups ($\equiv FeOH^{-0.5}$) of type a (N_S = 3.0 nm^{-2}) and b (N_S = 2.8 nm^{-2}), whereas (b) is for bidentate reactions that occur only with type b $\equiv FeOH^{-0.5}$ groups, according the ion complexation model for Fh of Hiemstra and Zhao.[8]

* From Hiemstra and Zhao.[8]

** From Hiemstra and Van Riemsdijk.[61]

*** The log*K* values (± SD) of the electrolytes Cl^- and ClO_4^- were derived from the self-consistent set of titrations performed with Fh_1. (n = 171, R^2 = 0.992).

The log*K* values of K^+ and Li^+ for Fh systems are extrapolations using the values for goethite as reference (See Figure 2.4).

2.3.2. Ion pair formation constants

2.3.2.1. Model parametrization

One of the objectives of our study is to derive a consistent set of thermodynamic affinity constants (logK_{ip}) for the interaction of electrolyte ions with Fh. In the present approach, the quantification of the logK_{ip} values has been done on a relative scale. For nano-particulate Fh, it is not feasible to derive the logK_{ip} values entirely independently by conventional fitting procedures because the SSA cannot be used

as independent input for scaling ion adsorption, in contrast to traditional metal (hydr)oxides. Therefore, we presently rely on the basic assumption that the logK_{ip} values for Na^+ and NO_3^-, derived for well-crystalized goethite,[61] are also applicable to Fh if consistently used with the size-dependent values of the molar mass (M_{nano}), the mass density (ρ_{nano}), and the Stern layer capacitance values (C_{nano}), as discussed above in Section 2.3.1.1.

The ion pair formation constants of Na^+ and NO_3^- for goethite are nearly symmetrical (Table 2.1), implying that the pH_{PPZC} can be well approximated from the values of pH_{CIP} (*i.e.* pH_{PPZC} = ~8.1) for the series of potentiometric titrations performed at different concentrations of $NaNO_3$ (Figure 2.1). Consequently, we can use in our 1-p*K* model for the titrations in $NaNO_3$ log$K_H \approx pH_{PPZC} \approx pH_{CIP}$. With this approach, the ion pair formation constants for the other anions of this study (Cl^- and ClO_4^-) can be derived (Table 2.1), interpreting the internally consistent H^+ adsorption data obtained with the Fh_1 suspensions (Figure 2.2), after scaling all data to the SSA derived with the titrations in $NaNO_3$.

In the modeling of the systems with Cl^- and ClO_4^-, we have accounted for the presence of a small quantity of $NaNO_3$. This amount originates from the preparation of the Fh_1 stock in 0.01 M $NaNO_3$. However, in the most extreme case, the concentration of NO_3^- ions did not exceed ~5% of the total anion concentration in the background solutions of both other anion systems. Our data show that ion pair formation constants strongly vary (Table 2.1). This is also illustrated in Figure 2.4, where we compare the logK_{ip} values for Fh and goethite. For both materials, the affinity constant of Cl^- is clearly higher than that of NO_3^- while the value for ClO_4^- is much lower. Goethite and Fh follow the same trend as shown in Figure 2.4 with colored symbols. For both materials, the values are set by definition equal for Na^+ and NO_3^-, but for the other anions (Cl^- and ClO_4^-) the values are closely related for both materials. Extrapolating the results to electrolyte ions not yet studied for Fh, the logK_{ip} values of Li^+ and K^+ can be specified using the values derived for goethite (open symbols). These logK_{ip} values will be applied in the next section.

2.3.2.2. Ion pair formation and PZC

As mentioned, the value of pristine point of zero charge (pH_{PPZC}) in our study is ~8.1 for Fh. In literature, significantly higher pH_{PZC} and pH_{CIP} values (~8.7) have been reported for two freeze-dried Fh materials.[43,75] Structural changes in the surface of Fh provoked by the drying process and/or inefficient CO_2 removal from the fresh-prepared materials have been suggested as reasons for the reported higher pH_{PZC} values of the freeze-dried Fh materials.[20,43] Yet, there is no conclusive evidence supporting this hypothesis. A higher pH_{PZC} value (~8.5) has also been found for a non-dried Fh suspension.[76,77] In the latter case, NaCl was used as background electrolyte. We consider asymmetry in ion pair formation as a major factor explaining the reported differences between the observed pH_{PZC} and the pH_{PPZC} of Fh.

Application of the logK_{ip} values of Figure 2.4 (Table 2.1) in our modeling of data collected from literature for Fh in KCl and KNO_3 shows that a good description of the charging behavior of Fh in these media can be achieved using logK_H = 8.1 rather than 8.7. For example, the H^+ adsorption data of freeze-dried Fh in KNO_3, as reported by Antelo et al.,[43] can be well-described with this approach using the SSA (A_H = 300 m^2 g^{-1}) as the only adjustable parameter. With the same approach, other H^+ titrations of Fh with a high reported pH_{PZC} measured in KCl[78] and NaCl[76] solutions can also be well interpreted (Figure S2.2 in the Supplementary Information). Table 2.2 shows the predicted (CD-MUSIC model) and experimental pH_{PZC} values for various Fh materials (both freeze-dried and wet materials) in different electrolyte solutions as reported in the literature. In general, the experimental and modeled pH_{PZC} values agree within the uncertainties.

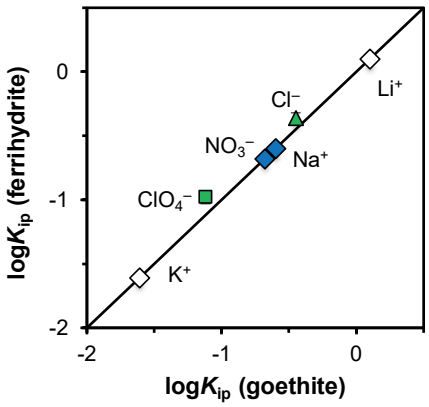

Figure 2.4. Comparison of the ion pair formation constants of Fh and goethite (colored symbols), using in the modeling common values for Na^+ and NO_3^- (blue diamonds). For comparison, the logK_{ip} values of K^+ and Li^+ for goethite are given (open diamonds) showing that a wide range of values can be found. For goethite, the logK_{ip} values are taken from the internally-consistent analysis presented by Hiemstra and Van Riemsdijk;[61] except for the value for ClO_4^-, which was fitted by modeling the consistent titration datasets presented by Rietra et al.[58]

Table 2.2. Comparison between the pH_{PZC} values reported in literature for various Fh materials (including freeze-dried and wet materials) and the pH_{PZC} values predicted with the CD model, using the logK_{ip} values given in Table 2.1 and Figure 2.4. The values of A_H were derived by modeling the reported surface charge.

Reference	Type	Background	pH_{PZC}		Fitted A_H ($m^2\ g^{-1}$)
			Reported	CD model	
Wang et al.[75,78]	Freeze-dried	KCl	8.7	8.7	455
Antelo et al.[43]	Freeze-dried	KNO_3	8.7	8.6	300
Jain et al.[76]	Wet	NaCl	8.5	8.4	670
Fukushi et al.[45]	Wet	NaCl	8.2	8.4	650
Other studies*	Wet	$NaNO_3$	8.0 ± 0.1	8.1	530–720

* For these wet Fh materials in $NaNO_3$ electrolyte solution, the pH_{PZC} value is an average (± SD) of the experimental values reported by a large number of authors and the A_H value shows the range of values found for these materials. Detailed information for each analyzed Fh suspension is presented in Table S2.2 of the Supporting Information.

2.3.2.3. Sensitivity analysis

In Figure 2.3, consistency was shown between the SSA values derived by probing the surface of Fh with protons (A_H) and phosphate (A_{PO_4}). Possibly, the consistency can be increased (Appendix E) by simultaneously optimizing the ion pair formations constants for all four ions used in this study (Na^+, NO_3^-, Cl^-, ClO_4^-) with the assumption of equality of A_H and A_{PO_4}. This leads to a slightly better agreement with the logK_{ip} values obtained for goethite. Modeling shows that the description of PO_4 adsorption to Fh is not sensitive to the exact value of the ion pair constants in the range of PO_4 concentrations used to derive A_{PO_4}. This is illustrated in Figure 2.5 for the variation of logK_{NO3} by ±

0.50 units. The relatively low sensitivity found for the usual concentration range of PO_4, as implemented in the probe-ion method, is due to the large difference in affinity of the PO_4 and NO_3^- ions.

The simultaneous optimization of the logK_{ip} for all four ions shows that the ion pair combination Na^+ and NO_3^- has the most symmetrical interaction with the surface groups of Fh (Figure S2.5a), supporting our initial assumption of logK_{Na} ≈ logK_{NO3}. Taking $A_H = A_{PO_4}$, the optimized values of logK_{Na} and logK_{NO3} for Fh are –0.68 ± 0.03 and –0.75 ± 0.03 respectively. These values are hardly different from the values derived for our reference goethite,[61] meaning that small variations (± 0.08) in the values of logK_{ip} will have only a small effect on the fitted A_H (~2%). Considering the uncertainty of the experimental and model approaches, using logK_{Na} and logK_{NO3} for goethite seems to be a valid assumption for describing the surface charge of Fh.

In the above analysis, the size dependency of the molar mass M_{nano}, mass density $\rho_{nano,}$ and the capacitance values ($C_{nano,1}$ and $C_{nano,2}$) of Fh is assumed. If changes due to surface curvature are ignored and the Stern Layer capacitances of the reference goethite are used, calculations for Fh_1 at 96 h aging show that the SSA measured with protons (A_H) would increase by 17% (Figure 2.6, A-B). Additionally, if the chemical composition of goethite (FeOOH = 89 g mol^{-1}) is used rather than the size-dependent composition of Fh, the SSA further increases by ~10% (Figure 2.6, B-C). Using the size density N_s of either goethite or Fh has only a minor impact (Figure 2.6, C-D) , because in the description of the surface charge of Fh the sum of sites densities of the singly and triply coordinated groups is similar for both Fe-(hydr)oxides. Consequently, the effect in the value of SSA is small if protons are used as probe ion.

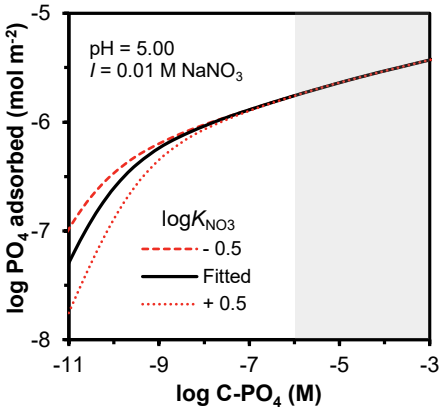

Figure 2.5. Adsorption isotherm of PO_4 to Fh at pH 5 and ionic strength of 0.01 M $NaNO_3$ (full line), modeled with the CD-MUSIC model using the parameters of Table 2.1. The dashed and dotted (red) lines illustrate the change of the predicted adsorption isotherm if the log$K$ value of the interaction between NO_3^- and Fh is changed by ± 0.5 units. The shaded region in the graph corresponds to the range of equilibrium PO_4 concentrations used for deriving the log$K$ values of PO_4 adsorption reactions and for assessing A_{PO4}, showing negligible influence of logK_{NO3}. PO_4 concentrations outside the shaded region (*i.e.* ~1 µM) are lower than the detection limit for P using ICP-OES.

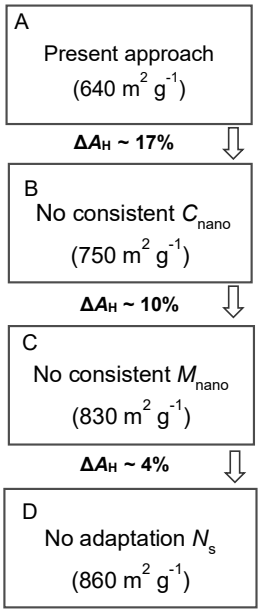

Figure 2.6. Changes in the fitted value A_H of Fh_1 derived with different modeling assumptions. The values of ΔA_H represent the percentage of change of the surface area in the direction showed by the arrows. A) SSA is fitted using the full approach proposed in Section 2.3.1.1. B) SSA is fitted without considering influence of surface curvature, *i.e.* without using size-dependent values for $C_{nano,1}$ and $C_{nano,2}$. The applied capacitance values are for well-crystallized goethite measured by Hiemstra and Van Riemsdijk.[61] C) SSA is fitted without additionally considering the size-dependent chemical composition of Fh. For Fh, the chemical composition and molar mass of goethite is assumed (see text). D) SSA is fitted without additionally considering difference in sites density (N_s) of Fh and goethite. All SSA values have been rounded to the nearest ten.

2.3.3. Applications and implications

The SSAs derived for Fh_1 at various times of aging show good agreement using either H^+ or PO_4 as probe ions (Figure 2.3). To enlarge our H^+ titration database, two additional Fh samples were synthesized, but at slightly different conditions. Fe(III) nitrate solution was titrated with NaOH to pH 6.0 (Fh_2) or pH 8.2 (Fh_3) and both preparations were aged for 24 h. The surface area was measured with the PO_4 probing methodology and with H^+ titrations in 0.05 and 1.0 M $NaNO_3$ (Figure S2.1). As shown in Table 2.3, the difference between A_H and A_{PO_4} is less than 1%. Comparing all data collected (including those for Fh_1) leads to a precision of ~2 %. The result is encouraging if compared to the precision of the measurement of the SSA with gas adsorption. For instance, replicate (n = 3) measurements of A_{BET} provide a precision in the order of ~5 % for Fh.[79]

Table 2.3. Specific surface area of Fh_2 and Fh_3 assessed by using H^+ (A_H) and PO_4 (A_{PO4}) as probe ions, as found by applying the CD-MUSIC model (Table 2.1) or by using the set of transfer functions. Both Fh suspensions were aged for 24 hours at a constant temperature of 20 °C before starting the H^+ and PO_4 adsorption experiments. The pH values at synthesis and subsequent aging of Fh_2 and Fh_3 were respectively 6.0 and 8.2.

		SSA (m^2 g^{-1})			
		CD-MUSIC model [a]		Transfer functions [b]	
Sample	pH aging	A_H	A_{PO4}	A_H	A_{PO4}
Fh_2	6.0	636 ± 8	627 ± 12	639	631
Fh_3	8.2	620 ± 10	633 ± 10	625	632

[a] A_H and A_{PO4} values derived by fitting the experimental adsorption data of H and PO_4 respectively, using the CD-MUSIC model parameters of Table 2.1.
[b] A_H and A_{PO4} values were derived, respectively, from the H^+ adsorption data in 1.0 M $NaNO_3$ and from the PO_4 adsorption data, using the set of practical transfer equations presented in the Appendixes G and H.

To enable a fast and convenient determination of the SSA, we have derived a helpful set of mathematical functions that translate the collected H^+ and PO_4 adsorption data straightforwardly into a value of SSA. These practical transfer functions have been parameterized with the CD-MUSIC model, using the parameter set of Table 2.1. The procedure followed to derive these transfer functions is explained in the Appendixes G and H of the Supplementary Information. For comparison with the results obtained with the CD-MUSIC model, the values of A derived with these functions are also presented in Table 2.3.

The SSA of our Fh_3, prepared at pH 8.2 and aged for 24 h (A_{PO_4} = 633 ± 10 m^2 g^{-1}), is in line with the value of the SSA predicted by our dynamic model (A_{DM} = 645 ± 7 m^2 g^{-1}). For Fh_1 (prepared at pH 6.0), we also found a good agreement between A_{PO4} and the SSA predicted by the model at different aging times (Figure 2.3). However, for Fh_2 prepared at pH 6.0 and aged for 24 h, the predicted value (A_{DM} = 672 ± 7 m^2 g^{-1}) is significantly higher than the one experimentally measured (A_{PO_4} = 627 ± 10 m^2 g^{-1}). The difference is related to an unusually low recovery of Fe (93%) in the synthesis of this hetero disperse material. At pH 6, Fh particles are positively charged, which hinders the aggregation of the primary particles into larger conglomerates in comparison to suspensions with a pH value close to the pH_{PZC}. Moreover, the separation of the liquid and solid phases by centrifugation was performed for Fh_2 almost immediately after the particle precipitation, whereas for Fh_1 this procedure was done ~2 h after precipitation. In the former case, the finest particles remained possibly in suspension due to incomplete aggregation, and therefore, were removed with the supernatant, making the SSA of the remaining Fh suspension lower. From the difference between the theoretical (model prediction) and experimental value of the SSA, one can calculate that the removed part of Fh_2 has a SSA of ~1250 ± 150 m^2 g^{-1} using $f/(1-f)$ (A_{DM}-A_{PO4}), in which f is the fraction of recovery (f = 0.93). The finest removed particles have an equivalent mean diameter of d ~ 1.5 nm and contains approximately n_{Fe} ~ 30 ± 15 Fe. Our result shows that slight differences in protocols for Fh synthesis may change the surface area and this advocates the use of ion probing as a tool to characterize individual batches of Fh with respect to SSA.

Overall, probing the Fh surface using either H^+ or PO_4 is a practical and consistent alternative to overcome the well-known limitations of the traditional BET method for assessing the SSA of Fe (hydr)oxide nanoparticles. For non-dried Fh suspensions, our modeling suggests that the reported A_{BET} underestimates the surface area by around ~50% in comparison to the fitted A_H value,[24,79] as already noticed in the early work of van der Giessen[74] when comparing A_{BET} and A_{TEM} measurements. The same can be concluded from the data of Michel et al.[49] showing a substantially lower A_{BET} than A_{TEM} for Fh with mean particle diameter of d < 5 nm (Figure S2.10). For re-suspended freeze-dried Fh, we found a surface area of A_H = 300 ± 9 m^2 g^{-1} when analyzing the H^+ adsorption data of Antelo et al.[43] while their reported A_{BET} is 229 m^2 g^{-1}. This difference suggests that the reduction of the SSA due to freeze-drying is partially counteracted by rewetting. If so, use of freeze-dried as a Fh proxy becomes questionable when A_{BET} is used for scaling.

As in general the SSA of Fh varies considerably (Table S2.2) between preparations,[10,20] future ion adsorption studies may benefit from calibrating this important property of Fh with ion surface probing. This may lead to more consistency between studies, which will facilitate the development of a self-consistent thermodynamic database for describing ion adsorption within a common theoretical framework. For this purpose, the use of PO_4 is most suitable, because this ion has a high affinity for Fh and its adsorption is more sensitive to variations in the surface area. Moreover, its measurement is rapid and accurate. Our proposed methodology has the advantage that it incorporates consistency amongst important properties such as molar mass, mass density, mean size and Stern layer capacitances, which

otherwise would be treated as fitting parameters or fixed to standard but unknown first order estimates,[80] even though they are variable.

In retro-perspective, the SSA of Fh derived in this study is actually found by calibrating it on the BET surface area of goethite accounting for differences in the site densities of both materials while assuming equal electrolyte ion affinity of Na^+ and NO_3^-. However, a correction is needed to account for the nano-character of Fh, implying a correction for the size dependency of the molar mass, the mass density, and the surface curvature. The latter follows from theoretical double layer considerations while both others are firmly based on experimental data that have been collected by Michel et al.[49] using TGA, TEM, and HEXS. Although the accuracy of the method remains disputable, its precision is very good, in the order of 2 % or better.

2.4. Conclusions

The following conclusions can be drawn from the present study:

- Scaling of the excess H^+ adsorption (ΔH/Fe) of Fh to a surface charge per unit mass (mC g^{-1}) requires the molar mass M_{nano} (g mol^{-1} Fe). However, this value is particle size-dependent due to the variable chemical composition of Fh ($FeO_{1.4}(OH)_{0.2}\cdot nH_2O$) as the result of the formation of OH/OH_2 surface groups, completing the coordination sphere of Fe at the surface.[57] Furthermore, scaling of the surface charge per unit mass (mC g^{-1}) to a surface charge per unit surface area (mC m^{-2}) requires a consistent value of the mass density of Fh (g cm^{-3}), which is also particle size-dependent. Therefore, the ΔH/Fe cannot be scaled and interpreted in a traditional manner, as is done for most other metal (hydr) oxides.

- With proton titration data in $NaNO_3$, the specific surface area of Fh (A_H) can be assessed consistently using the A_{BET} of well-crystallized goethite as reference, accounting for the difference in surface composition of both materials, while assuming equal ion pair formation constants ($\log K_{Na}$ and $\log K_{NO3}$). In our methodology, the size dependency of the molar mass, the mass density, and the surface curvature of Fh is taken into account, entirely based on respectively experimental data and theoretical double layer considerations.

- The specific surface area of Fh can also be assessed with specifically adsorbed oxyanions with a relatively high affinity, suppressing more effectively possible interferences by CO_2. In the present work, PO_4 has been chosen. Our work shows that within an uncertainty of ~2 % the specific surface area of Fh can be equally well assessed using either H^+ or PO_4 as probe ion, applying a common self-consistent modeling framework. However, PO_4 is most suitable for probing as it is quite sensitive to the values of SSA and can be conveniently, rapidly and accurately measured.

- The time-dependent change of the SSA of Fh is in agreement with a dynamic aging model that consistently resembles the mean particle size according to TEM. Since generally protocols for Fh synthesis lead to variation in the mean particle size, the use of ion surface probing is advocated to pinpoint the value of the SSA experimentally for individual batches of Fh, creating consistency in adsorption data collection.

- Assessment of the affinity of electrolyte ions at a relative scale shows that the affinity decreases in the order of $Cl^- > NO_3^- > ClO_4^-$ and the log*K* values are close to those obtained for goethite.[46,58] Based on the good agreement between the ion pair formation of goethite and Fh, the log*K* values of other electrolyte ions (Li^+ and K^+) can be provisionally assessed and have been tabulated in the present study.

- The pH_{PPZC} of Fh is close to 8.1. The higher pH_{PZC} values reported in literature for Fh can be largely understood from the asymmetric electrolyte ion affinity due to the use of KCl, KNO_3, and NaCl as background solutions, rather than $NaNO_3$.

- The presented concept of a consistent assessment of the SSA of Fh is a vital tool for the development of a coherent thermodynamic database with intrinsic affinity constants (log*K*) than can be applied in SCM.

Acknowledgments

We gratefully acknowledge the grant provided by the University of Costa Rica to the first author. The comments received from all the anonymous reviewers for improving this article are highly appreciated.

Supplementary Information

A. Experimental conditions of the potentiometric titrations

Table S2.1. Experimental conditions of the potentiometric titrations performed with three ferrihydrite suspensions.

Series	Synthesis pH [a]	Aging h [b]	Purging with N_2(g) [c]	[Fe] stock mM [d]	Vol stock Fh ml [e]	Vol_0 ml [f]	Background solution(s)	Salt level(s) M
Fh_1	6.0	96	20 h / pH 5.1	20.8	40.00	40.54	$NaNO_3$	0.05, 0.20, 1.0
		120	44 h/ pH 5.1	20.8	40.00	42.85	$NaNO_3$, NaCl, $NaClO_4$	0.20
		144	68 h/ pH 5.1	20.8	40.00	48.00	$NaNO_3$, NaCl, $NaClO_4$	0.50
Fh_2	6.0	24	20 h / pH 6.0 1h / pH ~4.7	18.6	50.00	51.35	$NaNO_3$	0.05, 1.0
Fh_3	8.2	24	20 h / pH 8.2 1h / pH ~4.7	20.9	75.00	76.85	$NaNO_3$	0.05, 1.0

[a] Final pH value reached after addition of base (0.02 M NaOH) to a $Fe(NO)_3$*$9H_20$ solution, which had been dissolved in 0.01 M HNO_3. The original suspensions produced by titration were concentrated by centrifugation, decanting, and resuspension in 0.01 M $NaNO_3$. If needed, the pH of these stock suspensions was readjusted to the targeted values.
[b] During aging, the stock suspensions had a background solution of 0.01 M $NaNO_3$. The contribution of this background solution to the final composition of the titration media has been considered in the model calculations.
[c] Duration of the purging step with moist purified N_2(g) and pH of the stock solution of Fh during this period.
[d] Concentration of Fe in the stock suspensions of ferrihydrite, measured in a matrix of 0.8 M H_2SO_4.
[e] Volume of the stock ferrihydrite suspensions pipetted into the reaction vessel for each titration experiment.
[f] Starting volume of the titration suspension upon adjustment of pH and/or the ionic strength and before titrants addition. For Fh_1, the ionic strength was adjusted using a 3.0 M stock solution of the corresponding electrolyte solution, whereas for Fh_2 and Fh_3 the ionic strength was adjusted with a 2.5 M $NaNO_3$ solution.

B. Potentiometric titration data for Fh_2 and Fh_3

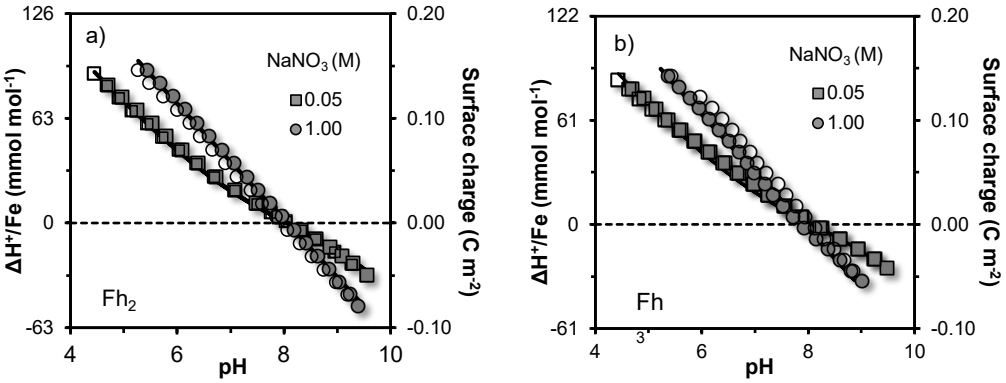

Figure S2.1. pH dependency of the excess H adsorption (left y-axis) and surface charge density (right y-axis) of Fh_2 (panel a) and Fh_3 (panel b). The ionic strength of the systems was fixed at 0.05 and 1.00 M, using $NaNO_3$ as electrolyte solution. Forward (closed symbols) and backward (open symbols) titrations were performed using (CO_2-free) 0.10 M solutions of NaOH and HNO_3 respectively. The lines are CD model simulations, using the ion pair formation constants for Na^+ and NO_3^- presented in Table 2.1 of the main text. For Fh_2, A_H = 636 ± 8 m^2 g^{-1} with a corresponding M_{nano}= 95.4 g Fh mol^{-1} Fe. For Fh_3, A_H = 620 ± 10 m^2 g^{-1} with a corresponding M_{nano}= 95.0 g Fh mol^{-1} Fe. The size-dependent capacitance values of the inner and outer Stern layers were consistently calculated using as reference the values C_1=0.90 F m^{-2} and C_2=0.74 F m^{-2} for a flat surface. The initial Fe concentration was 18.6 and 20.9 mM for Fh_2 and Fh_3 respectively.

C. Effect of electrolyte asymmetrical affinities on the pH_{PZC}

In literature, the reported range of pH_{PZC} values of Fh is ~7.9–8.7. Factors such as synthesis procedure, aging conditions, and an (in)efficient removal of CO_2 may contribute to this variation. Surprisingly, the variation in pH_{PZC} that results from the type of background electrolytes has not been analyzed yet following a systematic approach. The pH of the common intersection point (pH_{CIP}) of acid-base titrations performed at different salt levels is often used to find the reference zero-charge condition, assuming $pH_{PZC} \approx pH_{CIP}$. Only if the background anions (A^-) and cations (C^+) have the same affinity ($\log K_{A^-} = \log K_{C^+}$), the pH_{CIP} is equal to the pH_{PZC}, as well as to the pristine point of zero charge (pH_{PPZC}) of the material. If the background ions interact largely asymmetrically, then the pH_{CIP} deviates from the actual value of pH_{PPZC}. In general, if $\log K_{A^-} > \log K_{C^+}$ one gets $pH_{PZC} > pH_{PPZC}$. The opposite effect occurs if $\log K_{A^-} < \log K_{C^+}$. Asymmetrical interactions of electrolytes also shift the pH of the isoelectric point (pH_{IEP}) into an opposite direction than the shift in pH_{PZC}.[59] In the main text (Figure 2.4), we showed that Na^+–NO_3^- is likely the most symmetrical pair of electrolyte ions, based on the trends in affinity for Fh and goethite.[46,58,61] Therefore, the use of $NaNO_3$ as background solution is more recommended for Fh to get $pH_{CIP} \approx pH_{PZC} \approx pH_{PPZC}$.

The relatively high pH_{PZC} values (~ 8.5–8.7) of freeze-dried Fh materials have been attributed to changes in the surface structure that result from the drying procedure.[20,43] So far, there is no direct evidence supporting this assumption. Values of pH_{PZC} significantly larger than 8.1 have been also reported for a freshly prepared Fh suspension.[76] Below, we will show that the reported high values for the pH_{PZC} of various Fh materials (including freeze-dried and wet materials) can be largely explained by the asymmetrical affinity of the electrolyte ions used in the underlying experiments.

Figure S2.2 shows the pH–dependent surface charge density (C m^{-2}) of a selected number of freeze-dried and fresh Fh material. The potentiometric titrations were performed using KNO_3,[43] KCl,[78] NaCl,[76] or $NaNO_3$ [79] as background solutions. The reported pH_{PZC} values ranged between 8.0–8.7 (Table 2.2 in the main text). The surface charge of all these Fh preparations can be consistently described using a unique pH_{PPZC} value of 8.1. The corresponding $\log K_H = 8.1$ was also used for describing the surface charge of our Fh suspensions. The shift in the pH_{PZC} can be explained by the CD model, only considering the ion pair constants of the electrolyte ions involved (Table 2.1 and Figure 2.4 in the main text). In our approach, the capacitance values of the inner and outer Stern layers ($C_{nano,1}$ and $C_{nano,2}$) are not treated as fitting parameters. These values are particle-size dependent and have been calculated according to Hiemstra and Van Riemsdijk.[15] Only the specific surface area (SSA) was an adjustable parameter (see caption of Figure S2.2), and for each Fh suspension, its value has been iteratively calculated following the approach presented in Section 2.3.1.1 in the main text.

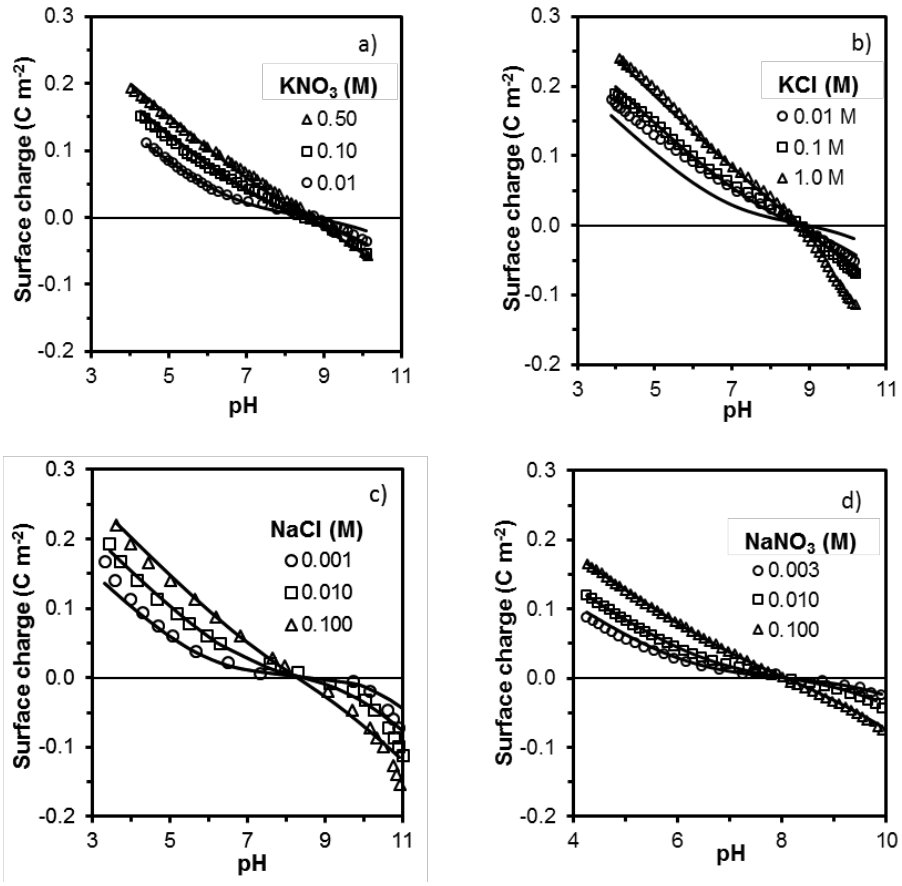

Figure S2.2. pH dependency of the surface charge of different freeze-dried Fh (panels a-b) and Fh materials kept in the wet state (panels c-d), as reported in literature. The different panels are for systems with different types of electrolyte solutions, which represent different degrees of asymmetry in the interaction with the surface groups of Fh. The lines are CD model predictions, using the ion pair constants of Table 2.1 and Figure 2.4 (see main text). The capacitance values are size-dependent,[15] using as reference C_1 = 0.90 F m^{-2} and C_2 = 0.74 F m^{-2} for a flat plane.[61] **Panel a**: Data are from Antelo et al.[43] using a freeze-dried Fh material and KNO_3 as background electrolyte. The SSA was fitted to 300 m^2 g^{-1} with a corresponding M_{nano} of 87.6 g Fh mol^{-1} Fe. Modeled lines were shifted by +0.005 units in the y-axis. **Panel b:** Data are from Wang et al.[78] using a freeze-dried Fh material and KCl as background electrolyte. The SSA was fitted to 455 m^2 g^{-1} with a corresponding M_{nano} of 91.1 g Fh mol^{-1} Fe. The description of the titration series at 0.01 M of KCl is inconsistent, and therefore not considered in the fitting of the SSA. Previous modeling attempts[20] have also reported an inconsistent description of surface charge of a Fh material prepared by the same research group.[75] All that presently matters is to show that the reported pH_{PZC} value can be well reproduced by the model, only considering the proper values of ion pair constants and $\log K_H$ = 8.1. **Panel c:** Data are from Jain et al.[76] using a fresh Fh suspension (aged at 2 °C for <10 d) and NaCl as background electrolyte. The SSA was fitted to 670 m^2 g^{-1} with a corresponding M_{nano} of 96.3 g Fh mol^{-1} Fe. Modeled lines are shifted by +0.004 units in the y-axis. **Panel d**: Data from Moon and Peacock[79] using a fresh Fh suspension and $NaNO_3$ as background electrolyte. The SSA was fitted to 570 m^2 g^{-1} with a corresponding M_{nano} of 93.8 g Fh mol^{-1} Fe. Experimental lines are shifted by +0.003 units in the y-axis. When the M_{nano} was not specified, nor the molar concentration of Fe, a molar mass of 89 g Fh mol^{-1} was assumed to transform the reported H^+ adsorption data from mol kg^{-1} to mol mol^{-1} Fe. As we advocated it in the main text, reporting this information for Fh is essential to consistently scale the primary H^+ adsorption data.

D. Probe ion method with PO_4 to assess the SSA of Fh

Figure S2.3 presents a scheme of the proposed method to assess the specific surface area of Fh using PO_4 as probe ion (A_{PO4}). At the left-hand side (red box), the range of experimental conditions and measured variables are depicted. Typically, the total PO_4 and Fe concentrations are in the order of 0.50 and 2.0 mM respectively (*i.e.* molar PO_4/Fe ration ~ 0.25). The final pH in the equilibrium solution ranges between ~4.5–8.0. The ionic strength of the systems is kept constant at 0.01 M, using $NaNO_3$ as background solution. Each adsorption series is composed of at least 4 evaluation points. The type and the concentration of the different reactants used to attain these conditions are explained in Section 2.2.3 of the main text. With this approach, adsorption envelopes of PO_4 are obtained (Figure S2.4a) in which the percentage adsorption varies between ~40–85%. The final PO_4 concentrations in the equilibrium solution range between ~0.05–0.30 mM. These conditions allow an accurate analytical determination of PO_4 concentrations, resulting in relatively high percentages of PO_4 adsorption found by calculating the difference between the total PO_4 concentration and the final PO_4 concentration in the equilibrium solution. For the proposed experimental conditions, the surface speciation of PO_4 in Fh systems has been calculated as a function of pH (Figure S2.4b). At pH < ~5.5, the protonated bidentate (BH) and doubly protonated monodentate (MH_2) species contribute significantly to the adsorption of PO_4 to Fh. At pH > ~5.5, the bidentate (B) and singly protonated monodentate (MH) are the dominant surface species.

In the right-hand side (green box) of Figure S2.3, the CD model parameters (input) are listed. The log*K* values and CD coefficients for the adsorption reactions of H^+, electrolyte ions, and PO_4 are given in Table 2.1 (main text). The site densities are based on the structural surface model for Fh discussed in Hiemstra and Zhao.[8] Experimental data of pH and total concentration of PO_4, Na^+, and NO_3^- are needed as model inputs. The solid-to-solution ratio (SSR in g L^{-1}) is also required. It corresponds to the product of total Fe concentration (mol L^{-1}) and the molar mass of Fh (M_{nano} in g mol^{-1} Fe). For Fh, M_{nano} is size-dependent and its value increases with increasing the SSA,[10,81] as described in the main text. Therefore, the value of the SSR is found iteratively, after a first approximation of the value for the SSA as input. In our approach, the capacitance values $C_{nano,1}$ and $C_{nano,2}$ are also size-dependent. Therefore, the values of $C_{nano,1}$ and $C_{nano,2}$ are also iteratively calculated using the values of well-crystallized goethite as reference. Equation 2.4 (main text) is used for calculating the size-dependency of the capacitance values for Fh.

In the workflow of Figure S2.3, the SSA is the only adjustable parameter and its value is found by scaling the experimental data of PO_4 adsorption (PO_4/Fe) to the values predicted by the CD model. Following this procedure, changes in the SSA of Fh, as a result of aging, can be consistently assessed.[23] This approach would also allow comparing differences in the surface reactivity of different Fh suspensions. This latter aspect is essential for developing an internally consistent thermodynamic database for applications in Surface Complexation Modeling (SCM).

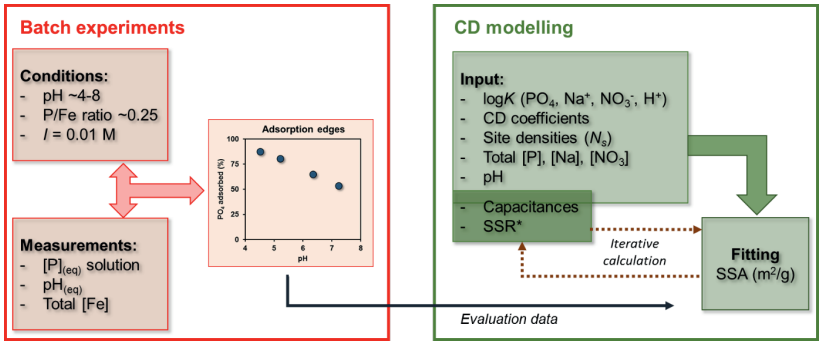

Figure S2.3. Workflow of the proposed method using PO_4 as probe ion for assessing the SSA of Fh suspensions. The left-hand side of the scheme (red square) depicts the experimental conditions of the batch adsorption experiments with PO_4. Generally, the determination of a PO_4 adsorption envelope with 4 evaluation points is enough to obtain reproducible and consistent evaluations. For an accurate evaluation of the PO_4 adsorption, we suggest the use of the pH range ~4.5–8.0 and a total molar ratio P/Fe ~ 0.25. The right-hand side of the scheme depicts the modeling procedure to fit the SSA iteratively. The experimental results of PO_4 adsorption (PO_4/Fe) are rescaled until the best description is achieved (dark-blue arrow), resulting in the optimum value of SSA. The fitting procedure is done iteratively to adjust the input values of capacitances (F m^{-2}) and SSR (g L^{-1}), as those parameters are size-dependent.

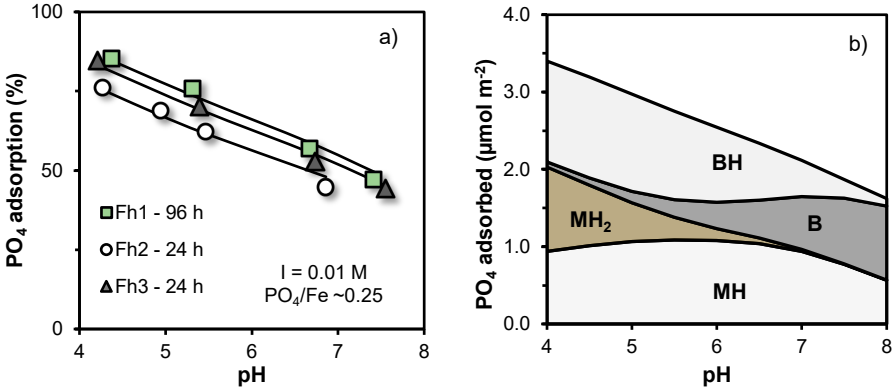

Figure S2.4. Panel a: Adsorption envelopes of PO_4 to three Fh suspensions used in this study. The experimental data (symbols) were collected following the proposed PO_4-method to assess the SSA of Fh (see text). The lines are CD model calculations performed with the parameters set of Table 2.1 (main text). In the modeling, the value of SSA is the only adjustable parameter. Panel b: Modelled surface speciation of PO_4 as a function of pH in single-ion systems with Fh. The adsorption conditions are the same as the experimental conditions used in the batch experiments presented in panel a; i.e. 0.01 M $NaNO_3$ as background solution, total PO_4 and Fe concentrations of 0.50 and 2.0 mM respectively. MH= singly protonated monodentate, MH_2 = doubly protonated monodentate, B = bidentate, BH = protonated bidentate complex.

E. Ion pair constants of Na and NO_3 based on scaling with A_{PO4}

Presently, for fresh Fh suspensions, it is not possible to derive by fitting procedures the $\log K_{ip}$ independently, i.e. free of assumptions. The reason is the absence of an independently derived value for the SSA. Traditionally, the BET method is used to assess the SSA of well-crystallized oxides, but this method is not suitable for freshly prepared Fh suspensions kept in the wet state. For this reason, we rely on goethite as reference material with a well characterized surface chemical behavior. The $\log K_{ip}$ values of Na^+ and NO_3^- are used to fit the relative affinity constants of other electrolyte anions, Cl^- and ClO_4^-. For the capacitances, well-crystallized goethite is also used as reference, accounting for the changes in surface curvature of the ultra-small Fh nanoparticles.

The electrolyte ion affinity constants of Fh and goethite are highly related, but a small deviation from the 1:1 line is found for Cl^- and ClO_4^-. By using A_{PO4} as an input for scaling the acid-base titration data of Fh_1 (Figures 2.1 and 2.2, main text), the $\log K_{ip}$ values of all four electrolyte ions (Na^+, NO_3^-, Cl^-, ClO_4^-) can be optimized simultaneously. Implicitly, we assume $A_H = A_{PO4}$. Overall, this leads to a minor shift of the $\log K_{ip}$ values minimizing the deviations from the 1:1 line (green symbols in Figure S2.5a). As the adsorption of PO_4 to Fh is not sensitive to the precise $\log K_{ip}$ of Na^+ and NO_3^- within the working range of PO_4 concentrations (Figure 2.5, main text), one may conclude that the adapted parameter set improves the consistency with the PO_4 adsorption.

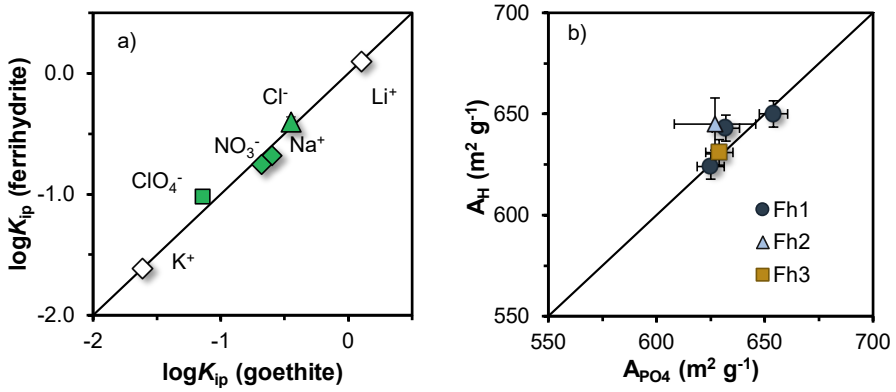

Figure S2.5. Panel a: Comparison of the ion pair formation constants of Fh and goethite (green symbols), using the values of A_{PO4} as input for scaling the H^+ adsorption data of Fh. In the modeling, the $\log K_{ip}$ for Na^+, NO_3^-, Cl^-, and ClO_4^- were fitted simultaneously, using the self-consistent dataset of Fh_1. Panel b: Comparison of the A_H and A_{PO4} values of our three Fh suspensions found using the optimized $\log K_{ip}$ values of Na^+ and NO_3^-.

Using the new set of $\log K_{ip}$ values, one can derive inversely from titration data, the best values of A_H for all Fh samples used in this study (Figure S2.5b). The data for Fh_1 (dark spheres) remain closely around the 1:1 line. Only for Fh_2 some deviation is observed, but this sample also has the largest uncertainty in the determination of the A_H and A_{PO4}. The uncertainty in the fitted A values, expressed in the error bars, is ~ 2% and remains within the expected accuracy of the ion probe method.

F. Assessment of A_H for freshly prepared Fh suspensions

Recently, Hiemstra[10] compiled a data set of acid-base titrations, reported in literature for Fh suspensions kept in the wet state and assessed the corresponding values of A_H using the CD model. Here, we have extended the literature data set and critically reinterpreted the H^+ adsorption data using the consistent approach presented in Section 2.3.1.1 of the main text. The results of this revaluation are presented in Table S2.2. The size-dependency of the molar mass (M_{nano}), mass density (ρ_{nano}) and capacitance values of the Stern layers ($C_{nano,1}$ and $C_{nano,2}$) has been systematically included in the assessment of A_H. For expressing the original data of Fukushi et al.[45] in terms of excess H/Fe ratio, the reported molar mass of 81.65 g mol^{-1} Fe was used. Scaling of all other data sets is based on M = 89 g mol^{-1} Fe, except for data of Moon and Peacock,[79] who used explicitly a value of M_{nano} = 96.0 g mol^{-1} Fe.

Table S2.2. Specific surface areas (A_H), molar masses (M_{nano}), and particle sizes (d) of Fh suspensions that have been kept in the wet state. The reported acid-base titrations have been interpreted with the CD model to derive the values of A_H, using the parameters set of Table 2.1 (main text).

Reference	Method	Aging	Electrolyte	PZC	A_H (m^2 g^{-1})	M_{nano} (g mol^{-1})	d (nm)
Pivovarov (2009)	b	2 days, pH 5	$NaNO_3$ / NaCl	8.1	720	97.6	~2.3
Hsi and Langmuir (1985)	c	4 h, pH 7	$NaNO_3$	8.0	680	96.5	~2.4
Jain et al. (1999)	a	< 10 days at 2 °C	NaCl	8.5	670	96.3	~2.4
Fukushi et al. (2013)	c*	4 h	NaCl	8.2	650	95.8	~2.5
Nagata et al. (2009)	c	4 h	$NaNO_3$	7.9	620	95.0	~2.6
Davis (1977)	c	4 h	$NaNO_3$	7.9	610	94.8	~2.6
Hiemstra (2018)	d	4 h	$NaNO_3$	8.1	610	94.8	~2.6
(Kinniburgh et al. 1975)	e	few days at 5 °C	$NaNO_3$	8.1	585[&]	94.1	~2.7
Moon and Peacock (2013)	a	5 days	$NaNO_3$	8.0	570	93.8	~2.7
Dyer et al. (2003)	a	24 h	$NaNO_3$	7.9	550	93.3	~2.8
Girvin et al. (1991)	f	24 h, pH 7	$NaNO_3$	8.0	530	92.8	~2.9

[a] Schwertmann and Cornell (1991) with 0.20 M $Fe(NO_3)_3$ or (a*) with 1 M $Fe(NO_3)_3$ and 3% citrate, neutralized with 1 M KOH and washed.
[b] Neutralization of 0.10 M $Fe(NO_3)_3$ to pH ~5.5.
[c] Davis and Leckie (1978) with 0.10 M $Fe(NO_3)_3$ or (c*) with 0.10 M $FeCl_3$.
[d] Neutralization of 0.01 M $Fe(NO_3)_3$ in 0.01 M HNO_3 with 0.02 M NaOH to pH =8.5.
[e] Neutralization of probably 1 M $Fe(NO_3)_3$ with 1.5 M NaOH to pH =7.0. The resulting suspension was stored in 1.0 $NaNO_3$ solution at 5 °C.
[f] Benjamin (1993) with 0.10 M $Fe(NO_3)_3$ and aging at pH = 7.0 .
[&]Calculated from the H^+ adsorption between pH 5.5 – 8.0 in 1.0 M $NaNO_3$, reported by Kinniburgh and Jackson (1982).

G. Transfer function to calculate A_H from proton titrations data

In practice, a single H^+ titration curve in $NaNO_3$ at a sufficiently high electrolyte concentration enables the assessment of the SSA. Experimental data and modeling calculations show that, at a high ionic strength (*I*) (*i.e.* > 0.50 M), the excess H^+ adsorption becomes linearly related to the pH within a pH range of ~5–9. Because of this linearity, no precise information about the pH_{PZC} value of the Fh material is needed for the assessment of A_H. The specific surface area can be directly related to the slope (*S*) of that relationship (*i.e.* Δ mmol H^+ mol^{-1} Fe per Δ pH).

To calibrate the transfer function for assessing A_H, we first modelled the surface charge density (C m^{-2}) for Fh systems in a 1.0 M $NaNO_3$ background electrolyte solution, using the CD model with the parameters set presented in Table 2.1 (main text). The pH range was ~ 5.0–9.6. The generated charge density data for particles of different size were transformed into H adsorption data per mole Fe (mmol H mol^{-1} Fe), applying the set of mathematical relationships that account for the size-dependency of the SSA and M_{nano}.[15,23] This was done for a range of SSA values between 500–800 m^2 g^{-1}.

These calculated H^+ adsorption series (mmol H mol^{-1} Fe) were plotted as a function of pH. The linearity of these relationships was checked (R^2 > 0.999) and their corresponding values for the slope (*S*) were determined. As shown in Figure S2.6, the values of *S* (Δ mmol mol^{-1} Fe per ΔpH) are linearly related to the values of A_H (R^2 = 0.999).

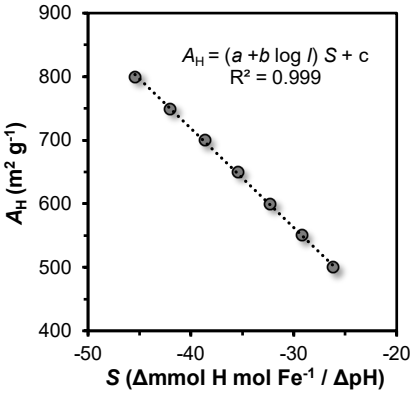

Figure S2.6. Relationship between the A_H of Fh and the slope *S* of the pH-dependent H^+ adsorption for titrations curves performed at 1.0. M $NaNO_3$.

The same calibration procedure was repeated for Fh systems with ionic strengths between *I* = 0.5–1.0 M. This reveals the variation in the proportionality factor between A_H and *S* as a function of *I*. This factor can be defined as $a + b \log I$. The resulting transfer function can be presented as:

$$A_H = (a + b \log I)\, S + c \qquad \text{(Equation S2.1)}$$

where A_H is the assessed SSA in m^2 g^{-1}, *I* is the ionic strength in mol L^{-1}, a = -15.61, b = 4.66, and c = 94 is a constant. Equation S2.1 can be applied to experimental data of proton adsorption and the resulting A_H values can be compared with those predicted with the full CD model approach discussed in the main text. Kinniburgh and Jackson[85] reported a constant slope of -32 mmol H^+ mol Fe^{-1} / pH for a Fh

suspension titrated in 1.0 M $NaNO_3$. Applying Equation S2.1 yields a value of A_H ~594 $m^2\ g^{-1}$, which agrees with the value previously calculated by Hiemstra[10] (A_H ~ 585 $m^2\ g^{-1}$) using the CD model. Applied to the H^+ adsorption data of our Fh_2 and Fh_3 suspensions (Figure S2.1), insignificant differences are found in the values of A_H derived with either the CD model or Equation S2.1 (Table 2.3, main text).

H. Transfer functions to calculate A_{PO4} from phosphate adsorption data

The SSA of Fh can also be assessed with surface probing using PO_4. For a Fh system with a given solid-to-solution ratio (SSR in g L^{-1}), the mass balance of PO_4 is related to the value of A_{PO4} ($m^2\ g^{-1}$) according to:

$$A_{PO_4} = \frac{PO_4(ini) - PO_4(eq)}{\Gamma_{PO_4} \times SSR} \qquad \text{(Equation S2.2)}$$

where PO_4(ini) and PO_4(eq) are respectively the initial and the final solution concentration of PO_4 (mol L^{-1}), and Γ_{PO_4} is the surface density of adsorbed PO_4 (mol m^{-2}).

As shown in Equation S2.2, the value of A_{PO4} can be derived from the mass balance of PO_4 in the Fh systems. An essential component of this mass balance is the value of Γ_{PO4}. This Γ_{PO4} value cannot be obtained directly from the experimental measurements as the primary information only yields the ratio PO_4/Fe, but it is derived by modeling. For a given condition of pH and ionic strength, there is a unique relationship between the equilibrium concentration of PO_4 in solution (PO_4(eq)) and Γ_{PO4}, *i.e.* the adsorption isotherm.

Using the CD model with the parameters of Table 2.1 (main text), we have generated a large number of data points in which the relationship PO_4(eq) ↔ Γ_{PO4} was evaluated for Fh. With these data, a multiple linear relationship (Equation S2.3) has been calibrated linking the value of Γ_{PO4} to the experimentally available information (pH and PO_4(eq)). It must be noted that this relationship is only valid for single PO_4 systems in the absence of any other specifically adsorbing (cat)-anion; *i.e.* it does not consider cooperative or competitive adsorption interactions with PO_4.

$$\Gamma_{PO_4} = a\ pH + b \log(PO_4(eq)) + c \qquad \text{(Equation S2.3)}$$

First, the empirical relationship was calibrated for Fh systems in 0.01 M $NaNO_3$, pH values between pH = 4.5–8.5, and Γ_{PO_4} of ~1.0–3.2 µmol m^{-2}. The results of the multiple linear regression are shown in Figure S2.7a, where c = 7.80, a = –0.51, and b = 0.58. The values of Γ_{PO4} predicted by the transfer function (y-axis) agree with the Γ_{PO4} derived by the full CD model (x-axis). In Figure S2.7b, we show the results for Fh in 0.1 M $NaNO_3$. The parameter values for this system are c = 7.59, a = –0.44, and b = 0.60.

The values of A_{PO4} derived for our Fh suspensions using Equation S2.2 and S2.3 are in good agreement with the values obtained with the CD model (Table 2.3 in the main text).

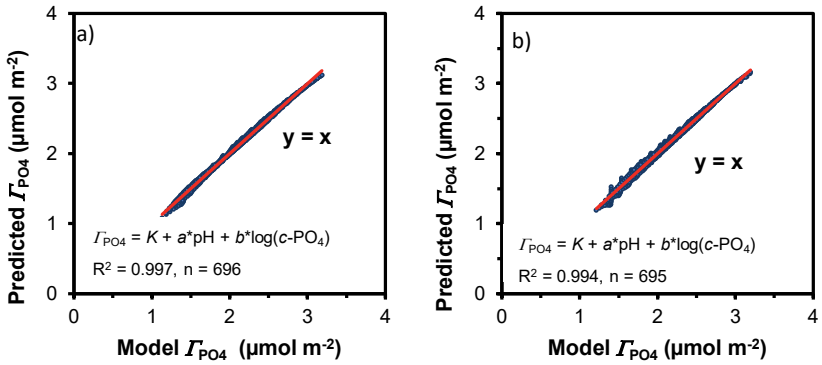

Figure S2.7. Relationship between the PO_4 surface loading values (Γ_{PO4}) derived with the CD model and predicted with the transfer functions. Panel a is for the multiple linear function calibrated for systems in 0.01 M $NaNO_3$, whose parameters were used in the A_{PO4} calculations of our Fh suspensions (main text). Panel b is for the multiple linear function calibrated for systems in 0.1 M $NaNO_3$.

I. Relationship between chemisorbed water and SSA

As explained in the main text, information about the chemical composition of Fh is required for the consistent scaling of ion adsorption phenomenon. The composition of Fh can be given as $FeO_{1.4}(OH)_{0.2}\cdot nH_2O\cdot mH_2O$, where nH_2O is the size-dependent amount of chemisorbed water and mH_2O is the physiosorbed water. Both values can be estimated experimentally from thermogravimetric analysis (TGA) data. Physisorbed water is removed at < 125 °C, and chemisorbed water between 125 and 350 °C, while at higher temperature (> 350 °C) the structural OH is removed as H_2O.[49,54] Figure S2.8 shows TGA data of a 2-line Fh material reported by Eggleton and Fitzpatrick,[26] in which the fractions of physisorbed, chemisorbed, and structural water are distinguished.

TGA data can be interpreted with the surface depletion (SD) model[57] to estimate the value of specific surface area (A_{TGA}) of Fh. A crucial aspect in this assessment is an accurate distinction between the amounts of the various water fractions involved. As shown in Figure S2.8, the slope of the relationship mass loss vs temperature is rather steep for temperatures around 125 °C, in contrast to the slope at a temperature of 350 °C. This leads to a relatively high uncertainty in the estimation of A_{TGA} (~ ±10%) for small differences in temperature (± 1 °C).

The approach illustrated in Figure S2.8 has been applied for interpreting the TGA data reported by Michel et al.[49] In Figure S2.9, the values of A_{TGA} are compared with the SSA values estimated from the average particle size obtained by TEM analysis (A_{TEM}). The latter values have been calculated iteratively using size-dependent values for the mass density (ρ_{nano}), as explained in Section 2.3.1.1 of the main text. For 2-line Fh with a high surface area and small particle size, good agreement exists between A_{TEM} and A_{TGA} within the uncertainties. At the lower end in the range of A ~ 20–750 $m^2\ g^{-1}$ the values found with TGA deviate. More water is removed than can be explained by the surface composition. This difference can be attributed to the presence of structural defects and can be caused by an imperfect particle growth by oriented attachment, as discussed in Hiemstra[86] and Hiemstra et al.[23]

In Figure S2.9, the values of A_{TEM} are also compared with the reported values of A_{BET}. A good agreement between both approaches is only found for the particles with the lowest A (~ < 250 $m^2\ g^{-1}$)

and corresponding largest particle size (d ~ > 5.5 nm). For higher A values, the A_{BET} values are significantly lower than those of A_{TEM}, indicating that the reduction in A_{BET} due aggregation of primary particles is more significant for Fh suspensions with the smaller mean particle size. Results in Figure S2.9 provide further evidence that the traditional BET method is not suitable for assessing the SSA of fresh Fh suspensions. Therefore, the use of PO_4 as probe ion has been advocated in the present contribution.

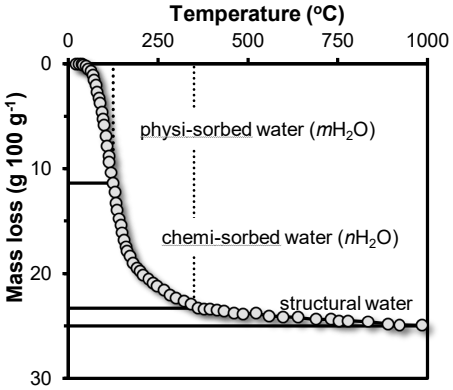

Figure S2.8. Thermogravimetric analysis (TGA) curve for a 2-line ferrihydrite preparation reported by Eggleton and Fitzpatrick.[26] The loss of mass below 125 °C is associated with the amount of physisorbed water, whereas the amount of chemisorbed water is related to mass loss occurring between 125 and 350 °C. Mass loss at > 350 °C is associated with structural water of the bulk mineral.

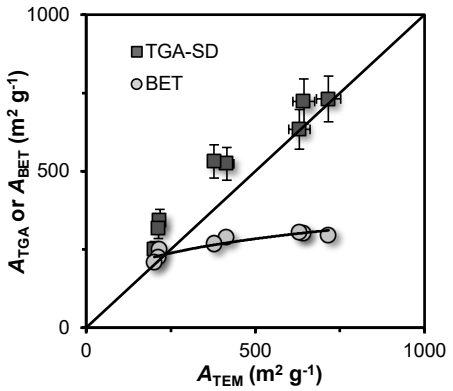

Figure S2.9. Relationship between the SSA of ferrihydrite derived from TEM data (A_{TEM}) with the SSA derived either from thermogravimetric analysis data (A_{TGA}) or gas adsorption (A_{BET}). Data are from Michel et al.[49] The A_{TEM} values were obtained from the reported average particle size obtained by TEM analysis, using size-dependent values of mass density (ρ_{nano}) as explained in the main text. The A_{TGA} values were obtained by interpreting the experimental amount of chemisorbed water (> 125 °C) according to the surface depletion model (SD).[57]

References

(1) Jambor, J. L.; Dutrizac, J. E. Occurrence and Constitution of Natural and Synthetic Ferrihydrite, a Widespread Iron Oxyhydroxide. *Chem. Rev.* **1998**, *98* (7), 2549–2586.

(2) Hochella, M. F.; Lower, S. K.; Maurice, P. A.; Penn, R. L.; Sahai, N.; Sparks, D. L.; Twining, B. S. Nanominerals, Mineral Nanoparticles, and Earth Systems. *Science (80-.).* **2008**, *319* (5870), 1631–1635.

(3) Guo, H.; Barnard, A. S. Naturally Occurring Iron Oxide Nanoparticles: Morphology, Surface Chemistry and Environmental Stability. *J. Mater. Chem. A* **2013**, *1* (1), 27–42.

(4) Tiberg, C.; Gustafsson, J. P. Phosphate Effects on Cadmium(II) Sorption to Ferrihydrite. *J. Colloid Interface Sci.* **2016**, *471*, 103–111.

(5) Trivedi, P.; Dyer, J. A.; Sparks, D. L. Lead Sorption onto Ferrihydrite. 1. A Macroscopic and Spectroscopic Assessment. *Environ. Sci. Technol.* **2003**, *37* (5), 908–914.

(6) Fariña, A. O.; Peacock, C. L.; Fiol, S.; Antelo, J.; Carvin, B. A Universal Adsorption Behaviour for Cu Uptake by Iron (Hydr)Oxide Organo-Mineral Composites. *Chem. Geol.* **2018**, *479*, 22–35.

(7) Liu, J.; Zhu, R.; Liang, X.; Ma, L.; Lin, X.; Zhu, J.; He, H.; Parker, S. C.; Molinari, M. Synergistic Adsorption of Cd(II) with Sulfate/Phosphate on Ferrihydrite: An in Situ ATR-FTIR/2D-COS Study. *Chem. Geol.* **2018**, *477*, 12–21.

(8) Hiemstra, T.; Zhao, W. Reactivity of Ferrihydrite and Ferritin in Relation to Surface Structure, Size, and Nanoparticle Formation Studied for Phosphate and Arsenate. *Environ. Sci. Nano* **2016**, *3*, 1265–1279.

(9) Wang, X.; Kubicki, J. D.; Boily, J. F.; Waychunas, G. A.; Hu, Y.; Feng, X.; Zhu, M. Binding Geometries of Silicate Species on Ferrihydrite Surfaces. *ACS Earth Sp. Chem.* **2018**, *2* (2), 125–134.

(10) Hiemstra, T. Ferrihydrite Interaction with Silicate and Competing Oxyanions: Geometry and Hydrogen Bonding of Surface Species. *Geochim. Cosmochim. Acta* **2018**, *238*, 453–476.

(11) Gu, C.; Wang, Z.; Kubicki, J. D.; Wang, X.; Zhu, M. X-Ray Absorption Spectroscopic Quantification and Speciation Modeling of Sulfate Adsorption on Ferrihydrite Surfaces. *Environ. Sci. Technol.* **2016**, *50* (15), 8067–8076.

(12) Adhikari, D.; Sowers, T.; Stuckey, J. W.; Wang, X.; Sparks, D. L.; Yang, Y. Formation and Redox Reactivity of Ferrihydrite-Organic Carbon-Calcium Co-Precipitates. *Geochim. Cosmochim. Acta* **2019**, *244*, 86–98.

(13) Li, F. Y.; Koopal, L.; Tan, W. F. Effect of Citrate on the Species and Levels of Al Impurities in Ferrihydrite. *Colloids Surfaces A Physicochem. Eng. Asp.* **2018**, *539*, 140–147.

(14) Han, L.; Sun, K.; Keiluweit, M.; Yang, Y.; Yang, Y.; Jin, J.; Sun, H.; Wu, F.; Xing, B. Mobilization of Ferrihydrite-Associated Organic Carbon during Fe Reduction: Adsorption versus Coprecipitation. *Chem. Geol.* **2019**, *503*, 61–68.

(15) Hiemstra, T.; Van Riemsdijk, W. H. A Surface Structural Model for Ferrihydrite I: Sites Related to Primary Charge, Molar Mass, and Mass Density. *Geochim. Cosmochim. Acta* **2009**, *73* (15), 4423–4436.

(16) Gunnarsson, M.; Abbas, Z.; Ahlberg, E.; Nordholm, S. Corrected Debye-Hückel Analysis of Surface Complexation: III. Spherical Particle Charging Including Ion Condensation. *J. Colloid Interface Sci.* **2004**, *274* (2), 563–578.

(17) Abbas, Z.; Labbez, C.; Nordholm, S.; Ahlberg, E. Size-Dependent Surface Charging of Nanoparticles. *J. Phys. Chem. C* **2008**, *112* (15), 5715–5723.

(18) Dzombak, D. A.; Morel, F. M. M. *Surface Complexation Modeling: Hydrous Ferric Oxide*; John Wiley & Sons, Inc.: New York, 1990.

(19) Cornell, R. M.; Schwertmann, U. *The Iron Oxides: Structure, Properties, Reactions, Ocurrence and Uses*, Second Edi.; WILEY-VCH, Germany, 2003.

(20) Bompoti, N.; Chrysochoou, M.; Machesky, M. Surface Structure of Ferrihydrite: Insights from Modeling Surface Charge. *Chem. Geol.* **2017**, *464*, 34–45.

(21) Burleson, D. J.; Penn, R. L. Two-Step Growth of Goethite from Ferrihydrite. *Langmuir* **2006**, *22* (1), 402–409.

(22) Mao, Y.; Ninh Pham, A.; Xin, Y.; David Waite, T. Effects of PH, Floc Age and Organic Compounds on the Removal of Phosphate by Pre-Polymerized Hydrous Ferric Oxides. *Sep. Purif. Technol.* **2012**, *91*, 38–45.

(23) Hiemstra, T.; Mendez, J. C.; Li, J. Evolution of the Reactive Surface Area of Ferrihydrite: Time, PH, and Temperature Dependency of Growth by Ostwald Ripening. *Environ. Sci. Nano* **2019**, *6* (3), 820–833.

(24) Hsi, C. D.; Langmuir, D. Adsorption of Uranyl onto Ferric Oxyhydroxides: Application of the Surface Complexation Site-Binding Model. *Geochim. Cosmochim. Acta* **1985**, *49* (9), 1931–1941.

(25) Yates, D. E.; Grieser, F.; Cooper, R.; Healy, T. W. Tritium Exchange Studies on Metal Oxide Colloidal Dispersions. *Aust. J. Chem.* **1977**, *30* (8), 1655–1660.

(26) Eggleton, R. A.; Fitzpatrick, R. W. New Data and a Revised Structural Model for Ferrihydrite. *Clays Clay Miner.*

1988, *36* (2), 111–124.

(27) Anderson, M. A.; Malotky, D. T. The Adsorption of Protolyzable Anions on Hydrous Oxides at the Isoelectric PH. *J. Colloid Interface Sci.* **1979**, *72* (3), 413–427.

(28) Pyman, M. A. F.; Posner, A. M. The Surface Areas of Amorphous Mixed Oxides and Their Relation to Potentiometric Titration. *J. Colloid Interface Sci.* **1978**, *66* (1), 85–94.

(29) Davis, J. A.; Leckie, J. O. Surface Ionization and Complexation at the Oxide/Water Interface II. Surface Properties of Amorphous Iron Oxyhydroxide and Adsorption of Metal Ions. *J. Colloid Interface Sci.* **1978**, *67* (1), 90–107.

(30) Brunauer, S.; Emmett, P. H.; Teller, E. Adsorption of Gases in Multimolecular Layers. *J. Am. Chem. Soc.* **1938**, *60* (2), 309–319.

(31) Zhuravlev, L. T. The Surface Chemistry of Amorphous Silica. Zhuravlev Model. *Colloids Surfaces A Physicochem. Eng. Asp.* **2000**, *173* (1–3), 1–38.

(32) Walton, K. S.; Snurr, R. Q. Applicability of the BET Method for Determining Surface Areas of Microporous Metal-Organic Frameworks. *J. Am. Chem. Soc.* **2007**, *129* (27), 8552–8556.

(33) Bae, Y. S.; Yazayd'n, A. Ö.; Snurr, R. Q. Evaluation of the BET Method for Determining Surface Areas of MOFs and Zeolites That Contain Ultra-Micropores. *Langmuir* **2010**, *26* (8), 5475–5483.

(34) Gómez-Gualdrón, D. A.; Moghadam, P. Z.; Hupp, J. T.; Farha, O. K.; Snurr, R. Q. Application of Consistency Criteria to Calculate BET Areas of Micro- and Mesoporous Metal-Organic Frameworks. *J. Am. Chem. Soc.* **2016**, *138* (1), 215–224.

(35) Weidler, P. G. BET Sample Pretreatment of Synthetic Ferrihydrite and Its Influence on the Determination of Surface Area and Porosity. *J. Porous Mater.* **1997**, *4* (3), 165–169.

(36) Strehlau, J. H.; Toner, B. M.; Arnold, W. A.; Penn, R. L. Accessible Reactive Surface Area and Abiotic Redox Reactivity of Iron Oxyhydroxides in Acidic Brines. *Geochim. Cosmochim. Acta* **2017**, *197*, 345–355.

(37) Tipping, E. The Adsorption of Aquatic Humic Substances by Iron Oxides. *Geochim. Cosmochim. Acta* **1981**, *45* (2), 191–199.

(38) Michen, B.; Geers, C.; Vanhecke, D.; Endes, C.; Rothen-Rutishauser, B.; Balog, S.; Petri-Fink, A. Avoiding Drying-Artifacts in Transmission Electron Microscopy: Characterizing the Size and Colloidal State of Nanoparticles. *Sci. Rep.* **2015**, *5* (1), 9793.

(39) Mendez, J. C.; Hiemstra, T. Carbonate Adsorption to Ferrihydrite: Competitive Interaction with Phosphate for Use in Soil Systems. *ACS Earth Sp. Chem.* **2019**, *3* (1), 129–141.

(40) Girvin, D. C.; Ames, L. L.; Schwab, A. P.; McGarrah, J. E. Neptunium Adsorption on Synthetic Amorphous Iron Oxyhydroxide. *J. Colloid Interface Sci.* **1991**, *141* (1), 67–78.

(41) Hansen, H. C. B.; Wetche, T. P.; Raulund-Rasmussen, K.; Borggaard, O. K. Stability Constants for Silicate Adsorbed to Ferrihydrite. *Clay Miner.* **1994**, *29* (03), 341–350.

(42) Pivovarov, S. Diffuse Sorption Modeling. *J. Colloid Interface Sci.* **2009**, *332* (1), 54–59.

(43) Antelo, J.; Fiol, S.; Pérez, C.; Mariño, S.; Arce, F.; Gondar, D.; López, R. Analysis of Phosphate Adsorption onto Ferrihydrite Using the CD-MUSIC Model. *J. Colloid Interface Sci.* **2010**, *347* (1), 112–119.

(44) Nagata, T.; Fukushi, K.; Takahashi, Y. Prediction of Iodide Adsorption on Oxides by Surface Complexation Modeling with Spectroscopic Confirmation. *J. Colloid Interface Sci.* **2009**, *332* (2), 309–316.

(45) Fukushi, K.; Aoyama, K.; Yang, C.; Kitadai, N.; Nakashima, S. Surface Complexation Modeling for Sulfate Adsorption on Ferrihydrite Consistent with in Situ Infrared Spectroscopic Observations. *Appl. Geochemistry* **2013**, *36*, 92–103.

(46) Rahnemaie, R.; Hiemstra, T.; van Riemsdijk, W. H. A New Surface Structural Approach to Ion Adsorption: Tracing the Location of Electrolyte Ions. *J. Colloid Interface Sci.* **2006**, *293* (2), 312–321.

(47) Towe, K. M.; Bradley, W. F. Mineralogical Constitution of Colloidal "Hydrous Ferric Oxides." *J. Colloid Interface Sci.* **1967**, *24* (3), 384–392.

(48) Drits, V. A.; Sakharov, B. A.; Salyn, A. L.; Manceau, A. Structural Model for Ferrihydrite. *Clay Miner.* **1993**, *28* (2), 185–207.

(49) Michel, F. M.; Barron, V.; Torrent, J.; Morales, M. P.; Serna, C. J.; Boily, J.-F.; Liu, Q.; Ambrosini, A.; Cismasu, A. C.; Brown, G. E. Ordered Ferrimagnetic Form of Ferrihydrite Reveals Links among Structure, Composition, and Magnetism. *Proc. Natl. Acad. Sci.* **2010**, *107* (7), 2787–2792.

(50) Maillot, F.; Morin, G.; Wang, Y.; Bonnin, D.; Ildefonse, P.; Chaneac, C.; Calas, G. New Insight into the Structure of Nanocrystalline Ferrihydrite: EXAFS Evidence for Tetrahedrally Coordinated Iron(III). *Geochim. Cosmochim. Acta* **2011**, *75* (10), 2708–2720.

(51) Peak, D.; Regier, T. Direct Observation of Tetrahedrally Coordinated Fe(III) in Ferrihydrite. *Environ. Sci. Technol.* **2012**, *46* (6), 3163–3168.

(52) Michel, F. M.; Ehm, L.; Antao, S. M.; Lee, P. L.; Chupas, P. J.; Liu, G.; Strongin, D. R.; Schoonen, M. A. A.; Phillips, B. L.; Parise, J. B. The Structure of Ferrihydrite, a Nanocrystalline Material. *Science* **2007**, *316* (5832), 1726–1729.

(53) Rancourt, D. G.; Meunier, J. F. Constraints on Structural Models of Ferrihydrite as a Nanocrystalline Material. *Am. Mineral.* **2008**, *93* (8–9), 1412–1417.

(54) Xu, W.; Hausner, D. B.; Harrington, R.; Lee, P. L.; Strongin, D. R.; Parise, J. B. Structural Water in Ferrihydrite and Constraints This Provides on Possible Structure Models. *Am. Mineral.* **2011**, *96* (4), 513–520.

(55) Harrington, R.; Hausner, D. B.; Xu, W.; Bhandari, N.; Michel, F. M.; Brown, G. E.; Strongin, D. R.; Parise, J. B. Neutron Pair Distribution Function Study of Two-Line Ferrihydrite. *Environ. Sci. Technol.* **2011**, *45* (23), 9883–9890.

(56) Pinney, N.; Kubicki, J. D.; Middlemiss, D. S.; Grey, C. P.; Morgan, D. Density Functional Theory Study of Ferrihydrite and Related Fe-Oxyhydroxides. *Chem. Mater.* **2009**, *21* (24), 5727–5742.

(57) Hiemstra, T. Surface and Mineral Structure of Ferrihydrite. *Geochim. Cosmochim. Acta* **2013**, *105*, 316–325.

(58) Rietra, R. P. J. J.; Hiemstra, T.; Van Riemsdijk, W. H. Electrolyte Anion Affinity and Its Effect on Oxyanion Adsorption on Goethite. *J. Colloid Interface Sci.* **2000**, *229* (1), 199–206.

(59) Lützenkirchen, J.; Preočanin, T.; Kovačević, D.; Tomišić, V.; Lövgren, L.; Kallay, N. Potentiometric Titrations as a Tool for Surface Charge Determination. *Croat. Chem. Acta* **2012**, *85* (4), 391–417.

(60) Hiemstra, T.; Van Riemsdijk, W. H. A Surface Structural Approach to Ion Adsorption: The Charge Distribution (CD) Model. *J. Colloid Interface Sci.* **1996**, *179* (2), 488–508.

(61) Hiemstra, T.; Van Riemsdijk, W. H. On the Relationship between Charge Distribution, Surface Hydration, and the Structure of the Interface of Metal Hydroxides. *J. Colloid Interface Sci.* **2006**, *301* (1), 1–18.

(62) Keizer, M. G.; van Riemsdijk, W. H. *ECOSAT, Equilibrium Calculation of Speciation and Transport. Technical Report. Department of Soil Quality. Wageningen Univeristy.*; 1998.

(63) Kinniburgh, D. G. *Fit, Technical Report WD/93/23*; Keyworth, Great Britain, 1993.

(64) Szekeres, M.; Tombácz, E. Surface Charge Characterization of Metal Oxides by Potentiometric Acid-Base Titration, Revisited Theory and Experiment. *Colloids Surfaces A Physicochem. Eng. Asp.* **2012**, *414*, 302–313.

(65) Čakara, D.; Kobayashi, M.; Skarba, M.; Borkovec, M. Protonation of Silica Particles in the Presence of a Strong Cationic Polyelectrolyte. *Colloids Surfaces A Physicochem. Eng. Asp.* **2009**, *339* (1–3), 20–25.

(66) Bompoti, N. M.; Chrysochoou, M.; Machesky, M. L. Assessment of Modeling Uncertainties Using a Multistart Optimization Tool for Surface Complexation Equilibrium Parameters (MUSE). *ACS Earth and Space Chemistry*. American Chemical Society January 10, 2019, p acsearthspacechem.8b00125.

(67) Boily, J. F.; Lützenkirchen, J.; Balmès, O.; Beattie, J.; Sjöberg, S. Modeling Proton Binding at the Goethite (α-FeOOH)-Water Interface. *Colloids Surfaces A Physicochem. Eng. Asp.* **2001**, *179* (1), 11–27.

(68) Hiemstra, T. Formation, Stability, and Solubility of Metal Oxide Nanoparticles: Surface Entropy, Enthalpy, and Free Energy of Ferrihydrite. *Geochim. Cosmochim. Acta* **2015**, *158*, 179–198.

(69) Snow, C. L.; Lilova, K. I.; Radha, A. V.; Shi, Q.; Smith, S.; Navrotsky, A.; Boerio-Goates, J.; Woodfield, B. F. Heat Capacity and Thermodynamics of a Synthetic Two-Line Ferrihydrite, FeOOH·0.027H2O. *J. Chem. Thermodyn.* **2013**, *58*, 307–314.

(70) Kozin, P. A.; Shchukarev, A.; Boily, J. F. Electrolyte Ion Binding at Iron Oxyhydroxide Mineral Surfaces. *Langmuir* **2013**, *29* (39), 12129–12137.

(71) Kallay, N.; Žalac, S. Charged Surfaces and Interfacial Ions. *Journal of Colloid and Interface Science*. Academic Press October 1, 2000, pp 1–11.

(72) Kozin, P. A.; Boily, J. F. Mineral Surface Charge Development in Mixed Electrolyte Solutions. *J. Colloid Interface Sci.* **2014**, *418*, 246–253.

(73) Lützenkirchen, J.; Boily, J. F.; Gunneriusson, L.; Lövgren, L.; Sjöberg, S. Protonation of Different Goethite Surfaces-Unified Models for NaNO3and NaCl Media. *J. Colloid Interface Sci.* **2008**, *317* (1), 155–165.

(74) van der Giessen, A. A. The Structure of Iron (III) Oxide-Hydrate Gels. *J. Inorg. Nucl. Chem.* **1966**, *28* (10), 2155–2159.

(75) Wang, X.; Li, W.; Harrington, R.; Liu, F.; Parise, J. B.; Feng, X.; Sparks, D. L. Effect of Ferrihydrite Crystallite Size on Phosphate Adsorption Reactivity. *Environ. Sci. Technol.* **2013**, *47* (18), 10322–10331.

(76) Jain, A.; Raven, K. P.; Loeppert, R. H. Arsenite and Arsenate Adsorption on Ferrihydrite: Surface Charge Reduction and Net OH - Release Stoichiometry. *Environ. Sci. Technol.* **1999**, *33* (8), 1179–1184.

(77) Raven, K. P.; Jain, A.; Loeppert, R. H. Arsenite and Arsenate Adsorption on Ferrihydrite: Kinetics, Equilibrium, and Adsorption Envelopes. *Environ. Sci. Technol.* **1998**, *32* (3), 344–349.

(78) Wang, X.; Liu, F.; Tan, W.; Li, W.; Feng, X.; Sparks, D. L. Characteristics of Phosphate Adsorption-Desorption Onto Ferrihydrite. *Soil Sci.* **2013**, *178* (1), 1–11.

(79) Moon, E. M.; Peacock, C. L. Modelling Cu(II) Adsorption to Ferrihydrite and Ferrihydrite-Bacteria Composites: Deviation from Additive Adsorption in the Composite Sorption System. *Geochim. Cosmochim. Acta* **2013**, *104*, 148–164.

(80) Bompoti, N. M.; Chrysochoou, M.; Machesky, M. L. A Unified Surface Complexation Modeling Approach for Chromate Adsorption on Iron Oxides. *Environ. Sci. Technol.* **2019**, *53* (11), 6352–6361.

(81) Hiemstra, T.; Riemsdijk, W. H. Van; Rossberg, A.; Ulrich, K.-U. A Surface Structural Model for Ferrihydrite II: Adsorption of Uranyl and Carbonate. *Geochim. Cosmochim. Acta* **2009**, *73* (15), 4437–4451.

(82) Davis, J. A. Adsorption of Trace Metals and Complexing Ligands at the Oxide/Water Interface., Standford University, California, USA, 1977.

(83) Kinniburgh, D. G.; Syers, J. K.; Jackson, M. L. Specific Adsorption of Trace Amounts of Calcium and Strontium by Hydrous Oxides of Iron and Aluminum. *Soil Sci. Soc. Am. J.* **1975**, *39* (3), 464–470.

(84) Dyer, J. A.; Trivedi, P.; Scrivner, N. C.; Sparks, D. L. Lead Sorption onto Ferrihydrite. 2. Surface Complexation Modeling. *Environ. Sci. Technol.* **2003**, *37* (5), 915–922.

(85) Kinniburgh, D. G.; Jackson, M. L. Concentration and PH Dependence of Calcium and Zinc Adsorption by Iron Hydrous Oxide Gel. *Soil Sci. Soc. Am. J.* **1982**, *46* (1), 56–61.

(86) Hiemstra, T. Surface Structure Controlling Nanoparticle Behavior: Magnetism of Ferrihydrite, Magnetite, and Maghemite. *Environ. Sci. Nano* **2018**, *5* (3), 752–764.

CHAPTER 3

Evolution of the reactive surface area of ferrihydrite: Time, pH, and temperature dependency of growth by Ostwald ripening

Tjisse Hiemstra, Juan C. Mendez, Jiayu Li

Published as:

Hiemstra, T., Mendez, J.C., Li, J. 2019. Evolution of the reactive surface area of ferrihydrite: Time, pH, and temperature dependency of growth by Ostwald ripening. *Environ. Sci. Nano* 6, 820–833. doi.org/10.1039/C8EN01198B

Abstract

Surface area is a crucial property of metal oxides for scaling ion adsorption phenomena. For ferrihydrite (Fh), the value is uncertain. Moreover, it rapidly changes with time, pH, and temperature. In this study, the dynamic change of the reactive surface area has been probed with phosphate for ferrihydrite, produced by ultra-fast neutralization at 20 ^{0}C. The initial nanoparticles are very small (d ~ 1.68 nm), have a remarkably large specific surface area (A ~ 1100 m^2 g^{-1}), and contain on average only 45 Fe atoms. Our data reveal the rapid change of the surface area showing that the rate of growth decreases by nearly three orders of magnitude (R ~ 0.01–10 μmol Fe m^{-2} h^{-1}) within one week of ageing. The rate of growth is proportional to the square of the super saturation of the solution $(Q_{so}/K_{so})^2$, which suggests a rate limitation by dual attachment of Fe to a surface site of growth. This process is significantly hindered by the presence of weakly bound organic molecules, particularly at low pH, implying for soils that natural organic matter may considerably contribute to the kinetic stability of the natural iron oxide fraction. Our data also show that the reaction pathways are very different in $NaNO_3$ and NaCl solutions. The decrease of surface area in $NaNO_3$, prepared in traditional batch experiments, can be described excellently with the above rate law implemented in our dynamic model. This model also covers the temperature dependency (4–120 °C) of Fh ageing using an activation energy of $E_a = 68 \pm 4$ kJ mol^{-1}. For traditionally prepared two-line Fh (2LFh), our model suggests that with solely dual Fe attachment, the growth of the primary particles is limited to d ~ 3–4 nm (A ~ 350–500 m^2 g^{-1}). Larger particles can be formed by oriented attachment, particularly at a high temperature. Using forced hydrolysis at 75 °C, large particles (d ~ 5.5 nm) can also be produced directly. According to our model, Ostwald ripening of such six-line Fh (6LFh) particles will be limited due to their low solubility.

3.1. Introduction

Ferrihydrite (Fh) is a nanoparticle omnipresent in nature and used in environmental engineering. Its properties contribute to the fate of many elements in the geochemical cycle and environmental technology. Ferrihydrite nanoparticles are highly reactive and have a high ion adsorption capacity that is relevant for applications. For this reason, it is used and widely studied as model material to elucidate the adsorption of cations, anions, and organic matter.[1–19] The surface area of Fh is an essential characteristic, particularly from the perspective of surface complexation modelling. One reason is that Fh particles are usually charged. This charge is scaled to a surface area. It allows the calculation of the variable electrostatic energy contribution that largely controls the variation in binding of ions to surfaces in relation to solution conditions.[16,20–24] In addition, the supposed surface area determines the number of available adsorption sites at a given surface site density. Therefore, a proper scaling is crucial for describing ion adsorption behaviour of Fh.

Ferrihydrite is easily synthesized in the laboratory.[25] However, variations in protocols lead to different and not well-known surface areas.[26,27] Moreover, the surface area of Fh will decrease with time because nanoparticles are thermodynamically unstable and will spontaneously grow. For Fh, the rate of change depends on controlling factors such as pH, adsorbed ions, and temperature.[28]

Relatively, little information is available about the evolution of the reactive surface area and particle size of Fh immediately after preparing the nanomaterial for use in for instance ion adsorption experiments. Formation of Fh starts with nucleation and it is followed by the binding of yet unreacted Fe(III), still present in the solution phase. The combination of nucleation and supplementary Fe adsorption results in a polydisperse suspension that initially contains ultra-small nanoparticles with a very high surface area, a high reactivity, and a high instability.

In a Fh suspension, the smallest particles will maintain a labile equilibrium between Fe in solution and the solid phase.[29] Ferrihydrite particles, larger than a critical size, will spontaneously grow at the expense of the smaller particles that dissolve. This will lead to an increase in the mean particle size. This process of simultaneous growth and dissolution was first described by Ostwald,[30] and therefore, we will refer to this process of coarsening as Ostwald ripening (OR).

For relatively large Fh particles, the rate of growth by classical Ostwald ripening becomes very small, as will be demonstrated in the present study. Nevertheless, experimental data show that Fh particles can still increase significantly in size.[31] This is due to growth by oriented particle attachment.[32] As soon as the Fh particles become sufficiently large, patches of specific crystal faces may develop that allow oriented attachment (OA).[33] Even larger particles may form by fusion as shown for ZnS.[34] Self-assembly of primary Fh particles results in rod-shaped entities as shown with TEM by Murphy et al.[35] and more recently, by Burleson and Penn.[31] These units get a typical aspect ratio of 5 ± 1.[31,35] The process of oriented particle attachment typically occurs for Fh particles with a size near ~ 4 nm and larger.[33] The rate of this particle–particle interaction is second-order-dependent on the suspension concentration of the primary nanoparticles and has a rate constant that depends on the pH and interface structure.[36] The process is most evident during aging at high temperature (60–120 ºC) and high pH (10–12).[31]

Ultimately, Fh transforms into more stable Fe (hydr)oxides. In the presence of dissolved Fe(II), the conversion is accelerated,[37] forming lepidocrocite and goethite within hours. Otherwise, Fh may convert into goethite, hematite, or maghemite.[38–41] This conversion occurs at a relatively large particle size[29] and therefore, it has often been studied at hydrothermal conditions. To quantify the degree of transformation, the difference in rate of dissolution in an oxalate[42–44] or ascorbate solution[45] has been used to assess the

amount of Fh left at transformation, or X-ray diffraction and/or EXAFS is used to estimate the amount of crystalline material formed.[41,46,47]

The initial size of primary Fh nanoparticles immediately formed after instantaneous hydrolysis of Fe(III) upon base addition is very small but not well-known. It has been proposed that the initial formation of Fh is *via* the formation of ultra-small Fe_{13} nuclei[48] with a Keggin structure having one central tetrahedral Fe. Similar clusters may form in ferritin when loaded with little Fe.[2] Fe_{13} nuclei are stable at very acid conditions but above pH ~ 2 they grow into Fh.[48] This growth is driven by the adsorption of dissolved Fe-complexes such as dimers.[49,50] Immediately after ultrafast synthesis of Fh at room temperature in a NaCl solution,[51] the particles have a mean particle size of d ~ 1.8 nm, a specific surface area of A ~ 1000 m^2 g^{-1}, and contain n_{Fe} ~ 60 Fe.[2]

With classical protocols for Fh synthesis, the specific surface area can be significantly smaller than with fast hydrolysis. Traditionally synthesized two-line Fh (2LFh) usually has a specific surface area in the range of just A ~ 530–710 m^2 g^{-1} when kept in the wet state.[27] The corresponding mean particle size is between d ~ 2.3–2.9 nm and the number of Fe per particle is n_{Fe} ~ 140–325 Fe. When dried, the particles are irreversibly bound together in porous aggregates having a significantly lower reactive surface area.[8,16,52–55]

The above overview illustrates that the particle size and surface area of Fh ultimately used in laboratory experiments may largely differ from the nanoparticles initially formed. During storage, the surface area will further decrease. The present study is meant to quantify the rate of ageing of freshly prepared Fh. We will study the change in reactive surface area of Fh in $NaNO_3$ for a time scale of up to one week, covering a particle size range of d ~ 1.7–3 nm. We aim to reveal the factors that control the change in specific surface area. The challenge is to elucidate the underlying mechanism of growth of the primary Fh particles due to Ostwald ripening in the early stage of growth. The ultimately goal is to develop a mechanistic model for describing the time-dependent change of particle size and surface area once the initial nanoparticles have been formed. With the collected insights, we will also disclose the size of the initial particles, immediately after formation.

There are several approaches to assess the reactive surface area of Fh. Traditionally the specific surface area of metal (hydr)oxides is determined by probing the surface with gas molecules (N_2, Ar, and Kr). For oxides in general, it gives good results compared to other methods.[56] The BET equation is used to derive the specific surface area from the collected gas adsorption data. This method cannot be applied to assess the specific surface area of Fh nanoparticles in the wet state. Use of transmission electron microscopy (TEM) can be seen as an alternative, but the approach is experimentally challenging as fresh Fh particles are very small, usually strongly aggregated, and have a particle size distribution.[40,57–60] In case of ZnS nanoparticles, peak broadening at X-ray diffraction has been used[34] to derive the mean particle size. The translation of size to specific surface area requires information about the particle shape,[61] while particle porosity should be unimportant.

Davis and Leckie[62] have suggested to use H^+ as probe-ion to assess the specific surface area of freshly-prepared Fh. In that approach, the pH-dependent proton adsorption is interpreted with surface complexation modelling. Basic assumptions are the value of the capacitance of the inner Stern layer and the value of the molar mass of Fh. Both are strongly size-dependent[2] but its variation can be consistently included, making the specific surface area the only adjustable parameter in a 1-pK approach.[27] Applying this approach to H^+ adsorption data from literature reveals a specific surface area ranging from 530–710 m^2 g^{-1} for the various Fh preparations.[27] The upper value corresponds to particles with a mean size of 2.3 nm, in agreement with TEM data for freshly-prepared Fh without specific ageing.[40]

An alternative to H^+ as probe-ion is the use of PO_4 ions.[2] The use of the latter has the advantage that the adsorption of PO_4 can be measured easily and accurately, since this anion has a high affinity for Fe. Comparison of the results found with proton titrations suggests good agreement[27] and is further supported by yet unpublished data. In the approach, the CD and MUSIC model recently developed for Fh has been used[2] and will also be applied in the present study.

In the present work, we will study the dynamic change of the reactive surface area of Fh kept in the wet state. We will start by producing Fh with high-speed titration of a Fe(III) nitrate solution with base, mixed in a flow chamber. For this material, the change of the specific surface area will be studied at a time scale between 0.1 hour and ~7 days for pH values of 5–9, maintained by means of organic pH buffer solutions, similarly as used recently by Mao et al.[51] In the second set of experiments, we will study the time and pH dependent ageing of traditionally produced Fh, and we will include in that study the temperature dependency (4–20 ºC). The results will be compared to data for Oswald ripening of primary particles at high temperature (60–120 ºC) collected with TEM.[31] For the latter data, we will show that the observed growth of the primary particles can be described with the same model that we developed for our freshly prepared Fh.

3.2. Experimental

Fh was produced by titrating a Fe(III) nitrate solution with NaOH, which was subsequently aged. The experiments were done in the presence and absence of organic pH buffers. In the latter case, temperature dependency was studied too. At each reaction time and pH condition, the specific surface area was measured using phosphate as probe-ion. The collected PO_4 adsorption isotherms or edges were interpreted with the charge distribution (CD) and multiple site complexation (MUSIC) model of Hiemstra and Zhao,[2] making the specific surface area the only adjustable parameter. From the value of the specific surface area, the mean particle size, and number of Fe ions per particle were calculated.

3.2.1. Ferrihydrite synthesis

3.2.1.1. High-speed neutralization

These experiments were conducted in a conditioned room (20 °C). All solutions were prepared with ultra-pure water (18.2 MΩcm at 25 °C, <1 ppb TOC) and chemical reactants of analytical grade. A mixture containing 100 mM $Fe(NO_3)_3$, 100 mM HNO_3, 38 mM MES ($C_6H_{13}NO_4S$) and 38 mM MOPs ($C_7H_{15}NO_4S$) was neutralized with 380 mM NaOH at a common tip in a tubing system and led over a glass electrode in a reaction vessel for nonstop recording of the pH (Figure S3.1). The rate of Fe addition was set to 8.0 mL min^{-1} and the rates of base addition were chosen such that the pH value remained initially ~ 0.5–1 pH units lower than the target value to be reached. The remaining NaOH addition (≤ ~5 % of the total added NaOH) was done at a lower speed while magnetically stirring the suspension produced. The system was purged continuously with moist and cleaned N_2 gas. Individual batches were produced for each reaction time and pH condition. The volume of added base solution varied only slightly between individual batches prepared for systems with the same target pH (CV% of base volume < 0.5%), *i.e.* the neutralization (OH/Fe ratio) was very reproducible.

For ageing, the suspensions produced were transferred into closed plastic bottles and shaken in a reciprocal shaker (180 strokes per minute). At a predefined reaction time between 0.1 hour and 7 days, the suspension was characterized with a PO_4 adsorption experiment using 6 different initial PO_4 concentrations, and the actual Fe concentration (~ 45 mM) was measured using Inductively coupled

plasma optical emission spectrometry (ICP-OES) after dissolving a sub sample in a final concentration of 0.1 M HNO_3.

3.2.1.2. Standard synthesis of ferrihydrite

A second set of Fh suspensions was produced with our standard methodology.[2] A freshly-prepared solution of about 1.1 L containing ~3.7 mM $Fe(NO_3)_3$ dissolved in 0.01 M HNO_3 was titrated with approximately 1.1 L of freshly-prepared 0.02 M NaOH. The initial neutralization of ~90 % was done at a rate of ~200 mL NaOH min^{-1} until a pH of 3.1–3.2 was reached. Additional 0.02 M NaOH solution was subsequently added in ~5 mL increments until the suspension reached a final pH of either 6.00 (Fh pH 6) or 8.20 (Fh pH 8.2). The pH was stabilized for 15 min and next, the Fh suspensions were centrifuged at 3330*g* for 45 minutes. Subsequently, the supernatant was carefully removed and the settled Fh particles were re-suspended in a 0.010 M $NaNO_3$ solution to a typical final volume of ~200 mL.

In some cases, the pH was slightly changed after re-suspending the particles in the final background electrolyte solution. In that case, the pH was re-adjusted to the target value by using either 0.01 M HNO_3 or 0.01 M NaOH solution. These ferrihydrite suspensions were aged in a closed bottle at 20 °C for 4 hours since neutralization. Part of this stock suspension was subsequently kept at 20 °C while another part was stored at 4 °C to determine the temperature dependency of ageing. The surface area of both suspensions was measured with PO_4 as probe-ion covering the time span of 4–168 h since neutralization. The total Fe concentration of the suspensions (~ 20 mM) was measured by ICP-OES in a matrix of 0.8 M H_2SO_4.

3.2.2. Phosphate adsorption experiments

3.2.2.1. Fh systems with pH-buffer

Systems for measuring the PO_4 adsorption were prepared in 50 mL polypropylene tubes. The total volume (V_T) was 30.0 mL and typically contained ~10 mM Fe. For each pH system, a ~10 mM PO_4 stock solution was prepared by mixing Na_2HPO_4 and NaH_2PO_4 in a ratio 1:99 (pH 5), 1:9 (pH 6), 1:1 (pH 7), 3:7 (pH 8), and 7:3 (pH 9). Six different initial PO_4 concentrations were used ranging from ~2.3–4.5 mM at low pH, to ~1.6–3.2 mM at high pH. In addition, two systems (pH 5 and 6) with a 10 fold higher initial PO_4 concentration range were used to test the possible influence of the buffer on the PO_4-adsorption, showing no evidence for this in agreement with the work of Mao et al.[51] The background electrolyte solution contained ~ 0.10 M NO_3, 3.8 mM MES, and 3.8 mM MOPs. Equilibration was established by shaking for 16 hours at 180 strokes per minute. Equilibration for 1 hour[51] was found to be not enough. After measuring the pH and subsequent centrifugation (3750*g* for 20 min), the supernatant was filtered over a 0.45 μm filter, acidified with 1 M HNO_3 and analysed for P with ICP-OES.

3.2.2.2. Standard Fh systems

For standard synthesized Fh, PO_4 adsorption was measured for five times of ageing at 20 °C (4, 24, 48, 72, and 166 or 168 hours), whereas for the Fh suspensions aged at 4 °C, two reaction times were used (72 and 166 or 168 hours). The phosphate adsorption experiments were done in a similar way as described above but in the absence of organic buffers and using different volumes and initial concentrations. The adsorption was measured in a background electrolyte solution of 0.010 M $NaNO_3$. Aliquots of 0.01 M acid (HNO_3) or base (NaOH) solutions were added to adjust the pH values to the desired pH range of about 4–8. The final volume was 40 mL and contained 0.50 mM PO_4 and about 2.0

mM Fe. Each adsorption edge was usually composed of four evaluation points at one initial PO_4 concentration but different pH values. The final pH after equilibration for 20 hours was between pH ~4.2–7.6 for the series prepared with Fh pH 6 and between pH ~5.0–8.0 for Fh pH 8.2. All adsorption experiments were done at 20 °C. After centrifugation (3300*g* for 15 minutes) and sampling with 0.45 µm filtration, the pH was measured in the re-suspended system. The sampled supernatant was similarly analysed for P with ICP-OES as described above. In a number of samples, Fe was also measured for verifying the quality of phase separation.

3.3. Results and Discussion

3.3.1. Primary adsorption data

The PO_4 adsorption isotherms have been measured for Fh systems aged at pH 5.0, 6.0, 7.0, 8.0, and 9.0. The pH was stabilized by using a combination of organic pH buffers (~ 0.02 M MES and ~ 0.02 M MOPS). Ageing times were 0.1, 1.5, 6, 24, and 168 hours in all pH experiments except pH 7, where 24, 48, 72, and 144 hours were selected to measure the particle growth. For the systems at pH 5 and 6, the growth was also characterized by studying it with a 10-fold higher initial PO_4 concentration (~ 15–35 mM). Figure 3.1 gives two examples of the decrease of the PO_4 adsorption isotherm with ageing. The trend of decrease with time of ageing is very similar in both cases. For pH 5, the P/Fe ratios are much higher than for pH 8, but this is mainly due to less PO_4 adsorption at higher pH values as follows from CD modelling. Initially, all particles are very small. The PO_4 adsorption is roughly halved after 168 hours of ageing, suggesting a change of the surface area by a factor of about 2.

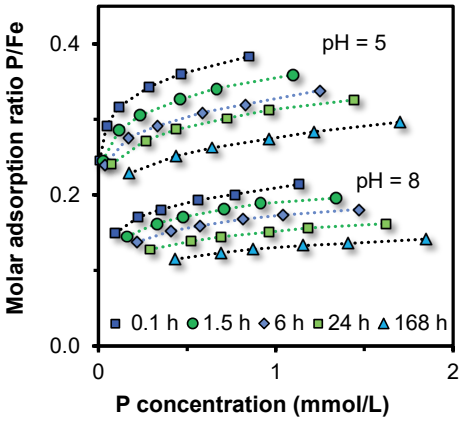

Figure 3.1. Time-dependent PO_4 adsorption isotherms in ~0.10 M $NaNO_3$ measured at pH 5.38 ± 012 and 8.01 ± 0.21 buffered with 3.8 mM MES and 3.8 mM MOPS (symbols). The Fh was formed and aged at pH 5.00 and 8.00 (20 °C) in solution containing finally ~0.10 M $NaNO_3$, ~19 mM MOPS, and ~19 mM MES. The lines have been calculated with the CD model, taking for each individual data point the corresponding experimental pH and total concentrations of Na, NO_3, PO_4, MES, MOPS, and Fe. The molar masses of Fh were found iteratively with CD modelling from the fitted specific surface area *A* (Equation 3.1). With time, it typically decreased from M_{nano} ~107 to ~94 g mol^{-1} Fe.

3.3.2. CD MUSIC modelling

The adsorption measured in the various systems can be described with the CD model. Previously, the PO_4 adsorption has been studied extensively[2] and the resulting parameter set has been applied to

describe the present data sets. In this approach, the reactive surface area is the only adjustable parameter and its value can be found by fitting the measured PO_4 adsorption isotherms. However, for a proper interpretation, the molar PO_4/Fe ratio needs to be translated into the PO_4 adsorption per unit mass of Fh. This requires the value of the molar mass. The latter is not constant but depends on the (yet unknown) specific surface area. The molar mass of the nanoparticle M_{nano} (g mol^{-1} Fe) is a function of the specific surface area A (m^2 g^{-1}) and the excess surface water density N_{H2O} (12.6 10^{-6} mol m^{-2}), as derived previously.[29,63]

$$M_{\text{nano}} = M_{\text{core}} \frac{A\, N_{\text{H}_2\text{O}} M_{\text{H}_2\text{O}}}{(1 - A\, N_{\text{H}_2\text{O}} M_{\text{H}_2\text{O}})} \qquad \text{(Equation 3.1)}$$

The reason for a variable molar mass is the presence of surface groups that lead to a change of the molar composition.

The molar composition of Fh can be given as $FeO_{1.4}(OH)_{0.2}{\cdot}nH_2O$ in which n is the molar amount of chemisorbed water in excess to the bulk composition $FeO_{1.4}(OH)_{0.2}$. This excess amount of coordinated water (n) can be calculated from the difference in the molar mass of the nanoparticle (M_{nano}) and mineral core or bulk (M_{core}), scaled to the molar mass of water M_{H2O}, according to:

$$n = \frac{M_{\text{nano}} - M_{\text{core}}}{M_{\text{H}_2\text{O}}} \qquad \text{(Equation 3.2)}$$

The molar mass M_{nano} (g mol^{-1}) and surface area A (m^2 g^{-1}) are iteratively found in a cycle of CD modelling and recalculation of the PO_4 adsorption per unit mass (mol kg^{-1}) from the primary molar PO_4/Fe ratio, and this is used to generate a new input for the fitting procedure. In this process, the values of the Stern layer capacitances are also continuously adapted to account for the surface curvature of the spherical particle with a diameter d calculated from the corresponding specific surface area A. In Figure S3.2, the influence of the surface curvature on the PO_4 adsorption is shown.

The translation from A (m^2 g^{-1}) to d (m) requires the value of the mass density of the nanoparticle ρ_{nano} (g m^{-3}), which is variable since the amount of coordinated water (n) adds more to the volume than to the mass of the particle. The relationship between the mass density and molar mass of a nanoparticle can be given as:

$$\rho_{\text{nano}} = \frac{M_{\text{nano}}}{V_{\text{O}} \times (n_{\text{O}} + n)} = \frac{M_{\text{nano}}}{V_{\text{O}} \times (n_{\text{O}} + (M_{\text{nano}} - M_{\text{core}})/M_{\text{H}_2\text{O}})} \qquad \text{(Equation 3.3)}$$

in which V_O is the lattice volume of Fh per oxygen in m^3 per mole oxygen ions, n_O is the number of oxygens per Fe in the bulk of Fh (1.6) and n is the amount of excess water defined in Equation 3.2.

In the above approach, the primary PO_4 adsorption data of Fh in the various systems have been used to derive the specific surface area. In a self-consistent manner, the effect of surface curvature is also included by translating the surface area to the corresponding spherical particle diameters d (m) according to:

$$d = \frac{6}{\rho_{\text{nano}}\, A} \qquad \text{(Equation 3.4)}$$

The corresponding number of Fe ions in the particle (n_{Fe}) follows from:

$$n_{\mathrm{Fe}} = \frac{\rho_{\mathrm{nano}}}{M_{\mathrm{nano}}} \frac{\pi d^3}{6} \mathrm{N_{Av}} \qquad \text{(Equation 3.5)}$$

in which N_{Av} is Avogadro's number. The above-described theoretical relation between chemical composition and particle size is shown for Fh in Figure 3.2 (line) together with experimental data (blue spheres) of Michel el al.,[40] as well as data derived by constructing Fh particles with Crystalmaker® (open squares) with a procedure described previously.[33,64] Good agreement exits between model and data, which implicitly indicates the correct calculation of molar mass M_{nano} and mass density ρ_{nano}.

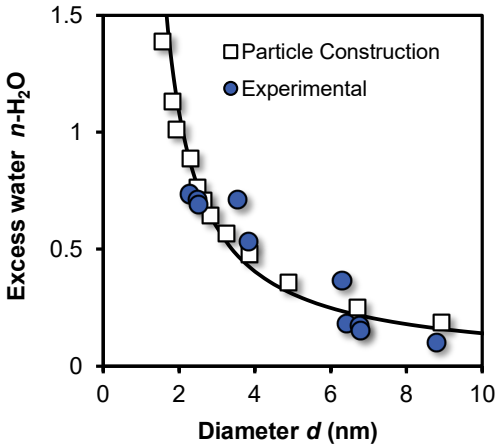

Figure 3.2. Excess water (n) of Fh ($FeO_{1.6}H_{0.2}\cdot nH_2O$) as a function of particle size. The blue spheres are data collected by Michel et al.[40] for a series of Fh particles aged at high temperature. The mean diameter has been found with high-resolution transmission electron microscopy (HR-TEM). The white squares have been derived by constructing near-spherical Fh particles from which all Fe2 and Fe3 were removed that formed singly coordinated surface groups.[33,64] The corresponding size was calculated based on the number of oxygen in the particle and the value for lattice volume expressed per oxygen V_O ($10.7\ 10^{-6}$ m^3 mol^{-1}). Using the principle of electro neutrality, the total number of H can be found for each particle from which one gets the excess number of protons by subtracting the number of structural H according to the composition $FeO_{1.4}(OH)_{0.2}$. It yields the corresponding amount of coordinated surface water. The model line is calculated applying Equations 3.1–3.4, showing good agreement with the data.

At very low pH (<2), small angle X-ray scattering (SAXS) points to the formation of ultra-small nuclei.[48] The reported Fe-dominated radius of r_o = 0.41 nm translates to a particle size by incorporating an effective O diameter of about ~0.20–0.25 nm, leading d ~1.22–1.32 nm, in agreement with our equivalent spherical diameter of ~1.25 nm calculated for Fe_{13}. A neutral Fe_{13} cluster will have a chemical composition of $Fe_{13}O_{40}H_{41}$. Compared to the bulk composition of Fh, the excess amount of coordinated water is n_{H2O} = 2.9, which is extremely above any of the values for excess water of Fh particles, given in Figure 3.2. It indicates that the Fh structure is significantly more condensed than any collection of aggregated Fe_{13} clusters. The core-shell structure suggested for the Fh[48] is in line with the particle size dependency of the ferrimagnetic behaviour of Fh as shown recently.[33] Other SAXS data[59,60] for characterizing Fh will be discussed later.

3.3.3. Particle evolution with time

In Figure 3.3, the pH and time dependent evolution of Fh is given showing the specific surface area A, the mean particle diameter d, and the number of Fe per particle n_{Fe} (symbols), obtained by interpreting the primary PO_4 adsorption data collected at the various pH values and times of ageing at 20 °C. At the logarithmic time scale, the measured specific surface area decreases almost linearly. After a few minutes of ageing, the particles are still very small. Depending on the pH, A = 1100–900 $m^2\ g^{-1}$, d = 1.7–1.9 nm, and n_{Fe} = 50–80.

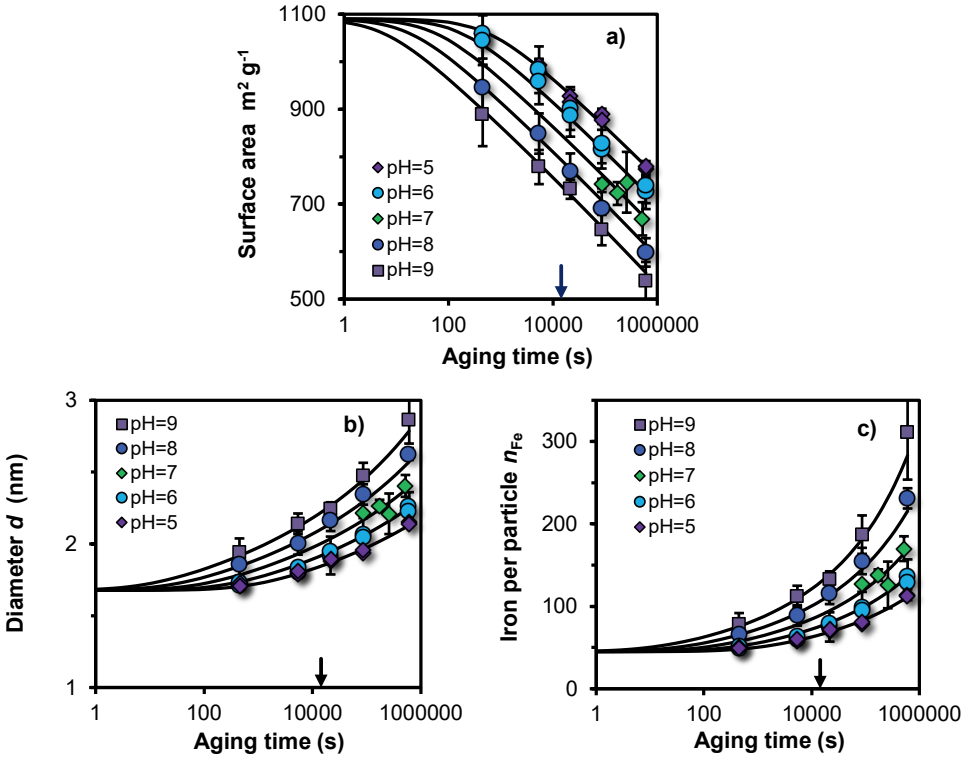

Figure 3.3. a) Evolution of the specific surface area (A), b) mean particle diameter (d), and c) number of Fe per particle (n_{Fe}) as a function of the logarithm of the ageing time for Fh produced and aged at 20 °C in a solution with 0.2 M $NaNO_3$, 19 mM MOPS, and 19 mM MES with pH values as indicated. The lines have been calculated with the dynamic simulation model presented and discussed using Equation 3.9 as rate law with $\log k_0$ = 4.80 ($m^{-2}\ s^{-1}$) or $\log k_0$ = -9.58 (μmol $m^{-2}\ s^{-1}$) and a = -0.5. The arrow at the x-axis indicates the ageing time of 4 hours that is often used in ion adsorption experiments with Fh.

3.3.4. Rate of growth

To get insight into the process of growth during Ostwald ripening, the collected data require rescaling to reveal the rate of growth that allows deriving the underlying rate law. During particle growth, there is a flux of Fe towards the surface. This flux (mol h^{-1}) can be expressed per unit surface area (mol $m^{-2}\ h^{-1}$). To do this scaling, the data have been described with a mathematical trial function that can excellently depict the evolution of the particle size (d) with time of ageing (t). The equation used is $d = a\ t^{1/n} + d_o$ in which the parameters a, d_o, and $1/n$ are derived by fitting. This can be done conveniently by plotting

the diameter d against the time parameter ($t^{1/n}$), evaluating linearity by searching for the best value of the exponent $1/n$ (Figure S3.3). The regression coefficients obtained are very high ($R^2 \geq 0.99$), *i.e.* this linear relationship describes the time dependency very well.

The parameterized trial functions can be used to calculate the rate of growth at the various times of ageing by taking the derivative ($\partial d/\partial t$) that also allows the calculation of the change of the number of Fe per particle (n_{Fe}) with time ($\partial n_{Fe}/\partial t$). By scaling to the corresponding surface area (m^2) of the particle ($A_{\#} = \pi d^2$), one derives the rate of growth R expressed as the number of Fe ions that become attached per unit surface area and time *i.e.* $R = (\partial n_{Fe}/\partial t) / A_{\#}$ with the unit μmol m^{-2} h^{-1}. At each reaction time, it represents the Fe-flux towards one unit of surface area. This rate of particle growth R is shown in Figure 3.4 as a function of time for the various systems studied.

3.3.5. Rate limiting step

It is obvious from Figure 3.4 that the rate of growth R is not constant. Initially, it is around 3–10 μmol m^{-2} h^{-1} but decreases dramatically by nearly three orders of magnitude during the course of the experiment. At the highest measured rates, the particles grow with less than one monolayer of Fe polyhedra per hour, as the Fe density of the Fh surfaces is 15–20 μmol m^{-2} (Figure S3.4). However, our dynamic model suggests significantly higher rates immediately after the formation of the initial, yet non-aged, particles (scale of seconds).

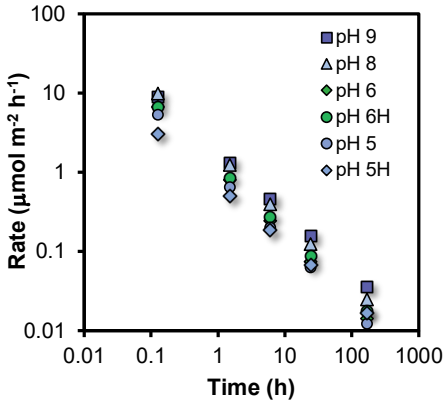

Figure 3.4. Development of rate of growth R with time for the Fh materials prepared and aged (20 ºC) at the various pH values indicated. The rate of Fe growth continuously decreases and changes by nearly three orders of magnitude for the time range studied. The change of the rate of growth is very similar for the Fh systems of different pH. For the systems pH5H and pH6H, the results have been obtained using a 10-fold higher PO_4 addition to measure the surface area.

As mentioned, the Fe-flux towards the surface becomes substantially less with time. Considering the process of growth as a chemical reaction of Fe in solution with specific reactive surface sites, the decrease of the rate of growth suggests that the solution concentration of Fe is considerably changing since the reactive site density can be seen as an intrinsic surface property of Fh.

At a given pH, the concentration of Fe in solution will be a function of the solubility product of Fh (Q_{so}). The solubility of nanoparticles is enhanced relatively to the intrinsic solubility of the bulk material (K_{so}). In a suspension with a given particle size distribution, the solubility is determined by a labile equilibrium between Fe in solution and particles in the critical state having the highest Gibbs free

energy.[29] All particles larger than the critical ones will have a lower chemical potential, a higher stability, and consequently, a lower solubility. For this reason, the vast majority of particles will grow, which will be at the expense of the smallest particles that dissolve in an attempt to maintain the solution concentration. This is the driving force for Ostwald ripening. The rate-limiting step of growth is the binding of Fe to the surface because the rate of dissolution of the smallest particles is sufficiently high to maintain an equilibrium concentration in the solution.

The solubility of the critical nuclei of Fh with a surface area A_{crit} (m^2 g^{-1}) can be described with the Ostwald-Freundlich equation, according to:

$$RT \ln \frac{Q_{so}}{K_{so}} = \frac{2}{3} M_{\mathrm{nano}} \gamma A_{\mathrm{crit}} \qquad \text{(Equation 3.6)}$$

in which Q_{so} is the activity product that we define as $Q_{so}= (Fe^{3+}) (OH^-)^3$ and K_{so} is the corresponding intrinsic value for the virtual bulk, being log K_{so} = -40.6 ± 0.2 (ref [29]) in agreement with calculations of Pinney et al.[65] Furthermore, M_{nano} is the molar mass (Equation 3.1), R is the gas constant, and T is the absolute temperature. For Fh, the surface Gibbs free energy γ (J m^{-2}) has recently been derived by Hiemstra[29] interpreting a set of thermochemical data of Majzlan et al.[66] and Snow et al.[67] The value of the surface Gibbs free energy is exceptionally low (γ = 0.186 ± 0.01 J m^{-2}) compared to the values for all other Fe (hydr)oxides.[68] It indicates that the surface of Fh has a relatively high stability, which can be explained by the absence of unstable Fe2 and Fe3 polyhedra at the surface according to the surface depletion model.[29] We assume that the value of γ is particle size independent, based on recent results obtained from silver nanoparticles.[69]

As follows from TEM data,[40,58] freshly prepared Fh has a particle size distribution in which the mean and minimum particle sizes are linearly correlated.[29] Introducing the ratio $\phi \equiv A_{\mathrm{crit}} / A_{\mathrm{mean}}$ between the specific surface area of the measurable mean (A_{mean}) and critical (A_{crit}) particle (m^2 g^{-1}), the Ostwald-Freundlich equation can be rewritten to:

$$RT \ln \frac{Q_{so}}{K_{so}} = \frac{2}{3} \phi M_{\mathrm{nano}} \gamma A_{\mathrm{mean}} \qquad \text{(Equation 3.7)}$$

Equation 3.7 shows that the super saturation of a solution relatively to the bulk material of infinite size (Q_{so}/K_{so}) is related to the specific surface area of Fh material (A_{mean}). This relation will be used in our derivation of the rate law of particle growth at Ostwald ripening. Analysis of the TEM data of Michel et al.[40] reveals a factor ϕ = 3/2.[29] The same conclusion follows from the data of Burrows et al.[58] Introducing this information (ϕ= 3/2) in the above Ostwald-Freundlich equation (Equation 3.7) leads to an equation without the factor 2/3 ϕ, known as the Ostwald equation.[29]

3.3.6. Rate law

As pointed out above, the process of growth can be considered as the attachment of dissolved Fe to reactive sites at the surface of Fh having a certain Fe-reactive site density N_r (mol m^{-2}). Since the solubility of Fh can be related to the mean specific surface area A (Equation 3.7), a relation between the rate of growth R and the ratio for super saturation Q_{so}/K_{so} is expected. In Figure 3.5, the growth rate R has been related to Q_{so}/K_{so} by plotting both on a logarithmic scale. The data for pH 7 have been omitted in this part of the analysis, because the time scale of the measurement is too limited due to the absence of data for short ageing times.

Figure 3.5a shows that the rate of growth varies with the super saturation of the solution (Q_{so}/K_{so}). Initially, the super saturation is typically ~1.000–10.000 (log Q_{so}/K_{so} = 3–4). After a few minutes of ageing, the mean size is 1.8 ± 0.1 nm and the corresponding solubility is about logQ_{so} ~ -37.2 ± 0.3, which matches within the uncertainties with the solubility (logQ_{so} ~ -37.5 ± 0.1) at rapid titration of Fe(II)/Fe(III) solution with NaOH in $NaClO_4$, back calculated to pH=PZC from the measured free [Fe^{3+}] concentration.[70]

The data in Figure 3.5a reveal a mean slope of s = 1.97 ± 0.18, which implies that within the uncertainty, the rate of growth R (µmol m^{-2} h^{-1}) is proportional to the square of the super saturation (Q_{so}/K_{so}). Therefore, the rate can be described with the conceptual equation:

$$R = k_r N_r \left(\frac{Q_{so}}{K_{so}}\right)^2 \equiv k \left(\frac{Q_{so}}{K_{so}}\right)^2 \qquad \text{(Equation 3.8)}$$

in which k_r is a reaction constant (h^{-1}) and N_r is the Fe-reactive site density of the surface (µmol m^{-2}). The precise value of the latter is unknown and therefore, it is combined with k_r to the pre-factor k (µmol m^{-2} h^{-1}).

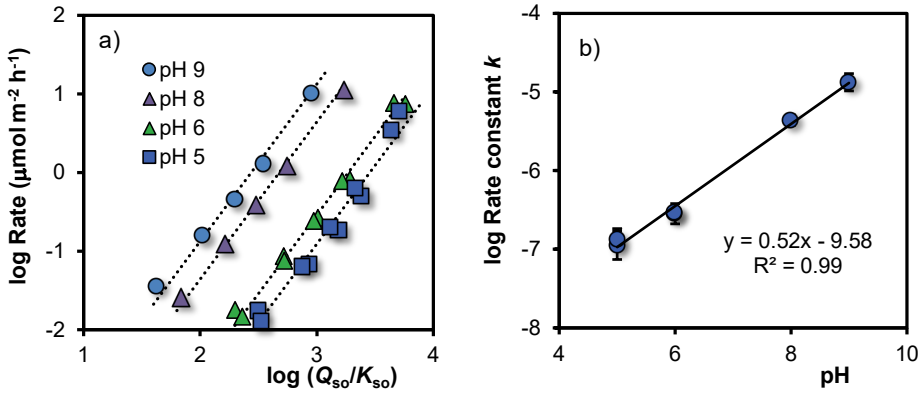

Figure 3.5. a) Logarithm of the rate of growth R (µmol m^{-2} h^{-1}) as a function of the logarithm of the super saturation of the solution (Q_{so}/K_{so}) for Fh in 0.2 M $NaNO_3$ buffered with 19 mM MES and 19 mM MOPS at the given pH values (T = 20 ºC). The slopes of the calculated lines (s) have been set to s = 2. The intercept at log(Q_{so}/K_{so}) = 0 equals the logarithm of the rate constant (log$k$), which is plotted in Figure 3.5 b) against the pH, revealing the pH dependency of log$k$ (Equation 3.8) with k in µmol m^{-2} h^{-1}.

The observation of a quadratic relation between rate and solubility can be interpreted as rate limitation by a site binding reaction of two Fe with one site (S + 2 Fe ⇨ SFe_2). The rate-limiting step is the simultaneous attachment of two Fe species forming together a stable surface complex. The value of 2 for the exponent of Q_{so}/K_{so} expresses the chance that two Fe species occupy simultaneous a single site of growth, resulting in a stable complex. If only one monomeric Fe species is attached, it may be labile and desorb again in dynamic events, while the binding of two Fe ions, *i.e.* formation of an adsorbed Fe-dimer, may be irreversibly. Possibly, the formation of the adsorbed Fe-dimer is *via* the attachment of individual Fe-monomers since aqueous Fe-dimers are typically formed at high total Fe-concentrations present in systems with very acidic conditions (pH~2), as confirmed experimentally.[49,50]

In Figure 3.5a, the intercept at the y-axis is equal to log$k$ of Equation 3.8. That intercept is pH dependent. The pH dependency of log$k$ can be revealed by plotting its value versus pH (Figure 3.5b). To reduce the interrelation between the intercept value and the slope (s) of the lines in Figure 3.5a, the

latter has been fixed to $s \equiv 2$. Incorporating the obtained pH dependency of the rate constant, we can rewrite Equation (8) to:

$$R = k_0 \, (\mathrm{H^+})^a \left(\frac{Q_{so}}{K_{so}}\right)^2 \qquad \text{(Equation 3.9)}$$

in which k_0 is a pH-independent rate constant and the exponent a determines the dependency of the growth rate R on the proton activity (H^+). The data of Figure 3.5b suggest $a = -0.5$.

3.3.7. Dynamic modelling

The above-derived rate law for Ostwald ripening of primary Fh particles in a suspension can be applied in dynamic modelling by defining a flux of Fe towards the surface of an Fh nanoparticle of certain mean size (d) and surface area of $A_\# = \pi d^2$. The Fe flux F (mol h^{-1}) can be related to the rate of surface growth of the particle R (mol m^{-2} h^{-1}), according to:

$$F = R \, A_\# \qquad \text{(Equation 3.10)}$$

in which the surface area $A_\#$ has the unit m^2. In our dynamic model, the rate of growth R is described with the rate law (Equation 3.9) that has been derived with the above data analysis (Figure 3.5). The results of these simulations are shown in Figure 3.3 with lines.

At each (small) time step (Δt) in the modelling, the total number of Fe in the particle (n_{Fe}) has been calculated according to $n_{Fe} = n_{Fe(t=0)} + \Sigma \, \Delta n_{Fe}/\Delta t$. Additionally, a corresponding set of related parameters was calculated, *i.e.* the molar mass M_{nano} (g mol^{-1}), mass density ρ_{nano} (g m^{-3}), diameter d (m), particle surface area $A_\#$ (m^2), and the specific surface area $A_{mean} = N_{Av}/(n_{Fe} \, M_{nano})$ $A_\#$ (m^2 g^{-1}). Combining the latter with the surface Gibbs free energy γ (J m^{-2}) and molar mass M_{nano} (g mol^{-1}) allows the calculation (Equation 3.7) of the relative solubility Q_{so}/K_{so} ($\phi = 3/2$), which is subsequently applied in the rate equation (Equation 3.9) to find $\Delta n_{Fe}/\Delta t$ before calculating the next time step.

In the modelling approach, the initial particle size at $t = 0$ is an adjustable parameter. Application of the model shows that we can describe the evolution of the size and specific surface area of the particles using a single value for the number of Fe present in the initial particle, independent of the pH. The data indicate that the non-aged particle (made at room temperature) has an equivalent spherical size of $d \sim$ 1.68 nm and a corresponding Fe content of $n_{Fe} \sim 45$. One may construct such a representative particle by linking two Fe_{13} moieties and extend it with attaching additionally Fe polyhedra in accordance to the surface depletion model as given in Figure S3.5.

For different pH values, we find at the first sampling point ($t = 0.1$ h) a significant difference with the calculated initial size at $t = 0$. At pH=9, $n_{Fe} \sim 80$, while for pH = 5, $n_{Fe} \sim 50$ for t =0.1 h. The reason for this difference is the variation in the rate of growth. The model curves in Figure 3.3c show that practically no difference exits in the calculated number of Fe per particle (n_{Fe}) at the typically time scale of about a second. This is also the time scale of physical mixing of the Fe(III) and base solution in the flow chamber. The differences in size observed at the first sampling point, a few minutes after the formation, are due to differences in rate of growth by Ostwald ripening, being relatively high at pH 9 and low at pH 5. We note that the data for the first sampling point at $t = 0.1$ h are potentially affected by the kinetics of the adsorption of PO_4. However, one may expect that the added PO_4 will promptly stop the ageing process when adsorbed, even though full equilibration[2] may take more time.

Visual inspection of the process of formation in a flow chamber and connected tubing system shows a rapid change in colour from pale-yellow to a yellow-brown upon mixing of the reactants. In the next

seconds, the transparency changes and one starts to observe the formation of aggregated, reddish-brown Fe (hydr)oxide that contains micro-aggregates with a size of about 50 nm or larger.[48,60,71] Formation of loose flocs (~mm) in the tubing system is nearly completed in less than 30 seconds. These observations illustrate the ultra-high speed of the formation reaction of Fh and the subsequent very fast physical process of aggregation and floc formation.

3.3.8. Ageing of transitionally synthesized Ferrihydrite

Above, we find that flash neutralization of Fe(III) in a pH-buffered solution leads to the synthesis of relatively small particles that reach a specific surface area of 750–950 $m^2 g^{-1}$ after ageing for 4 hours (Figure 3.3a). These values are significantly higher than the typical values of 550–710 $m^2 g^{-1}$ found with the classical synthesis of two-line Fh (2LFh) described in literature.[27] This difference is an important motivation to extend our work by including Fh synthesized with the traditional approach of Fe(III) neutralization.

To extend the lifetime of freshly prepared 2LFh, researchers have stored their suspensions at low temperature in a refrigerator. Therefore, we have also studied the ageing at 4 °C to derive the temperature dependency of the particle growth. Our results refer to a single 2LFh material made by neutralizing a 3.3 mM Fe(III) nitrate solution with a 0.02 M NaOH solution to a pH value of pH 6.0 or 8.2 and an initial ageing for 4 hours since neutralization. After sampling, the ageing was continued at temperatures of either 4 °C or 20 °C. The experimental results are shown in Figure 3.6.

Analysis of the data of particle growth at pH 8.2 along the same lines as presented above (Figure 3.5) revealed that the rate dependency of the particle growth is basically the same as in the systems of Figure 3.3, in the sense that the exponent for the dependency on the solubility is the same, *i.e.* $R \propto (Q_{so}/K_{so})^2$. It strongly suggests that the ageing process has the same rate-limiting step as found above, *i.e.* a dual attachment of Fe.

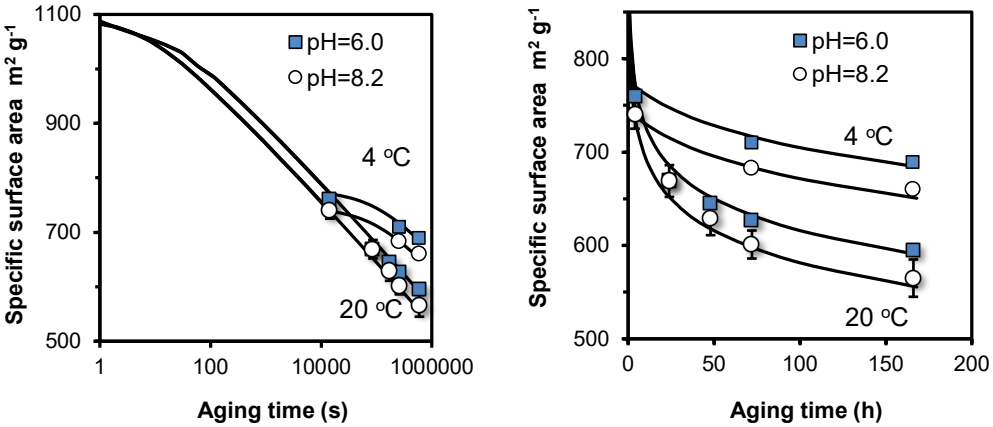

Figure 3.6. Time dependency of the specific surface area ($m^2 g^{-1}$) for traditionally synthesized Fh, aged in 0.01 M $NaNO_3$ in the absence organic pH buffers. After synthesis at pH 6.0 or 8.2, the Fh materials were aged for 4 hours since neutralization before a first sample was taken. The remaining suspensions were split and further aged at either 4 °C or 20 ° C. The lines have been calculated with the model (Equation 3.8), only adjusting the rate constant k. At 20 ° C, $\log k$ = 9.25 (pH=8.2) and 9.00 (pH=6), and at 4 ° C, $\log k$ = 8.35 (pH=8.2) and 8.10 (pH=6) with k in Fe per m^2 per second. Subtracting a value of 14.22 from these $\log k$ values gives $\log k$ in the unit μmol $m^{-2} s^{-1}$.

When the dynamic model was applied, we found that we can use the same value for the initial size of the non-aged primary Fh particles (n_{Fe} = 45) as in the experiments with the formation of Fh in the flow chamber in the presence of organic pH buffers. However, a somewhat higher value is also possible as our data only refer to a relatively long time of ageing (≥ 4 h), making the approach less sensitive to pinpointing the precise initial value at t=0. This is illustrated in Figure S3.6, showing that an increase of the initial size hardly affects the particle size at a longer time of ageing (> day). The modelling of Figure S3.6 also shows that it is difficult to grow Fh particles to sizes larger than ~3–4 nm by the process of Ostwald ripening at room temperature and circumneutral pH values. However, additionally growth will occur by oriented attachment.[31]

3.3.9. Evolution of ferrihydrite according to TEM

The growth of Fh can also be studied by directly observing the change in particle size with TEM. This was done by Burleson and Penn[31] studying the ageing of Fh for 20–2000 h as a function of temperature (60, 90, and 120 ºC) and pH. The initial Fh sample was prepared by neutralizing a Fe(III) solution with $NaHCO_3$, followed by dialysis at 4 ºC during 5 days with a final pH of ~ 3.5. The created particles have a mean diameter of 3.0 nm (Black square in Fig. 7a) and will contain about 360 Fe.

The TEM data of Burleson and Penn[31] show the simultaneous presence of relatively small primary particles as well as larger particles with another aspect ratio (~5) that have formed by oriented attachment, particularly at pH ~10–12. However, the data in Figure 3.7a refer only to the growth of the fraction of primary particles. The other particles have been excluded and were evaluated differently by Burleson and Penn.[31] With increase of temperature, the rate of growth of the primary particles increases. Despite the high temperature, the Ostwald ripening of these particles is still relatively slow. At 120 ºC, the mean diameter increases with only ~1–1.5 nm in one day.

Fh particles can also grow by oriented attachment.[31] This typically occurs at high temperature, similarly as found for ZnS.[34] Oriented attachment of Fh may occur once the particle size of Fh is large enough to develop preferred crystal faces. Ferrihydrite, hydrothermally aged at 175 ºC,[40] shows a rapid near-doubling of the mean particle size as soon as the particles reach a mean size of about 3.5–4 nm.[33] Simultaneously, the magnetic saturation becomes less than expected for defect free Fh,[33] which suggests imperfect attachments. Upon further hydrothermal ageing, the reduction of the magnetic saturation (*i.e.* defects) gradually disappears, signifying completion of the particle fusion. These particles are large enough (~ 8 nm [29]) to transform into hematite.[40]

The TEM data (symbols) of Figure 3.7a have been described with our kinetic model (lines) by only adjusting the rate constant k of Equation 3.8 while using the reported experimentally value (3 nm) as initial particle size. These rate constants have been given as open squares in Fig. 7b as a function of the inverse of the temperature ($1/T$). The k value is given in the unit $m^{-2}\ s^{-1}$ but can be expressed in $\mu mol\ m^{-2}\ h^{-1}$ using Avogadro's number and 1 h = 3600 s. The blue spheres in Figure 3.7b refer to the log$k$ values obtained from our data collected at the same pH (pH = 6) in 0.01 M $NaNO_3$.

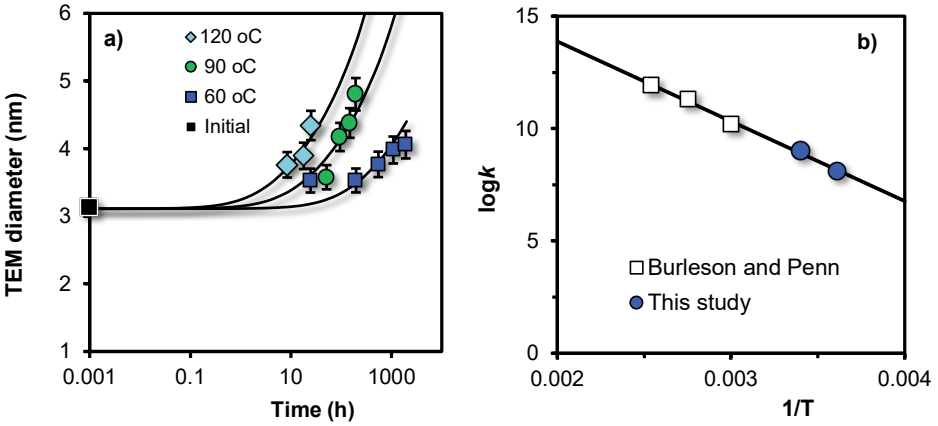

Figure 3.7. a) Time dependency of the mean size of primary particles in Fh suspensions, measured with TEM at pH=6 by Burleson and Penn.[31] for different temperatures (symbols). The data only refer to the fraction of primary particles in the suspension, excluding the particles that formed by oriented particle attachment. The k value (Equation 3.8) in Figure 3.7b) is given in the unit Fe per m^2 per second. The slope of the line is equivalent to an activation energy of E_{act} = 68 ± 4 kJ mol^{-1} (see text).

3.3.10. Temperature dependency

The temperature dependency of the rate constants k obtained by modelling (Figure 3.7b) can be described with the classical Arrhenius equation:

$$k = A\, e^{-E_{act}/RT} \qquad \text{(Equation 3.11)}$$

in which A is a pre-exponential factor related to the frequency and E_{act} is the energy of activation (J mol^{-1}). If applied to the overall rate constant k for particle growth of Fh at pH = 6 (Figure 3.7b), assuming no other factors of temperature dependency, it provides an apparent energy of activation of E_{act} = 68 ± 4 kJ mol^{-1}. This activation energy is of the same order as found in literature for the conversion of Fh to goethite (52 ± 4 kJ mol^{-1}) at high pH (12) and the dissolution of various Fe oxides in hydrochloric acid (67–94 kJ mol^{-1}) as summarized by Cornell and Schwertmann.[28] Growth by oriented attachment is more temperature dependent than growth by Ostwald ripening, *i.e.* has a higher activation energy,[34] and ion diffusion in water is less temperature dependent.

3.3.11. Time dependency

Burleson and Penn[31] have previously used the classical model of Lifshitz and Slyozov[72] to evaluate the growth of the primary Fh particles. In that model, the rate of growth is limited by the diffusion of Fe between the free solution and particle surface. In the model, the Ostwald-Freundlich equation is linearized which is increasingly justified for systems with little supersaturation (Figure S3.7). For a polydisperse system, Lifshitz and Slyozov[72] derived that the particle volume increases linearly with time ($\Delta V_{mean} \propto t$). This increase is equivalent to a time-dependent change of the particle diameter according to $\Delta d \propto t^{1/3}$. However, our data do not show this time dependency. It can be shown that the growth of Fh is likely not limited by diffusion across the solid-solution interface (Figure S3.8, Table S3.1). The process is much slower.

For a polydisperse system, Wagner[73] derived a time dependency of the mean size of $\Delta d \propto t^{1/2}$ if the growth is limited by a chemical reaction that is first order in concentration (c^1). In case of a surface

reaction that is second order with respect to the concentration (c^2), the rate will be more time-dependent. Our data analysis and model suggest $\Delta d \propto t^{1/n}$ with $n = 3.9 \pm 0.7$ (Figure S3.3), *i.e.* approximately $\Delta d \propto t^{1/4}$. Remarkably, the theoretical growth of lens-shaped particles at the boundary between two matrices may exhibit the same time dependency,[74] indicating that time dependency should be interpreted with care.[34]

Six-line Fh (6LFh) can be made by forced hydrolysis at 75 °C in about 10–12 minutes[25] without base addition. It leads to particles with a size of ~ 5.5 nm according to TEM[57] and SAXS.[59] If formed by prompt adsorption of Fe to Fe_{13} nuclei, about 7 ± 1 monolayers of Fe polyhedra are needed (Figure S3.4). This assumption implies less nucleation in the solution than at the formation of 2LFh by Fe(III) neutralization with base at room temperature. The 6LFh particles with $d = 5.5$ nm typically contain n_{Fe} ~ 2600 Fe. Further growth by classical Ostwald ripening will be little at room temperature according to our model (Figure S3.9). This is due to the very low solubility and super saturation ($\log Q_{so}/K_{so} \sim 0.6$) of the solution. Indeed, no ageing occurs during storage for months at room temperature, according to SAXS.[59] Apparently, oriented attachment or particle fusion does not play a significant role in that case.

3.3.12. pH dependency

The logarithms of the rate constants, log*k* (Equation 3.8), for Fh aged in the absence and presence of organic pH buffers are compared in Figure 3.8. At low pH, the rate constants for growth are much lower in the presence of organic pH buffers (MES and MOPS), resulting in a larger pH-dependency. At low pH, the rates constants are strongly reduced compared to Fh systems without these organics. It suggests that at low pH the organic molecules are present at the surface, hindering the process of Fe adsorption. The interaction of these organic molecules with the surface will be relatively weak since these ions do not influence the adsorption of PO_4 at the concentration scales studied.[51] These organic molecules are negatively charged in the pH range studied (at 20 °C and $I = 0.1$ M, $\log K_H = 6.16$ for MES add $\log K_H = 7.17$ for MOPS) and may interact by electrostatic forces with the positively charged surface groups at a pH below the value of the PZC (~8.2). At higher pH, the interaction will largely disappear leading to the same rates as in the pure Fh systems.

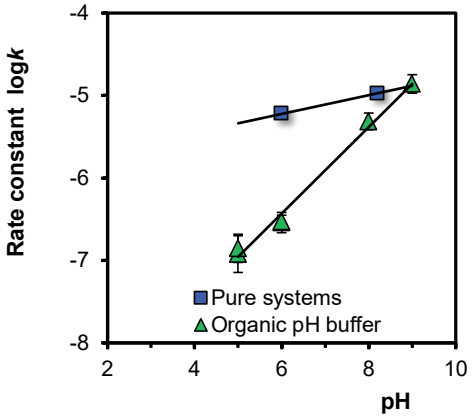

Figure 3.8. pH dependency of the rate constant of growth of Fh at 20 °C (log*k* of Equation 3.8 with *k* in μmol m^{-2} h^{-1}) in the absence (squares) and presence (triangles) of an organic pH buffer solution. In the latter case, the rate is strongly reduced at low pH, which can be explained by a weak interaction of the organic molecules with the surface.

3.3.13. Role of organic matter and anions

The above indicates that any disturbance of the Fe attachment by the presence of organic molecules may highly reduce the rate of transformation. As organic matter is readily available in nature, it implies that Fh particles may have significantly lower rates of transformation in the natural environment. This will contribute to the nano-character of the natural iron oxide fraction of many top soils.[75] The primary iron and aluminium (hydr)oxide particles remain ultra-small, and are embedded in and/or covered by organic matter, since for the soils a good correlation is found between the reactive oxide surface area and the organic matter content.[75]

As oxyanions may also interfere in the formation of Fh,[44] primary particles may remain small if these anions adsorb.[2] For instance, the adsorption of Si reduces the coherent length of scattering of Fh.[76] This explains the small size (2 nm) of siliceous Fh particles produced in drinking water facilities at aeration of groundwater with Fe(II).[27] Interference of oxyanions may also explain the small size of 2LFh (pH = 8) prepared in the presence of $As(OH)_3$.[60] The characterization with SAXS suggested a size near 2 × (0.8 + 0.2) = ~2 nm.[60] Such particles will have a surface area of ~850 m^2 g^{-1}. According to our model (Fig.6), this would require ageing for ~0.5 hours while the particles were aged for 24 h. The difference may be due to the adsorption of $As(OH)_3$, suppressing the rate of ageing.

In literature,[51] Fh has been prepared and aged in the presence of Cl as major anion. The measured growth is very different from the growth observed in systems with NO_3 as major anion, as shown in Figure 3.9 (squared colored symbols). Initially, the particles have nearly the same size in both systems. Shortly later, the time dependency of growth becomes very different. In $NaNO_3$, the rate of growth on a volume basis decreases continuously, while in NaCl the volume or number of Fe per particle (n_{Fe}) increases linearly with time.[2] This linearity is typical for a diffusion-controlled growth in systems with little super saturation, as derived by Lifshitz and Slyozov,[72] resulting in $\Delta V \propto t$ or $n_{Fe} \propto t$.

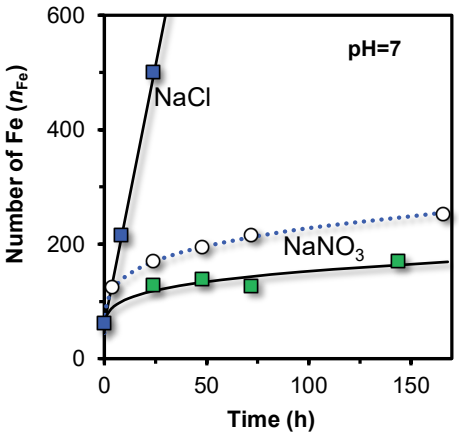

Figure 3.9. Ageing of ultra-fast synthesized Fe (hydr)oxide in 0.1 M NaCl[51] and 0.1 M $NaNO_3$ (present study) at pH=7 in the presence of organic pH buffers (squares). The reaction pathways start to deviate significantly after ~4 hours of ageing. In NaCl, the number of Fe per particle (volume) increases linearly with time while it is non-linear in $NaNO_3$. The open symbols and dotted line are for Fh aged in 0.01 M $NaNO_3$ at pH 7 in the absence of organic pH buffers, derived by interpolation of the data collected at pH 6.0 and pH 8.2 (Figure 3.6).

The data in Figure 3.9 illustrate that the reaction pathways followed in NaCl and $NaNO_3$ are very different. In Cl systems, akaganéite (β-FeOOH.*x*HCl) may form as found by X-ray diffraction[77] and with HRTEM.[78] This mineral has internal sites occupied with Cl ions, given rise to a Cl/Fe ratio of x ~ 0.15-0.19.[79,80] One may expect that such internal sites are still relatively unimportant in the initial particles from which akaganéite is formed because initially, most Fe is part of the surface and little is part of the bulk.

3.4. Conclusions

Fh is thermodynamically unstable and will ultimately transform into a more stable Fe (hydr)oxide. When initially formed, the particles are ultra-small and subject to Oswald ripening in which the smallest particles dissolve and the larger ones grow, resulting in a decrease of the reactive surface area. In the present study this pH, temperature, and time-dependent process has been probed using PO_4. We show how the time-dependent change of the surface area can be translated into the rate of growth per unit surface area (μmol Fe m^{-2} h^{-1}). In all calculations, we have accounted for the size dependency of molar mass and mass density that is the result of a variable contribution of coordinated surface water (n) in excess to the bulk composition ($FeO_{1.4}(OH)_{0.2}{\cdot}nH_2O$).

The rate of growth R is highly time-dependent and decreases by nearly three orders of magnitude at ageing from a few minutes to one week. It varies between $R \sim 0.01$–10 μmol m^{-2} h^{-1}. These rates can be considered as low because particle growth of Fh by a monolayer of Fe polyhedra requires 15–20 μmol m^2, *i.e.* hours or days are needed to grow a single monolayer at room temperature. Additionally, we showed that the rate of growth of Fh is too low to be limited by a diffusion flux across the solid-solution interface.

Our data only refer to primary particles (d = 1.7–2.9 nm) for which we show that the rate of growth is related to the solubility of Fh. The data analysis reveals that the rate of growth is proportional to the square of the super saturation of the solution, expressed in the ratio of the solubility product of the actual particle (Q_{so}) and the virtual bulk (K_{so}). In our analysis, the size dependency of the solubility and super saturation is calculated using the surface Gibbs free energy of Fh (γ = 0.186 J m^{-2}) that is implemented in the Ostwald-Freundlich equation accounting for the difference in surface area of the critical and mean particle (ϕ = 3/2). The squared proportionality of the super saturation in the rate law can be interpreted as a rate limitation by a chemical reaction with dual attachment of Fe to a single site of growth (S + 2 Fe ⇨ SFe_2). The time dependency of the change of the diameter is close to $\Delta d \propto t^{1/4}$ for model and data.

The rate constant for the process of growth is pH dependent. The presence of organic pH buffers reduces the rate constant for Ostwald ripening at low pH by a factor 10 or more, but its effect disappears at high pH, which is explained by the variable interference of the organic molecules in the Fe attachment. Interference will be enhanced if Fh is covered by natural organic matter and consequently, organic matter contributes to the kinetic stability of Fh in soils.

Application of our dynamic model for particle growth discloses the initial size of non-aged Fh particles of $d \sim 1.68$ nm and the corresponding specific surface area of $A \sim 1100$ m^2 g^{-1}. These particles formed at room temperature contain on average ~ 45 Fe. Dynamic modelling further shows that the growth of the primary particles by Ostwald ripening is usually limited to a size of ~ 3.5–4 nm ($A \sim 350$–500 m^2 g^{-1}). Additional growth will be by (oriented) particle attachment at the onset of the formation of crystal faces. This is typically observed at ageing in high temperature systems, particularly at high pH.

If 6LFh is produced with the classical method of forced hydrolysis at 75 °C, the initial particles are significantly larger (~ 5.5 nm). According to our model, Ostwald ripening becomes little because these particles have a relatively low solubility.

Combining various data for growth of primary Fh particles at pH = 6, collected with TEM and PO_4 probing, reveals an activation energy of $E_a = 68 \pm 4$ kJ mol^{-1} for the growth by Ostwald ripening, which will be lower than that for growth by oriented attachment.

The reaction pathway of Ostwald ripening in NaCl is very different from that in $NaNO_3$. In NaCl, the particle volume increases linearly with time while in $NaNO_3$, it is clearly non-linear. In NaCl, akaganéite may start to form according to evidence obtained by X-ray diffraction.

Acknowledgements

We grateful acknowledge the modelling contributions of Imtiaz Miah. Part of this project has been funded by a grant provided by the University of Costa Rica (UCR) and by NanoNextNL (FES 5120756-02), both being gratefully acknowledged.

Supplementary Information

A. Flow chamber design

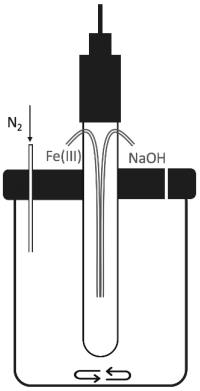

Figure S3.1. Experimental setup for mixing a Fe nitrate and Na hydroxide solution added with motor burets. The tips, where mixing occurs, is mounted about halfway on a pH electrode hanging in a vessel that is kept under N_2 atmosphere. This allows continuous pH-recording of the mixed solution, passing the glass membrane before it flows into the vessel where it is stirred magnetically. The pH-recording allows the setting of the rate of the NaOH addition at a constant rate (8 mL min^{-1}) of the Fe nitrate addition, keeping the pH value about 0.5-1.0 pH unit below the final target value. Progressively, the vessel gets filled and the recorded pH then refers to the suspension as a whole that is subsequently increased to the final pH once the addition of partially neutralized Fe-nitrate solution has stopped (~3 minutes). The final NaOH addition to reach the target pH value is done at a lower speed.

B. Size-dependent Stern layer capacitances and adsorption

Primary charge

The capacitance of a spherical capacitor ($C_{1,r}$) can be given as:

$$C_{1,r} = \frac{r+\Delta r}{r} C_1 \quad \text{(Equation S3.1)}$$

in which r is the inner radius of the sphere and Δr the thickness of the layer.

In case of an Extended Stern (ES) layer model[81] with two Stern layers, a value of Δr_1 = 0.35 nm is used to calculate the inner Stern layer capacitance from C_1 of a flat layer at a given particle radius r.

The capacitance of the second spherical Stern layer ($C_{2,r}$) is found with:

$$C_{2,r} = \frac{r+\Delta r_1+\Delta r_2}{r+\Delta r_1} C_2 \quad \text{(Equation S3.2)}$$

using Δr_2 = 0.35 nm as derived for the compact double layer with a total thickness of 0.7 nm, equivalent with the packed size of nearly three water molecules.[81] In the calculation, C_2 is the capacitance of the outer Stern layer of a flat layer.

For Fh, the Stern layer capacitance values for the flat layer ($r \rightarrow \infty$) have been set equal to the numbers found for well-crystallized goethite, *i.e.* C_1 = 0.9 F m^{-2} and C_2 = 0.74 F m^{-2}.[81] For 2LFh, the typical capacitance values with a diameter of ~2.5 nm are C_1 = 1.15 F m^{-2} and C_2 = 0.90 F m^{-2}.[2] These values

are very different from the values given by Antelo et al.,[52,55] *i.e.* C_1= 0.74 F m^{-2} and C_2 = 0.93 F m^{-2}. The much lower value for C_1 indicates a lower surface charge density.

Phosphate adsorption and curvature

The effect of the surface curvature on the PO_4 adsorption at a given pH and PO_4 equilibrium concentration is shown in Figure S3.2 (left panel). At decrease of the particle size, the electrostatic effects decrease. The reduction of the field strength allows the adsorption of more ions. The field becomes less limiting. In case of a constant PO_4 loading (right panel), the increase of the capacitance at decrease of the particle size will lead to a lower equilibrium concentration of phosphate.

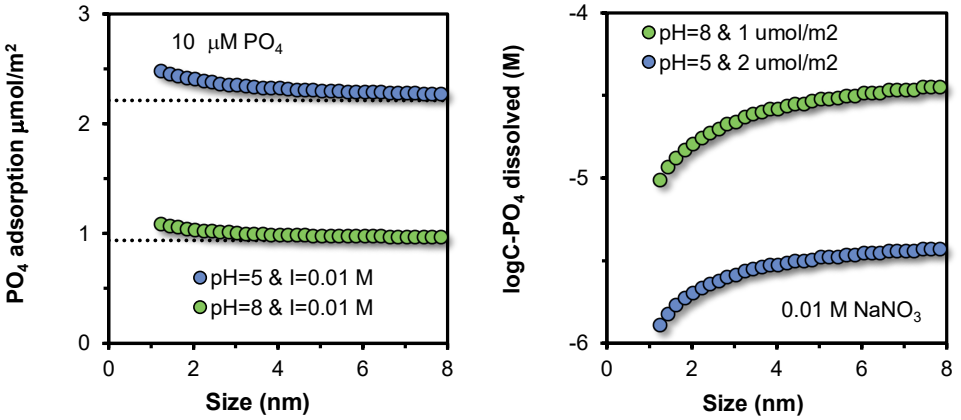

Figure S3.2. Left panel. Adsorption of phosphate as a function of particle size, in case of spherical Stern layers (ES model) for Fh at the conditions given. The adsorption increases by ~10% or less compared to the adsorption at a flat surface. A similar size dependency of the adsorption due to a variable capacity has been illustrated in Hiemstra and Zhao.[2] Right panel. Logarithm of the equilibrium concentration of PO_4 at a constant surface loading (1 and 2 µmol PO_4 m^{-2} at respectively pH=8 and pH=5 in 0.01 M $NaNO_3$). The equilibrium concentration decreases substantially.

C. Deriving the rate of growth *R* (mol m^{-2} h^{-1})

Time-dependency of the particle size

For obtaining the experimental rate of growth *R*, the function

$$d = kt^{1/n} + d_o \qquad \text{(Equation S3.3)}$$

has been used in the data analysis (Figure S3.3). Equation SI–3.3 is a general equation for describing the growth of particles with different theories and mechanisms.[34] The value of exponent *n* depends on the rate limitation and conditions assumed. At crystal growth controlled by diffusion of ions across the solid-solution interface, *n* is equal to the value *n* = 3. In that case, the volume ($V \propto d^3$) increases linearly with the ageing time *t* as derived by Lifshitz and Slyozov,[72] and Wagner.[73] However, our data for ageing of Fh in a $NaNO_3$ solution show a non-linear relation of the volume *V* with time. For Fh, the process of growth has another time dependency. The growth decreases more quickly with time.

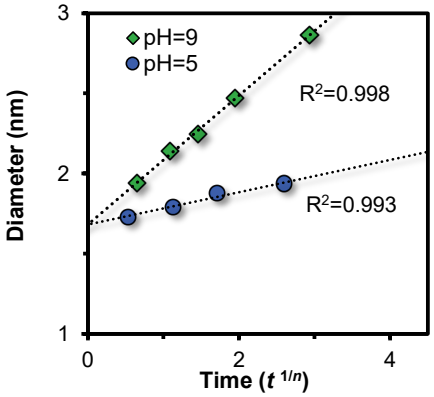

Figure S3.3. Particle diameter (d) related to a power function of time ($t^{1/n}$) for ageing at pH 5 and 9. For each pH, the best value of the exponent $1/n$ of the time (h) is optimized to get the best description with a linear function $d = k\, t^{1/n} + d_o$, in which d_o is the diameter at $t = 0$.

In the pH range 5–9, the fitted value of exponent $1/n$ equals 0.21 ± 0.06 if the value of d_o is simultaneously fitted. The value d_o represents the initial size at $t = 0$. It is the intercept in the plot. If a common value of d_o is assumed (d_o = 1.68 nm), $1/n = 0.26 \pm 0.05$. In the latter case, the corresponding inverse value is $n = 3.9 \pm 0.7$.

Rate of growth

With the above function (Equation S3.3), the rate of growth R has been derived by fitting the values k, d_o, and $1/n$ for each data set (Figure S3.3). The calculation of R starts by taking numerically the derivatives of the optimized function at a chosen time t. The procedure requires simultaneously the calculation of the mass density ρ_{nano} according to Hiemstra[27]:

$$\rho_{\text{nano}} = \frac{M_{\text{core}}}{n_O V_O} - \left(\frac{M_{\text{core}}}{n_O} - \mathrm{M_{H_2O}}\right)\frac{6}{d}\, N_{\mathrm{H_2O}} \qquad \text{(Equation S3.4)}$$

and specific surface area A according to:

$$A = \frac{6}{\rho_{\text{nano}}\, d} \qquad \text{(Equation S3.5)}$$

followed by calculating the molar mass M_{nano} according to:

$$M_{\text{nano}} = M_{\text{core}} \frac{1}{(1 - A\, N_{\mathrm{H_2O}} M_{\mathrm{H_2O}})} \qquad \text{(Equation S3.6)}$$

In combination (ρ_{nano}, M_{nano}), one can obtain the corresponding number of Fe per particle (n_{Fe}), according to:

$$n_{\mathrm{Fe}} = \frac{\rho_{\text{nano}}}{M_{\text{nano}}} \frac{\pi d^3}{6}\, \mathrm{N_{Av}} \qquad \text{(Equation S3.7)}$$

In the above equations, N_{H2O} is the surface density of coordinated water (12.6 10^{-6} mol m^{-2}),[29] n_O is the amount of oxygen per Fe in the bulk (1.6), M_{core} is the molar mass of the Fh core (81.65 g mol^{-1}), M_{H2O} is the molar mass of water (18 g mol^{-1}), and N_{Av} is Avogadro's number (6.022 10^{23} mol^{-1}).

In equation SI–3.4, V_O is the lattice volume, expressed per mol oxygen. The value of V_O can be estimated from the relation between mass density (g m^{-3}) and molar mass per oxygen (g / mol O)[63] or alternatively, it can be calculated from the chemical composition combined with the volume of the unit cell that provides the mass density of the bulk:

$$V_O = \frac{M_{core}}{n_O \rho_{core}} \qquad \text{(Equation S3.8)}$$

For Fe (hydr)oxides in general, $V_O \sim 10.8\ 10^{-6}$ m^3 mol^{-1} O.[63] Based on the unit cell dimensions derived by Wang et al.[82] and Pinney et al.,[65] $V_O = 10.7\ 10^{-6}$ m^3 mol^{-1} O. The number is equivalent with a mass density of ρ_{core} = 4.77 10^6 g m^{-3}, but might be slightly higher (~ 2%) according to other parametrizations[40,83,84] leading to $\rho_{core} = 4.92 \pm 0.03\ 10^6$ g m^{-3} and $V_O = 10.5\ 10^{-6}$ m^3 mol^{-1} O.

Ultimately, the rate of growth R (mol m^{-2} h^{-1}) follows from the change of n_{Fe} with change of time t, scaled to the surface area of the particle ($A_\# = \pi d^2$) at the corresponding time, according to:

$$R = \frac{\frac{dn_{Fe}}{dt}}{A_\#} \qquad \text{(Equation S3.9)}$$

D. A monolayer of Fe: surface density

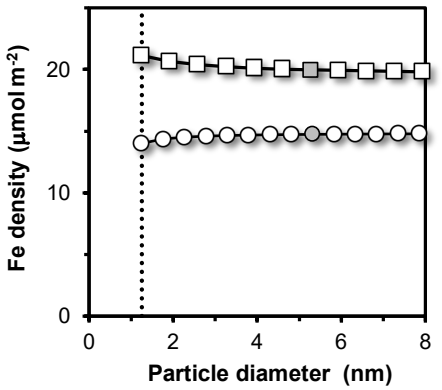

Figure S3.4. Mean surface density of Fe (spheres) at the repetitive growth of Fh using the *a*-direction of the unit cell with a = 0.587 nm as measure for the representative distance.[85] The surface density has been derived by step-wise increasing the particle diameter d with the repetitive Fe-Fe distance ($L = ½\sqrt{3}\ a/2$ = 0.25 nm), *i.e.* $d + 2L$, and calculate self-consistently with the equations given in the main text the increase of the amount of Fe in the volume of the layer with thickness L. By scaling to the corresponding particle surface area $A_\# = \pi d^2$, the Fe surface density follows. Another approach is to use the mean Fe-Fe distance in the Fh lattice as repetitive distance (L = 0.33 ± 0.02 nm), leading to a higher surface density (squares). If individual crystal faces are considered, similar values are found for the mean repetitive growth, *i.e.* ~15 µmol m^{-2} for the 100 or 010 face, and ~20 µmol m^{-2} for the 001 face. The orange color gives the size of 6LFh (~ 5.5 nm, n_{Fe} ~ 2600), formed by forced hydrolysis of Fe(III) at 75 °C.[57,59] If formed by Fe adsorption to Fe_{13} nuclei, the formation of this 6LFH particle is equivalent with the binding of ~6-8 monolayers of Fe.

E. Polyhedral representation of a non-aged initial Fh particle

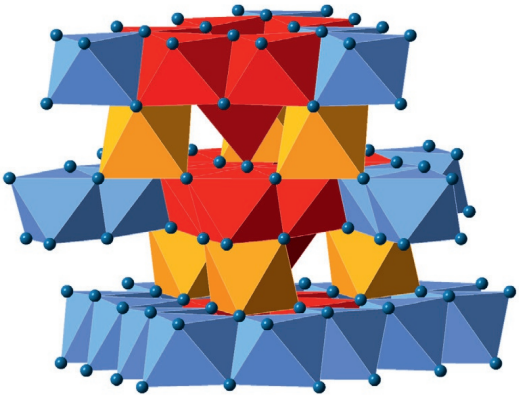

Figure S3.5. A ferrihydrite particle built from 45 Fe polyhedra with the composition $Fe_{45}O_{132}H_{129}$. This is equivalent to $FeO_{1.4}(OH)_{0.2}.nH_2O$ with $n = 1.5$. The blue spheres are oxygen ions. The protons are not shown. The particle has a Fe_{13} signature and contains two linked Fe_{13} units that are given with red, dark red, and orange-colored polyhedra. Additionally attached Fe polyhedra are given in blue. The constructed particle is surface depleted by Fe2 (orange) octahedra and Fe3 (dark red) tetrahedra because these polyhedra are considered as less stable at the surface of Fh when forming singly coordinated surface groups.[64]

F. Influence of initial particle size on ageing

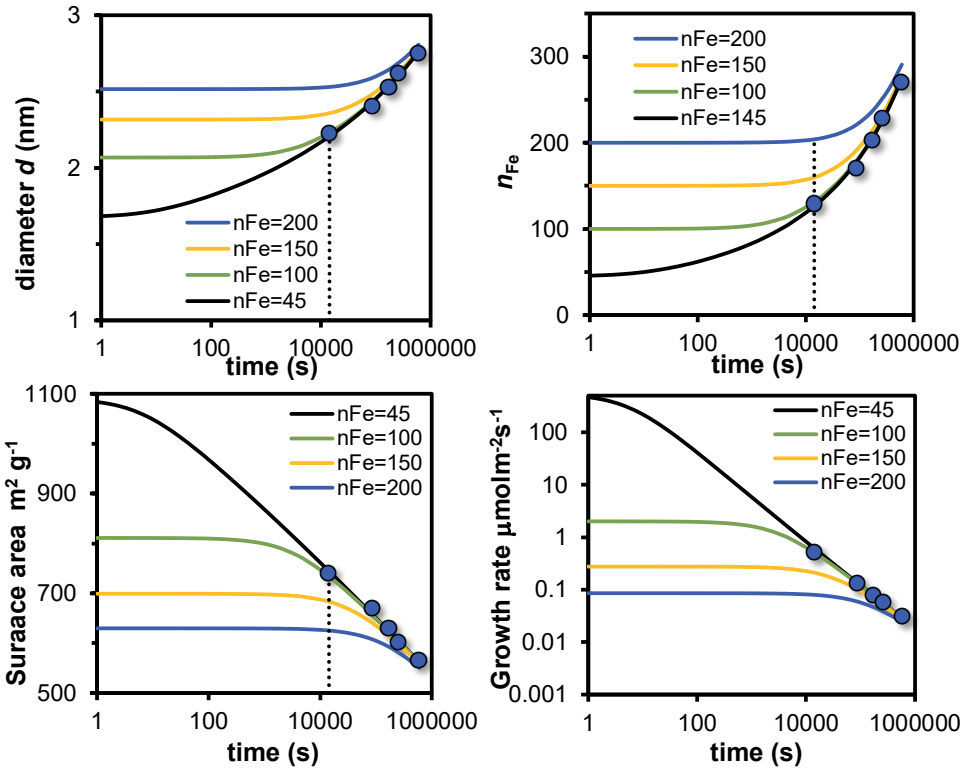

Figure S3.6. Time dependency of the mean particle diameter d (nm), number of Fe per particle n_{Fe}, specific surface area A ($m^2\ g^{-1}$), and rate of growth R (µmol $m^{-2}\ h^{-1}$) of traditionally synthesized Fh, produced and aged at pH 8.2 in 0.01 M $NaNO_3$ at 20 °C (spheres) for $t \geq 4$ hours. The lines have been calculated with the dynamic model for log$k$ = -4.97 (Equation 3.8, main text) using different values for the amount of Fe present in the initial particles.

The model results of Figure S3.6 show that increase of the size of the initial particles (n_{Fe}) does not lead to a considerable increase of the particle size at prolonged ageing. The reason is that the increase of the particle size leads to a substantial decrease of the solubility and super saturation, acting as a very strong negative feedback on the rate of growth R. However, the choice of the value of n_{Fe} at time $t = 0$ becomes critical at shorter times of ageing as used in the experiment with the organic pH buffers (t = 0.1 and 1.5 hours). The dotted vertical line indicates 4 hours of ageing.

G. Rate limitation by diffusion across the solid-water interface

The rate limitation of growth by diffusion from the solution to the surface leads to a time dependent growth of the diameter according to $\Delta d = k\ t^{1/n}$ with n =3, according to Lifshitz and Slyozov.[72] This theory is based on combining Fick first law with the Ostwald-Freundlich equation for describing the solubility as a function of the particle size. The latter equation is used in its linearized form.

The classical Ostwald-Freundlich (OF) equation can be given as:

$$RT\ln\frac{Q_{so}}{K_{so}} = \frac{2}{3}\gamma A_c = \frac{M_{nano}}{\rho_{nano}}\frac{2\gamma}{r_c} \quad \text{(Equation S3.10)}$$

in which Q_{so} and K_{so} are respectively the solubility products of the actual Fh of given radius of the critical particles and the virtual bulk, and A_c is the specific surface area ($m^2\ mol^{-1}$) of the critical particle in the size distribution.

Taking the exponential of Equation S3.10 and simplifying with $e^x = 1 + x$ for $x \to 0$, one gets the linearized Ostwald-Freundlich (L-OF) equation:

$$\frac{Q_{so}}{K_{so}} = e^{\frac{1}{RT}\frac{M_{nano}}{\rho_{nano}}\frac{2\gamma}{r_c}} \approx 1 + \frac{2\gamma}{RT}\frac{M_{nano}}{\rho_{nano}}\frac{1}{r_c} \quad \text{(Equation S3.11)}$$

With increase of the critical radius r_c, linearization of the equation is increasingly justified as shown in Figure S3.7. In Figure S3.7, we have given the difference in super saturation. Only at a large size, the relative difference in the calculated solution concentration of OF and L-OF becomes small. For d ~6.5 nm, $\Delta(Q_{so}/K_{so}) = 1$ as indicated in the graph with the black sphere. In that case, Q_{so}/K_{so} (OF) ~ 3 and Q_{so}/K_{so} (L-OF) ~ 2, *i.e.* the super saturation calculated with the OF approach is 50% higher. The difference quickly increases at a smaller particle size.

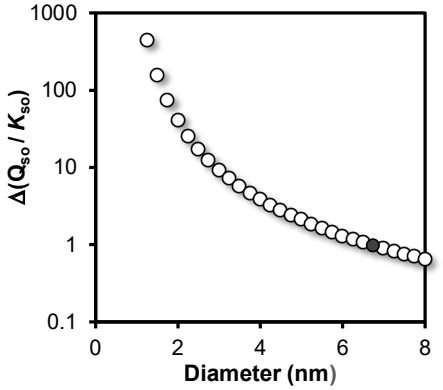

Figure S3.7. Size-dependent difference in relative solution concentration (ΔQ_{so}) of Fh calculated with the classical and the linearized Ostwald-Freundlich equation scaled to the solubility of the virtual bulk of Fh (K_{so}). The calculated concentration difference is orders of magnitude different when particles are small. The black sphere locates the system in which the relative difference has decreased to $\Delta(Q_{so}/K_{so}) = 1$, where the super saturation calculated by the OF equation is 50% higher than with the L-OF approach.

The factors Q_{so} and K_{so} can be linked to the concentration of dissolved aqueous species (aq) at a given pH in equilibrium with respectively a particle of critical size (c_{rc}) and virtual bulk material at infinite size c_∞, leading to:

$$c_{r_c} = c_\infty + \frac{2\gamma}{RT}\frac{M_{nano}}{\rho_{nano}}\frac{1}{r_c}c_\infty \equiv c_\infty + \frac{\alpha}{r_c} \quad \text{(Equation S3.12)}$$

By defining super saturation of the solution as $\Delta \equiv c_o - c_\infty$ in which c_o is actual solution, Lifshitz and Slyozov[72] derived for the concentration gradient between solution and surface of the growing particles with radius r

$$c_{r_c} - c_o = \left(\frac{\alpha}{r_c} + c_\infty\right) - (\Delta - c_\infty) = \frac{\alpha}{r_c} + \Delta \qquad \text{(Equation S3.13)}$$

This concentration difference is introduced in the Fick's first law of diffusion.

Required length of diffusion explaining the rate of growth of Fh

Our measured rates of growth (R) are typically in the order of $R \sim 0.01$ - 10 µmol m^{-2} h^{-1} or $R \sim 3\ 10^{-12}$ - $3\ 10^{-9}$ mol m^{-2} s^{-1}. Assuming that the rate of growth is limited by diffusion across the solid-solution interface, one may calculate the diffusion length required to explain the experimental rate of growth R by using Fick's first law as a first approach that is combined with the classical Ostwald Freundlich equation. According to Fick's first law, we may write for the flux F (mol s^{-1}):

$$F = -DA_{\#}\frac{\partial c}{\partial x} \qquad \text{(Equation S3.14)}$$

in which D is the diffusion coefficient in m^2 s^{-1}, $A_{\#}$ is the surface area (m^2), and $\partial c/\partial x$ is the linear concentration gradient with the concentration c in mol m^{-3} and the diffusion length x in m.

Rewriting Equation S.3.14 leads to an expression for the length of the diffusion path L between the solution ($x = 0$) and surface ($x = x$):

$$L = \frac{1}{F/A_{\#}}\ D\ (c_o - c_{surf}) \sim \frac{D}{R} c_{eq} \qquad \text{(Equation S3.15)}$$

in which the flux F per unit surface area $A_{\#}$ represents the rate R of growth ($R = F/A_{\#}$ in mol m^{-2} s^{-1}). The concentration in the solution (c_o) is determined by the solubility of the critical particle with size d_{crit} and the concentration at the surface (c_{surf}) is determined by that of Fh particle of mean size d_{mean}. For a polydisperse Fh suspension, both sizes are related by a factor of about $\phi = d_{mean} / d_{crit} = 3/2$. The corresponding equilibrium concentrations can be calculated with the Ostwald-Freundlich equation. If the difference c_o - c_{surf} is relatively large, one may simplify to c_o - $c_{surf} = c_{eq}$ in which the latter is the equilibrium concentration maintained by the critical particles.

In Figure S3.8, the distance L at which the rate is limited by diffusion is given. It has been calculated for a suspension with Fh particles of different mean size having a rate of growth in the range $R = 0.01$–10 µmol m^{-2} h^{-1} or ~ 3–300 10^{-12} mol m^{-2} s^{-1}, taken from Figure 3.4 in the main text. The corresponding size dependent solubility products ($\log Q_{so} = \log(Fe^{3+}) + 3\log(OH^-)$) can be used to calculate the solution concentrations as a function of pH. Depending on the size, the concentrations at neutral pH are in the order of about 10^{-7} -10^{-9} M or 10^{-4} -10^{-6} mol m^{-3}.

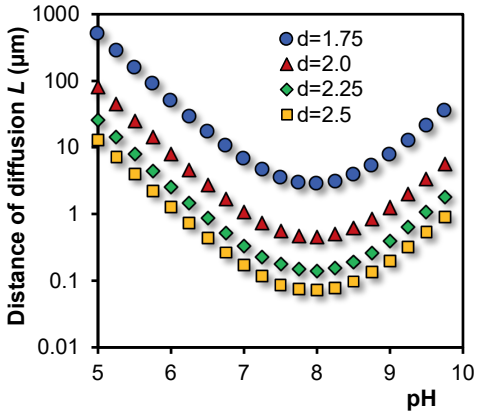

Figure S3.8. Interfacial length of diffusion L (µm) that can explain the observed rates of growth (R) of Fh with mean sizes (d_{mean} in nm) as given. Compared to the mean particle size of Fh (~nm), the diffusion length L (~ µm) is very large, making rate limitation by interfacial transport unlikely, particularly because the Fh particles in the actual suspension are aggregated. The Fh solubility has been calculated with the Ostwald-Freundlich equation (Equation 3.7 main text) using a surface Gibbs free energy of 0.186 J m^{-2}, a size distribution ratio of $\phi = d_{mean} / d_{crit}$ = 3/2, and a solubility product for Fh bulk of $\log K_{so}$ = -40.6. The rates (µmol m^{-2} h^{-1}) used to calculate L are 10 (blue spheres), 1.0 (red triangles), 0.1 (green diamonds), and 0.01 (yellow squares), typically for a timescale of ageing being respectively about 0.1, 1, 10, and 100 h.

Using a representative value for the diffusion coefficient, for instance $D = 0.6\ 10^{-9}$ m^2 s^{-1} for Fe^{3+}, the calculated distance L (Figure S3.8) at which the rate becomes limited by diffusion is typically in the order around one µm, depending on the particle size and pH in solution (Figure S3.8). As these distances are relatively large compared to the size of the Fh nanoparticle (> 100–1000 times), the calculated result supports our interpretation that the rate of growth is not limited by diffusion across the solid-solution interface but by another process. Moreover, Figure S3.8 shows that if diffusion would be rate-controlling, the diffusion length would not change with size or time, whereas our data would point to a significant change (Figure S3.8).

Mean particle-particle distance in suspensions

One may calculate the mean equivalent distance x (m) between Fh particles in a suspension in the case of a homogenous distribution over space (no aggregation), taking the one-dimensional distance of the Fh particle density in the suspension according to:

$$x = \left(\frac{n_{Fe} M_{nano}}{N_{Av}\, \rho_{sus}} \right)^{1/3} \qquad \text{(Equation S3.16)}$$

in which n_{Fe} is the number of Fe per particle and N_{av} is Avogadro's number (mol^{-1}), M_{nano} is the molar mass of Fh (g Fh mol^{-1} Fe), and ρ_{sus} is the suspension concentration (g m^{-3}). In combination, this gives the Fh particle density (Fh particles m^{-3}). The third root of this particle density can be seen as representative for the mean particle distance x (m). The calculated mean distance for representative particles of certain size (d-Fh) is given in the table below.

Table S3.1. Mean particle-particle distance in a supposed homogeneous suspension with a concentration of 1 g Fh L^{-1} ($\rho_{sus} = 10^{-3}$ g m^{-3}). Note that Fh with 5 and 10 nm has not been studied in this paper, but it has been added for comparison.

d-Fh (nm)	M_{nano} (g mol^{-1})	n_{Fe}	*x* (nm)
1.7	108	47	20
2.0	101	88	25
2.5	95	195	31
3.0	92	363	38
5	87	1930	65
10	84	16930	133

Collectively, the above shows that rate limitation by diffusion across the interface cannot explain the rate of growth of Fh. The growth of Fh is much slower. In literature, rates of growth of materials are often limited by diffusion. This will occur if the reaction at the surface is fast, creating relatively large particles and low super saturation, *i.e.* low concentration gradient. Finally, it is interesting to note that the rate of Fe attachment is rather comparable with the rate of the adsorption of ions such as PO_4, being typically in the order of the scale of µmol m^{-2} h^{-1}.

H. Ageing of 6LFh

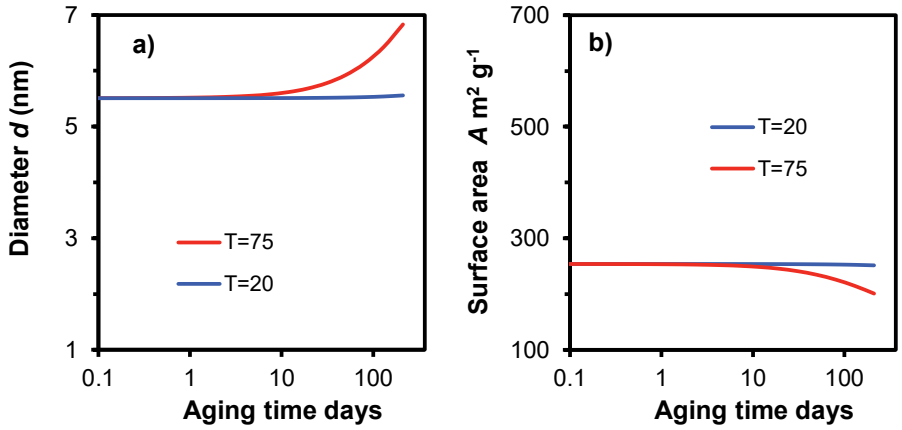

Figure S3.9. Time dependency of the mean particle diameter *d* (nm), and specific surface area *A* (m^2 g^{-1}) of 6LFh. If synthesized by forced hydrolysis at 75 °C for 10–12 minutes, according to the method of Schwertmann and Cornell,[25] the initial size is about 5.5 nm.[57,59] According to our model (lines), storage and long-term ageing of the material at 20 °C leads to no notable change in size and surface area by Ostwald ripening, in agreement with recent data collected by SAXS[59] after 1 and 9 months of ageing. At 75 °C, some classical Ostwald ripening may occur according to our model, but more significant changes may be expected from oriented particle attachment and/or fusion, which is typical for ageing at high temperature.[31]

References

(1) Tiberg, C.; Sjöstedt, C.; Persson, I.; Gustafsson, J. P. Phosphate Effects on Copper(II) and Lead(II) Sorption to Ferrihydrite. *Geochim. Cosmochim. Acta* **2013**, *120*, 140–157.

(2) Hiemstra, T.; Zhao, W. Reactivity of Ferrihydrite and Ferritin in Relation to Surface Structure, Size, and Nanoparticle Formation Studied for Phosphate and Arsenate. *Environ. Sci. Nano* **2016**, *3*, 1265–1279.

(3) Senn, A. C.; Kaegi, R.; Hug, S. J.; Hering, J. G.; Mangold, S.; Voegelin, A. Effect of Aging on the Structure and Phosphate Retention of Fe(III)-Precipitates Formed by Fe(II) Oxidation in Water. *Geochim. Cosmochim. Acta* **2017**, *202*, 341–360.

(4) Johnston, C. P.; Chrysochoou, M. Mechanisms of Chromate, Selenate, and Sulfate Adsorption on Al-Substituted Ferrihydrite: Implications for Ferrihydrite Surface Structure and Reactivity. *Environ. Sci. Technol.* **2016**, *50* (7), 3589–3596.

(5) Rossberg, A.; Ulrich, K.-U.; Weiss, S.; Tsushima, S.; Hiemstra, T.; Scheinost, A. C. Identification of Uranyl Surface Complexes on Ferrihydrite: Advanced EXAFS Data Analysis and CD-MUSIC Modeling. *Environ. Sci. Technol.* **2009**, *43* (5), 1400–1406.

(6) Larsson, M. A.; Persson, I.; Sjöstedt, C.; Gustafsson, J. P. Vanadate Complexation to Ferrihydrite: X-Ray Absorption Spectroscopy and CD-MUSIC Modelling. *Environ. Chem.* **2017**, *14* (3), 141–150.

(7) Francisco, P. C. M.; Sato, T.; Otake, T.; Kasama, T.; Suzuki, S.; Shiwaku, H.; Yaita, T. Mechanisms of Se(IV) Co-Precipitation with Ferrihydrite at Acidic and Alkaline Conditions and Its Behavior during Aging. *Environ. Sci. Technol.* **2018**, *52* (8), 4817–4826.

(8) Wang, X.; Kubicki, J. D.; Boily, J. F.; Waychunas, G. A.; Hu, Y.; Feng, X.; Zhu, M. Binding Geometries of Silicate Species on Ferrihydrite Surfaces. *ACS Earth Sp. Chem.* **2018**, *2* (2), 125–134.

(9) Swedlund, P. J.; Holtkamp, H.; Song, Y.; Daughney, C. J. Arsenate-Ferrihydrite Systems from Minutes to Months: A Macroscopic and IR Spectroscopic Study of an Elusive Equilibrium. *Environ. Sci. Technol.* **2014**, *48* (5), 2759–2765.

(10) Zhang, S.; Williams, P. N.; Zhou, C. Y.; Ma, L. Q.; Luo, J. Extending the Functionality of the Slurry Ferrihydrite-DGT Method: Performance Evaluation for the Measurement of Vanadate, Arsenate, Antimonate and Molybdate in Water. *Chemosphere* **2017**, *184*, 812–819.

(11) Wang, X.; Hu, Y.; Tang, Y.; Yang, P.; Feng, X.; Xu, W.; Zhu, M. Phosphate and Phytate Adsorption and Precipitation on Ferrihydrite Surfaces. *Environ. Sci. Nano* **2017**, *4* (11), 2193–2204.

(12) Tian, L.; Shi, Z.; Lu, Y.; Dohnalkova, A. C.; Lin, Z.; Dang, Z. Kinetics of Cation and Oxyanion Adsorption and Desorption on Ferrihydrite: Roles of Ferrihydrite Binding Sites and a Unified Model. *Environ. Sci. Technol.* **2017**, *51* (18), 10605–10614.

(13) Meng, S.; Wang, H.; Liu, H.; Yang, C.; Wei, Y.; Hou, D. Evaluation of the Ability of Ferrihydrite to Bind Heavy Metal Ions: Based on Formation Environment, Adsorption Reversibility and Ageing. *Appl. Geochemistry* **2014**, *45*, 114–119.

(14) Liu, J.; Zhu, R.; Xu, T.; Xu, Y.; Ge, F.; Xi, Y.; Zhu, J.; He, H. Co-Adsorption of Phosphate and Zinc(II) on the Surface of Ferrihydrite. *Chemosphere* **2016**, *144*, 1148–1155.

(15) Pieczara, G.; Rzepa, G. The Effect of Si Content on Ferrihydrite Sorption Capacity for Pb(II), Cu(II), Cr(VI), AND P(V). *Environ. Eng. Manag. J.* **2016**, *15* (9), 2095–2107.

(16) Dzombak, D. A.; Morel, F. M. M. *Surface Complexation Modeling: Hydrous Ferric Oxide*; John Wiley & Sons, Inc.: New York, 1990.

(17) Fu, H.; Yang, Y.; Zhu, R.; Liu, J.; Usman, M.; Chen, Q.; He, H. Superior Adsorption of Phosphate by Ferrihydrite-Coated and Lanthanum-Decorated Magnetite. *J. Colloid Interface Sci.* **2018**, *530*, 704–713.

(18) Sowers, T. D.; Stuckey, J. W.; Sparks, D. L. The Synergistic Effect of Calcium on Organic Carbon Sequestration to Ferrihydrite. *Geochem. Trans.* **2018**, *19* (1), 4.

(19) Tian, L.; Liang, Y.; Lu, Y.; Peng, L.; Wu, P.; Shi, Z. Pb(II) and Cu(II) Adsorption and Desorption Kinetics on Ferrihydrite with Different Morphologies. *Soil Sci. Soc. Am. J.* **2018**, *82* (1), 96–105.

(20) Stumm, W.; Huang, C. P.; Jenkins, S. R. Specific Chemical Interaction Affecting the Stability of Dispersed Systems. *Croat. Chem. Acta* **1970**, *42* (2), 223–245.

(21) Davis, J. A.; James, R. O.; Leckie, J. O. Surface Ionization and Complexation at the Oxide/Water Interface: I. Computation of Electrical Double Layer Properties in Simple Electrolytes. *J. Colloid Interface Sci.* **1978**, *63* (3), 480–499.

(22) Abbas, M.; Parvatheeswara Rao, B.; Naga, S. M.; Takahashi, M.; Kim, C. Synthesis of High Magnetization Hydrophilic Magnetite (Fe3O 4) Nanoparticles in Single Reaction - Surfactantless Polyol Process. *Ceram. Int.* **2013**,

39 (7), 7605–7611.

(23) Yates, D. E.; Levine, S.; Healy, T. W. Site-Binding Model of the Electrical Double Layer at the Oxide/Water Interface. *J. Chem. Soc. Faraday Trans. 1 Phys. Chem. Condens. Phases* **1974**, *70*, 1807–1818.

(24) Hiemstra, T.; Van Riemsdijk, W. H. A Surface Structural Approach to Ion Adsorption: The Charge Distribution (CD) Model. *J. Colloid Interface Sci.* **1996**, *179* (2), 488–508.

(25) Schwertmann, U.; Cornell, R. M. *Iron Oxides in the Laboratory*; VCH Publishers, 1991.

(26) Bompoti, N.; Chrysochoou, M.; Machesky, M. Surface Structure of Ferrihydrite: Insights from Modeling Surface Charge. *Chem. Geol.* **2017**, *464*, 34–45.

(27) Hiemstra, T. Ferrihydrite Interaction with Silicate and Competing Oxyanions: Geometry and Hydrogen Bonding of Surface Species. *Geochim. Cosmochim. Acta* **2018**, *238*, 453–476.

(28) Cornell, R. M.; Schwertmann, U. *The Iron Oxides: Structure, Properties, Reactions, Ocurrence and Uses*, Second Edi.; WILEY-VCH, Germany, 2003.

(29) Hiemstra, T. Formation, Stability, and Solubility of Metal Oxide Nanoparticles: Surface Entropy, Enthalpy, and Free Energy of Ferrihydrite. *Geochim. Cosmochim. Acta* **2015**, *158*, 179–198.

(30) Ostwald, W. The Formation and Changes of Solids (Translated from German). *Z Phys Chem* **1897**, *22*, 289–330.

(31) Burleson, D. J.; Penn, R. L. Two-Step Growth of Goethite from Ferrihydrite. *Langmuir* **2006**, *22* (1), 402–409.

(32) Li, D.; Nielsen, M. H.; Lee, J. R. I.; Frandsen, C.; Banfield, J. F.; De Yoreo, J. J. Direction-Specific Interactions Control Crystal Growth by Oriented Attachment. *Science (80-.).* **2012**, *336* (6084), 1014 LP – 1018.

(33) Hiemstra, T. Surface Structure Controlling Nanoparticle Behavior: Magnetism of Ferrihydrite, Magnetite, and Maghemite. *Environ. Sci. Nano* **2018**, *5* (3), 752–764.

(34) Huang, F.; Zhang, H.; Banfield, J. F. Two-Stage Crystal-Growth Kinetics Observed during Hydrothermal Coarsening of Nanocrystalline ZnS. *Nano Lett.* **2003**, *3* (3), 373–378.

(35) Murphy, P. J.; Posner, A. M.; Quirk, J. P. Characterization of Partially Neutralized Ferric Chloride Solutions. *J. Colloid Interface Sci.* **1976**, *56* (2), 284–297.

(36) Burrows, N. D.; Hale, C. R. H.; Penn, R. L. Effect of PH on the Kinetics of Crystal Growth by Oriented Aggregation. *Cryst. Growth Des.* **2013**, *13* (8), 3396–3403.

(37) Boland, D. D.; Collins, R. N.; Miller, C. J.; Glover, C. J.; Waite, T. D. Effect of Solution and Solid-Phase Conditions on the Fe(II)-Accelerated Transformation of Ferrihydrite to Lepidocrocite and Goethite. *Environ. Sci. Technol.* **2014**, *48* (10), 5477–5485.

(38) Jiang, Z.; Liu, Q.; Roberts, A. P.; Barrón, V.; Torrent, J.; Zhang, Q. A New Model for Transformation of Ferrihydrite to Hematite in Soils and Sediments. *Geology* **2018**, *46* (11), 987–990.

(39) Cao, L.; Jiang, Z. X.; Du, Y. H.; Yin, X. M.; Xi, S. B.; Wen, W.; Roberts, A. P.; Wee, A. T. S.; Xiong, Y. M.; Liu, Q. S.; et al. Origin of Magnetism in Hydrothermally Aged 2-Line Ferrihydrite Suspensions. *Environ. Sci. Technol.* **2017**, *51* (5), 2643–2651.

(40) Michel, F. M.; Barron, V.; Torrent, J.; Morales, M. P.; Serna, C. J.; Boily, J.-F.; Liu, Q.; Ambrosini, A.; Cismasu, A. C.; Brown, G. E. Ordered Ferrimagnetic Form of Ferrihydrite Reveals Links among Structure, Composition, and Magnetism. *Proc. Natl. Acad. Sci.* **2010**, *107* (7), 2787–2792.

(41) Mitsunobu, S.; Muramatsu, C.; Watanabe, K.; Sakata, M. Behavior of Antimony(V) during the Transformation of Ferrihydrite and Its Environmental Implications. *Environ. Sci. Technol.* **2013**, *47* (17), 9660–9667.

(42) Roden, E. E.; Zachara, J. M. Microbial Reduction of Crystalline Iron(III) Oxides: Influence of Oxide Surface Area and Potential for Cell Growth. *Environ. Sci. Technol.* **1996**, *30* (5), 1618–1628.

(43) Schwertmann, U.; Stanjek, H.; Becher, H.-H. Long-Term in Vitro Transformation of 2-Line Ferrihydrite to Goethite/Hematite at 4, 10, 15 and 25°C. *Clay Miner.* **2004**, *39* (4), 433–438.

(44) Gálvez, N.; Barrón, V.; Torrent, J. Effect of Phosphate on the Crystallization of Hematite, Goethite, and Lepidocrocite from Ferrihydrite. *Clays Clay Miner.* **1999**, *47* (3), 304–311.

(45) Raiswell, R.; Vu, H. P.; Brinza, L.; Benning, L. G. The Determination of Labile Fe in Ferrihydrite by Ascorbic Acid Extraction: Methodology, Dissolution Kinetics and Loss of Solubility with Age and de-Watering. *Chem. Geol.* **2010**, *278* (1), 70–79.

(46) Michael Bolanz, R.; Bläss, U.; Ackermann, S.; Ciobotă, V.; Rösch, P.; Tarcea, N.; Popp, J.; Majzlan, J. The Effect of Antimonate, Arsenate, and Phosphate on the Transformation of Ferrihydrite to Goethite, Hematite, Feroxyhyte, and Tripuhyite. *Clays Clay Miner.* **2013**, *61* (1), 11–25.

(47) Das, S.; Hendry, M. J.; Essilfie-Dughan, J. Transformation of Two-Line Ferrihydrite to Goethite and Hematite as a Function of PH and Temperature. *Environ. Sci. Technol.* **2011**, *45* (1), 268–275.

(48) Weatherill, J. S.; Morris, K.; Bots, P.; Stawski, T. M.; Janssen, A.; Abrahamsen, L.; Blackham, R.; Shaw, S. Ferrihydrite Formation: The Role of Fe13 Keggin Clusters. *Environ. Sci. Technol.* **2016**, *50* (17), 9333–9342.

(49) Collins, R. N.; Rosso, K. M.; Rose, A. L.; Glover, C. J.; David Waite, T. An in Situ XAS Study of Ferric Iron Hydrolysis and Precipitation in the Presence of Perchlorate, Nitrate, Chloride and Sulfate. *Geochim. Cosmochim. Acta* **2016**, *177*, 150–169.

(50) Zhu, M.; Frandsen, C.; Wallace, A. F.; Legg, B.; Khalid, S.; Zhang, H.; Mørup, S.; Banfield, J. F.; Waychunas, G. A. Precipitation Pathways for Ferrihydrite Formation in Acidic Solutions. *Geochim. Cosmochim. Acta* **2016**, *172*, 247–264.

(51) Mao, Y.; Ninh Pham, A.; Xin, Y.; David Waite, T. Effects of PH, Floc Age and Organic Compounds on the Removal of Phosphate by Pre-Polymerized Hydrous Ferric Oxides. *Sep. Purif. Technol.* **2012**, *91*, 38–45.

(52) Antelo, J.; Arce, F.; Fiol, S. Arsenate and Phosphate Adsorption on Ferrihydrite Nanoparticles. Synergetic Interaction with Calcium Ions. *Chem. Geol.* **2015**, *410*, 53–62.

(53) Wang, X.; Liu, F.; Tan, W.; Li, W.; Feng, X.; Sparks, D. L. Characteristics of Phosphate Adsorption-Desorption Onto Ferrihydrite. *Soil Sci.* **2013**, *178* (1), 1–11.

(54) Cerkez, E. B.; Bhandari, N.; Reeder, R. J.; Strongin, D. R. Coupled Redox Transformation of Chromate and Arsenite on Ferrihydrite. *Environ. Sci. Technol.* **2015**, *49* (5), 2858–2866.

(55) Antelo, J.; Fiol, S.; Pérez, C.; Mariño, S.; Arce, F.; Gondar, D.; López, R. Analysis of Phosphate Adsorption onto Ferrihydrite Using the CD-MUSIC Model. *J. Colloid Interface Sci.* **2010**, *347* (1), 112–119.

(56) Van den Hul, H. J.; Lyklema, J. Determination of Specific Surface Areas of Dispersed Materials. Comparison of the Negative Adsorption Method with Some Other Methods. *J. Am. Chem. Soc.* **1968**, *90* (12), 3010–3015.

(57) Guyodo, Y.; Banerjee, S. K.; Lee Penn, R.; Burleson, D.; Berquo, T. S.; Seda, T.; Solheid, P. Magnetic Properties of Synthetic Six-Line Ferrihydrite Nanoparticles. *Phys. Earth Planet. Inter.* **2006**, *154* (3), 222–233.

(58) Burrows, N. D.; Hale, C. R. H.; Penn, R. L. Effect of Ionic Strength on the Kinetics of Crystal Growth by Oriented Aggregation. *Cryst. Growth Des.* **2012**, *12* (10), 4787–4797.

(59) Gentile, L.; Wang, T.; Tunlid, A.; Olsson, U.; Persson, P. Ferrihydrite Nanoparticle Aggregation Induced by Dissolved Organic Matter. *J. Phys. Chem. A* **2018**, *122* (38), acs.jpca.8b05622.

(60) Guénet, H.; Davranche, M.; Vantelon, D.; Gigault, J.; Prévost, S.; Taché, O.; Jaksch, S.; Pédrot, M.; Dorcet, V.; Boutier, A.; et al. Characterization of Iron–Organic Matter Nano-Aggregate Networks through a Combination of SAXS/SANS and XAS Analyses: Impact on As Binding. *Environ. Sci. Nano* **2017**, *4* (4), 938–954.

(61) Lee Penn, R.; Erbs, J. J.; Gulliver, D. M. Controlled Growth of Alpha-FeOOH Nanorods by Exploiting-Oriented Aggregation. *J. Cryst. Growth* **2006**, *293* (1), 1–4.

(62) Davis, J. A.; Leckie, J. O. Surface Ionization and Complexation at the Oxide/Water Interface II. Surface Properties of Amorphous Iron Oxyhydroxide and Adsorption of Metal Ions. *J. Colloid Interface Sci.* **1978**, *67* (1), 90–107.

(63) Hiemstra, T.; Van Riemsdijk, W. H. A Surface Structural Model for Ferrihydrite I: Sites Related to Primary Charge, Molar Mass, and Mass Density. *Geochim. Cosmochim. Acta* **2009**, *73* (15), 4423–4436.

(64) Hiemstra, T. Surface and Mineral Structure of Ferrihydrite. *Geochim. Cosmochim. Acta* **2013**, *105*, 316–325.

(65) Pinney, N.; Kubicki, J. D.; Middlemiss, D. S.; Grey, C. P.; Morgan, D. Density Functional Theory Study of Ferrihydrite and Related Fe-Oxyhydroxides. *Chem. Mater.* **2009**, *21* (24), 5727–5742.

(66) Majzlan, J.; Navrotsky, A.; Schwertmann, U. Thermodynamics of Iron Oxides: Part III. Enthalpies of Formation and Stability of Ferrihydrite (~Fe(OH)3), Schwertmannite (~FeO(OH)3/4(SO4)1/8), and ε-Fe2O3. *Geochim. Cosmochim. Acta* **2004**, *68* (5), 1049–1059.

(67) Snow, C. L.; Lilova, K. I.; Radha, A. V.; Shi, Q.; Smith, S.; Navrotsky, A.; Boerio-Goates, J.; Woodfield, B. F. Heat Capacity and Thermodynamics of a Synthetic Two-Line Ferrihydrite, FeOOH·0.027H2O. *J. Chem. Thermodyn.* **2013**, *58*, 307–314.

(68) Navrotsky, A.; Mazeina, L.; Majzlan, J. Size-Driven Structural Thermodynamic Complexity in Iron Oxides. *Science (80-.).* **2008**, *319* (March), 1635–1639.

(69) Molleman, B.; Hiemstra, T. Size and Shape Dependency of the Surface Energy of Metallic Nanoparticles: Unifying the Atomic and Thermodynamic Approaches. *Phys. Chem. Chem. Phys.* **2018**, *20* (31), 20575–20587.

(70) Byrne, R. H.; Luo, Y.-R. Direct Observations of Nonintegral Hydrous Ferric Oxide Solubility Products: Kso*=[Fe3+][H+]-2.86. *Geochim. Cosmochim. Acta* **2000**, *64* (11), 1873–1877.

(71) Li, F.; Koopal, L.; Tan, W. Roles of Different Types of Oxalate Surface Complexes in Dissolution Process of Ferrihydrite Aggregates. *Sci. Rep.* **2018**, *8* (1), 2060.

(72) Lifshitz, I. M.; Slyozov, V. V. The Kinetics of Precipitation from Supersaturated Solid Solutions. *J. Phys. Chem.*

Solids **1961**, *19* (1), 35–50.

(73) Wagner, C. Theorie Der Alterung von Niederschlägen Durch Umlösen (Ostwald-Reifung). *Zeitschrift für Elektrochemie, Berichte der Bunsengesellschaft für Phys. Chemie* **1961**, *65* (7-8), 581–591.

(74) Speight, M. V. Growth Kinetics of Grain-Boundary Precipitates. *Acta Metall.* **1968**, *16* (1), 133–135.

(75) Hiemstra, T.; Antelo, J.; Rahnemaie, R.; van Riemsdijk, W. H. Nanoparticles in Natural Systems I: The Effective Reactive Surface Area of the Natural Oxide Fraction in Field Samples. *Geochim. Cosmochim. Acta* **2010**, *74* (1), 41–58.

(76) Cismasu, A. C.; Michel, F. M.; Tcaciuc, A. P.; Tyliszczak, T.; Brown Gordon E., J. Composition and Structural Aspects of Naturally Occurring Ferrihydrite. *Comptes Rendus Geosci.* **2011**, *343* (2), 210–218.

(77) Biedermann, G.; Chow, J. T.; Kujanpää, T.; von Hofsten, B.; Williams, D. H.; Bunnenberg, E.; Djerassi, C.; Records, R. Studies on the Hydrolysis of Metal Ions. Part 57. Hydrolysis of the Iron(III) Ion and the Solubility Product of Fe(OH)2.70Cl0.30 in 0.5 M (Na+)Cl- Medium. *Acta Chem. Scand.* **1966**, *20*, 1376–1388.

(78) Legg, B. A.; Zhu, M.; Zhang, H.; Waychunas, G.; Gilbert, B.; Banfield, J. F. A Model for Nucleation When Nuclei Are Nonstoichiometric: Understanding the Precipitation of Iron Oxyhydroxide Nanoparticles. *Cryst. Growth Des.* **2016**, *16* (10), 5726–5737.

(79) Kozin, P. A.; Boily, J.-F. Proton Binding and Ion Exchange at the Akaganéite/Water Interface. *J. Phys. Chem. C* **2013**, *117* (12), 6409–6419.

(80) Kersten, M.; Karabacheva, S.; Vlasova, N.; Branscheid, R.; Schurk, K.; Stanjek, H. Surface Complexation Modeling of Arsenate Adsorption by Akagenéite (β-FeOOH)-Dominant Granular Ferric Hydroxide. *Colloids Surfaces A Physicochem. Eng. Asp.* **2014**, *448*, 73–80.

(81) Hiemstra, T.; Van Riemsdijk, W. H. On the Relationship between Charge Distribution, Surface Hydration, and the Structure of the Interface of Metal Hydroxides. *J. Colloid Interface Sci.* **2006**, *301* (1), 1–18.

(82) Wang, X.; Zhu, M.; Koopal, L. K.; Li, W.; Xu, W.; Liu, F.; Zhang, J.; Liu, Q.; Feng, X.; Sparks, D. L. Effects of Crystallite Size on the Structure and Magnetism of Ferrihydrite. *Environ. Sci. Nano* **2016**, *3* (1), 190–202.

(83) Harrington, R.; Hausner, D. B.; Bhandari, N.; Strongin, D. R.; Chapman, K. W.; Chupas, P. J.; Middlemiss, D. S.; Grey, C. P.; Parise, J. B. Investigation of Surface Structures by Powder Diffraction: A Differential Pair Distribution Function Study on Arsenate Sorption on Ferrihydrite. *Inorg. Chem.* **2010**, *49* (1), 325–330.

(84) Maillot, F.; Morin, G.; Wang, Y.; Bonnin, D.; Ildefonse, P.; Chaneac, C.; Calas, G. New Insight into the Structure of Nanocrystalline Ferrihydrite: EXAFS Evidence for Tetrahedrally Coordinated Iron(III). *Geochim. Cosmochim. Acta* **2011**, *75* (10), 2708–2720.

(85) Harrington, R.; Hausner, D. B.; Xu, W.; Bhandari, N.; Michel, F. M.; Brown, G. E.; Strongin, D. R.; Parise, J. B. Neutron Pair Distribution Function Study of Two-Line Ferrihydrite. *Environ. Sci. Technol.* **2011**, *45* (23), 9883–9890.

CHAPTER 4

High and low affinity sites of ferrihydrite for metal ion adsorption: Data and modeling of the alkaline-earth ions Be, Mg, Ca, Sr, Ba, and Ra

Juan C. Mendez, Tjisse Hiemstra

Accepted for publication in *Geochimica et Cosmochimica Acta* in a revised version

Abstract

The alkaline-earth metal ions series comprises Be, Mg, Ca, Sr, Ba, and Ra. Calcium (Ca) and magnesium (Mg) are the most abundant alkaline-earth metal ions in nature and their interaction with the mineral surfaces of metal (hydr)oxides (*e.g.* ferrihydrite, Fh) affects the bioavailability, mobility, and geochemical cycling of many relevant ions. The adsorption of Ca^{2+} and Mg^{2+} ions to well-characterized freshly precipitated Fh has not been extensively measured yet in systems with a large variation in pH (4–10), ionic strength (0.01–1 M), and ion adsorption (0.002–2 μmol m^{-2}). Nor have such adsorption data been interpreted with a surface complexation model that regards the structure of the adsorbed complexes and state-of-the-art insights into the surface structure of Fh. The primary adsorption data collected in this study (M^{2+}/Fe) were scaled in a consistent manner to the surface area derived with a recently developed probe-ion methodology, before these data were interpreted with the charge distribution (CD) model, using MO/DFT/B3LYP/6-31+G** optimized hydrated geometries to obtain independently the CD coefficients. The pH-dependent adsorption behavior of Ca and Mg is rather similar. Both cations (M^{2+}) form predominantly bidentate inner-sphere surface complexes ($\equiv(FeOH)_2^{\Delta z0}M^{\Delta z1}$), most possibly present as a binuclear bidentate double corner (^{2}C) complex according to EXAFS data from literature for other divalent cations. This binding mechanism explains the relatively high H/Ca exchange ratio and the related pH-dependency of the Ca^{2+} adsorption. Modeling of the adsorption data reveals and quantifies the surface site heterogeneity of Fh, distinguishing high and low affinity sites for binding M^{2+} ions. Depending on the Fh preparation, the high affinity sites have a surface site density of ~0.3 ± 0.1 nm^{-2}, equivalent to the binding of ~3 metal ions per particle. The surface structure of Fh has been evaluated to rationalize this phenomenon and identify possible surface configurations. Undersaturation of the charge of oxygen ions shared by specific sets of Fe1 octahedra at the surface and the bulk mineral may cause a redistribution of charge within these surface Fe1 polyhedra, leading to an increase of the $\equiv$FeOH-M^{2+} bond strength of the adsorbed ion. The surface density of $\equiv$FeOH (0.28 ± 0.08 nm^{-2}) involved, according to our surface analysis of constructed 2.2–2.8 nm Fh particles, matches with the above surface site density of high affinity sites found by ion adsorption modeling. Extending our analysis to ion adsorption data from literature, comprising the full series of alkaline-earth ions, showed an increase in the adsorption affinity with increase in the ionic radius of these cations, *i.e.* $Be^{2+} < Mg^{2+} < Ca^{2+} \approx Sr^{2+} < Ba^{2+} < Ra^{2+}$, which is opposite to the affinity trend observed for other Fe-(hydr)oxides (*e.g.* hematite, goethite). Our analysis suggests that a difference in the order of affinity (log*K*) can be explained by a different energy contribution of the interfacial water in the binding of the metal ions, pointing to a relatively strong binding of physisorbed water by Fh in comparison to other Fe (hydr)oxides.

Keywords: calcium, magnesium, iron oxide nanoparticles, surface complexation modeling, CD model, cooperative and synergistic binding, electrostatic interactions, anion-bridged complexes

4.1. Introduction

Ferrihydrite (Fh) is a naturally occurring Fe-(hydr)oxide nanoparticle ($Fe_{ox}NP$) ubiquitously present in soils, aquifers, and oceans, and it is also found in for instance mine waste drainage.[1,2] Fh can be formed by either hydrolysis of ferric Fe(III) or oxidation of ferrous Fe(II) species.[3] Thermodynamically, Fh is the most stable $Fe_{ox}NP$ at the ultra-small nano-size scale.[4] Precipitated Fh particles are precursors of other more crystalline Fe-(hydr)oxides.[5–7] The (bio)geochemical cycle of Fh is coupled with that of many other elements, comprising nutrients, inorganic pollutants, and organic molecules.[8–13] Therefore, analyzing the interfacial processes of Fh at the nanoscale is essential to understand ion adsorption behavior at the macroscopic scale.

The extraordinarily high ion adsorption capacity of Fh is in the first place determined by its large specific surface area (SSA).[14] For freshly precipitated Fh, the SSA is in the order of ~600–1100 $m^2\ g^{-1}$.[15] Proton adsorption by the various types of surface groups of Fh results in an amphoteric behavior that is important for the pH-dependent binding of both metal cations and oxyanions. The mechanisms of ion adsorption to Fh have been extensively studied in a long history of surface complexation modeling (SCM), *in situ* spectroscopy, and quantum chemical computations (*e.g.* references [14,16–30]). For metal ion adsorption, most of the studies have focused on analyzing the interactions of heavy metal ions with Fh, probably because of their potential harmful effects in the environment. In contrast, the interaction of alkaline-earth metal ions with Fh has received considerably less attention, yet these elements are highly abundant in the environment and can affect significantly the behavior of other compounds.[31,32]

Historically, the rather enigmatic and elusive structure of Fh has impeded the development of a mechanistic SCM for this material, yet important contributions have been added over the last decade for clarifying the mineral and the surface structure of Fh.[33–38] According to the surface model of Fh,[35] the polyhedral composition of the Fh surface is different from that of the mineral core. In addition, the mineral core of Fh is H-poor while its surface is water-rich due to the large contribution of ≡FeOH and $\equiv FeOH_2$ surface groups. The overall composition of Fh, given as $FeO_{1.4}(OH)_{0.2}{\cdot}nH_2O$, is particle size-dependent due to the variable molar contribution of chemisorbed water (nH_2O) that completes the coordination spheres of Fe atoms at the surface of Fh.[35] This directly affects several Fh properties, including its molar mass M_{nano} (g mol^{-1} Fe) and mass density ρ_{nano} (g m^{-3}). Changes in M_{nano} and ρ_{nano} affect the relationship between the specific surface area ($m^2\ g^{-1}$) and the mean particle size. In the present study, the size-dependency of these properties will be included for consistently scaling and interpreting ion adsorption data.[39]

Surface site heterogeneity has been recognized as an important aspect of Fh for describing the binding of divalent metal ions.[14,24,40] A minor fraction of the reactive sites has a relatively high affinity for metal ions compared to most other sites. In the present approach, we will use M^{2+} adsorption data to estimate the quantity of the high affinity sites and will discuss a possible structural rationale for the presence of these sites in relation to the binding mode and types of ions involved. The challenge is to contribute to develop a general surface complexation model for describing simultaneously the adsorption of an entire suite of cat- and anions to Fh, in a mechanistic physical-chemical manner.

Based on all the above, the objective of the present study is to assess the binding of the alkaline-earth metal ions Ca and Mg to the surfaces of freshly prepared Fh suspensions. In the present work, the adsorption data will be interpreted with an advanced ion complexation model for Fh,[30] which considers state-of-the-art insights into the surface structure of Fh[35] in junction with the mineral structure proposed by Michel et al.[33] Using the mechanistic insights derived from the interpretation of Ca and Mg adsorption

data, we will generalize our interpretation to describe the adsorption of the full series of alkaline-earth metal ions, comprising Be^{2+}, Mg^{2+}, Ca^{2+}, Sr^{2+} Ba^{2+}, and Ra^{2+}. The alkaline-earth ions form a unique class of divalent metal cations with distinct properties that differ from those of other divalent cations (*e.g.* heavy metal ions). Interpreting adsorption data of Fh reported in literature for strontium (Sr),[41,42] as well as radium (Ra) and barium (Ba),[43] the adsorption of this series of ions will be evaluated in a consistent manner to disclose their variation in affinities (log*K*) for the surface sites of Fh, and to compare the results with the behavior found for other Fe (hydr)oxides (*e.g.* goethite).

4.2. Experimental section

Ultra-pure water (18.2 MΩcm at 25 °C, 1 ppb TOC) and chemical reactants of analytical grade were used to prepare all stock solutions and Fh suspensions. Contact between solutions and air was minimized to avoid the interference of CO_2(g) during the adsorption experiments.

4.2.1. Synthesis of ferrihydrite

Ferrihydrite nanoparticles were synthesized as described previously by Hiemstra et al.[15] Briefly, approximately 1.0 L of a solution containing ~3.7 mM of $Fe(NO_3)_3 \cdot 9H_2O$, dissolved in 0.01 M HNO_3, was hydrolyzed by adding a freshly-prepared solution of 0.02 M NaOH. The base solution was initially added at a rate of ~200 mL NaOH min^{-1} until a pH of ~3.1 was reached. More NaOH solution was subsequently added in ~5 mL increments until the suspension reached a final pH of ~8.2. Once the pH was stabilized (over 15 min), the Fh suspension was centrifuged at 3300*g* for 45 min. Then, the supernatant was carefully removed, and the settled Fh particles were re-suspended in a solution of 0.01 M $NaNO_3$ to a final volume of typically ~160 mL. Each freshly-prepared Fh suspension was aged in closed bottles for 4 h at 20 °C before starting the adsorption experiments. The total Fe concentration of each Fh suspension was measured by ICP-OES in a matrix of 0.8 M H_2SO_4. On average, the total Fe concentration in these stock suspensions was 20.5 ± 0.5 mM (~2 g L^{-1}). The specific surface area (SSA in m^2 g^{-1}) of each Fh batch was independently measured using PO_4 as probe ion.[39] In this approach, the pH-dependent adsorption of PO_4 is measured in single-ion systems. The primary adsorption data (*i.e.* mol PO_4 mol^{-1} Fe) are then iteratively interpreted with the CD model, defining the SSA as the only adjustable parameter and accounting for the size dependency of the molar mass (M_{nano}) and mass density (ρ_{nano}) of Fh, as well as the size dependency of the Stern layer capacitance.[39]

4.2.2. Adsorption experiments

The adsorption of Ca and Mg in single-ion systems was determined in a series of batch experiments with freshly prepared Fh suspensions as a function of the pH and the total molar M^{2+}/Fe ratio. Most of the experiments were performed in a background solution of 0.01 M $NaNO_3$. For some Ca systems, higher background electrolyte concentrations of 0.10, 0.50, or 1.0 M $NaNO_3$ were used to evaluate the ionic strength dependency of the Ca adsorption. An overview of the chemical conditions is given in Table S4.1 of the Supporting Information (SI).

Each adsorption system was prepared in 50 mL polypropylene tubes kept under moist-purified N_2(g) to prevent intrusion of CO_2(g) during the preparation of the systems. First, a solution of $NaNO_3$ was added according to the intended background electrolyte level (0.01–1.0 M $NaNO_3$). Next, a volume of 3.0, 7.5, or 15.0 mL of Fh stock suspension was added. The pH values of the suspensions were then adjusted within the desired range (*i.e.* pH 6 to 10) using 0.01 M solutions of either HNO_3 or NaOH.

Finally, an aliquot of a stock solution of either $Ca(NO_3)_2$ or $Mg(NO_3)_2$ was added to achieve the intended total cation concentration M^{2+} within the range of ~0.01–1.0 mM. The final volume of each adsorption system was 40.0 mL. For Mg, an adsorption isotherm was additionally determined at a constant pH (8.82 ± 0.02) and constant ionic strength (0.01 M $NaNO_3$). For this, different volumes of Fh stock suspension (8.0 to 20.0 mL) were combined with different total Mg concentrations (~0.02 to 1.0 mM) to obtain a wide range of Mg adsorption densities. All the adsorption systems were constantly shaken (120 strokes min^{-1}) at 20 °C. After 20 h of equilibration, the suspensions were centrifuged at 3330*g* for 20 min to separate the solid and liquid phases. An aliquot of 10 mL was taken from the supernatant of each adsorption system, filtered through a 0.45 µm membrane filter, and acidified with HNO_3 for analyzing the equilibrium concentration of the corresponding cation. The analysis was done using either ICP-OES or ICP-MS, depending on the final M^{2+} concentration. The settled Fh particles were re-suspended in the 50 mL polypropylene tube to measure the equilibrium pH with a combined glass electrode.

4.2.3. Modeling

The results of the adsorption experiments have been interpreted with the charge distribution (CD) model[44] in combination with a recent multisite ion complexation (MUSIC) model for Fh.[30] Details about this structural surface complexation model are described in Section 4.4.1. The electrical double layer (EDL) is described with the extended Stern layer approach.[45] As Fh is a ultra-small nanoparticle, the effect of surface curvature on the capacitance values ($C_{nano,1}$ and $C_{nano,2}$) of the inner- and outer- Stern layers are made size-dependent, using as a reference the capacitance values of a goethite surface with nearly zero surface curvature.[46] The protonation reactions determining the primary surface charge and the interactions of the background electrolyte ions with the surface groups of Fh are described according to Mendez and Hiemstra.[39]

CD modeling was performed with the software ECOSAT (version 4.9).[47] The affinity constants (log*K*) of the adsorption reactions of Ca and Mg were optimized using the program FIT (version 2.581).[48] The solution speciation reactions used in the modeling are given in Table S4.2 of the SI. In our modeling, we used CD coefficients for the various alkaline-earth metal ions that we derived with a Brown bond valence analysis[49,50] from the geometries of complexes optimized with molecular orbital (MO) calculations, applying density function theory (DFT) implemented in the software Spartan18 parallel of Wavefunction, Inc. Details about the template of the Fe cluster used in the geometry optimizations were recently described by Mendez and Hiemstra.[17]

4.3. Results

4.3.1. Adsorption of calcium

4.3.1.1. Effect of pH and molar Ca/Fe ratio

The Ca adsorption was studied in single-ion systems by varying either the Ca (Figure 4.1a) or Fe concentration (Figure 4.1b) in the Fh systems. In addition, the total concentrations of Ca and Fe were changed at a fixed molar Ca/Fe ratio (Figure 4.1c). The adsorption of Ca to Fh increases with increasing the pH, which is typical for the pH-dependent binding of metal ions to Fe-(hydr)oxides,[14] as there is a net release of protons upon metal ion adsorption.[51] The pH at which the Ca adsorption occurs is rather high compared to the adsorption pH values of divalent transition metal ions (*e.g.* Cd^{2+}, Pb^{2+}, Cu^{2+},

Zn^{2+}).[14,24,25,29,52] This reflects the relatively low affinity of this alkaline-earth metal ion for Fh, in comparison to heavy metal ions.

As follows from Figure 4.1, the pH-dependency of the adsorption edges of Ca becomes less pronounced at increasing the molar Ca/Fe ratios. For systems with the same Ca/Fe ratio but different total concentrations of Ca and Fe, the adsorption edges of Ca are shifted towards higher pH values for the systems with a lower total concentration of Ca and Fe (Figure 4.1c). Similar observations have been described for the adsorption of Cd to Fh,[53] and can be attributed to the non-linearity of the adsorption isotherms of these cations. The adsorption of Ca to Fh, expressed in mol mol^{-1} Fe or µmol m^{-2} (Figure S4.1), initially increases with increasing the total molar Ca/Fe ratio. Fh adsorbs more Ca than goethite per unit of Fe, especially at the higher pH range,[54] which is mainly due to the much larger specific surface area (m^2 g^{-1}) of Fh.

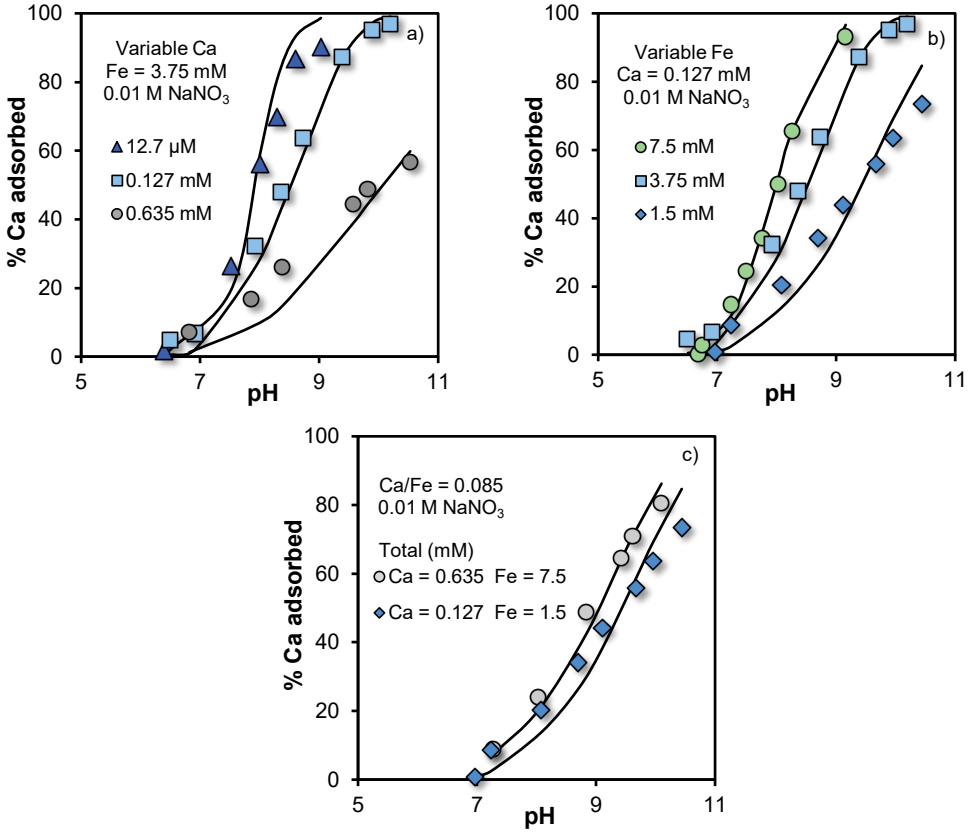

Figure 4.1. pH-dependent percentage of Ca adsorbed to ferrihydrite in single-ion systems. The specific surface area of these Fh suspensions was A = 684 ± 15 m^2 g^{-1} with a corresponding molar mass of M_{nano}= 96.6 g mol^{-1} Fe. The symbols are experimental data and the lines are CD model calculations obtained with the parameters set of Table 4.1. The translation of the data to surface loading is given in Figure S4.1 showing a variation over nearly 3 orders of magnitude (~0.002 and ~1 µmol m^{-2}). **Panel a)** presents the Ca adsorption at a fixed total Fe but variable Ca content in 0.01 M $NaNO_3$. **Panel b)** presents the Ca adsorption at a fixed initial Ca but variable Fe concentration in 0.01 M $NaNO_3$. **Panel c)** presents the Ca adsorption at fixed molar Ca/Fe ratio but different total Ca and Fe concentrations for systems in 0.01 M $NaNO_3$.

4.3.1.2. *Effect of ionic strength*

The effect of the ionic strength on the adsorption of Ca is presented in Figure 4.2 for two sets of Fh systems with contrasting total molar Ca/Fe ratios. For a given pH, the effect of the ionic strength depends on the adsorption density of Ca. For systems with the lowest total molar Ca/Fe ratio (Figure 4.2a), the adsorption of Ca clearly decreases when the ionic strength increases from 0.01 to 1.0 M $NaNO_3$. This trend has been reported previously for the adsorption of Ca to Fh[32] and goethite.[55] The adsorption of Ca to Fh occurs predominantly in the pH range above the point of zero charge (PZC), which is pH_{PZC} ~8.1 for Fh suspensions in $NaNO_3$.[39] Under these pH conditions, the surface of Fh is negatively charged, which creates a set of negative electrical double layer potentials that are attractive for Ca^{2+} ions. At increasing the ionic strength, this attractive field diminishes and consequently, the Ca adsorption decreases too. At a high Ca/Fe ratio (Figure 4.2b), the effect of ionic strength on the Ca adsorption is less evident, possibly because the relative high adsorption density in these systems contributes by itself to the compensation of the surface charge, reducing the change of the field by the background electrolyte.

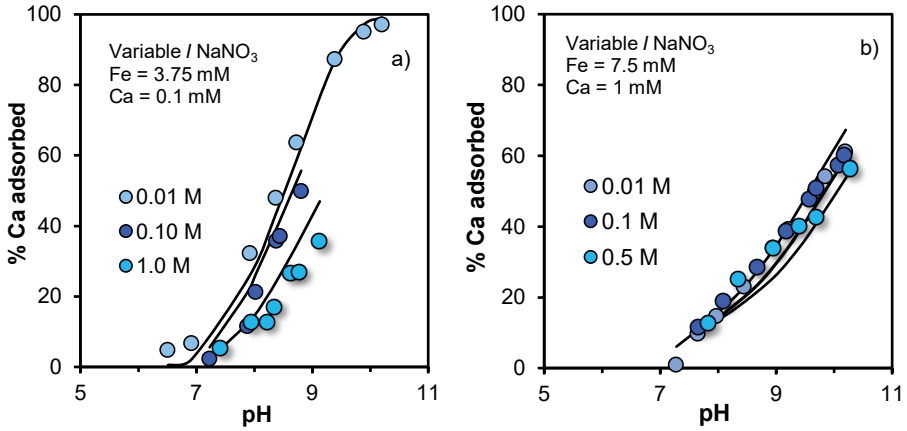

Figure 4.2. pH-dependent percentage of the Ca adsorption to ferrihydrite in single-ion systems at different $NaNO_3$ concentrations, added as background electrolyte solution. Panel **a**) and **b**) are for systems with total molar Ca/Fe ratios of ~0.03 and ~0.13, equivalent to an initial loading of ~0.4 and ~2.0 µmol m^{-2}. The symbols are experimental data and the lines are CD model calculations obtained with the parameters set of Table 4.1. The specific surface area of Fh was A = 684 ± 15 m^2 g^{-1} with a corresponding molar mass of M_{nsano}= 96.6 g mol^{-1} Fe.

4.3.2. Adsorption of magnesium

Despite the potential relevance of Mg in various marine and terrestrial environments, its interaction with Fh has not been studied in any detail yet. Here, we quantify the adsorption of Mg to freshly-prepared Fh in single-ion systems (Figure 4.3a) with different total molar Mg/Fe ratios. Like in the case of Ca, the adsorption edges of Mg are right-hand shifted when the total molar Mg/Fe ratio increases, and this behavior can be attributed to the non-linearity of the adsorption isotherm (Figure 4.3b). The adsorption of Mg is about proportional to its solution concentration (c) according to c^n with n ~ 0.4 (*i.e.* a Freundlich adsorption behavior) rather than n = 1 (*i.e.* a linear adsorption isotherm).

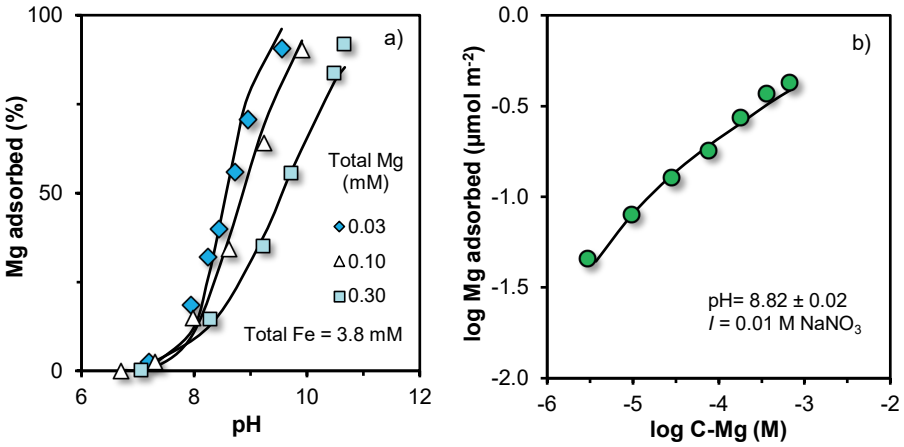

Figure 4.3. (**a**) pH-dependency of the Mg adsorption to ferrihydrite in single-ion systems with three total Mg concentrations (0.03, 0.10, and 0.30 mM) and one total Fe concentration (3.8 mM). The specific surface area of these Fh suspensions was A = 720 ± 10 m^2 g^{-1} with a corresponding molar mass of M_{nano} = 97.6 g mol^{-1} Fe. The initial loading varied between ~0.1 and ~1.1 µmol m^{-2} (**b**) Adsorption isotherm of Mg to ferrihydrite at pH 8.82 ± 0.02. The specific surface area of this Fh was A = 690 ± 17 m^2 g^{-1} with a corresponding molar mass of M_{nano} = 96.8 g mol^{-1} Fe. In both cases (panels a and b), the ionic strength was kept constant at I = 0.01 M $NaNO_3$. The symbols are experimental data and the lines are CD model calculations obtained with the parameters set of Table 4.1.

4.3.3. Ca versus Mg adsorption

In Figure 4.4, the adsorption behavior of Ca and Mg is compared for Fh systems with two different molar M^{2+}/Fe ratios. Both datasets show that, at the same experimental conditions, more Ca (spheres) than Mg (squares) is adsorbed to Fh, illustrating the higher adsorption affinity of Ca for Fh in comparison to Mg. This also follows from the higher log$K$ values for the adsorption of Ca presented in Table 4.1. A higher binding affinity of Ca compared to Mg has also been found for TiO_2.[56,57] Interestingly, the opposite affinity trend has been found for other Fe (hydr)oxides, including goethite and hematite.[58–61] This difference in affinity trend will be discussed in the Section 4.4.2.5.

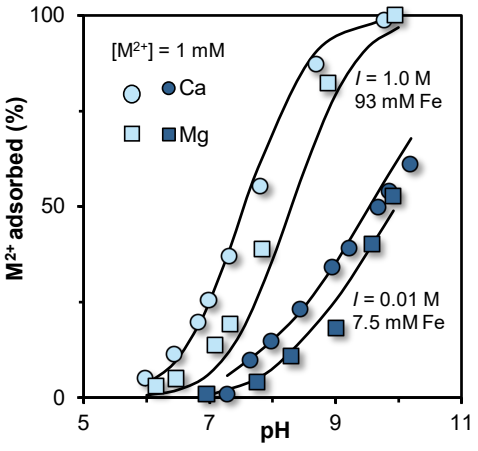

Figure 4.4. pH-dependency of Ca (circles) and Mg (squares) adsorption to ferrihydrite in single-ion systems. The total concentration of either Ca or Mg is $[M^{2+}]$ = 1 mM. The dark-blue symbols are experimental data collected in the present study in systems with an ionic strength of I = 0.01 M $NaNO_3$ and a total Fe concentration of 7.5 mM. The average specific surface area of this ferrihydrite is A = 700 ± 20 m^2 g^{-1} and the initial M^{2+} loading is ~2 µmol m^{-2}. The light-blue symbols are experimental data from Kinniburgh et al.[62] in systems with an ionic strength of I = 1.0 M and a total Fe concentration of 93 mM. The initial M^{2+} loading is ~0.2 µmol m^{-2}. The specific surface area of this ferrihydrite material is A = 585 m^2 g^{-1}, as calculated by Hiemstra[63] from proton adsorption data. The lines are model simulations obtained with the parameter set of Table 4.1.

4.4. Discussion

4.4.1. Multisite ion complexation model for Fh

Michel et al.[33,34] proposed a new structural model for Fh that has been subsequently supported by additional evidence.[36,37,64] Since Fh particles are ultra-small, the surface will dominantly contribute to the overall behavior of this nanomaterial. Many microscopic and macroscopic properties of Fh are size-dependent. The particle size dependency of a suite of physical-chemical properties of Fh can be understood from the difference in the polyhedral composition of the mineral core and the surface.[4,35,63,65] As mentioned in the Introduction section, Hiemstra and Zhao[30] have developed a mechanistic multi-site ion complexation model for Fh in which the types of sites, and corresponding densities, of this nanomaterial were derived independently with a surface structural analysis. The model includes the size-dependent variation of the molar mass (M_{nano}) and the mass density (ρ_{nano}) that results from the variable contribution of chemisorbed water (nH_2O) to the overall chemical composition of Fh ($FeO_{1.4}(OH)_{0.2}\cdot nH_2O$).[15]

In this structural multi-site Fh model, three types of surface groups have been defined, which differ in their coordination number to Fe: *i.e.* singly ($\equiv FeOH^{-0.5}$), doubly ($\equiv Fe_2OH^0$), and triply ($\equiv Fe_3O^{-0.5}$) coordinated groups. Furthermore, two types of singly coordinated groups can be distinguished structurally, namely $\equiv FeOH(a)^{-0.5}$ and $\equiv FeOH(b)^{-0.5}$, which can form respectively either single edge (^{1}E) or double corner (^{2}C) bidentate surface complexes, having a surface density of $N_s(a) = 3.0$ nm^{-2} and $N_s(b) = 2.8 \pm 0.6$ nm^{-2}. Both types of singly coordinated groups may also form single corner (^{1}C) monodentate surface complexes. The triply coordinated groups do not participate in ligand exchange reactions but contribute to the development of primary surface charge with an effective site density of $N_s(T) = 1.4 \pm 0.5$ nm^{-2}. The $\equiv Fe_2OH^0$ groups are apparently uncharged and do not react with protons at common pH conditions. This surface model has been applied to describe consistently the adsorption of a range of oxyanions, such as PO_4 and AsO_4,[30] $Si(OH)_4$,[63] and CO_3.[17] In the present study, this ion adsorption framework for Fh will be extended by introducing the concept of high affinity sites to describe the adsorption of alkaline-earth metal cations, and this can be relevant for metal ion adsorption in general.

4.4.2. Modeling

4.4.2.1. Adsorption mechanism

To the best of our knowledge, no *in-situ* structural information is available about the binding modes of Ca and Mg to Fh. However, extended X-ray absorption fine structure (EXAFS) has been used in the past to analyze the surface complex structure of another alkaline-earth metal ion, namely strontium (Sr^{2+}).[66] With EXAFS, a Sr-Fe distance of 375 ± 6 pm has been found at a total molar Sr/Fe ratio of 0.1,[66] which is equivalent to an estimated initial loading of ~1.5 μmol m^{-2}. Under extreme conditions with a tenfold higher (1:1) Sr/Fe ratio, the reported Sr-Fe distance is shorter, *i.e.* 340 ± 11 pm. The short Fe-Sr distance may be due to edge (E) sharing while double corner sharing may lead to the larger Fe-Sr distance. Comparison to the structure of Sr ferrite $SrFe(III)_2O_4(s)$[67] supports this, although we notice that in ferrites Fe is 4-fold rather than 6-fold coordinated.

For a further interpretation, we have optimized the geometry of a hydrated $SrFe_2(OH,OH_2)_{10}$ cluster with MO/DFT. Our MO/DFT/B3LYP/6-31+G** optimizations of various equilibrium geometries show an intricate picture of possible complexes in which, the initial location of the Sr ion, its coordination

number (CN), and the predefined water network play a role in the final outcome. For optimized hydrated double corner complexes of Sr^{2+} (CN = 8), we can find an equilibrium Fe-Sr distance of 426 ± 3 pm as well as 385 ± 25 pm. In case of the removal of one water molecule from the latter structure, the Fe-Sr distance decreases to 362 ± 15 pm. In that complex, the Sr^{2+} ion coordinates additionally to a doubly Fe-coordinated OH-ligand (≡Fe_2OH) in our cluster. In fact, a tridentate complex is then formed with double edge (^{2}E) sharing. In case of the formation of a single edge (^{1}E) complex, we find a similar value for the Fe-Sr distance (369 pm). Our optimizations suggest that a short Sr-Fe distance can be attributed to edge formation and the larger Sr-Fe distances refer to the formation of binuclear bidentate double corner complexes.

For goethite, EXAFS data do not show convincing evidence for the presence of Fe in the coordination sphere of Sr at pH 7 and in the absence of a background electrolyte.[68] However, adsorption data and CD modeling suggest inner-sphere complex formation at a neutral pH. Inner-sphere surface complexes are observed for goethite with EXAFS at very high pH (10-13) showing *d*(Fe-Sr) = 430 pm,[69] or *d*(Fe-Sr) = 358 and 448 pm.[70] Considering our MO/DFT calculations, the larger distance can be explained by the formation of a binuclear bidentate complex and the short distance points to the formation of a mononuclear bidentate complex.

Based on the above, and after an extensive modeling search (Appendix K), we assume for the binding of M^{2+} to Fh the formation of binuclear bidentate complexes as the dominant binding mechanism, according to:

$$2\ \equiv\mathrm{FeOH(b)}^{-0.5} + \mathrm{M}^{2+}(\mathrm{aq}) \leftrightarrow \equiv (\mathrm{FeOH(b)})_2^{-1+\Delta z0}\mathrm{M}^{\Delta z1} \qquad \log K_{\mathrm{BM}} \qquad \text{(Equation 4.1)}$$

in which $\equiv\mathrm{FeOH(b)}^{-0.5}$ represents the singly coordinated groups (type b) that can form double corner complexes and Δz_0 and Δz_1 are the charge attributions to respectively the surface and 1- Stern plane. These coefficients have been derived with a Brown bond valence analysis[49,50] of the MO/DFT/B3LYP/6-31+G** optimized geometry of the M^{2+} complexes (Table S4.4).

Since both Ca^{2+} and Cd^{2+} are divalent cations of nearly equal ionic radius and have the same coordination number (CN = 6), the optimized structure of a hydrated $CdFe_2(OH,OH_2)_{10}$ cluster used as a starting point for optimizing the structure of the various alkaline-earth metal ions. The experimental *d*(Fe-Cd) = 376 ± 4 pm reported by Tiberg and Gustafsson[29] for this Cd complex is well-reproduced with our MO/DFT/B3LYP/6-31+G** calculations, resulting in *d*(Fe-Cd) = 370 ± 6 pm. The latter value represents the average (± S.D.) of the Fe-Cd distances found by optimizing 4 different Fe(III) clusters (see Appendix G).

After replacing Cd^{2+} by Ca^{2+} in these Fe(III) clusters and subsequent geometry re-optimization, the equilibrium Ca-OH(H) distances obtained have been used to calculate the interfacial charge distribution coefficients, yielding for Ca^{2+} Δz_0 = +0.94 v.u. and Δz_1 = +1.06 v.u. The mean Fe-Ca distance in the optimized clusters is *d*(Fe-Ca) = 372 ± 8 pm. Similarly, we found for Mg (CN = 6), Sr (CN = 8), and Ba (CN = 8) respectively *d*(M-Fe) = 362 ± 4, 427 ± 5, and 440 ± 20 pm. Be (CN = 4) has the shortest M-Fe distance, *i.e.* 323 ± 6 pm. In Table S4.3, the Fe-M^{2+} and M^{2+}-OH(H) distances are given for a case in which the Fe(III) ions are fixed in the cluster, *i.e.* no Fe(III) relaxation is allowed.

In Figure 4.5a, the optimized structure of one of the alkaline-earth metal ions (Ca^{2+}) is given as an example. In addition, we show in Figure 4.5b the interfacial charge attribution (Δz_0) values for the various optimized complexes (also given in Table 4.2) in comparison to the values that are calculated assuming a symmetrical distribution of charge within the coordination sphere of each adsorbed metal ion, *i.e.* using Pauling bond valences. A linear relationship is observed between the Δz_0 values derived from the Brown bond valance analysis of the MO-DFT optimized geometries and the Δz_0 values calculated using Pauling bond valences. However, this relationship is shifted in the y-axis by about +0.20 v.u. (black arrow) with respect to the 1:1 line (dashed line). This shift may be rationalized in the first place as a change in charge distribution imposed by the coordinating –OH ligands of the Fe(III) cluster used in optimizations, rather than by the type of adsorbing metal ion.

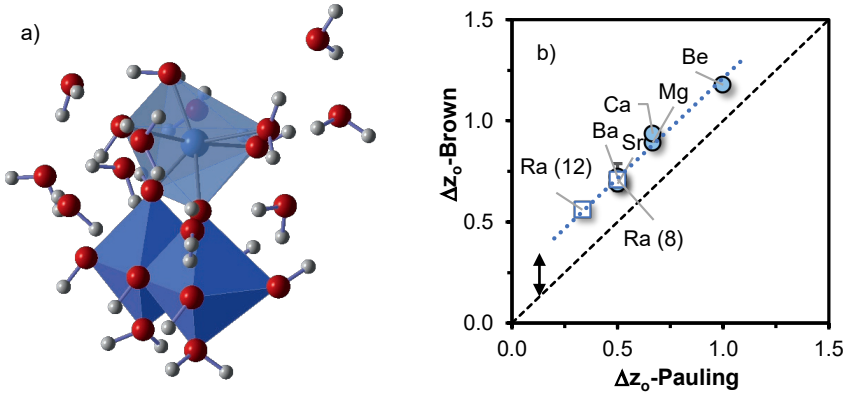

Figure 4.5. a) Optimized geometry of a Fe (hydr)oxide cluster ($Fe_2(OH)_8(OH_2)_2$) with a binuclear bidentate double corner complex of Ca^{2+} with 14 surrounding water molecules. **b**) Comparison of the interfacial charge attribution (Δz_0) of the common surface -OH ligands of various binuclear bidentate double corner complexes of M^{2+} ions, calculated with a Brown bond valence analysis (y-axis) applied to the optimized MO/DFT/B3LYP/6-31+G** geometries (Table 4.2) and by assuming an equal charge distribution over the ligands in the M^{2+} coordination spheres (x-axis), *i.e.* using the Pauling bond valence approach. For Ra (open symbols), the Δz_0-Brown values were calculated by extrapolating the results of the other ions, considering a coordination number of CN = 8 or 12.

In theory, bidentate complex formation of Ca can also be inferred by a thermodynamic consistency analysis of macroscopic data, using either the net release of H^+ per mol of adsorbed Ca^{2+} at constant pH, or the pH-dependency of the Ca adsorption, provided that the adsorption is dominated by only one binding mode. The H/Ca exchange ratio reflects the change in the net surface charge upon specific ion adsorption at fixed pH values.[14,51,71] For Fh suspensions in 1.0 M $NaNO_3$, the experimental H/Ca exchange ratio is 0.92 ± 0.03 as reported by Kinniburgh.[51] In systems with 0.01 M $NaNO_3$, the predicted H/Ca exchange ratio will be even larger, about ~1.7 (Figure S4.2). This points to a relatively strong electrostatic interaction of the Ca^{2+} ion with the protons bound at the surface and consequently, to a large pH dependency of the Ca adsorption. Our modeling predicts a H/Ca ratio of ~1.0 for Fh systems in 1.0 M $NaNO_3$ in the case of bidentate complex formation, which is in close agreement with the experimental data, while the ratio would be only H/Ca ~0.5 in the case of monodentate complex formation. In addition, the formation of monodentate complex as main binding mechanisms is inconsistent with the description of the adsorption of Ca and PO_4 in the binary systems (Chapter 5). All this evidence obtained from macroscopic data supports our assumption that bidentate complex formation is most probably the dominant binding mechanism of Ca to Fh.

4.4.2.2. *"High" and "low" affinity sites of Fh*

Surface site heterogeneity is a commonly reported phenomenon for the binding of metal ions to Fh.[14] From an electrostatic perspective, metal ions may bind stronger at a lower than at a higher surface loading. Heterogeneity is only evident if the metal adsorption is studied over a sufficiently large range of surface loadings. Kinniburgh and Jackson[25] have collected an impressive set of Ca^{2+} adsorption data to Fh, covering a large concentration range of ~5 orders of magnitude (Figure 4.6a). The pH was also strongly varied (Figure 4.6b). Defining in our modeling approach the formation of bidentate complexes as the main binding mode of Ca (Equation 4.1), these dataset could be well described only by introducing in the CD modeling sites with a relatively high affinity for Ca, in addition to sites with a lower affinity. Excluding site heterogeneity from the modeling led to unacceptable deviations in the model predictions, particularly in systems with a high Ca loading. Evaluation other modeling options with different binding mechanisms of Ca neither provided an accurate description of the experimental adsorption data (see Appendix K in the SI). In addition, chemical heterogeneity was required for describing our own adsorption data of Ca (Figure 4.1) as well as for data from literature for Sr, Ba, and Ra adsorption as given in Figures S4.5, S4.6, and S4.7, respectively.

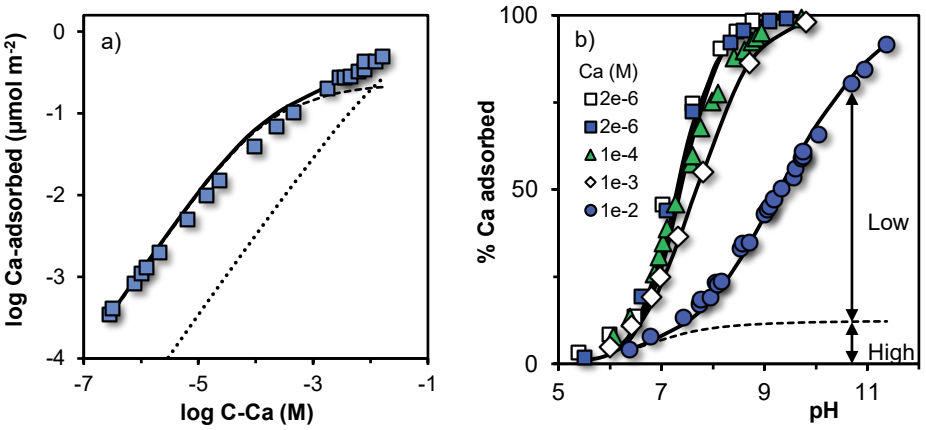

Figure 4.6. a) Adsorption isotherm of Ca to Fh at pH 8.0 and **b**) pH dependency of the Ca adsorption to Fh for a broad range of total Ca concentrations in 1.0 M $NaNO_3$ and at a total Fe concentration of 93 mM. Data are from Kinniburgh and Jackson.[25] The full lines give the model result, using for Fh a derived specific surface area of A = 585 m^2 g^{-1}. The dashed and dotted lines in panel a) give respectively the contribution of the high and low affinity sites to the binding of Ca. The dashed line in panel b gives the contribution of the high affinity site at the highest Ca addition (10^{-2} M). The site densities for the high and low affinity sites are 0.29 ± 0.02 and 2.51 nm^{-2} respectively. Applying the CD model, the pH dependency of the data show that the Ca^{2+} ions bind to Fh predominantly as a bidentate complex. The CD values have been derived independently from MO/DFT optimized geometries, leading to a good description of the data (R^2 = 0.99, n= 89). The model parameters are presented in Table 4.1.

The shape of the isotherm in Figure 4.6a is characteristic for the adsorption of metal ions to the surfaces of Fh.[14] At low surface coverages, the adsorption density of Ca increases almost linearly with the concentration of Ca in solution. The reason is the nearly constant electrostatic contribution to the overall adsorption energy, due to the insignificant introduction of interfacial charge by the adsorbed metal ion and the absence of site saturation. This results in a slope s of ~1 in the log-log plot (Figure 4.6a). Linearity can also be deduced from the absence of a pH-shift in the adsorption edges of Ca for the series with the lowest total Ca additions (Figure 4.6b). According to Figure 4.6a, there is a loss in

linearity at increasing Ca adsorption densities. Our modeling shows that at high loadings, this loss in linearity cannot be explained by just changes in the electrostatic adsorption energy.[14,24,40] A significant quantity of additional sites with a substantially lower intrinsic affinity for Ca is present at the Fh surface.

In Figure 4.6, our modeling outcomes for Ca^{2+} are given with lines. In the modeling, we used a specific surface area of A = 585 m^2 g^{-1} that is based on the reported proton titration in the pH range of ~5.0–8.2.[39] The consistent value of molar mass is M_{nano} = 94.1 g mol^{-1} Fe. The dashed and dotted lines in Figure 4.6a represent the adsorption to respectively the high and low affinity sites. The modeling shows that in this data set, the Ca adsorption at pH 8 is dominated by the binding to the high affinity sites. At pH 8, the high affinity sites get saturated only at solution concentrations of ~10^{-2} M Ca. Conversely, at pH 10, the adsorption of Ca is dominated by low affinity sites over a wider range of solution concentrations (Figure S4.3).

In Figure 4.6a, the contribution of the low affinity sites to the overall Ca adsorption is still relatively low. However, at higher pH, it can be substantially larger, as given in Figure 4.6b. These data at high pH and high loading can be consistently described only if a combination of low and high affinity sites is included in our modeling approach (Appendix K). At the surface of Fh, the low affinity sites dominate (N_s = 2.51 nm^{-2}), but its contribution to the Ca adsorption is usually limited to a relatively high pH and Ca concentration, as is given in Figure 4.6 with the dashed lines. Calculations show that there is only a relatively small number of high affinity sites (N_s = 0.29 ± 0.02 nm^{-2}). This is also experienced in the modeling of our own data, where the contribution of the low affinity sites becomes only evident at high pH. The good agreement between the data and modeling advocates the presence of two types of sites that strongly differ in their affinity for Ca and in their surface density. The intrinsic log$K$ values found for these high and low affinity sites differ by ~2.5 log$K$ units and are respectively logK_{BhCa} = 5.13 ± 0.02 and logK_{BlCa} = 2.62 ± 0.03 (Table 4.1).

Table 4.1. Surface species, CD coefficients, and fitted log$K$ for the binding reactions of Ca (n = 89, R^2 = 0.99) and Mg (n = 32, R^2 = 0.98) to Fh. The surface site densities used are from Hiemstra and Zhao[30] with ≡FeOH(a) = 3.0 nm^{-2}, ≡FeOH(b) = 2.8 nm^{-2} and ≡Fe_3O = 1.4 nm^{-2}. Two types of ≡FeOH(b) groups were defined to account for site heterogeneity ≡FeOH(bl) for low and ≡FeOH(bh) for high affinity sites. The site densities of these surface groups were fitted respectively to 2.48 ± 0.02 and 0.32 ± 0.02 nm^{-2} for our Fh suspensions. The capacitance values for the extended Stern layers of Fh ($C_{nano,1}$ and $C_{nano,2}$) are size-dependent and are calculated taking the capacitance values of a flat plane as reference (C_1 = 0.90 F m^{-2} and C_2 = 0.74 F m^{-2}).

Species	ID*	≡FeOH(bl)$^{-0.5}$	≡FeOH(bh)$^{-0.5}$	Δz_0**	Δz_1	Δz_2	H^+	Ca^{2+}	Mg^{2+}	log$K$ ± SE***
(≡FeOH)$_2$Ca	BCa(l)	2	0	0.94	1.06	0	0	1	0	2.62 ± 0.03
(≡FeOH)$_2$Ca	BCa(h)	0	2	0.94	1.06	0	0	1	0	5.13 ± 0.02
(≡FeOH)$_2$Mg	BMg(l)	2	0	0.89	1.11	0	0	0	1	1.87 ± 0.06
(≡FeOH)$_2$Mg	BMg(h)	2	2	0.89	1.11	0	0	0	1	4.09 ± 0.04

* BCa(l) = Bidentate (double-corner) Ca with low affinity sites; BCa(h) = Bidentate (double-corner) Ca with high affinity sites; BMg(l) = Bidentate (double-corner) Mg with low affinity sites; BMg(h) = Bidentate (double-corner) Mg with high affinity sites

** The CD coefficients have been derived from MO/DFT optimized geometries.

*** The log$K$ values for Ca were optimized using the Ca adsorption data Kinniburgh and Jackson.[25] See text.

4.4.2.3. Structural interpretation high affinity sites

Presently, it is difficult to indisputably link the observed difference in metal ion affinity to a comprehensive structural surface configuration of Fh. In literature, the presence of sites for crystal growth has been proposed as explanation for the existence of high affinity sites.[72] However, for Fh the crystal growth occurs by a simultaneous attachment of Fe octahedra in pairs,[15] whereas the Ca^{2+} and Mg^{2+} adsorption refers to the binding of a single ion, making sites of crystal growth less likely as the reckoned high affinity sites. We propose that the high affinity character of a small fraction of the singly coordinated groups is related to the presence a selective number of surface -OH ligands that are less well neutralized by the Fe(III) ions of the solid. Consequently, these sites will have a higher affinity for binding metal (M^{2+}) ions. Stronger ≡FeOH-M^{2+} bonds can then be formed. Below, we present the result of a surface structural analysis, in an attempt to identify a possible set of ≡FeOH sites that may have a high affinity character. There are two criteria in the search for such a structure, namely, it gives a) an explanation for the number of high affinity sites found in our modeling and 2) there is a rationale for its high affinity character.

A major characteristic of the Fh structure is that the Fe1 octahedra (60%) are organized in single sheets that are bound together by Fe in Fe2 octahedra (20%) and Fe3 tetrahedra (20%).[33] At the surface, the Fe1 polyhedra are relatively protruded.[35] In Figure 4.7, a snapshot is given of a part of the surface of a Fh particle, showing in yellow the layers with Fe1 octahedra that are bound together by highly distorted Fe2 (dark blue octahedra) and Fe3 (light blue tetrahedra). Both rose-colored Fe1 octahedra with singly coordinated ≡FeOH groups in the front can form a binuclear bidentate complex (^{2}C) with a metal ion, having a supposed high affinity.

In Figure 4.7, the two turquoise-colored spheres of the high affinity moiety represent two O3 oxygen ions, whereas the two white spheres are two O4 oxygen ions. These oxygen ions have the same coordination number (CN) as in the bulk mineral, namely CN=3 and CN=4 respectively, and without surface relaxation, these oxygen ions are under-saturated in bond valence charge, being respectively –0.18 and –0.07 v.u.[35]

The dark-blue spheres of the edge of the Fe1 octahedra are both undercoordinated due to the absence of a Fe3 tetrahedron, changing the coordination number from CN = 4 to CN = 3 (although this is not visible in the present representation). Due to the absence of a Fe3 tetrahedron, a bond valence charge of 0.75 v.u. is lacking. For the upper dark-blue O4 oxygen ion, this leads to a charge of $–0.07 – 0.75 \approx –0.82$ v.u. Upon interaction with the water network with charge donation of ~0.2 v.u., the net oxygen charge will be reduced to ~0.62 v.u., equivalent to an estimated value of $logK_H$ ~12.[73] Consequently, the oxygen ion will carry a proton, which saturates the oxygen valence (≈ 0 v.u.). The lower dark-blue O2 oxygen ion had originally a charge of +0.23 v.u.,[35] but due to the absence of a Fe3 tetrahedron, its charge changes to $+0.23 – 0.75 \approx –0.5$ v.u. This charge will decrease by ~ 0.2 v.u. in case of hydrogen bond formation with interfacial water, leading to a relatively low value for the protonation constant, $logK_H \sim 6$,[73] effectively preventing protonation. The dotted black spheres are “ordinary” uncharged, doubly coordinated ≡Fe_2OH^0 surface groups.

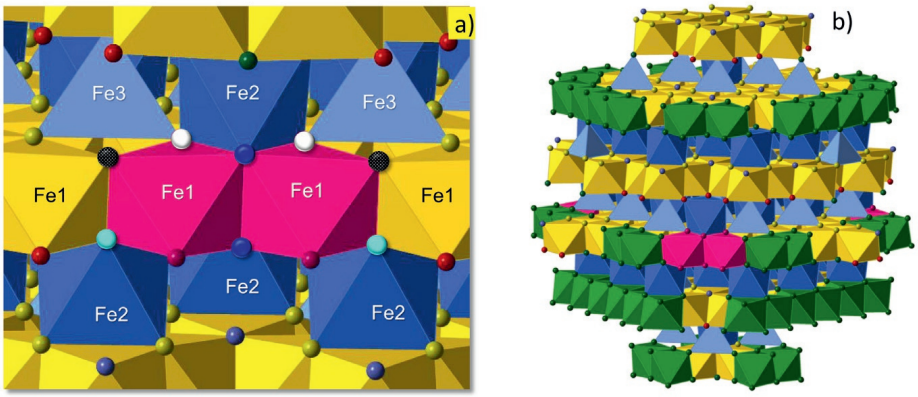

Figure 4.7. a) Snapshot of the surface of a Fh particle showing layers with Fe1 octahedra (yellow), bound together by Fe2 (dark blue) and Fe3 (light blue) polyhedra with two rose-colored Fe1 octahedra having two singly coordinated ≡FeOH groups forming a high affinity site. The various types of oxygen ions of the Fe1 octahedra that are shared with the Fe octahedra of the solid are undercoordinated and contribute in a different degree (see text) to a redistribution of the charge within the Fe1 octahedra. The shift of charge leads to an increased demand for saturation of both singly coordinated ≡FeOH surface groups that can be delivered by the coordination of an adsorbed M^{2+} ion, yielding high affinity sites with a density of 0.28 ± 0.08 nm^{-2} for representative Fh particles of different size. **b)** Fh particle (2.7 nm) with 3 pairs of Fe1 octahedra (rose-colored) with high affinity ≡FeOH sites and 27 pairs of other ≡FeOH sites (green) with a low affinity that both can form binuclear bidentate complexes.

Collectively, the oxygen ions of both rose-colored Fe1 octahedra shared with the bulk may cause a redistribution of charge within the Fe1 moiety. Upon relaxation, bond valence charge may move towards the oxygen ions shared with the solid, decreasing the charge neutralization of the oxygen ligands of the ≡FeOH surface groups having the lowest Fe coordination. This shift in charge will lead to an increased demand for saturation of the charge of both ≡FeOH surface groups that can be delivered by a M^{2+} ion that adsorbs. In Figure 4.7b, we present a 2.7 nm Fh particle that has three pairs of high affinity Fe1 octahedra (rose-colored) and 27 other Fe1 pairs with a supposed low affinity for forming binuclear bidentate complexes.

By constructing Fh nanoparticles of various sizes, we found some variations on the structure of Figure 4.7a, in which for instance the lower dark-blue O2 oxygen ion retained its coordination with the tetrahedral Fe3 (Figure S4.8a) or in which the Fe1octahedra at either side of the high affinity octahedra were absent (Figure S4.8b). Therefore, high affinity sites probably form a class of structural configurations rather than a single one. All these sites are affected to a greater or less extent by a shift of charge within the Fe1 octahedra to satisfy charge of the oxygen ions shared with the mineral bulk. The increase in affinity of the corresponding singly coordinated ≡FeOH groups is in the order of ~2–3 log*K* units for alkaline-earth metal ions (Tables 4.1 and 4.2) according to our data analysis.

In our model approach, the class of high affinity sites is represented by a single site and a mean log*K* value. Actually, a small variation in log*K* may exist within this class of high affinity sites. If so, this will lead to less linearity in the adsorption isotherms at low loading where the electrostatic energy contribution is practically constant, unaffected by the metal ion loading. This may be the reason why the slope of the experimental isotherm in Figure 4.6a changes slightly more than the model prediction. By explicitly introducing within the high affinity sites a distribution of affinities, as done for proton and ion adsorption to organic matter,[74,75] one may improve the model description, but this development is beyond the scope of the present paper.

We have constructed a few Fh particles of different sizes (2.2–2.8 nm) for counting the number of groups related to the above-described surface structures. The particles had a specific surface area between SSA 550–750 $m^2\ g^{-1}$. At the surfaces of these particles, only one to three high affinity moieties were found. This is equivalent to a typical density of high affinity ≡FeOH sites of 0.28 ± 0.08 nm^{-2}, which is 10% of the total amount of ≡FeOH(b) sites. This number obtained for the high affinity sites matches satisfactorily with the site densities found by fitting of M^{2+} adsorption data.

4.4.2.4. *Modeling our Ca and Mg adsorption data*

Our adsorption data for Ca cover a broad range of conditions, comprising different molar Ca/Fe ratios, pH values, and ionic strength. This extensive data set can be described using the Ca^{2+} ion as probe to derive the site density of the high affinity sites. In the approach, we use the intrinsic log*K* values derived above for the data collected by Kinniburgh and Jackson[25] (Table 4.1). By only adjusting slightly the site density of the high affinity sites, our entire data set can be well described as illustrated with the model lines in Figures 4.1 and 4.2. The optimized site density for the high sites of our Fh preparations is N_s(bh) = 0.32 ± 0.02 nm^{-2} (R^2 = 0.951, n = 78) and the corresponding site density for the low affinity sites is set to N_s(bl) = 2.48 nm^{-2}, as the sum of both types of $FeOH(b)^{-0.5}$ groups is 2.8 nm^{-2}.[30] The fitted N_s(bh) value is in excellent agreement with the density of high affinity sites derived from the adsorption data of Kinniburgh and Jackson[25] and from the surface structural analysis of Fh. Using the parameters set of Table 4.1, the Ca adsorption data from Dempsey and Singer[76] can also be well-described (Figure S4.4).

For goethite, formation of inner-sphere monodentate complexes with the singly coordinated groups has been proposed as the dominant binding mode of Ca.[54,59,60,77–79] For a freeze-dried Fh material, Antelo et al.[21] have also used in the modeling monodentate inner-sphere complexes, combining non-hydrolyzed (≡$FeOHCa^{+1.5}$) and hydrolyzed (≡$FeOHCaOH^{+0.5}$) surface species. Applying these surfaces species in our modeling, with and without including outer-sphere complex formation, did not allow a good description of our data if the aim is to describe simultaneously and consistently also the extensive dataset of Kinniburgh and Jackson[25] (Appendix K). Moreover, as mentioned in Section 4.4.2, defining monodentate complexes as the main binding mechanism of Ca is inconsistent with the description of Ca and PO_4 adsorption in the binary Ca-PO_4 systems (Chapter 5).

For Mg, modeling of the adsorption data in single-ion systems suggests that the binding mechanism of this cation is similar to that of Ca. Formation of inner-sphere bidentate complexes is the dominant binding mode of Mg to the surfaces of Fh (Equation 4.1). Surface site heterogeneity is also required to describe properly the adsorption edges (Figure 4.3a) and the adsorption isotherm (Figure 4.3b) of this cation. In our modeling of the Mg adsorption data, we used the same site densities for the high and low affinity sites of Fh as derived above from our Ca adsorption data. The CD model parameters for Mg are presented in Table 4.1. These parameters provide a good description of the adsorption data of Mg in single ion systems (R^2 = 0.98, n = 32).

4.4.2.5. *Variation in affinity of alkaline-earth ions*

Table 4.1 shows that the log*K* values of the high and low affinity sites for Mg are lower than the corresponding log*K* values for Ca. This model outcome agrees with the parallel shift in the adsorption edges of Ca and Mg along the pH scale seen in Figure 4.4, illustrating the difference in binding affinity between these two ions. The trend in affinity $Ca^{2+} > Mg^{2+}$ observed for Fh is also found for TiO_2,[56,57] but remarkably not for other Fe (hydr)oxides, such as hematite[61] and goethite[58–60] nor for SiO_2.[80] The

trend in affinity is related in a complex manner to the size of the adsorbed ion. Ca^{2+} and Mg^{2+} are just two members of the series of alkaline-earth metal ions, comprising Be^{2+}, Mg^{2+}, Ca^{2+}, Sr^{2+}, Ba^{2+} and Ra^{2+}.

To generalize our work and confirm the observed trend in affinity for the whole series of ions, we have included in our adsorption modeling relevant data for other alkaline-earth metal ions (Figures S4.5 – S4.7) as far as data are available in literature (Table 4.2). In the modeling approach, the formation of binuclear bidentate complexes (Equation 4.1) has been defined as the main binding mechanism, similar as defined for Ca and Mg. The CD values used in the modeling are provided in the legend of Table 4.2. In Figure 4.8, the variation in adsorption affinity (log*K*) as a function of the ionic radius of M^{2+}(aq) is illustrated for both the high and the low affinity sites. In both cases, the log*K* values increase at increasing the ionic radius of the alkaline-earth metal ions.

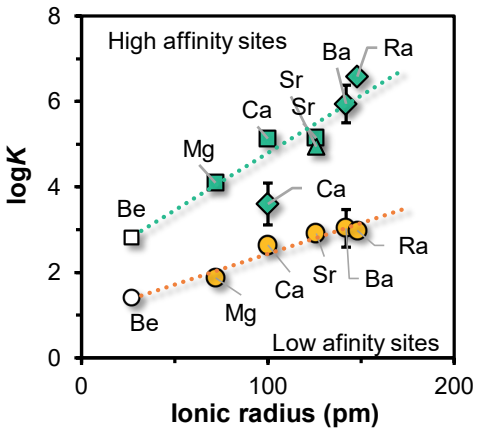

Figure 4.8 Affinity constants of high affinity sites (logK_{bh}) for the series of alkaline-earth metal ions (green symbols). The modeling is based on our own experimental data and those of Kinniburgh et al.[25,41] (green squares), Kolařík[42] (green triangle), and Sajih et al.[43] (green diamonds). The corresponding logK_{bl} values for the low affinity sites are given as orange spheres. The logK_{bh} and logK_{bl} values for Be (open symbols) have been calculated by a linear extrapolation of the logK_b values of the other alkaline-earth metal ions. The ionic radius data are from Shannon.[81] The details of the CD modeling are given in the Supporting Information (Figures S4.5 – 4.7).

The formation of M^{2+} inner-sphere surface complexes can be split into a sequential number of reactions, comprising 1) partial dehydration of the aqueous M^{2+} ion, 2) removal and rearrangement of interfacial water upon surface attachment of this partially hydrated M^{2+}, and 3) bond formation of the adsorbed M^{2+} ion with the surface -OH groups. For each of the reactions an energy change can be attributed that in summation leads to the overall adsorption energy change ΔE_{ads}. The dehydration enthalpy or energy ($-E_h$) is nearly linearly related to the ionic size.[80] Smaller M^{2+} ions are more difficult to dehydrate than larger ones due to the formation of shorter and stronger M-OH_2 bonds. Simultaneously, one may expect for smaller M^{2+} ions stronger bonds with the -OH groups at the surface of Fh. If the formation energy of the latter (E_f) is proportionally larger than the dehydration energy ($-E_h$) for each type of ion, *i.e.* $E_f = f E_h$ with $f>1$, the smaller alkaline-earth ions will have a higher adsorption energy $\Delta E_{ads} = E_f - E_h = (f-1) E_h$, since more energy is gained than invested. In this way, one can explain the affinity trend for M^{2+} binding to metal (hydr)oxides such as hematite, goethite, and silica ($Mg^{2+} > Ca^{2+} > Ba^{2+}$).

However, for other (hydr)oxides including Fh, the affinity trend is opposite ($Mg^{2+} < Ca^{2+} < Ba^{2+}$) to the trend found for *e.g.* goethite and hematite. This suggests that another energy term is involved, which overrules the above proportional difference in bond strength of the metal ion with water molecules and surface -OH ligands (*i.e.* the ligand exchange energy). Removal and restructuring of interfacial water might be a possibility (step 2) to explain the opposite trend for Fh given in Figure 4.8. The energy for the removal of interfacial water (E_{int}) should be negatively related to the metal ion size (d_M), according to $E_{int} = -k\, d_M$. In this approach, the value of k can change the affinity trend. If k is small or zero, the affinity trend follows the order of the Hofmeister series. However, if the value of k becomes relatively large, the affinity trend reverses, leading to a decrease in the value of ΔE_{ads} with an increase in the size of the metal ion. In that case, the energy gained by release and restructuring of interfacial water (E_{int}) is relatively large, leading to an increase in the log$K$ value with the ion size as observed for Fh (Figure 4.8).

Table 4.2. Fitted site densities (N_s) and affinity constants (log$K$) for the surface complex formation of Sr, Ba, and Ra derived using the data sets of various authors. The data and model lines are given in the Figures S4.5-4.7. The charge distribution coefficients (CD) found from the MO/DFT optimized geometries are: $\Delta z_0 = 0.69$, $\Delta z1 = 1.31$ v.u. for BB-Sr; $\Delta z_0 = 0.70$, $\Delta z1 = 1.30$ v.u. for E-Sr; $\Delta z_0 = 0.70$, $\Delta z1 = 0.30$ v.u. for E-SrOH. For BB-Ba, $\Delta z_0 = 0.72$, $\Delta z1 = 1.28$ v.u. For Ra, we used $\Delta z_0 = 0.73$, $\Delta z1 = 1.27$ v.u., found by correlation using CN = 8 in Figure 4.5. For Be, $\Delta z_0 = 1.18$, $\Delta z1 = 0.82$ v.u. and the estimate log$K$ values for the high and low affinity sites (Figure 4.7) are log$K$(h) = 2.8 and log$K$(l) = 1.4.

Author(s)	N_s(h)	N_s(l)	BB-Sr(h)	BB-Sr(l)	E-Sr #	E-SrOH #	R^2
Kinniburgh et al.[41]	0.29±0.02	2.51	5.14±0.02	-	-	-	0.999
Kolarik[42]	0.16±0.03	2.64	4.94±0.09	2.91±0.08	1.48±0.3	-10.78±0.2	0.987

Present at high pH ~10-13 and Sr/Fe = 0.05 and found with EXAFS at Sr/Fe = 1 [66]

Author(s)	N_s(h)	N_s(l)	BB-Ba(h)	BB-Ba(l)	BB-Ra(h)	BB-Ra(l)	R^2
Sajid et al.[43]	0.1±0.09	2.7	5.94 ±0.44	3.03 ±0.44	6.60 ±0.02	2.93 ±0.11	0.968/0.993

4.5. Summary and conclusions

In this study, the adsorption of the alkaline-earth metal ions Ca and Mg (M^{2+}) to Fh has been quantified in single-ion systems. The collected data have been interpreted with the CD model in combination with a multisite ion complexation (MUSIC) model for Fh that is based on a surface structural analysis of this nanomaterial. Presently, this MUSIC framework has been extended for describing the adsorption of cations that may bind to specific surface sites with a high and low affinity.

The primary adsorption data (M^{2+}/Fe) were scaled in a consistent manner to the surface area of Fh, measured with a recently developed ion probing methodology that is based on the measurement of the adsorption envelope of PO_4 to Fh.[39] Optimized geometries of the adsorbed M^{2+}complexes, obtained with MO/DFT/B3LYP/6-31+G** calculations, have been used to derive independently the interfacial CD coefficients. Ca and Mg bind to Fh forming predominantly inner-sphere bidentate complexes $\equiv(FeOH)_2^{\Delta z0}M^{\Delta z1}$, most probably as a binuclear double corner (^{2}C) complex based on our combined interpretation of MO/DFT geometry optimizations and EXAFS data reported in the literature for the adsorption of other divalent cations to Fe (hydr)oxides.[29,66,68–70] The formation of bidentate complexes is also supported by the H^+/M^{2+} exchange ratio for Ca and by the correspondingly marked pH-

dependency of the Ca adsorption. Modeling of the adsorption of alkaline-earth ions (Mg, Ca, Sr, Ba, and Ra) over a wide range of solution concentrations reveals surface site heterogeneity. Most sites for binuclear bidentate complex formation have a low affinity (~90 %), but a small fraction of the binding sites for M^{2+} ions has a high affinity (~10 %). The fitted surface site density is about ~0.3 ± 0.1 nm^{-2}, depending on the Fh sample considered. This is equivalent with the binding of about ~3 ± 1 alkaline-earth metal ions per Fh particle.

The Fh surface structure has been analyzed to rationalize the high affinity phenomenon and identify possible surface configurations. The high affinity character of these sites can be related to a significant charge redistribution within specific pairs of Fe1 octahedra that have a large number of -O ligands (8) common with the bulk of the material. These common oxygen ions demand for additional charge saturation of the not yet entirely saturated oxygen charge that can be delivered by both singly coordinated ≡FeOH surface ligands of the Fe1 octahedra. A redistribution of charge increases the affinity leading in the case of M^{2+} adsorption to a higher ≡FeOH-M^{2+} bond strength. A surface structural analysis of a number of constructed Fh particles of different size (~2.5 ± 0.3 nm) reveals a typical surface density of these ≡FeOH(bh) groups of 0.28 ± 0.08 nm^{-2}, which matches well with the mean surface site density of the high affinity sites according to our ion adsorption modeling.

Extending our analysis to data reported in the literature, comprising the full series of the alkaline-earth ions, showed an increase in the binding affinity (log*K*) with an increase in the ionic radius of these cations, *i.e.* $Be^{2+} < Mg^{2+} < Ca^{2+} \approx Sr^{2+} < Ba^{2+} < Ra^{2+}$. This is found for the M^{2+} binding to the high affinity and low affinity sites. A similar trend in affinity has also been found for TiO_2, but remarkably, it is opposite to the affinity trend found for other Fe-(hydr)oxides such as goethite and hematite. The difference in the order of affinity between various types of metal (hydr)oxide can be attributed to differences in the adsorption energy of physisorbed water in the interface. If the energy contribution of interfacial water change is relatively low, a decrease in affinity is expected when the ionic radius increases, while the opposite occurs if this energy term is relatively large compared to the contribution of the ligand exchange energy.

Acknowledgements

The grant provided by the University of Costa Rica (UCR) to the first author is gratefully acknowledged. We thank Peter Nobels from the Chemistry and Biology Soil Laboratory (CBLB) for his attentive work regarding the ICP-OES and ICP-MS analyses.

Supplementary Information

A. Conditions of the batch adsorption experiments

Table S4.1. Chemical conditions of the batch adsorption experiments in single-ion systems with the alkaline-earth metals (M^{2+}) Ca and Mg. The specific surface area (SSA) and molar mass (M_{nano}) of ferrihydrite were assessed using PO_4 as probe ion, as described in Mendez and Hiemstra.[39]

Series	System	Figure number	I	M^{2+}	Fe	SSA	M_{nano}	C_1	C_2
			M	mM	mM	$m^2\ g^{-1}$	g mol^{-1} Fe	F m^{-2}	
Ca-A.1	Single-Ca	4.1a	0.01	0.013	3.75	684 ± 15	96.6	1.17	0.91
Ca-A.2	Single-Ca	4.1a/4.1b/4.2a	0.01	0.127	3.75	684 ± 15	96.6	1.17	0.91
Ca-B.1	Single-Ca	4.1a	0.01	0.635	3.75	684 ± 15	96.6	1.17	0.91
Ca-B.2	Single-Ca	4.1c	0.01	0.635	7.50	684 ± 15	96.6	1.17	0.91
Ca-C.1	Single-Ca	4.1b/4.1c	0.01	0.127	1.50	684 ± 15	96.6	1.17	0.91
Ca-C.2	Single-Ca	4.1b	0.01	0.127	7.50	684 ± 15	96.6	1.17	0.91
Ca-D.1	Single-Ca	4.2a	0.10	0.108	3.75	684 ± 15	96.6	1.17	0.91
Ca-D.2	Single-Ca	4.2a	1.00	0.096	3.75	684 ± 15	96.6	1.17	0.91
Ca-E	Single-Ca	4.2b/4.4	0.01	0.955	7.50	684 ± 15	96.6	1.17	0.91
Ca-F	Single-Ca	4.2b	0.10	1.020	7.50	684 ± 15	96.6	1.17	0.91
Ca-G	Single-Ca	4.2b	0.50	0.998	7.50	684 ± 15	96.6	1.17	0.91
Mg-A.1	Single-Mg	4.3a	0.01	0.100	3.90	720 ± 10	97.6	1.18	0.91
Mg-A.2	Single-Mg	4.3a	0.01	0.300	3.90	720 ± 10	97.6	1.18	0.91
Mg-B.1	Single-Mg	4.4	0.01	1.00	7.50	720 ± 10	97.6	1.18	0.91
Mg-B.2	Single-Mg	4.3a	0.01	0.030	3.75	720 ± 10	97.6	1.18	0.91
Mg-C	Mg isotherm	4.3b	0.01	~ 0.02–1.0	4.35–10.0	690 ± 15	96.8	1.17	0.91

B. Thermodynamic database used in the modeling

Table S4.2. Aqueous speciation reactions used in the model calculations. The log*K* values are for $I = 0$.

Species	Reaction			log*K*	
$NaOH^0$	$Na^+ + OH^-$	↔	$NaOH^0$	-0.20	[a]
$NaNO_3^0$	$Na^+ + NO_3^-$	↔	$NaNO_3^0$	-0.60	[a]
$NaHPO_4^-$	$PO_4^{3-} + Na^+ + H^+$	↔	$NaHPO_4^-$	13.40	[b]
$NaPO_4^{2-}$	$PO_4^{3-} + Na^+$	↔	$NaPO_4^{2-}$	2.05	[b]
HPO_4^{2-}	$PO_4^{3-} + H^+$	↔	HPO_4^{2-}	12.35	[a]
$H_2PO_4^-$	$PO_4^{3-} + 2H^+$	↔	$H_2PO_4^-$	19.55	[a]
$H_3PO_4^0$	$PO_4^{3-} + 3H^+$	↔	$H_3PO_4^0$	21.70	[a]
$CaOH^+$	$Ca^{2+} + OH^-$	↔	$CaOH^+$	1.30	[a]
$Ca(OH)_2^0$	$Ca^{2+} + 2OH^-$	↔	$Ca(OH)_2^0$	0.01	[a]
$CaNO_3^+$	$Ca^{2+} + NO_3^-$	↔	$CaNO_3^+$	0.70	[c]
$Ca(NO_3)_2^0$	$Ca^{2+} + 2NO_3^-$	↔	$Ca(NO_3)_2^0$	-4.50	[a]
$MgOH^+$	$Mg^{2+} + OH^-$	↔	$MgOH^+$	2.55	[a]
$Mg(OH)_2^0$	$Mg^{2+} + 2OH^-$	↔	$Mg(OH)_2^0$	0.01	[a]
$Mg(NO_3)_2^0$	$Mg^{2+} + 2NO_3^-$	↔	$Mg(NO_3)_2^0$	-0.01	[a]
$SrOH^+$	$Sr^{2+} + OH^-$	↔	$SrOH^+$	0.22	[a]
$BaOH^+$	$Ba^{2+} + OH^-$	↔	$BaOH^+$	0.65	[a]

[a] From Lindsay.[82]
[b] From Rahnemaie et al.[83]
[c] From De Robertis et al.[84]

C. Adsorption density of Ca

In Figure 4.1 (main text), the pH-dependent adsorption of Ca was presented as the fraction of total added Ca that is bound to the surfaces of Fh. In Figure S4.1, the adsorption of Ca is expressed in terms of μmol m^{-2} (left y-panel) and mol mol^{-1} Fe (right y-axis) for systems with increasing total molar Ca/Fe ratios. The latter form represents the primary data obtained in the adsorption experiments, *i.e.* before any interpretation is done to account for the specific surface area and molar mass of Fh. Information in Figure S4.1 provides further information about the degree of surface coverage by Ca ions. For a given pH value, the adsorption of Ca increases as the total molar Ca/Fe ratio increases from 0.003 to 0.09. At a further increase of the total Ca/Fe ratio, the adsorption of Ca no longer increases significantly, indicating that the maximum adsorption density is nearly approached. At pH ~10, the maximum adsorption density of Ca to Fh is ~1.2 μmol m^{-2} or ~0.8 mol mol^{-1} Fe.

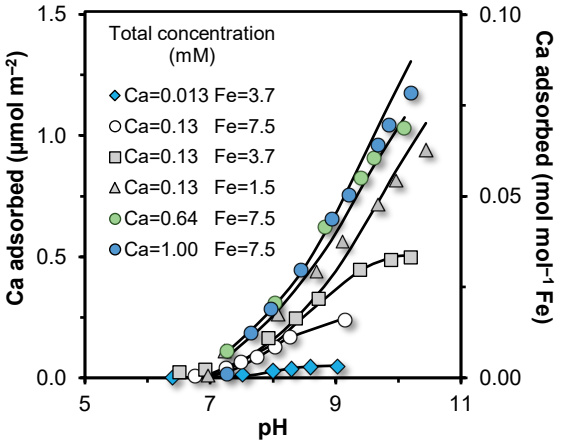

Figure S4.1. pH-dependent adsorption density of Ca expressed in μmol m^{-2} (left y-axis) and mol mol^{-1} Fe (right y-axis) for ferrihydrite systems with different total molar Ca/Fe ratios. The symbols are experimental data and the lines are CD model calculations obtained with the parameters set of Table 4.1 (main text). The total Ca concentrations varied from 0.013 to 1.00 mM in combination with three total Fe concentrations of 1.5, 3.7 or 7.5 mM. The Ca/Fe ratios ranged from ~0.003 to 0.13. The ionic strength was kept constant at I = 0.01 M $NaNO_3$. The specific surface area of Fh was A = 684 m^2 g^{-1} with a corresponding molar mass of M_{nano} = 96.6 g mol^{-1} Fe.

D. Exchange ratio H^+/Ca

Upon specific binding of Ca, and metal ions in general, protons are released from the surfaces of metal (hydr)oxides. This H^+/Ca exchange ratio (χ) indicates the change in the net surface charge upon specific ion adsorption at fixed pH values. Figure S4.2 shows the predicted χ values for Fh systems in 0.01 M and 1.0 M $NaNO_3$ and fixed pH of 9.0. The calculations were performed with the CD model parameters presented in Table 4.1 (main text).

For systems in 1.0 M $NaNO_3$, the predicted exchange ratio (χ = ~1.0) is in line with the experimental value (χ = ~0.92 ± 0.03) reported by Kinniburgh.[51] For systems with an ionic strength of 0.01 M $NaNO_3$ the model predicts a higher H/Ca exchange ratio of χ = ~1.7. The increase in the value of χ at decreasing ionic strength levels can be understood by the weaker screening of the interfacial charge by the counter

ions present in the diffuse double layer (DDL), which increases the electrostatic repulsion of H^+ from the surface. The H^+/Ca exchange ratio is independent of pH value for both ionic strength conditions (data not shown).

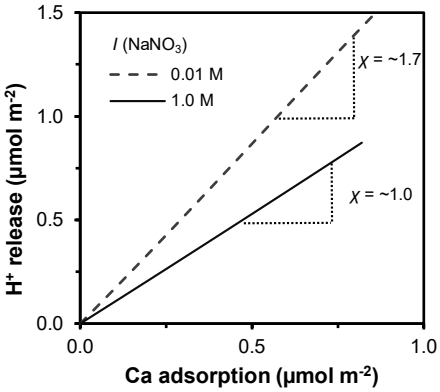

Figure S4.2. Modeled proton release as a result of the adsorption of Ca to ferrihydrite in 0.01 M and 1.0 $NaNO_3$ at constant pH of 9.0. The calculations were performed with the CD-MUSIC model using the parameter set presented in Table 4.1. The extended Stern layer approach[45] was applied for describing the compact part of the electrical double layer (EDL). The value of χ represent the mean H^+/Ca exchange ratio at the surfaces of Fh.

E. Adsorption isotherms of Ca to Fh in 0.01 M $NaNO_3$

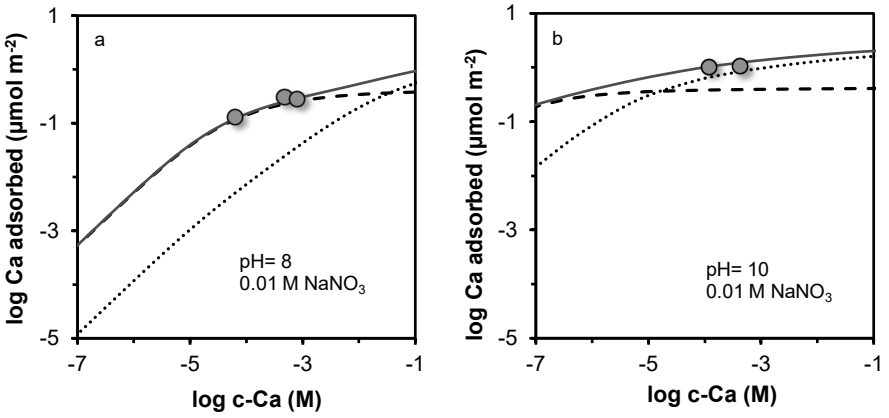

Figure S4.3. Adsorption isotherms of Ca to ferrihydrite at pH 8.0 (panel a) and pH 10 (panel b) for conditions representative of the adsorption experiments performed in the present study: I = 0.01 M $NaNO_3$, Fe = 7.5 mM, and specific surface area of Fh A= 684 m^2 g^{-1}. The symbols are experimental data points taken in this study for the given conditions. The isotherms were calculated with the CD model parameters presented in Table 4.1. The dashed and dotted lines give respectively the contribution of the binding of Ca to high and low affinity sites. The solid lines represent the total adsorption of Ca to Fh.

F. Additional Ca adsorption data from literature

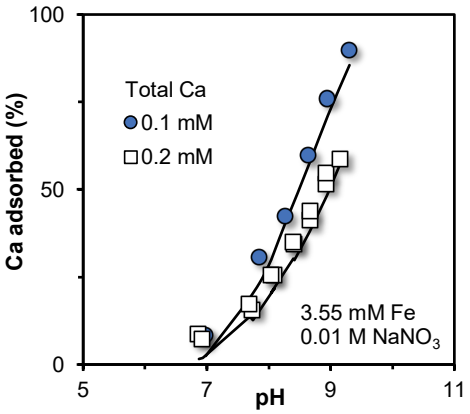

Figure S4.4. pH-dependent adsorption of Ca in single ion systems with ferrihydrite. The ionic strength was kept constant at I = 0.01 M $NaNO_3$. The specific surface area of Fh was taken as A = 650 m^2 g^{-1} with a corresponding molar mass of M_{nano} = 95.8 g mol^{-1} Fe. The symbols are experimental data from Dempsey and Singer[76] as reported by Dzombak and Morel.[14] The lines are CD model calculations using the parameters set of Table 4.1. The surface densities of the high and low affinity sites are respectively 0.32 and 2.48 nm^{-2}, which were set equal as for the Fh suspensions prepared in this study.

G. Brown bond analysis of optimized geometries

The MO/DFT/B3LYP/6-31+G** optimized geometries have been used to derive the CD coefficients (Δz_0 and Δz_1) of the adsorbed complexes of alkaline-earth metal ions. A template with two edge-linked Fe octahedra was used to represent the adsorption sites at the surface of Fh. Details about the template are given in Rahnemaie et al.[83] Inner-sphere binuclear bidentate (^{2}C) complexes were defined (see main text). The optimized geometries were interpreted with the Brown valence concept,[49] which relates the bond length (R) to a bond valence (ν) according to:

$$\nu = \exp\left(-\frac{R-\mathrm{R_o}}{\mathrm{B}}\right) \qquad \text{(Equation S4.1)}$$

In equation S4.1, B is an empirical constant (B = 37 pm) and R_o (pm) is a reference distance whose value is chosen such that the sum of ν is equal to the formal valence of the adsorbing ion. Table S4.3 presents the R (pm) and the respective ν values (v.u) for entire series of alkaline-earth metals, except for Ra. The given Fe-M^{2+} and M^{2+}-OH(H) distances were obtained using a template in which the Fe(III) ions are fixed, i.e. no Fe(III) relaxation. Allowing relaxation of Fe(III) ions in the cluster and/or changing the initial position of the M^{2+} ion on either side of the apices of the Fe(III) cluster only had a minor influence on the equilibrium bond lengths and on the estimation of the final CD values.

From the ν values, the ionic charge distribution values (n_0 and n_1) are calculated. The final CD coefficients (Δz_0, Δz_1) include the charge of the protons involved in the formation reactions (n_{H0}, n_{H1}) and a correction term ($\pm\ \varphi_m \Lambda_0$) for the interfacial water dipole orientation, where φ_m is a constant (0.17 ± 0.02) and Λ_0 is the change of charge relatively to that of the reference state from which the reaction is defined. Details about the calculations are explained by Hiemstra and van Riemsdijk.[85] The final CD coefficients for all alkaline-earth metals are summarized in Table S4.4.

Table S4.3. Bond lengths (R) and a bond valence (v) of the optimized geometries of the bidentate binuclear surface complexes for a series of alkaline-earth metals (M^{2+}). The geometries were optimized with MO/DFT using the 6-31+G** basis set and the functional B3LYP, using a $M^{2+}Fe_2(OH,OH_2)_{10}$ template in which the Fe(III) ions are fixed, *i.e.* no Fe(III) relaxation was allowed in the cluster, and the M^{2+} ions are located to the right hand side of the apices in the Fe(III) octahedra. The v values (v.u.) were calculated with the Brown valence analysis.

$(FeOH)_2Be$			$(FeOH)_2Mg$			$(FeOH)_2Ca$			$(FeOH)_2Sr$			$(FeOH)_2Ba$		
Bond	**R (pm)**	**v (v.u)**	**Bond**	**R (pm)**	**v (v.u)**	**Bond**	**R (pm)**	**v (v.u)**	**Bond**	**R (pm)**	**v (v.u)**	**Bond**	**R (pm)**	**v (v.u)**
FeOH-Be*	158.9	0.59	FeOH-Mg*	206.5	0.38	FeOH-Ca*	228.5	0.43	FeOH-Sr*	262.3	0.31	FeOH-Ba*	281.9	0.34
FeOH-Be*	156.3	0.63	FeOH-Mg*	200.0	0.46	FeOH-Ca*	223.5	0.50	FeOH-Sr*	263.2	0.31	FeOH-Ba*	282.6	0.33
Be-H2O	177.4	0.36	Mg-H2O	217.2	0.29	Ca-H2O	245.1	0.28	Sr-H2O	279.8	0.19	Ba-H2O	294.6	0.24
Be-H2O	170.5	0.43	Mg-H2O	216.3	0.29	Ca-H2O	240.5	0.31	Sr-H2O	264.5	0.29	Ba-H2O	283.8	0.32
Sum υ		2.00	Mg-H2O	214.1	0.31	Ca-H2O	249.4	0.25	Sr-H2O	278.9	0.20	Ba-H2O	394.8	0.02
Ro	139.2		Mg-H2O	220.8	0.26	Ca-H2O	250.8	0.24	Sr-H2O	273.0	0.23	Ba-H2O	292.1	0.26
CN**	4			Sum υ	2.00		Sum υ	2.00	Sr-H2O	277.6	0.21	Ba-H2O	293.2	0.25
			Ro	171.1		Ro	197.5		Sr-H2O	270.4	0.25	Ba-H2O	292.8	0.25
			CN**	6		CN**	6			Sum υ	2.00		Sum υ	2.00
									Ro	219.3		Ro	241.7	
									CN**	8		CN**	8	
Fe-Be	324.2		Fe-Mg	360.8		Fe-Ca	377.6		Fe-Sr	424.5		Fe-Ba	447.9	
Fe-Be	328.3		Fe-Mg	366.5		Fe-Ca	378.2		Fe-Sr	428.2		Fe-Ba	451.5	
mean	326.3		mean	363.7		mean	377.9		mean	426.4		mean	449.7	

* OH-M^{2+} represents the bonds that are share with Fe at the surface of ferrihydrite
** Coordination number of the M^{2+} cation in the final optimized geometry

H. Surface complexes of alkaline-earth metals in ferrihydrite

Table S4.4. Compilation of the surface species and CD coefficients for the binding reactions of the entire series of alkaline-earth metals (M^{2+}) to ferrihydrite. The surface site densities are from Hiemstra and Zhao[30] with ≡FeOH(a) = 3.0 nm^{-2}, ≡FeOH(b) = 2.8 nm^{-2} and ≡Fe_3O = 1.4 nm^{-2}. Two types of ≡FeOH(b) groups were defined to account for site heterogeneity ≡FeOH(bl) for low and ≡FeOH(bh) for high affinities. The site densities of these groups were fitted respectively to 2.48 ± 0.02 and 0.32 ± 0.02 nm^{-2} for our Fh suspensions. The capacitance values for the extended Stern layers of Fh ($C_{nano,1}$ and $C_{nano,2}$) are size-dependent and are calculated taking the capacitance values for a flat plane as reference (C_1 = 0.90 F m^{-2} and C_2 = 0.74 F m^{-2}).

Species	ID*	≡FeOH(bl)$^{-0.5}$	FeOH(bh) $^{-0.5}$	FeOH(a) $^{-0.5}$	Δz_0**	Δz_1	Δz_2	H^+	M^{2+}	log*K*
(≡FeOHb)$_2$Be	BB-Be(l)	2	0	0	1.18	0.82	0	0	1	log*K* Be(l)
(≡FeOHb)$_2$Be	BB-Be(h)	0	2	0	1.18	0.82	0	0	1	log*K* Be(h)
(≡FeOHb)$_2$Mg	BB-Mg(l)	2	0	0	0.89	1.11	0	0	1	log*K* Mg(l)
(≡FeOHb)$_2$Mg	BB-Mg(h)	0	2	0	0.89	1.11	0	0	1	log*K* Mg(h)
(≡FeOHb)$_2$Ca	BB-Ca(l)	2	0	0	0.94	1.06	0	0	1	log*K* Ca(l)
(≡FeOHb)$_2$Ca	BB-Ca(h)	0	2	0	0.94	1.06	0	0	1	log*K* Ca(h)
(≡FeOHb)$_2$Sr	BB-Sr(l)	2	0	0	0.69	1.31	0	0	1	log*K* Sr(l)
(≡FeOHb)$_2$Sr	BB-Sr(h)	0	2	0	0.69	1.31	0	0	1	log*K* Sr(h)
(≡FeOHa)$_2$Sr	E-Sr(l)	0	0	2	0.70	1.30	0	0	1	log*K* Sr(e)
(≡FeOHa)$_2$SrOH	E-SrOH(l)	0	0	2	0.70	0.30	0	-1	1	log*K* SrOH(e)
(≡FeOH)$_2$Ba	BB-Ba(l)	2	0	0	0.72	1.28	0	0	1	log*K* Ba(l)
(≡FeOH)$_2$Ba	BB-Ba(h)	0	2	0	0.72	1.28	0	0	1	log*K* Ba(h)
(≡FeOH)$_2$Ra	BB-Ra(l)	2	0	0	0.71**	1.29	0	0	1	log*K* Ra(l)
(≡FeOH)$_2$Ra	BB-Ra(h)	0	2	0	0.71**	1.29	0	0	1	log*K* Ra(h)

* BB = Binuclear Bidentate or double-corner complex, E = Edge or Mononuclear Monodentate, (h) = high affinity sites of ≡FeOH(b); (l) = low affinity sites of ≡FeOH(b)

** The CD coefficients have been derived from the MO/DFT optimized geometries except for BB-Ra whose value was found by correlation from Figure 4.5 assuming the same coordination number (CN) number as for Ba and Sr, *i.e.* CN = 8.

I. Adsorption data of Sr, Ba, and Ra to ferrihydrite

Data from literature describing the adsorption of strontium (Sr),[41,42] and radium (Ra) and barium (Ba)[43] to fresh ferrihydrite suspensions have been interpreted here with the CD-MUSIC model. The set of adsorption reactions and CD coefficients are presented in Table S4.4. The CD coefficients for Sr and Ba were derived from the MO/DFT optimized geometries, whereas for Ra these values were found by correlation (Figure 4.5, main text) assuming the same coordination number as for Ba and Sr, *i.e.* CN = 8. The affinity constants (log*K*) of the corresponding adsorption reactions, as well as the site density (N_s) of the high affinity groups were set as adjustable parameters in the modeling (Table 4.2, main text).

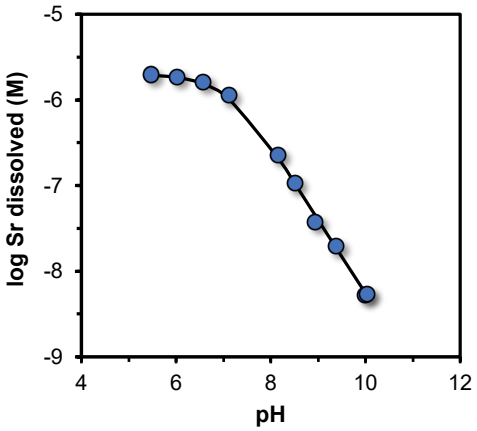

Figure S4.5a. pH-dependent solution concentration of strontium (Sr) in the equilibrium solution of ferrihydrite systems prepared at constant ionic strength of I = 1.0 M $NaNO_3$. The total added Sr concentration was $2 \cdot 10^{-6}$ M and the total Fe concentration was 0.65 mM. The symbols are the experimental data are taken from Kinniburgh et al.[41] The line has been calculated with the CD-model using the parameters set of Table 4.2 (main text). Only the formation of binuclear bidentate (BB) complexes with the high affinity sites $\equiv FeOH^{-0.5}$(bh) (N_s = 0.29 nm^{-2}) was required to describe this data set. The specific surface area of the ferrihydrite suspension is A = 585 $m^2\ g^{-1}$ with a corresponding molar mass of M_{nano} = 94.1 g mol^{-1} Fe, as described by Hiemstra (2018).[63] R^2 = 0.999, n = 8.

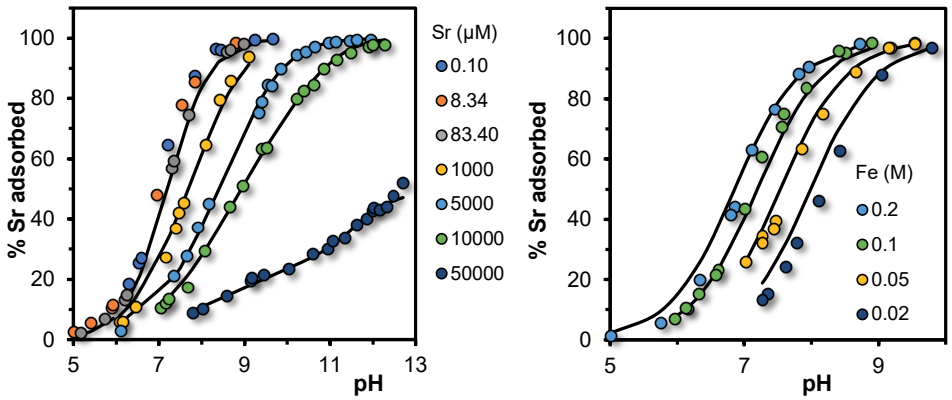

Figure S4.5b pH-dependent adsorption of strontium (Sr) to ferrihydrite in systems prepared at constant ionic strength of I = 1.0 M $NaNO_3$. Left panel, the total added Sr concentration varied from 0.1 μM to 50 mM and the total Fe concentration was 100 mM. Right panel, the total added Sr concentration was 0.5 μM and the total Fe concentrations varied between 0.02 and 0.2 M. The symbols are the experimental data taken from Kolařík.[42] The lines have been calculated with the CD-model using the parameters set of Table 4.2 (main text). Formation of binuclear bidentate (BB) and edge-sharing (E) was required to describe this adsorption data set. The BB complexes are formed with both high (≡$FeOH^{-0.5}$(bh)) (N_s = 0.16 ± 0.03 nm^{-2}) and low (≡$FeOH^{-0.5}$(bl)) (N_s = 2.64 nm^{-2}) affinity surface groups, whereas the E complexes are formed with the (≡$FeOH^{-0.5}$(a)) surface groups. The latter complexes are required to describe the extremely high Sr adsorption at pH > ~ 10. The specific surface area of the ferrihydrite suspension was assumed to be the same as for the Fh suspension in 1 M $NaNO_3$ of Kinniburgh,[51] *i.e.* A = 585 m^2 g^{-1} with a corresponding molar mass of M_{nano} = 94.1 g mol^{-1} Fe. R^2 = 0.989, n = 137.

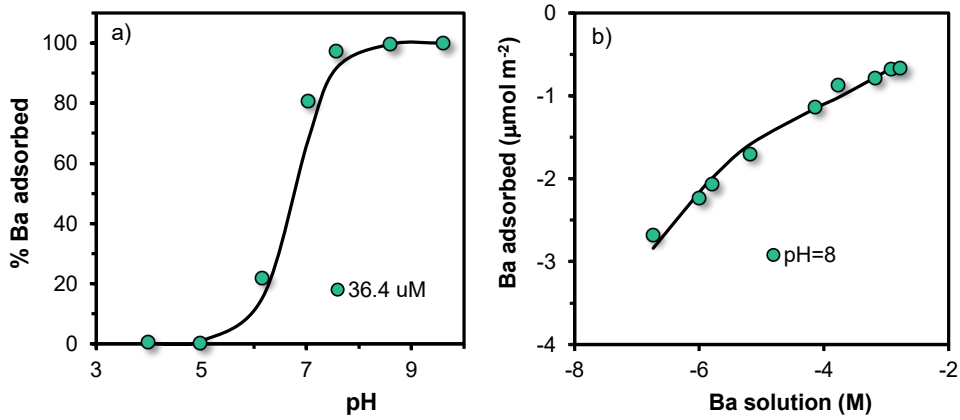

Figure S4.6. pH-dependent adsorption of barium (Ba) to ferrihydrite represented as an adsorption edge (**a**) and as an adsorption isotherm at pH 8.0 ± 0.05 (**b**) in systems with constant ionic strength of I = 0.1 M $NaClO_4$. Ferrihydrite was added as a wet paste at a concentration of 10 g L^{-1} based on a dry weight. The symbols are the experimental data taken from Sajih et al.[43] The lines have been calculated with the CD-model using the parameters set of Table 4.2 (main text). Formation of binuclear bidentate (BB) with high (≡$FeOH^{-0.5}$(bh)) (N_s = 0.10 ± 0.09 nm^{-2}) and low (≡$FeOH^{-0.5}$(bl)) (N_s = 2.7 nm^{-2}) affinity surface groups was required to describe this adsorption data set. The specific surface area of the ferrihydrite suspension was set to a standard value of A = 610 m^2 g^{-1}. R^2 = 0.968, n = 16.

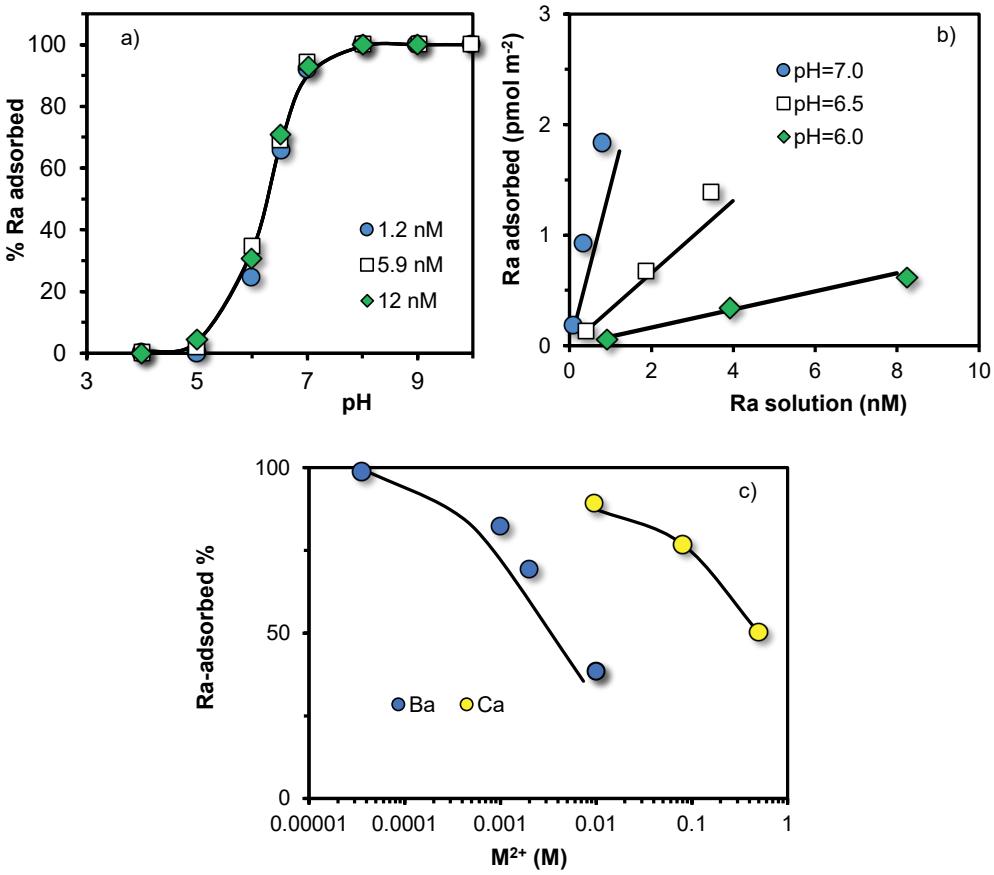

Figure S4.7. **Panels a-b**: pH-dependent adsorption of radium (Ra) to ferrihydrite represented as adsorption edges (**a**), and adsorption isotherms at pH 6.0, 6.5 and 7.0 ± 0.05 (**b**). **Panel c**: Adsorption of Ra to ferrihydrite as a function of the concentration of either Ca (pH = 7.0 ± 0.05) or Ba (pH = 7.0 ± 0.05) acting as competitor cations with Ra. The ionic strength of all systems was kept constant at I = 0.1 M $NaClO_4$. Ferrihydrite was added as a wet paste at a concentration of 10 g L^{-1} based on a dry weight. The symbols are the experimental data taken from Sajih et al.[43] The lines have been calculated with the CD model using the parameters set of Table 4.2 (main text). Formation of binuclear bidentate (BB) complexes with high (≡$FeOH^{-0.5}$(bh)) (N_s = 0.1 nm^{-2}) and low (≡$FeOH^{-0.5}$(bl)) (N_s = 2.7 nm^{-2}) affinity surface groups was required to describe this data set. The specific surface area of the ferrihydrite suspension were set to the standard value of A = 610 m^2 g^{-1}. R^2 = 0.993, n = 41.

J. Additional surface configurations for high affinity sites

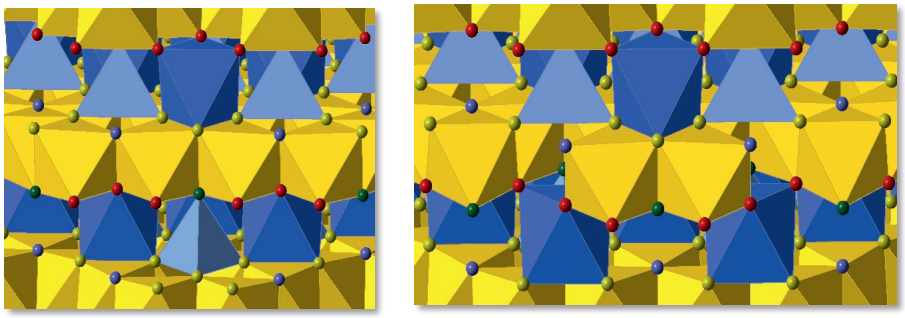

Figure S4.8 Left panel. A surface configuration comparable with the structure given in the main text (Figure 4.7) with a difference in the presence of a Fe3 tetrahedron, fixing the O2 ligand (green) at the common edge of the two Fe1 octahedra of the high affinity site. **Right panel**. A surface configuration comparable with the structure given in the main text (Figure 4.7) with a difference in the absence of a Fe1 octahedron at either side of both Fe1 octahedra with a high affinity.

K. Alternative descriptions of the data set of Kinniburgh 1982

The starting point of our modeling is the assumption that Ca forms predominantly double corner (^{2}C) bidentate complex with two -OH groups at the surfaces of Fh, in line with spectroscopic information for Sr and Cd binding to Fh (see main text). For the interaction of Ca, we first assume a reaction with all the ≡FeOH(b) sites with a site density of N_s = 2.8 nm^{-2} according to the MUSIC model of Fh.[30] The CD coefficients are Δz_0 = 0.94 and Δz_1 = 1.06, which were derived from the MO/DFT optimized geometries. In this first option, there is only 1 adjustable parameter. The fitted logK_{BC} value is 3.84 ± 0.05. The quality of the description is rather poor (R^2 = 0.78, n = 89). Figure S4.9 shows that there is a systematic deviation. Overprediction of the experimental Ca adsorption data occurs in systems with the highest Ca loadings.

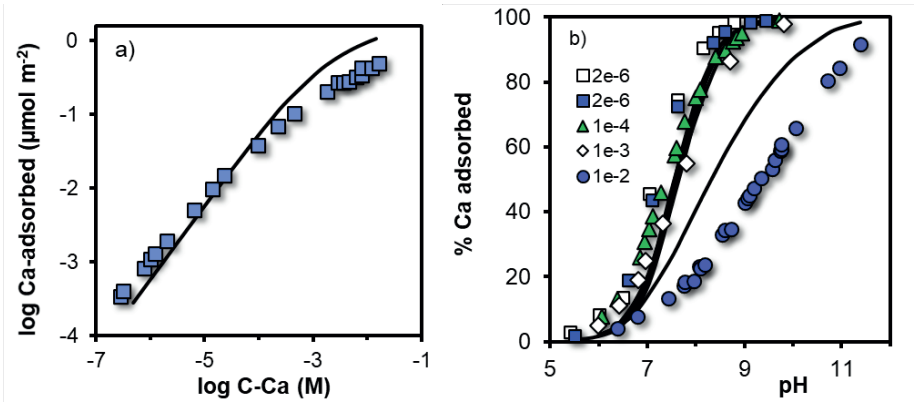

Figure S4.9. a) Adsorption isotherm of Ca to Fh at pH = 8 in 1.0 M $NaNO_3$. **b**) pH-dependent adsorption edges of Ca in 1.0 M $NaNO_3$ at different initial Ca concentration (M) for Fh systems with 93 mM Fe. Data (symbols) are from Kinniburgh and Jackson.[25] The SSA is set to 585 m^2 g^{-1} and the consistent molar mass is M_{nano} = 94.1 g mol^{-1}Fe. The applied capacitance values are $C_{1,nano}$ = 1.14 F m^{-2} and $C_{2,nano}$ = 0.89 F m^{-2}. The lines have been calculated assuming for Ca double corner (^{2}C) bidentate complex formation to all ≡FeOH(b) sites (N_s = 2.8 nm^{-2}).

In an attempt to improve the description of Figure S4.9, the CD coefficient of the surface plane was made to an adjustable parameter, yielding a lower value, namely $\Delta z_0 = 0.43 \pm 0.03$. This modeling choice did improve the quality of the fit ($R^2 = 0.93$). However, the deviation between the model and experimental data has a clear systematic trend, particularly in systems with high initial Ca concentration (10^{-2} M). The deviations are larger than the variation that one may expect from random errors related to the uncertainty in the measurements. In the 0.01M Ca system, there is an overprediction at low pH, and at high pH, there is an underprediction of the experimental data. Introducing additionally the formation of a hydrolyzed adsorbed Ca complexes, *i.e.* CaOH complexes, did not lead to any substantial improvement of the description ($\log K_{\mathrm{BCa}} = 3.84 \pm 0.03$ and $\log K_{\mathrm{BCaOH}} = -8.06 \pm 0.86$ with R^2=0.93). In both cases, minimization of the deviations between experimental and modeling data leads to the same low value for the CD coefficient ($\Delta z_0 = 0.43$ v.u.). Such a CD value is typical for monodentate complex formation, not bidentate complex formation.

Switching to the formation of monodentate complexes (^{1}C) by interaction with only the ≡FeOH(b) sites ($N_s = 2.8$ nm^{-2}) leads to a decrease in the quality of description ($R^2 = 0.88$). Assuming monodentate interaction with all ≡FeOH sites (*i.e.* the sum of ≡FeOH(a) + ≡FeOH(b) = 5.8 nm^{-2}) leads to an even further decrease in the fitting quality ($R^2 = 0.87$). This trend suggests that using a lower site density may improve the quality of the fit. Making the site density of ≡FeOH sites to an adjustable parameter within this modeling option, with the constraint of a constant total site density of N_s= 5.8 nm^{-2} for the sum of all singly coordinated groups, the quality of the description indeed increases to $R^2 = 0.93$. However, the deviation between model and experimental data still has a clear systematic deviation, as illustrated in Figure S4.10. This indicates that focusing on the R^2 value only may not be enough in objective fitting procedures. For the option with monodentate ^{1}C complexes, the fitted values are $N_{s(\mathrm{Monodentate})} = 0.78 \pm 0.05$ nm^{-2}, $\log K_{\mathrm{MCa}} = 4.06 \pm 0.05$, $\log K_{\mathrm{MCaOH}} = -6.85 \pm 2.28$ and $\Delta z_0 = 0.53 \pm 0.05$ v.u. The large uncertainty in $\log K_{\mathrm{MCaOH}}$ indicates that a contribution of such a complex does not significantly contribute to the quality of the fit and could be ignored.

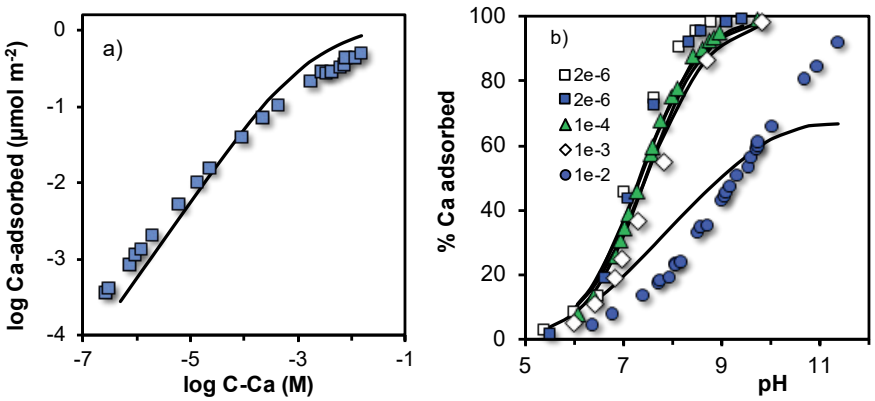

Figure S4.10. a) Adsorption isotherm of Ca to Fh at pH = 8 in 1.0 M $NaNO_3$. **b**) pH-dependent adsorption edges of Ca in 1.0 M $NaNO_3$ at different initial Ca concentration (M) for Fh systems with 93 mM Fe. Data (symbols) are from Kinniburgh and Jackson.[25] The SSA is set to 585 m^2 g^{-1} and the consistent molar mass is $M_{\mathrm{nano}} = 94.1$ g mol^{-1}Fe. The applied capacitance values are $C_{1,\mathrm{nano}} = 1.14$ F m^{-2} and $C_{2,\mathrm{nano}} = 0.89$ F m^{-2}. The lines have been calculated assuming monodentate complex formation to a selected number of ≡FeOH sites. Interaction with other ≡FeOH sites is excluded. The total site density of ≡FeOH is N_s = 5.8 nm^{-2}, of which a fitted fraction ($N_s = 0.78 \pm 0.07$ nm^{-2}) binds Ca and CaOH ions, see text.

In a next attempt to improve the modeling option using monodentate complexes, we have added ion pair formation of Ca ions, interacting with all ≡FeOH and ≡Fe_3O sites. A single logK_{OS} value is fitted for the outer-sphere (OS) complex formation. This does not lead to a substantial increase of the quality of the descriptions (R^2 = 0.93). The fitted values are $N_{s(Monodentate)}$ = 0.48 ± 0.13 nm^{-2}, logK_{MCa}= 4.30 ± 0.09, logK_{MCaOH} = -5.34 ± 1.58 and Δz_0 = 0.77 ± 0.17 v.u. The introduction of the formation of OS complexes leads to a significant increase in the value of the CD coefficient. This fitted value for the CD coefficient is not in line with the assumption of formation of monodentate complexes. It could suggest that Ca is bound by the combination of outer-sphere and bidentate inner-sphere complex formation.

Changing to an option that combines formation of bidentate inner-sphere and outer-sphere complexes, using a fitted value for the number of ≡FeOH sites involved ($N_{s≡FeOH,\ bidentate}$) with the constraint for the total number of ≡FeOH sites, *i.e.* N_s = 5.8 nm^{-2}, leads to: $N_{s≡FeOH,\ bidentate}$ = 1.22 ± 0.13 nm^{-2}, logK_{BCa}= 4.29 ± 0.27, logK_{BCaOH} = -5.24 ± 0.88, logK_{OS} = 1.85 ± 0.47, and Δz_0 = 0.70 ± 0.12 v.u. with R^2 = 0.95. Indeed, the quality increases. However, despite the relatively large number of adjustable parameters (n = 5), the model still deviates systematically from the data, as shown in Figure S4.11.

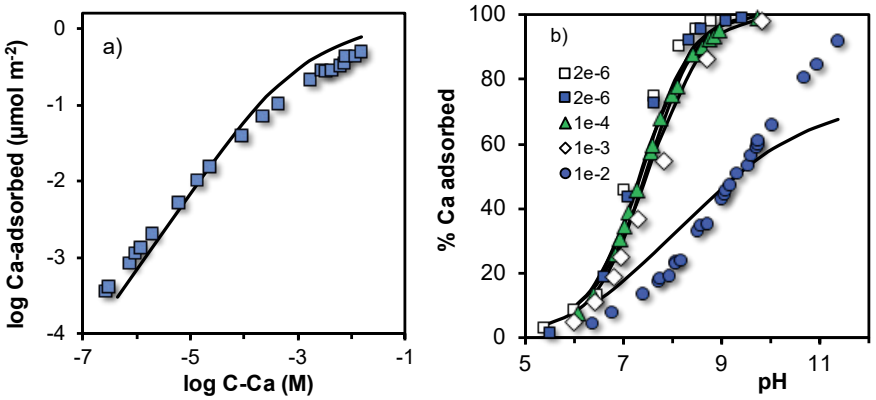

Figure S4.11. a) Adsorption isotherm of Ca to Fh at pH = 8 in 1.0 M $NaNO_3$. **b**) pH-dependent adsorption edges of Ca in 1.0 M $NaNO_3$ at different initial Ca concentration (M) for Fh systems with 93 mM Fe. Data (symbols) are from Kinniburgh and Jackson.[25] The SSA is set to 585 m^2 g^{-1} and the consistent molar mass is M_{nano} = 94.1 g mol^{-1} Fe. The applied capacitance values are $C_{1,nano}$ = 1.14 F m^{-2} and $C_{2,nano}$ = 0.89 F m^{-2}. The lines have been calculated assuming bidentate complex formation to a selected number of ≡FeOH sites with a fitted site density of N_s = 1.22 ± 0.13 nm^{-2} and a total ≡FeOH site density of N_s = 5.8 nm^{-2}. The CD value is fitted (Δz_0 = 0.70 ± 0.12). A hydrolyzed inner-sphere bidentate complex and outer-sphere complex were also included in the modeling (see text).

Based on the above, a good model option would be that one with only a few adjustable parameters, which is constrained by information about the surface structure with corresponding sited densities, and that additionally gives credits to spectroscopy data for the adsorption of Sr ions to Fh. The model option presented in the main text, which defines formation of bidentate double corner (^{2}C) complex with the ≡FeOH(b) surface groups and distinguishes sites with high and low affinity, satisfies these criteria.

Assuming complex formation by edge sharing (^{1}E) is not required for the above data set of Kinniburgh and Jackson.[25] However, under extreme solution conditions (*e.g.* high pH values and high initial ion loadings), the formation of ^{1}E complexes might not be excluded. For a good description of Sr adsorption to Fh, using the dataset reported by Kolařík,[42] we found that complexation with ^{1}E complexes

is required as an additional binding reaction. The reason may be that in these experiments, part of the experiment data were collected in Fh systems with a very high initial solution concentration and for pH values in the range pH ~10–13 (see Figure S4.5b). This might be in line with the EXAFS finding of Axe et al.[66] for systems with an extreme molar Sr/Fe ratio (1/1).

References

(1) Jambor, J. L.; Dutrizac, J. E. Occurrence and Constitution of Natural and Synthetic Ferrihydrite, a Widespread Iron Oxyhydroxide. *Chem. Rev.* **1998**, *98* (7), 2549–2586.

(2) Hochella, M. F.; Lower, S. K.; Maurice, P. A.; Penn, R. L.; Sahai, N.; Sparks, D. L.; Twining, B. S. Nanominerals, Mineral Nanoparticles, and Earth Systems. *Science (80-.).* **2008**, *319* (5870), 1631–1635.

(3) Cornell, R. M.; Schwertmann, U. *The Iron Oxides: Structure, Properties, Reactions, Ocurrence and Uses*, Second Edi.; WILEY-VCH, Germany, 2003.

(4) Hiemstra, T. Formation, Stability, and Solubility of Metal Oxide Nanoparticles: Surface Entropy, Enthalpy, and Free Energy of Ferrihydrite. *Geochim. Cosmochim. Acta* **2015**, *158*, 179–198.

(5) Liu, J.; Zhu, R.; Xu, T.; Xu, Y.; Ge, F.; Xi, Y.; Zhu, J.; He, H. Co-Adsorption of Phosphate and Zinc(II) on the Surface of Ferrihydrite. *Chemosphere* **2016**, *144*, 1148–1155.

(6) Guo, H.; Barnard, A. S. Naturally Occurring Iron Oxide Nanoparticles: Morphology, Surface Chemistry and Environmental Stability. *J. Mater. Chem. A* **2013**, *1* (1), 27–42.

(7) Schwertmann, U.; Friedl, J.; Stanjek, H. From Fe(III) Ions to Ferrihydrite and Then to Hematite. *J. Colloid Interface Sci.* **1999**, *209* (1), 215–223.

(8) Borch, T.; Kretzschmar, R.; Kappler, A.; Cappellen, P. Van; Ginder-Vogel, M.; Voegelin, A.; Campbell, K. Biogeochemical Redox Processes and Their Impact on Contaminant Dynamics. *Environ. Sci. Technol.* **2010**, *44* (1), 15–23.

(9) Mejia, J.; He, S.; Yang, Y.; Ginder-Vogel, M.; Roden, E. E. Stability of Ferrihydrite–Humic Acid Coprecipitates under Iron-Reducing Conditions. *Environ. Sci. Technol.* **2018**, *52* (22), 13174–13183.

(10) Li, G.-X.; Chen, X.-P.; Wang, X.-N.; Chen, Z.; Bao, P. Sulfur Redox Cycling Dependent Abiotic Ferrihydrite Reduction by a *Desulfitobacterium Hafniense*. *ACS Earth Sp. Chem.* **2018**, *2* (5), 496–505.

(11) Jones, A. M.; Collins, R. N.; Waite, T. D. Redox Characterization of the Fe(II)-Catalyzed Transformation of Ferrihydrite to Goethite. *Geochim. Cosmochim. Acta* **2017**, *218*, 257–272.

(12) Burton, E. D.; Hockmann, K.; Karimian, N.; Johnston, S. G. Antimony Mobility in Reducing Environments: The Effect of Microbial Iron(III)-Reduction and Associated Secondary Mineralization. *Geochim. Cosmochim. Acta* **2019**, *245*, 278–289.

(13) Adhikari, D.; Sowers, T.; Stuckey, J. W.; Wang, X.; Sparks, D. L.; Yang, Y. Formation and Redox Reactivity of Ferrihydrite-Organic Carbon-Calcium Co-Precipitates. *Geochim. Cosmochim. Acta* **2019**, *244*, 86–98.

(14) Dzombak, D. A.; Morel, F. M. M. *Surface Complexation Modeling: Hydrous Ferric Oxide*; John Wiley & Sons, Inc.: New York, 1990.

(15) Hiemstra, T.; Mendez, J. C.; Li, J. Evolution of the Reactive Surface Area of Ferrihydrite: Time, PH, and Temperature Dependency of Growth by Ostwald Ripening. *Environ. Sci. Nano* **2019**, *6* (3), 820–833.

(16) Davis, J. A.; Leckie, J. O. Surface Ionization and Complexation at the Oxide/Water Interface II. Surface Properties of Amorphous Iron Oxyhydroxide and Adsorption of Metal Ions. *J. Colloid Interface Sci.* **1978**, *67* (1), 90–107.

(17) Mendez, J. C.; Hiemstra, T. Carbonate Adsorption to Ferrihydrite: Competitive Interaction with Phosphate for Use in Soil Systems. *ACS Earth Sp. Chem.* **2019**, *3* (1), 129–141.

(18) Liu, J.; Zhu, R.; Liang, X.; Ma, L.; Lin, X.; Zhu, J.; He, H.; Parker, S. C.; Molinari, M. Synergistic Adsorption of Cd(II) with Sulfate/Phosphate on Ferrihydrite: An in Situ ATR-FTIR/2D-COS Study. *Chem. Geol.* **2018**, *477*, 12–21.

(19) Trivedi, P.; Dyer, J. A.; Sparks, D. L. Lead Sorption onto Ferrihydrite. 1. A Macroscopic and Spectroscopic Assessment. *Environ. Sci. Technol.* **2003**, *37* (5), 908–914.

(20) Swedlund, P. J.; Miskelly, G. M.; McQuillan, A. J. Silicic Acid Adsorption and Oligomerization at the Ferrihydrite - Water Interface: Interpretation of ATR-IR Spectra Based on a Model Surface Structure. *Langmuir* **2010**, *26* (5), 3394–3401.

(21) Antelo, J.; Arce, F.; Fiol, S. Arsenate and Phosphate Adsorption on Ferrihydrite Nanoparticles. Synergetic Interaction

with Calcium Ions. *Chem. Geol.* **2015**, *410*, 53–62.

(22) Bompoti, N. M.; Chrysochoou, M.; Machesky, M. L. A Unified Surface Complexation Modeling Approach for Chromate Adsorption on Iron Oxides. *Environ. Sci. Technol.* **2019**, *53* (11), 6352–6361.

(23) Waite, T. D.; Davis, J. A.; Payne, T. E.; Waychunas, G. A.; Xu, N. Uranium(VI) Adsorption to Ferrihydrite: Application of a Surface Complexation Model. *Geochim. Cosmochim. Acta* **1994**, *58* (24), 5465–5478.

(24) Benjamin, M. M.; Leckie, J. O. Multiple-Site Adsorption of Cd, Cu, Zn, and Pb on Amorphous Iron Oxyhydroxide. *J. Colloid Interface Sci.* **1981**, *79* (1), 209–221.

(25) Kinniburgh, D. G.; Jackson, M. L. Concentration and PH Dependence of Calcium and Zinc Adsorption by Iron Hydrous Oxide Gel. *Soil Sci. Soc. Am. J.* **1982**, *46* (1), 56–61.

(26) Zachara, J. M.; Girvin, D. C.; Schmidt, R. L.; Resch, C. T. Chromate Adsorption on Amorphous Iron Oxyhydroxide in the Presence of Major Groundwater Ions. *Environ. Sci. Technol.* **1987**, *21* (6), 589–594.

(27) Wang, X.; Kubicki, J. D.; Boily, J. F.; Waychunas, G. A.; Hu, Y.; Feng, X.; Zhu, M. Binding Geometries of Silicate Species on Ferrihydrite Surfaces. *ACS Earth Sp. Chem.* **2018**, *2* (2), 125–134.

(28) Johnston, C. P.; Chrysochoou, M. Mechanisms of Chromate, Selenate, and Sulfate Adsorption on Al-Substituted Ferrihydrite: Implications for Ferrihydrite Surface Structure and Reactivity. *Environ. Sci. Technol.* **2016**, *50* (7), 3589–3596.

(29) Tiberg, C.; Gustafsson, J. P. Phosphate Effects on Cadmium(II) Sorption to Ferrihydrite. *J. Colloid Interface Sci.* **2016**, *471*, 103–111.

(30) Hiemstra, T.; Zhao, W. Reactivity of Ferrihydrite and Ferritin in Relation to Surface Structure, Size, and Nanoparticle Formation Studied for Phosphate and Arsenate. *Environ. Sci. Nano* **2016**, *3*, 1265–1279.

(31) Katz, L. E.; Criscenti, L. J.; Chen, C.; Larentzos, J. P.; Liljestrand, H. M. Temperature Effects on Alkaline Earth Metal Ions Adsorption on Gibbsite: Approaches from Macroscopic Sorption Experiments and Molecular Dynamics Simulations. *J. Colloid Interface Sci.* **2013**, *399*, 68–76.

(32) Cowan, C. E.; Zachara, J. M.; Resch, C. T. Cadmium Adsorption on Iron Oxides in the Presence of Alkaline-Earth Elements. *Environ. Sci. Technol.* **1991**, *25* (3), 437–446.

(33) Michel, F. M.; Ehm, L.; Antao, S. M.; Lee, P. L.; Chupas, P. J.; Liu, G.; Strongin, D. R.; Schoonen, M. A. A.; Phillips, B. L.; Parise, J. B. The Structure of Ferrihydrite, a Nanocrystalline Material. *Science* **2007**, *316* (5832), 1726–1729.

(34) Michel, F. M.; Barron, V.; Torrent, J.; Morales, M. P.; Serna, C. J.; Boily, J.-F.; Liu, Q.; Ambrosini, A.; Cismasu, A. C.; Brown, G. E. Ordered Ferrimagnetic Form of Ferrihydrite Reveals Links among Structure, Composition, and Magnetism. *Proc. Natl. Acad. Sci.* **2010**, *107* (7), 2787–2792.

(35) Hiemstra, T. Surface and Mineral Structure of Ferrihydrite. *Geochim. Cosmochim. Acta* **2013**, *105*, 316–325.

(36) Maillot, F.; Morin, G.; Wang, Y.; Bonnin, D.; Ildefonse, P.; Chaneac, C.; Calas, G. New Insight into the Structure of Nanocrystalline Ferrihydrite: EXAFS Evidence for Tetrahedrally Coordinated Iron(III). *Geochim. Cosmochim. Acta* **2011**, *75* (10), 2708–2720.

(37) Xu, W.; Hausner, D. B.; Harrington, R.; Lee, P. L.; Strongin, D. R.; Parise, J. B. Structural Water in Ferrihydrite and Constraints This Provides on Possible Structure Models. *Am. Mineral.* **2011**, *96* (4), 513–520.

(38) Pinney, N.; Kubicki, J. D.; Middlemiss, D. S.; Grey, C. P.; Morgan, D. Density Functional Theory Study of Ferrihydrite and Related Fe-Oxyhydroxides. *Chem. Mater.* **2009**, *21* (24), 5727–5742.

(39) Mendez, J. C.; Hiemstra, T. Surface Area of Ferrihydrite Consistently Related to Primary Surface Charge, Ion Pair Formation, and Specific Ion Adsorption. *Chem. Geol.* **2020**, *532*, 119304.

(40) Kinniburgh, D. G.; Barker, J. A.; Whitfield, M. A Comparison of Some Simple Adsorption Isotherms for Describing Divalent Cation Adsorption by Ferrihydrite. *J. Colloid Interface Sci.* **1983**, *95* (2), 370–384.

(41) Kinniburgh, D. G.; Syers, J. K.; Jackson, M. L. Specific Adsorption of Trace Amounts of Calcium and Strontium by Hydrous Oxides of Iron and Aluminum. *Soil Sci. Soc. Am. J.* **1975**, *39* (3), 464–470.

(42) Kolařík, Z. Sorption Radioaktiver Isotopen an Niederschlägen VI. System Eisen(III)-Hydroxyd-Strontiumnitratlösung Und Die Allgemeinen Gesetzmäsigkeiten Der Sorption Am Eisen(III)-Hydroxyd. *Collect. Czechoslov. Chem. Commun.* **1962**, *27* (4), 938–950.

(43) Sajih, M.; Bryan, N. D.; Livens, F. R.; Vaughan, D. J.; Descostes, M.; Phrommavanh, V.; Nos, J.; Morris, K. Adsorption of Radium and Barium on Goethite and Ferrihydrite: A Kinetic and Surface Complexation Modelling Study. *Geochim. Cosmochim. Acta* **2014**, *146*, 150–163.

(44) Hiemstra, T.; Van Riemsdijk, W. H. A Surface Structural Approach to Ion Adsorption: The Charge Distribution (CD) Model. *J. Colloid Interface Sci.* **1996**, *179* (2), 488–508.

(45) Hiemstra, T.; Van Riemsdijk, W. H. On the Relationship between Charge Distribution, Surface Hydration, and the

Structure of the Interface of Metal Hydroxides. *J. Colloid Interface Sci.* **2006**, *301* (1), 1–18.

(46) Hiemstra, T.; Van Riemsdijk, W. H. A Surface Structural Model for Ferrihydrite I: Sites Related to Primary Charge, Molar Mass, and Mass Density. *Geochim. Cosmochim. Acta* **2009**, *73* (15), 4423–4436.

(47) Keizer, M. G.; van Riemsdijk, W. H. *ECOSAT, Equilibrium Calculation of Speciation and Transport. Technical Report. Department of Soil Quality. Wageningen Univeristy.*; 1998.

(48) Kinniburgh, D. G. *Fit, Technical Report WD/93/23*; Keyworth, Great Britain, 1993.

(49) Brown, I. D.; Altermatt, D. Bond-Valence Parameters Obtained from a Systematic Analysis of the Inorganic Crystal Structure Database. *Acta Crystallogr. Sect. B Struct. Sci.* **1985**, *41* (4), 244–247.

(50) Brown, I. D. Recent Developments in the Methods and Applications of the Bond Valence Model. *Chem. Rev.* **2009**, *109* (12), 6858–6919.

(51) Kinniburgh, D. G. The H+/M2+ Exchange Stoichiometry of Calcium and Zinc Adsorption by Ferrihydrite. *J. Soil Sci.* **1983**, *34* (4), 759–768.

(52) Tiberg, C.; Sjöstedt, C.; Persson, I.; Gustafsson, J. P. Phosphate Effects on Copper(II) and Lead(II) Sorption to Ferrihydrite. *Geochim. Cosmochim. Acta* **2013**, *120*, 140–157.

(53) Swedlund, P. J.; Webster, J. G.; Miskelly, G. M. The Effect of SO4 on the Ferrihydrite Adsorption of Co, Pb and Cd: Ternary Complexes and Site Heterogeneity. *Appl. Geochemistry* **2003**, *18* (11), 1671–1689.

(54) Weng, L. P.; Koopal, L. K.; Hiemstra, T.; Meeussen, J. C. L.; Van Riemsdijk, W. H. Interactions of Calcium and Fulvic Acid at the Goethite-Water Interface. *Geochim. Cosmochim. Acta* **2005**, *69* (2), 325–339.

(55) Ali, M. A.; Dzombak, D. A. Effects of Simple Organic Acids on Sorption of Cu2+ and Ca2+ on Goethite. *Geochim. Cosmochim. Acta* **1996**, *60* (2), 291–304.

(56) Jang, H. M.; Fuerstenau, D. W. The Specific Adsorption of Alkaline-Earth Cations at the Rutile/Water Interface. *Colloids and Surfaces* **1986**, *21* (C), 235–257.

(57) Ridley, M. K.; Machesky, M. L.; Wesolowski, D. J.; Palmer, D. A. Calcium Adsorption at the Rutile-Water Interface: A Potentiometric Study in NaCl Media to 250°C. *Geochim. Cosmochim. Acta* **1999**, *63* (19–20), 3087–3096.

(58) Gao, Y.; Mucci, A. Individual and Competitive Adsorption of Phosphate and Arsenate on Goethite in Artificial Seawater. *Chem. Geol.* **2003**, *199* (1–2), 91–109.

(59) Rahnemaie, R.; Hiemstra, T.; van Riemsdijk, W. H. Inner- and Outer-Sphere Complexation of Ions at the Goethite–Solution Interface. *J. Colloid Interface Sci.* **2006**, *297* (2), 379–388.

(60) Stachowicz, M.; Hiemstra, T.; van Riemsdijk, W. H. Multi-Competitive Interaction of As(III) and As(V) Oxyanions with Ca2+, Mg2+, PO3−4, and CO2−3 Ions on Goethite. *J. Colloid Interface Sci.* **2008**, *320* (2), 400–414.

(61) Breeuwsma, A.; Lyklema, J. Interfacial Electrochemistry of Hematite (Fe2O3). *Discuss. Faraday Soc.* **1971**, *52* (0), 324–333.

(62) Kinniburgh, D. G.; Jackson, M. L.; Syers, J. K. Adsorption of Alkaline Earth, Transition, and Heavy Metal Cations by Hydrous Oxide Gels of Iron and Aluminum1. *Soil Sci. Soc. Am. J.* **1976**, *40* (5), 796.

(63) Hiemstra, T. Ferrihydrite Interaction with Silicate and Competing Oxyanions: Geometry and Hydrogen Bonding of Surface Species. *Geochim. Cosmochim. Acta* **2018**, *238*, 453–476.

(64) Harrington, R.; Hausner, D. B.; Xu, W.; Bhandari, N.; Michel, F. M.; Brown, G. E.; Strongin, D. R.; Parise, J. B. Neutron Pair Distribution Function Study of Two-Line Ferrihydrite. *Environ. Sci. Technol.* **2011**, *45* (23), 9883–9890.

(65) Hiemstra, T. Surface Structure Controlling Nanoparticle Behavior: Magnetism of Ferrihydrite, Magnetite, and Maghemite. *Environ. Sci. Nano* **2018**, *5* (3), 752–764.

(66) Axe, L.; Bunker, G. B.; Anderson, P. R.; Tyson, T. A. An XAFS Analysis of Strontium at the Hydrous Ferric Oxide Surface. *J. Colloid Interface Sci.* **1998**, *199* (1), 44–52.

(67) Kahlenberg, V.; Fischer, R. X. Structural Characterization of Strontium Monoferrite SrFe2O4, a New Stuffed Framework Compound. *Solid State Sci.* **2001**, *3* (4), 433–439.

(68) Nie, Z.; Finck, N.; Heberling, F.; Pruessmann, T.; Liu, C.; Lützenkirchen, J. Adsorption of Selenium and Strontium on Goethite: EXAFS Study and Surface Complexation Modeling of the Ternary Systems. *Environ. Sci. Technol.* **2017**, *51* (7), 3751–3758.

(69) Collins, C. R.; Sherman, D. M.; Vala Ragnarsdóttir, K. The Adsorption Mechanism of Sr2+ on the Surface of Goethite. *Radiochim. Acta* **1998**, *81* (4), 201–206.

(70) Fuller, A. J.; Shaw, S.; Peacock, C. L.; Trivedi, D.; Burke, I. T. EXAFS Study of Sr Sorption to Illite, Goethite, Chlorite, and Mixed Sediment under Hyperalkaline Conditions. *Langmuir* **2016**, *32* (12), 2937–2946.

(71) Rietra, R. P. J. J.; Hiemstra, T.; Van Riemsdijk, W. H. Electrolyte Anion Affinity and Its Effect on Oxyanion

Adsorption on Goethite. *J. Colloid Interface Sci.* **2000**, *229* (1), 199–206.

(72) Spadini, L.; Schindler, P. W.; Charlet, L.; Manceau, A.; Ragnarsdottir, K. V. Hydrous Ferric Oxide: Evaluation of Cd-HFO Surface Complexation Models Combining CdK EXAFS Data, Potentiometric Titration Results, and Surface Site Structures Identified from Mineralogical Knowledge. *J. Colloid Interface Sci.* **2003**, *266* (1), 1–18.

(73) Hiemstra, T.; Venema, P.; Van Riemsdijk, W. H. Intrinsic Proton Affinity of Reactive Surface Groups of Metal (Hydr)Oxides: The Bond Valence Principle. *J. Colloid Interface Sci.* **1996**, *184* (2), 680–692.

(74) Koopal, L. K.; Saito, T.; Pinheiro, J. P.; Van Riemsdijk, W. H. Ion Binding to Natural Organic Matter: General Considerations and the NICA-Donnan Model. In *Colloids and Surfaces A: Physicochemical and Engineering Aspects*; Elsevier B.V., 2005; Vol. 265, pp 40–54.

(75) Kinniburgh, D. G.; Van Riemsdijk, W. H.; Koopal, L. K.; Borkovec, M.; Benedetti, M. F.; Avena, M. J. Ion Binding to Natural Organic Matter: Competition, Heterogeneity, Stoichiometry and Thermodynamic Consistency. In *Colloids and Surfaces A: Physicochemical and Engineering Aspects*; Elsevier Science Publishers B.V., 1999; Vol. 151, pp 147–166.

(76) Dempsey, B. A.; Singer, P. C. The Effects of Calcium on the Adsorption of Zinc by MnOx(s) and Fe(OH)3 (Am). In *Contaminants and Sediments, Vol 2*; Baker, R. A., Ed.; Ann Arbor Science, 1980; pp 333–352.

(77) Hiemstra, T.; Antelo, J.; Rahnemaie, R.; van Riemsdijk, W. H. Nanoparticles in Natural Systems I: The Effective Reactive Surface Area of the Natural Oxide Fraction in Field Samples. *Geochim. Cosmochim. Acta* **2010**, *74* (1), 41–58.

(78) Rietra, R. P. J. J.; Hiemstra, T.; van Riemsdijk, W. H. Interaction between Calcium and Phosphate Adsorption on Goethite. *Environ. Sci. Technol.* **2001**, *35* (16), 3369–3374.

(79) Talebi, M.; Rahnemaie, R.; Goli Kalanpa, E.; Davoodi, M. H. Competitive Adsorption of Magnesium and Calcium with Phosphate at the Goethite Water Interface: Kinetics, Equilibrium and CD-MUSIC Modeling. *Chem. Geol.* **2016**, *437*, 19–29.

(80) Allen, N.; Machesky, M. L.; Wesolowski, D. J.; Kabengi, N. Calorimetric Study of Alkali and Alkaline-Earth Cation Adsorption and Exchange at the Quartz-Solution Interface. *J. Colloid Interface Sci.* **2017**, *504*, 538–548.

(81) Shannon, R. D. Revised Effective Ionic Radii and Systematic Studies of Interatomic Distances in Halides and Chalcogenides. *Acta Crystallogr. Sect. A* **1976**, *32* (5), 751–767.

(82) Lindsay, W. L. *Chemical Equilibria in Soils*; Wiley-Interscience Publication; Wiley, 1979.

(83) Rahnemaie, R.; Hiemstra, T.; Van Riemsdijk, W. H. Geometry, Charge Distribution, and Surface Speciation of Phosphate on Goethite. *Langmuir* **2007**, *23* (7), 3680–3689.

(84) De Robertis, A.; Di Giacomo, P.; Foti, C. Ion-Selective Electrode Measurements for the Determination of Formation Constants of Alkali and Alkaline Earth Metals with Low-Molecular-Weight Ligands. *Anal. Chim. Acta* **1995**, *300* (1–3), 45–51.

(85) Hiemstra, T.; van Riemsdijk, W. H. Biogeochemical Speciation of Fe in Ocean Water. *Mar. Chem.* **2006**, *102* (3), 181–197.

CHAPTER 5

Ternary complex formation of phosphate with Ca and Mg ions binding to ferrihydrite: Experiments and mechanisms

Juan C. Mendez, Tjisse Hiemstra

Published as:

Mendez, J.C., Hiemstra, T. 2020. Ternary complex formation of phosphate with Ca and Mg ions binding to ferrihydrite: Experiments and mechanisms. *ACS Earth and Space Chemistry*. 4(4) 545-557 doi/10.1021/acsearthspacechem.9b00320

Abstract

Calcium (Ca) and magnesium (Mg) are the most abundant alkaline-earth metals in nature, and their interaction with ferrihydrite (Fh) affects the geochemical cycling of relevant ions, including phosphate (PO_4). The interfacial interactions of Ca and Mg (M^{2+}) with PO_4 have not been analyzed yet for freshly precipitated Fh. Here, we studied experimentally this interaction in binary M^{2+}-PO_4 systems over a wide range of pH, M^{2+}/PO_4 ratios, and ion loadings. The primary adsorption data were scaled to the surface area of Fh using a recent ion-probing methodology that accounts for the size-dependent chemical composition of this nanomaterial ($FeO_{1.4}(OH)_{0.2}\cdot nH_2O$). The results have been interpreted with the charge distribution (CD) model, combined with a state-of-the-art structural surface model for Fh. The CD coefficients have been derived independently using MO/DFT/B3LYP/6-31+G** optimized geometries. M^{2+} and PO_4 mutually enhance their adsorption to Fh. This synergy results from the combined effect of ternary surface complex formation and increased electrostatic interactions. The type of ternary complex formed (*i.e.* anion *vs* cation-bridged) depends on the relative binding affinities of the co-adsorbing ions. For our Ca-PO_4 systems, modeling suggests the formation of two anion-bridged ternary complexes, *i.e.* $\equiv(FeO)_2PO_2Ca$ and $\equiv FeOPO_3Ca$. The latter is most prominently present, leading to a relative increase in the fraction of monodentate PO_4 complexes. In Mg-PO_4 systems, only the formation of the ternary $\equiv FeOPO_3Mg$ complex has been resolved. In the absence of Ca, the pH dependency of PO_4 adsorption is stronger for Fh than for goethite, but this difference is largely, although not entirely, compensated in the presence of Ca. This study enables the use of Fh as a proxy for the natural oxide fraction, which will contribute to improve our understanding of the mutual interactions of PO_4 and M^{2+} in natural systems.

Keywords: calcium, magnesium, iron oxide nanoparticles, surface complexation modeling, CD model, cooperative and synergistic binding, electrostatic interactions, anion-bridged complexes

5.1. Introduction

Ferrihydrite (Fh) is a nanoparticulate Fe-(hydr)oxide present in almost all natural systems including soils, aquifers, and oceans, and it is also found in mine waste drainage water.[1–3] Due to its relatively low surface energy in comparison to other Fe-(hydr)oxides, Fh is the most thermodynamically stable Fe-(hydr)oxide at a nano-size range of ~2–8 nm.[4] It is the earliest Fe(III) product that precipitates and works as a precursor of other more crystalline Fe-(hydr)oxides.[5–7] Ferrihydrite has a high ion adsorption capacity and a large affinity for binding inorganic ions and organic compounds.[8–13] In the environment, the (bio)geochemical cycle of many nutrients and pollutants is largely determined by adsorption processes occurring at the Fh–solution interface.[1] Hence, grasping the interfacial processes of ion binding is essential for understanding the adsorption behavior of ions observed at the macroscopic scale.

A major reason for the extraordinarily high ion adsorption capacity of Fh is its large specific surface area (SSA),[14,15] which, for freshly precipitated Fh is in the order of ~ 600 – 1100 $m^2\ g^{-1}$.[16] Moreover, Fh has a relatively high surface site density of particularly singly coordinated (≡FeOH) groups,[17] which are able to bind cations and anions. The singly (≡FeOH) and triply (≡Fe_3O) coordinated surface groups of Fh may bind protons, resulting in a pH-dependent net surface charge. The result is an amphoteric behavior of Fh being important for the pH dependency of the adsorption of both metal ions and oxyanions. The mechanisms of ion complexation have been extensively studied for Fh in a long history of *in situ* spectroscopy, quantum chemical computations and surface complexation modeling, *e.g.* refs [[14,18–32]]. Remarkably, the interaction of Ca and Mg with Fh nanoparticles has received relatively little attention, whereas both elements are highly abundant in the environment and may significantly affect the adsorption of other compounds, particularly oxyanions, such as phosphate (PO_4), arsenate (AsO_4), and selenite (SeO_3).[33–36] In systems with well-crystallized goethite, it has been shown that the adsorption of PO_4 and SeO_3 increases in the presence of, respectively, the alkaline-earth metal ions Ca^{2+} and Sr^{2+}.[34,36,37] Qualitatively, similar results have been reported for the adsorption of AsO_4 and PO_4 in the presence of Ca^{2+} ions in systems with freeze-dried Fh.[23]

From a quantitative perspective, Ca^{2+} is generally the most important metal cation in soil and groundwater.[38] Across different environments, the solution concentration of Ca varies over several orders, being low as ~10^{-5} M and high as 10^{-1} M. Magnesium ions (Mg^{2+}) can also be abundant in natural environments. It dominates the composition of divalent cations in marine systems and is important in areas irrigated with Mg-rich water.[36,39] Both alkaline-earth cations (hereinafter jointly referred to as M^{2+}) can specifically adsorb to the surfaces of Fe-(hydr)oxides, affecting the physicochemical properties of the mineral–solution interface and the adsorption of organic and inorganic compounds,[13,33–35] including PO_4.

In aquatic and terrestrial systems, the PO_4 availability is largely controlled by adsorption to the nano-size fraction of Fe- and Al-(hydr)oxides[40–42] that can be dissolved in an acid ammonium oxalate solution.[43,44] Thus, Fh can be considered as a relevant model material for studying the mechanisms of PO_4 binding to the natural fraction of metal-(hydr)oxides. In most environments, PO_4 is simultaneously present with Ca^{2+} and Mg^{2+} ions and will interact in combination at the Fh–solution interface. The adsorption of Ca^{2+} ions promotes the binding of PO_4 to Fe-(hydr)oxides and *vice versa*.[34,45] This cooperative interaction has been noticed by soil chemists since long ago,[46,47] yet the mechanism of the pH-dependent interplay of PO_4 and Ca^{2+} ions at the surfaces of Fe-(hydr)oxides remains indistinct. However, understanding and quantifying these mutual interactions is highly relevant from a practical perspective of soil chemical analysis. For predicting the availability and mobility of PO_4 in the environment, field samples are often taken and routinely extracted with unbuffered electrolyte

solutions.[48,49] These solutions may strongly differ in the concentration of Ca, for instance soil extractions with 0.01 M $CaCl_2$ solution[50] *vs* soil extractions with demineralized water.[48] The differences in the Ca concentration of the extracting solutions will affect the equilibration of PO_4.[48,51] Translation of these measurements to field conditions not only requires insights into the interfacial interactions of PO_4 and the alkaline-earth metal ions but also their quantification.

Three main mechanisms have been proposed for explaining the synergistic interaction between PO_4 and Ca^{2+} ions at the metal-(hydr)oxide surfaces, namely, (i) increase in the interfacial electrostatic interactions; (ii) formation of ternary surface complexes; and (iii) surface precipitation of Ca-PO_4 mineral phases, which may be particularly relevant at high adsorption densities.[20,52–54] Moreover, formation of Fe-PO_4-Ca networks has been reported when Fe(III) coprecipitates in the presence of PO_4 and Ca^{2+} ions.[55] A chemical interaction between Ca^{2+} and PO_4 is conceivable as these ions can precipitate in a range of minerals whose thermodynamic stability increases when the Ca/PO_4 ratio increases.[56] Rationalizing the interfacial interaction between Ca^{2+} and PO_4 only on the basis of electrostatics has been done for goethite,[34,36] while the additional formation of a ternary Fe-PO_4-Ca complex has been assumed in the case of a freeze-dried Fh material.[23]

For freeze-dried Fh, the cooperative interaction between Ca^{2+} and PO_4 ions has been previously investigated.[23] However, the ion adsorption behavior of this material differs from that of freshly-prepared Fh because drying leads to irreversible aggregation of the primary particles.[57] It may lead to changes in the crystal morphology, phase transformation of Fh,[58] and undefined reduction of the reactive surface area.[59] Therefore, freshly prepared Fh is chosen in the present study. For this material, we have developed recently a methodology to determine the SSA in a consistent manner with the description of the primary surface charge and specific ion adsorption.[59] For freshly prepared Fh, the cooperative interaction of PO_4 with Ca^{2+} ions has never been studied nor has it been done for Mg^{2+} ions. Another advantage of using freshly prepared Fh is the possibility to interpret the collected adsorption data with advanced surface complexation modeling. In addition, we consider freshly prepared Fh as a good proxy for the natural Fe-(hydr)oxide fraction of soils and sediments, since Fh particles may precipitate without extensive aggregation if formed in the presence of natural organic matter, which contributes to the thermodynamic stability of Fh and prevents its phase transformation into more stable Fe-(hydr)oxide minerals.[6,60,61]

Based on the above, the objective of the present study is to assess experimentally and by surface complexation modeling the interaction of the alkaline-earth metal ions Ca^{2+} and Mg^{2+} with PO_4 in systems with well-defined, freshly precipitated Fh. In our analysis, we will apply a state-of-art modeling framework that includes recent insights into the surface structure of Fh,[32] and the interfacial charge distribution of the complexes formed that will be derived independently from MO/DFT/B3LYP/6-31+G** optimized hydrated clusters. In addition, we will account for the chemical heterogeneity of the reactive sites of Fh for binding divalent metal ions, defining in our modeling sites with high and low affinities for binding Ca^{2+} and Mg^{2+} ions.

For a consistent data interpretation, we will measure the SSA of Fh with a recently developed ion-probing methodology[59] that we will use to scale our primary adsorption data (*i.e.* ion/Fe ratios). In this scaling, we will consistently account for the size dependency of the molar mass of Fh. The latter is due to a particle size-dependent contribution of chemisorbed water (nH_2O), completing the coordination spheres of Fe atoms at the surface of Fh leading to $FeO_{1.4}(OH)_{0.2}{\cdot}nH_2O$.[17] The size-dependent composition also affects the mass density ρ_{nano} (g cm^{-3}) of Fh. This ρ_{nano} will be used to translate the specific surface area into a mean particle diameter that is used to derive the values of the Stern layer

capacitances of the compact part of the electrical double layer because this nanomaterial is strongly curved. All the above-mentioned factors will be collectively included in the present CD modeling approach together with a recent evaluation of the primary charge of Fh.[59] In our work, we will explore the ternary complex formation, for which we will be considering a suite of complexes as candidates to describe our extensive adsorption dataset. Finally, we will address the question of how much Fh differs from well-crystallized goethite in relation to the cooperative binding of Ca-PO_4, and what are the possible implications of using these materials as proxies for the natural oxide fraction in soils.

5.2. Experimental section

Ultra-pure water (18.2 MΩcm at 25 °C, 1 ppb TOC) and chemical reactants of analytical grade were used to prepare all stock solutions and Fh suspensions. Contact between solutions and air was minimized to avoid the interference of CO_2(g) during the adsorption experiments.

5.2.1. Synthesis of ferrihydrite

Ferrihydrite was synthesized according to Hiemstra et al.[16] Briefly, ~1.0 L of a solution containing ~3.7 mM $Fe(NO_3)_3 \cdot 9H_2O$ dissolved in 0.01 M HNO_3 was titrated by adding a freshly prepared solution of 0.02 M NaOH. The NaOH solution was initially added at a rate of ~200 mL min^{-1} until a pH of ~3.1 was reached. Subsequently, additional base solution was added in ~5 mL increments until the suspension reached a final pH of ~8.2. Once the pH was stabilized (~15 min), the Fh suspension was centrifuged at 3300*g* for 45 min. Next, the supernatant was carefully removed, and the settled Fh particles were re-suspended in a solution of 0.01 M $NaNO_3$ to a final volume of typically ~160 mL. Each freshly prepared Fh suspension was aged for 4 h at 20 °C in closed bottles before starting the adsorption experiments. The total Fe concentration of each Fh suspensions was determined in a matrix of 0.8 M H_2SO_4 using ICP-OES. Typically, the total Fe concentration in these suspensions was 20.5 ± 0.5 mM (~2 g L^{-1}). The specific surface area (SSA, m^2 g^{-1}) of each Fh batch was independently measured using surface probing with PO_4.[59] In this approach, the pH-dependent adsorption of PO_4 is measured in single-ion systems. The primary adsorption data (*i.e.* mol PO_4/mol Fe) are then iteratively interpreted with the CD model, defining the SSA as the only adjustable parameter and accounting for the size dependency of the molar mass (M_{nano}) and mass density (ρ_{nano}) of Fh, as well as the size dependency of the Stern layer capacitance.[59]

5.2.2. Adsorption experiments

The adsorption interaction between the alkaline-earth cations (Ca^{2+} and Mg^{2+}) and PO_4 was evaluated in binary systems with freshly precipitated Fh. The pH of the adsorption systems ranged between ~5 and 10, and the background electrolyte concentration was kept constant at 0.01 M $NaNO_3$. Each adsorption system was prepared in 50 mL polypropylene tubes kept under moist-purified N_2(g) to prevent intrusion of CO_2(g) during the preparation of the systems. For the Ca-PO_4 experiments, nine adsorption series were prepared with different total molar Ca:PO_4:Fe ratios. Additional series with no Ca addition were prepared and used as a reference for the adsorption of PO_4 in single-ion systems. For the Mg-PO_4 experiments, three adsorption series were prepared at different total molar Mg:PO_4:Fe ratios. Details about the chemical conditions of each adsorption series are presented in Tables S5.1 and S5.2 of the Supporting Information (SI). The pH of the adsorption systems was adjusted within the desired range by adding 1.0–2.0 mL of 0.01 M solutions of either HNO_3 or NaOH. Stock solutions of

NaH_2PO_4, $Ca(NO_3)_2$, and $Mg(NO_3)_2$ were used to add respectively the ions PO_4^{3-}, Ca^{2+}, and Mg^{2+}. To minimize the risk of any precipitation of Ca-PO_4 and Mg-PO_4 solid phases, the systems were pre-equilibrated with PO_4 for 1 h before the corresponding alkaline-earth ion was added. The final volume of each adsorption system was 40.0 mL. All adsorption systems were constantly shaken (120 strokes min^{-1}) at 20 °C for 20 h, and next the suspensions were centrifuged at 3330*g* for 20 min to separate the solid and liquid phases. An aliquot of 10 mL was taken from the supernatant of each adsorption system, filtered through a 0.45 µm membrane filter, and acidified with HNO_3 for analysis of the equilibrium concentration of M^{2+} and PO_4. The analysis was done using either ICP-OES or ICP-MS, depending on the final concentrations of the analyzed elements. The settled Fh particles were re-suspended in the 50 mL polypropylene tube to measure the equilibrium pH with a combined glass electrode.

5.2.3. Modeling

5.2.3.1. Charge distribution (CD) model

The results of the M^{2+}-PO_4 adsorption experiments have been interpreted with the charge distribution (CD) model[62] in combination with a recent multisite ion complexation (MUSIC) model for Fh.[32] Details about this structural surface model are described in Section 5.2.3.2. The electrical double layer (EDL) is described with the extended Stern layer approach.[63] Since Fh is an ultra-small nanoparticle with a strong surface curvature, the capacitance values ($C_{nano,1}$ and $C_{nano,2}$) of the inner and outer Stern layers are made size-dependent, using well-crystallized goethite as a reference with a near zero surface curvature.[64] The primary surface charge is described according to Mendez and Hiemstra.[59]

CD modeling was done with ECOSAT version 4.9.[65] The affinity constants (log*K*) of the adsorption reactions of the ternary Fe-PO_4-M^{2+} complexes were optimized using the program FIT version 2.581.[66] The entire set of solution speciation and primary protonation reactions used in the modeling are presented respectively in Tables S5.3 and S5.4 of the SI. The software Spartan18 parallel of Wavefunction, Inc. was used to optimize the geometries of the ternary Fe-PO_4-Ca and Fe-PO_4-Mg complexes with molecular orbital (MO) calculations, applying density function theory (DFT). This approach has been also applied to optimize the geometries of the M^{2+} [67] and PO_4 [32] complexes adsorbed to Fh. These optimized geometries were interpreted with Brown valence analysis[68,69] to assess the charge distribution of the adsorbed complexes with a small correction for water dipole orientation.[63] The charge attribution to the surface plane (Δz_0) was based on the optimized MO-DFT geometries, whereas the charge distribution over the Stern planes (Δz_1 and Δz_2) was derived for the ternary complexes by fitting to the experimental adsorption data. Details about the template of Fh used in the geometry optimizations are given in Mendez and Hiemstra.[19]

5.2.3.2. Multisite ion complexation model for Fh

For Fh, a new structural model has been proposed by Michel et al.[70,71] The surface structure has been described by Hiemstra.[17] Since Fh particles are ultra-small, the surface will dominantly contribute to the overall behavior of this nanomaterial. Many microscopic and macroscopic properties of Fh are size-dependent. A whole suite of physical-chemical properties can be understood from the difference in the polyhedral composition of the mineral core and the surface.[4,17,72,73] With a surface structural analysis of this material, Hiemstra and Zhao[32] have developed a mechanistic multisite ion complexation model for Fh distinguishing various types of sites and deriving corresponding densities. The model also includes the size-dependent variation of the molar mass (M_{nano}) and the mass density (ρ_{nano}) that results from the variable contribution of chemisorbed water ($n H_2O$) to the overall chemical composition of Fh ($FeO_{1.4}(OH)_{0.2} \cdot n H_2O$).[16]

In the above structural multisite model, three types of surface groups have been defined, which differ in their coordination number with Fe, *i.e.* singly ($\equiv FeOH^{-0.5}$), doubly ($\equiv Fe_2OH^0$), and triply ($\equiv Fe_3O^{-0.5}$) coordinated groups. Structurally, two types of singly coordinated groups can be distinguished, *i.e.* $\equiv FeOH(a)^{-0.5}$ and $\equiv FeOH(b)^{-0.5}$, which may form, respectively, either single-edge (^1E) or double-corner (^2C) bidentate surface complexes having, respectively, a surface density of $N_s(a) = 3.0 \pm 0.6$ nm^{-2} and $N_s(b) = 2.8 \pm 0.6$ nm^{-2}. Both types of singly coordinated groups may also form single corner (^1C) monodentate surface complexes. The triply coordinated groups do not participate in ligand exchange reactions, but they contribute to the development of the primary surface charge. At the surfaces of Fh, different types of triply coordinated groups are found with a large variation in their proton affinity ($\log K_H$). The surface charge introduced by groups with a low $\log K_H$ ($\equiv Fe_3O^{-0.5}$) is compensated by groups with a high $\log K_H$ ($\equiv Fe_3OH^{+0.5}$), leading to an effective site density of $N_{s,(T)} = 1.4 \pm 0.5$ nm^{-2}, if the charging behavior of these triply coordinated groups is represented by an equivalent surface site with a $\log K_H = \sim 8.1$, as for the singly coordinated groups.[32] The $\equiv Fe_2OH^0$ groups are presumably uncharged and do not react with protons under common pH conditions. This model has been applied to describe consistently the primary surface charge[59] and the adsorption of a range of oxyanions, such as PO_4, AsO_4, $As(OH)_3$,[32] $Si(OH)_4$,[72] and CO_3[19] as well as the adsorption of the whole series of alkaline-earth metal cations.[67]

5.2.3.3. *Description of ion adsorption in single systems*

In a parallel study, we have shown that the CD model can describe very well the adsorption of Ca^{2+} and Mg^{2+} ions (M^{2+}) to Fh in single-ion systems over a broad range of solution conditions, comprising different initial M^{2+} concentrations and molar M^{2+}/Fe ratios, as well as pH and ionic strength levels.[67] The data can be described by defining in the modeling the formation of a binuclear bidentate complex according to:

$$2 \equiv FeOH(b)^{-0.5} + M^{2+} \leftrightarrow \equiv (FeOH(b))_2^{-1+\Delta z0}M^{\Delta z1} \qquad \log K_{BM} \qquad \text{(Equation 5.1)}$$

where Δz_0 and Δz_1 are the CD coefficients derived from the Brown bond valence analysis applied to the MO/DFT optimized geometries (Table 5.1). Bidentate complex formation is supported by our combined interpretation of MO/DFT geometry optimizations[67] and EXAFS data for the adsorption of divalent cation to Fe-(hydr)oxides.[31,37,74–76] This binding mechanism is also supported by the thermodynamic analysis of macroscopic data such as the H^+/M^{2+} exchange ratio reported for Ca[77] and the marked pH dependency of Ca adsorption observed in our adsorption experiments.

In that same parallel study, we have also shown that the adsorption sites of Fh for binding M^{2+} exhibit chemical heterogeneity, which is a common reported phenomenon for the binding of metal ions to Fh.[14,26,78] The high affinity sites dominate the adsorption at low M^{2+} concentrations, and for our Fh preparation, these surface sites have a density of $N_s(bh) = 0.32 \pm 0.02$ nm^{-2}. The corresponding site density for the low affinity sites can be set to $N_s(bl) = 2.48$ nm^{-2}, as the sum of both types of surface $FeOH(b)^{-0.5}$ groups is 2.8 nm^{-2}.[32]

For describing the adsorption of PO_4 in single-ion systems, we have used the set of CD model parameters derived by Hiemstra and Zhao.[32] For the adsorption of oxyanions that strongly interact with Fh such as PO_4, we do not experience explicitly in our modeling the presence of high affinity sites in line with previous suggestions given by Dzombak and Morel.[14] Probably, the high affinity character of these sites is masked by the already rather large PO_4 loading of the low affinity sites. Therefore, we have used in our modeling the same set of $\log K$ values for PO_4 binding to both types of $FeOH(b)^{-0.5}$ groups (Table 5.2 and Table S5.4).

Table 5.1. Surface species, CD coefficients, and fitted log*K* for the binding reactions of Ca and Mg to Fh derived in our parallel study.[67] The surface site densities are from Hiemstra and Zhao[32] with ≡FeOH(a) = 3.0 nm^{-2}, ≡FeOH(b) = 2.8 nm^{-2} and ≡Fe_3O = 1.4 nm^{-2}. Two types of ≡FeOH(b) groups were defined to account for site heterogeneity ≡FeOH(bl) for low affinity and ≡FeOH(bh) for high affinity, having a site density of respectively 2.48 ± 0.02 and 0.32 ± 0.02 nm^{-2} for our Fh preparations. The capacitance values for the extended Stern layers of Fh ($C_{nano,1}$ and $C_{nano,2}$) are size-dependent[59] (see Tables S5.1 and S5.2) and were calculated by taking as a reference the capacitance values of goethite (C_1 = 0.90 F m^{-2} and C_2 = 0.74 F m^{-2}).

Species	ID*	≡FeOH(bl)$^{-0.5}$	≡FeOH(bh)$^{-0.5}$	Δz_0**	Δz_1	Δz_2	H^+	Ca^{2+}	Mg^{2+}	log*K* ±SE
$(\equiv FeOH)_2Ca$	BCa(l)	2	0	0.94	1.06	0	0	1	0	2.64 ± 0.03
$(\equiv FeOH)_2Ca$	BCa(h)	0	2	0.94	1.06	0	0	1	0	5.13 ± 0.02
$(\equiv FeOH)_2Mg$	BMg(l)	2	0	0.89	1.11	0	0	0	1	1.87 ± 0.06
$(\equiv FeOH)_2Mg$	BMg(h)	0	2	0.89	1.11	0	0	0	1	4.09 ± 0.04

* BCa(l) = bidentate (double-corner) Ca with low affinity sites; BCa(h) = bidentate (double-corner) Ca with high affinity sites;
BMg(l) = bidentate (double-corner) Mg with low affinity sites; BMg(h) = bidentate (double-corner) Mg with high affinity sites

** The CD coefficients have been derived from MO/DFT optimized geometries.

5.3. Results and discussion

5.3.1. Interaction of calcium and magnesium with phosphate: experimental results

The interaction of the alkaline-earth metal ion Ca^{2+} with PO_4 in Fh systems has been studied extensively in the present work. In Figures 5.1 and 5.2, the left panels show the adsorption edges of Ca to Fh in the binary Ca-PO_4 systems, whereas the right panels show the corresponding PO_4 adsorption data. In Figure 5.1, the upper panels are for a total Ca concentration of ~0.05 mM, and the lower panels are for systems with a 5-fold higher concentration of added Ca (~0.25 mM). In Figure 5.2, we give the adsorption data for binary Ca-PO_4 systems with a higher Fh concentration. This allows an accurate measurement of the adsorption of Ca to Fh at higher total added Ca concentrations, *i.e.* ~1.0 mM (upper panels) and ~0.62 mM (lower panels). For comparison, we also present in Figures 5.1 and 5.2 the model predictions (dotted lines) and/or the measured adsorption data (open symbols) of the corresponding single-ion systems at the same initial ion loading.

At a given pH, the adsorption of Ca to Fh increases simultaneously with an increase in the initial concentration of PO_4. In comparison to the single-ion systems, the adsorption edges of Ca are significantly shifted toward lower pH values (~2.0 pH units) in the presence of PO_4. For systems with the same total Fe content, this shift of the adsorption edges is more pronounced for systems with lower total molar Ca/PO_4 ratios. Simultaneously, the adsorption of PO_4 to Fh increases in the presence of Ca, but the synergistic effect of Ca on the PO_4 adsorption is less pronounced than the corresponding effect of PO_4 on the adsorption of Ca.

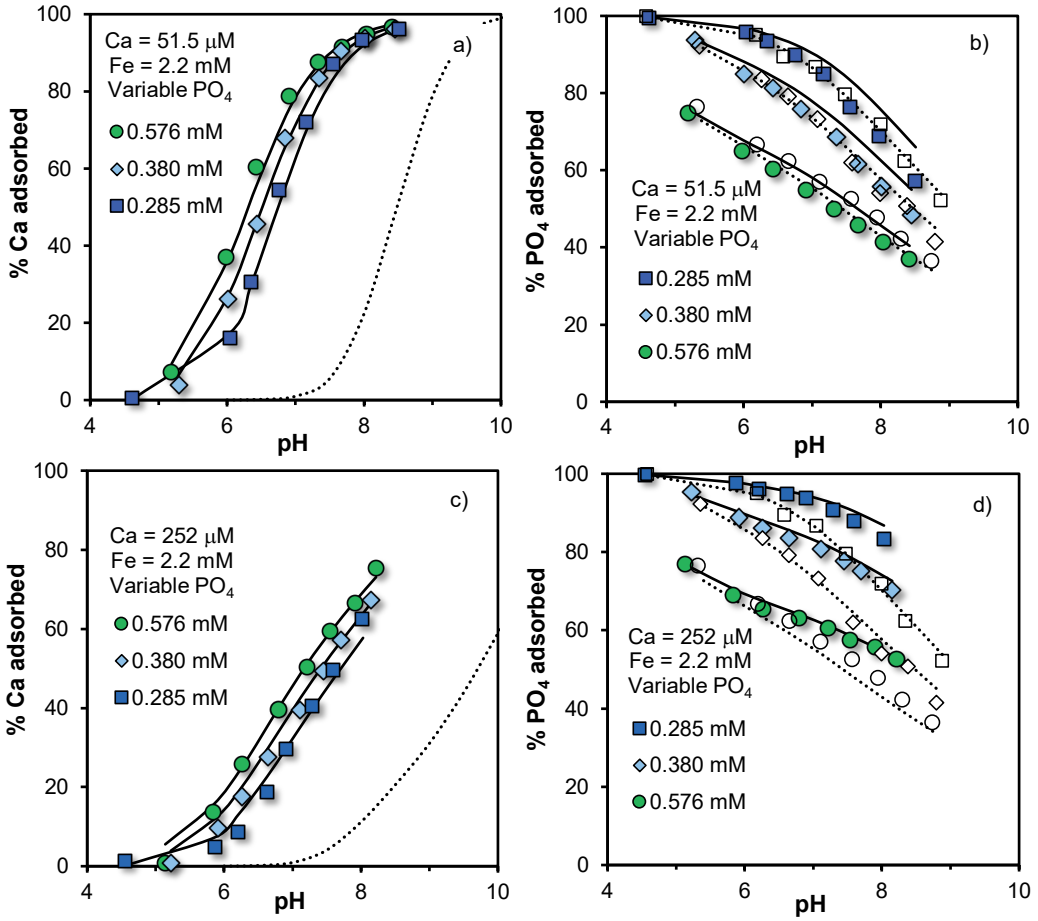

Figure 5.1. pH-dependent adsorption of Ca (left panels) and PO_4 (right panels) in binary ion systems with Fh. The ionic strength was kept constant at I = 0.01 M $NaNO_3$, and the specific surface area of this Fh suspension was A = 684 ± 15 m^2 g^{-1} with a corresponding molar mass of M_{nano} = 96.6 g mol^{-1} Fe. The symbols are experimental data and the lines are CD model calculations obtained with the parameter sets of Table 5.1 and 5.2. The adsorption parameters of PO_4 in single-ion systems are taken from Hiemstra and Zhao.[32] The total concentrations of Fe, Ca, and PO_4 are given in each panel. The initial Ca loadings in systems a,b and c,d are equivalent to respectively ~0.4 and ~1.7 μmol m^{-2}, and the equivalent initial PO_4 loadings vary from ~2.0 to 3.9 μmol m^{-2}. For comparison, model predictions are given for the corresponding single-ion systems, *i.e.* without addition of either Ca or PO_4 (dotted lines). For PO_4, the adsorption in single-ion systems was additionally measured for each experimental condition (open symbols). The adsorption of Ca and PO_4 is promoted in the binary systems by mutual electrostatic interactions and the formation of ternary PO_4-Ca surface complexes.

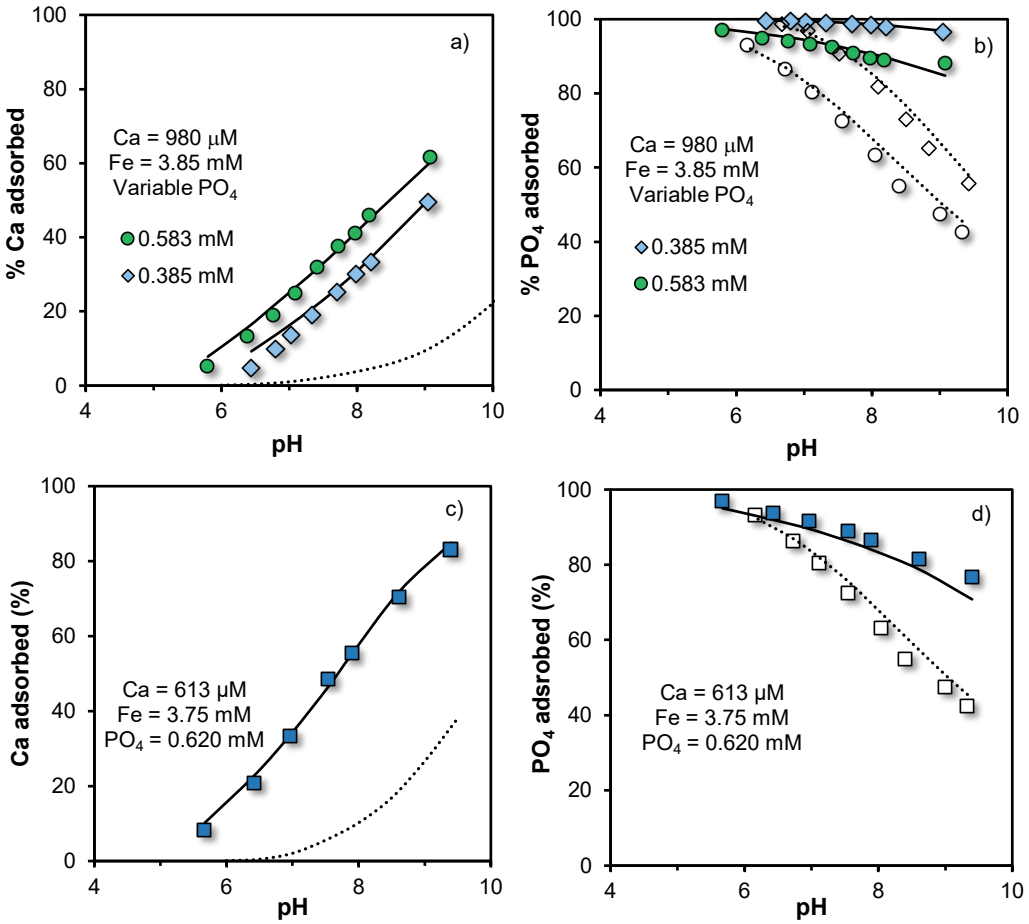

Figure 5.2. pH-dependent adsorption of Ca (left panels) and PO_4 (right panels) in single and binary ion systems with Fh in I = 0.01 M $NaNO_3$. The specific surface area of this Fh suspension was A = 684 ± 15 m^2 g^{-1} with a corresponding molar mass of M_{nano} = 96.6 g mol^{-1} Fe. The total concentrations of Fe, Ca, and PO_4 are given in each panel. The initial Ca loading in systems a,b and c,d are equivalent to respectively ~3.9 and ~2.5 µmol m^{-2}. The initial PO_4 loadings are equivalent to ~1.5–2.3 µmol m^{-2} in systems a,b and ~2.5 in systems c,d. The closed symbols and the full lines are respectively experimental data and CD model calculations for binary systems. For comparison, the model predictions are given for single-ion systems, *i.e.* without addition of either Ca or PO_4 (dotted lines). For PO_4, the adsorption in single-ion systems was also measured for each experimental condition (open symbols). The CD model parameter sets are given in Tables 5.1 and 5.2. The adsorption parameters of PO_4 in single-ion systems are taken from Hiemstra and Zhao.[32]

The cooperative interaction of ions adsorbed to Fh was also evaluated in the binary Mg-PO_4 systems. Figure 5.3 a,c shows that in the presence of PO_4, the adsorption edges of Mg are shifted toward lower pH values (closed symbols), in comparison to the adsorption of Mg in the single-ion systems (open symbols). In Figure 5.3b, the adsorption of PO_4 in the absence (open symbols) and presence (closed symbols) of Mg is compared for Fh systems with two different values for the total molar Mg/PO_4 ratios: 0.5 (circles) and 0.05 (squares). The percentage of PO_4 adsorbed increases in the presence of Mg.

Additionally, the pH-dependency of the PO_4 adsorption is strongly reduced in the systems with a relatively high molar Mg/PO_4 ratio, *e.g.* ~1.6 (Figure 5.3d).

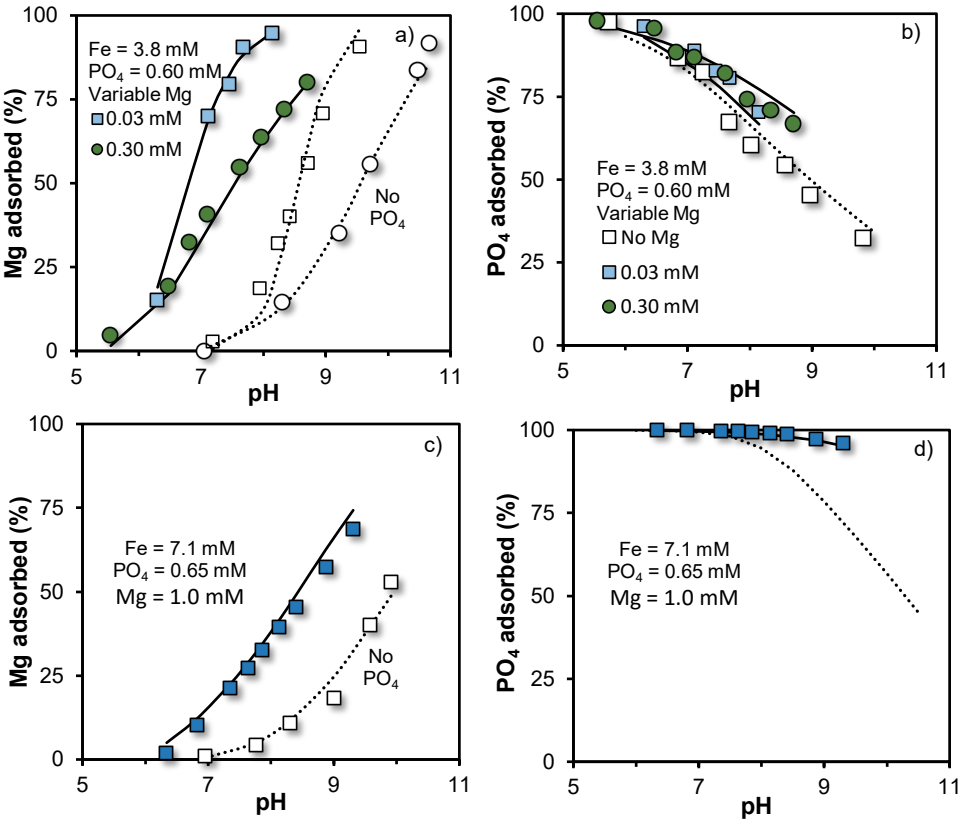

Figure 5.3. pH-dependent adsorption of Mg (left panels) and PO_4 (right panels) in single (open symbols) and binary ion systems (closed symbols) with Fh in $I = 0.01$ M $NaNO_3$. The specific surface area of this Fh suspension was $A = 720 \pm 10$ m^2 g^{-1} with a corresponding molar mass of $M_{nano} = 97.6$ g mol^{-1} Fe. The symbols are experimental data and the lines are CD model results obtained with the parameter sets of Tables 5.1 and 5.2. The adsorption parameters of PO_4 in single-ion systems are taken from Hiemstra and Zhao.[32] The total concentrations of Fe, Mg, and PO_4 are given in each panel. The initial loadings of Mg are equivalent to ~0.1 and ~1.1 µmol m^{-2} in systems a,b and ~2.0 µmol m^{-2} in systems c,d. The initial PO_4 loadings are equivalent to, respectively, ~2.2 and 1.3 µmol m^{-2} in systems a,b and c,d. For comparison, the respective adsorption series in single-ion systems have been measured (open symbols) and/or modelled (dotted line).

The model lines in Figures 5.1–5.3 show the capability of the CD model to describe accurately the interfacial interactions of the alkaline-earth metal ions Ca^{2+} and Mg^{2+} with PO_4 over a wide range of conditions in the Fh systems. Synergy between these cations and PO_4 has been also reported for freeze-dried Fh,[23] goethite (α-FeOOH),[34–36] hydrous zirconium oxide (HZO),[79] and manganese dioxide (δ-MnO_2).[80] However, the dominant mechanisms explaining these interactions might differ between these oxide materials. For Fh, details about the mechanisms of synergetic binding will be discussed in the next section.

5.3.2. Modeling and mechanisms of M^{2+}–PO_4 adsorption synergy

5.3.2.1. Effect of electrostatic interactions

The adsorption of M^{2+} is significantly promoted by PO_4 in all binary systems in comparison to the corresponding single-ion systems (dotted lines and/or open symbols in the left panels of Figures 5.1–5.3). In contrast, the PO_4 adsorption in the binary systems (right panels in Figures 5.1–5.3) increases mainly at high pH and high initial M^{2+} concentration due to the presence of M^{2+}. The reason for this difference is the higher affinity of PO_4 for the adsorption to Fh, in comparison with the adsorption affinity of M^{2+}. The large quantities of adsorbed PO_4 can change substantially the net particle charge of Fh, whereas the presence of M^{2+} in the binary systems affects notably less the net particle charge, as it can be shown by modeling.

In the absence of specific ion adsorption, the point of zero charge of Fh in $NaNO_3$ solutions is pH_{PZC} ~8.1.[59] Our CD modeling shows that the adsorption of PO_4 to Fh provokes a decrease in the isoelectric point (IEP) to pH_{IEP} ~4.5–5.0 (Figure S5.1a). It implies that, under these conditions, a negative double layer potential (ψ) is created in a major part of the pH range of our study. This induces a shift of the adsorption edges of Ca and Mg in the presence of PO_4 (Figures 5.1–5.3) and stimulates the formation of ternary surface species (Section 5.3.2.2). The binding of Ca^{2+} or Mg^{2+} ions in the binary systems with PO_4 partly compensates the negative charge created by the adsorbed PO_4 ions and in turn, this promotes the adsorption of PO_4 in the binary systems, particularly at high pH. It can be shown that at a sufficiently high Ca concentration, binary Ca-PO_4 systems with Fh may have two pH values where the particle charge switches, *i.e.* two pH_{IEP} values, one at low pH and one at high pH (Figure S5.1b).

Figure 5.4 presents the concentrations of Ca (panel a) and PO_4 (panel b) in the equilibrium solution of the respective single (open symbols) and binary (closed symbols) Fh systems. The experimental data of the binary systems cannot be explained using in the modeling only the adsorption reactions found for the single-ion systems (dotted lines). Figure 5.4 illustrates that mutual electrostatic interactions alone are not enough to explain the adsorption data in binary Ca-PO_4 systems. This finding contrasts with that in goethite systems, in which the cooperative binding of Ca^{2+} and Mg^{2+} ions with PO_4 could be well-predicted assuming only electrostatic interactions.[34–36] Differences in the adsorption interaction Ca-PO_4 between Fh and goethite are discussed in Section 5.3.4. In our Fh systems, precipitation of a calcium phosphate mineral cannot explain the significant reduction in concentrations in the Ca and PO_4 systems neither, as illustrated in Appendix D of the SI. For the Mg-PO_4 systems, the same results are observed (Figure S5.4).

5.3.2.2. Formation of ternary Ca-PO_4 surface complexes

The adsorption data of Ca and PO_4 in the binary systems can only be described by including in our modeling approach the formation of ternary surface complexes. In general, Ca and PO_4 have contrasting affinities for binding to metal (hydr)oxides. Ca^{2+} ions have a much lower intrinsic affinity than PO_4 ions for the binding sites at the surface of Fh. However, Ca^{2+} ions do have a high affinity for PO_4, which is reflected by the increasing stability of Ca-PO_4 minerals at increasing the molar Ca/PO_4 ratio of these minerals.[56] In the case of ternary complex formation, it is therefore more likely that a Ca^{2+} ion will bind to an adsorbed PO_4 ion rather than the opposite. This idea is supported by literature data of Fe-PO_4-Ca co-precipitation showing direct complexation of PO_4 to Fe(III) polymers, where these units form larger networks that are interconnected by Ca^{2+} ions.[55,81] High energy X-ray scattering (HEXS) with Pair distribution function (PDF) analysis showed double corner $\equiv(FeO)_2PO_2$ complexes linked together by Ca^{2+} ions bound as single corner complexes[55] with a Ca-P distance of 360 pm. *In situ* spectroscopic

studies have also suggested the formation of PO_4-bridged ternary complexes with Ca in adsorption systems with hydrous zirconium oxide[79] and titanium dioxide (TiO_2).[82]

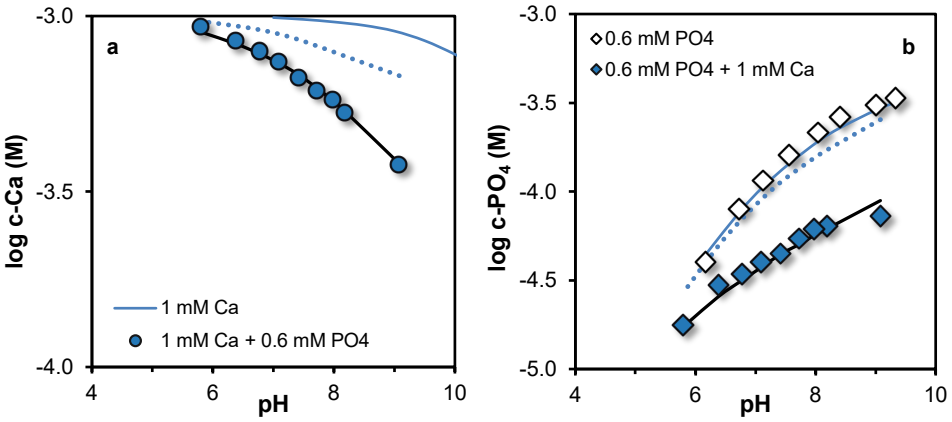

Figure 5.4. Logarithm of the (a) Ca and (b) PO_4 concentrations in the equilibrium solution of systems with Fh in $I = 0.01$ M $NaNO_3$. The total Fe concentration was 3.9 mM and the specific surface area of this Fh suspension was $A = 684 \pm 15$ m^2 g^{-1} with a respective molar mass $M_{nano} = 96.6$ g mol^{-1} Fe. Closed symbols are for the binary Ca-PO_4 systems with total concentrations of Ca = 1.0 mM and PO_4 = 0.6 mM, and the open symbols are for the single-ion systems. The dotted lines are the CD model predictions using only the adsorption parameters of the single-ion systems of Ca (Table 5.1) and PO_4,[32] whereas the full lines are the modeling results including for the binary systems the formation of ternary surface complexes (Table 5.2).

The binding of Ca^{2+} cations to already adsorbed PO_4 anions (*i.e.* formation of anion-bridged ternary complexes) is also supported by the modeling of the Ca and PO_4 adsorption data of our binary Ca-PO_4 systems with Fh (Figure 5.1 and 5.2). Our extensive modeling of these systems shows that the use of cation-bridged ternary complexes (*i.e.* Fe-Ca-PO_4) did not provide a good description of the adsorption of both Ca and PO_4 in the binary systems. Instead, our modeling advocates the formation of anion-bridged complexes in which the Ca^{2+} ion is located at a larger distance from the surface.

The formation reactions of the ternary complexes ultimately derived after extensive modeling are:

$$\equiv FeOH^{-0.5} + H^+(aq) + PO_4^{3-}(aq) + Ca^{2+}(aq) \leftrightarrow \equiv FeO^{-0.5+\Delta z0}PO_3^{\Delta z1}Ca^{\Delta z2} + H_2O(l) \quad \log K_{MTC} \quad \text{(Equation 5.2)}$$

$$2\equiv FeOH^{-0.5} + 2\ H^+(aq) + PO_4^{3-}(aq) + Ca^{2+}(aq) \leftrightarrow \equiv (FeO)_2^{-1+\Delta z0}PO_2^{\Delta z1}Ca^{\Delta z2} + 2\ H_2O(l) \quad \log K_{BTC} \quad \text{(Equation 5.3)}$$

where Δz_0, Δz_1, and Δz_2 are the CD coefficients of the 0–, 1– and 2– plane in the extended Stern layer model. The corresponding set of adsorption parameters is given in Table 5.2.

Table 5.2. Surface species, CD coefficients and fitted log*K* for the formation reactions of ternary surface complexes in the binary systems PO_4-Ca (R^2 = 0.99, *n*= 72) and PO_4-Mg (R^2 = 0.99, *n*= 22) with Fh. The surface site densities are taken from Hiemstra and Zhao[32] with ≡FeOH(a) = 3 nm^{-2}, ≡FeOH(b) = 2.8 nm^{-2} and ≡Fe_3O = 1.4 nm^{-2}. Two types of ≡FeOH(b) groups were defined to account for the surface site heterogeneity of the adsorption of M^{2+} (≡FeOH(bl) and ≡FeOH(bh) for low and high affinities, respectively).

Species	ID	≡FeOH(a)[a]	≡FeOH(bl)[a]	≡FeOH(bh)[a]	Δz_0	Δz_1	Δz_2	H^+	M^{2+}	PO_4^{3-}	log*K* ±SE***
≡$FeOPO_3Ca$*	MPCa(a)	1	0	0	0.24	-1.30	1.06	1	1	1	22.27 ± 0.12
≡$FeOPO_3Ca$*	MPCa(bl)	0	1	0	0.24	-1.30	1.06	1	1	1	22.27 ± 0.12
≡$FeOPO_3Ca$*	MPCa(bh)	0	0	1	0.24	-1.30	1.06	1	1	1	22.27 ± 0.12
≡ $(FeO)_2PO_2Ca$**	BPCa(bl)	0	2	0	0.62	-1.08	1.46	2	1	1	30.09 ± 0.12
≡ $(FeO)_2PO_2Ca$**	BPCa(bh)	0	0	2	0.62	-1.08	1.46	2	1	1	30.09 ± 0.12
≡$FeOPO_3Mg$*	MPMg(a)	1	0	0	0.22	-1.55	1.33	1	1	1	22.00 ± 0.10
≡$FeOPO_3Mg$*	MPMg(bl)	0	1	0	0.22	-1.55	1.33	1	1	1	22.00 ± 0.10
≡$FeOPO_3Mg$*	MPMg(bh)	0	0	1	0.22	-1.55	1.33	1	1	1	22.00 ± 0.10

*Δz_2 = 1.06 v.u. (± 0.06) can be explained as the Ca complexation to adsorbed PO_4 in ≡$FeOPO_3$-Ca-$(OH_2)_n$ with remaining charge attribution of Ca to 3 OH_2 ligands in the outer Stern plane. For the ternary complexes MPMg, a higher Δz_2 value of 1.33 v.u. (± 0.07) suggest that Mg is more loosely bound to PO_4 than Ca (see text).
**Δz_2 = 1.46 v.u. (± 0.17) can be explained as the Ca complexation to adsorbed PO_4 in ≡$(FeO)_2PO_2$-Ca-$(OH_2)_n$ with remaining charge attribution of Ca to 4 OH_2 ligands in the outer Stern plane.
*** log*K* values derived in this study by fitting of the experimental data obtained in the binary Ca-PO_4 and Mg-PO_4 systems.
[a] ≡$FeOH(a)^{-0.5}$ forms with PO_4 only monodentate complexes, whereas ≡$FeOH(b)^{-0.5}$ forms both mono- and bidentate (double-corner) complexes (See section 5.2.3.2).

For both the above surface complexes, the values of Δz_0 have been derived with the Brown bond valence analysis[68,69] of the optimized geometries of these ternary complexes that we obtained with MO/DFT/B3LYP/6-31+G** calculations (Appendix E in the SI), whereas the values of Δz_1 and Δz_2 were adjusted by fitting the model to the adsorption data using the constraint $\Delta z_{tot} = \Delta z_0 + \Delta z_1 + \Delta z_2$. The optimized MO/DFT structures of the ternary complexes defined with Equations 5.2 and 5.3 are represented in Figure 5.5 a,b, respectively. Both the mononuclear monodentate ≡$FeOPO_3$ complex (Figure 5.5a) and the binuclear bidentate ≡$(FeO)_2PO_2$ complex (Figure 5.5b) interact with Ca by forming one single Ca-O-P bond. In the former complex, the calculated Ca-P distance was 367 pm and, in the latter, it was 327 pm. In a hydrated calcium phosphate mineral, brushite ($CaHPO_4{\cdot}2H_2O$), a Ca-P distance of 370 ± 2 pm can be found in the case of single Ca-O-P bridging, which is close to the distance (360 pm) observed in ≡$(FeO)_2PO_2Ca$ networks[55] and found also in hydroxyapatite. In brushite, a shorter Ca-P distance of 312 pm is also found for single Ca-O-P linkages.

The ternary complex in which PO_4 is bound to Fh in a monodentate configuration (MPCa) (Equation 5.2) is the most relevant ternary surface species for describing our experimental data of the binary Ca–PO_4 systems (see below Figure 5.6). This complex can be formed with both types of singly coordinated groups ≡$FeOH(a)^{-0.5}$ and ≡$FeOH(b)^{-0.5}$. A similar type of complex was used by Antelo et al.[23] for describing Ca-PO_4 binary systems with freeze-dried Fh. However, their data set covers a relatively small range of solution conditions compared to our work in which we collected adsorption data at a wider range of Ca/Fe ratios. This allows us to reveal by modeling the formation of an additional ternary complex (BPCa) in which Ca is bound to an adsorbed PO_4 present in the bidentate configuration

(Equation 5.3). Moreover, in our modeling we have implemented the difference in high and low affinity sites for Ca, enabling a good description of the Ca binding over a wide range of Ca-loadings. With the two ternary complexes resolved, an excellent and consistent description of the simultaneous adsorption of Ca and PO_4 is possible ($R^2 = 0.99$, $n = 72$), as shown in Figures 5.1 and 5.2 with the modeled lines.

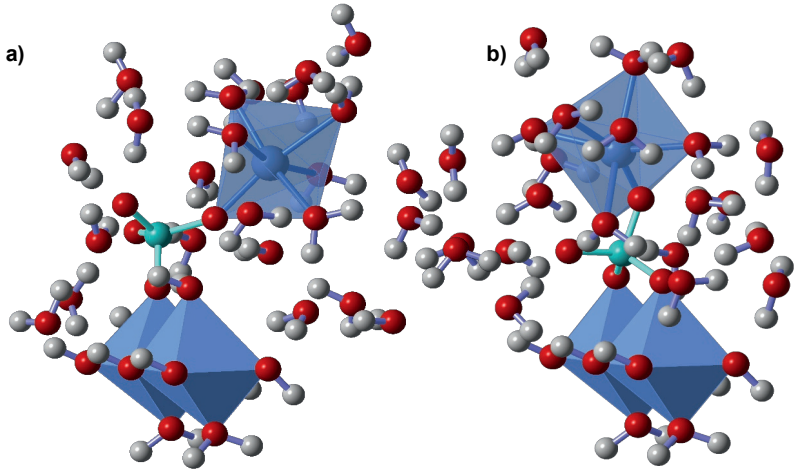

Figure 5.5. Hydrated geometries of the ternary Fe-PO_4-Ca complexes optimized with MO-DFT/B3LYP/6-31+G**. Panel a): single corner complex of ≡$FeOPO_3$ (d(Fe-P) = 348 pm) with a Ca ion that is bound to PO_4 as a Ca-O-P single corner (^{1}C) complex (d(P-Ca) = 367 pm), formed according to Equation 5.2. Panel b): double corner complex of ≡$(FeO)_2PO_2$ (d(Fe-P) = 320 ± 4 pm) with a Ca^{2+} ion that is bound to PO_4 as a Ca-O-P single corner (^{1}C) complex (d(P-Ca) = 327 pm), formed according to Equation 5.3. The $Fe_2(OH)_6(OH_2)_3PO_4$-Ca cluster (a) has 26 water molecules for hydration and the other one has 21 (b).

For the binary Mg-PO_4 systems, only the formation of one ternary complex is required for describing adequately the interaction of these two ions with the surfaces of Fh ($R^2 = 0.99$, n =22). In this ternary complex, PO_4 is bound to Fh in a monodentate configuration (MPMg), similar to that for the ternary Fe-PO_4-Ca complex formulated in Equation 5.2. The respective adsorption reaction is formulated as:

$$\equiv FeOH^{-0.5} + H^+(aq) + PO_4^{3-}(aq) + Mg^{2+}(aq) \leftrightarrow \equiv FeO^{-0.5+\Delta z0}PO_3^{\Delta z1}Mg^{\Delta z2} + H_2O(l) \quad \log K_{MTC} \quad \text{(Equation 5.4)}$$

Presently, we have not been able to clearly reveal the formation of the ternary Fe-PO_4-Mg complex in which PO_4 is bound to Fh in a bidentate configuration (BPMg), as we did resolve for the Ca-PO_4 systems. Introduction of such BPMg does not improve the description of our adsorption data in the Mg-PO_4 systems and a large uncertainty is found in the fitting of the CD coefficients of the 1- and 2- planes (*i.e.* Δz_1 and Δz_2) of this ternary species. It must be noticed that for the Mg-PO_4 systems, we have collected a more limited dataset, covering a narrower range of solution conditions in comparison to the Ca-PO_4 systems. This may have affected the resolution of our modeling approach to distinguish the

potential formation of an additional ternary complex species. Considering this constraint, we have implemented in our final modeling only the formation of the ternary complex MPMg.

In the series of alkaline-earth metal ions, Ca^{2+} interacts stronger than Mg^{2+} with Fh, which is reflected in its higher log*K* values ($\Delta \log K$ ~0.9) for the high as well as for the low affinity sites (Table 5.1). This difference in log*K* might be attributed to an exchange of interfacial water, releasing Gibbs free energy.[67] For the formation of monodentate ternary complexes (Equations 5.2, 5.4), we find a difference in affinity of $\Delta \log K_{MTC}$ ~0.3 between the ternary complexes with Ca and Mg, which is possibly also due to an exchange of interfacial water, because in solution both association constants ($CaHPO_4^0$(aq) and $MgHPO_4^0$(aq)) are rather similar.[83] The stronger interaction of Ca with PO_4 at the surface of Fh can be also inferred from our MO/DFT calculations. Ca^{2+} ions neutralize the negative charge of PO_4 ligands better than Mg^{2+} ions, which leads to lower attribution of the negative charge by PO_4 to the surface and, consequently, to slightly higher Δz_0 values for the MPCa complex. In addition, the fitted Δz_2 value is higher for the MPMg than for the MPCa complex (Table 5.2), suggesting that a higher fraction of Mg^{2+} charge remains in the outer Stern layer region. Overall, these results suggest that Mg^{2+} is more loosely bound to PO_4 than Ca^{2+} at the surfaces of Fh. In Figure S5.6 of the SI, we modeled the PO_4 binding to Fh in the presence of either Ca or Mg. At the same solution condition (*i.e.* pH and M^{2+} concentration), the adsorption of PO_4 is more enhanced in the presence of Ca in comparison to Mg.

In literature, formation of both anion-bridged (*e.g.* Fe-PO_4-M^{2+}) and metal-bridged (*e.g.* Fe-M^{2+}-PO_4) ternary complexes have been proposed.[53] In general, the type of ternary complexes formed would depend on the relative affinity of the co-adsorbing ions for the Fe-(hydr)oxide surfaces.[53] If the anion interaction with the surface is relatively weak, metal-bridged ternary complexes dominate as found for instance in Cd-SO_4 and Pb-SO_4 systems.[20,84,85] In our case, the anion (PO_4^{3-}) is much stronger bound to Fh than the cation (Ca^{2+} or Mg^{2+}) and this leads to the formation of anion-bridged complexes.

In specific cases, it is also possible that both cations and anions react directly with the surfaces,[31,53,86] as found in Pb–PO_4 systems.[87] In that type of complex, both ions are bound to the surface in a monodentate manner, but there is an additional chemical (lateral) interaction between the adsorbed cation and anion.[53] Conceptually, all charges are then located in the inner Stern layer region (0- and 1-plane). When a ternary anion-bridged surface complex is formed, part of the complex (M^{2+}) may physically enter the outer Stern layer region (2- plane). This is found with our CD modeling for the ≡$(FeO)_2PO_2$-Ca and ≡$FeOPO_3$-Ca complexes. According to the CD model, ~ 2/3 of the Ca^{2+} charge in the ≡$(FeO)_2PO_2$-Ca complex is at the 2-plane ($\Delta z_2 = 1.46 \pm 0.17$ v.u.), which could suggest that ~2/3 of the Ca ligands are in the outer Stern layer. This attribution of positive charge of the ternary Fe-PO_4-Ca complexes to the 2-plane will have important implications for describing the pH-dependent PO_4 adsorption in Ca media, as it will be discussed in Section 5.3.4.

5.3.3. Surface speciation: single *vs* binary ion systems

In Figure 5.6, the surface speciation of PO_4 and Ca in single-ion systems (left panels) is compared to the corresponding surface speciation of these ions in the binary Ca-PO_4 systems (right panels). The calculations have been done with the CD model and the simulated conditions of the binary Ca–PO_4 systems are similar to the experimental conditions for the data shown in Figures 5.2 a,b and 5.4.

In relation to the PO_4 adsorption, comparing Figures 5.6 a and b shows that the Ca-PO_4 synergy is more notorious at high pH values in agreement with our experimental results (Figures 5.1 and 5.2). The ternary complex formation is mainly due to the formation of MPCa. The ternary complex formation

reduces the contribution of the bidentate PO_4 surface complexes (B, BH) to the overall PO_4 adsorption, while the speciation of both monodentate PO_4 species (MH, MH_2) is hardly affected. A similar result is found for the PO_4 surface speciation in binary Mg-PO_4 systems (Figure S5.5).

Comparing Figures 5.6 c and d shows that the Ca adsorption strongly increases in the presence of PO_4. At low pH values, Ca is mainly bound as a ternary complex in the binary Ca-PO_4 systems. In the absence of PO_4 (Figure 5.6c), hardly any Ca is bound at low pH. The stimulating role of PO_4 due to favorable electrostatics is mainly visible at high pH. In the presence of PO_4, more Ca is clearly bound as bidentate species (BCa), as it is evident from comparing Figures 5.6 c and d. Especially, the Ca adsorption to the low affinity sites (BCa(l)) is enhanced at high pH conditions. The Ca binding to the high sites (BCa(h)) is hardly affected, which is due to near-saturation of these sites, as observed already in the single-ion systems in the absence of PO_4.

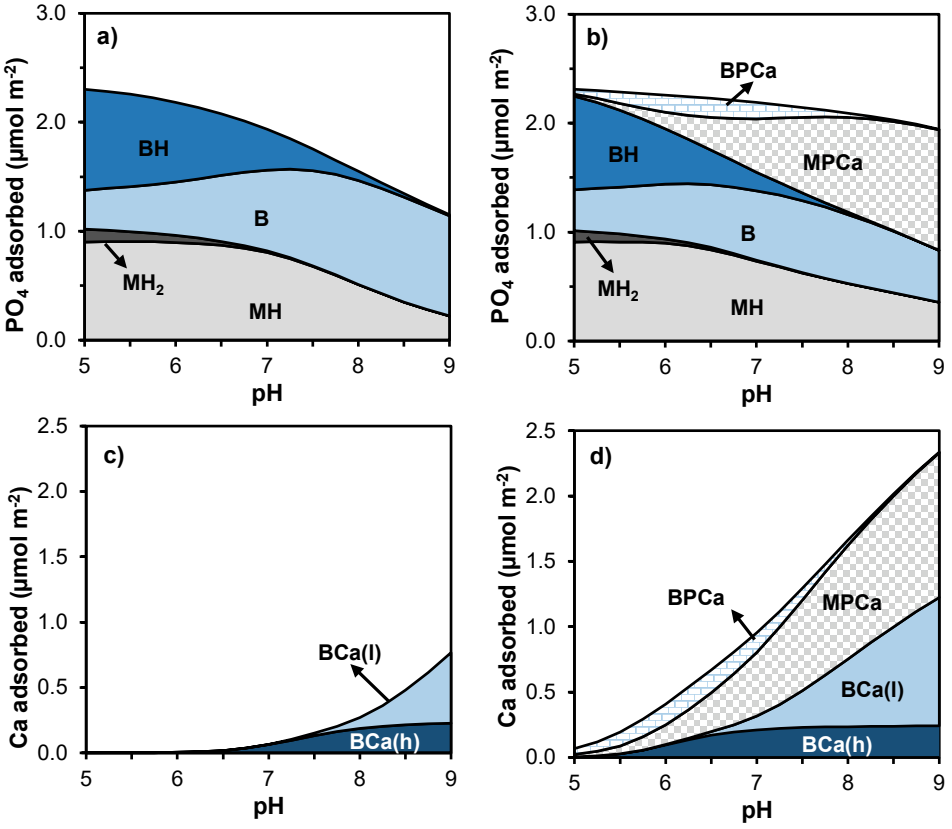

Figure 5.6. pH-dependent surface speciation of PO_4 (upper panels) and Ca (lower panels) in the corresponding single-ion (left panels) and binary Ca–PO_4 (right panels) systems with Fh in 0.01 M $NaNO_3$. The conditions of the systems are similar to those of the adsorption experiments shown in Figure 5.2 a,b and Figure 5.4. The total Fe concentration is 3.90 mM and the specific surface area of Fh is A = 684 m^2 g^{-1} with a corresponding molar mass of M_{nano} = 96.6 g mol^{-1}. The total PO_4 and Ca concentrations are respectively 0.60 mM and 1.0 mM. For PO_4: MH= monodentate protonated; MH_2 = monodentate doubly protonated; B = bidentate; BH = bidentate protonated. For Ca: BCa(l)= bidentate at the low affinity sites; BCa(h)= bidentate at the high affinity sites. For the ternary species: MPCa = ternary complex in which PO_4 is bound as a monodentate; BPCa = ternary complex in which PO_4 is bound as a bidentate. The calculations have been done using the CD model with the parameter sets of Tables 5.1, 5.2 and Table S5.4 in the SI.

5.3.4. Comparing ferrihydrite and goethite

The synergistic interaction of Ca with PO_4 has been studied extensively in the past for well-crystallized goethite,[34] allowing us to compare it with the interaction presently measured for Fh. In Figure 5.7, the PO_4 adsorption isotherms of Fh (panel a) and goethite (panel b) have been calculated for systems at pH 5 and 7 in the presence (symbols) and absence (lines) of Ca at a constant ionic strength of 3 mM. In the absence of Ca, the pH dependency of the PO_4 adsorption is much larger for Fh than for goethite, which can be attributed to more protonation of adsorbed PO_4 at low pH values.[32] In the presence of Ca, the pH dependency is much smaller for the reasons discussed below.

The intrinsic difference in the pH dependency of the PO_4 adsorption of Fh and goethite is illustrated in Figure 5.7 a,b with model lines calculated for systems at pH 5 and 7 in $NaNO_3$ solution. This pH dependency is much higher for Fh than for goethite. At pH 7, the PO_4 adsorption in $NaNO_3$ is very similar for Fh and goethite (dotted lines). However, at pH 5 the adsorption of PO_4 in $NaNO_3$ is much higher for Fh (full lines) than for goethite. As mentioned above, this is particularly due to a difference in protonation of the adsorbed PO_4 species.[32] For Fh (Figure 5.7a), the presence of Ca^{2+} ions hardly affects the PO_4 adsorption at pH 5 (green squares *vs* full line), although some Ca^{2+} ions do adsorb but this is mainly in the form of ternary Fe-PO_4-Ca complexes. The corresponding adsorbed Ca^{2+} does not have a strong electrostatic interaction with the other types of adsorbed PO_4 ions because a significant part of the Ca^{2+} charge is outside the inner Stern region according to our CD analysis (see Δz_2 in Table 5.2). In contrast, in the Ca systems, there is a substantial increase in the PO_4 adsorption at pH = 5 for goethite (Figure 5.7b), which is due to a strong electrostatic interaction of the adsorbed Ca^{2+} ions with adsorbed PO_4. For goethite, most of the divalent charge of Ca^{2+} is present at the 1-plane (Δz_1) and acts on the negatively charge of the outer oxygen ligands of PO_4 that reside there. This strong electrostatic interaction of Ca^{2+} also occurs at pH 7, increasing the PO_4 adsorption to similar levels as that for pH 5. For Fh at pH 7, the PO_4 adsorption is also increased in the presence of Ca^{2+} (blue circles vs dotted line). However, this increase is mainly due to the significant formation of ternary Ca-PO_4 complexes and it is less important than the increase in the PO_4 adsorption on goethite by electrostatic interaction of the large fraction of Ca^{2+} charge present in the 1-plane.

The above-mentioned difference in the pH-dependent adsorption behavior of PO_4 for both Fe-(hydr)oxide minerals will be important in applications of surface complexation modeling in natural systems. It is evident that the choice of a proxy for the natural oxide fraction will be crucial for the outcome of predictions, particularly the pH dependency, as illustrated in Figure 5.7. In future applications to soils, this will be evaluated.

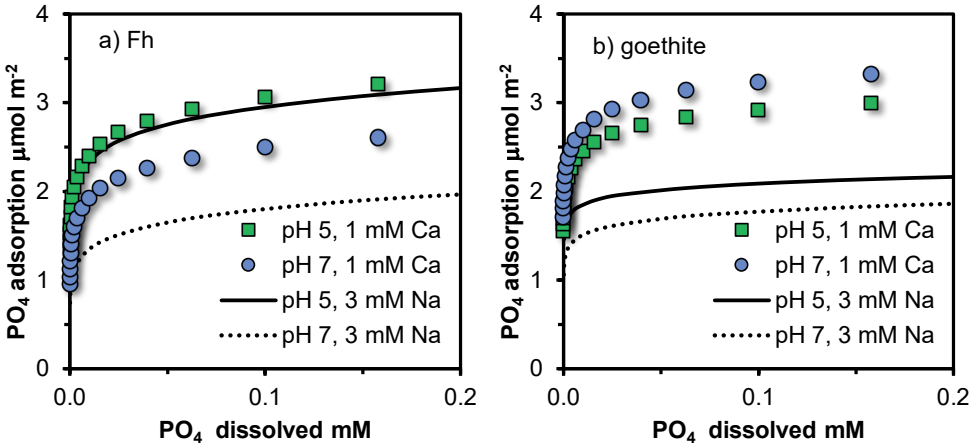

Figure 5.7. PO_4 adsorption isotherms of (a) ferrihydrite and (b) goethite at pH 5 and 7 in the absence (lines) and presence (symbols) of Ca at a constant ionic strength of 3 mM. The intrinsic pH dependency of the PO_4 adsorption in the $NaNO_3$ solutions is much higher for Fh than for goethite (lines). This difference is largely, though not entirely, compensated by the presence of Ca (symbols). For Fh, the PO_4 adsorption is increased by ternary Ca-PO_4 complex formation, particularly at high pH (Figure 5.6), and for goethite, the increase is due to a strong electrostatic interaction of adsorbed Ca^{2+} by introducing positive charge mainly to the first Stern plane where the negatively charged outer ligands of the adsorbed PO_4 ions reside (see text). For Fh, the adsorption of PO_4 has been calculated using the parameter sets of Tables 5.1 and 5.2 and Table S5.4 in the SI. For goethite, the adsorption has been calculated with the parameter set of Hiemstra et al.[43]

5.4. Conclusions

In this study, the surface interaction of the alkaline-earth metal ions Ca^{2+} and Mg^{2+} with adsorbed PO_4 has been quantified for well-characterized, freshly precipitated Fh. The collected data have been interpreted with the CD model in combination with a recently developed multisite ion complexation model for Fh, in which reactive site densities are based on analysis of the surface structure. In addition, high and low affinity (log*K*) sites are distinguished in the model, derived from the adsorption of alkaline-earth metal ions (M^{2+}) covering a wide range of surface loadings. The corresponding adsorption densities have been quantified in a parallel study using single-ion systems.[67] According to that study, the alkaline-earth metal ions form binuclear double-corner (^{2}C) inner-sphere complexes $\equiv(FeOH)_2^{\Delta z=0}M^{\Delta z=1}$, for which the CD coefficients have been derived with a Brown bond valence analysis using MO/DFT optimized geometries of complexes.

In the present study with binary M^{2+}-PO_4 systems, the adsorption of Ca^{2+} and Mg^{2+} ions to Fh is found to be enhanced in the presence of adsorbed PO_4 and *vice versa*. For Fh, this synergistic effect is due to the combined effect of an enhanced electrostatic interaction and the formation of ternary surface complexes. For the Ca-PO_4 systems, our model reveals the formation of two anion-bridged surface ternary complexes: $\equiv FeOPO_3Ca$ and $\equiv (FeO)_2PO_2Ca$, the former being most prominently present. The charge attribution to the surface (Δz_0) has been derived for both complexes from the MO/DFT/B3LYP/6-31+G** optimized geometries. The Ca^{2+} ion charge is distributed between the inner (Δz_1) and outer Stern (Δz_2) plane, which we found by analysis of the adsorption data with CD modeling. For the Mg-PO_4 systems, only the formation of the ternary complex $\equiv FeOPO_3Mg$ could be revealed under the investigated adsorption conditions. Our results are in line with the general notion that the dominant type

of ternary complex (*i.e.* metal-bridged *vs* anion-bridged) depends on the relative affinity of the co-adsorbing ions for the metal (hydr)oxide surface. PO_4 has a significantly higher intrinsic affinity than Ca and Mg for binding sites at the surface of Fh, favoring the formation of anion-bridged ternary complexes. This is indeed found in our CD modeling. In addition, our modeling reveals that the distribution between monodentate and bidentate surface complexes of PO_4 is different in the single-ion and binary systems. In the presence of M^{2+}, more PO_4 is bound to Fh in a monodentate configuration compared to the single-ion systems.

The pH dependency of the intrinsic PO_4 adsorption in $NaNO_3$ solution is much larger for Fh than for goethite. However, this difference is largely compensated by the binding of Ca^{2+}. For Fh, the increase in PO_4 adsorption is predominantly due to the formation of ternary Fe-PO_4-Ca surface complexes, and in the case of goethite, the increase is entirely due to a mutual electrostatic interaction of adsorbed Ca^{2+} and PO_4. From an environmental perspective, the present study is highly relevant because Ca^{2+} and Mg^{2+} ions are abundant in natural systems. The interaction of Ca^{2+} and Mg^{2+} ions with the surfaces of metal-(hydr)oxides affects the chemical behavior and fate of other important ions, particularly anions, as shown here for PO_4. Fh can be used as a proxy for the natural oxide fraction and application of the results of the present study will contribute to improved understanding of the mutual interactions of PO_4 and M^{2+} in soils, aquifers, and natural water bodies.

Acknowledgements

The grant provided by the University of Costa Rica (UCR) to the first author is gratefully acknowledged. We thank the work of He Wei and Frank van Raffe in collecting part of the Ca-PO_4 and Mg-PO_4 adsorption data, respectively. We also thank Peter Nobels from the Chemistry and Biology Soil Laboratory (CBLB) for his attentive work regarding the ICP-OES and ICP-MS analyses.

Supplementary Information

A. Conditions of the batch adsorption experiments

Table S5.1. Chemical conditions of the batch experiments in single-ion (PO_4) and binary Ca–PO_4 adsorption systems. The specific surface area (SSA) and molar mass (M_{nano}) of ferrihydrite was assessed using PO_4 as probe ion, as described in Mendez and Hiemstra.[59] The capacitance values for the extended Stern layers of Fh ($C_{nano,1}$ and $C_{nano,2}$) are size-dependent and were calculated by taking the capacitance values of goethite as a reference (C_1 = 0.90 F m^{-2} and C_2 = 0.74 F m^{-2}).

Series	System	Figure number	I	Ca	PO_4	Fe	SSA	M_{nano}	$C_{nano,1}$	$C_{nano,2}$
			M	mM	mM	mM	m^2 g^{-1}	g mol^{-1} Fe	F m^{-2}	
H.1	Binary	5.2c/5.2d	0.01	0.613	0.620	3.75	684 ± 15	96.6	1.17	0.91
I.1	Single-PO_4	5.1b/5.1d	0.01	-	0.285	2.20	684 ± 15	96.6	1.17	0.91
I.2	Single-PO_4	5.1b/5.1d/S5.2	0.01	-	0.380	2.20	684 ± 15	96.6	1.17	0.91
I.3	Single-PO_4	5.1b/5.1d	0.01	-	0.576	2.20	684 ± 15	96.6	1.17	0.91
J.1	Binary	5.1a/5.1b	0.01	0.051	0.285	2.20	684 ± 15	96.6	1.17	0.91
J.2	Binary	5.1a/5.1b	0.01	0.051	0.380	2.20	684 ± 15	96.6	1.17	0.91
J.3	Binary	5.1a/5.1b	0.01	0.051	0.576	2.20	684 ± 15	96.6	1.17	0.91
K.1	Binary	5.1c/5.1d	0.01	0.252	0.285	2.20	684 ± 15	96.6	1.17	0.91
K.2	Binary	5.1c/5.1d/S5.2	0.01	0.252	0.380	2.20	684 ± 15	96.6	1.17	0.91
K.3	Binary	5.1c/5.1d	0.01	0.252	0.576	2.20	684 ± 15	96.6	1.17	0.91
L.1	Single-PO_4	5.2b	0.01	-	0.385	3.85	684 ± 15	96.6	1.17	0.91
L.2	Single-PO_4	5.2b/5.4b/S5.2	0.01	-	0.583	3.85	684 ± 15	96.6	1.17	0.91
M.1	Binary	5.2a/5.2b	0.01	0.98	0.385	3.85	684 ± 15	96.6	1.17	0.91
M.2	Binary	5.2a/5.2b/4/S5.2	0.01	0.98	0.583	3.85	684 ± 15	96.6	1.17	0.91

Table S5.2. Chemical conditions of the batch experiments in binary Mg–PO_4 adsorption systems. The specific surface area (SSA) and molar mass (M_{nano}) of ferrihydrite was assessed using PO_4 as probe ion, as described in Mendez and Hiemstra.[59] The capacitance values for the extended Stern layers of Fh ($C_{nano,1}$ and $C_{nano,2}$) are size-dependent and were calculated by taking the capacitance values of goethite as a reference (C_1 = 0.90 F m^{-2} and C_2 = 0.74 F m^{-2}).

Series	System	Figure number	I	Mg	PO_4	Fe	SSA	M_{nano}	$C_{nano,1}$	$C_{nano,2}$
			M	mM	mM	mM	m^2 g^{-1}	g mol^{-1} Fe	F m^{-2}	
D.1	Binary	5.3a/5.3b	0.01	0.030	0.600	3.94	720 ± 10	97.6	1.18	0.91
D.2	Binary	5.3a/5.3b	0.01	0.300	0.600	3.94	720 ± 10	97.6	1.18	0.91
E	Binary	5.3c/5.3d/S5.4	0.01	1.00	0.658	7.13	720 ± 10	97.6	1.18	0.91

B. Thermodynamic databases used in the modeling

Table S5.3. Aqueous speciation reactions used in the model calculations. The log*K* values are for $I = 0$.

Species	Reaction			log*K*	
$NaOH^0$	$Na^+ + OH^-$	↔	$NaOH^0$	-0.20	[a]
$NaNO_3^0$	$Na^+ + NO_3^-$	↔	$NaNO_3^0$	-0.60	[a]
$NaHPO_4^-$	$PO_4^{3-} + Na^+ + H^+$	↔	$NaHPO_4^-$	13.40	[b]
$NaPO_4^{2-}$	$PO_4^{3-} + Na^+$	↔	$NaPO_4^{2-}$	2.05	[b]
HPO_4^{2-}	$PO_4^{3-} + H^+$	↔	HPO_4^{2-}	12.35	[a]
$H_2PO_4^-$	$PO_4^{3-} + 2H^+$	↔	$H_2PO_4^-$	19.55	[a]
$H_3PO_4^0$	$PO_4^{3-} + 3H^+$	↔	$H_3PO_4^0$	21.70	[a]
$CaOH^+$	$Ca^{2+} + OH^-$	↔	$CaOH^+$	1.30	[a]
$Ca(OH)_2^0$	$Ca^{2+} + 2OH^-$	↔	$Ca(OH)_2^0$	0.01	[a]
$CaNO_3^+$	$Ca^{2+} + NO_3^-$	↔	$CaNO_3^+$	0.70	[c]
$Ca(NO_3)_2^0$	$Ca^{2+} + 2NO_3^-$	↔	$Ca(NO_3)_2^0$	-4.50	[a]
$CaPO_4^-$	$PO_4^{3-} + Ca^{2+}$	↔	$CaPO_4^-$	6.46	[a]
$CaHPO_4^0$	$PO_4^{3-} + Ca^{2+} + H^+$	↔	$CaHPO_4^0$	15.09	[a]
$CaH_2PO_4^+$	$PO_4^{3-} + Ca^{2+} + 2H^+$	↔	$CaH_2PO_4^+$	20.95	[a]
$MgOH^+$	$Mg^{2+} + OH^-$	↔	$MgOH^+$	2.55	[a]
$Mg(OH)_2^0$	$Mg^{2+} + 2OH^-$	↔	$Mg(OH)_2^0$	0.01	[a]
$Mg(NO_3)_2^0$	$Mg^{2+} + 2NO_3^-$	↔	$Mg(NO_3)_2^0$	-0.01	[a]
$MgPO_4^-$	$PO_4^{3-} + Mg^{2+}$	↔	$MgPO_4^-$	4.65	[d]
$MgHPO_4^0$	$PO_4^{3-} + Mg^{2+} + H^+$	↔	$MgHPO_4^0$	15.26	[a]

[a] From Lindsay.[88]
[b] From Rahnemaie et al.[89]
[c] From De Robertis et al.[90]
[d] MINTEQ (version 3.1)

Table S5.4. Adsorption reactions, CD coefficients, and log*K* values for the complete set of surface species used in the CD model. Site densities are from Hiemstra and Zhao[32] with N_s(≡FeOH$^{-0.5}$(a)) = 3.0 nm^{-2}, N_s (≡FeOH$^{-0.5}$(b)) =2.8 nm^{-2} and N_s(≡Fe$_3$O$^{-0.5}$) = 1.4 nm^{-2}. Two types of ≡FeOH$^{-0.5}$(b) have been defined to distinguish between the high (bh) and low (bl) affinity sites for M^{2+}. The capacitances of the Stern layers are size-dependent and were calculated as described in Mendez and Hiemstra,[59] using reference values of C_1 = 0.90 and C_2 = 0.74 F m^{-2} of goethite representing a flat plane.

Species	ID	Surface group[a]	Adsorption reaction	Δz_0	Δz_1	Δz_2	log*K*
≡FeOH$_2$		S (a, bl, bh)	≡FeOH$^{-0.5}$ + H$^+$ ↔ ≡FeOH$_2^{+0.5}$	1	0	0	8.10*
≡Fe$_3$OH		T	≡Fe$_3$O$^{-0.5}$ + H$^+$ ↔ ≡Fe$_3$OH$^{+0.5}$	1	0	0	8.10*
≡FeOH--Na		S (a, bl, bh)	≡FeOH$^{-0.5}$ + Na$^+$ ↔ ≡FeOH$^{-0.5}$--Na$^+$	0	1	0	-0.60 ± 0.02**
≡Fe$_3$O--Na		T	≡Fe$_3$O$^{-0.5}$ + Na$^+$ ↔ ≡Fe$_3$O$^{-0.5}$--Na$^+$	0	1	0	-0.60 ± 0.02**
≡FeOH$_2$--NO$_3$		S (a, bl, bh)	≡FeOH$^{-0.5}$ + H$^+$ + NO$_3^-$ ↔ ≡FeOH$_2^{+0.5}$--NO$_3^-$	1	-1	0	7.42 ± 0.02**
≡Fe$_3$OH--NO$_3$		T	≡Fe$_3$O$^{-0.5}$ + H$^+$ + NO$_3^-$ ↔ ≡Fe$_3$OH$^{+0.5}$--NO$_3^-$	1	-1	0	7.42 ± 0.02**
≡FeOPO$_2$OH	MPH	S (a, bl, bh)	≡FeOH$^{-0.5}$ + PO$_4^{3-}$ + 2H$^+$ ↔ ≡FeO$^{-0.22}$PO$_2$OH$^{-1.28}$ + H$_2$O	0.28	-1.28	0	26.36 ± 0.20*
≡FeOPO(OH)$_2$	MPH$_2$	S (a, bl, bh)	≡FeOH$^{-0.5}$ + PO$_4^{3-}$ + 3H$^+$ ↔ ≡FeO$^{-0.17}$PO(OH)$_2^{-0.33}$ + H$_2$O	0.33	-0.33	0	29.84 ± 0.23*
(≡FeO)$_2$PO$_2$	BP	S (bl, bh)	2≡FeOH$^{-0.5}$ + PO$_4^{3-}$ + 2H$^+$ ↔ ≡(FeO)$_2^{-0.54}$PO$_2^{-1.46}$ + 2H$_2$O	0.46	-1.46	0	28.31 ± 0.04*
(≡FeO)$_2$POOH	BPH	S (bl, bh)	2≡FeOH$^{-0.5}$ + PO$_4^{3-}$ + 3H$^+$ ↔ ≡(FeO)$_2^{-0.35}$POOH$^{-0.65}$ + 2H$_2$O	0.65	-0.65	0	33.52 ± 0.13*
(≡FeO)$_2$Ca	BCa	S (bl)	2≡FeOH$^{-0.5}$ + Ca^{2+} ↔ ≡FeO$^{-0.06}$Ca$^{+1.06}$	0.94	1.06	0	2.64 ± 0.03***
(≡FeO)$_2$Ca	BCa	S (bh)	2≡FeOH$^{-0.5}$ + Ca^{2+} ↔ ≡FeO$^{-0.06}$Ca$^{+1.06}$	0.94	1.06	0	5.13 ± 0.02***
(≡FeO)$_2$Mg	BMg	S (bl)	2≡FeOH$^{-0.5}$ + Mg^{2+} ↔ ≡FeO$^{-0.11}$Mg$^{+1.11}$	0.89	1.11	0	1.87 ± 0.06***
(≡FeO)$_2$Mg	BMg	S (bh)	2≡FeOH$^{-0.5}$ + Mg^{2+} ↔ ≡FeO$^{-0.11}$Mg$^{+1.11}$	0.89	1.11	0	4.09 ± 0.04***
≡FeOPO$_3$Ca	MPCa	S (a, bl, bh)	≡FeOH$^{-0.5}$ + PO$_4^{3-}$ + Ca^{2+} + H$^+$ ↔ ≡FeO$^{-0.26}$PO$_3^{-1.30}$Ca$^{+1.06}$ + H$_2$O	0.24	-1.30	1.06	22.27 ± 0.12
(≡FeO)$_2$PO$_2$Ca	BPCa	S (bl, bh)	2≡FeOH$^{-0.5}$ + PO$_4^{3-}$ + Ca^{2+} + 2H$^+$ ↔ (≡FeO)$_2^{-0.38}$PO$_2^{-1.08}$Ca$^{+1.46}$ + 2H$_2$O	0.62	-1.08	1.46	30.09 ± 0.12
≡FeOPO$_3$Mg	MPMg	S (a, bl, bh)	≡FeOH$^{-0.5}$ + PO$_4^{3-}$ + Mg^{2+} + H$^+$ ↔ ≡FeO$^{-0.28}$PO$_3^{-1.55}$Mg$^{+1.33}$ + H$_2$O	0.22	-1.55	1.33	22.00 ± 0.10

[a] Type of reactive surface group participating in the corresponding reactions. S and T stand for singly (≡FeOH$^{-0.5}$) and triply (≡Fe$_3$OH$^{-0.5}$) coordinated groups, respectively. For S two types are distinguished: type "a" that forms single corner (^{1}C) monodentate and single edge (^{1}E) bidentate complexes, and type "b" that forms single corner (^{1}C) monodentate and bidentate double-corner (^{2}C) complexes. The high and low affinity sites are represented respectively by (bh) and (bl)

* Taken from Hiemstra and Zhao[32]

** Taken from Mendez and Hiemstra[59]

*** Taken from Mendez and Hiemstra[67]

C. Effect of phosphate adsorption on the net charge of ferrihydrite

Figure S5.1 shows the net particle charge density (σ_P in mC m^{-2}) of Fh for single-ion systems with PO_4 (panel a) and for binary PO_4-Ca systems (panel b). The calculations were obtained with the CD model, combined with the extended Stern Layer approach for describing the electrostatics of the Fh–solution interphase. In this approach, the net particle charge density is defined as $\sigma_P = \sigma_0 + \sigma_1 + \sigma_2$, where 0, 1 and 2 are the charge density at the surface plane, the inner Stern layer, and the outer Stern layer, respectively.

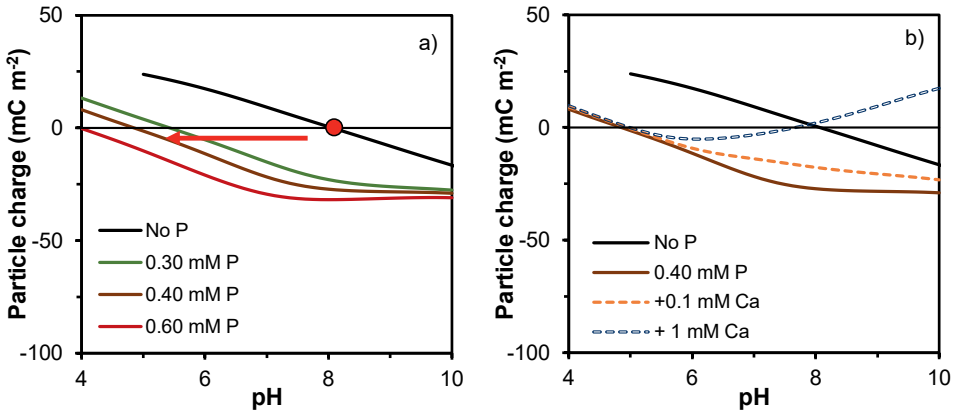

Figure S5.1. pH-dependency of the net charge density (σ_P) of ferrihydrite particles in single-ion systems at three levels of added PO_4: 0.30, 0.40 and 0.60 mM (panel a) and in binary PO_4-Ca systems with a fixed total PO_4 concentration (0.40 mM) and two Ca levels: 0.10 and 1.0 mM (panel b). The ionic strength of the system is fixed at 0.01 M using a $NaNO_3$ solution. As a reference, the net charge density of ferrihydrite in the absence of specific ion adsorption ions is also represented (black full lines). The red point at pH ~8.1 (panel a) represents the net zero charge condition of Fh in a background solution of $NaNO_3$ and the red arrow indicates the shift in the zero-charge condition upon specific adsorption of PO_4. The calculations were done with the CD model using the parameters set of Table S5.4. The extended Stern Layer approach[63] was used for describing the compact part of the electrical double layer (EDL).

In the absence of specific ion adsorption, the net particle charge σ_P is zero at pH ~8.1 (black lines), which corresponds with the point of zero charge, *i.e.* pH_{PZC}. Upon specific adsorption of PO_4, an excess amount of negative charge is introduced into the mineral-solution interface, shifting the condition of zero net particle charge ($\sigma_0 + \sigma_1 + \sigma_2$) towards lower pH values (Figure S5.1a). Consequently, a negative electrostatic potential (ψ) is developed in the interface over almost the entire range of pH values evaluated in our adsorption experiments. This partly explains the observed shift of the adsorption edges of Ca in the binary systems toward lower pH values (ΔpH ~ –2) compared to the single-ion systems.

In the binary Ca–PO_4 systems (Figure S5.1b), the net charge of Fh above the isoelectric point (IEP) will become less negative due to the pH-dependent adsorption of Ca, introducing positive charge, particularly to the 2- plane. At a given pH, the uplift of the curve (compared to the single PO_4 systems) depends on the Ca concentration in the system, determining the corresponding Ca adsorption. At a sufficiently high pH and Ca concentration, the net particle charge may even switch, creating a second iso-electric point (IEP) at high pH.

D. Precipitation of Ca-PO_4 minerals

In the binary Ca–PO_4 systems, the equilibrium solution concentration of both Ca and PO_4 ions is lower than in the corresponding equilibrium solution of the monocomponent systems (see Figure 5.4, main text). The reason is the mutual interaction between Ca and PO_4 that enhances the binding of both ions to Fh. We have shown by modeling that the experimental concentrations of Ca and PO_4 in the binary systems cannot be explained only based on the electrostatic interactions between these two ions. Therefore, an additional mechanism must contribute to the cooperative binding between Ca and PO_4.

We exclude that the lower concentrations of Ca and PO_4 in the binary systems with Fh are due to the precipitation of Ca-PO_4 minerals. Thermodynamic calculations show that, for most of the binary systems, the solution at the start of the adsorption experiments is undersaturated with respect to octa-Ca-PO_4 ($Ca_4H(PO_4)_3{\cdot}2.5H_2O(s)$), *i.e.* the saturation index $SI = \log(Q_{so}/K_{so}) < 0$ for the solubility reaction:

$$Ca_4H(PO_4)_3{\cdot}2.5H_2O(s) + 5H^+(aq) \leftrightarrow 4Ca^{2+}(aq) + 3H_2PO_4^-(aq) + 2.5H_2O(l), \quad \log K_{so} = 11.76 \quad \text{(Equation S5.1)}$$

Modeling of the binary systems including Equation S5.1 does not explain the decrease in the equilibrium concentration of Ca and PO_4. In Figure S5.2, the modeling results including precipitation of octa-Ca-PO_4 are shown for PO_4 (red dashed lines) in systems with two different total molar Ca/PO_4 ratios of 0.8 and 1.7. Precipitation of octa-Ca-PO_4 may have occurred only for the data point at the highest pH value (~9) of the series with the total molar Ca/PO_4 ratio of 1.7 (panel b). As we explained in the main text, the formation of ternary surface complexes (≡Fe-PO_4-Ca) is the mechanism explaining the larger adsorption of PO_4 and Ca in the binary systems, which cannot be explained only by considering electrostatic interactions.

In the modeling of Figure S5.2, octa-Ca-phosphate has been chosen. This mineral is a meta-stable phase in the series insoluble Ca-PO_4 minerals, as illustrated in Figure S5.3. The *Ostwald-Lussac* rule of mineral formation states that when several solid phases can precipitate, the most soluble phase will precipitate first. This rule has a thermodynamic foundation governed by the relation between mineral stability and surface Gibbs free energy.[4] With increase of the bulk stability of minerals, the energy of surface formation increases too, which implies a higher investment of energy to create a nanoparticle. Consequently, a mineral with a higher bulk stability will have a higher solubility at the ultra-small nanometer scale, and a mineral with a lower bulk stability will be less soluble. In other words, the stability / solubility relationship is shifted at the nanoscale. Once a nanophase is formed, kinetic aspects of particle growth upon aging may play a role in the conversion of this product into a more stable phase. Additional modeling assuming equilibrium of $Ca^{2+}(aq)$ and $PO_4^{3-}(aq)$ with the more insoluble mineral HAP (as bulk mineral) did neither explain the decreased solution concentrations of these ions in the binary systems (not shown).

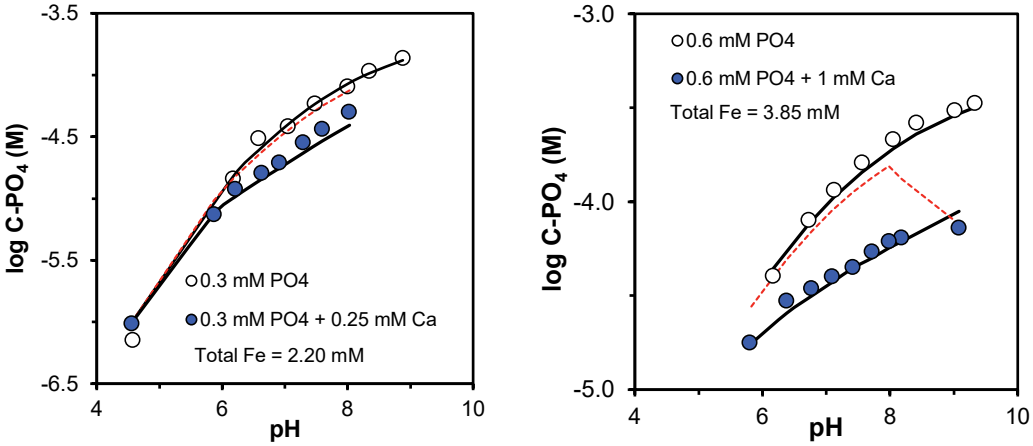

Figure S5.2. Logarithm of the PO_4 concentration in the equilibrium solution of ferrihydrite systems with total molar Ca/PO_4 ratios of ~0.8 (panel a) and ~1.7 (panel b) at constant ionic strength of I = 0.01 M $NaNO_3$. Open symbols are for single PO_4 systems and closed symbols are for binary Ca-PO_4 systems. The black lines are the CD predictions using the set of adsorption parameters presented in Table S5.4, considering the formation of ternary surface complexes. The red-dashed lines are CD model simulations in which the formation of ternary complexes is not considered and instead equilibrium with a mineral phase of octa-calcium-phosphate was assumed. The specific surface area of Fh was A= 684 m^2 g^{-1} with a corresponding molar mass M_{nano} = 96.6 g mol^{-1} Fe.

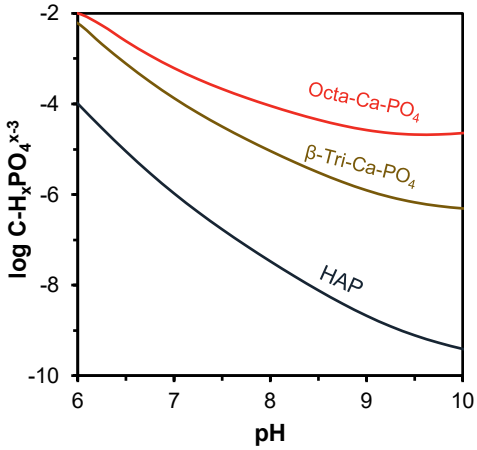

Figure S5.3. Solubility diagram of the calcium phosphate minerals octa-Ca-phosphate ($Ca_4H(PO_4)_3 \cdot 2.5H_2O$), β-tri-Ca-phosphate ($Ca_3(PO_4)_2$), and hydroxyapatite (HAP) ($Ca_5(PO_4)_3OH$) in closed systems with no CO_2. The Ca^{2+} activity in solution is fixed at 10^{-3} M. Calculations were performed with the speciation software ECOSAT, using logK_{so} values from Lindsay (1979).

E. Charge distribution of the ternary complexes

The MO/DFT/B3LYP/6-31+G** optimized geometries of the hydrated ternary Fe-PO_4-M^{2+} have been used to derive the corresponding Δz_0 values. Details about the template used are given in Rahnemaie et al.[89] and Mendez and Hiemstra.[19] The optimized geometries were interpreted with the Brown valence concept,[68] which relates bond length (R) to a bond valence (ν) according to:

$$\nu = \exp\left(-\frac{R-R_o}{B}\right) \qquad \text{(Equation S5.2)}$$

In equation S5.2, B is an empirical constant (B = 37 pm) and R_o (pm) is a reference distance whose value is chosen such that the sum of ν (v.u.) is equal to the formal valence of the central adsorbing ion. Details about the calculations are explained elsewhere.[63,89] Table S5.5 shows the optimized bond lengths (R) and bond valence values (ν) for the Fe-PO_4-M^{2+} used in our model (see Table 5.2 in the main text). The surface charge attribution derived includes a correction for change in water dipole orientation, leading to the interfacial CD value Δz_0.

Table S5.5. Bond lengths (R) and a bond valence (ν) of the optimized geometries of the ternary Fe-PO_4-M^{2+} complexes used in the modeling. The geometries were optimized with MO/DFT using the 6-31+G** basis set and the functional B3LYP. The corresponding bond valences (ν) are obtained with the Brown valence analysis.

$FeOPO_3$-Ca			**$(FeO)_2PO_2$-Ca**			**$FeOPO_3$-Mg**		
Bond	***R* (pm)**	**ν (v.u)**	**Bond**	***R* (pm)**	**ν (v.u)**	**Bond**	***R* (pm)**	**ν (v.u)**
FeO-P*	159.2	1.19	FeO-P*	157.0	1.25	FeO-P*	160.1	1.16
P-O-H_2O	154.5	1.35	FeO-P*	155.9	1.29	P-O-H_2O	154.8	1.34
P-O-H_2O	158.3	1.22	P-O-H_2O	158.7	1.20	P-O-H_2O	158.1	1.22
P-O-Ca	157.4	1.25	P-O-Ca	157.0	1.25	P-O-Mg	156.3	1.28
	Sum υ	5.00		Sum υ	5.00		Sum υ	5.00
R_o	165.6		R_o	165.4		R_o	165.5	
Other d			**Other d**			**Other d**		
Ca-O-P	224.4		Ca-O-P	229.5		Mg-O-P	202.1	
Ca-H_2O	244.7		Ca-H_2O	249.0		Mg-H_2O	208.0	
Ca-H_2O	250.3		Ca-H_2O	247.7		Mg-H_2O	218.5	
Ca-H_2O	248.6		Ca-H_2O	255.0		Mg-H_2O	211.9	
Ca-H_2O	240.8		Ca-H_2O	238.1		Mg-H_2O	226.6	
Ca-H_2O	239.1		Ca-H_2O	243.6		Mg-H_2O	215.2	

* O-P* represents the bonds that are shared with Fe at the surface of ferrihydrite

The value for Δz_0 has been derived as described above. The Δz_1 and Δz_2 values were found by fitting the adsorption data of the binary Ca–PO_4 and Mg–PO_4 systems, using the constraint $\Delta z_{tot} = \Delta z_0 + \Delta z_1 + \Delta z_2$ or $\Delta z_1 + \Delta z_2 = \Delta z_{tot} - \Delta z_0$. In this approach, the charge of the M^{2+} ions bound to adsorbed PO_4 complexes is conceptually distributed over the inner and outer Stern plane. For instance, according to our results for Δz_1 and Δz_2, about 1/2 of the Ca^{2+} charge in the ≡$FeOPO_3Ca$ complex is located at the outer Stern plane. For ≡ $(FeO)_2PO_2Ca$ complex, it is about ~2/3. The final set of CD coefficients is presented above in the Table S5.4.

F. Modeling of Mg–PO_4 interaction with no ternary complex formation

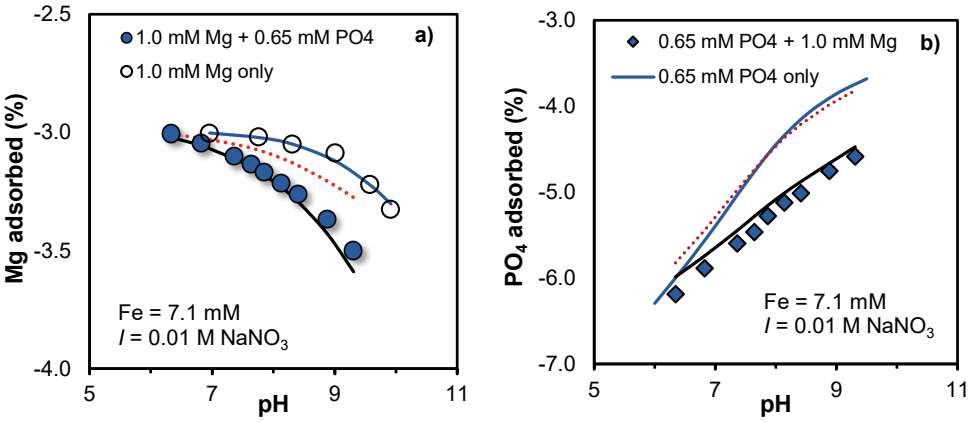

Figure S5.4. Logarithm of the Mg (panel a) and PO_4 (panel b) concentration in the equilibrium solution of ferrihydrite systems in $I = 0.01$ M $NaNO_3$. The total Fe concentration was ~7.1 mM and the specific surface area of this Fh suspension was $A = 720 \pm 10$ m^2 g^{-1} with a corresponding molar mass $M_{nano} = 97.6$ g mol^{-1} Fe. Closed symbols are for binary Mg–PO_4 systems with total concentrations of Mg = 1.0 mM and PO_4 = 0.65 mM, and the open symbols are for the corresponding single-ion systems. The dotted (red) lines are the CD model predictions for the binary Mg–PO_4 systems using only the adsorption parameters of the single-ion systems of Mg (Table 5.1 main text) and PO_4 (ref [32]); *i.e.* considering the effect of electrostatic interactions only. The full (black) lines are the modeling results including additionally the formation of ternary surface complexes for the binary Mg–PO_4 systems (Table 5.2 in the main text).

G. Surface speciation of PO_4 and Mg in ferrihydrite systems

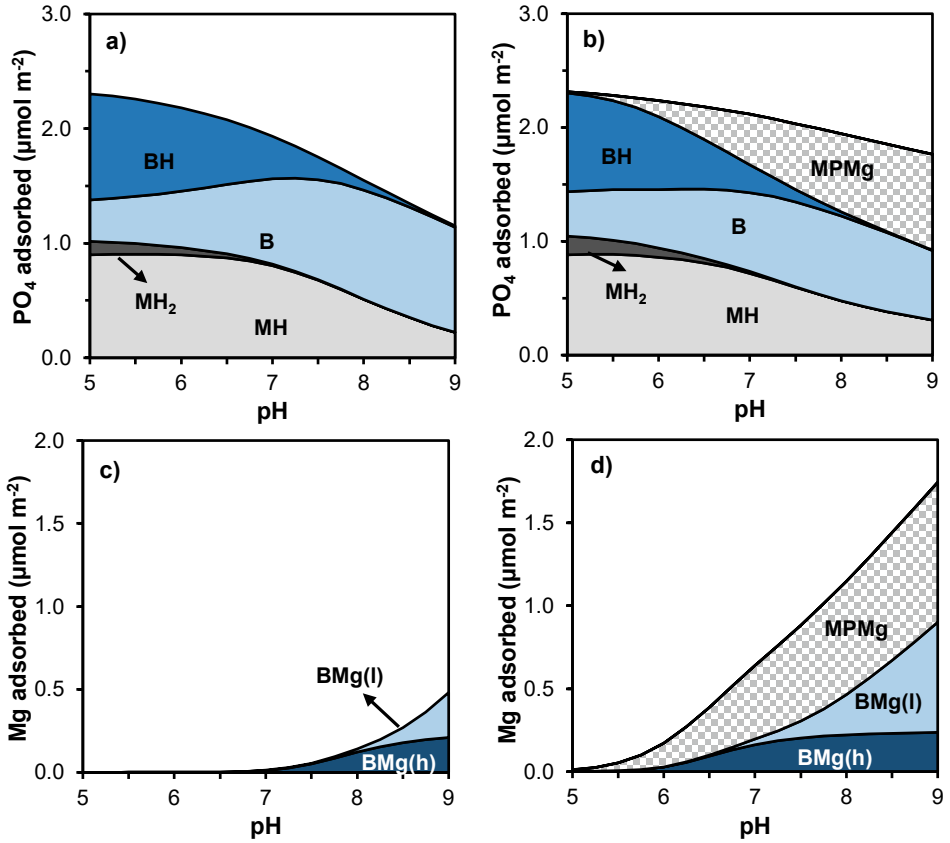

Figure S5.5. pH-dependent surface speciation of PO_4 (upper panels) and Mg (lower panels) in the single-ion (left panels) and binary Mg–PO_4 (right panels) systems with Fh in 0.01 M $NaNO_3$. The calculations have been done with the CD model, using the parameter sets presented in Tables 5.1 and 5.2 of the main text. The parameters for PO_4 adsorption in single-ion systems are taken from Hiemstra and Zhao.[32] The total Fe concentration is 3.90 mM and the specific surface area of Fh is A = 684 m^2 g^{-1} with a corresponding molar mass of M_{nano} = 96.6 g mol^{-1}. The total PO_4 concentration in the single PO_4 and binary Mg–PO_4 systems is 0.60 mM. The total Mg concentration in the single Mg and binary Mg–PO_4 systems is 1.0 mM. For PO_4: MH = monodentate protonated; MH_2 = monodentate doubly protonated; B = bidentate; BH = bidentate protonated. For Mg: BMg(l) = bidentate with low affinity sites; BMg(h) = bidentate with high affinity sites. For ternary species: MPMg = ternary complex in which PO_4 is bound to Fh as a monodentate complex.

In the presence of Mg, the relative contribution of bidentate PO_4 complexes (B, BH) is reduced in comparison to the surface speciation of PO_4 in single-ion systems. Moreover, the presence of PO_4 promotes the binding of Mg to the low affinity sites, particularly at high pH values. Similar results were observed for the binary Ca-PO4 systems (Figure 5.6, main text).

H. Modeling PO_4 binding: Ca vs Mg systems

The increased PO_4 binding to Fh in the presence of either Ca or Mg has been analyzed by modeling as shown in Figure S5.6. For a given pH and total M^{2+} concentration, the adsorption of PO_4 is enhanced more in the presence of Ca in comparison to Mg. At low total M^{2+} concentrations (*e.g.* 0.10 mM), the difference in PO_4 adsorption is small between systems with Ca and Mg but it becomes more significant at higher total M^{2+} concentrations. The modeling results in Figure S5.6 agree qualitatively with the larger PO_4 uptake by fresh Fe(III)-precipitates in background Ca solutions, in comparison with Mg solutions at equal M^{2+}/Fe ratio.[91] Figure S5.6 also shows that the pH-dependency of the PO_4 adsorption is reduced in the presence of co-adsorbing M^{2+} ions. This reduction is more obvious in the Ca-PO_4 systems. From a practical perspective, this observation is relevant as unbuffered water and $CaCl_2$ solutions are often used for assessing the soil P status in agricultural and grasslands. A better understanding of the interfacial interactions between M^{2+} and PO_4 will allow better interpretations of the phosphorus behavior in natural environments.

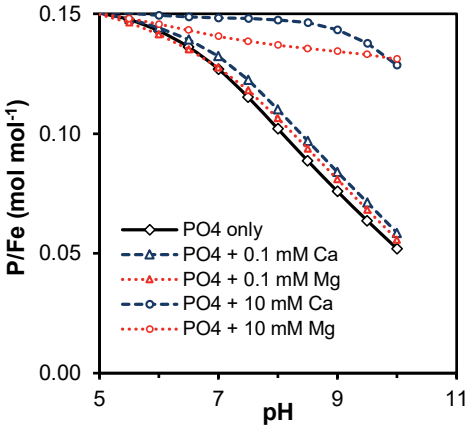

Figure S5.6. Modeled pH-dependent PO_4 adsorption to ferrihydrite, expressed as the ratio P/Fe (mol mol^{-1}), for systems with 0 (diamonds), 0.1 (triangles) or 10 mM (circles) total concentration of either Ca (blue series) or Mg (red series). Model calculations were performed with the parameters set presented in Table S5.4. The ionic strength was kept constant at I = 0.01 M $NaNO_3$, and the total concentrations of PO_4, and Fe were respectively 0.60 and 3.90 mM.

References

(1) Jambor, J. L.; Dutrizac, J. E. Occurrence and Constitution of Natural and Synthetic Ferrihydrite, a Widespread Iron Oxyhydroxide. *Chem. Rev.* **1998**, *98* (7), 2549–2586.

(2) Hochella, M. F.; Lower, S. K.; Maurice, P. A.; Penn, R. L.; Sahai, N.; Sparks, D. L.; Twining, B. S. Nanominerals, Mineral Nanoparticles, and Earth Systems. *Science (80-.).* **2008**, *319* (5870), 1631–1635.

(3) Qafoku, N. P. *Terrestrial Nanoparticles and Their Controls on Soil-/Geo-Processes and Reactions*; 2010; Vol. 107.

(4) Hiemstra, T. Formation, Stability, and Solubility of Metal Oxide Nanoparticles: Surface Entropy, Enthalpy, and Free Energy of Ferrihydrite. *Geochim. Cosmochim. Acta* **2015**, *158*, 179–198.

(5) Liu, J.; Zhu, R.; Xu, T.; Xu, Y.; Ge, F.; Xi, Y.; Zhu, J.; He, H. Co-Adsorption of Phosphate and Zinc(II) on the Surface of Ferrihydrite. *Chemosphere* **2016**, *144*, 1148–1155.

(6) Guo, H.; Barnard, A. S. Naturally Occurring Iron Oxide Nanoparticles: Morphology, Surface Chemistry and Environmental Stability. *J. Mater. Chem. A* **2013**, *1* (1), 27–42.

(7) Schwertmann, U.; Friedl, J.; Stanjek, H. From Fe(III) Ions to Ferrihydrite and Then to Hematite. *J. Colloid Interface Sci.* **1999**, *209* (1), 215–223.

(8) Borch, T.; Kretzschmar, R.; Kappler, A.; Cappellen, P. Van; Ginder-Vogel, M.; Voegelin, A.; Campbell, K. Biogeochemical Redox Processes and Their Impact on Contaminant Dynamics. *Environ. Sci. Technol.* **2010**, *44* (1), 15–23.

(9) Mejia, J.; He, S.; Yang, Y.; Ginder-Vogel, M.; Roden, E. E. Stability of Ferrihydrite–Humic Acid Coprecipitates under Iron-Reducing Conditions. *Environ. Sci. Technol.* **2018**, *52* (22), 13174–13183.

(10) Li, G.-X.; Chen, X.-P.; Wang, X.-N.; Chen, Z.; Bao, P. Sulfur Redox Cycling Dependent Abiotic Ferrihydrite Reduction by a *Desulfitobacterium Hafniense*. *ACS Earth Sp. Chem.* **2018**, *2* (5), 496–505.

(11) Jones, A. M.; Collins, R. N.; Waite, T. D. Redox Characterization of the Fe(II)-Catalyzed Transformation of Ferrihydrite to Goethite. *Geochim. Cosmochim. Acta* **2017**, *218*, 257–272.

(12) Burton, E. D.; Hockmann, K.; Karimian, N.; Johnston, S. G. Antimony Mobility in Reducing Environments: The Effect of Microbial Iron(III)-Reduction and Associated Secondary Mineralization. *Geochim. Cosmochim. Acta* **2019**, *245*, 278–289.

(13) Adhikari, D.; Sowers, T.; Stuckey, J. W.; Wang, X.; Sparks, D. L.; Yang, Y. Formation and Redox Reactivity of Ferrihydrite-Organic Carbon-Calcium Co-Precipitates. *Geochim. Cosmochim. Acta* **2019**, *244*, 86–98.

(14) Dzombak, D. A.; Morel, F. M. M. *Surface Complexation Modeling: Hydrous Ferric Oxide*; John Wiley & Sons, Inc.: New York, 1990.

(15) Cornell, R. M.; Schwertmann, U. *The Iron Oxides: Structure, Properties, Reactions, Ocurrence and Uses*, Second Edi.; WILEY-VCH, Germany, 2003.

(16) Hiemstra, T.; Mendez, J. C.; Li, J. Evolution of the Reactive Surface Area of Ferrihydrite: Time, PH, and Temperature Dependency of Growth by Ostwald Ripening. *Environ. Sci. Nano* **2019**, *6* (3), 820–833.

(17) Hiemstra, T. Surface and Mineral Structure of Ferrihydrite. *Geochim. Cosmochim. Acta* **2013**, *105*, 316–325.

(18) Davis, J. A.; Leckie, J. O. Surface Ionization and Complexation at the Oxide/Water Interface II. Surface Properties of Amorphous Iron Oxyhydroxide and Adsorption of Metal Ions. *J. Colloid Interface Sci.* **1978**, *67* (1), 90–107.

(19) Mendez, J. C.; Hiemstra, T. Carbonate Adsorption to Ferrihydrite: Competitive Interaction with Phosphate for Use in Soil Systems. *ACS Earth Sp. Chem.* **2019**, *3* (1), 129–141.

(20) Liu, J.; Zhu, R.; Liang, X.; Ma, L.; Lin, X.; Zhu, J.; He, H.; Parker, S. C.; Molinari, M. Synergistic Adsorption of Cd(II) with Sulfate/Phosphate on Ferrihydrite: An in Situ ATR-FTIR/2D-COS Study. *Chem. Geol.* **2018**, *477*, 12–21.

(21) Trivedi, P.; Dyer, J. A.; Sparks, D. L. Lead Sorption onto Ferrihydrite. 1. A Macroscopic and Spectroscopic Assessment. *Environ. Sci. Technol.* **2003**, *37* (5), 908–914.

(22) Swedlund, P. J.; Miskelly, G. M.; McQuillan, A. J. Silicic Acid Adsorption and Oligomerization at the Ferrihydrite - Water Interface: Interpretation of ATR-IR Spectra Based on a Model Surface Structure. *Langmuir* **2010**, *26* (5), 3394–3401.

(23) Antelo, J.; Arce, F.; Fiol, S. Arsenate and Phosphate Adsorption on Ferrihydrite Nanoparticles. Synergetic Interaction with Calcium Ions. *Chem. Geol.* **2015**, *410*, 53–62.

(24) Bompoti, N. M.; Chrysochoou, M.; Machesky, M. L. A Unified Surface Complexation Modeling Approach for Chromate Adsorption on Iron Oxides. *Environ. Sci. Technol.* **2019**, *53* (11), 6352–6361.

(25) Waite, T. D.; Davis, J. A.; Payne, T. E.; Waychunas, G. A.; Xu, N. Uranium(VI) Adsorption to Ferrihydrite: Application of a Surface Complexation Model. *Geochim. Cosmochim. Acta* **1994**, *58* (24), 5465–5478.

(26) Benjamin, M. M.; Leckie, J. O. Multiple-Site Adsorption of Cd, Cu, Zn, and Pb on Amorphous Iron Oxyhydroxide. *J. Colloid Interface Sci.* **1981**, *79* (1), 209–221.

(27) Kinniburgh, D. G.; Jackson, M. L. Concentration and PH Dependence of Calcium and Zinc Adsorption by Iron Hydrous Oxide Gel. *Soil Sci. Soc. Am. J.* **1982**, *46* (1), 56–61.

(28) Zachara, J. M.; Girvin, D. C.; Schmidt, R. L.; Resch, C. T. Chromate Adsorption on Amorphous Iron Oxyhydroxide in the Presence of Major Groundwater Ions. *Environ. Sci. Technol.* **1987**, *21* (6), 589–594.

(29) Wang, X.; Kubicki, J. D.; Boily, J. F.; Waychunas, G. A.; Hu, Y.; Feng, X.; Zhu, M. Binding Geometries of Silicate Species on Ferrihydrite Surfaces. *ACS Earth Sp. Chem.* **2018**, *2* (2), 125–134.

(30) Johnston, C. P.; Chrysochoou, M. Mechanisms of Chromate, Selenate, and Sulfate Adsorption on Al-Substituted Ferrihydrite: Implications for Ferrihydrite Surface Structure and Reactivity. *Environ. Sci. Technol.* **2016**, *50* (7), 3589–3596.

(31) Tiberg, C.; Gustafsson, J. P. Phosphate Effects on Cadmium(II) Sorption to Ferrihydrite. *J. Colloid Interface Sci.* **2016**, *471*, 103–111.

(32) Hiemstra, T.; Zhao, W. Reactivity of Ferrihydrite and Ferritin in Relation to Surface Structure, Size, and Nanoparticle Formation Studied for Phosphate and Arsenate. *Environ. Sci. Nano* **2016**, *3*, 1265–1279.

(33) Ali, M. A.; Dzombak, D. A. Effects of Simple Organic Acids on Sorption of Cu2+ and Ca2+ on Goethite. *Geochim. Cosmochim. Acta* **1996**, *60* (2), 291–304.

(34) Rietra, R. P. J. J.; Hiemstra, T.; van Riemsdijk, W. H. Interaction between Calcium and Phosphate Adsorption on Goethite. *Environ. Sci. Technol.* **2001**, *35* (16), 3369–3374.

(35) Stachowicz, M.; Hiemstra, T.; van Riemsdijk, W. H. Multi-Competitive Interaction of As(III) and As(V) Oxyanions with Ca2+, Mg2+, PO3−4, and CO2−3 Ions on Goethite. *J. Colloid Interface Sci.* **2008**, *320* (2), 400–414.

(36) Talebi, M.; Rahnemaie, R.; Goli Kalanpa, E.; Davoodi, M. H. Competitive Adsorption of Magnesium and Calcium with Phosphate at the Goethite Water Interface: Kinetics, Equilibrium and CD-MUSIC Modeling. *Chem. Geol.* **2016**, *437*, 19–29.

(37) Nie, Z.; Finck, N.; Heberling, F.; Pruessmann, T.; Liu, C.; Lützenkirchen, J. Adsorption of Selenium and Strontium on Goethite: EXAFS Study and Surface Complexation Modeling of the Ternary Systems. *Environ. Sci. Technol.* **2017**, *51* (7), 3751–3758.

(38) Likens, G. E.; Driscoll, C. T.; Buso, D. C.; Siccama, T. G.; Johnson, C. E.; Lovett, G. M.; Fahey, T. J.; Reiners, W. A.; Ryan, D. F.; Martin, C. W.; et al. The Biogeochemistry of Calcium at Hubbard Brook. *Biogeochemistry* **1998**, *41* (2), 89–173.

(39) Qadir, M.; Schubert, S.; Oster, J. D.; Sposito, G.; Minhas, P. S.; Cheraghi, S. A. M.; Murtaza, G.; Mirzabaev, A.; Saqib, M. High-magnesium Waters and Soils: Emerging Environmental and Food Security Constraints. *Sci. Total Environ.* **2018**, *642*, 1108–1117.

(40) Weng, L.; Vega, F. A.; van Riemsdijk, W. H. Competitive and Synergistic Effects in PH Dependent Phosphate Adsorption in Soils: LCD Modeling. *Environ. Sci. Technol.* **2011**, *45* (19), 8420–8428.

(41) Slomp, C. P.; Van Der Gaast, S. J.; Van Raaphorst, W. Phosphorus Binding by Poorly Crystalline Iron Oxides in North Sea Sediments. *Mar. Chem.* **1996**, *52* (1), 55–73.

(42) Gottselig, N.; Nischwitz, V.; Meyn, T.; Amelung, W.; Bol, R.; Halle, C.; Vereecken, H.; Siemens, J.; Klumpp, E. Phosphorus Binding to Nanoparticles and Colloids in Forest Stream Waters. *Vadose Zo. J.* **2017**, *16* (3), 0.

(43) Hiemstra, T.; Antelo, J.; Rahnemaie, R.; van Riemsdijk, W. H. Nanoparticles in Natural Systems I: The Effective Reactive Surface Area of the Natural Oxide Fraction in Field Samples. *Geochim. Cosmochim. Acta* **2010**, *74* (1), 41–58.

(44) Koopmans, G. F. F.; Hiemstra, T.; Vaseur, C.; Chardon, W. J. J.; Voegelin, A.; Groenenberg, J. E. E. Use of Iron Oxide Nanoparticles for Immobilizing Phosphorus In-Situ: Increase in Soil Reactive Surface Area and Effect on Soluble Phosphorus. *Sci. Total Environ.* **2020**, *711*, 135220.

(45) Weng, L.; van Riemsdijk, W. H.; Hiemstra, T. Factors Controlling Phosphate Interaction with Iron Oxides. *J. Environ. Qual.* **2012**, *41* (3), 628–635.

(46) Schofield, R. K. Can a Precise Meaning Be given to Available Soil Phosphorus? *Soils Fertil.* **1955**, *18*, 373–375.

(47) Aslyng, H. C. Phosphate Potential and Phosphate Status of Soils. *Acta Agric. Scand.* **1964**, *14* (4), 261–285.

(48) Koopmans, G. F.; Chardon, W. J.; Dekker, P. H. M.; Römkens, P. F. A. M.; Schoumans, O. F. Comparing Different Extraction Methods for Estimating Phosphorus Solubility in Various Soil Types. *Soil Sci.* **2006**, *171* (2), 103–116.

(49) Houba, V. J. G.; Temminghoff, E. J. M.; Gaikhorst, G. A.; van Vark, W. Soil Analysis Procedures Using 0.01 M Calcium Chloride as Extraction Reagent. *Commun. Soil Sci. Plant Anal.* **2000**, *31* (9–10), 1299–1396.

(50) Houba, V. J. G.; Novozamsky, I.; Huybregts, A. W. M.; van der Lee, J. J. Comparison of Soil Extractions by 0.01M CaCl2, by EUF and by Some Conventional Extraction Procedures. *Plant Soil* **1986**, *96* (3), 433–437.

(51) Sánchez-Alcalá, I.; del Campillo, M. C.; Torrent, J. Extraction with 0.01 m CaCl 2 Underestimates the Concentration of Phosphorus in the Soil Solution. *Soil Use Manag.* **2014**, n/a-n/a.

(52) Weesner, F. J.; Bleam, W. F. Binding Characteristics of Pb2+on Anion-Modified and Pristine Hydrous Oxide Surfaces Studied by Electrophoretic Mobility and x-Ray Absorption Spectroscopy. *J. Colloid Interface Sci.* **1998**, *205* (2), 380–389.

(53) Elzinga, E. J.; Kretzschmar, R. In Situ ATR-FTIR Spectroscopic Analysis of the Co-Adsorption of Orthophosphate and Cd(II) onto Hematite. *Geochim. Cosmochim. Acta* **2013**, *117*, 53–64.

(54) Swedlund, P. J.; Webster, J. G.; Miskelly, G. M. The Effect of SO4 on the Ferrihydrite Adsorption of Co, Pb and Cd: Ternary Complexes and Site Heterogeneity. *Appl. Geochemistry* **2003**, *18* (11), 1671–1689.

(55) van Genuchten, C. M.; Gadgil, A. J.; Peña, J. Fe(III) Nucleation in the Presence of Bivalent Cations and Oxyanions Leads to Subnanoscale 7 Å Polymers. *Environ. Sci. Technol.* **2014**, *48* (20), 11828–11836.

(56) Wang, L.; Nancollas, G. H. Calcium Orthophosphates: Crystallization and Dissolution. *Chem. Rev.* **2008**, *108* (11), 4628–4669.

(57) Scheinost, A. C.; Abend, S.; Pandya, K. I.; Sparks, D. L. Kinetic Controls on Cu and Pb Sorption by Ferrihydrite. *Environ. Sci. Technol.* **2001**, *35* (6), 1090–1096.

(58) Greffié, C.; Amouric, M.; Parron, C. HRTEM Study of Freeze-Dried and Untreated Synthetic Ferrihydrites: Consequences of Sample Processing. *Clay Miner.* **2001**, *36* (3), 381–387.

(59) Mendez, J. C.; Hiemstra, T. Surface Area of Ferrihydrite Consistently Related to Primary Surface Charge, Ion Pair Formation, and Specific Ion Adsorption. *Chem. Geol.* **2020**, *532*, 119304.

(60) Thomasarrigo, L. K.; Kaegi, R.; Kretzschmar, R. Ferrihydrite Growth and Transformation in the Presence of Ferrous Iron and Model Organic Ligands. *Environ. Sci. Technol.* **2019**, *53* (23), 13636–13647.

(61) Lu, Y.; Hu, S.; Wang, Z.; Ding, Y.; Lu, G.; Lin, Z.; Dang, Z.; Shi, Z. Ferrihydrite Transformation under the Impact of Humic Acid and Pb: Kinetics, Nanoscale Mechanisms, and Implications for C and Pb Dynamics. *Environ. Sci. Nano* **2019**, *6* (3), 747–762.

(62) Hiemstra, T.; Van Riemsdijk, W. H. A Surface Structural Approach to Ion Adsorption: The Charge Distribution (CD) Model. *J. Colloid Interface Sci.* **1996**, *179* (2), 488–508.

(63) Hiemstra, T.; Van Riemsdijk, W. H. On the Relationship between Charge Distribution, Surface Hydration, and the Structure of the Interface of Metal Hydroxides. *J. Colloid Interface Sci.* **2006**, *301* (1), 1–18.

(64) Hiemstra, T.; Van Riemsdijk, W. H. A Surface Structural Model for Ferrihydrite I: Sites Related to Primary Charge, Molar Mass, and Mass Density. *Geochim. Cosmochim. Acta* **2009**, *73* (15), 4423–4436.

(65) Keizer, M. G.; van Riemsdijk, W. H. *ECOSAT, Equilibrium Calculation of Speciation and Transport. Technical Report. Department of Soil Quality. Wageningen Univeristy.*; 1998.

(66) Kinniburgh, D. G. *Fit, Technical Report WD/93/23*; Keyworth, Great Britain, 1993.

(67) Mendez, J. C.; Hiemstra, T. High and Low Affinity Sites of Ferrihydrite for Metal Ion Adsorption: Data and Modeling of the Alkaline-Earth Ions Be, Mg, Ca, Sr, Ba, and Ra. *Geochim. Cosmochim. Acta* **2020**, *Accepted*.

(68) Brown, I. D.; Altermatt, D. Bond-Valence Parameters Obtained from a Systematic Analysis of the Inorganic Crystal Structure Database. *Acta Crystallogr. Sect. B Struct. Sci.* **1985**, *41* (4), 244–247.

(69) Brown, I. D. Recent Developments in the Methods and Applications of the Bond Valence Model. *Chem. Rev.* **2009**, *109* (12), 6858–6919.

(70) Michel, F. M.; Ehm, L.; Antao, S. M.; Lee, P. L.; Chupas, P. J.; Liu, G.; Strongin, D. R.; Schoonen, M. A. A.; Phillips, B. L.; Parise, J. B. The Structure of Ferrihydrite, a Nanocrystalline Material. *Science* **2007**, *316* (5832), 1726–1729.

(71) Michel, F. M.; Barron, V.; Torrent, J.; Morales, M. P.; Serna, C. J.; Boily, J.-F.; Liu, Q.; Ambrosini, A.; Cismasu, A. C.; Brown, G. E. Ordered Ferrimagnetic Form of Ferrihydrite Reveals Links among Structure, Composition, and Magnetism. *Proc. Natl. Acad. Sci.* **2010**, *107* (7), 2787–2792.

(72) Hiemstra, T. Ferrihydrite Interaction with Silicate and Competing Oxyanions: Geometry and Hydrogen Bonding of Surface Species. *Geochim. Cosmochim. Acta* **2018**, *238*, 453–476.

(73) Hiemstra, T. Surface Structure Controlling Nanoparticle Behavior: Magnetism of Ferrihydrite, Magnetite, and Maghemite. *Environ. Sci. Nano* **2018**, *5* (3), 752–764.

(74) Axe, L.; Bunker, G. B.; Anderson, P. R.; Tyson, T. A. An XAFS Analysis of Strontium at the Hydrous Ferric Oxide Surface. *J. Colloid Interface Sci.* **1998**, *199* (1), 44–52.

(75) Collins, C. R.; Sherman, D. M.; Vala Ragnarsdóttir, K. The Adsorption Mechanism of Sr2+ on the Surface of Goethite. *Radiochim. Acta* **1998**, *81* (4), 201–206.

(76) Fuller, A. J.; Shaw, S.; Peacock, C. L.; Trivedi, D.; Burke, I. T. EXAFS Study of Sr Sorption to Illite, Goethite, Chlorite, and Mixed Sediment under Hyperalkaline Conditions. *Langmuir* **2016**, *32* (12), 2937–2946.

(77) Kinniburgh, D. G. The H+/M2+ Exchange Stoichiometry of Calcium and Zinc Adsorption by Ferrihydrite. *J. Soil Sci.* **1983**, *34* (4), 759–768.

(78) Kinniburgh, D. G.; Barker, J. A.; Whitfield, M. A Comparison of Some Simple Adsorption Isotherms for Describing Divalent Cation Adsorption by Ferrihydrite. *J. Colloid Interface Sci.* **1983**, *95* (2), 370–384.

(79) Lin, J.; Zhan, Y.; Wang, H.; Chu, M.; Wang, C.; He, Y.; Wang, X. Effect of Calcium Ion on Phosphate Adsorption onto Hydrous Zirconium Oxide. *Chem. Eng. J.* **2017**, *309*, 118–129.

(80) Yao, W.; Millero, F. J. Adsorption of Phosphate on Manganese Dioxide in Seawater. *Environ. Sci. Technol.* **1996**, *30* (2), 536–541.

(81) Voegelin, A.; Kaegi, R.; Frommer, J.; Vantelon, D.; Hug, S. J. Effect of Phosphate, Silicate, and Ca on Fe(III)-

Precipitates Formed in Aerated Fe(II)- and As(III)-Containing Water Studied by X-Ray Absorption Spectroscopy. *Geochim. Cosmochim. Acta* **2010**, *74* (1), 164–186.

(82) Ronson, T. K.; McQuillan, A. J. Infrared Spectroscopic Study of Calcium and Phosphate Ion Coadsorption and of Brushite Crystallization on TiO2. *Langmuir* **2002**, *18* (12), 5019–5022.

(83) Daniele, P. G.; Foti, C.; Gianguzza, A.; Prenesti, E.; Sammartano, S. Weak Alkali and Alkaline Earth Metal Complexes of Low Molecular Weight Ligands in Aqueous Solution. *Coordination Chemistry Reviews*. Elsevier May 1, 2008, pp 1093–1107.

(84) Zhang, G. Y.; Peak, D. Studies of Cd(II)–Sulfate Interactions at the Goethite–Water Interface by ATR-FTIR Spectroscopy. *Geochim. Cosmochim. Acta* **2007**, *71* (9), 2158–2169.

(85) Ostergren, J. D.; Brown, G. E.; Parks, G. A.; Persson, P. Inorganic Ligand Effects on Pb(II) Sorption to Goethite (α-FeOOH) - II. Sulfate. *J.Colloid Interface Sci.* **2000**, *225* (2), 483–493.

(86) Liu, J.; Zhu, R.; Liang, X.; Ma, L.; Lin, X.; Zhu, J.; He, H.; Parker, S. C.; Molinari, M. Synergistic Adsorption of Cd(II) with Sulfate/Phosphate on Ferrihydrite: An in Situ ATR-FTIR/2D-COS Study. *Chem. Geol.* **2018**, *477*, 12–21.

(87) Tiberg, C.; Sjöstedt, C.; Persson, I.; Gustafsson, J. P. Phosphate Effects on Copper(II) and Lead(II) Sorption to Ferrihydrite. *Geochim. Cosmochim. Acta* **2013**, *120*, 140–157.

(88) Lindsay, W. L. *Chemical Equilibria in Soils*; Wiley-Interscience Publication; Wiley, 1979.

(89) Rahnemaie, R.; Hiemstra, T.; Van Riemsdijk, W. H. Geometry, Charge Distribution, and Surface Speciation of Phosphate on Goethite. *Langmuir* **2007**, *23* (7), 3680–3689.

(90) De Robertis, A.; Di Giacomo, P.; Foti, C. Ion-Selective Electrode Measurements for the Determination of Formation Constants of Alkali and Alkaline Earth Metals with Low-Molecular-Weight Ligands. *Anal. Chim. Acta* **1995**, *300* (1–3), 45–51.

(91) Senn, A.-C.; Kaegi, R.; Hug, S. J.; Hering, J. G.; Mangold, S.; Voegelin, A. Composition and Structure of Fe(III)-Precipitates Formed by Fe(II) Oxidation in Water at near-Neutral PH: Interdependent Effects of Phosphate, Silicate and Ca. *Geochim. Cosmochim. Acta* **2015**, *162*, 220–246.

CHAPTER 6

Carbonate adsorption to ferrihydrite: Competitive interaction with phosphate for use in soil systems

Juan C. Mendez, Tjisse Hiemstra

Published as:

Mendez, J.C., Hiemstra, T. 2019. Carbonate adsorption to ferrihydrite: Competitive interaction with phosphate for use in soil systems. *ACS Earth and Space Chemistry.* 3(1) 129-141. doi.org/10.1021/acsearthspacechem.8b00160

Abstract

Carbonate (CO_3) interacts with Fe-(hydr)oxide nanoparticles, affecting the availability and geochemical cycle of other important oxyanions in nature. Here, we studied the carbonate–phosphate interaction in closed systems with freshly prepared ferrihydrite (Fh), using batch experiments that cover a wide range of pH values, ionic strength, and CO_3 and PO_4 concentrations. The surface speciation of CO_3 has been assessed by interpreting the ion competition with the Charge Distribution (CD) model, using CD coefficients derived from MO/DTF optimized geometries. Adsorption of CO_3 occurs predominately *via* formation of bidentate inner-sphere complexes, either $(\equiv FeO)_2CO$ or $(\equiv FeO)_2CO\cdots Na^+$. The formation of the latter complex is electrostatically promoted at high pH and in the presence of adsorbed PO_4. Additionally, a minor complex is present at high CO_3 loadings. The CD model, solely parametrized by measuring the pH-dependent PO_4 adsorption as a function of the CO_3 concentration, successfully predicts the CO_3 adsorption to Fh in single-ion systems. The adsorption affinity of CO_3 to Fh is higher than to goethite, particularly at high pH and CO_3 loadings due to the enhanced formation $(\equiv FeO)_2CO\cdots Na^+$. The PO_4 adsorption isotherm in 0.5 M $NaHCO_3$ can be well described, which is relevant for assessing the reactive surface area of the natural oxide fraction with soil extractions and CD modeling. Additionally, we have evaluated the enhanced Fh solubility due to Fe(III)-CO_3 complex formation and resolved a new species ($Fe(CO_3)_2(OH)_2^{3-}(aq)$), which is dominant in closed systems at high pH. The measured solubility of our Fh agrees with the size-dependent solubility predicted using the surface Gibbs free energy of Fh.

Keywords: ferrihydrite, goethite, nanoparticles, ion adsorption, surface complexation, competition, CD model, solubility

6.1. Introduction

The adsorption of ions to the natural Fe-(hydr)oxides of soils is a key process that regulates the bioavailability, toxicity, and mobility of specific nutrients and contaminants in the environment.[1] Particularly, understanding the interaction between Fe-(hydr)oxide nanoparticles (Fe_{ox}NPs) and oxyanions such as phosphate (PO_4^{3-}), sulfate (SO_4^{2-}), silicate (SiO_4^{4-}), and arsenate (AsO_4^{3-}) is of great relevance as their behavior varies under a wide range of environmental conditions.[2–6] Moreover, recent developments in nanotechnology have shown promising results for the application of engineered Fe_{ox}NPs in a series of environmental and industrial clean-up applications, such as drinking and wastewater treatment.[7–9]

In relation to the ion adsorption capacity, ferrihydrite (Fh) is one of the most reactive Fe_{ox}NPs. The large reactivity of Fh is mainly due to its high specific surface area (SSA ≥ 600 $m^2\ g^{-1}$) and high density of reactive surface groups.[10,11] Fh is ubiquitously present in terrestrial and aquatic systems[12,13] and, from the thermodynamic perspective, it is the most stable Fe-(hydr)oxide at the nanometer scale.[14] Therefore, studying the fundamental processes that regulate the interaction of ions with Fh is essential to understand and predict the adsorption behavior of these ions in a variety of systems.

Dissolved inorganic carbon, hereinafter called dissolved carbonate (CO_3), is another ubiquitous component in terrestrial and aquatic systems. The concentration of CO_3 in natural systems such as rivers and groundwater ranges over about two orders of magnitude (~0.1–10 mM).[15,16] An important property of CO_3 is its capacity to interact with the mineral surfaces of Fe-(hydr)oxides,[17,18] affecting the solid-solution partitioning of a whole suite of important ions in the environment,[19–28] including phosphate ions, hereinafter referred to as PO_4.[29,30]

From an environmental perspective, quantifying the CO_3–PO_4 interaction on the surfaces of the Fe-(hydr)oxides is important for understanding the reactivity of the natural oxide fraction. This aspect is essential for assessing the fate of nutrients and pollutants in the environment with Surface Complexation Modeling (SCM). The CO_3–PO_4 interaction has been previously used to assess the reactive surface area (RSA) of soil samples.[31] In that approach, the PO_4 buffer capacity of soils is measured by equilibrating the soil with a 0.5 M $NaHCO_3$ solution (pH = 8.5) at different soil-to-solution ratios. The resulting desorption curves have been interpreted with a SCM that was calibrated for the CO_3–PO_4 interaction with goethite (α-FeOOH). This material was chosen because of the existence of an internally consistent database with intrinsic adsorption constants. However, the application of this methodology to field samples revealed that the natural oxide fraction of topsoils is dominated by nanoparticles (d ~ 2–10 nm) with a corresponding high specific surface area (SSA ~200–1200 $m^2\ g^{-1}$). It suggests that Fh, rather than well-crystalized goethite, may be a better proxy for the natural oxide fraction in topsoils.[31]

To date, no information is available about the competitive interaction of CO_3 and PO_4 at the surface of Fh. In addition, only a single data set is available in the literature with respect to CO_3 adsorption in monocomponent systems with Fh.[24] These data have been collected using ^{14}C dating, assuming no source of CO_3 in the system other than the ^{14}C added. Moreover, the adsorption was only studied at very low concentrations of CO_3 (μM level), which are much lower than the natural concentration range. The lack of reliable information about the adsorption of CO_3 to Fh, in systems with and without PO_4 ion competition, underlines the scientific and practical relevance of the present research. Our study has a wide perspective as CO_3 is omnipresent in nature and will interfere in many geochemical processes, as mentioned above.[6,19–30]

In the present study, our main objective is to measure the interaction of CO_3 with the surfaces of freshly prepared Fh in a series of batch experiments that cover a wide range of chemical conditions. Since measuring the CO_3 adsorption is challenging from an analytical perspective, a significant part of our experimental study will refer to the assessment of the interaction of CO_3 with PO_4 as a function of pH (~7–12), ionic strength (0.05–0.5 M), total CO_3 concentration (4 mM–0.5 M), and PO_4 loading (0.68–1.48 μmol m^{-2}). The interaction of CO_3 with Fh will be parametrized by measuring the competitive effect of this anion in the adsorption of PO_4. A similar approach has been used successfully to derive the CO_3 interaction with goethite.[29]

The charge distribution (CD) model[32] will be used to interpret the collected competition data, in combination with state-of-the-art knowledge about the mineral and surface structure of Fh.[10,11,33] To limit the number of adjustable parameters to one per complex (*i.e.* log*K*), the CD coefficients will be derived with a bond valence analysis[34,35] of the optimized geometry of the CO_3 surface complexes, obtained with molecular orbital (MO) calculations, applying density functional theory (DFT).

Since Fh is a nanoparticle *pur sang*, most of its properties are size dependent. The molar mass (M_{nano}) will increase with smaller particle size[11] due to the change of the chemical composition $FeO_{1.4}(OH)_{0.2}\cdot nH_2O$ by the presence of surface groups, giving rise to a size dependent amount of chemisorbed water (nH_2O). This will also lead to a decrease of the mass density (ρ_{nano}) as this chemisorbed water does contribute more to the volume of the particle than to its mass.[36] These changes in M_{nano} and ρ_{nano} will affect the relation between the specific surface area of Fh and its particle size. The particle size will also change the capacitance values of the Stern layers used in the electrostatic part of the model.[36] The size-dependence of the above properties will be considered in our modeling, using a consistent set of equations.[36,37]

In addition to the CO_3–PO_4 competition data, the CO_3–Fh interaction will be studied for single-ion systems. The CD model, parametrized for the PO_4-CO_3 interaction, will be applied to compare the experimental adsorption of CO_3 with the model predictions for single-ion systems. With the derived adsorption parameters, we will evaluate the surface speciation of CO_3 in Fh systems as a function of solution conditions such as pH, ionic strength, and anion concentrations. In the last part of the paper, we will compare the CO_3 interaction of Fh and goethite and show that the significant differences between both materials can be understood from the difference of the interaction of Na^+ with adsorbed CO_3. This will lead to a strong difference in the competitive behavior of CO_3 with PO_4 bound by either Fh or goethite. It will have important implications for assessing the RSA of field soil samples, as we will discuss briefly.

6.2. Experimental Section

For all the adsorption experiments, ultrapure water (18.2 MΩ cm at 25 °C, <1 ppb TOC) and chemical reactants of analytical grade were used to prepare the stock solutions and the Fh suspensions. Contact between solutions and air was minimized to reduce the interference of atmospheric CO_2(g) during the adsorption experiments.

6.2.1. Ferrihydrite Synthesis

Fh suspensions were prepared by fast titrating with 0.02 M NaOH a solution of ~3.7 mM of $Fe(NO_3)_3$ dissolved in 0.010 M HNO_3. Freshly prepared acid and base solutions were always used. The base

addition was initially done at a rate of ~200 mL NaOH min^{-1} until a pH of ~3.2 was reached. More NaOH solution was subsequently added in ~5 mL increments until the suspension reached a final stable pH (over 15 min) of ~8.2 for the binary CO_3–PO_4 adsorption experiments, or pH ~6.0 for the CO_3 adsorption experiments in monocomponent systems. The Fh suspensions were centrifuged at 3500*g* for 45 min, the supernatant was carefully removed, and the settled Fh particles were resuspended in a 0.01 M $NaNO_3$ solution. The Fh suspensions were aged at 20 °C for 4 h since formation, before starting the CO_3–PO_4 competition experiments. Due to the relatively low level of added CO_3, the results of the adsorption experiments of CO_3 in single-ion systems may be particularly sensitive to interference of atmospheric CO_2(g). Therefore, the Fh suspensions used in these systems were first acidified to pH ~5.5 and purged during 24 h with moist purified N_2(g) before starting the adsorption experiments. The total Fe concentration ($Fe_{[T]}$) of each Fh suspension was measured by ICP-OES in a matrix of 0.8 M H_2SO_4. The $Fe_{[T]}$ was typically 19.3 ± 0.7 mM, which is equivalent to 1.90 ± 0.07 g Fh L^{-1} (for a mean Fh molar mass of M_{nano}= 97.6 g Fh mol^{-1} Fe). The specific surface area (SSA in m^2 g^{-1}) of each Fh suspension was assessed independently by using PO_4 as probe ion.[37] The values of $Fe_{[T]}$, SSA, and M_{nano} corresponding to each Fh preparation are presented in Table S6.1 of the Supplementary Information (SI).

6.2.2. Competitive Adsorption Carbonate–Phosphate

The competitive interaction of CO_3 with PO_4 was experimentally evaluated by determining the adsorption edges of PO_4 in a series of closed Fh systems with different concentrations of both oxyanions. Each individual system was prepared in 50 mL polypropylene tubes and contained a total volume of 40.0 mL. First, the required volume of ultrapure water and 4 M $NaNO_3$ solution was added into the tubes according to the intended final volume and background electrolyte level. Next, aliquots of 10.0 or 15.0 mL of the freshly prepared Fh were pipetted into the tubes and the pH of the suspensions was adjusted by adding acid (HNO_3) or base (NaOH) solutions, leading to pH ~6.5–11. Adsorption systems with pH values below 6.5 were not prepared to prevent the escape of HCO_3^- to the atmosphere as CO_2(g). Finally, volumes of the stock solution of NaH_2PO_4 (0.010 M) and $NaHCO_3$ (0.10 or 1.0 M) were simultaneously pipetted into the tubes. The $NaHCO_3$ solutions were freshly prepared before each experiment. Total PO_4 concentrations ($PO_{4[T]}$) of 0.25 and 0.50 mM were used in the systems with a low Fh content, whereas $PO_{4[T]}$ of 0.50 and 0.75 mM were used in the systems with a high Fh content. These combinations resulted in systems with a total PO_4 loading ($PO_{4(T)}$) equivalent to 0.68, 1.07, and 1.48 μmol m^{-2}. The total CO_3 concentrations ($CO_{3[T]}$) varied between 4.0 mM and 0.50 M. Most of the experiments were performed at a constant ionic strength of I = 0.50 M. Additional experiments were done at I = 0.050 and 0.10 M for evaluating the effect of different Na^+ levels on the competitive interaction of CO_3–PO_4. A summary of the chemical conditions for each experimental series is presented in Table S6.1 of the Supplementary Information (SI).

The thus-prepared CO_3–PO_4 systems with Fh were constantly shaken (120 strokes min^{-1}) in a conditioned room at 20 °C. After 20 h of equilibration, the suspensions were centrifuged at 3500*g* for 20 min to separate the Fh nanoparticles and the liquid phase. The equilibrium pH of the solution was measured with a glass electrode, and immediately after this, an aliquot of 10 mL was taken from the supernatant for chemical analysis. This aliquot was filtered through a 0.45 μm filter and acidified with HNO_3 to analyze the total concentration of P in solution by either ICP-OES or ICP-MS, depending on the final concentration of P. The concentration of Fe was also measured in the supernatant of a selected number of samples to test if significant dissolution of Fh occurred during the adsorption experiments, due to the formation of aqueous Fe(III)-CO_3 complexes.[38]

6.2.3. Carbonate Adsorption in Monocomponent Systems

The adsorption of CO_3 in monocomponent systems with Fh was experimentally evaluated following a similar procedure to that used for the binary CO_3–PO_4 systems. The pH of the adsorption systems ranged from ~6.5 to ~10.5, and the ionic strength was kept constant at I = 0.10 $NaNO_3$. Aliquots of 10, 20, or 30 mL of Fh suspension, aged for 24 h, were pipetted into the systems with a final solution volume of 40 mL. The $CO_{3[T]}$ was 1 mM, which was added using a freshly prepared 0.010 M $NaHCO_3$ stock solution. The gas-to-solution ratio of the systems was 0.25 mL mL^{-1}, which was used in the model calculations to account for the distribution of the total added CO_3 over the gas and liquid phases. The samples were equilibrated for 20 h at 20 ºC, and after centrifugation, a volume of 10 mL of solution was rapidly taken for analysis of the CO_3 concentration. The equilibrium pH was immediately measured in the remaining supernatant. The CO_3 concentration in solution was measured with a TOC analyzer, which converts the dissolved inorganic carbon into CO_2(g) by means of an internal acidification step. The concentration of produced CO_2(g) is then measured with an IR detector. Internal standard solutions with known concentrations of total dissolved CO_3 were also analyzed to verify the accuracy of our measurements. At every moment, maximum care was taken to minimize the escape/intrusion of CO_2(g) to/from the atmosphere.

6.2.4. CD Modeling and MO/DFT Calculations

The interaction between CO_3 and PO_4 at the mineral–solution interface of Fh has been described using the charge distribution (CD) model[32] in combination with the extended Stern layer model[39] that describes the compact part of the electrical double layer (EDL). In this electrostatic model, we have accounted for the effect of the nano-sized spherical particles on the capacitance values (C_1 and C_2) of the inner and outer Stern layers, in relation to the capacitance values of a flat plane.[36] The types of sites and the corresponding site densities have been derived with a surface structural analysis of Fh[37] based on recent insights into the mineral and surface structure of this Fe-(hydr)oxide material.[10,11,33] Primary charge reactions have been described according to Hiemstra.[5] CD model parameters for describing the adsorption of PO_4 to Fh were taken from Hiemstra and Zhao,[37] whereas the parameters for CO_3 have been derived in the present study from modeling the competition experiments with PO_4. CD modeling was done with the software Ecosat,[40] version 4.9. The adsorption parameters for CO_3 were optimized using the program FIT,[41] version 2.581. The complete set of solution speciation reactions and primary charge reactions used in the modeling are presented respectively in Tables S6.2 and S6.3 given in the Supplementary Information.

The geometries of the hydrated CO_3 complexes were optimized with molecular orbital (MO) calculations, using the Spartan14 parallel of Wavefunction, Inc. Density functional theory (DFT) was applied, using a range of functionals (BP86, B3LYP, EDF1, EDF2, BLYP, ωP97X-D). For the geometries optimization, we have used $(H_2O)_2Fe_2(OH)_6$ as template with fixed atomic positions[42] to which a hydrated moiety with CO_3^{2-}, HCO_3^-, or $NaCO_3^-$ was attached to form an inner-sphere complex that was allowed to freely relax. The average O–C bond lengths obtained with the different DFT functionals were interpreted with the Brown valence concept.[34,35] The resulting charge distribution coefficients have been corrected for the electrostatic contribution of water dipole orientation.[39]

6.3. Results and Discussion

6.3.1. Dissolution of Ferrihydrite in Carbonate Media

Carbonate may significantly increase the solubility of Fe-(hydr)oxides[38,43,44] by forming aqueous Fe(III)–CO_3 complexes, particularly above neutral pH. As this may have influenced our interpretation of the CO_3–PO_4 adsorption experiments, we have first evaluated the solubility of Fh in a number of binary CO_3–PO_4 adsorption systems by measuring the concentration of Fe in the supernatant of these systems (Figure 6.1).

According to Grivé et al.,[38] two aqueous Fe(III)–CO_3 complexes may form in carbonate solutions, *i.e.* a neutral $FeOHCO_3^0$ complex that dominates the Fe(III) solution speciation at pH ~4–7; and a $Fe(CO_3)_3^{3-}$ complex that controls the Fe(III) speciation above pH 7. Formation of the latter species leads to a significant increase of the solubility of Fe-(hydr)oxides in open systems with high partial CO_2 pressures (Figure S6.2). However, such partial pressures are not present in our closed systems because the total concentration of CO_3 remains constant with pH, in contrast to the open systems used by Grivé et al.[38] For the latter system, one may calculate the solubility of Fh as a function of pH, using the above given Fe(III)-CO_3 complexes. Representing Fh as $Fe(OH)_3(s)$, the formation reactions of these Fe(III)–CO_3 complexes can be given as:

$$Fe(OH)_3(s) + HCO_3^-(aq) + H^+(aq) \Leftrightarrow FeOHCO_3^0(aq) + 2\ H_2O(l) \quad \text{(Equation 6.1)}$$

$$Fe(OH)_3(s) + 3\ HCO_3^-(aq) \Leftrightarrow Fe(CO_3)_3^{3-}(aq) + 3\ H_2O(l) \quad \text{(Equation 6.2)}$$

For solutions with a constant concentration of HCO_3^-, the overall solubility of Fh will be pH-independent, if the solution speciation of Fe is dominated by $Fe(CO_3)_3^{3-}(aq)$. As $HCO_3^-(aq)$ gradually transforms into $CO_3^{2-}(aq)$ at high pH, the solubility of Fh is predicted to decrease (dotted lines in Figure 6.1), whereas our data show an opposite trend with pH. The difference can be explained by the formation of an additional Fe(III)–CO_3 species. Our experimental data for the dissolved Fe concentrations can be described by assuming the formation of an extra Fe(III)–CO_3 complex, according to the reaction:

$$Fe(OH)_3(s) + 2\ HCO_3^-(aq) \Leftrightarrow Fe(CO_3)_2(OH)_2^{3-}(aq) + H^+(aq) + 1\ H_2O(l) \quad \text{(Equation 6.3)}$$

The log$K$ values of reactions 4.1–4.3 are respectively log$K$ = 24.86 ± 0.09, 24.86 ± 0.09, and 31.71 ± 0.13. Details on deriving these constants as well as the solubility product of our Fh material can be found in Appendix E of the Supplementary Information.

In Figure 6.1, the right y-axis gives the fraction of the total Fe that is dissolved in our systems. For the systems with a $CO_{3[T]}$ of 0.50 M, less than ~0.5% of the total Fe is dissolved at the highest pH. This implies that the effect of CO_3 on the dissolution of Fh is negligible under our experimental conditions, as nearly 100% of the total Fe in the systems remains as part of the solid phase.

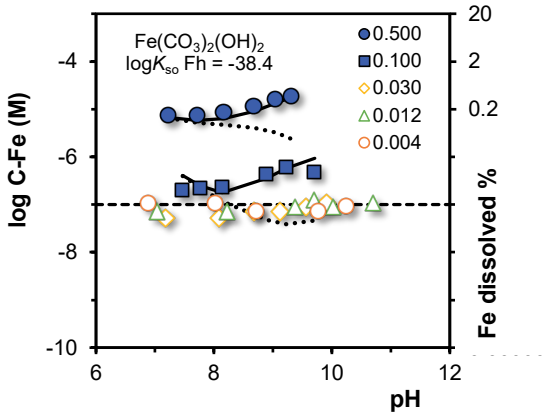

Figure 6.1. Logarithm of the experimental Fe concentrations (symbols) in the supernatants (left y-axis) and percentages of dissolved Fh (right y-axis) measured in our binary CO_3–PO_4–Fh systems as a function of pH for different $CO_{3[T]}$ with a fixed total concentration of Fe (4.9 mM) and PO_4 (0.25 mM) at a constant ionic strength (I = 0.5 M). Only the systems with 0.50 and 0.10 M $CO_{3[T]}$ have Fe concentrations that are clearly above the detection limit (dashed line) of our ICP-MS measurements. This detection limit is relatively high due to the very high electrolyte concentration that requires dilution. Dotted lines are model predictions including only the Fe(III)–CO_3 complexes proposed by Grivé et al.,[38] whereas the solid lines are model predictions using additionally $Fe(CO_3)_2(OH)_2^{3-}$(aq) (See text). The solubility of our Fh was found to be $\log Q = \log(Fe^{3+}) + 3\log(OH^-) = -38.4 \pm 0.1$, which is in line with the solubility calculated for Fh with a mean particle size of ~2.2 nm and a specific surface area of 765 $m^2\ g^{-1}$ ($\log Q_{so} = -38.2 \pm 0.2$) applying the Ostwald equation with a surface Gibbs free energy of 0.186 ± 0.01 J m^{-2} and an intrinsic (bulk) solubility of $\log K_{so} = -40.6 \pm 0.1$ as described elsewhere.[14]

6.3.2. Interaction Carbonate–Phosphate in Ferrihydrite Systems

6.3.2.1. Influence of pH and Carbonate Concentration

Figure 6.2 presents the adsorption edges of PO_4 to Fh for systems with different $CO_{3[T]}$ at two levels of $PO_{4(T)}$ equivalent to 0.68 (a) and 1.07 (b) µmol m^{-2}. The background Na^+ concentration was kept constant at 0.50 M by adding appropriate amounts of $NaNO_3$. A series of observations can be made focusing on these data. First, with increase of $CO_{3[T]}$, the PO_4 adsorption decreases. This illustrates the competition between both ions for the same binding sites at the surfaces of Fh. Second, the percentage of adsorbed PO_4 decreases when the solution pH increases. This pH-dependency is characteristic for oxyanions in general (PO_4, AsO_4, SO_4) binding to the surfaces of Fe-(hydr)oxides.[45–47] With the increase in pH, the protonated singly ($\equiv FeOH_2^{+0.5}$) and triply ($\equiv Fe_3OH^{+0.5}$) coordinated surface groups will gradually release protons. This will lead to a decrease in the electrostatic surface potential and, consequently, to less attraction of the negatively charged PO_4 ions by the surface.

Additionally, the adsorption of PO_4 to Fh does not decrease proportionally to the increase in the $CO_{3[T]}$ (Figure 6.2). This non proportional effect is related to the higher affinity of PO_4 for the adsorption to Fh, in comparison with CO_3. A quite high concentration of CO_3 ions is needed before the adsorption of PO_4 to Fh is significantly suppressed. The competitive effect of CO_3 on the adsorption of PO_4 depends on the relative concentration of both ions in solution ($[PO_4] / [PO_4+CO_3]$).

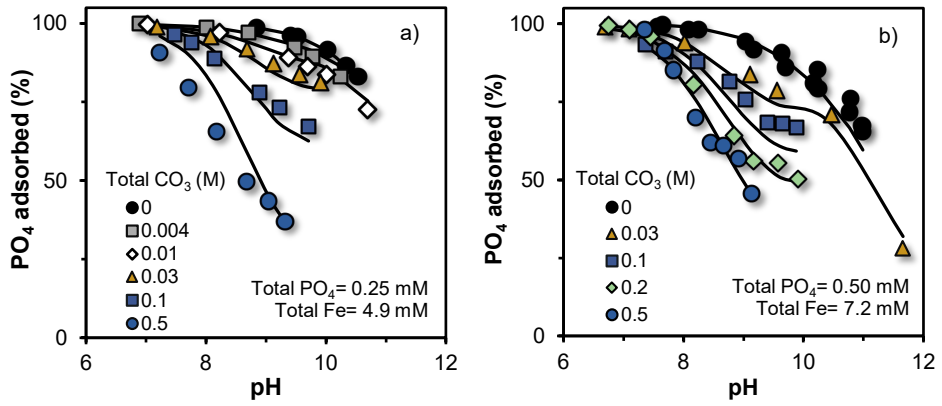

Figure 6.2. Adsorption edges of the competitive PO_4 binding to Fh in closed CO_3 systems at constant ionic strength of 0.50 M created by adding additionally $NaNO_3$. The symbols are experimental results and the lines are CD model calculations applying the parameter set of Table 6.1. The zero-carbonate system has been used to derive the specific surface area of Fh, being for system (a) 765 and (b) 672 $m^2\ g^{-1}$ at a molar mass of respectively M_{nano} = 98.76 and 96.33 g mol^{-1} Fe. The initial PO_4 loadings are equivalent to 0.68 (a) and 1.07 (b) µmol m^{-2}.

The relatively high affinity of PO_4 for binding to Fh can be depicted by constructing a normalized adsorption isotherm for binary CO_3–PO_4 systems. In this isotherm, the amount of adsorbed PO_4 as well as its solution concentration are presented on a relative scale (0–100%) with respect to the total amount adsorbed and total solution concentration of oxyanions ([PO_4+CO_3]). The constructed isotherm (Figure S6.4) shows that only a small fraction of dissolved PO_4 is needed to dominate the oxyanion adsorption onto Fh. This is very different for the adsorption of PO_4 in binary systems with a stronger competitor, as for instance AsO_4, where the normalized adsorption isotherm is much closer to a 1:1 line, as shown in Figure S6.4 of the Supplementary Information.

6.3.2.2. Influence of Phosphate Loading and Electrolyte Concentration

Figure 6.3a shows the equilibrium concentration of PO_4 in solution as a function of pH for systems that differ in surface loading with PO_4 (0.68 and 1.48 µmol m^{-2}) in the presence and absence of CO_3. Due to the competition with CO_3, the equilibrium concentration of PO_4 is higher in the systems with 0.03 M CO_3 in comparison to the corresponding PO_4 monocomponent systems. However, for a given pH, the extent of the CO_3 effect depends on the PO_4 level in the system. Addition of 0.03 M CO_3 leads to a larger increase of the PO_4 concentration in the systems with the lower initial PO_4 loading.

Figure 6.3a also shows that CO_3 enhances the equilibrium concentration of PO_4 more at a lower pH. This is related to the pH dependency of the CO_3 adsorption reaching a maximum near pH ~7, as we will show later in Section 6.3.4.1. This has also been found for goethite[16,25] and matches qualitatively also with other data obtained for goethite using the same experimental approach.[29]

In Figure 6.3b, the effect of the ionic strength on the competitive interaction between CO_3 and PO_4 is shown. In general, a rather small effect of the ionic strength is observed, which is consistent with the formation of predominantly inner-sphere surface complexes for PO_4.[45,48–50] The largest differences are found at high pH and at relatively low loading with PO_4.

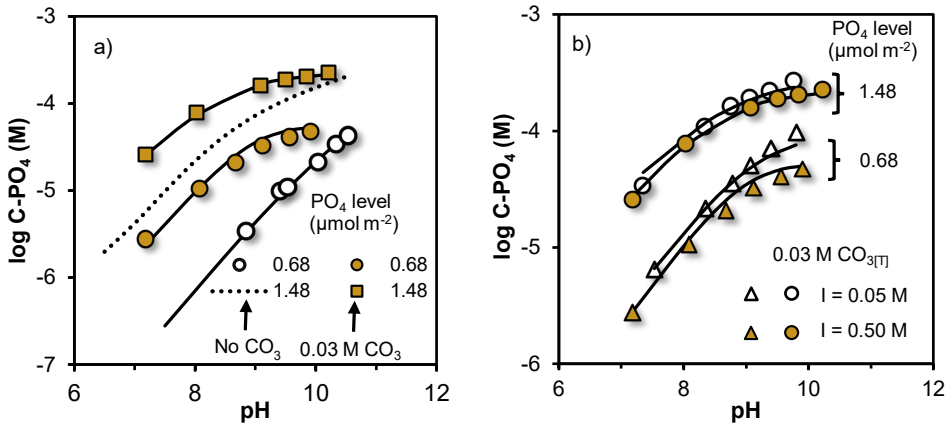

Figure 6.3. Logarithm of the equilibrium concentration of PO_4 as a function of pH in closed systems with Fh. Symbols are experimental results, and lines are CD model calculations using the parameter set of Table 6.1. The total Fe content was 4.5 mM for all the series, except for the colored triangle series in panel b, whose total Fe concentration was 4.9 mM. The calibrated specific surface area of the Fh suspensions used here was SSA = 765 $m^2\ g^{-1}$ at a molar mass of M_{nano} = 98.76 g mol^{-1} Fe. Panel a shows the effect of the addition of 0.03 M CO_3 (colored symbols) on the equilibrium PO_4 concentration for systems with two initial PO_4 loadings (0.68 and 1.48 µmol PO_4 m^{-2}). As reference, the equilibrium concentration of PO_4 in monocomponent systems has been measured and/or modeled (open symbols and dotted line). All data correspond to systems with an ionic strength of 0.5 M, made by adding additionally $NaNO_3$. Panel b presents the effect of the ionic strength (0.05 M for open symbols, 0.5 M for colored symbols) on the equilibrium PO_4 concentration for systems with a total $CO_{3[T]}$ = 0.03 M for two initial PO_4 loadings, as given.

The increase of the PO_4 adsorption with the increase in ionic strength can be understood from a better screening of the repulsive interface charge at a higher ionic strength. The trend observed in Figure 6.3b agrees with the ionic strength dependency of the specific adsorption of anions in general as reported for monocomponent systems with Fh.[37,45,48] The adsorption of CO_3 contributes also to this trend as discussed in Section 6.3.3.2.

6.3.3. Surface Complexation Modeling

In this section, we will explore the main mechanisms of the CO_3 adsorption to Fh by interpreting with the CD model the results of the competitive CO_3–PO_4 adsorption experiments.[32] A similar approach was successfully applied previously by Rahnemaie et al.[29] for describing the adsorption of CO_3 onto goethite.

6.3.3.1. Surface Structure of Ferrihydrite

Presently, we will apply the multisite ion adsorption model recently developed for Fh.[37] A structural analysis of the surface [37] reveals the presence of two types of reactive surface groups at the surface of Fh, namely singly ($\equiv FeOH^{-1/2}$) and the triply ($\equiv Fe_3O^{-1/2}$) coordinated groups. The singly coordinated groups are dominantly present having a total site density of 5.8 ± 0.3 nm^{-2} or 9.6 µmol m^{-2}. Based on the surface structure, two types of singly coordinated groups are defined: those that only allow the formation of monodentate surface complexes ($\equiv FeOH(a)^{-1/2}$), and those that in addition allow the formation of binuclear bidentate surfaces complexes ($\equiv FeOH(b)^{-1/2}$) with *e.g.* PO_4 and AsO_4 ions.[37] The

site densities of these $\equiv FeOH(a)^{-1/2}$ and $\equiv FeOH(b)^{-1/2}$ groups are 3.0 ± 0.6 and 2.8 ± 0.6 nm^{-2}, respectively. The triply coordinated groups ($\equiv Fe_3O^{-1/2}$) do not participate directly in the ligand exchange reactions with oxyanions, but they contribute to the development of primary surface charge. The value for the effective site density of the $\equiv Fe_3O^{-1/2}$ groups (1.4 ± 0.5 nm^{-2}) has been derived by fitting PO_4 adsorption data to Fh.[37]

In the model, the proton affinity of both singly and triply coordinated groups has been set equal to the value of the point of zero charge (PZC) of Fh, according to:

$$\equiv FeOH^{-0.5} + H^+ \Leftrightarrow \equiv FeOH_2^{+0.5} \qquad \log K_H = PZC = 8.1 \qquad \text{(Equation 6.4)}$$

$$\equiv Fe_3O^{-0.5} + H^+ \Leftrightarrow \equiv Fe_3OH^{+0.5} \qquad \log K_H = PZC = 8.1 \qquad \text{(Equation 6.5)}$$

The above surface groups may also react with the background electrolyte ions (*i.e.* Na^+, NO_3^-) forming ion pairs. For reasons of consistency, we will rely on the set of adsorption parameters recently published by Hiemstra and Zhao[37] to describe the PO_4 adsorption to Fh.

6.3.3.2. Carbonate Surface Complexes

Structural information about surface complexes obtained with *in situ* spectroscopy studies is useful to formulate, within the CD model approach, a set of reactions that realistically reflect the molecular picture of the adsorption mechanisms. For CO_3, the surface speciation at the mineral–solution interface of metal-(hydr)oxides has been analyzed in several *in situ* spectroscopy studies.

Attenuated total reflectance-Fournier transformed infrared (ATR-FTIR) spectra have been interpreted previously as evidence for the dominant formation of inner-sphere monodentate CO_3 complexes at the surfaces of goethite.[51–53] The basis of this interpretation was the extent of peak splitting of the v_3 band (Δv_3) of the O–C–O asymmetric stretching frequency, taking as a reference the Δv_3 value (80–137 cm^{-1}) for the formation of inner-sphere monodentate Co(III)-carbonato complexes in solution.[54] A critical evaluation by Hiemstra et al.,[55] combined with interpreting the charge distribution of the CO_3 surface species with SCM, suggested the dominant formation of inner-sphere bidentate complexes of CO_3 adsorbed to goethite. Bargar et al.[56] characterized the adsorption of CO_3 onto the hematite surface at various values of pH and ionic strength with ATR-FTIR spectroscopy and vibrational frequency calculations. The formation of an inner-sphere bidentate complex dominated the adsorption of CO_3 to hematite, especially at a high background electrolyte concentration (*i.e.* 0.1 M NaCl), whereas outer-sphere complexes may be relevant at a low pH and a low ionic strength. Kubicki et al.[57] applied MO/DFT calculations on molecular clusters to model the IR vibrational frequencies of the surface complex structures for a series of oxyanions (*i.e.* CO_3^{2-}, PO_4^{3-}, SO_4^{2-}, AsO_4^{3-}). A good agreement was found between the MO/DFT derived frequencies of a hydrated CO_3 bidentate complex and the experimental frequencies reported by Bargar et al.[56]

For Fh, recent evidence obtained with *in situ* ATR-FTIR spectroscopy and DFT calculations also suggests the formation of inner-sphere bidentate complex as one of the main adsorption mechanisms for CO_3 under atmospheric moisture conditions.[17] Therefore, we will first consider in our modeling the formation of a binuclear bidentate carbonate complex (BC) with ligand exchange according to:

$$2 \equiv FeOH(b)^{-0.5} + 2H^+(aq) + CO_3^{2-}(aq) \Leftrightarrow \equiv (FeO)_2^{-1+\Delta z=0}CO^{\Delta z=1} + 2\,H_2O(l) \quad \log K_{BC} \qquad \text{(Equation 6.6)}$$

in which Δz_0 and Δz_1 are the charge attributed to the surface and inner Stern plane by the adsorbed ions ($\Delta z_0 + \Delta z_1 = 0$).

Solely considering this BC complex in the modeling provides a good description of the experimental PO_4 adsorption data for the series with $CO_{3[T]}$ levels, below 0.03 M. However, the quality of fitting the entire experimental data set was rather poor ($R^2 = 0.85$, $n = 146$). The pH-dependency of the PO_4 adsorption to Fh was underestimated at the higher values of $CO_{3[T]}$, especially in the systems with the largest amount of added PO_4 (*i.e.* 1.07 and 1.48 μmol m^{-2}). Additionally, the effect of ionic strength on the PO_4–CO_3 competition was not well described.

In solution, Na^+ and CO_3^{2-} ions may interact forming relatively weak, yet important, ion pairs.[58,59] A similar interaction may occur at solid–solution interfaces. For a subset of data ($n = 58$), comprising only the adsorption series with $CO_{3[T]}$ of 0.03 and 0.1 M at three ionic strength levels ($I = 0.05$, 0.1, or 0.5 M), good description ($R^2 = 0.97$) was found if a ternary complex was included. The formation of a binuclear bidentate complex of CO_3 interacting with a Na^+ ion (BCNa) has been suggested previously for goethite[29,51] and can be formulated as:

$$2 \equiv FeOH(b)^{-0.5} + 2\ H^+(aq) + CO_3^{2-}(aq) + Na^+(aq) \Leftrightarrow \equiv(FeO)_2{}^{-1+\Delta z0}CO\cdots Na^{+1+\Delta z1} + 2\ H_2O(l) \qquad \log K_{BCNa} \qquad \text{(Equation 6.7)}$$

Modeling the results of our CO_3–PO_4 competition experiments suggests attribution of the full Na^+ charge to the 1-plane of the Stern layer (Section 6.3.3.3). It does not necessarily imply that Na^+ forms an inner-sphere complex with the outer O- ligand of the adsorbed CO_3. According to Bargar et al.,[56] a mechanism of $NaCO_3$ inner-sphere complexation is less likely, based on MO/DFT calculations comparing the experimental and calculated vibrational frequencies of CO_3 adsorbed to hematite. If the Na^+ ion of our resolved BCNa complex binds as a $Na^{\cdots}CO_3$ ion pair, the Na^+ ion may search for the interfacial location that allows the strongest electrostatic attraction, which will be the 1-plane as the electric potential of the inner Stern plane is most negative in our PO_4–CO_3 systems.

By using two CO_3 inner-sphere complexes, a substantial part of our experimental data set can be well described. However, the adsorption of PO_4 to Fh is slightly over predicted by the model in our systems with the highest $CO_{3[T]}$ levels (0.2 and 0.5 M), *i.e.* the competitive effect of CO_3 is still insufficiently predicted by the model ($R^2 = 0.90$, $n = 146$). It is possible that an additional CO_3 surface complex contributes to the CO_3–PO_4 interaction. To explore the possibilities, we have defined additionally the formation of a monodentate carbonate (MC) complex according to:

$$\equiv FeOH^{-0.5} + H^+(aq) + CO_3^{2-}(aq) \Leftrightarrow \equiv FeO^{-0.5+\Delta z0}CO_2{}^{\Delta z1} + 1\ H_2O(l) \qquad \log K_{MC} \qquad \text{(Equation 6.8)}$$

Note that the MC complex can be formed by reacting with both types of singly $\equiv FeOH^{-1/2}$ groups ($(\equiv FeOH^{-1/2}(a)$ as well as $\equiv FeOH^{-1/2}(b)$). For the surface complex in Equation 6.8, we searched for the charge distribution by free fitting of the CD coefficients, resulting in $\Delta z_0 = 0.26 \pm 0.08$ and $\Delta z_1 = -1.26 \pm 0.08$ v.u. The obtained charge distribution shows that about 2/3 of the charge of the divalent CO_3^{2-} ion is present at the Stern plane and about 1/3 is at the surface. According to the Pauling bond valence concept, this can be interpreted as the formation of a monodentate inner-sphere complex having one O-ligand common with the Fe in the surface while both other O-ligands are outside the surface. The values for the CD coefficients found by fitting are in good agreement with the ones found by optimizing the geometry of that complex with MO/DFT, *i.e.* $\Delta z_0 = +0.34$, $\Delta z_1 = -1.34$ v.u., which will be discussed in Section 6.3.3.3.

The log*K* value for the above set of reactions is presented in Table 6.1 and corresponds to the average value found by evaluating the data at four different evaluation scales (*i.e.* % PO_4 adsorbed, PO_4 solution concentration, log PO_4 solution concentration, and μmol PO_4 adsorbed m^{-2}). In Table S6.4 of the Supplementary Information, the log*K* values fitted for each evaluation scale are given. The use of the parameter set presented in Table 6.1 and Table S6.4 resulted in a good description of the entire data set ($R^2 > 0.94$, for all different scales).

Table 6.1. Table defining the surface species, CD values, and log*K* for the adsorption reactions of CO_3 and PO_4 to ferrihydrite. The log*K* values for the CO_3 surfaces species were found by fitting the experimental results of the binary adsorption systems CO_3-PO_4 (n = 146). The surface site densities are from Hiemstra and Zhao[37] with ≡FeOH(a) = 3.0 nm^{-2}, ≡FeOH(b) = 2.8 nm^{-2}, and ≡Fe_3O = 1.4 nm^{-2}. The capacitance values for the extended Stern layer model are C_1 = 1.15 F m^{-2} and C_2 = 0.90 F m^{-2}.

Surface species	ID[ǂ]	≡FeOH(a)$^{-0.5}$[&]	≡FeOH(b)$^{-0.5}$[&]	≡$Fe_3O^{-0.5}$	Δz_0	Δz_1	Δz_2	H^+	CO_3^{2-}	Na^+	PO_4^{3-}	log*K*
(≡FeO)$_2$CO(b)	BC	0	2	0	0.66	-0.66	0	2	1	0	0	21.73 ± 0.09*
(≡FeO)$_2$CO--Na(b)	BCNa	0	2	0	0.65	0.35	0	2	1	1	0	22.38 ± 0.09*
≡FeOCO$_2$(a)	MC	1	0	0	0.34	-1.34	0	1	1	0	0	11.60 ± 0.01*
≡FeOCO$_2$(b)	MC	0	1	0	0.34	-1.34	0	1	1	0	0	11.60 ± 0.01*
(≡FeO)$_2$PO$_2$(b)	BP	0	2	0	0.46	-1.46	0	2	0	0	1	28.31 ± 0.04[s]
(≡FeO)$_2$POOH(b)	BPH	0	2	0	0.65	-0.65	0	3	0	0	1	33.52 ± 0.13[s]
≡FeOPO$_2$OH(a)	MPH	1	0	0	0.28	-1.28	0	2	0	0	1	26.36 ± 0.20[s]
≡FeOPO$_2$OH(b)	MPH	0	1	0	0.28	-1.28	0	2	0	0	1	26.36 ± 0.20[s]
≡FeOPO(OH)$_2$(a)	MPH_2	1	0	0	0.33	-0.33	0	3	0	0	1	29.84 ± 0.23[s]
≡FeOPO(OH)$_2$(b)	MPH_2	0	1	0	0.33	-0.33	0	3	0	0	1	29.84 ± 0.23[s]
		ρAN_{s1}[#]	ρAN_{s2}[#]	ρAN_{s3}[#]	Σ_1[#]	Σ_2[#]	Σ_3[#]	H_{tot}	$CO_{3,tot}$	Na_{tot}	$PO_{4,tot}$	

ǂ BC = Bidentate CO_3 inner-sphere; BCNa = Bidentate CO_3 inner-sphere with Na; MC = Monodentate CO_3 inner-sphere, BP = Bidentate PO_4 inner-sphere; BPH = Bidentate PO_4 inner-sphere protonated; MPH = Monodentate PO_4 inner-sphere protonated; MPH_2 = Monodentate PO_4 inner-sphere doubly protonated.

& ≡FeOH(a)$^{-0.5}$ forms only monodentate complexes with PO_4 and CO_3, whereas ≡FeOH(b)$^{-0.5}$ can form mono and bidentate complexes, according to the ion adsorption model for Fh from Hiemstra and Zhao.[37]

* Values of log*K* (mean ± SD) are the average of the values obtained using four different fitting scales (see SI).

s Taken from Hiemstra and Zhao.[37]

Sums of these columns are equal to the change of charge as defined Hiemstra and van Riemsdijk.[32]

Presently, we cannot entirely rule out for CO_3 the formation of an outer-sphere complex at the surfaces of Fh. In our modeling, considering the formation of outer-sphere complexes instead of the monodentate inner-sphere yields a similar quality of fitting (Appendix D in the SI) and describes the adsorption of CO_3 to Fh in monocomponent systems well. Spectroscopic information does suggest the formation of CO_3 outer-sphere complexes at the interfaces of Fe-(hydr)oxides. However, these complexes were particularly found at low pH and a low to very low ionic strength.[56] For other oxyanions (SeO_4^{2-}, CrO_4^{2-}, SO_4^{2-}), recent spectroscopy suggests a combination of inner- and outer-sphere complexes as mechanism to explain the adsorption to Fe-(hydr)oxides.[47,60,61] However, all that presently matters is that according to the CD model any additional complex (either outer-sphere or inner-sphere complex) is contributing little in our systems. Binuclear bidentate complex formation of CO_3 is found to be dominant, as shown later in detail.

It is important to note that the introduction of a HCO_3^- surface complex did not improve the description of our data, yet HCO_3^- dominates the solution speciation of CO_3 over most of our experimental pH range. This agrees with the observation that surface complexes with CO_3^{2-} complexes

dominate the surface speciation under atmospheric moisture conditions, whereas HCO_3^- complexes are only preferentially formed upon dehydration.[17,62,63] In addition, our optimization of the geometry of a monodentate HCO_3^- complex with MO/DFT shows that the proton of the adsorbed HCO_3 spontaneously shifts toward an adjacent $\equiv FeOH^{-1/2}$ group if present in an O–H···O bond. This spontaneous shift leads formally to the formation of a $\equiv FeOH_2^{+1/2}$ group and deprotonation of monodentate inner-sphere complex.

6.3.3.3. Charge Distribution Coefficients

In the CD model, the ionic charge of an inner-sphere complex is distributed over two different electrostatic planes at the interface. This interfacial charge distribution is accounted for by means of the CD coefficients (Δz_0, Δz_1). In the original approach,[32] the CD coefficients were estimated by assuming symmetrical distribution of the charge of the central ion over its ligands (Pauling bond valence). However, differences in the bond lengths between the central ion and the coordinating ligands will lead to an asymmetrical charge distribution. Bond length differences can be interpreted with the semi-empirical Brown valence concept,[34,35] which relates bond length (R) to a bond valence (s).

In our approach, we have used MO/DFT calculations to optimize the geometry of a series of different CO_3–Fe complexes and derive subsequently the values of the CD coefficients. This approach has the advantage of restricting the number of adjustable parameters per surface species to one (*i.e.* log$K$). In Table 6.2, the ionic charge distribution values (n_0, n_1) are presented for the different CO_3 surface species considered in our modeling (Section 6.3.3.2). Detailed information about the bond length distances and the application of the Brown bond concept is given in Appendix I of the Supplementary Information. The final CD coefficients (Δz_0, Δz_1) include the change of charge that results from the protons involved (n_{H0}, n_{H1}) in the formation reactions (Equations 6.6 – 6.8). In addition, there is a correction term ($\pm \varphi_m \Lambda_0$) for the interfacial water dipole orientation. The factor φ_m is a constant (0.17 ± 0.02),[42] and Λ_0 is the change of charge relative to that of the reference state from which the reaction is defined. Therefore, $\Lambda_0 = n_0 + n_{H0} + \Sigma\, n_{ref} \times z_{ref}$ in which n_{ref} and z_{ref} are the number and the charge of the reference surface groups involved, respectively.[39]

As follows from the n_0 and n_1 values presented in Table 6.2, there is some asymmetry in the distribution of the central C^{4+} charge over the different -O ligands of the CO_3 surface complexes. Slightly more negative charge is attributed to the Fe–O–C bonds in comparison to the symmetrical charge distribution according to the Pauling bond valence concept. The interaction of the bidentate carbonate complex with a Na^+ ion does not affect significantly the n_0 and n_1 values of the O-ligands in this ternary complex, which implies that no significant transfer of charge occurs from the Na^+ to the O- ligands of the bidentate complex. Free fitting of the CD coefficients of the BCNa complex suggests a full attribution of the Na^+ charge to the 1-plane of the Stern layer. The Δz_1 value of the BCNa complex in Table 6.2 includes the charge of Na^+.

The results presented in Table 6.2 are for complexes optimized using an uncharged $(H_2O)_2Fe_2(OH)_6(OH_2)_2$ template (A) that has also been used previously to derive the CD coefficients for the PO_4 surface species.[37,42] It has been shown that the charge of the template may influence the calculated CD coefficients;[29] that is, the charge distribution may depend on the protonation/deprotonation of the overall moiety.[5] Calculations performed with a positive charged template, $(H_2O)_2Fe_2(OH)_4(OH_2)_4$ (B) resulted in more transfer of negative charge (–0.09 v.u.) to the common O- ligands for the binuclear bidentate CO_3 complexes in comparison with template A. Nevertheless, this variation is still low in comparison with the uncertainty of the CD coefficients (± 0.25

v.u.) found at free fitting of the CD value using our experimental data. For the CO_3–PO_4 competition experiments, the same quality of the fitting was obtained using either template A or B as model. However, use of template A leads to a better prediction of the adsorption of CO_3 in monocomponent systems.

Table 6.2. Charge Distribution values (n_0, n_1) of relevant CO_3 surface complexes derived from the MO/DFT optimized geometries, applying the Brown bond valence concept. The CD coefficients (Δz_0, Δz_1) include the change of charge due to the reaction with protons (n_{H0}, n_{H1}) and a correction for the interfacial water dipole orientation.

Surface species	ID[‡]	n_0[&]	n_1[&]	Δz_0	Δz_1	Δz_2
$(\equiv FeO)_2CO$(b)	BC	-1.40 ± 0.01	-0.60 ± 0.01	0.66	-0.66	0
$(\equiv FeO)_2CO$--Na(b)	BCNa	-1.42 ± 0.02	-0.58 ± 0.02	0.65	0.35	0
$\equiv FeOCO_2$(a)	MC	-0.70 ± 0.01	-1.30 ± 0.01	0.34	-1.34	0
$\equiv FeOCO_2$(b)	MC	-0.70 ± 0.01	-1.30 ± 0.01	0.34	-1.34	0

[‡] BC = Bidentate CO_3 inner-sphere; BCNa = Bidentate CO_3 inner-sphere with Na; MC = Monodentate CO_3 inner-sphere.
[&] Mean values (±SD) obtained from six different quantum chemical models (BP86, B3LYP, EDF1, EDF2, BLYP, ωP97X-D).

6.3.4. Model Applications

6.3.4.1. Carbonate Adsorption in Single-Ion Systems

The suitability of the above-derived CD model parameters for describing the adsorption of CO_3 in single-ion systems with Fh will be evaluated here. Batch adsorption experiments were performed using three $Fe_{[T]}$ levels (5.1, 10.4, and 15.5 mM) at a fixed initial $CO_{3[T]}$ of 1 mM and a constant ionic strength of 0.10 M $NaNO_3$. The pH of the systems varied from 6.9 to 10.5. As shown in Figure 6.4a, the adsorption of CO_3 to Fh continuously decreases as the solution pH increases from 7 to 10 (symbols). The solid lines are the corresponding CD model predictions for the adsorption of CO_3 in these systems, using the parameter values of Table 6.1. Interestingly, these parameters have been derived without any direct measurement of the CO_3 adsorption. The excellent prediction obtained for the single-ion systems shows that the CD model can be well parametrized for CO_3 by only measuring the competitive effect of this anion on the adsorption of PO_4 to Fh. In addition, it is noted that the total concentration of CO_3 is 4 to 500 times lower in the single-ion experiments than applied in the competition experiments. The good agreement between the experimental adsorption edges and the model predictions evidences the reliability of the CD model to describe the adsorption of CO_3 over a broad range of conditions. This is highly relevant from an environmental point of view as CO_3 is omnipresent in soils, sediments, rivers, groundwater, and marine systems at highly variable conditions. It will contribute to an improved modeling of the geochemical cycle of a range of compounds relevant from the environmental perspective.[64–66]

According to our model simulations (Figure 6.4a), the adsorption maximum of CO_3 to Fh occurs around pH ~6.5–7.0. This maximum is nearly independent from the solid-to-solution ratio of the system. Above pH ~6.5, the CO_3 adsorption decreases at increasing the pH values, while the opposite occurs below pH ~6.5. This behaviour has also been found for goethite by Villalobos and Leckie[16] and can be predicted very well with the CD model.[29] A similar pH-dependency has also been found by Zachara *et al.*[24] for single-ion systems with Fh. Even though measured for very low CO_3 concentrations (*i.e.* µM

levels), the pH-dependency of this data set can also be predicted well with the present CD model (Table 6.1), as shown in Figure S6.6 in the Supplementary Information.

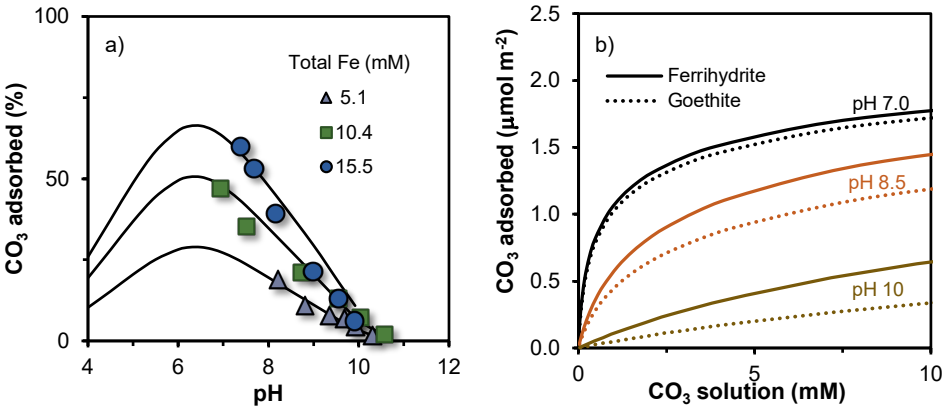

Figure 6.4. (a) Adsorption edges of CO_3 in single-ion systems with ferrihydrite at a constant ionic strength (I = 0.1 M $NaNO_3$). The black lines are CD model predictions using the parameter set of Table 6.1, that has been derived based on only interpreting competitive PO_4 adsorption data in carbonate systems. The adsorption edges are for systems with $CO_{3[T]}$ = 1 mM and three $Fe_{[T]}$ (5.1, 10.4, and 15.5 mM). The specific surface area of ferrihydrite was A = 625 m^2 g^{-1} at a corresponding molar mass of M_{nano} = 95.14 g mol^{-1} Fe. (b) Modeled adsorption isotherms of CO_3 to ferrihydrite (full lines) and goethite (dotted lines) at a constant ionic strength (I = 0.10 M) and three pH values: 7.0, 8.5, and 10.0. Model parameters for ferrihydrite are from Table 6.1, whereas for goethite they are taken from Rahnemaie et al.[29]

The characteristic pH-dependency of the CO_3 adsorption with a maximum in the adsorption edge (Figure 6.4a) is due to a change in solution speciation. The pH-dependency of adsorption is a trade-off between proton binding to surface and solution species. According to the thermodynamic consistency principle,[39,67,68] the change (∂) of the logarithm of the solution concentration with pH is:

$$\left(\frac{\partial \log C_{CO3(T)}}{\partial pH}\right)_{\Gamma_{CO3}} = \left(\chi_H - n_H\right)_{pH} \qquad \text{(Equation 6.9)}$$

in which χ_H is the molar ratio of the proton excess adsorption upon adsorption of CO_3, known as proton co-adsorption ratio, and n_H is the mean number of protons bound to dissolved CO_3 species, both defined relatively to a chosen reference species. Calculations show that the proton co-adsorption is about χ_H~ 1.5 at neutral pH. Using CO_3^{2-}(aq) as reference, n_H = +2 when H_2CO_3(aq) dominates the system at pH < logK_{H2} = 6.35, and $\chi_H - n_H < 0$, while $\chi_H - n_H > 0$ for n_H=+1 in a solution dominated by HCO_3^- (aq) (pH > 6.35). The change of n_H leads to the remarkable switch in pH-dependency shown in Figure 6.4a. At pH ~ logK_{H2}, n_H=1.5 and $\chi_H - n_H$~0. This implies that at this condition, there will be no pH-dependency of the CO_3 adsorption. This coincides with the top of the curves in Figure 6.4a. The above thermodynamic consistency principle can also be applied to the adsorption of other ions, including the adsorption of Si to Fh, as discussed recently in detail.[5]

In Figure 6.4b, the modeled adsorption isotherms of CO_3 to Fh (full lines) are presented for systems at pH 7.0, 8.5, and 10.0. For comparison, the corresponding adsorption isotherms to goethite (α-FeOOH) have also been modeled (dotted lines), using the CD model parameters from Rahnemaie et al.[29] At pH 7.0, the adsorption of CO_3 to both Fe-(hydr)oxide minerals is similar over the entire range of solution concentrations. As the pH increases, more CO_3 is adsorbed to Fh than to goethite, under similar solution

conditions. This difference is more significant at increased CO_3 loadings, and it can be related to differences in the surface speciation of CO_3 of both minerals. Particularly important is the enhanced formation of the BCNa complex in the Fh systems. Formulating the formation of the BCNa complex according to:

$$\equiv(FeO)_2^{-1+\Delta z0}CO^{\Delta z1} + Na^+(aq) \Leftrightarrow \equiv(FeO)_2^{-1+\Delta z0}CO\cdots Na^{+1+\Delta z1} \quad \text{(Equation 6.10)}$$

the corresponding equilibrium constant of the reaction is log$K$ +0.65 for Fh and log$K$ +0.02 for goethite. The difference shows that for a given solution condition, the formation of the BCNa is more favored at the surfaces of Fh. The pH and concentration dependence of the CO_3 surface speciation in Fh is presented in Figure 6.5 and Figure S6.5 (see SI), respectively.

6.3.4.2. Carbonate Surface Speciation

In this section, we evaluate the effect of pH, total CO_3 concentration, and the presence of PO_4 on the surface speciation of adsorbed CO_3 (Figure 6.5). It is observed that the distribution of the adsorbed CO_3 over the different surface species is strongly affected by the pH of the solution. The BC complex is the dominant CO_3 surface species in the low pH range (Figure 6.5a–d). As the pH increases, the relative contribution of the BCNa complex to the total CO_3 adsorption gradually increases. The relative importance of the BCNa complex further increases at a high loading of CO_3 and/or PO_4 (Figure 6.5 c and d), which can be understood from the increase of the negative value of the electrostatic potential in the inner Stern (1-) plane. This leads for the Na^+ ions to a stronger attraction and formation of the ternary surface species.

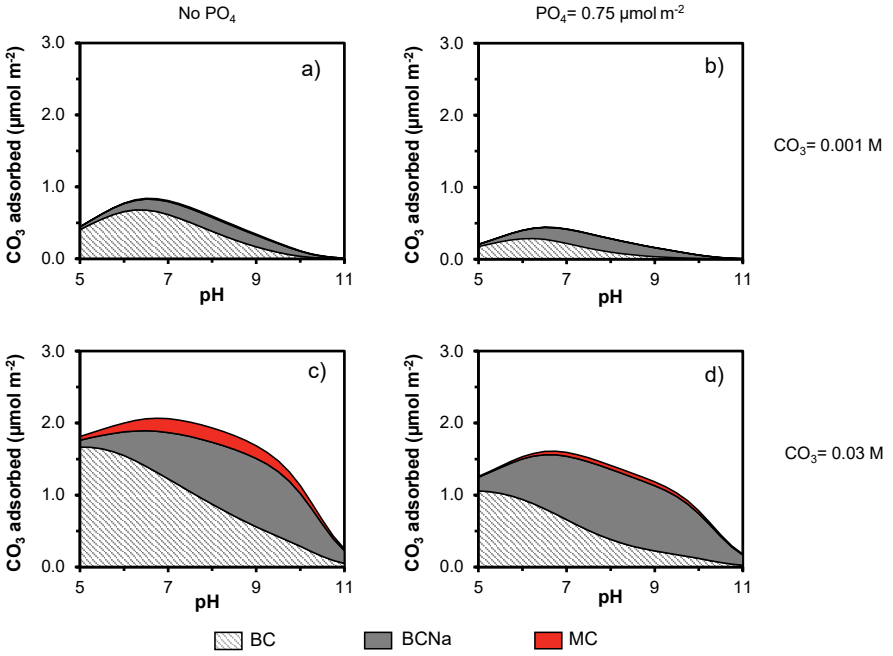

Figure 6.5. Surface speciation of CO_3 on ferrihydrite as a function of pH for single CO_3 systems (left panels) and binary CO_3–PO_4 systems (right panels). The CD model calculations were performed with the CO_3 and PO_4 parameter set presented Table 6.1. The upper panels (a and b) are for systems with a $CO_{3[T]}$ = 0.001 M, whereas the lower panels (c and d) are for systems with $CO_{3[T]}$ = 0.03 M. The ferrihydrite concentration was 0.5 g L^{-1} with an assumed SSA of 670 m^2 g^{-1}. The ionic strength in all the systems was adjusted to 0.05 M by adding $NaNO_3$.

Figure 6.5 also shows that the formation of the MC complex is almost negligible at a low $CO_{3[T]}$ level (Figures 6.5 a and b vs c and d). This fits with our modeling experience (Section 6.3.3.2) that the incorporation of this MC species was only necessary to describe the results of the CO_3–PO_4 competition experiments at the high $CO_{3[T]}$ levels. In addition, comparison of the single and binary ion systems in Figures 6.5 shows that at the chosen $CO_{3[T]}$ level, the formation of the MC complex is reduced when PO_4 is present. This effect also follows from electrostatic considerations. As mentioned before, the specific adsorption of PO_4 induces uncompensated negative charge that increases the negative electrostatic potential of the inner Stern or 1-plane (Figure S6.7 in the SI). Since the MC complex introduces more negative charge in the 1-plane (Δz_1= -1.34 v.u.) than the BC complex (Δz_1= -0.66 v.u.), the formation of the former surface complex is most suppressed in the presence of PO_4.

6.3.4.3. PO_4 Extraction with Carbonate Solution

The competitive interaction CO_3–PO_4 has been traditionally used in soil chemical analysis to evaluate the soil PO_4 availability in natural and agricultural systems.[69,70] More recently, this interaction has been applied to derive the effective reactive surface area (RSA) of soils.[31] In the present study, we have measured the PO_4 adsorption isotherm for Fh in 0.5 M $NaHCO_3$ (pH = 8.70 ± 0.01) over a range of equilibrium PO_4 concentrations (~5–650 µM) that represents the conditions typically found when natural and fertilized field soil samples are extracted with 0.5 M $NaHCO_3$.[70] The lines in Figure 6.6a are predictions with the CD model, showing an accurate prediction of the PO_4 adsorption density (in µmol m^{-2}) for the systems in competition with CO_3, using the set of adsorption parameters presented in Table 6.1. As an example of the competitive effect of added $NaHCO_3$ at a pH condition relevant in soil extractions, additional PO_4 adsorption isotherms have been calculated for systems with an increasing $CO_{3[T]}$ (dashed lines), as well as for systems with no CO_3 addition (red dotted line). CO_3 is a good competitor at high concentrations, removing a significant amount of adsorbed PO_4 from the surfaces of Fh. It diminishes the high affinity character (shape) of the PO_4 adsorption isotherm (Figure 6.6a).

Figure 6.6b shows the adsorption isotherms of PO_4 for goethite (α-FeOOH) calculated with the CD model parameters derived by Rahnemaie et al.[29] The latter material has been used to derive the RSA soil samples, while results suggests that the natural oxide fraction is dominated by nanoparticles (*e.g.* Fh).[31] In the absence of CO_3, the adsorption of PO_4 is similar for both Fe-(hydr)oxide materials. However, CO_3 removes less PO_4 from goethite than from Fh at the same solution conditions. The PO_4 adsorption isotherm in goethite remains steeper. The results in Figure 6.6 agree with the model simulations presented previously in Figure 6.4b, which showed that at high pH, CO_3 has a higher adsorption affinity for Fh than for goethite. This results in a stronger competition with PO_4 in the systems with Fh.

With the collected information on Figure 6.6, one may assess the RSA (m^2 g^{-1} soil) based on the change (Δ) of the PO_4 amount in solution and the change in surface loading $\Delta\Gamma_{PO4}$ (mol m^{-2}), according to:

$$\mathrm{RSA} = \frac{\Delta\,(c_{PO_4} \times \mathrm{SSR})}{\Delta\,\Gamma_{PO_4}} \qquad \text{(Equation 6.11)}$$

in which C_{PO4} is the experimental PO_4 concentration (mol L^{-1}) and SSR is the solution-to-soil ratio (in L kg^{-1}). The measured change in concentration ΔC_{PO4} (mol L^{-1}) is translated into a corresponding change in PO_4 surface loading $\Delta\Gamma_{PO4}$ (µmol m^{-2}) calculated with the CD model.

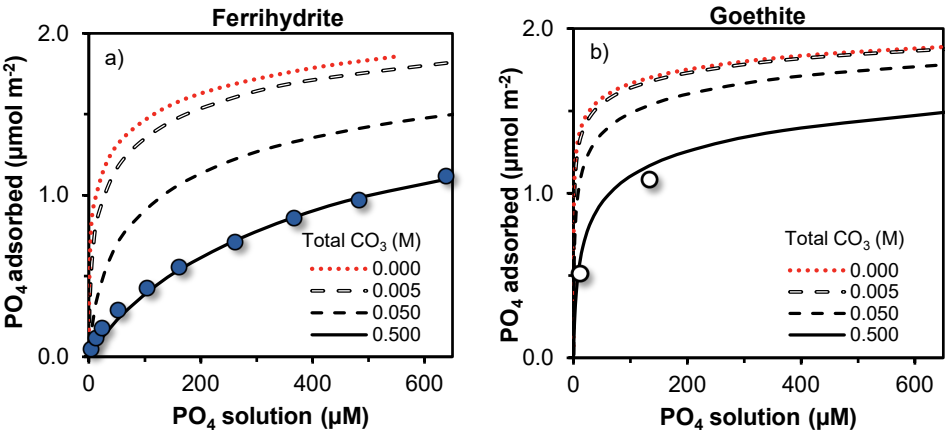

Figure 6.6. **Panel a**: Adsorption isotherm of PO_4 to ferrihydrite in 0.5 M $NaHCO_3$ at pH 8.70 ± 0.01. The specific surface area of the ferrihydrite was A = 735 m^2 g^{-1} with a respective molar mass of M_{nano}= 97.98 g mol^{-1} Fe. The total reactive area was 375 m^2 L^{-1}. The symbols are experimental data and the (full) line is the model prediction. For comparison, the calculated PO_4 adsorption isotherms for systems with 0 (red dotted line), 0.005 (open-dashed line), and 0.05 M (dashed line) $CO_{3[T]}$ have also been included in the graph. The ionic strength was fixed at 0.5 M by adding $NaNO_3$ when required. CD model calculations were performed with the parameters presented in Table 6.1. **Panel b**: Modeled adsorption isotherms of PO_4 to goethite in the absence (red dotted line) and presence (black lines) of CO_3 for the same solution as used in panel a. Modeling parameters and PO_4 adsorption data points were taken from Rahnemaie et al.[29]

As follows from Figure 6.6, the relation between ΔC_{PO4} and $\Delta\Gamma_{PO4}$ value is clearly determined by the slope of the adsorption isotherm and consequently depends on the type of Fe-(hydr)oxide used as reference material. A steeper adsorption isotherm will lead to more buffering of the PO_4 concentration, *i.e.* smaller ΔC_{PO4} at the same $\Delta\Gamma_{PO4}$, leading to a lower value for the calculated RSA. In 0.5 M $NaHCO_3$, goethite has a PO_4 adsorption isotherm that is relatively flat at a high PO_4 concentration compared to Fh. This implies that its use as reference oxide to calculate the reactive surface area of soils will lead to a higher value than with the use of Fh as reference oxide. It illustrates that precise information about the adsorption isotherm of the natural oxide fraction is essential for a correct assessment of the effective RSA of soil samples. In a forthcoming contribution, we will evaluate the use of Fh as nanoparticulate proxy for the natural metal oxide fraction of soils by applying the information collected in the present study.

6.4. Conclusions

In the present study, we aim to quantify the interaction of CO_3 with Fh by measuring its competitive effect on the adsorption of PO_4 in closed systems. Our analysis starts by evaluating the effect of high CO_3 concentrations on the solubility of Fh, since Fe(III)-CO_3 complexes may form while our freshly prepared Fh is relatively soluble. Three aqueous species $FeOHCO_3^0$(aq), $Fe(CO_3)_3^{3-}$(aq), and $Fe(CO_3)_2(OH)_2^{3-}$(aq) are found to be relevant according to modeling literature[38] and our own data. The latter species is most important in our closed systems, while both others are more relevant in open systems. At the chosen conditions in the adsorption experiments, only a very small fraction of Fh (< 0.4%) was dissolved, enabling straightforward interpretation of the collected CO_3 adsorption data.

CO_3 competes with PO_4 for the adsorption sites of the Fh surface. However, PO_4 has a significantly larger affinity than CO_3 for these binding sites, meaning that high CO_3/PO_4 concentration ratios are needed to remove PO_4 efficiently from the surface of Fh. The competitive interaction CO_3–PO_4 in Fh systems was successfully described with the CD model using only the experimental PO_4 adsorption data for parametrization. The CD coefficients of the CO_3 surfaces complexes were derived independently from the MO/DFT optimized geometries. Our study provides insights into the surface speciation of CO_3 that are consistent with the state-of-the-art knowledge of the mineral and surface structure of Fh. CO_3 is predominantly bound as an inner-sphere bidentate (double-corner) complex. At high CO_3 and/or PO_4 loading and a high Na^+ concentration, this $\equiv(FeO)_2CO$ complex interacts with Na^+ forming a ternary $\equiv(FeO)_2CO^{\cdots}Na^+$ complex in which Na^+ most likely forms an ion pair with the adsorbed CO_3. At high CO_3 loading, an additionally surface complex is formed that may be an inner-sphere monodentate complex ($\equiv FeOCO_2$).

We have shown that the CD model, only parametrized with the PO_4 adsorption data from the CO_3–PO_4 competition experiments, can predict the experimental adsorption of CO_3 in monocomponent systems with $CO_{3[T]}$ levels that are relevant in the natural environment (soil, river, groundwater, and seawater). The adsorption of CO_3 in the monocomponent systems reaches a maximum at pH ~6.5 in full agreement with literature results and is thermodynamically consistent with the surface speciation derived. Our CD modeling demonstrates that the CO_3 surface speciation is mainly governed by effects of charge, particularly acting on the potential of the inner Stern layer. Change in environmental conditions such as pH, ionic strength, and concentration of competitive anions will change the relative distribution over the different CO_3 surface species.

Finally, it is shown that our CD model can predict very well the measured adsorption isotherm of PO_4 in Fh systems with 0.5 M $NaHCO_3$ at high pH. In comparison with goethite, CO_3 has a significantly higher adsorption affinity to Fh, which leads to a marked decrease in the high affinity character of the adsorption isotherm of PO_4 in 0.5 M $NaHCO_3$. The higher adsorption of CO_3 to Fh is particularly evident at high pH values and it is related to the enhanced interaction of Na^+ with the BC complex forming BCNa. The parametrized CO_3–PO_4 interaction can be used to interpret the equilibration data of soil extractions in 0.5 M $NaHCO_3$ solution to reveal RSA, using Fh as reference material for the natural oxide fraction. A consistent determination of the RSA may improve the prediction of the adsorption behavior of nutrients and pollutants in environmental samples with surface complexation modeling.

Acknowledgements

We highly appreciate the work of Jelle Jansen in collecting part of the CO_3–PO_4 competition data. We are also grateful for the accurate and attentive work regarding the sample analysis by Peter Nobels and Johan Uijtenbroek, from the Chemistry and Biology Soil Laboratory (CBLB). The grant provided by the University of Costa Rica (UCR) to the first author is gratefully acknowledged.

Supplementary Information

A. Experimental conditions of the batch adsorption systems

Table S6.1. Chemical conditions and characteristics of the ferrihydrite suspensions used in the batch experiments in binary CO_3-PO_4 competition systems and in monocomponent systems with CO_3.

Fh series	Batch number	Ionic strength	Total CO_3	Total PO_4	Total Fe	M_{nano}	SSA	Fh
		M	M	mM	mM	g mol^{-1} Fe	m^2 g^{-1}	g L^{-1}
A	1-Binary	0.5	0.030	0.500	7.20	96.33	672	0.69
B	2-Binary	0.5	0.100	0.500	7.20	96.33	672	0.69
C	3-Binary	0.5	0.200	0.500	7.20	96.33	672	0.69
D	4-Binary	0.5	0.500	0.500	7.20	96.33	672	0.69
E	5-Binary	0.5	0.100	0.750	7.31	96.33	672	0.70
F	6-Binary	0.5	0.500	0.750	7.31	96.33	672	0.70
G	7-Binary	0.1	0.030	0.500	7.46	96.33	672	0.72
H	8-Binary	0.1	0.100	0.500	7.46	96.33	672	0.72
I	9-Binary	0.5	0.004	0.251	4.88	98.79	765	0.48
	10-Binary	0.5	0.012	0.251	4.88	98.79	765	0.48
J	11-Binary	0.5	0.030	0.251	4.88	98.79	765	0.48
	12-Binary	0.5	0.100	0.251	4.88	98.79	765	0.48
	13-Binary	0.5	0.500	0.251	4.88	98.79	765	0.48
K	14-Binary	0.05	0.030	0.251	4.48	98.79	765	0.44
	15-Binary	0.05	0.030	0.502	4.48	98.79	765	0.44
	16-Binary	0.5	0.030	0.502	4.48	98.79	765	0.44
L	17-Binary (Isotherm)	0.5	0.500	0.021-1.06	5.20	97.98	735	0.51
M	1-Mono	0.1	0.001	-	10.4	95.14	625	0.99
N	2-Mono	0.1	0.001	-	15.3	95.14	625	1.46
	3-Mono	0.1	0.001	-	5.10	95.14	625	0.50

B. Additional phosphate adsorption series in competition with carbonate

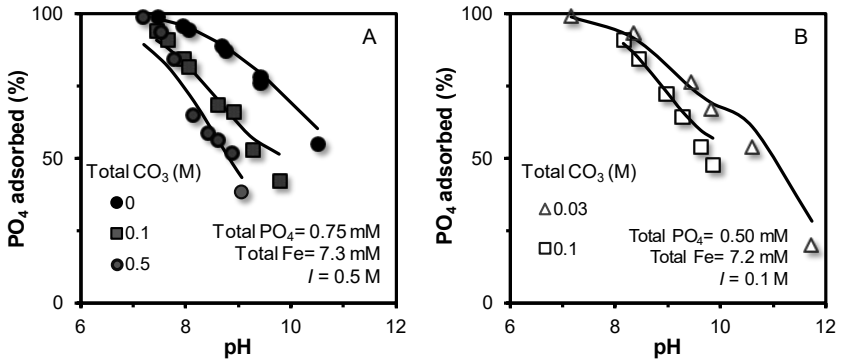

Figure S6.1. Adsorption edges of PO_4 to ferrihydrite in competition systems with CO_3. The symbols are experimental results and the lines are CD model calculations using the parameters set presented in Table 6.1 (main text). The SSA of the ferrihydrite suspensions was A = 672 m^2 g^{-1} with a molar mass of M_{nano}= 96.33 g mol^{-1} Fe. **Panel A**: Total PO_4 and Fe concentrations are 0.75 and 7.3 mM, respectively. The ionic strength was adjusted to 0.5 M using $NaNO_3$ when required. **Panel B**: Total PO_4 and Fe concentrations are 0.50 and 7.2 mM, respectively. The ionic strength was adjusted to 0.1 M, using $NaNO_3$ when required.

C. Thermodynamic databases used in the CD modeling

Table S6.2. Thermodynamic database used in the modeling for the aqueous speciation reactions. Log$K$ values are for I = 0.

Species	Reaction	logK
$NaOH^0$	$Na^+ + OH^- \leftrightarrow NaOH^0$	-0.20 *
$NaNO_3^0$	$Na^+ + NO_3^- \leftrightarrow NaNO_3^0$	-0.60 *
HPO_4^{2-}	$PO_4^{3-} + H^+ \leftrightarrow HPO_4^{2-}$	12.35 *
$H_2PO_4^-$	$PO_4^{3-} + 2H^+ \leftrightarrow H_2PO_4^-$	19.55 *
$H_3PO_4^0$	$PO_4^{3-} + 3H^+ \leftrightarrow H_3PO_4^0$	21.70 *
HCO_3^-	$CO_3^{2-} + H^+ \leftrightarrow HCO_3^-$	10.33 *
$H_2CO_3^0$	$CO_3^{2-} + 2H^+ \leftrightarrow H_2CO_3^0$	16.69 *
$CO_2(g)$	$CO_3^{2-} + 2H^+ \leftrightarrow CO_2(g) + H_2O(l)$	18.15 *
$Na_2CO_3^0$	$CO_3^{2-} + 2Na^+ \leftrightarrow Na_2CO_3^0$	0.01 *
$NaCO_3^-$	$CO_3^{2-} + Na^+ \leftrightarrow NaCO_3^-$	1.27 #
$NaHCO_3^0$	$CO_3^{2-} + Na^+ + H^+ \leftrightarrow NaHCO_3^0$	10.02 #
$NaHPO_4^-$	$PO_4^{3-} + Na^+ + H^+ \leftrightarrow NaHPO_4^-$	13.40 ‡
$NaPO_4^{2-}$	$PO_4^{3-} + Na^+ \leftrightarrow NaPO_4^{2-}$	2.05 ‡

* From Lindsay (1979)
\# From NIST database 46.7
‡ From Rahnemaie *et al.* (2007).

Table S6.3. Table defining formation reactions, CD coefficients and logK values for the entire set of surface species used in the CD model. The surface site densities are from Hiemstra and Zhao[37] with N_s (≡FeOH$^{-0.5}$(a)) = 3.0 nm^{-2}, N_s (≡FeOH$^{-0.5}$(b)) =2.8 nm^{-2} and N_s (≡$Fe_3O^{-0.5}$) = 1.4 nm^{-2}. The capacitance values for the extended Stern layer are size dependent. For instance, for ferrihydrite with SSA = 615 m^2 g^{-1}, C_1 =1.15 F m^{-2} and C_2 = 0.90 F m^{-2}.

Species	≡FeOH(a)$^{-0.5}$[&]	≡FeOH(b)$^{-0.5}$[&]	≡$Fe_3O^{-0.5}$	Δz_0	Δz_1	Δz_2	H^+	CO_3^{2-}	Na^+	PO_4^{3-}	NO_3^-	log*K*
FeOH(a)$^{-0.5}$	1	0	0	0	0	0	0	0	0	0	0	0
$FeOH_2(a)^{+0.5}$	1	0	0	1	0	0	1	0	0	0	0	8.1[s]
FeOH(a)$^{-0.5}\cdots Na^+$	1	0	0	0	1	0	0	0	1	0	0	-0.60 ± 0.03[ł]
$FeOH_2(a)^{+0.5}\cdots NO_3^-$	1	0	0	1	1	0	1	0	0	0	1	7.42 ± 0.03[ł]
FeOH(b)$^{-0.5}$	0	1	0	0	0	0	0	0	0	0	0	0
$FeOH_2(b)^{+0.5}$	0	1	0	1	0	0	1	0	0	0	0	8.1[s]
FeOH(b)$^{-0.5}\cdots Na^+$	0	1	0	0	1	0	0	0	1	0	0	-0.60 ± 0.03[ł]
$FeOH_2(b)^{+0.5}\cdots NO_3^-$	0	1	0	1	1	0	1	0	0	0	1	7.42 ± 0.03[ł]
$Fe_3O^{-0.5}$	0	0	1	0	0	0	0	0	0	0	0	0
$Fe_3OH^{+0.5}$	0	0	1	1	0	0	1	0	0	0	0	8.1[s]
$Fe_3O^{-0.5}\cdots Na^+$	0	0	1	0	1	0	0	0	1	0	0	-0.60 ± 0.03[ł]
$Fe_3OH^{+0.5}\cdots NO_3^-$	0	0	1	1	1	0	1	0	0	0	1	7.42 ± 0.03[ł]
$(FeO)_2CO$(b)	0	2	0	0.66	-0.66	0	2	1	0	0	0	21.73 ± 0.09*
$(FeO)_2CO\cdots Na$(b)	0	2	0	0.65	0.35	0	2	1	1	0	0	22.38 ± 0.09*
$FeOCO_2$(a)	1	0	0	0.34	-1.34	0	1	1	0	0	0	11.60 ± 0.01*
$FeOCO_2$(b)	0	1	0	0.34	-1.34	0	1	1	0	0	0	11.60 ± 0.01*
$(FeO)_2PO_2$(b)	0	2	0	0.46	-1.46	0	2	0	0	1	0	28.31 ± 0.04[s]
$(FeO)_2POOH$(b)	0	2	0	0.65	-0.65	0	3	0	0	1	0	33.52 ± 0.13[s]
$FeOPO_2OH$(a)	1	0	0	0.28	-1.28	0	2	0	0	1	0	26.36 ± 0.20[s]
$FeOPO_2OH$(b)	0	1	0	0.28	-1.28	0	2	0	0	1	0	26.36 ± 0.20[s]
$FeOPO(OH)_2$(a)	1	0	0	0.33	-0.33	0	3	0	0	1	0	29.84 ± 0.23[s]
$FeOPO(OH)_2$(b)	0	1	0	0.33	-0.33	0	3	0	0	1	0	29.84 ± 0.23[s]

[&] ≡FeOH(a)$^{-0.5}$ form only monodentate surface complexes, whereas ≡FeOH(b)$^{-0.5}$ can form mono- and bidentate surface complexes, according to the ion adsorption model for ferrihydrite of Hiemstra and Zhao[37]

* log*K* (mean ± SD) are the average of the values obtained in this study using four different scales of evaluation

ł Taken from Hiemstra and van Riemsdijk[39]

[s] Taken from Hiemstra and Zhao[37]

D. Evaluation of carbonate adsorption parameters at different scales

The formation constants (log*K*) of the CO_3 surface complexes were derived by fitting the experimental data of PO_4 adsorption to ferrihydrite in the competition systems with CO_3. In the fitting procedure, four evaluation scales were used to optimize the log*K* values: relative PO_4 adsorption (%), equilibrium PO_4 concentration in solution (C-PO_4 in mol L^{-1}), log_{10} of the equilibrium PO_4 concentration (log C-PO_4 in mol L^{-1}), and adsorption density of PO_4 (µmol m^{-2}). The results (log*K* ± SD) are given in Table S6.4**.**

Within the uncertainty of the fitting procedure, the log*K* values presented in Table S6.4 are consistent amongst the different evaluation scales (less than 1% difference). Testing for this consistency is important, as the response variable to be predicted by the model may differ from one situation to another (*e.g.* adsorption density *vs* solution concentration). The R^2 value and the root mean square error (RMSE) were used to evaluate the quality of the fitting and to compare the performance of the model under different alternative approaches.

Table S6.4. Log*K* values of the carbonate surface species, derived from the competitive effect of CO_3 on the adsorption of PO_4 to ferrihydrite, fitted at four evaluation scales: percentage of PO_4 adsorbed, equilibrium concentration of PO_4 in solution, log_{10} equilibrium concentration of PO_4 in solution, and adsorption density of PO_4 in µmol m^{-2}. Results are presented for two different scenarios in which the formation of the monodentate inner-sphere complex (Option A) is replaced by the formation an outer-sphere complex (Option B).

Option A	**log*K* values**				
Surface species	**% PO_4 adsorbed**	**log C-PO_4**	**C-PO_4**	**µmol PO_4 m^{-2}**	**Average‡**
$(\equiv FeO)_2CO$	21.85 ± 0.08	21.63 ± 0.10	21.69 ± 0.17	21.75 ± 0.12	21.73 ± 0.09
$(\equiv FeO)_2CO\cdot\cdot Na$	22.25 ± 0.09	22.42 ± 0.11	22.45 ± 0.09	22.41 ± 0.08	22.38 ± 0.09
$\equiv FeOCO_2$ (a/b)	11.61 ± 0.05	11.61 ± 0.08	11.59 ± 0.05	11.59 ± 0.05	11.60 ± 0.01
R^2 *	0.952	0.941	0.964	0.974	
RMSE *	4.12	0.15	2.09E-05	0.046	

Option B	**log*K* values**				
Surface species	**% PO_4 adsorbed**	**log C-PO_4**	**C-PO_4**	**µmol PO_4 m^{-2}**	**Average‡**
$(\equiv FeO)_2CO$	21.93 ± 0.06	21.63 ± 0.08	21.84 ± 0.08	21.88 ± 0.07	21.82 ± 0.13
$(\equiv FeO)_2CO\cdot\cdot Na$	21.91 ± 0.10	22.19 ± 0.12	22.16 ± 0.09	22.16 ± 0.09	22.11 ± 0.13
$\equiv FeOH_2\cdot\cdot CO_3$ (a/b)	11.34 ± 0.07	11.52 ± 0.10	11.32 ± 0.06	11.31 ± 0.06	11.37 ± 0.10
$\equiv Fe_3OH\cdot\cdot CO_3$	11.34 ± 0.07	11.52 ± 0.10	11.32 ± 0.06	11.31 ± 0.06	11.37 ± 0.10
R^2 *	0.945	0.941	0.960	0.970	
RMSE *	4.38	0.15	2.19E-05	0.049	

‡ Average log*K* values ± the standard deviation (SD) found by fitting the data using four evaluation scales. The values of Option A are also given in Table 6.4. of the main text and were used for calculating the mode lines in the various figures.

* R^2 and root means square error (RMSE) obtained with the FIT program express the quality of the fitting of the data set.

In Table S6.4, an alternative approach is presented (option B) to describe the competitive effect of CO_3 on the adsorption of PO_4 adsorption to ferrihydrite. In this approach, the formation of the inner-sphere monodentate complex is replaced by the formation of an outer-sphere complex with the singly ($\equiv FeOH^{-0.5}$) and triply ($\equiv Fe_3O^{-0.5}$) coordinated surface groups. A free fitting of the CD coefficients of this defined outer-sphere complex suggests that some negative charge is placed in the surface (0-plane) of ferrihydrite. In comparison with option A, similar quality of the fitting was obtained when the CD coefficients are set to $\Delta z_0 = +0.70$ v.u. and $\Delta z_1 = -1.70$ v.u. These charge distribution values can possibly result from a weak interaction between the CO_3 anions and the reactive surface groups, as for instance via H^+ bonding.

According to the model, there is a small contribution of an additional species (either inner-sphere monodentate or outer-sphere). It is tempting to attribute this to the formation of outer-sphere complexes, since these have been observed with *in-situ* spectroscopy at the interfaces of Fe-(hydr)oxides.[56] These outer-sphere species are especially found at low ionic strength and low pH values. In most of our experiments, the conditions are different. Moreover, outer-sphere complexation is rather weak (low $\log K_{intrinsic}$) and will only occur at favorable electrostatic conditions. These are not present at the interface if large quantities of oxyanions (CO_3 and/or PO_4) are specifically adsorbed, strongly reducing the electrostatic potential of the Stern (1-) plane (see Figure S6.7). This leads to a strong competition with any anion bound as an outer-sphere complex. As mentioned in the main text, a free search for the CD of the additional carbonate species points to monodentate complex formation (option A), however, using instead outer-sphere complexation (option B) also give a description of nearly the same quality. In the main text we have applied option A.

E. Aqueous complex formation of Fe carbonates

Open systems with constant pCO_2

Grivé et al.[38] have recently studied the complexation of Fe by CO_3 ions in open systems for different partial pressures of CO_2 (pCO_2 = 0, 0.98, 29.45, and 98.15 kPa). Fe-(hydr)oxide in 0.5 M $NaClO_4$ solution at 25 ºC was used to fix the activity of Fe^{3+}(aq). A two-line (2LFh) ferrihydrite material was produced. The product was dried in a non-specified manner and then sieved to sizes between 50 and 100 µm or 50.000 and 100.000 nm, *i.e.* large aggregates were used in an attempt to avoid colloidal material during the solubility experiments. The product had a BET surface area of ~200 $m^2\ g^{-1}$ meaning that the aggregates are porous considering their very large size. X-ray diffraction confirmed the presence of 2LFh. The reported solubility product is $\log Q_{so} = \log (Fe^{3+}) + 3 \log (OH^-) = -40.8 \pm 0.4$ at zero ionic strength ($I = 0$). Equilibration was relatively slow and lasted typically at least two or more weeks.

The data set of Grivé et al.[38] is presented in Figure S6.2. In the range of pH ~ 4.0–7.0, the solution concentration of Fe in equilibrium with the Fe-(hydr)oxide is nearly independent of the pH but clearly depends on the pCO_2 level. This can be explained by the formation of $FeOHCO_3^0$(aq) according to the reaction:

$$Fe^{3+}(aq) + OH^-(aq) + CO_3^{2-}(aq) \Leftrightarrow FeOHCO_3^o\ (aq) \qquad \log K_{FeOHCO3} \qquad \text{(Equation S6.1)}$$

At higher pH, the solubility increases suddenly and depends very strongly on the pCO_2 and pH. This behavior can be understood from the formation of $Fe(CO_3)_3^{3-}$(aq) according to:

$$Fe^{3+}(aq) + 3\ CO_3^{2-}(aq) \Leftrightarrow Fe(CO_3)_3^{3-}\ (aq) \qquad \log K_{Fe(CO3)3} \qquad \text{(Equation S6.2)}$$

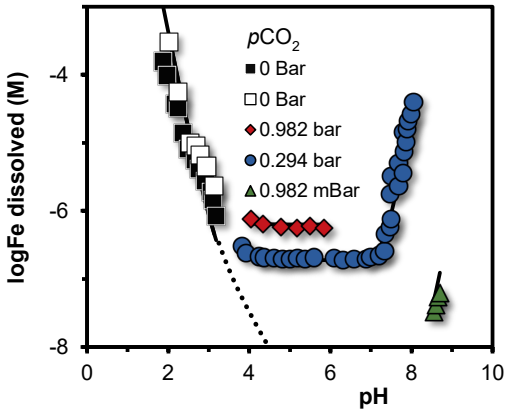

Figure S6.2. Concentration of Fe in solution in equilibrium with Fe-(hydr)oxide as a function of the pH and different pCO_2, measured in 0.5 M $NaClO_4$ at 25 °C. The experimental data (symbols) are from Grivé et al.[38] and the lines are results of model calculations obtained by re-evaluating the data using the reactions defined in Table S6.5. The solubility of the Fe-(hydr)oxide used by Grivé et al.[38] is very low ($\log Q_{so}$= -40.9 ± 0.06) pointing to the presence of a very stable mineral phase, despite the reported predominance of 2LFh. The unusual stability suggests that the surfaces of the large aggregates (50.000-100.000 nm) are covered by some rather crystalline material that determines the solubility. Importantly, for the determination of the log*K* values of the aqueous Fe(III)-CO_3 complexes, the precise cause of the high stability is irrelevant. The dotted line gives the extrapolated solubility in the absence of CO_3. It demonstrates that the measured solubility in the presence of CO_2 is significantly different. It implies that the formation constants for these Fe(III)-CO_3 complexes can be derived rather accurately.

The above behavior has been re-evaluated in order to be applied in our systems. The fitted values for the formation constants of $FeOHCO_3^0$ (aq) and $Fe(CO_3)_3^{3-}$ (aq) are respectively $\log K_{FeOHCO3}$ = 24.86 (± 0.09) and $\log K_{Fe(CO3)3}$ = 24.86 (± 0.09), using the reactions defined above. NB. The numerical value of both log*K* values is coincidentally the same.

According to our data analysis, the hydrolysis constant of $Fe(OH)_3^o$(aq), $Fe(OH)_4^-$(aq), $Fe_2(OH)_2^{4+}$(aq), and $Fe_3(OH)_4^{5+}$(aq) are fortunately not relevant for the interpretation of these data as these values are rather uncertain. Only the values for the first and second hydrolysis constant are relevant. The intrinsic log*K* values (I = 0) of these species have been taken from the most recent critical review given by Lemire et al.,[71] recommending $\log K_{FeOH2+}$ = 11.85 ± 0.03 and $\log K_{Fe(OH)2}$ = 23.20 ± 0.40. In our analysis, we used the Davies equation to account for the effect of the ionic strength, applying a value of D = 0.2. The $\log Q_{so}$ of the Fe-(hydr)oxide material used by Grivé et al.[38] was simultaneously fitted resulting in $\log Q_{so}$= log (Fe^{3+}) + 3 log (OH^-) = – 40.9 ± 0.06. Our values are very close to the values reported by Grivé et al.[38] (Table S6.5). The quality of the description was good (R^2 = 0.93, RMSE = 0.26).

The solubility product fitted for the Fe-(hydr)oxide material of Grivé et al.[38] is extremely low ($\log K_{so}$= – 40.9) and difficult to attribute to 2LFh. Most other studies report for 2LFh and 6LFh a much higher solubility being typically about two orders of magnitude higher with $\log K_{so}$ values that range from about – 38.5 to – 39.5.[14,71] A recent interpretation of thermochemical data of Majzlan et al.[72] by Hiemstra[14] reveals the intrinsic $\log K_{so}$ value for the solubility of Fh ($\log K_{so}$(bulk) = – 40.6 ± 0.1) when virtually present as a bulk material of infinite size. This $\log K_{so}$ (bulk) value fits well with the $\log K_{so}$ derived by Pinney et al.[73] using MO/DFT calculations. Moreover, actual Fh particles are nano-sized and

therefore, will be significantly less stable than its virtual bulk material due to a significant surface Gibbs free energy contribution.[14]

Using the recently derived surface Gibbs free energy values for goethite and hematite[14] in combination with the intrinsic logK_{so} values for both materials,[74] we estimate that the observed solubility product (logK_{so}= – 40.9) is equivalent to spherical particles with a size of about 14 ± 2 nm in the presence of nano-goethite or nano-hematite. This size is beyond the critical size of 8 nm for thermodynamic stability of Fh[14]. This is illustrated in Figure S6.3. Therefore, we hypothesize that the material of Grivé et al.[38] is likely to be 2LFh aggregated in extremely large particles (50.000 – 100.000 nm) whose surfaces have transformed into a more crystalline material, while still being a nano-size, but with a much lower solubility due to the higher crystallinity.

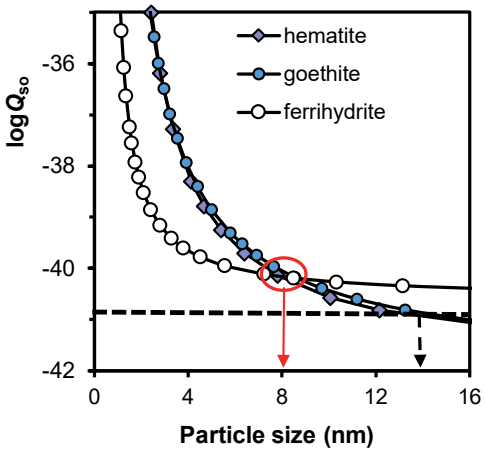

Figure S6.3. Particle size dependency of the solubility (logQ_{so}) of ferrihydrite, goethite, and hematite calculated with the thermodynamic data set provided by Hiemstra[14] concerning the intrinsic solubility of the various bulk materials and corresponding surface Gibbs free energies. At small sizes, Fh is the most stable Fe-(hydr)oxide material. Above a diameter of about 8 nm (red arrow), it is less stable than goethite and hematite. The value of logQ_{so} = – 40.9 (dashed line) is equivalent the solubility of goethite or hematite with a size of about 14 ± 2 nm (dashed arrow).

Closed systems

The above-derived formation constants for the aqueous Fe(III)-CO_3 complexes reported by Grivé et al.[38] can be used in evaluating the Fh solubility for our systems. Our closed systems have constant total CO_3 concentrations, while the pH varies. In this respect, our systems are different from the systems of Grivé et al.[38]. In closed systems the pCO_2 varies with changes in pH, whereas in the open systems of Grivé et al.[38] the pCO_2 is constant, leading to a simultaneous increase of the total CO_3 concentrations when the pH increases.

In Figure 6.1 of the main text, the measured concentration of dissolved Fe is given as a function of pH for systems with different levels of added CO_3. The ionic strength in the systems has been fixed to 0.5 M by the addition of appropriate amounts of $NaNO_3$. The experimental data at the lowest total CO_3 concentrations are close to the detection limit of Fe (dashed line) with ICP-MS. The value of the detection limit is relatively high (log $C_{Fe,total}$ = – 7 M) for our systems because dilution (50x) was needed to reduce the salt load during the analytical measurements. Therefore, we can only evaluate the solubility

of our Fh in 0.1 and 0.5 M CO_3 solutions. These solutions also contain some PO_4. The Fh used has been probed with PO_4 to determine the specific surface area, yielding A = 765 m^2 g^{-1} at a molar mass M_{nano} = 98.79 g mol^{-1}. The corresponding mean diameter of the particles is ~2.2 nm as calculated with a set of equations given by Hiemstra and Zhao.[37]

With the formation constants for $FeOHCO_3^0$(aq) and $Fe(CO_3)_3^{2-}$(aq), one is not able to describe the observed increase of the solubility in Figure 6.1 (main text) at increase of the pH. Instead, a decrease is predicted as illustrated with dotted lines in that figure. It suggests that there is an additional contribution by another Fe(III)-CO_3 species. Modeling shows that the higher pH-dependency of the solubility of Fh can be understood with the formation of $Fe(CO_3)_2(OH)_2^{3-}$(aq) according to the reaction:

$$Fe^{3+}(aq) + 2\ CO_3^{2-}(aq) + 2\ OH^-(aq) \Leftrightarrow Fe(CO_3)_2(OH)_2^{3-}(aq) \qquad \log K_{Fe(CO3)2(OH)2} \qquad \text{(Equation S6.3)}$$

The fitted log$K$ value for this reaction is $\log K_{Fe(CO3)2(OH)2}$ = 31.78 ± 0.13. Simultaneously, the solubility of our Fh has been derived by fitting, resulting in $\log Q_{so}$= – 38.55 ± 0.08. The quality of the description is very good (R^2 = 0.97, RMSE =0.16).

The solubility obtained for our Fh is in good agreement with the particle size derived with PO_4 probing. For Fh with d = 2.2 nm, we calculate $\log Q_{so}$= – 38.2 ± 0.2 applying the Ostwald equation with a surface Gibbs free energy of γ = 0.186 ± 0.01 J m^{-2} and the intrinsic solubility of $\log K_{so}$= – 40.6 ± 0.1 for Fh as virtual bulk material of infinite size.[14] An overview of the formation constants used in our modeling is given in Table S6.5. These values have been used in calculating the full lines the relevant graphs.

Table S6.5. Formation constants of aqueous Fe(III)-CO_3 complexes and the log$K$ values for the solubility of Fe-(hydr)oxide materials used in this study and by Grivé et al.

Species	**log*K***	**error**	
$FeOHCO_3^0$ (aq)	24.86*	0.09	Grivé et al.[38]
$Fe(CO_3)_3^{3-}$ (aq)	24.86*	0.09	Grivé et al.[38]
$Fe(CO_3)_2(OH)_2^{3-}$ (aq)	31.71	0.13	This study
$FeOH^{2+}$ (aq)	11.85	0.03	Lemire et al.[71]
$Fe(OH)_2^+$ (aq)	23.20	0.4	Lemire et al.[71]
Fh(s)*	-38.55	0.08	This study
Fe (hydr)oxide (s)	-40.90*	0.06	Grivé et al.[38]

* Log$K$ values as re-evaluated in the present study

F. Normalized competitive adsorption isotherms

Figure S6.4 presents the normalized adsorption isotherms of PO_4 to ferrihydrite, in competition systems with either CO_3 (black lines) or AsO_4 (green lines). The isotherms have been calculated with the CD model. The figure illustrates the relatively high affinity of PO_4 compared to CO_3. A small fraction of PO_4 in solution gives already a high relative PO_4 adsorption. In contrast, the affinities of PO_4 and AsO_4 are quite similar leading to relative isotherms that are close to the 1:1 line.

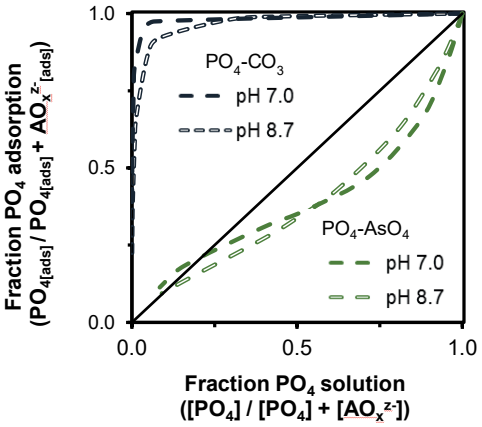

Figure S6.4. Normalized adsorption isotherms of PO_4 to ferrihydrite in the presence of competing oxyanions. Black lines are for binary systems with PO_4–CO_3, whereas the green lines are for binary systems with PO_4–AsO_4. The x-axis shows the concentration of PO_4 in solution, relative to the total concentration of oxyanions in solution ($[PO_4] + [AO_x^{z-}]$), being $[AO_x^{z-}]$ the competitor oxyanion concentration. The y-axis shows the relative adsorption of PO_4 to ferrihydrite, defined as $PO_{4[ads]} / (PO_{4[ads]} + AO_X^{z-}{}_{[ads]})$. The isotherms were calculated with the CD model. The model parameters for CO_3 were taken from Table 6.1 (main text), whereas the parameters for PO_4 and AsO_4 are from Hiemstra and Zhao.[37] The ionic strength was $I = 0.5$ M, using $NaNO_3$ as background electrolyte.

G. Adsorption isotherms: carbonate surface speciation

In Figure S6.5, the surface speciation of CO_3 in Fh systems has been modeled and presented in the form of adsorption isotherms. The chemical conditions in this modeling exercise are the same as in the systems presented in Figure 6.4 of the main text. At neutral pH (panel A), the bidentate complex (BC) dominates the adsorption of CO_3 over the entire range of solution concentrations. The relative contribution of the bidentate complex with Na (BCNa) and the monodentate complex (MC) increases with increasing the surface loading of CO_3. At pH 8.5 (panel B), the surface loading of CO_3 decreases in comparison with the systems presented in panel A. This decrease is expected, due to the analyzed pH-dependence of CO_3 adsorption. In addition, the surface speciation shifts toward a preferential formation of the BCNa complex. This change is mainly a result of electrostatic interactions, as explained in Section 6.3.4.2 of the main text.

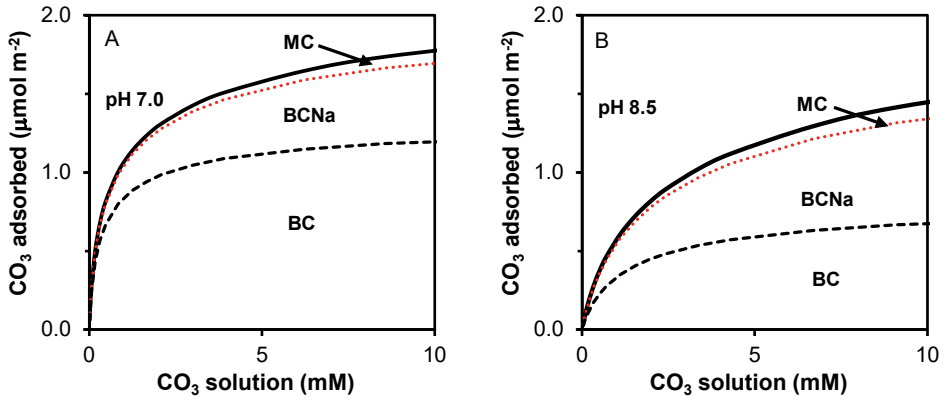

Figure S6.5. Surface speciation of carbonate as a function of the solution concentration in single-ion systems with ferrihydrite at pH 7.0 (A) and 8.5 (B). The CD model parameters set for carbonate, presented in Table 6.1 of the main text was used in the calculations. The ionic strength of the systems was fixed at 0.10 M by adding the corresponding amounts of $NaNO_3$. BC= Bidentate carbonate complex; BCNa= Bidentate carbonate complex with Na; MC= Monodentate carbonate complex.

H. Adsorption data of carbonate from literature

Figure S6.6 presents the adsorption edges of CO_3 reported by Zachara et al.[24] for single-ion systems with $CO_{3[T]}$ = 4.6 µM and two $Fe_{[T]}$ (0.87 and 8.7 mM). The black lines are the CD model predictions obtained with the parameters set presented in Table 6.1 of the main text. The specific surface area of Fh was set to A = 600 $m^2\ g^{-1}$. With our modeling, we reproduced very well the observed pH dependence of the CO_3 adsorption in this data set. The maximum adsorption of CO_3 to Fh occurs at pH ~6.5. Below this pH value, the adsorption of CO_3 decreases markedly. The observed pH-dependency of the CO_3 adsorption, with a maximum in the adsorption edge, is related to the change in the solution speciation of CO_3.

At pH values below ~7.0, the description of the CO_3 adsorption to Fh slightly improves when the formation of outer-sphere complexes is considered in the modeling, instead of the monodentate inner-sphere complex (red dotted lines). The formation of outer-sphere complexes can be favoured in conditions of low pH and low ionic strength levels, especially in the absence of competitor anions such as PO_4.

As observed in Figure S6.6, overestimations of the percentage of CO_3 adsorption are predicted by the model at higher pH values (pH > 7.0). A lower log$K$ value than the reported in Table 6.1 (main text) for the formation reaction of the BC surface complex is needed to improve the description of the experimental data. However, the study of Zachara et al.[24] was performed with $CO_{3[T]}$ at the µM level (*i.e.* $10^3 - 10^5$ times lower than in the present study), measuring ^{14}C scintillation and assuming no other source of CO_3 in the system than the ^{14}C added. The data are rather unreliable, as follows from the large scattering. Despite these methodological considerations and the evident uncertainty in the CO_3 adsorption measurements, the work of Zachara et al.[24] has been used since then as a reference to model the effect of CO_3 on the adsorption of other ions to Fh (*e.g.* UO_2^{2+} and AsO_4^{3-}).[21,22,75] The lack of reliable CO_3 adsorption data to Fh underlies the relevance of our present contribution.

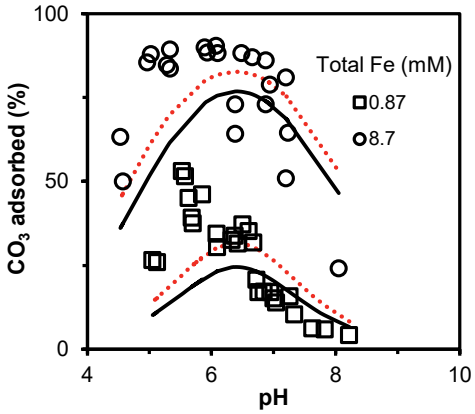

Figure S6.6. Adsorption edges of carbonate in single-ion systems with ferrihydrite. Data are taken from Zachara et al.[24] for systems with $CO_{3[T]}$= 4.6 µM and two total Fe concentrations (0.87 and 8.7 mM). The ionic strength of the systems is I = 0.10 M, using $NaNO_3$ as background electrolyte. The specific surface area of the ferrihydrite suspensions was set to A = 600 m^2 g^{-1} with a respective molar mass of M_{nano} = 94.51 g mol^{-1} Fe. The black full lines are model calculations, obtained with the set of CD model parameters set presented in Table 6.1 of the main text. The red dotted lines are CD model predictions considering the formation of outer-sphere complexes instead of monodentate inner-sphere complexes (See Option B in Table S6.4).

I. Bond length and Brown bond valence concept

The geometries of the inner-sphere bidentate (BC and BCNa) and monodentate (MC) carbonate complexes have been optimized with Molecular Orbital (MO) calculations, applying density functional theory (DFT) with six different functional (BP86, B3LYPyp, EDF1, EDF2, BLYPlyp, ωPWB97X-D) and 6-31+G** as basis set. The calculations have been done with Spartan'14 parallel software of Wavefunction, Inc.

An uncharged template composed of two Fe octahedra was used as defined previously by Rahnemaie et al.[42] to optimize the geometries of the PO_4 surface complexes. The lower part of the template, i.e. $(H_2O)_2Fe_2(OH)_6$, has a fix geometry. Inner-sphere complexation of CO_3 was defined and the structure was hydrated with water molecules to explicitly account for hydration. The optimized geometries of (a) CO_3 bidentate (BC), (b) $NaCO_3$ bidentate (BCNa) and (c) CO_3 monodentate (MC) complex have respectively an overall charge of respectively -2, -1, and -2. The average bond distances has been used to calculate the bond valence ν (v.u.) according to the Brown bond concept:[34]

$$\nu = \exp\left(-\frac{R-R_o}{B}\right) \qquad \text{(Equation S6.4)}$$

In Equation S6.4, B is an empirical constant (B = 37 pm), R (pm) is the bond length distance and R_o (pm) is a reference distance calibrated for each element using the sum bond valence rule. Table S6.6 presents the average bond distance (pm), obtained from the six different functionals, and the respective ν values (v.u) for the three CO_3 complexes used in our model: CO_3 bidentate (BC), $NaCO_3$ bidentate (BCNa) and CO_3 monodentate (MC).

From the ν values, the bond valence coefficients (n_0 and n_1) can be calculated, and after considering the charge contribution of the protons involved in the formation reaction (n_{H0} and n_{H1}), and a correction

for the interfacial water dipole orientation, then the interfacial charge distribution coefficients (Δz_0 and Δz_1) are derived. The n_0 and n_1 coefficients and the final Δz_0 and Δz_1 values are presented in Table 6.2 of the main text.

Table S6.6. Average bond lengths in the optimized geometries of the carbonate surface complexes obtained with MO/DFT using the 6-31+G** basis set and six different functionals (BP86, B3LYP, EDF1, EDF2, BLYP, ωP97X-D). The corresponding bond valences (ν) are obtained with the Brown valence analysis.

BC			BCNa			MC		
Bond	**Distance (pm)#**	**ν (v.u)**	**Bond**	**Distance (pm)#**	**ν (v.u)**	**Bond**	**Distance (pm)#**	**ν (v.u)**
FeO-CO*	130.8 ± 0.8	1.298	FeO-CO*	130.7 ± 1.1	1.296	FeO-CO*	130.7 ± 0.7	1.305
FeO-CO*	130.8 ± 0.7	1.301	FeO-CO*	130.9 ± 1.3	1.287	FeOC-O	129.7 ± 1.0	1.341
FeOC=O	128.0 ± 1.1	1.402	FeOC=O	127.4 ± 1.5	1.417	FeOC=O	129.4 ± 1.4	1.353
	Sum υ	4.000		Sum υ	4.000		Sum υ	4.000
Fe-C	302.4 ± 2.9		Fe-C	308.1 ± 1.5		Fe-C	301.8 ± 3.8	
Fe-C	302.9 ± 3.1		Fe-C	302.3 ± 1.4				
R_o	140.5		R_o	140.2		R_o	140.6	

* C-O bonds that are share with Fe at the surface of ferrihydrite
# Average (± SD) obtained from the optimized geometries applying six different DFT functionals (BP86, B3LYP, EDF1, EDF2, BLYP, ωP97X-D)

J. Effect of phosphate adsorption on the surface charge of ferrihydrite

The interaction of PO_4 with CO_3 at the solid-solution interface of ferrihydrite affects both the total amount of CO_3 adsorbed and the surface speciation of this oxyanion. For instance, as shown in Figure 6.5 of the main text, the relative contribution of the CO_3 bidentate complex interacting with Na^+ (BCNa) increases in the presence of PO_4. Conversely, increase in the total PO_4-loading of the systems strongly reduces the formation of the inner-sphere monodentate CO_3 complex (MC). The electrostatic interactions between both oxyanions play a crucial role in determining the surface speciation of CO_3.

In the extended Stern layer approach,[39] the net charge density of the ferrihydrite particles (σ_P = C m^{-2}) is given by the sum of the charge density in the different electrostatic planes (*i.e.* 0, 1, and 2) defined as: $\sigma_P = \sigma_0 + \sigma_1 + \sigma_2$. If the specific surface area (SSA in m^2 kg^{-1}) of ferrihydrite is considered, one can obtain the total net particle charge (Q_P in C kg^{-1}). Based on the principle of overall electroneutrality, the surface charge Q_P is compensated by the net counter ion charge present in the Diffuse Double Layer (Q_{DDL} in C kg^{-1}). The charge balance can be defined as $Q_{DDL} + Q_P = 0$. Upon specific PO_4 adsorption to positively charged ferrihydrite, a considerable amount of negative charge is introduced to the surface and inner Stern plane. Consequently, there will be a reduction in the net charge density and the electrostatic potential of the 1-plane (ψ_1) of the Stern Layer will diminish. CD model calculations show that in our binary systems with CO_3 and PO_4 particle charge (σ_P) is negative over the entire experimental pH range (Figure S6.7 A,C). Likewise, for a given pH value (5–10), the electrostatic potential ψ_1 decreases continuously when the total PO_4-loading of the systems increases (Figure S6.7 B,D). The more negative potential in the inner Stern plane (ψ_1) is unfavorable for the formation of a CO_3 monodentate complex, because two of the negatively charged ligands of the CO_3 complex are located in the 1-plane. On the other hand, the interaction of Na^+ ions with the outer ligand of the bidentate CO_3 complex will be favored by the presence of this negative electrostatic potential (ψ_1).

For systems with an ionic strength of I = 0.5 M, the decreases in the inner Stern plane potential ψ_1 upon specific anion adsorption is less pronounced than for the systems with I = 0.05 M (Figure S6.7 B,D). At higher values of the ionic strength, the counter ions (Na^+) present in the DDL will better screen the negative charge present in the 1-plane. This will result in a higher adsorption of PO_4 and CO_3 due to less electrostatic repulsion. This observation agrees with the experimental results presented in Figure 6.3b of the main text showing a lower solution concentration of PO_4 in binary adsorption systems with a higher ionic strength.

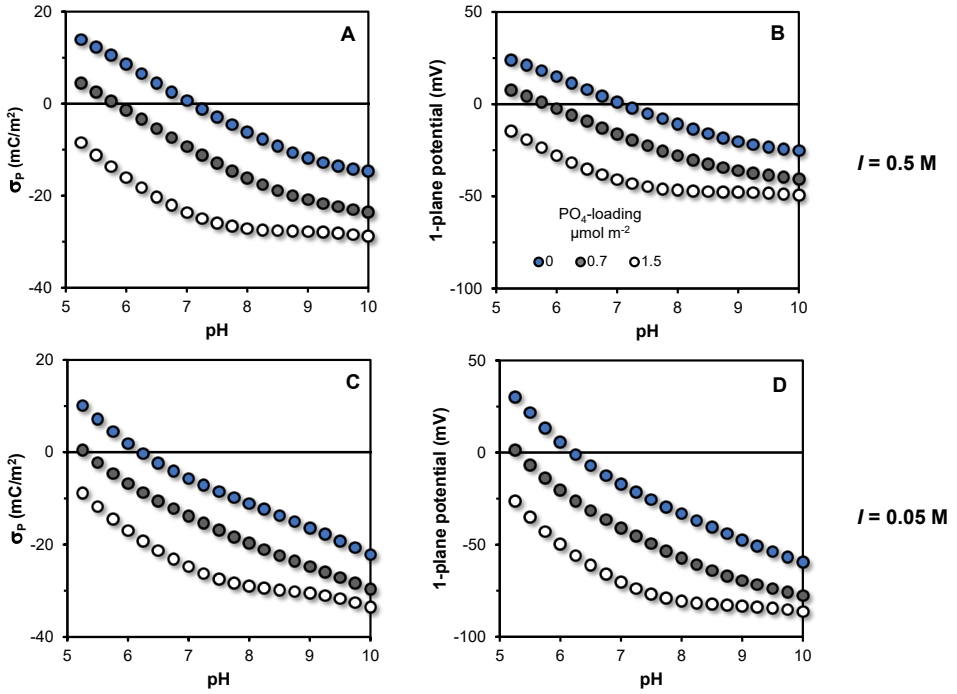

Figure S6.7. Model calculations of the net charge density (σ_P) of the ferrihydrite particles (A and C) and electrostatic potential in the 1-plane (ψ_1) of the Extended Stern Layer of the ferrihydrite-water interface (B and D) for a series of Fh systems with three PO_4-loadings (0, 0.7, and 1.5 µmol m^{-2}) in the presence of CO_3 (0.03 M). The upper panels correspond to systems with an ionic strength of I = 0.5 M and the lower panels are for systems with I = 0.05 M, using $NaNO_3$ as background electrolyte. The model calculations were performed with the parameters presented in Table 6.1 of the main text.

References

(1) Hochella, M. F.; Lower, S. K.; Maurice, P. A.; Penn, R. L.; Sahai, N.; Sparks, D. L.; Twining, B. S. Nanominerals, Mineral Nanoparticles, and Earth Systems. *Science (80-.).* **2008**, *319* (5870), 1631–1635.

(2) van der Zee, C.; Roberts, D. R.; Rancourt, D. G.; Slomp, C. P. Nanogoethite Is the Dominant Reactive Oxyhydroxide Phase in Lake and Marine Sediments. *Geology* **2003**, *31* (11), 993–996.

(3) Hiemstra, T.; Antelo, J.; van Rotterdam, A. M. D.; van Riemsdijk, W. H. Nanoparticles in Natural Systems II: The Natural Oxide Fraction at Interaction with Natural Organic Matter and Phosphate. *Geochim. Cosmochim. Acta* **2010**, *74* (1), 59–69.

(4) Wang, X.; Kubicki, J. D.; Boily, J. F.; Waychunas, G. A.; Hu, Y.; Feng, X.; Zhu, M. Binding Geometries of Silicate Species on Ferrihydrite Surfaces. *ACS Earth Sp. Chem.* **2018**, *2* (2), 125–134.

(5) Hiemstra, T. Ferrihydrite Interaction with Silicate and Competing Oxyanions: Geometry and Hydrogen Bonding of Surface Species. *Geochim. Cosmochim. Acta* **2018**, *238*, 453–476.

(6) Liu, J.; Zhu, R.; Liang, X.; Ma, L.; Lin, X.; Zhu, J.; He, H.; Parker, S. C.; Molinari, M. Synergistic Adsorption of Cd(II) with Sulfate/Phosphate on Ferrihydrite: An in Situ ATR-FTIR/2D-COS Study. *Chem. Geol.* **2018**, *477*, 12–21.

(7) Zhang, Y.; Wu, B.; Xu, H.; Liu, H.; Wang, M.; He, Y.; Pan, B. Nanomaterials-Enabled Water and Wastewater Treatment. *NanoImpact* **2016**, *3–4*, 22–39.

(8) Xu, P.; Zeng, G. M.; Huang, D. L.; Feng, C. L.; Hu, S.; Zhao, M. H.; Lai, C.; Wei, Z.; Huang, C.; Xie, G. X.; et al. Use of Iron Oxide Nanomaterials in Wastewater Treatment: A Review. *Sci. Total Environ.* **2012**, *424*, 1–10.

(9) Gora, S.; Liang, R.; Zhou, Y. N.; Andrews, S. Settleable Engineered Titanium Dioxide Nanomaterials for the Removal of Natural Organic Matter from Drinking Water. *Chem. Eng. J.* **2018**, *334*, 638–649.

(10) Michel, F. M.; Ehm, L.; Antao, S. M.; Lee, P. L.; Chupas, P. J.; Liu, G.; Strongin, D. R.; Schoonen, M. A. A.; Phillips, B. L.; Parise, J. B. The Structure of Ferrihydrite, a Nanocrystalline Material. *Science* **2007**, *316* (5832), 1726–1729.

(11) Hiemstra, T. Surface and Mineral Structure of Ferrihydrite. *Geochim. Cosmochim. Acta* **2013**, *105*, 316–325.

(12) Jambor, J. L.; Dutrizac, J. E. Occurrence and Constitution of Natural and Synthetic Ferrihydrite, a Widespread Iron Oxyhydroxide. *Chem. Rev.* **1998**, *98* (7), 2549–2586.

(13) Guo, H.; Barnard, A. S. Naturally Occurring Iron Oxide Nanoparticles: Morphology, Surface Chemistry and Environmental Stability. *J. Mater. Chem. A* **2013**, *1* (1), 27–42.

(14) Hiemstra, T. Formation, Stability, and Solubility of Metal Oxide Nanoparticles: Surface Entropy, Enthalpy, and Free Energy of Ferrihydrite. *Geochim. Cosmochim. Acta* **2015**, *158*, 179–198.

(15) Stumm, W.; Morgan, J. J. *Aquatic Chemistry: Chemical Equilibria and Rates in Natural Waters*; John Wiley & Sons, 2012; Vol. 126.

(16) Villalobos, M.; Leckie, J. O. Carbonate Adsorption on Goethite under Closed and Open CO2 Conditions. *Geochim. Cosmochim. Acta* **2000**, *64* (22), 3787–3802.

(17) Hausner, D. B.; Bhandari, N.; Pierre-Louis, A. M.; Kubicki, J. D.; Strongin, D. R. Ferrihydrite Reactivity toward Carbon Dioxide. *J. Colloid Interface Sci.* **2009**, *337* (2), 492–500.

(18) Taifan, W.; Boily, J.-F.; Baltrusaitis, J. Surface Chemistry of Carbon Dioxide Revisited. *Surf. Sci. Rep.* **2016**, *71* (4), 595–671.

(19) Ostergren, J. D.; Brown, G. E.; Parks, G. A.; Persson, P. Inorganic Ligand Effects on Pb(II) Sorption to Goethite (α-FeOOH) - II. Sulfate. *J.Colloid Interface Sci.* **2000**, *225* (2), 483–493.

(20) Wazne, M.; Korfiatis, G. P.; Meng, X. Carbonate Effects on Hexavalent Uranium Adsorption by Iron Oxyhydroxide. *Environ. Sci. Technol.* **2003**, *37* (16), 3619–3624.

(21) Hiemstra, T.; Riemsdijk, W. H. Van; Rossberg, A.; Ulrich, K.-U. A Surface Structural Model for Ferrihydrite II: Adsorption of Uranyl and Carbonate. *Geochim. Cosmochim. Acta* **2009**, *73* (15), 4437–4451.

(22) Appelo, C. A. J.; Van Der Weiden, M. J. J.; Tournassat, C.; Charlet, L. Surface Complexation of Ferrous Iron and Carbonate on Ferrihydrite and the Mobilization of Arsenic. *Environ. Sci. Technol.* **2002**, *36* (14), 3096–3103.

(23) Stachowicz, M.; Hiemstra, T.; Van Riemsdijk, W. H. Arsenic-Bicarbonate Interaction on Goethite Particles. *Environ. Sci. Technol.* **2007**, *41* (16), 5620–5625.

(24) Zachara, J. M.; Girvin, D. C.; Schmidt, R. L.; Resch, C. T. Chromate Adsorption on Amorphous Iron Oxyhydroxide in the Presence of Major Groundwater Ions. *Environ. Sci. Technol.* **1987**, *21* (6), 589–594.

(25) van Geen, A.; Robertson, A. P.; Leckie, J. O. Complexation of Carbonate Species at the Goethite Surface: Implications for Adsorption of Metal Ions in Natural Waters. *Geochim. Cosmochim. Acta* **1994**, *58* (9), 2073–2086.

(26) Brechbühl, Y.; Christl, I.; Elzinga, E. J.; Kretzschmar, R. Competitive Sorption of Carbonate and Arsenic to Hematite : Combined ATR-FTIR and Batch Experiments. *J. Colloid Interface Sci.* **2012**, *377* (1), 1–18.

(27) Biswas, A.; Gustafsson, J. P.; Neidhardt, H.; Halder, D.; Kundu, A. K.; Chatterjee, D.; Berner, Z.; Bhattacharya, P. Role of Competing Ions in the Mobilization of Arsenic in Groundwater of Bengal Basin: Insight from Surface Complexation Modeling. *Water Res.* **2014**, *55*, 30–39.

(28) Peter, A.; Lamert, H.; Beyer, M.; Hornbruch, G.; Heinrich, B.; Schulz, A.; Geistlinger, H.; Schreiber, B.; Dietrich, P.; Werban, U.; et al. Investigation of the Geochemical Impact of CO2 on Shallow Groundwater: Design and Implementation of a CO2 Injection Test in Northeast Germany. *Environ. Earth Sci.* **2012**, *67* (2), 335–349.

(29) Rasoul; Hiemstra, T.; van Riemsdijk, W. H. Carbonate Adsorption on Goethite in Competition with Phosphate. *J. Colloid Interface Sci.* **2007**, *315* (2), 415–425.

(30) Flower, H.; Rains, M.; Lewis, D.; Zhang, J.-Z.; Price, R. Control of Phosphorus Concentration through Adsorption and Desorption in Shallow Groundwater of Subtropical Carbonate Estuary. *Estuar. Coast. Shelf Sci.* **2016**, *169*, 238–

247.

(31) Hiemstra, T.; Antelo, J.; Rahnemaie, R.; van Riemsdijk, W. H. Nanoparticles in Natural Systems I: The Effective Reactive Surface Area of the Natural Oxide Fraction in Field Samples. *Geochim. Cosmochim. Acta* **2010**, *74* (1), 41–58.

(32) Hiemstra, T.; Van Riemsdijk, W. H. A Surface Structural Approach to Ion Adsorption: The Charge Distribution (CD) Model. *J. Colloid Interface Sci.* **1996**, *179* (2), 488–508.

(33) Michel, F. M.; Barron, V.; Torrent, J.; Morales, M. P.; Serna, C. J.; Boily, J.-F.; Liu, Q.; Ambrosini, A.; Cismasu, A. C.; Brown, G. E. Ordered Ferrimagnetic Form of Ferrihydrite Reveals Links among Structure, Composition, and Magnetism. *Proc. Natl. Acad. Sci.* **2010**, *107* (7), 2787–2792.

(34) Brown, I. D.; Altermatt, D. Bond-Valence Parameters Obtained from a Systematic Analysis of the Inorganic Crystal Structure Database. *Acta Crystallogr. Sect. B Struct. Sci.* **1985**, *41* (4), 244–247.

(35) Brown, I. D. Recent Developments in the Methods and Applications of the Bond Valence Model. *Chem. Rev.* **2009**, *109* (12), 6858–6919.

(36) Hiemstra, T.; Van Riemsdijk, W. H. A Surface Structural Model for Ferrihydrite I: Sites Related to Primary Charge, Molar Mass, and Mass Density. *Geochim. Cosmochim. Acta* **2009**, *73* (15), 4423–4436.

(37) Hiemstra, T.; Zhao, W. Reactivity of Ferrihydrite and Ferritin in Relation to Surface Structure, Size, and Nanoparticle Formation Studied for Phosphate and Arsenate. *Environ. Sci. Nano* **2016**, *3*, 1265–1279.

(38) Grivé, M.; Duro, L.; Bruno, J. Fe(III) Mobilisation by Carbonate in Low Temperature Environments: Study of the Solubility of Ferrihydrite in Carbonate Media and the Formation of Fe(III) Carbonate Complexes. *Appl. Geochemistry* **2014**, *49*, 57–67.

(39) Hiemstra, T.; Van Riemsdijk, W. H. On the Relationship between Charge Distribution, Surface Hydration, and the Structure of the Interface of Metal Hydroxides. *J. Colloid Interface Sci.* **2006**, *301* (1), 1–18.

(40) Keizer, M. G.; van Riemsdijk, W. H. *ECOSAT, Equilibrium Calculation of Speciation and Transport. Technical Report. Department of Soil Quality. Wageningen Univeristy.*; 1998.

(41) Kinniburgh, D. G. *Fit, Technical Report WD/93/23*; Keyworth, Great Britain, 1993.

(42) Rahnemaie, R.; Hiemstra, T.; Van Riemsdijk, W. H. Geometry, Charge Distribution, and Surface Speciation of Phosphate on Goethite. *Langmuir* **2007**, *23* (7), 3680–3689.

(43) Bruno, J.; Stumm, W.; Wersin, P.; Brandberg, F. On the Influence of Carbonate in Mineral Dissolution: I. The Thermodynamics and Kinetics of Hematite Dissolution in Bicarbonate Solutions at T = 25°C. *Geochim. Cosmochim. Acta* **1992**, *56* (3), 1139–1147.

(44) Hummel, W. Comment on "On the Influence of Carbonate in Mineral Dissolution: 1. The Thermodynamics and Kinetics of Hematite Dissolution in Bicarbonate Solutions at T = 25°C" by J. Bruno, W. Stumm, P. Wersin, and F. Brandberg. *Geochim. Cosmochim. Acta* **2000**, *64* (12), 2167–2171.

(45) Antelo, J.; Fiol, S.; Pérez, C.; Mariño, S.; Arce, F.; Gondar, D.; López, R. Analysis of Phosphate Adsorption onto Ferrihydrite Using the CD-MUSIC Model. *J. Colloid Interface Sci.* **2010**, *347* (1), 112–119.

(46) Stachowicz, M.; Hiemstra, T.; van Riemsdijk, W. H. Multi-Competitive Interaction of As(III) and As(V) Oxyanions with Ca2+, Mg2+, PO3−4, and CO2−3 Ions on Goethite. *J. Colloid Interface Sci.* **2008**, *320* (2), 400–414.

(47) Gu, C.; Wang, Z.; Kubicki, J. D.; Wang, X.; Zhu, M. X-Ray Absorption Spectroscopic Quantification and Speciation Modeling of Sulfate Adsorption on Ferrihydrite Surfaces. *Environ. Sci. Technol.* **2016**, *50* (15), 8067–8076.

(48) Arai, Y.; Sparks, D. L. ATR–FTIR Spectroscopic Investigation on Phosphate Adsorption Mechanisms at the Ferrihydrite–Water Interface. *J. Colloid Interface Sci.* **2001**, *241* (2), 317–326.

(49) Mallet, M.; Barthélémy, K.; Ruby, C.; Renard, A.; Naille, S. Investigation of Phosphate Adsorption onto Ferrihydrite by X-Ray Photoelectron Spectroscopy. *J. Colloid Interface Sci.* **2013**, *407*, 95–101.

(50) Goldberg, S.; Johnston, C. T. Mechanisms of Arsenic Adsorption on Amorphous Oxides Evaluated Using Macroscopic Measurements, Vibrational Spectroscopy, and Surface Complexation Modeling. *J. Colloid Interface Sci.* **2001**, *234* (1), 204–216.

(51) Villalobos, M.; Leckie, J. O. Surface Complexation Modeling and FTIR Study of Carbonate Adsorption to Goethite. *J. Colloid Interface Sci.* **2001**, *235* (1), 15–32.

(52) Wijnja, H.; Schulthess, C. P. Carbonate Adsorption Mechanism on Goethite Studied with ATR – FTIR, DRIFT, and Proton Coadsorption Measurements. *Soil Sci. Soc. Am. J.* **2001**, *65* (2), 324–330.

(53) Su, C.; Suarez, D. L. In Situ Infrared Speciation of Absorbed Carbonate on Aluminum and Iron Oxides. *Clays Clay Miner.* **1997**, *45*, 814–825.

(54) Goldsmith, J. A.; Ross, S. D. Factors Affecting the Infra-Red Spectra of Planar Anions with D3h Symmetry—IV The

Vibrational Spectra of Some Complex Carbonates in the Region 4000-400 Cm−1. *Spectrochim. Acta Part A Mol. Spectrosc.* **1968**, *24* (8), 993–998.

(55) Hiemstra, T.; Rahnemaie, R.; Van Riemsdijk, W. H. Surface Complexation of Carbonate on Goethite: IR Spectroscopy, Structure and Charge Distribution. *J. Colloid Interface Sci.* **2004**, *278* (2), 282–290.

(56) Bargar, J. R.; Kubicki, J. D.; Reitmeyer, R.; Davis, J. A. ATR-FTIR Spectroscopic Characterization of Coexisting Carbonate Surface Complexes on Hematite. *Geochim. Cosmochim. Acta* **2005**, *69* (6), 1527–1542.

(57) Kubicki, J. D.; Kwon, K. D.; Paul, K. W.; Sparks, D. L. Surface Complex Structures Modelled with Quantum Chemical Calculations: Carbonate, Phosphate, Sulphate, Arsenate and Arsenite. *Eur. J. Soil Sci.* **2007**, *58* (4), 932–944.

(58) Capewell, S. G.; Buchner, R.; Hefter, G.; May, P. M. Dielectric Relaxation of Aqueous Na2CO3 Solutions. *Phys. Chem. Chem. Phys.* **1999**, *1* (8), 1933–1937.

(59) Rudolph, W. W.; Irmer, G.; Königsberger, E. Speciation Studies in Aqueous HCO_3^-–CO_3^{2-} Solutions. A Combined Raman Spectroscopic and Thermodynamic Study. *Dalt. Trans.* **2008**, *0* (7), 900–908.

(60) Johnston, C. P.; Chrysochoou, M. Mechanisms of Chromate, Selenate, and Sulfate Adsorption on Al-Substituted Ferrihydrite: Implications for Ferrihydrite Surface Structure and Reactivity. *Environ. Sci. Technol.* **2016**, *50* (7), 3589–3596.

(61) Wang, X.; Wang, Z.; Peak, D.; Tang, Y.; Feng, X.; Zhu, M. Quantification of Coexisting Inner- and Outer-Sphere Complexation of Sulfate on Hematite Surfaces. *ACS Earth Sp. Chem.* **2018**, *2* (4), 387–398.

(62) Baltrusaitis, J.; Schuttlefield, J. D.; Zeitler, E.; Jensen, J. H.; Grassian, V. H. Surface Reactions of Carbon Dioxide at the Adsorbed Water-Oxide Interface. *J. Phys. Chem. C* **2007**, *111* (40), 14870–14880.

(63) Baltrusaitis, J.; Schuttlefield, J.; Zeitler, E.; Grassian, V. H. Carbon Dioxide Adsorption on Oxide Nanoparticle Surfaces. *Chem. Eng. J.* **2011**, *170* (2–3), 471–481.

(64) Zheng, L.; Apps, J. A.; Spycher, N.; Birkholzer, J. T.; Kharaka, Y. K.; Thordsen, J.; Beers, S. R.; Herkelrath, W. N.; Kakouros, E.; Trautz, R. C. Geochemical Modeling of Changes in Shallow Groundwater Chemistry Observed during the MSU-ZERT CO2injection Experiment. *Int. J. Greenh. Gas Control* **2012**, *7*, 202–217.

(65) Trautz, R. C.; Pugh, J. D.; Varadharajan, C.; Zheng, L.; Bianchi, M.; Nico, P. S.; Spycher, N. F.; Newell, D. L.; Esposito, R. A.; Wu, Y.; et al. Effect of Dissolved CO2 on a Shallow Groundwater System: A Controlled Release Field Experiment. *Environ. Sci. Technol.* **2013**, *47* (1), 298–305.

(66) Tsakiroglou, C. D.; Terzi, K.; Aggelopoulos, C.; Theodoropoulou, M. CO2-Induced Release of Copper and Zinc from Model Soil in Water. *Int. J. Greenh. Gas Control* **2018**, *76*, 150–157.

(67) Perona, M. J.; Leckie, J. O. Proton Stoichiometry for the Adsorption of Cations on Oxide Surfaces. *J. Colloid Interface Sci.* **1985**, *106* (1), 64–69.

(68) Rietra, R. P. J. J.; Hiemstra, T.; Van Riemsdijk, W. H. Electrolyte Anion Affinity and Its Effect on Oxyanion Adsorption on Goethite. *J. Colloid Interface Sci.* **2000**, *229* (1), 199–206.

(69) Olsen, S. R.; Cole, C. V.; Watanabe, F. S.; Dean, L. A. *Estimation of Available Phosphorous in Soils by Extraction with Sodium Bicarbonate*; 1954.

(70) Barrow, N. J.; Shaw, T. C. Sodium Bicarbonate as an Extractant for Soil Phosphate, I. Separation of the Factors Affecting the Amount of Phosphate Displaced from Soil from Those Affecting Secondary Adsorption. *Geoderma* **1976**, *16* (2), 91–107.

(71) Lemire, R. J.; Berner, U.; Musikas, C.; Palmer, D. A.; Taylor, P.; Tochiyama, O. *Chemical Thermodynamics of Iron Part 1*; 2013; Vol. 13a.

(72) Majzlan, J.; Navrotsky, A.; Schwertmann, U. Thermodynamics of Iron Oxides: Part III. Enthalpies of Formation and Stability of Ferrihydrite (~Fe(OH)3), Schwertmannite (~FeO(OH)3/4(SO4)1/8), and ε-Fe2O3. *Geochim. Cosmochim. Acta* **2004**, *68* (5), 1049–1059.

(73) Pinney, N.; Kubicki, J. D.; Middlemiss, D. S.; Grey, C. P.; Morgan, D. Density Functional Theory Study of Ferrihydrite and Related Fe-Oxyhydroxides. *Chem. Mater.* **2009**, *21* (24), 5727–5742.

(74) Navrotsky, A.; Mazeina, L.; Majzlan, J. Size-Driven Structural Thermodynamic Complexity in Iron Oxides. *Science (80-.).* **2008**, *319* (March), 1635–1639.

(75) Waite, T. D.; Davis, J. A.; Payne, T. E.; Waychunas, G. A.; Xu, N. Uranium(VI) Adsorption to Ferrihydrite: Application of a Surface Complexation Model. *Geochim. Cosmochim. Acta* **1994**, *58* (24), 5465–5478.

CHAPTER 7

Assessing the reactive surface area of soils with ferrihydrite as proxy for natural oxide nanoparticles

Juan C. Mendez, Tjisse Hiemstra, Gerwin F. Koopmans

In peer review for *Environmental Science & Technology*

Abstract

Assessment of the surface reactivity of natural metal (hydr)oxide nanoparticles is necessary for predicting ion adsorption phenomena in soils, using surface complexation modeling. Here, we describe how the equilibrium concentrations of PO_4, obtained with 0.5 M $NaHCO_3$ extractions at different solution-to-soil ratios, can be interpreted with a state-of-the-art ion adsorption model for ferrihydrite to assess the reactive surface area (RSA) of agricultural top-soils. Simultaneously, the method reveals the fraction of reversibly adsorbed soil PO_4 (*R*-PO_4). The applied ion-probing methodology shows that ferrihydrite, rather than goethite, is a better proxy for consistently assessing RSA and *R*-PO_4. The *R*-PO_4 pool agrees well with ammonium oxalate (AO) extractable phosphorous, but only if measured as ortho-phosphate. The RSA varied between ~2–20 m^2/g soil. The corresponding specific surface area (SSA) of the natural (hydr)oxide fraction is ~350–1400 m^2/g, illustrating that the SSA is highly variable and cannot be represented by a single "standard" value, based on the AO-extractable oxide content. The surface loading of soil organic carbon (SOC) increases linearly not only with the increase in RSA but remarkably, also with the mean particle size (1.5–5 nm). To explain these observations, we present a structural model for organo-mineral associations based on the coordination of SOC particles to metal (hydr)oxide cores.

7.1. Introduction

The chemical behavior of many nutrients and pollutants in the environment is largely controlled by sorption phenomena occurring at the surfaces of metal (hydr)oxides.[1,2] These surfaces are also crucial for the formation of organo-mineral complexes, contributing to ion adsorption competition[3,4] and to the long-term stabilization of organic carbon in soils and sediments.[5,6] Particularly, nanocrystalline Fe and Al (hydr)oxides may dominate the reactive metal (hydr)oxide fraction, in for instance, podzols and agricultural top-soils.[1,2,7,8]

Surface complexation models (SCM) can be powerful tools for describing ion adsorption to Fe and Al (hydr)oxides. Presently, the Charge Distribution (CD) model,[9] combined with a multisite ion complexation (MUSIC)[10,11] model, is one of the most advanced approaches.[12–14] This approach was originally developed using the surface structure of well-crystallized metal oxides.[9,10,15–17] Recently, it has been extended for modeling the adsorption of ions to metal (hydr)oxide nanoparticles, particularly ferrihydrite (Fh),[11,18,19] incorporating recent insights into the mineral and surface structure of this nanomaterial.[18,20–22] The CD and MUSIC framework can also be implemented for describing the solid-solution partitioning of oxyanions in soils.[7,23–25] However, for a realistic modeling of ion adsorption phenomena in soils, information about the reactive surface area (RSA) of the natural metal (hydr)oxide fraction is an indispensable prerequisite, and therefore, this is the main topic of the present contribution.

An accurate and consistent assessment of the RSA in soil samples is a challenging task. The use of the traditional gas adsorption method (*i.e.* Brunauer–Emmett–Teller, BET) is not suitable because drying and outgassing processes during sample preparation lead to irreversible aggregation of colloidal nanoparticles, resulting in a underestimation of the RSA.[26–30] Therefore, in SCM studies the RSA is often estimated based on selective extractions of Fe and Al.[23,25,31] For instance, the nanocrystalline fraction of metal-(hydr)oxides is often assessed using the traditional acid ammonium oxalate (AO) extraction[32,33] with conversion to the RSA (m^2/g soil), using standard values for the molar mass (M_{nano}) and for the specific surface area (SSA). However, this approach may lead to inconsistent results because these two properties depend on the size of nanoparticles,[34,35] which can greatly differ amongst soil samples.[36–38]

Hiemstra et al.[7] have developed a probe-ion method for assessing the effective RSA of soils in which soil samples with added activated carbon are equilibrated with 0.5 M $NaHCO_3$ (pH 8.5) at different solution-to-soil ratios (SSR), followed by analysis of the equilibrium PO_4 concentration. These data are then modeled with the CD model to retrieve the RSA, using a chosen metal (hydr)oxide as a reference to represent the natural metal (hydr)oxide fraction in soils. At the time of development, well-crystallized goethite was chosen as proxy because the PO_4–CO_3 interaction had only been studied extensively for this material.[39] However, application of this proxy[7,40] revealed that the metal (hydr)oxide fraction of the studied soils has SSA values that are typical for nano-sized particles with diameters of ~2–8 nm, which is in conflict with the use of well-crystalized goethite as a proxy. Recently, the interaction of PO_4–CO_3 has been measured and modeled for Fh nanoparticles.[41] It has been recently shown that both oxyanions have a rather different competitive adsorption interaction when compared to goethite systems.[41] It implies that using Fh as a proxy will inevitably affect the RSA estimated by modeling of the soil probing data, and therefore, this will be studied here.

The above ion-probing methodology reveals simultaneously the effective RSA resulting from the presence of metal (hydr)oxides in soils, as well as and the pool of reversibly bound PO_4 (R-PO_4) associated to these metal (hydr)oxides. The latter can be compared with the pool of ortho-phosphate

extracted with *e.g.* ammonium oxalate (AO-PO_4). We consider the agreement between *R*-PO_4 and AO-PO_4 as a keystone in making the ion-probing methodology a valid and valuable instrument for consistently assessing the RSA of soils, and for describing the ion adsorption behavior of the natural oxide fraction of soils. However, in the earlier approach,[7] it was overlooked that in the data collection total soluble phosphorus (P_{tot}) rather than inorganic ortho-PO_4 was measured in the AO-extracts, while the samples may contain a variable amount of organic P.[42–44] Therefore, new AO-PO_4 data have been collected in the present study.

The aforementioned ion adsorption framework for Fh includes a systematic implementation of the size-dependency of fundamental properties of this nano-oxide material, including molar mass (M_{nano}) and mass density (ρ_{nano}), which are both crucial for a consistent interpretation and modeling of the ion adsorption data.[45,46] However, in our application of SCM to soils, a complicating factor is that not only Fe but also Al contributes to the composition of the natural metal (hydr)oxides. This will affect, amongst other things, the M_{nano} and particularly, the ρ_{nano} of the natural oxide fraction. The latter property is essential for translating the SSA of the nano-oxide fraction into a corresponding mean particle diameter, which in turn may affect SCM calculations.[46] In this study, our goal is to unravel such a cross-linkage and to develop a systematic and consistent approach in the modelling of ion adsorption data in soils, when this process is governed by the presence of Fe and Al (hydr)oxide nanoparticles. Finally, our data analysis will show that the calculated RSA and the soil organic (SOC) content are tightly related in our soils. Therefore, we explored this relation and developed a conceptual model that describes the possible structural arrangement of the nano-scale associations between metal (hydr)oxide and organic matter particles. This is important because the organo-mineral associations are considered as a key factor contributing to the long-term stability of SOC.[5,26,47]

7.2. Methodology

7.2.1. Soil samples

We used the dataset of Hiemstra et al.[7,48] of 19 soil samples, which were selected from a larger collection of representative Dutch agricultural top-soils.[49] The selected samples cover a wide range of pH values (~4.0–7.0), SOC (~1–15%), clay content (~3–30%), 0.01 M $CaCl_2$-soluble PO_4 (~1–30 μM), and Fe- and Al-(hydr)oxides extractable with AO[32] ($[Fe+Al]_{AO}$, 14–361 mmol/kg) and in dithionite–citrate–bicarbonate (DCB) ($[Fe+Al]_{DCB}$, 22–879 mmol/kg). The chemical properties of these soil samples are presented in Table S7.1 of the Supporting Information (SI). The underlying data are taken from Hiemstra et al,[7] where details about the analytical procedures are given. In the present study, for all soil samples (except for soil 11), we additionally determined colorimetrically, using a molybdenum-blue method[50] with a Segmented Flow Analyzer (SFA), the ortho-phosphate concentration in AO soil extracts (AO-PO_4) after dilution with deionized-water (×100) to eliminate the interference of oxalate in the AO-PO_4 measurements,[42,44] for which we have tested.

7.2.2. Phosphate desorption data

The PO_4 desorption data are from Hiemstra et al,[7] which were obtained by equilibrating soil samples (~10–15 days) with freshly–prepared solutions of 0.5 M $NaHCO_3$ (pH 8.5) at six solution-to-soil ratios (SSR) ranging between 5–300 L/kg. The equilibrium PO_4 concentrations were measured colorimetrically,[50] using a SFA instrument. To remove dissolved organic matter released during the

$NaHCO_3$ extractions, powdered activated carbon was added (0.40 g/g soil) to the soil suspensions. Details about the experimental procedure are given in Hiemstra et al.[7]

7.2.3. Surface complexation modeling

The competitive PO_4–CO_3 interaction in the 0.5 M $NaHCO_3$ soil extracts was interpreted with a model framework built from the combination of the CD model[9] and a novel structural multi-site surface complexation (MUSIC) model for Fh.[11] The compact part of the electrical double layer was described with the extended curved Stern layer approach.[51,52] The surface and solution speciation reactions for Fh are presented in Tables S7.2 and S7.3, respectively. The latter includes the complexation of protons, electrolyte ions, PO_4, and CO_3.[11,41] The pH, $NaHCO_3$ concentration, SSR (L/kg) , and gas-to-solution volume ratio (L/L) were used as input data for the modeling. The effective reactive surface area (RSA) and total reversibly bound PO_4 (R-PO_4) were the only adjustable parameters, which were fitted simultaneously by iterative CD model calculations (Section 7.3.1). Model calculations were done with the software Ecosat[53] (version 4.9) in combination with the FIT[54] program for parameters optimization.

7.3. Results and Discussion

7.3.1. Background

For each soil sample, a pool of reversibly bound ortho-phosphate, R-PO_4 (mol/kg) is defined for which the value is fixed at the time of sampling in the field. During equilibration in closed systems with 0.5 M $NaHCO_3$ solution at different SSR (L/kg), R-PO_4 is then redistributed over the solid and solution phases according to the mass balance:

$$R\text{-}PO_4 = A\,\Gamma + SSR\,c \qquad \text{(Equation 7.1)}$$

where A is the effective RSA of the soil (m^2/kg soil), Γ is the PO_4 surface density of the metal (hydr)oxide fraction present in the soil (mol/m^2), and c is the equilibrium PO_4 concentration in solution (mol/L).

Using this mass balance, one can derive iteratively the surface area A and R-PO_4, by measuring the equilibrium concentrations c_i at various SSR_i. The measurement of c as a function of SSR results in PO_4 desorption curves as shown Figure S7.1. Key in the methodology to calculate the surface area A and R-PO_4 is the translation of the measured concentrations c_i into the PO_4 surface loading Γ_i. Actually, the relationship $\Gamma_i - c_i$ is the competitive adsorption isotherm of PO_4 in the $NaHCO_3$ solution, whose interpretation will depend on the type of metal (hydr)oxide used as reference in the CD model calculations.[41] For a chosen reference oxide, a minimum set of two (i =2) combinations of c_i and SSR_i allows the calculation of the surface area A according to:

$$A = \frac{\Delta(SSR_i \times c_i)}{\Delta\,\Gamma_i} \qquad \text{(Equation 7.2)}$$

with Δ indicating the change in the values of the respective parameters with index i = 1 and 2.

The calculation of the PO_4 adsorption density is sensitive to uncertainty in the experimental c value in the 0.5 M $NaHCO_3$ extracts. Therefore, six SSRs are used in the present study. These data reveal part of the desorption isotherm that can be interpreted with the CD model to derive the values of A and R-PO_4 by iterative optimization.

7.3.2. PO_4 adsorption in model systems: ferrihydrite vs goethite

The competitive adsorption isotherm applied in Equations 7.1 and 7.2 to relate Γ_i and c_i will depend on the type of metal (hydr)oxide. This implies that the calculation of both A and R-PO_4 will be influenced by the choice of either Fh or goethite as reference oxide in the modeling and interpretation of the data collected with the probe-ion method. Recently, it has been shown that CO_3 ions compete much stronger with PO_4 for adsorption to Fh, than in case of goethite.[41] As shown in Figure 7.1a for a system with 0.5 M $NaHCO_3$ (pH 8.5), the difference between goethite and Fh is loading-dependent. In other words, the results obtained with the probe-ion method for A and R-PO_4 will be different.

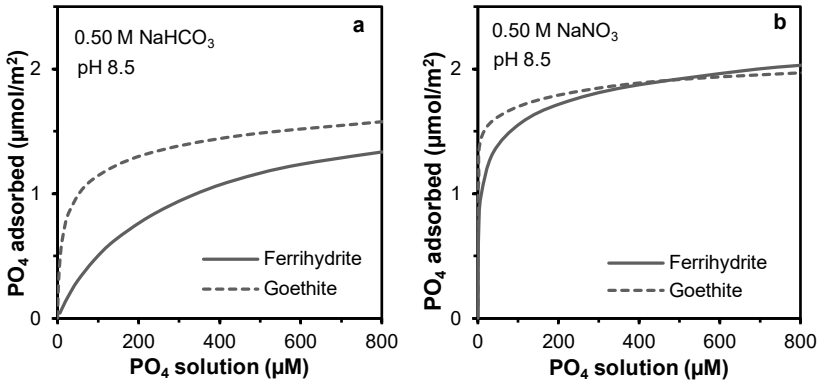

Figure 7.1. Phosphate (PO_4) adsorption isotherms of ferrihydrite (full lines) and goethite (dashed lines) in systems with 0.5 M $NaHCO_3$ (**a**) and 0.5 $NaNO_3$ (**b**) at pH 8.5, calculated with the CD model, using parameters sets from Hiemstra and Zhao[11] and Mendez and Hiemstra[41] for ferrihydrite and Rahnemaie et al.[39] for goethite.

In 0.5 M $NaHCO_3$ systems (Figure 7.1a), the adsorption of PO_4 to both oxides is lower than in systems with 0.5 M $NaNO_3$ (Figure 7.1b). This is due to the competition of CO_3 and PO_4 for the same binding sites at the mineral surfaces. In the presence of CO_3, the decrease in the PO_4 adsorption is most distinct for Fh (Figure 7.1a), particularly at low PO_4 concentrations, illustrating that CO_3 suppresses more efficiently the adsorption of PO_4 to the surface of Fh[41] than to the surfaces of goethite.[39,41] Differences in the surface speciation of CO_3 may explain the different CO_3–PO_4 interaction in both oxides (Figure S7.2).

In 0.5 M $NaHCO_3$ Fh preserves less well the high affinity character of PO_4 adsorption, which is visible in the form of a lower slope of the isotherm, particularly at low PO_4 concentrations. This implies that Fh has a lower capacity to buffer the PO_4 concentration during extraction of soil with 0.5 M $NaHCO_3$. This property will have implications for the probe-ion method in assessing the RSA of soils. Hence, a fundamental question arises of which Fe (hydr)oxide most accurately represents the ion adsorption behavior of the natural oxide fraction of top-soils, *i.e.* which reference material is a better proxy for the natural oxide fraction? This will be answered in the following section.

7.3.3. Reversibly adsorbed phosphate: experimental and model results

For testing which reference oxide material, either Fh or goethite, is a better proxy for describing with SCM the reactivity of the natural metal (hydr)oxide in top-soils, one may collect experimental information regarding the size of the reversibly bound PO_4 pool in soils and compare these results with

the calculated *R*-PO_4 pool from the probe-ion method. The extraction of soil with AO is often used for assessing the fraction of metal (hydr)oxides present in soil as nanoparticles, because it has been shown that Fh is completely dissolved with that procedure, in contrast to well-crystallized metal (hydr)oxides.[1,33,55] The AO extraction method is also used to assess the degree of P saturation of soils,[56–58] by measuring with ICP-OES simultaneously the amount of P released. Laboratory experiments using a P sink technique have shown that all P_{tot} extractable from soil with AO is potentially desorbable.[59] This P_{tot} pool was also largely available for uptake by grass in a long-term P-mining experiment.[60] However, part of the measured P_{tot} in the AO extracts may not be present as ortho-phosphate,[42,61] whereas the probe-ion method is based on the measurement of the equilibrium PO_4 concentration in the $NaHCO_3$ extracts. Therefore, in this study the molybdenum-blue method[50] has been applied to measure the ortho-PO_4 pool in the AO extracts.[43,44] For our soils, the difference between the total amount of P (AO-P_{tot}) and ortho-PO_4 (AO-PO_4) measured in the AO extracts is on average ~40 ± 9 %. The difference could be attributed mainly to the presence of organic P (P_{org}).[43] Indeed, a significant relationship ($R^2 = 0.60$, $p < 0.001$) is found between P_{org} = AO-P_{tot} minus AO-PO_4 and the bulk SOC content (Figure S7.3b).

The presence of P_{org} in the AO-extracts implies that the validation of the probe-ion method cannot be based on the comparison between the calculated *R*-PO_4 and the amount of AO-P_{tot}, as it was done previously.[7] In other SCM studies, using AO-P_{tot} as a proxy of *R*-PO_4 has led to overestimations of the PO_4 concentration in soil leachates[62] and soil extraction solutions.[25] However, in these studies, the contribution of P_{org} to the AO-P_{tot} was not explicitly assessed. Based on these results, the authors have proposed the use of isotopically exchangeable PO_4 (*E*-value) as a proxy for *R*-PO_4 in SCM. However, the results of this methodology are inherently associated to the kinetics of P exchange and are influenced by the chosen evaluation time.[63]

In Figure 7.2, the modeled *R*-PO_4 pool is compared with the experimental measurements of AO-PO_4. When goethite is used as a reference oxide material in the interpretation of the probe-ion method, the calculated amount of *R*-PO_4 are approximately ~2 times higher than the measured AO-PO_4 pool. This clearly indicates that the PO_4 adsorption behavior of the metal (hydr)oxide fraction of soils in 0.5 M $NaHCO_3$ solutions cannot be well-represented by goethite. However, when Fh is used as a reference oxide material, a good agreement (1:1 line) between modeled and measured amounts of reversibly adsorbed PO_4 is found, indicating that Fh is a better proxy for the natural oxide fraction of our top-soils.

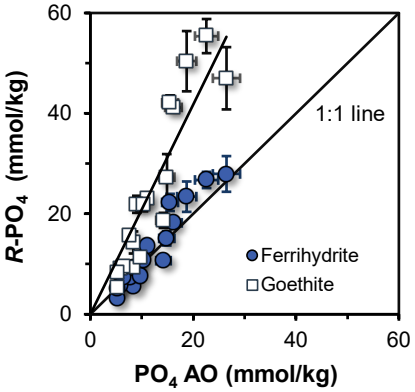

Figure 7.2. Relationship between the ammonium oxalate extractable ortho-phosphate (AO-PO_4) and the amount of reversibly adsorbed PO_4 in soils (*R*-PO_4), calculated with the CD model using either goethite (squares) or ferrihydrite (circles) as reference oxide. In the latter case, the data are closer to the 1:1 line. For sample 11, no data for AO-PO_4 is available, and therefore, this sample is not included in the analysis.

7.3.4. Reactive surface area of Fe and Al-(hydr)oxides

In Figure 7.3, the calculated values of effective RSA are given for the set of top-soil samples used in this study. When Fh is used as reference oxide in the CD modeling (closed symbols), the RSA values vary by a factor of ~10 across this soil series, *i.e.* ~2–20 m^2/g. If goethite is used as reference oxide, the RSA values are on average ~1.5 times higher. The lower RSA in case of Fh, combined with the calculated surface PO_4 loading in the 0.5 M $NaHCO_3$ solutions (Figure 7.1), explain the amount of ortho-phosphate measured in the AO soil extracts (Figure 7.2). The latter cannot be said when goethite is used as a proxy for the natural metal oxide fraction of our top-soils.

As expected, the content of AO-extractable Fe and Al ($[Fe+Al]_{AO}$ in mmol/kg) positively correlates with the RSA calculated with the probe-ion method. In Figure 7.3, the slope of the line represents the mean value of the specific surface area, being SSA = 65 ± 12 m^2/mmol using Fh as model oxide. Translating this value using a mean molar mass of *e.g.* 89 g/mol Fe+Al yields a mean value of SSA = 730 ± 130 m^2/g oxide. For the erroneous case of using goethite as a proxy, the corresponding mean value would be SSA = 1120 ± 250 m^2/g oxide. Using in the scaling $[Fe+Al]_{DCB}$ instead of $[Fe+Al]_{AO}$ (Figure S7.4), these SSA values will decrease because $[Fe+Al]_{AO}$ in our soil samples represents on average ~60 ± 15% of the total metal (hydr)oxide content. The difference from $[Fe+Al]_{DCB}$ minus $[Fe+Al]_{AO}$ is attributed to the presence of well-crystallized metal (hydr)oxides. However, this fraction is supposed to have a significantly lower SSA. In laboratory preparations, crystalline Fe (hydr)oxides usually have SSAs that are up to ~10 smaller than the SSA of Fh.[1,35] Hence, in our soil samples, the well-crystallized oxides will contribute more in terms of mass than in terms of surface reactivity. Indeed, the $[Fe+Al]_{AO}$ fraction represents ~90 ± 10% of the total metal (hydr)oxide reactivity on a surface area basis, according to exploratory calculations discussed in Figure S7.5.

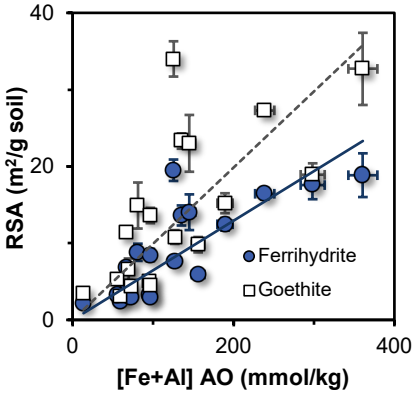

Figure 7.3. Relationship between Fe and Al content, extracted with an acid ammonium oxalate solution (AO, pH 3), and the effective reactive surface area (RSA) of the soil samples obtained by modeling the results of the probe-ion method, using either goethite or ferrihydrite as reference oxide. The slope of the lines indicates the mean specific surface area which in case of using goethite as reference material is very high, about SSA ~100 m^2/mmol. With the use of ferrihydrite as reference oxide material, a more realistic value for the mean specific surface area is obtained, SSA ~65 m^2/mmol.

The RSA values derived with the probe-ion method represent an "effective" reactive surface area, resulting from probing all surfaces in soil that bind PO_4 and whose adsorption interactions are described using a well-characterized proxy, which in our case is Fh. The metal (hydr)oxide fraction is thought to

be the most important reactive material for the binding of PO_4 in soils, due to its much higher affinity for oxyanions and larger SSA in comparison with other reactive soil surfaces.[24,42,64] The oxidic edges of clay minerals can also contribute to the RSA of fine-textured soils.[65] The possible contribution of clays to the RSA of the soil can be inferred from the regression analysis of the relationship between RSA and $[Fe+Al]_{AO}$ (Figure 7.3), if the clay and metal (hydr)oxide content are not correlated. A positive and significant intercept of the linear regression line in Figure 7.3 might then suggest a contribution of clay minerals to the RSA. However, such a contribution cannot be resolved statistically for our data. Our regression analysis shows that the intercept is not significantly different from zero ($p < 0.001$).

The physicochemical properties of naturally formed metal (hydr)oxide nanoparticles may differ from those of their synthetic counterparts.[1,66] In nature, the nanocrystalline structure and particle size distribution of Fh is affected when it precipitates in the presence of organic matter,[67–70] or inorganic ions (*e.g.* Al^{3+}, Si^{4+}).[71–73] This has raised concerns about the use of SCM, parametrized for synthetic oxides, for describing ion adsorption to the natural metal (hydr)oxide fraction of soils.[66] However, despite the molecular-scale differences found for the binding preferences of PO_4 to Al/Fe coprecipitates, the macroscopic adsorption of PO_4 was indistinguishable from that of pure Fh at Al/(Fe+Al) molar ratios < 0.50.[74] Similarly, our results show than the overall macroscopic adsorption behavior of PO_4 to the metal (hydr)oxides in soils can be well-described using Fh as reference material. From a practical perspective, the present study is relevant as it supports the use of Fh as a single model oxide for describing with SCM the interaction of oxyanions with metal (hydr)oxide in top-soils.

7.3.5. Size-dependent properties of natural metal (hydr)oxides

Translation of the specific surface area SSA (m^2/mol) to an equivalent mean particle size d (m) of natural metal-(hydr)oxide nanoparticles requires a consistent set of values for the molar mass M_{nano} (g/mol) and mass density ρ_{nano} (g/m^3). These values can be assessed using a set of mathematical relationships, as given by Hiemstra.[45] Since M_{nano} and ρ_{nano} are both particle size-dependent, they cannot be calculated directly, but their values are derived iteratively as explained in Appendix E of the SI.

The M_{nano} and ρ_{nano} of Fe- and Al-(hydr)oxide nanoparticles depend on the chemical composition of these minerals. For Fh, the chemical composition can be given as $FeO_{1.4}(OH)_{0.2}{\cdot}nH_2O$, where $FeO_{1.4}(OH)_{0.2}$ is the composition of the bulk mineral and nH_2O is the amount of chemisorbed water completing the coordination sphere of the Fe atoms present at the surface.[18,35] Similarly, one may write for nano-particulate Al hydroxide the composition $Al(OH)_3{\cdot}nH_2O$. In both cases, the fraction of metal ions forming surface groups will increase when the particle size decreases, leading to an increase in nH_2O. Consequently, M_{nano} will increase at decreasing particle size, whereas ρ_{nano} will simultaneously decrease because the surface groups ($–OH_2$ and –OH) contribute more to the particle volume than to the mass.[35]

In Figure 7.4a, the excess amount of chemisorbed water (nH_2O) of Fh and $Al(OH)_3$ nanoparticles is presented as a function of the SSA. For Fh (colored squares), the data are from Hiemstra.[75] For comparison, experimental data of Michel et al.[20] (open squares) are given. The data for $Al(OH)_3$ have been derived in the present study following a whole particle construction approach, as described previouly.[18,75] Briefly, near-spherical nanoparticles with different size are constructed with the Crystalmaker® software and the amount of coordinative water of these particles is calculated after completion of the coordination spheres of the metal ions at the surface by adding additional –OH and $–OH_2$ groups.[75] As follows from Figure 7.4a, the excess amount of water is less for $Al(OH)_3$ nanoparticles (circles) than for Fh (squares). The reason is that for $Al(OH)_3$, part of the surface ligands are already

present as -OH, while this is mainly -O in case of Fh. The slope of the linear relationships of Figure 7.4a represents the surface loading of excess chemisorbed water, being N_{H2O} = 12.6 µmol/m^2 for Fh and N_{H2O} = 6.3 µmol/m^2 for $Al(OH)_3$.

In Figure 7.4b, the relation between specific surface area (SSA) and the equivalent spherical particle size, calculated with Equation S7.3, is given for Fh (full line) and nano-particulate $Al(OH)_3$ (dashed line). For spherical particles with the same diameter, the SSA is considerably different for Fh and $Al(OH)_3$. The latter material has a much higher SSA at a given particle diameter, because $Al(OH)_3$ has a much lower mass density since the oxygen ions of the lattice are neutralized by light (Al) and very light (H) elements, in contrast to Fh where most neutralizing cations are heavy (Fe). The higher SSA of $Al(OH)_3$ at the same particle size may contribute to the observed higher PO_4 adsorption capacity of Al-(hydr)oxides compared to Fe-(hydr)oxides, when expressed in mol PO_4 per mol Al/Fe.[74] Similar results have been recently reported for the adsorption of PO_4 and AsO_4 to mixtures of nanocrystalline Fe and Al (hydr)oxides.[76]

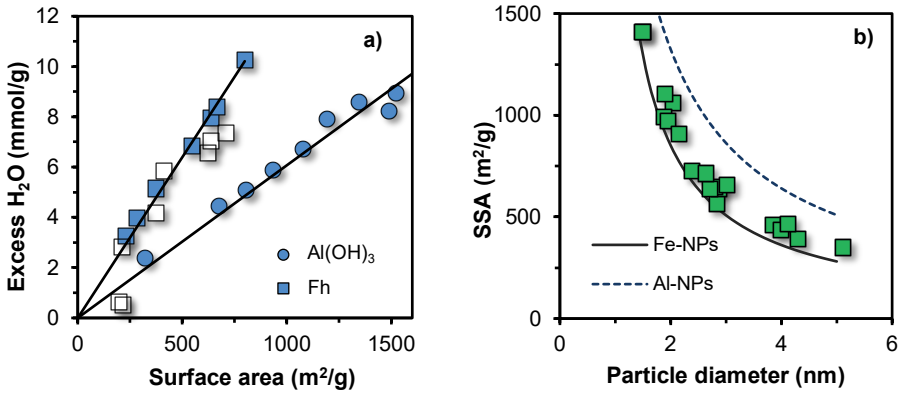

Figure 7.4. (**a**) Relationship between the specific surface area and the excess amount of chemisorbed water of Fh (squares) and $Al(OH)_3$ (circles) nanoparticles, derived by a whole particle construction approach.[75] Open symbols are experimental data for Fh taken from Michel et al.[20] (**b**) Theoretical relationship between the mean particle size and the specific surface area of Fh (dashed lines) and $Al(OH)_3$ (dotted lines) nanoparticles, calculated using the set of mathematical relationships given by Hiemstra[45] and described in Appendix E of the SI. Symbols are for the natural oxide fraction of top-soils studied here (see text).

Figure 7.4b also shows the equivalent particle diameter (d) of the natural metal (hydr)oxides in the various soils of this study (symbols). The calculated equivalent particle size varies between ~1.5–5 nm. The smallest particles would contain typically ~50 metal ions and the largest ones ~2000. The calculated diameter values are between those of Fh and $Al(OH)_3$ because the natural metal (hydr)oxides contain ~5–50% Al as found in the AO extracts (Table S7.1). This Al can be partly present in the Fe-(hydr)oxides by Al-substitution.[1] When Fh is synthesized in the presence of Al, substitutions of up to ~20–30 mol% Al have been reported for the formed Fh before precipitation of secondary Al-(hydr)oxide phases occurs.[77,78]

The above equivalent particle diameters for the natural oxide fraction (Figure 7.4b) have been calculated applying the set of equations given by Hiemstra.[45] In the present approach, equal size is assumed for all metal (hydr)oxide particles in a soil, irrespectively of the Al/Fe ratio found in the AO extract. For each soil sample, the overall SSA of the reactive metal (hydr)oxide fraction has been

calculated as the mass-weighted average of the surface area of the fractions represented by the Fe (A_{Fe}) and Al (A_{Al}) (hydr)oxides. Details of the calculation procedure are given in Appendix E of the SI.

Table 7.1 summarizes a series of size-dependent properties of the metal (hydr)oxide fractions derived for our soils. The values for each individual sample are given in Table S7.1. The SSA of the reactive metal (hydr)oxide largely varies between ~350–1400 m^2/g, illustrating that the use of "standard" SSA values (*i.e.* 600 m^2/g) for the AO-extractable Fe and Al-(hydr)oxides, as generally done in SCM studies,[25,31,62] may lead to large deviations in the estimated amount of available reactive sites for ion adsorption.

Table 7.1. Summary of the particle size-dependent characteristics of reactive metal (hydr)oxide nanoparticles for a set of agricultural top-soil samples from the Netherlands.

	Diameter *d*	**M_{nano} (g/mol)[a]**		**ρ_{nano} (g/cm^3)[a]**		**SSA[b]**
	(nm)	**Fe**	**Al**	**Fe**	**Al**	**(m^2/g oxide)**
average	2.83	96.6	88.9	3.78	2.30	760
min	1.50	87.0	82.7	3.10	2.21	350
max	5.13	115.4	98.5	4.28	2.36	1400

[a] The reactive metal (hydr)oxide fraction is assumed to be composed by only Fe and Al-(hydr)oxides, whose content is estimated from the amount of AO-extractable Fe and Al. The values of ρ_{nano} and M_{nano} are calculated with equations S7.1 and S7.2 respectively, assuming a common equivalent particle diameter for the Fe and Al-(hydr)oxide nanoparticles (see Appendix E in the SI).

[b] The SSA was calculated iteratively (Equations S7.5-S7.6) to account for the size dependency of ρ_{nano} and M_{nano}. It represents the overall SSA of the whole oxide fraction, which is a mass-weighted average, based on the content Fe and Al extracted with AO. The SSA values are rounded to the nearest ten.

The M_{nano} values of the Fe and Al-(hydr)oxides nanoparticles are on average ~15–20% higher than the corresponding molar mass of the bulk minerals $FeO_{1.4}(OH)_{0.2}$ and $Al(OH)_3$. The equivalent diameters (*d*) range between ~1.5–5.0 nm, in agreement with previous studies stating that nano-size particles dominate the reactive metal (hydr)oxide in top-soils.[7,37,79] Direct measurements for the size of natural nanoparticles in soils are scarce in literature. Using Asymmetric Field-Flow Fractionation, a size range of ~2–10 nm was found for Fe-(hydr)oxide nanoparticles dispersed with pyrophosphate from a podzol soil, with maximum concentrations found at a particle size of ~5 nm.[36] These results provided direct evidence for the presence of reactive nano-size particles in the metal (hydr)oxide fraction of that soil.

7.4. Organo-mineral interaction: structural arrangement

In the literature, the relationship between soil organic carbon (SOC) and metal (hydr)oxide content has been well-recognized for various soil types.[26,80,81] With our probe-ion methodology, the relationship between SOC and the calculated values of RSA can now be evaluated, contributing to obtain more insights into the interaction between natural metal (hydr)oxide nanoparticles and humic substances. This interaction is important because it contributes to the long-term stabilization of SOC,[26,47,82,83] and to the apparent high stability in the environment of otherwise metastable metal (hydr)oxide nanoparticles.[35,84] Moreover, the SOC-metal (hydr)oxide interaction is important for predicting the fate of oxyanions in the environment, as shown in Figure S7.6 for PO_4.

In the agricultural soils of this study, the total SOC content is well-related to RSA ($R^2 = 0.50$, $n = 18$). This relationship becomes even clearer when the samples are categorized according to the soil texture, as shown in Figure 7.5a. Sample 11 has been excluded from this analysis since this is a peaty soil. The slopes of the lines in Figure 7.5a give the maximum amount of organic carbon that can be associated with minerals (MOC). For the soils with low clay content (< 20%), the maximum MOC value is ~2.2 mg C/m^2 oxide. For the soils with a high clay content (>= 20 %), the maximum MOC value is ~2 fold higher (~4 mg C/m^2 oxide), probably due to an additional contribution of SOC interacting with the clay surfaces, for instance *via* Ca^{2+} bridging.[85,86] Moreover, mineral associations between clays and oxides may contribute to physical-chemical stabilization of SOC when organized in micro-aggregates.[8,47,81,86]

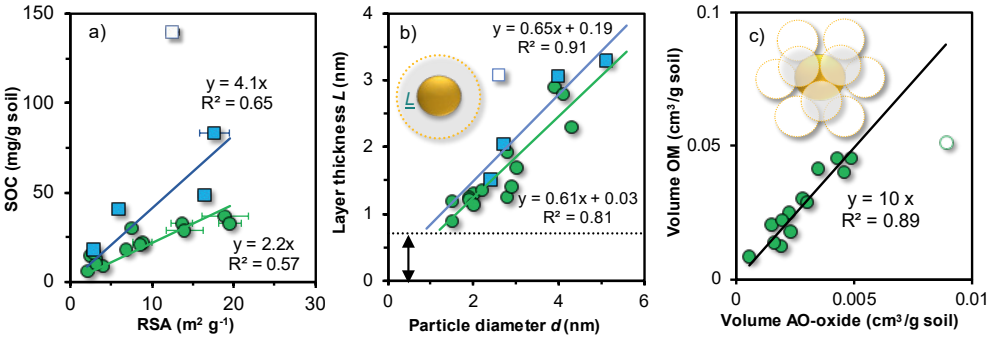

Figure 7.5. (**a**) Relationship between bulk soil organic carbon (SOC) and effective reactive surface area (RSA) for our mineral top-soils with a clay content < 20 % (circles) and ≥ 20 % (squares). The slope of the lines represents the mean adsorption density of OC (mg/m^2). Sample 11 (open symbol) was excluded from the regression analysis due to the exceptionally high SOC content of this peaty soil. (**b**) Relationship between the layer thickness *L* of SOM and the mean particle diameter of the reactive metal (hydr)oxide fraction, according to a core-surface layer model (inset), showing that larger oxide particles are associated with more organic matter. (**c**) Relationship between the volumes of SOM and the volumes of the Fe+Al nano-oxide fraction, extractable with AO, both expressed in cm^3/g soil. The open symbol refers to a soil with an exceptionally high Fe+Al oxide content (soil 3) and therefore it has been excluded from the calculation of the mean volume ratio R_v, which is for our data set $R_v = 10 \pm 2$. If this R_v is interpreted as a coordination number (CN), the arrangement of SOM particles around a metal (hydr)oxide core varies between cubic (CN = 8) and cub octahedral (CN = 12). The latter is shown in the inset.

To sketch the contours of the interaction of SOC with metal (hydr)oxide nanoparticles, one may consider a mineral core–surface layer model in which all SOC is accommodated in a layer around the metal (hydr)oxide particles (inset Figure 7.5b). In this approach, the fitted layer thickness *L* varies between ~1–3 nm. The underlying calculations are given in Appendix I of the SI. The calculated layers (*L*) are larger than the thickness of the compact part of the double layer, being ~0.7 nm,[51] indicated with an arrow in Figure 7.5b. Only the smallest (hydr)oxide particles of Figure 7.5b with a low value of *L* could in theory accommodate a significant fraction of the total SOC in the compact part of the double layer.

Remarkably and counter-intuitively, the calculated layer thickness *L* increases linearly ($R^2 = 0.81$) with increasing the mean size of the metal (hydr)oxide particles in the soils, as given in Figure 7.5b. If this is due to a physical and/or chemical protection of SOC against microbial decomposition,[5,26,47] the relation suggests a more efficient protection when particles are relatively large. This picture might be

understood from a more robust organization of the organo-mineral particles forming larger micro-aggregates.

The SOC-mineral interaction can also be interpreted with another structural picture in which the organo-mineral association is seen as a collection of discrete particles of metal (hydr)oxide and SOM. Excluding the soils with a high clay content, a significant relationship is found ($R^2 = 0.89$, $p < 0.001$) between the volume of both types of particles, yielding volume ratio of 10 ± 2. This ratio is high in comparison to the value of ~1 estimated at maximum adsorption of SOM to synthetic Fe (hydr)oxides.[87,88] If the high volumetric ratio of Figure 7.5c is interpreted as a particle coordination number (CN), the structural arrangement varies between a cubic (CN = 8) and a cub-octahedral (CN = 12) configuration. According to Pauling's first rule, such an arrangement requires a ratio of particle radii of respectively 0.73 (CN = 8) and 1.0 (CN = 12). This suggests that the primary particles of SOC and metal (hydr)oxide in a given soil tend to be rather similar in size. In light of the relation given in Figure 7.5b, an increase in the size of the metal (hydr)oxide particle is accompanied by a corresponding increase of the mean SOC particle size. As mentioned, this might be related to the formation of larger micro-aggregates, which are more resistant against degradation.

In soils, Ca^{2+} ions play an important role in the colloidal stabilization of negatively charged SOM molecules[89,90] and negatively charged metal (hydr)oxide particles that carry adsorbed oxyanions, such as PO_4.[91] In the case of Fh, the Ca^{2+} ions are predominantly bound in ternary ≡Fe-PO_4-Ca complexes,[91] which strongly reduce the net particle charge (Figure S7.7). The corresponding Ca^{2+} ions are mainly present in the outer Stern layer, and therefore, may serve as cation bridges that link by interaction with functional $RCOO^-$ groups of SOC both types of particles together, contributing to the formation of a relatively large network of these particles.

Acknowledgements

We gratefully acknowledge the financial support of the University of Costa Rica.

Supplementary Information

A. Results of the probe-ion method (0.5 M $NaHCO_3$ extractions)

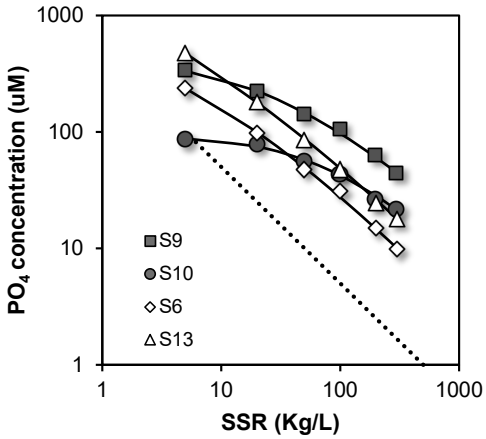

Figure S7.1 Equilibrium phosphate (PO_4) concentration in the 0.5 M $NaHCO_3$ soil extracts as a function of solution-to-soil ratio (SSR) for four selected soil samples (symbols). Lines are CD model calculations obtained with the parameter set presented in Table S3 and using ferrihydrite as a proxy for the metal-(hydr)oxide fraction of the selected top-soils. The dotted line represents a linear dilution curve, where a 10-fold increase in SSR (x-axis) would result in a 10-fold decrease in the PO_4 concentration in solution. This linear dilution curve would predict the PO_4 concentration if soils would not release any additional PO_4 via desorption upon further dilution of the soil samples with 0.5 M $NaHCO_3$ solution.

B. **Properties of the selected soil samples**

Table S7.1. Chemical characteristics of the agricultural top-soils from the Netherlands selected for the present study and properties of the natural metal (hydr)oxide fraction of these soils, which have been derived in the present study from the application of the probe-ion method and data interpretation with the CD model, using ferrihydrite as reference oxide material.

				DCB [c]		AO [d]									A [f]		M_{nano} [f]		ρ_{nano} [f]		
Soil	pH [a]	OC [b]	Clay	Fe	Al	Fe	Al	P_{tot}	PO_4	PO_4 [a]	DOC [a]	*R*-PO_4 [e]	RSA [e]	*d* [f]	Fe	Al	Fe	Al	Fe	Al	SSA [g]
		mg/g	%	mmol/kg		mmol/kg				µM	mg/L	mmol/kg	m^2/g soil	nm	m^2/g		g/mol		g/cm^3		m^2/g
1	4.3	18	5	48	41	32	34	20	11	30.0	11.6	13.6 ± 0.6	6.8 ± 0.5	2.0	823	1288	100.4	91.6	3.55	2.27	1060
2	5.2	22	7	119	39	49	33	23	15	17.7	19.6	15.1 ± 1.4	8.8 ± 1.1	1.9	907	1391	102.8	92.9	3.46	2.26	1099
3	5.6	37	8	852	27	342	19	38	19	1.6	16.2	23.4 ± 3.0	18.9 ± 2.8	2.8	544	915	93.1	87.2	3.89	2.31	563
4	5.6	33	11	125	34	93	33	32	23	6.8	13.7	26.7 ± 1.6	19.5 ± 1.4	1.5	1277	1796	114.9	98.3	3.11	2.22	1406
5	4.9	13	15	168	30	76	20	15	8	2.3	19.5	5.5 ± 0.2	3.2 ± 0.2	4.3	333	594	88.3	83.7	4.19	2.35	387
6	5.0	15	9	68	25	43	16	8.6	5	1.9	12.6	3.2 ± 0.1	2.4 ± 0.1	3.9	378	666	89.3	84.5	4.12	2.34	457
7	5.7	9	11	135	27	50	19	15	8	17.1	8.7	9.3 ± 0.7	4.0 ± 0.6	2.9	536	904	93.0	87.1	3.90	2.31	637
8	5.0	30	14	101	32	96	31	19	8	1.6	26.6	7.4 ± 0.3	7.5 ± 0.3	2.8	553	929	93.4	87.3	3.88	2.31	645
9	4.6	49	21	242	36	211	28	35	16	2.6	37.0	18.2 ± 0.7	16.4 ± 0.7	2.4	672	1094	96.3	89.2	3.73	2.29	720
10	4.9	83	25	318	59	252	46	26	9	0.6	32.0	9.0 ± 0.8	17.6 ± 1.8	2.7	574	959	93.9	87.7	3.85	2.31	634
11	5.5	140	28	146	N.D.	132	58	20	N.D.	2.9	71.7	8.5 ± 0.4	12.5 ± 0.8	2.6	593	985	94.3	88.0	3.83	2.30	712
12	4.5	33	13	233	29	114	21	30	15	27.1	23.9	22.3 ± 1.7	13.6 ± 1.3	1.9	917	1402	103.1	93.0	3.45	2.26	990
13	7.2	18	26	178	32	65	32	14	6	2.3	13.8	5.7 ± 0.1	2.9 ± 0.1	5.1	273	497	87.0	82.7	4.28	2.36	347
14	6.8	6	3	16	6	11	3	7.8	6	17.1	4.9	7.3 ± 0.1	2.1 ± 0.1	1.5	1294	1812	115.6	98.6	3.10	2.21	1403
15	6.4	41	28	200	30	117	39	24	14	5.8	17.7	10.7 ± 0.2	5.9 ± 0.2	4.0	362	641	89.0	84.2	4.14	2.34	432
16	6.0	10	6	84	34	31	24	16	10	9.4	6.0	7.6 ± 0.1	3.2 ± 0.1	3.0	502	855	92.2	86.5	3.95	2.32	654
17	7.1	29	12	277	32	116	29	40	26	23.9	12.5	27.9 ± 3.6	14.0 ± 2.3	2.0	873	1350	101.8	92.4	3.50	2.26	968
18	5.6	21	12	116	36	68	29	19	10	4.2	17.5	10.8 ± 0.8	8.5 ± 0.8	2.2	773	1225	99.0	90.8	3.61	2.28	906
19	6.3	16	17	153	59	42	30	11	5	4.2	12.0	5.0 ± 0.1	2.9 ± 0.1	4.1	349	620	88.7	84.0	4.16	2.34	461

[a] Measured in 0.01 M $CaCl_2$ extract (solution-to-solid ratio SSR = 10 L/kg, time = 2 h).[49]
[b] Measured according to Kurmies method.
[c] Dithionite-citrate-bicarbonate extraction as reported by Hiemstra et al.[7] based on Holmgren.[92]
[d] Acid ammonium oxalate extraction as reported by Hiemstra et al.[7] based on Schwertmann.[32]
[e] Reactive surface area (RSA) and total reversibly bound PO_4 (*R*-PO_4) derived with the CD model by interpreting the results of the probe-ion method, using Fh as reference oxide material.
[f] Properties of the nanocrystalline Fe and Al (hydr)oxides, derived from the scaling of RSA to the content of Fe and Al extractable in AO (see Appendix E for explanation).
[g] Mean SSA of the whole metal (hydr)oxide fraction, which has been mass-weighted based on the AO extractable content of Fe and Al (see Appendix E for explanation).

C. Thermodynamic databases used in the modelling

Table S7.2. Thermodynamic database including surface species, charge distribution (CD) coefficients and log*K* values for the surface complexation reactions implemented in the CD model, using ferrihydrite as reference oxide material. The surface sites densities are from Hiemstra and Zhao[11] with ≡FeOH(a) = 3.0 nm^{-2}, ≡FeOH(b) = 2.8 nm^{-2}, and Fe_3O = 1.4 nm^{-2}.

Species	≡FeOH(a)$^{-0.5}$ &	≡FeOH(b)$^{-0.5}$ &	≡$Fe_3O^{-0.5}$	Δz_0	Δz_1	Δz_2	H^+	CO_3^{2-}	Na^+	PO_4^{3-}	NO_3^-	log*K*
FeOH(a)$^{-0.5}$	1	0	0	0	0	0	0	0	0	0	0	0
$FeOH_2$(a)$^{+0.5}$	1	0	0	1	0	0	1	0	0	0	0	8.1*
FeOH(a)$^{-0.5}\cdots Na^+$	1	0	0	0	1	0	0	0	1	0	0	-0.60 ± 0.03*
$FeOH_2$(a)$^{+0.5}\cdots NO_3^-$	1	0	0	1	-1	0	1	0	0	0	1	7.42 ± 0.03*
FeOH(b)$^{-0.5}$	0	1	0	0	0	0	0	0	0	0	0	0
$FeOH_2$(b)$^{+0.5}$	0	1	0	1	0	0	1	0	0	0	0	8.1*
FeOH(b)$^{-0.5}\cdots Na^+$	0	1	0	0	1	0	0	0	1	0	0	-0.60 ± 0.03*
$FeOH_2$(a)$^{+0.5}\cdots NO_3^-$	0	1	0	1	-1	0	1	0	0	0	1	7.42 ± 0.03*
$Fe_3O^{-0.5}$	0	0	1	0	0	0	0	0	0	0	0	0
$Fe_3OH^{+0.5}$	0	0	1	1	0	0	1	0	0	0	0	8.1*
$Fe_3O^{-0.5}\cdots Na^+$	0	0	1	0	1	0	0	0	1	0	0	-0.60 ± 0.03*
$FeOH_2$(a)$^{+0.5}\cdots NO_3^-$	0	0	1	1	-1	0	1	0	0	0	1	7.42 ± 0.03*
$(FeO)_2CO$(b)	0	2	0	0.66	-0.66	0	2	1	0	0	0	21.73 ± 0.09**
$(FeO)_2CO\cdots Na$(b)	0	2	0	0.65	0.35	0	2	1	1	0	0	22.38 ± 0.09**
$FeOCO_2$(a)	1	0	0	0.34	-1.34	0	1	1	0	0	0	11.60 ± 0.01**
$FeOCO_2$(b)	0	1	0	0.34	-1.34	0	1	1	0	0	0	11.60 ± 0.01**
$(FeO)_2PO_2$(b)	0	2	0	0.46	-1.46	0	2	0	0	1	0	28.31 ± 0.04***
$(FeO)_2POOH$(b)	0	2	0	0.65	-0.65	0	3	0	0	1	0	33.52 ± 0.13***
$FeOPO_2OH$(a)	1	0	0	0.28	-1.28	0	2	0	0	1	0	26.36 ± 0.20***
$FeOPO_2OH$(b)	0	1	0	0.28	-1.28	0	2	0	0	1	0	26.36 ± 0.20***
$FeOPO(OH)_2$(a)	1	0	0	0.33	-0.33	0	3	0	0	1	0	29.84 ± 0.23***
$FeOPO(OH)_2$(b)	0	1	0	0.33	-0.33	0	3	0	0	1	0	29.84 ± 0.23***

& ≡FeOH(a)$^{-0.5}$ forms only monodentate complexes with PO_4 and CO_3, whereas ≡FeOH(b)$^{-0.5}$ forms both mono- and bidentate (double-corner) complexes with PO_4 and CO_3, according to the ion adsorption model for ferrihydrite from Hiemstra and Zhao.[11]

* From Mendez and Hiemstra.[46]

** From Mendez and Hiemstra.[41]

*** From Hiemstra and Zhao.[11]

Table S7.3. Thermodynamic database of the aqueous speciation reactions used in the CD modelling. Log*K* values are given for $I = 0$.

Species	Reaction			log*K*	
$NaOH^0$	$Na^+ + OH^-$	↔	$NaOH^0$	-0.20	*
$NaNO_3^0$	$Na^+ + NO_3^-$	↔	$NaNO_3^0$	-0.60	*
HPO_4^{2-}	$PO_4^{3-} + H^+$	↔	HPO_4^{2-}	12.35	*
$H_2PO_4^-$	$PO_4^{3-} + 2H^+$	↔	$H_2PO_4^-$	19.55	*
$H_3PO_4^0$	$PO_4^{3-} + 3H^+$	↔	$H_3PO_4^0$	21.70	*
HCO_3^-	$CO_3^{2-} + H^+$	↔	HCO_3^-	10.33	*
$H_2CO_3^0$	$CO_3^{2-} + 2H^+$	↔	$H_2CO_3^0$	16.69	*
$CO_2(g)$	$CO_3^{2-} + 2H^+$	↔	$CO_2(g) + H_2O(l)$	18.15	*
$Na_2CO_3^0$	$CO_3^{2-} + 2Na^+$	↔	$Na_2CO_3^0$	0.01	*
$NaCO_3^-$	$CO_3^{2-} + Na^+$	↔	$NaCO_3^-$	1.27	**
$NaHCO_3^0$	$CO_3^{2-} + Na^+ + H^+$	↔	$NaHCO_3^0$	10.02	**
$NaHPO_4^-$	$PO_4^{3-} + Na^+ + H^+$	↔	$NaHPO_4^-$	13.40	***
$NaPO_4^{2-}$	$PO_4^{3-} + Na^+$	↔	$NaPO_4^{2-}$	2.05	***

* From Lindsay (1979)
** From NIST database 46.7
*** From Rahnemaie et al. (2007)

D. **Surface speciation of CO_3 in competitive systems with PO_4**

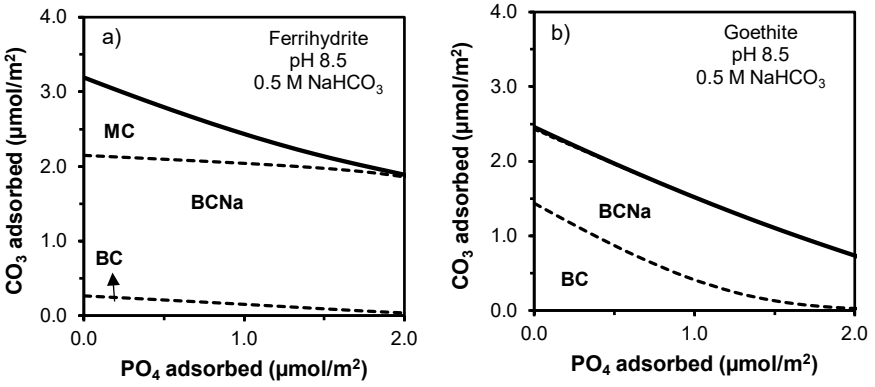

Figure S7.2. Surface speciation of carbonate (CO_3) as a function of the surface loading of phosphate (PO_4) in ferrihydrite (panel a) and goethite (panel b) systems in 0.5 M $NaHCO_3$ solutions (pH 8.5). The calculations have been performed with the CD model, using the parameter sets for the CO_3-PO_4 interaction reported by Mendez and Hiemstra[41] and Rahnemaie et al.[39] for ferrihydrite and goethite, respectively. BC = inner-sphere bidentate (double corner) CO_3 complex; BCNa = inner-sphere bidentate (double corner) CO_3 complex in which a Na^+ ion interacts with the adsorbed CO_3, forming a ternary complex; MC = inner-sphere monodentate (single-corner) CO_3 complex.

For a given PO_4 surface loading, the adsorption of CO_3 is larger to ferrihydrite than to goethite (thick full line), showing the higher adsorption affinity of CO_3 for ferrihydrite. The surface speciation of CO_3 differs between both Fe (hydr)oxides. In 0.5 M $NaHCO_3$ systems, the formation of the MC complexes contributes significantly to the adsorption of CO_3 to ferrihydrite, whereas formation of this MC complex has not been revealed for goethite. Instead, formation of an outer-sphere complex has been proposed for goethite systems.[39] However, this outer-sphere complex is not relevant in the 0.5 M $NaHCO_3$ system with goethite. Moreover, the distribution over the bidentate complexes BC and BCNa is different for both materials. More BCNa is formed when CO_3 interacts with ferrihydrite in $NaHCO_3$ than with goethite. For this ternary BCNa complex, the $\Delta \log K$ value between ferrihydrite and goethite is ~0.60.[41] For ferrihydrite, the decrease in the formation of BCNa is less sensitive to the increase in the PO_4 adsorption than for goethite.

E. **Calculation of size-dependent properties of metal oxide nanoparticles**

As explained in the main text, a number of important properties are particle-size dependent for ferrihydrite (Fh) and metal-(hydr)oxide nanoparticles in general, including the specific surface area (SSA, m^2/g), molar mass (M_{mass}, g/mol metal ion), and mass density (ρ_{nano}, g/m^3). It is essential to take this size-dependency into account for a consistent scaling and interpretation of ion adsorption data. In the present work, we have implemented a set of mathematical relationships (Equations S1-S3), previously given by Hiemstra,[45] to derive a consistent set of values of SSA, M_{mass}, and ρ_{nano} for the natural fraction of metal-(hydr)oxides in our set of top-soil samples.

Using the particle diameter (d, in m) as starting point in the calculations, the ρ_{nano} of metal (hydr)oxide nanoparticles can be calculated as:

$$\rho_{\mathrm{nano}} = \left(\frac{M_{\mathrm{core}}}{n_0 V_0}\right) - \left(\frac{M_{\mathrm{core}}}{n_0} - M_{\mathrm{H_2O}}\right) \times \frac{6}{d} N_{\mathrm{H_2O}} \qquad \text{(Equation S7.1)}$$

where M_{core} is the molar mass of the bulk mineral (in g/mol), n_O is the mol of oxygen atoms per mol metal ions in the mineral core, V_O is the lattice volume (in m^3/mol O), and N_{H2O} is the excess water

density (in mol/m^2). In Table S7.4, the values of these parameters are given for Fh ($FeO_{1.4}(OH)_{0.2}{\cdot}nH_2O$) and Al hydroxide ($Al(OH)_3{\cdot}nH_2O$) nanoparticles. In Equation S7.1, M_{H2O} is the molar mass of water (18 g/mol).

Using the value of ρ_{nano} derived in Equation S7.1, the molar mass (M_{nano}, g/mol metal ion) and specific surface area (A,m^2/g) of the metal (hydr)oxide nanoparticles follow respectively from:

$$M_{\mathrm{nano}} = \frac{M_{\mathrm{core}}}{\left(1-\left(\frac{6}{\rho_{\mathrm{nano}} \times d}\right) \times N_{\mathrm{H_2O}} \times M_{\mathrm{H_2O}}\right)} \quad \text{(Equation S7.2)}$$

$$A = \frac{6}{\rho_{\mathrm{nano}} \times d} \quad \text{(Equation S7.3)}$$

Additionally, the number (n_m) of metal atoms (*i.e.* Fe^{3+} or Al^{3+}) in each individual nanoparticle follows from:

$$n_{\mathrm{m}} = \frac{\rho_{\mathrm{nano}}}{\mathrm{M_{nano}}} \frac{\pi d^3}{6} N_{\mathrm{av}} \quad \text{(Equation S7.4)}$$

where N_{av} is Avogadro's number (6.02 10^{23} mol^{-1}).

Table S7.4. Parameters of the mineral core and density of chemisorbed water (N_{H2O}) of ferrihydrite and Al hydroxide nanoparticles, which have been implemented in the mathematical relationships applied for the calculation of a consistent set of values of mass density (ρ_{nano}), molar mass (M_{nano}), and surface area (A) of metal (hydr)oxide nanoparticles (Equations S7.1-S7.3).

Parameter	Units	Fh	$Al(OH)_3$
Formula core		$FeO_{1.4}OH_{0.2}$	$Al(OH)_3$
M_{core}	g / mol metal ion	81.65	78.00
ρ_{core}	g / m^3	4.77x10^6 [a]	2.42x10^6
V_O [a]	m^3 / mol oxygen	1.07x10^{-5}	1.07x10^{-5}
N_{H2O} [b]	mol / m^2	12.6x10^{-6}	6.4x10^{-6}
n_O	mol O/ mol metal ion	1.6	3.0

[a] The mass density ρ_{core} of Fh is based on the lattice parameterization of Pinney et al.[93] and Wang et al.[94] The related lattice volume Vo can be calculated from $Vo = M_{core} / n_O \rho_{core}$, as described in Hiemstra et al.[35]
[b] The density of chemisorbed water (N_{H2O}) for ferrihydrite is from Hiemstra,[18] whereas for $Al(OH)_3$, it has been derived in this study (see Section 7.3.5 in the main text).

Using the above set of equations we have scaled the values of the reactive surface area (RSA) of soils, obtained with the ion-probe method, to the content of AO extractable Fe and Al (hydr)oxides in an internally consistent manner. With this approach important information is derived about the properties of the naturally occurring metal (hydr)oxides, particularly SSA, mean particle size and spherical surface curvature, revealing the nano-sized nature of the reactive fraction of metal (hydr)oxide in soils.

The reactive metal (hydr)oxide fraction in our soils is composed mainly by Fe and Al (hydr)oxides. Therefore, our analysis started by assuming that the AO-extractable Fe and Al originate from two separate (hydr)oxide phases with a common equivalent diameter (d). These Fe and Al solid phases are represented respectively by Fh and $Al(OH)_3$ nanoparticles. For a chosen starting d value, a consistent set

of $\rho_{nano,}$ M_{nano}, and A values are calculated for both Fh and $Al(OH)_3$, using Equations S7.1–S7.3 and parameters of Table S7.4. Next, the overall SSA of the metal (hydr)oxide fraction is calculated from the A values derived for Fh and $Al(OH)_3$, which are weighted based on the molar amount of Fe and Al extracted with AO. This weighted average can be called the theoretical SSA (SSA_{theor}) and is calculated as:

$$SSA_{theor} = (A_{Fe} \times f_{Fe}) + (A_{Al} \times (1 - f_{Fe})) \quad \text{(Equation S7.5)}$$

where A_{Fe} and A_{Al} are respectively the surface areas of Fh and $Al(OH)_3$ nanoparticles derived with Equation S7.3, and f_{Fe} is the molar fraction of Fe in the AO extract, which is defined as f_{Fe} = Fe / [Fe+Al].

The SSA of the metal (hydr)oxide fraction can be also estimated by scaling the calculated RSA (m^2/kg soil) of the soil to the amount of Fe and Al-(hydr)oxide extracted with AO. This provides an estimation of the experimental SSA (SSA_{exp}). For the scaling, the M_{nano} values of Fh and $Al(OH)_3$ nanoparticles are required for transforming the molar amount of Fe and Al in the AO extracts (mol/kg) into a corresponding content of metal (hydr)oxide (g/kg). However, these M_{nano} values are not known *a priori* since these are particle size dependent. Therefore, these M_{nano} values need to be calculated iteratively. The SSA_{exp} values are calculated as:

$$SSA_{exp} = \frac{RSA}{(Fe_{AO} \times M_{nano,Fh}) + (Al_{AO} \times M_{nano,Al})} \quad \text{(Equation S7.6)}$$

where Fe_{AO} and Al_{AO} are respectively the amount of Fe and Al (in mol/kg) measured in the AO extracts.

For each top-soil sample, an iterative calculation was performed until a particle diameter d was found at which SSA_{theor} = SSA_{exp}. The results of these iterative calculations are presented in Table S7.1 for each individual soil sample.

F. Ortho-phosphate vs organic phosphorus in the ammonium oxalate soil extracts

In Figure S7.3 (panel a), the amounts of ortho-phosphate and organic phosphorus (P_{org}) measured in the acid ammonium oxalate (AO) extracts are presented for our set of soil samples (left y-axis). The P_{org} is calculated as total AO-extractable P (AO-P_{tot}) minus AO-extractable ortho-PO_4 pool (AO-PO_4). The red symbols show the fraction of inorganic ortho-PO_4 in relation to the total P measured in the AO extracts (right y-axis). On average, ~60 ± 10 % of the total AO-extractable P is present in our soils as inorganic ortho-PO_4, whereas the remaining fraction is due to the presence of other P species, most probably as P_{org}. This result shows the importance of distinguishing between both pools, AO-P_{tot} and AO-PO_4, in the application of the probe-ion method for assessing the reactive surface area of soils.

In Figure S7.3 (panel b), the P_{org} pool measured in the AO soil extracts is linearly related to the bulk content of soil organic carbon (SOC) (R^2 = 0.60, n = 18). The slope s of this linear relationship s = 230 mol C/mol P_{org} defines the mean C:P molar ratio of the soil organic matter (SOM) in our set of soils, if all P_{org} was released in the AO extractions. If less is released, the C:P ratio increases. A C/P ratio of 230, is close to the lowest range of C:P stoichiometry, expected for a nutrient rich SOM.[95]

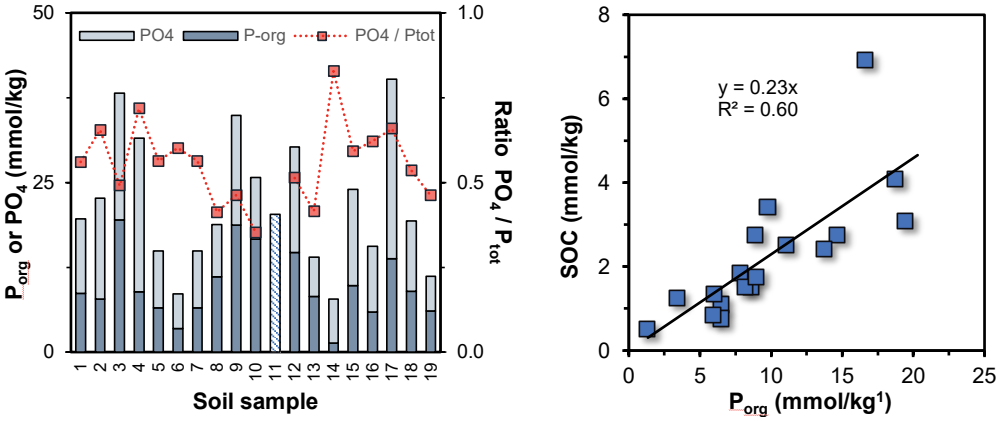

Figure S7.3. **Panel a**: Content of inorganic ortho-phosphate (AO-PO_4) and organic P (P_{org}) extracted with ammonium oxalate (left y-axis), and fraction of AO-PO_4 in relation to the total AO-extractable P pool (AO-P_{tot}) (right y-axis). The P_{org} content is estimated as AO-P_{tot} minus AO-PO_4. For soil 11, no data for AO-PO_4 is available and the bar indicates the measured total P pool in the AO extract. **Panel b**: Relationship between bulk SOC content and the P_{org} content estimated as the difference between the ammonium oxalate extractable total P and PO_4.

G. **Relationship RSA vs. DCB extractable oxides**

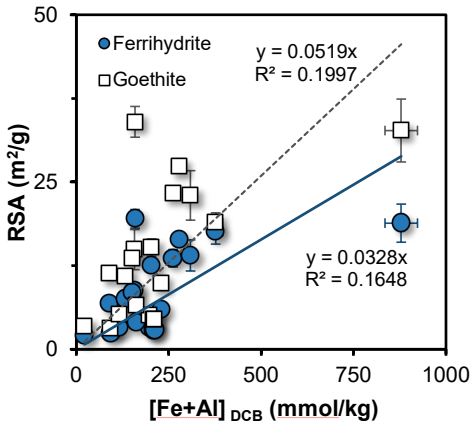

Figure S7.4. Relationship between Fe and Al content, extracted with dithionite-citrate-bicarbonate (DCB) solution, and the calculated reactive surface area (RSA) of the soil samples derived by CD modeling of the results obtained with the probe-ion method, using either goethite (squares) or ferrihydrite (circles) as reference oxides. The slope of the lines indicates the mean specific surface area (SSA) if the DCB-extractable Fe and Al (hydr)oxides ($[Fe+Al]_{DCB}$) are used in the scaling of RSA. The SSA values correspond to 51 ± 15 and 33 ± 9 m^2/mmol using goethite and ferrihydrite as model oxides in the CD model, respectively. These SSA values are approximatively half of the corresponding values derived in Figure 7.3 (main text) in which, the RSA has been scaled to the content of AO-extractable Fe and Al (hydr)oxides ($[Fe+Al]_{AO}$). The reason for this difference is that $[Fe+Al]_{DCB}$ includes both the nanocrystalline (*i.e.* Fh-like) and the well-crystalline oxide fractions. From the difference $[Fe+Al]_{DCB}$ minus $[Fe+Al]_{AO}$ the fraction of well-crystallized metal (hydr)oxides can be estimated. In our soils, the well-crystallized fraction contributes more in terms of mass than in terms of surface reactivity to the total soil content of metal (hydr)oxides (see Appendix H).

H. **Relative molar and surface area contribution of the nanocrystalline and well-crystallized (hydr)oxides in soils**

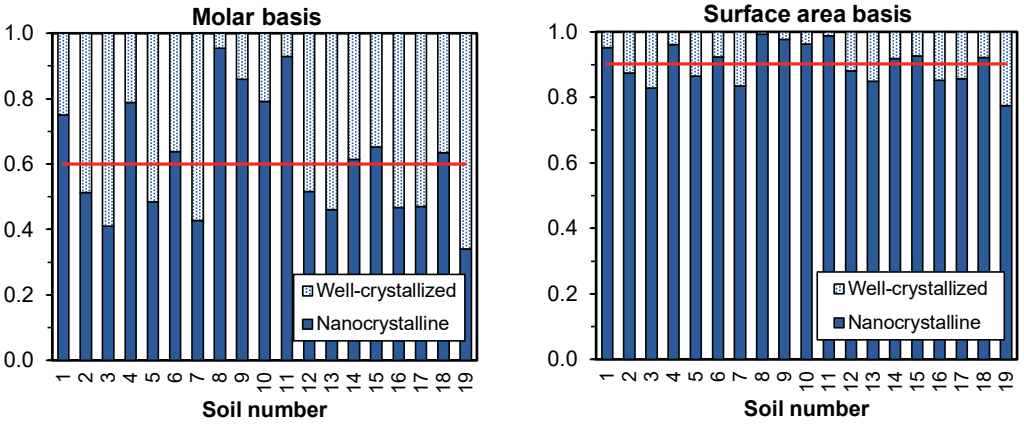

Figure S7.5. Relative contribution of the nanocrystalline and well-crystallized fractions to the total content of Fe and Al (hydr)oxides expressed on a molar basis (**panel a**) and in a surface area basis (**panel b**). The red lines indicate the corresponding average contribution of the nanocrystalline oxide fraction across all soil samples. The nanocrystalline fraction is estimated from the amount of AO extractable Fe and Al ($[Fe+Al]_{AO}$), whereas the well-crystallized fraction is estimated as $[Fe+Al]_{DCB}$ minus $[Fe+Al]_{AO}$. In panel b, the relative contribution of surface area was calculated exploratively and only for illustrative purposes, assuming "standard" mean values for the molar mass (M_{nano}) and for the specific surface area (SSA) of the natural Fe- and Al-(hydr)oxides so as to transform the molar amounts of AO-extractable Fe and Al (mmol/kg soil) into a reactive surface area (m^2/kg soil) for each soil. For the nanocrystalline fraction the assumed molar mass M_{nano} was 96 and 89 g/mol for the Fe- and Al-(hydr)oxides, respectively. For the well-crystallized metal-(hydr)oxides, M_{nano} was 89 and 78 g/mol for the Fe- and Al-(hydr)oxides, respectively, taking goethite (FeOOH) and gibbsite ($Al(OH)_3$) as a reference. The SSA of the nanocrystalline Fe- and Al-(hydr)oxide was set at 650 m^2/g, whereas the SSA of the well-crystallized Fe- and Al-(hydr)oxides was 100 m^2/g. With these assumptions, on average, ~90% of the reactive surface area of the soils is due to the presence of nanocrystalline Fe- and Al-(hydr)oxides, even though their relative contribution on a molar basis is only about ~60%.

I. **Calculation of SOC layer thickness**

Metal (hydr)oxide nanoparticles and soil organic matter (SOM) are tightly related as demonstrated in Figure 7.5a of the main text. Different structural views can be used to interpret the observed relationship between reactive surface area and soil organic carbon (SOC). One view is considering the metal (hydr)oxides of the soils as a collection of particles coated by organic matter, *i.e.* considering a core-layer model (Figure 7.5b). Another view is considering metal (hydr)oxide and SOM as a collection of discrete particles that interact with each other (Figure 7.5c).

Option 1

One may consider the particles of the natural metal (hydr)oxide fraction of soils as a metal (hydr)oxide core coated by a layer of organic matter. For each soil, the representative layer thickness L is found by calculating the volume of organic matter ΔV_{OM} and then transforming this value into a corresponding mass (M_{OM}) of organic matter covering the surfaces of the metal (hydr)oxide particles with a mean radius r, according to:

$$\Delta V_{OM} = V_{(r+L)} - V_r = 4/3\ \pi\ \{(r+L)^3 - r^3\} \quad \text{(Equation S7.7)}$$

$$M_{OM} = \rho_{OM}\ \Delta V_{OM} \quad \text{(Equation S7.8)}$$

Using a mass density of ρ_{OM} = 1250 10^3 g/m^3, the value of L can be found iteratively until the experimental SOM content with a carbon content of 58% equals the calculated value of M_{OM} (Equation S7.8).

Option 2

Soils seem to have proportionally more organic carbon if the metal (hydr)oxide particles are larger (Figure 7.5b, see main text). Consequently, one may interpret the organo-mineral associations as a collection of discrete particles that interact with each other. The amounts of SOM and AO-extractable metal (hydr)oxide can be given on a volume basis, assuming for SOM a carbon content of 58% and a mass density of ρ_{OM} = 1250 10^3 g/m^3, and for the Fe and Al (hydr)oxide particles, variable mass densities (ρ_{Ox}) consistent with the mean particle size and Al/Fe ratio, being in the range of ~2850–3750 10^3 g/m^3 (Table S7.1).

J. Organic matter content related to PO_4 surface loading

The interaction of SOC with metal (hydr)oxide surfaces will affect the environmental fate of many important inorganic oxyanions, including PO_4 and AsO_4. Part of the functional groups of SOC, typically $RCOO^-$, may form inner-sphere complexes and compete with these oxyanions for the same binding sites at the metal (hydr)oxide surfaces. Additionally, mutual electrostatic repulsion might contribute to this competitive interaction. This may explain the significant negative correlation (r= -0.85, p < 0.001) between the SOC content and the surface PO_4-loading observed for our soils (Figure S7.6). The PO_4-loadings have been calculated from the model outputs as $\Gamma_{PO4} = R_{ev}$ / RSA. Similar results were found for a series of forest and arable soils with variable SOC content.[96] These results show that the interaction between oxyanions and SOC at the metal (hydr)oxide surfaces must be included in SCM for effectively predicting the availability of oxyanions in field soil samples.[23,24,48]

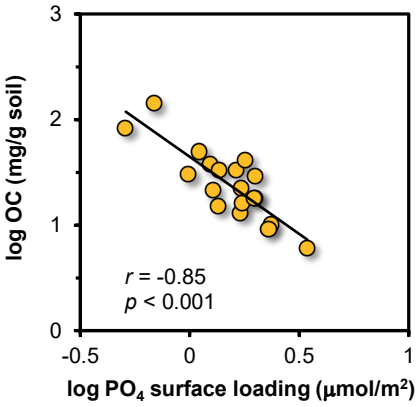

Figure S7.6. Linear decrease (log-log plot) of the PO_4 surface loading the soil organic carbon content of the agricultural top-soil samples used in this study increases.

K. Particle charge of Fh in Ca – PO_4 systems

The charge of Fh is pH-dependent. In pure Fh systems without specific ion adsorption, Fh particles are positively charged at pH values below the point of zero charge (PZC), being pH_{PZC} ~8.1 for this material. When phosphate ions adsorb, negative charge is introduced in the interface. By lowering the pH, additional protons can bind to the remaining surface groups. When these adsorbed protons fully compensate the charge of the adsorbed PO_4 ions, the particle becomes zero-charged again. The corresponding pH at which this occurs is called the iso-electrical point (IEP). At a PO_4 concentration of 1–10 µM, the pH_{IEP} is ~ 4. Above this pH, the Fh particles become negatively charged. When, Ca^{2+} ions are additionally present in the system, most of this charge will be compensated by the adsorption of Ca^{2+}, mainly bound in the form of ternary ≡Fe-PO_4-Ca complexes.[91] This is illustrated in Figure S7.7, showing the particle charge as a function of the pH for Fh-PO_4 systems with and without Ca, at an ionic strength of 3 mM (left panel) and 30 mM (right panel) and equilibrium PO_4 concentrations of 1, 3, and 10 µM. In the pH range 5–7, the particle charge is near zero when Ca is present, and the strong reduction of the negative particle charge of Fh with adsorbed PO_4 may contribute to an interaction with SOC particles forming stable micro aggregates.

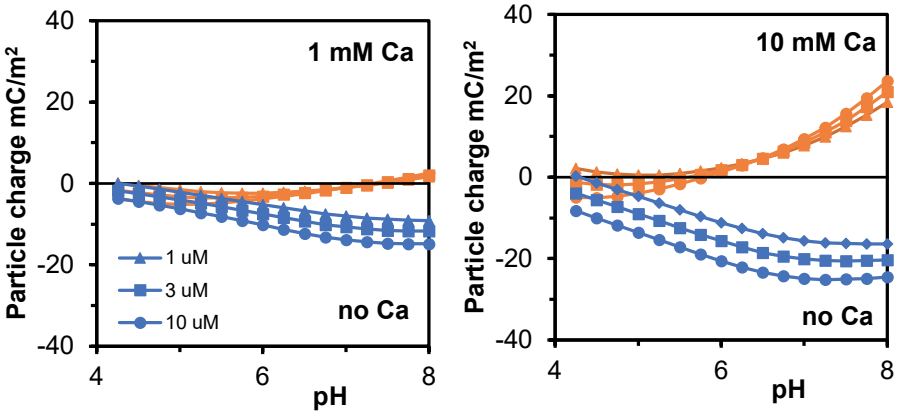

Figure S7.7. pH dependent particle charge of ferrihydrite in systems with Ca (orange lines) and without Ca (blue lines) at an ionic strength of 3 mM (left panel) and 30 mM (right panel), for PO_4 equilibrium concentrations of 1, 3, and 10 µM. In the absence of Ca, the pH_{IEP} ~ ≤ 4. In the presence of Ca, two values for the pH_{IEP} are possible, one at pH ≤ 4 and a pH_{IEP} value at higher pH values. The latter pH_{IEP} are near to pH ~7 in systems with 0.001 M Ca and around pH ~6 in systems with 0.01 M Ca.

References

(1) Cornell, R. M.; Schwertmann, U. *The Iron Oxides: Structure, Properties, Reactions, Ocurrence and Uses*, Second Edi.; WILEY-VCH, Germany, 2003.

(2) Guo, H.; Barnard, A. S. Naturally Occurring Iron Oxide Nanoparticles: Morphology, Surface Chemistry and Environmental Stability. *J. Mater. Chem. A* **2013**, *1* (1), 27–42.

(3) Xue, Q.; Ran, Y.; Tan, Y.; Peacock, C. L.; Du, H. Arsenite and Arsenate Binding to Ferrihydrite Organo-Mineral Coprecipitate: Implications for Arsenic Mobility and Fate in Natural Environments. *Chemosphere* **2019**, *224*, 103–110.

(4) Weng, L.; van Riemsdijk, W. H.; Hiemstra, T. Humic Nanoparticles at the Oxide−Water Interface: Interactions with Phosphate Ion Adsorption. *Environ. Sci. Technol.* **2008**, *42* (23), 8747–8752.

(5) Kleber, M.; Eusterhues, K.; Keiluweit, M.; Mikutta, C.; Mikutta, R.; Nico, P. S. Mineral-Organic Associations: Formation, Properties, and Relevance in Soil Environments. *Adv. Agron.* **2015**, *130*, 1–140.

(6) Lalonde, K.; Mucci, A.; Ouellet, A.; Gélinas, Y. Preservation of Organic Matter in Sediments Promoted by Iron. *Nature* **2012**, *483* (7388), 198–200.

(7) Hiemstra, T.; Antelo, J.; Rahnemaie, R.; van Riemsdijk, W. H. Nanoparticles in Natural Systems I: The Effective Reactive Surface Area of the Natural Oxide Fraction in Field Samples. *Geochim. Cosmochim. Acta* **2010**, *74* (1), 41–58.

(8) Pronk, G. J.; Heister, K.; Kögel-Knabner, I. Iron Oxides as Major Available Interface Component in Loamy Arable Topsoils. *Soil Sci. Soc. Am. J.* **2011**, *75* (6), 2158–2168.

(9) Hiemstra, T.; Van Riemsdijk, W. H. A Surface Structural Approach to Ion Adsorption: The Charge Distribution (CD) Model. *J. Colloid Interface Sci.* **1996**, *179* (2), 488–508.

(10) Hiemstra, T.; Venema, P.; Van Riemsdijk, W. H. Intrinsic Proton Affinity of Reactive Surface Groups of Metal (Hydr)Oxides: The Bond Valence Principle. *J. Colloid Interface Sci.* **1996**, *184* (2), 680–692.

(11) Hiemstra, T.; Zhao, W. Reactivity of Ferrihydrite and Ferritin in Relation to Surface Structure, Size, and Nanoparticle Formation Studied for Phosphate and Arsenate. *Environ. Sci. Nano* **2016**, *3*, 1265–1279.

(12) Komárek, M.; Antelo, J.; Králová, M.; Veselská, V.; Číhalová, S.; Chrastný, V.; Ettler, V.; Filip, J.; Yu, Q.; Fein, J. B.; et al. Revisiting Models of Cd, Cu, Pb and Zn Adsorption onto Fe(III) Oxides. *Chem. Geol.* **2018**, *493*, 189–198.

(13) Groenenberg, J. E.; Lofts, S. The Use of Assemblage Models to Describe Trace Element Partitioning, Speciation, and Fate: A Review. *Environ. Toxicol. Chem.* **2014**, *33* (10), 2181–2196.

(14) Koopal, L.; Tan, W.; Avena, M. Equilibrium Mono- and Multicomponent Adsorption Models: From Homogeneous Ideal to Heterogeneous Non-Ideal Binding. *Adv. Colloid Interface Sci.* **2020**, 102138.

(15) Hiemstra, T.; Yong, H.; Van Riemsdijk, W. H. Interfacial Charging Phenomena of Aluminum (Hydr)Oxides. *Langmuir* **1999**, *15* (18), 5942–5955.

(16) Machesky, M. L.; Wesolowski, D. J.; Palmer, D. A.; Ridley, M. K. On the Temperature Dependence of Intrinsic Surface Protonation Equilibrium Constants: An Extension of the Revised MUSIC Model. *J. Colloid Interface Sci.* **2001**, *239* (2), 314–327.

(17) Machesky, M. L.; Předota, M.; Wesolowski, D. J.; Vlcek, L.; Cummings, P. T.; Rosenqvist, J.; Ridley, M. K.; Kubicki, J. D.; Bandura, A. V.; Kumar, N.; et al. Surface Protonation at the Rutile (110) Interface: Explicit Incorporation of Solvation Structure within the Refined MUSIC Model Framework. *Langmuir* **2008**, *24* (21), 12331–12339.

(18) Hiemstra, T. Surface and Mineral Structure of Ferrihydrite. *Geochim. Cosmochim. Acta* **2013**, *105*, 316–325.

(19) Hiemstra, T. Surface Structure Controlling Nanoparticle Behavior: Magnetism of Ferrihydrite, Magnetite, and Maghemite. *Environ. Sci. Nano* **2018**, *5* (3), 752–764.

(20) Michel, F. M.; Barron, V.; Torrent, J.; Morales, M. P.; Serna, C. J.; Boily, J.-F.; Liu, Q.; Ambrosini, A.; Cismasu, A. C.; Brown, G. E. Ordered Ferrimagnetic Form of Ferrihydrite Reveals Links among Structure, Composition, and Magnetism. *Proc. Natl. Acad. Sci.* **2010**, *107* (7), 2787–2792.

(21) Michel, F. M.; Ehm, L.; Antao, S. M.; Lee, P. L.; Chupas, P. J.; Liu, G.; Strongin, D. R.; Schoonen, M. A. A.; Phillips, B. L.; Parise, J. B. The Structure of Ferrihydrite, a Nanocrystalline Material. *Science* **2007**, *316* (5832), 1726–1729.

(22) Harrington, R.; Hausner, D. B.; Xu, W.; Bhandari, N.; Michel, F. M.; Brown, G. E.; Strongin, D. R.; Parise, J. B. Neutron Pair Distribution Function Study of Two-Line Ferrihydrite. *Environ. Sci. Technol.* **2011**, *45* (23), 9883–9890.

(23) Gustafsson, J. P. Arsenate Adsorption to Soils: Modelling the Competition from Humic Substances. *Geoderma* **2006**, *136* (1–2), 320–330.

(24) Weng, L.; Vega, F. A.; van Riemsdijk, W. H. Competitive and Synergistic Effects in PH Dependent Phosphate Adsorption in Soils: LCD Modeling. *Environ. Sci. Technol.* **2011**, *45* (19), 8420–8428.

(25) Verbeeck, M.; Hiemstra, T.; Thiry, Y.; Smolders, E. Soil Organic Matter Reduces the Sorption of Arsenate and Phosphate: A Soil Profile Study and Geochemical Modelling. *Eur. J. Soil Sci.* **2017**, *68* (5), 678–688.

(26) Kaiser, K.; Guggenberger, G. The Role of DOM Sorption to Mineral Surfaces in the Preservation of Organic Matter

in Soils. In *Organic Geochemistry*; Pergamon, 2000; Vol. 31, pp 711–725.

(27) Strehlau, J. H.; Toner, B. M.; Arnold, W. A.; Penn, R. L. Accessible Reactive Surface Area and Abiotic Redox Reactivity of Iron Oxyhydroxides in Acidic Brines. *Geochim. Cosmochim. Acta* **2017**, *197*, 345–355.

(28) Heister, K. The Measurement of the Specific Surface Area of Soils by Gas and Polar Liquid Adsorption Methods—Limitations and Potentials. *Geoderma* **2014**, *216*, 75–87.

(29) Dzombak, D. A.; Morel, F. F. M. M. *Surface Complexation Modeling: Hydrous Ferric Oxide*; John Wiley & Sons, 1990.

(30) Mendez, J. C.; Hiemstra, T. Surface Area of Ferrihydrite Consistently Related to Primary Surface Charge, Ion Pair Formation, and Specific Ion Adsorption. *Chem. Geol.* **2020**, *532*.

(31) Bonten, L. T. C.; Groenenberg, J. E.; Weng, L.; van Riemsdijk, W. H. Use of Speciation and Complexation Models to Estimate Heavy Metal Sorption in Soils. *Geoderma* **2008**, *146* (1), 303–310.

(32) Schwertmann, U. Differenzierung Der Eisenoxide Des Bodens Durch Extraktion Mit Ammoniumoxalat-Lösung. *Zeitschrift für Pflanzenernährung, Düngung, Bodenkd.* **1964**, *105* (3), 194–202.

(33) Borggaard, O. K. Dissolution of Poorly Crystalline Iron Oxides in Soils by EDTA and Oxalate. *Zeitschrift für Pflanzenernährung und Bodenkd.* **1992**, *155* (5), 431–436.

(34) Hochella, M. F.; Lower, S. K.; Maurice, P. A.; Penn, R. L.; Sahai, N.; Sparks, D. L.; Twining, B. S. Nanominerals, Mineral Nanoparticles, and Earth Systems. *Science (80-.).* **2008**, *319* (5870), 1631–1635.

(35) Hiemstra, T.; Mendez, J. C.; Li, J. Evolution of the Reactive Surface Area of Ferrihydrite: Time, PH, and Temperature Dependency of Growth by Ostwald Ripening. *Environ. Sci. Nano* **2019**, *6* (3), 820–833.

(36) Regelink, I. C.; Weng, L.; Koopmans, G. F.; van Riemsdijk, W. H. Asymmetric Flow Field-Flow Fractionation as a New Approach to Analyse Iron-(Hydr)Oxide Nanoparticles in Soil Extracts. *Geoderma* **2013**, *202–203*, 134–141.

(37) Eusterhues, K.; Rumpel, C.; Kögel-Knabner, I. Organo-Mineral Associations in Sandy Acid Forest Soils: Importance of Specific Surface Area, Iron Oxides and Micropores. *Eur. J. Soil Sci.* **2005**, *56* (6), 753–763.

(38) Theng, B. K. G.; Yuan, G. Nanoparticles in the Soil Environment. *Elements* **2008**, *4* (6), 395–399.

(39) Rasoul; Hiemstra, T.; van Riemsdijk, W. H. Carbonate Adsorption on Goethite in Competition with Phosphate. *J. Colloid Interface Sci.* **2007**, *315* (2), 415–425.

(40) Koopmans, G. F. F.; Hiemstra, T.; Vaseur, C.; Chardon, W. J. J.; Voegelin, A.; Groenenberg, J. E. E. Use of Iron Oxide Nanoparticles for Immobilizing Phosphorus In-Situ: Increase in Soil Reactive Surface Area and Effect on Soluble Phosphorus. *Sci. Total Environ.* **2020**, *711*, 135220.

(41) Mendez, J. C.; Hiemstra, T. Carbonate Adsorption to Ferrihydrite: Competitive Interaction with Phosphate for Use in Soil Systems. *ACS Earth Sp. Chem.* **2019**, *3* (1), 129–141.

(42) Cui, Y.; Weng, L. Arsenate and Phosphate Adsorption in Relation to Oxides Composition in Soils: LCD Modeling. *Environ. Sci. Technol.* **2013**, *47* (13), 7269–7276.

(43) Wolf, A. M.; Baker, D. E. Colorimetric Method for Phosphorus Measurement in Ammonium Oxalate Soil Extracts. *Commun. Soil Sci. Plant Anal.* **1990**, *21* (19–20), 2257–2263.

(44) Hass, A.; Loeppert, R. H.; Messina, M. G.; Rogers, T. D. Determination of Phosphate in Selective Extractions for Soil Iron Oxides by the Molybdenum Blue Method in an Automated Continuance Flow Injection System. *Commun. Soil Sci. Plant Anal.* **2011**, *42* (14), 1619–1635.

(45) Hiemstra, T. Ferrihydrite Interaction with Silicate and Competing Oxyanions: Geometry and Hydrogen Bonding of Surface Species. *Geochim. Cosmochim. Acta* **2018**, *238*, 453–476.

(46) Mendez, J. C.; Hiemstra, T. Surface Area of Ferrihydrite Consistently Related to Primary Surface Charge, Ion Pair Formation, and Specific Ion Adsorption. *Chem. Geol.* **2020**, *532*, 119304.

(47) Wagai, R.; Mayer, L. M. Sorptive Stabilization of Organic Matter in Soils by Hydrous Iron Oxides. *Geochim. Cosmochim. Acta* **2007**, *71* (1), 25–35.

(48) Hiemstra, T.; Antelo, J.; van Rotterdam, A. M. D.; van Riemsdijk, W. H. Nanoparticles in Natural Systems II: The Natural Oxide Fraction at Interaction with Natural Organic Matter and Phosphate. *Geochim. Cosmochim. Acta* **2010**, *74* (1), 59–69.

(49) van Erp, P. J.; Houba, Y. J. G.; Van Beusichem, M. L. One Hundredth Molar Calcium Chloride Extraction Procedure. Part I: A Review of Soil Chemical, Analytical, and Plant Nutritional Aspects. *Commun. Soil Sci. Plant Anal.* **1998**, *29* (11–14), 1603–1623.

(50) Murphy, J.; Riley, J. P. A Modified Single Solution Method for the Determination of Phosphate in Natural Waters. *Anal. Chim. Acta* **1962**, *27* (C), 31–36.

(51) Hiemstra, T.; Van Riemsdijk, W. H. On the Relationship between Charge Distribution, Surface Hydration, and the Structure of the Interface of Metal Hydroxides. *J. Colloid Interface Sci.* **2006**, *301* (1), 1–18.

(52) Hiemstra, T.; Van Riemsdijk, W. H. A Surface Structural Model for Ferrihydrite I: Sites Related to Primary Charge, Molar Mass, and Mass Density. *Geochim. Cosmochim. Acta* **2009**, *73* (15), 4423–4436.

(53) Keizer, M. G.; van Riemsdijk, W. H. *ECOSAT, Equilibrium Calculation of Speciation and Transport. Technical*

Report. Department of Soil Quality. Wageningen Univeristy.; 1998.

(54) Kinniburgh, D. G. *Fit, Technical Report WD/93/23*; Keyworth, Great Britain, 1993.

(55) Schwertmann, U.; Schulze, D. G.; Murad, E. Identification of Ferrihydrite in Soils by Dissolution Kinetics, Differential X-Ray Diffraction, and Mössbauer Spectroscopy1. *Soil Sci. Soc. Am. J.* **1982**, *46* (4), 869–875.

(56) van der Zee, S. E. A. T. M.; van Riemsdijk, W. H. Model for Long-Term Phosphate Reaction Kinetics in Soil. *J. Environ. Qual.* **1988**, *17* (1), 35–41.

(57) Koopmans, G. F.; Chardon, W. J.; De Willigen, P.; Van Riemsdijk, W. H. Phosphorus Desorption Dynamics in Soil and the Link to a Dynamic Concept of Bioavailability. *J. Environ. Qual.* **2004**, *33* (4), 1393–1402.

(58) Maguire, R. O.; Foy, R. H.; Bailey, J. S.; Sims, J. T. Estimation of the Phosphorus Sorption Capacity of Acidic Soils in Ireland. *Eur. J. Soil Sci.* **2001**, *52* (3), 479–487.

(59) Lookman, R.; Freese, D.; Merckx, R.; Vlassak, K.; van Riemsdijk, W. H. Long-Term Kinetics of Phosphate Release from Soil. *Environ. Sci. Technol.* **1995**, *29* (6), 1569–1575.

(60) Koopmans, G. F.; Chardon, W. J.; Ehlert, P. A. I.; Dolfing, J.; Suurs, R. A. A.; Oenema, O.; van Riemsdijk, W. H. Phosphorus Availability for Plant Uptake in a Phosphorus-Enriched Noncalcareous Sandy Soil. *J. Environ. Qual.* **2004**, *33* (3), 965–975.

(61) Jørgensen, C.; Turner, B. L.; Reitzel, K. Identification of Inositol Hexakisphosphate Binding Sites in Soils by Selective Extraction and Solution 31P NMR Spectroscopy. *Geoderma* **2015**, *257–258*, 22–28.

(62) Warrinnier, R.; Goossens, T.; Amery, F.; Vanden Nest, T.; Verbeeck, M.; Smolders, E. Investigation on the Control of Phosphate Leaching by Sorption and Colloidal Transport: Column Studies and Multi-Surface Complexation Modelling. *Appl. Geochemistry* **2019**, *100* (November 2018), 371–379.

(63) Frossard, E.; Sinaj, S. The Isotope Exchange Kinetic Technique: A Method to Describe the Availability of Inorganic Nutrients. Applications to K, P, S and Zn. *Isotopes Environ. Health Stud.* **1997**, *33* (1), 61–77.

(64) Goldberg, S. Competitive Adsorption of Arsenate and Arsenite on Oxides and Clay Minerals. *Soil Sci. Soc. Am. J.* **2002**, *66* (2), 413.

(65) Gérard, F. Clay Minerals, Iron/Aluminum Oxides, and Their Contribution to Phosphate Sorption in Soils — A Myth Revisited. *Geoderma* **2016**, *262*, 213–226.

(66) Perret, D.; Gaillard, J. F.; Dominik, J.; Atteia, O. The Diversity of Natural Hydrous Iron Oxides. *Environ. Sci. Technol.* **2000**, *34* (17), 3540–3546.

(67) Chen, C.; Dynes, J. J.; Wang, J.; Sparks, D. L. Properties of Fe-Organic Matter Associations via Coprecipitation versus Adsorption. *Environ. Sci. Technol.* **2014**, *48* (23), 13751–13759.

(68) Chen, K. Y.; Chen, T. Y.; Chan, Y. T.; Cheng, C. Y.; Tzou, Y. M.; Liu, Y. T.; Teah, H. Y. Stabilization of Natural Organic Matter by Short-Range-Order Iron Hydroxides. *Environ. Sci. Technol.* **2016**, *50* (23), 12612–12620.

(69) Eusterhues, K.; Wagner, F. E.; Häusler, W.; Hanzlik, M.; Knicker, H.; Totsche, K. U.; Kögel-Knabner, I.; Schwertmann, U. Characterization of Ferrihydrite-Soil Organic Matter Coprecipitates by X-Ray Diffraction and Mössbauer Spectroscopy. *Environ. Sci. Technol.* **2008**, *42* (21), 7891–7897.

(70) Mikutta, R.; Lorenz, D.; Guggenberger, G.; Haumaier, L.; Freund, A. Properties and Reactivity of Fe-Organic Matter Associations Formed by Coprecipitation versus Adsorption: Clues from Arsenate Batch Adsorption. *Geochim. Cosmochim. Acta* **2014**, *144*, 258–276.

(71) Cismasu, A. C.; Levard, C.; Michel, F. M.; Brown, G. E. Properties of Impurity-Bearing Ferrihydrite II: Insights into the Surface Structure and Composition of Pure, Al- and Si-Bearing Ferrihydrite from Zn(II) Sorption Experiments and Zn K-Edge X-Ray Absorption Spectroscopy. *Geochim. Cosmochim. Acta* **2013**, *119*, 46–60.

(72) Lee, S.; Xu, H. One-Step Route Synthesis of Siliceous Six-Line Ferrihydrite: Implication for the Formation of Natural Ferrihydrite. *ACS Earth Sp. Chem.* **2019**, *3* (4), 503–509.

(73) Hofmann, A.; Vantelon, D.; Montargès-Pelletier, E.; Villain, F.; Gardoll, O.; Razafitianamaharavo, A.; Ghanbaja, J. Interaction of Fe(III) and Al(III) during Hydroxylation by Forced Hydrolysis: The Nature of Al-Fe Oxyhydroxy Co-Precipitates. *J. Colloid Interface Sci.* **2013**, *407*, 76–88.

(74) Liu, Y. T.; Hesterberg, D. Phosphate Bonding on Noncrystalline Al/Fe-Hydroxide Coprecipitates. *Environ. Sci. Technol.* **2011**, *45* (15), 6283–6289.

(75) Hiemstra, T. Formation, Stability, and Solubility of Metal Oxide Nanoparticles: Surface Entropy, Enthalpy, and Free Energy of Ferrihydrite. *Geochim. Cosmochim. Acta* **2015**, *158*, 179–198.

(76) Tiberg, C.; Sjöstedt, C.; Eriksson, A. K.; Klysubun, W.; Gustafsson, J. P. Phosphate Competition with Arsenate on Poorly Crystalline Iron and Aluminum (Hydr)Oxide Mixtures. *Chemosphere* **2020**, *255*, 126937.

(77) Adra, A.; Morin, G.; Ona-Nguema, G.; Menguy, N.; Maillot, F.; Casiot, C.; Bruneel, O.; Lebrun, S.; Juillot, F.; Brest, J. Arsenic Scavenging by Aluminum-Substituted Ferrihydrites in a Circumneutral PH River Impacted by Acid Mine Drainage. *Environ. Sci. Technol.* **2013**, *47* (22), 12784–12792.

(78) Cismasu, A. C.; Michel, F. M.; Stebbins, J. F.; Levard, C.; Brown, G. E. Properties of Impurity-Bearing Ferrihydrite I. Effects of Al Content and Precipitation Rate on the Structure of 2-Line Ferrihydrite. *Geochim. Cosmochim. Acta*

2012, *92*, 275–291.

(79) Kiem, R.; Kögel-Knabner, I. Refractory Organic Carbon in Particle-Size Fractions of Arable Soils II: Organic Carbon in Relation to Mineral Surface Area and Iron Oxides in Fractions < 6 Mm. *Org. Geochem.* **2002**, *33* (12), 1699–1713.

(80) Kleber, M.; Mikutta, R.; Torn, M. S.; Jahn, R. Poorly Crystalline Mineral Phases Protect Organic Matter in Acid Subsoil Horizons. *Eur. J. Soil Sci.* **2005**, *56* (6), 717–725.

(81) Wiseman, C. L. S.; Püttmann, W. Interactions between Mineral Phases in the Preservation of Soil Organic Matter. *Geoderma* **2006**, *134* (1–2), 109–118.

(82) Eusterhues, K.; Neidhardt, J.; Hädrich, A.; Küsel, K.; Totsche, K. U. Biodegradation of Ferrihydrite-Associated Organic Matter. *Biogeochemistry* **2014**, *119* (1–3), 45–50.

(83) Mikutta, R.; Kleber, M.; Torn, M. S.; Jahn, R. Stabilization of Soil Organic Matter: Association with Minerals or Chemical Recalcitrance? *Biogeochemistry* **2006**, *77* (1), 25–56.

(84) Hu, S.; Lu, Y.; Peng, L.; Wang, P.; Zhu, M.; Dohnalkova, A. C.; Chen, H.; Lin, Z.; Dang, Z.; Shi, Z. Coupled Kinetics of Ferrihydrite Transformation and As(V) Sequestration under the Effect of Humic Acids: A Mechanistic and Quantitative Study. *Environ. Sci. Technol.* **2018**, *52* (20), 11632–11641.

(85) Liu, H.; Yuan, P.; Qin, Z.; Liu, D.; Tan, D.; Zhu, J.; He, H. Thermal Degradation of Organic Matter in the Interlayer Clay-Organic Complex: A TG-FTIR Study on a Montmorillonite/12-Aminolauric Acid System. *Appl. Clay Sci.* **2013**, *80–81*, 398–406.

(86) Wattel-Koekkoek, E. J. W.; Van Genuchten, P. P. L.; Buurman, P.; Van Lagen, B. Amount and Composition of Clay-Associated Soil Organic Matter in a Range of Kaolinitic and Smectitic Soils. *Geoderma* **2001**, *99* (1–2), 27–49.

(87) Kaiser, K.; Guggenberger, G. Sorptive Stabilization of Organic Matter by Microporous Goethite: Sorption into Small Pores vs. Surface Complexation. *Eur. J. Soil Sci.* **2007**, *58* (1), 45–59.

(88) Weng, L. P.; Van Riemsdijk, W. H.; Hiemstra, T. Adsorption of Humic Acids onto Goethite: Effects of Molar Mass, PH and Ionic Strength. *J. Colloid Interface Sci.* **2007**, *314* (1), 107–118.

(89) Sowers, T. D.; Adhikari, D.; Wang, J.; Yang, Y.; Sparks, D. L. Spatial Associations and Chemical Composition of Organic Carbon Sequestered in Fe, Ca, and Organic Carbon Ternary Systems. *Environ. Sci. Technol.* **2018**, *52* (12), 6936–6944.

(90) Mikutta, R.; Mikutta, C.; Kalbitz, K.; Scheel, T.; Kaiser, K.; Jahn, R. Biodegradation of Forest Floor Organic Matter Bound to Minerals via Different Binding Mechanisms. *Geochim. Cosmochim. Acta* **2007**, *71* (10), 2569–2590.

(91) Mendez, J. C.; Hiemstra, T. Ternary Complex Formation of Phosphate with Ca and Mg Ions Binding to Ferrihydrite: Experiments and Mechanisms. *ACS Earth Sp. Chem.* **2020**, *4* (4), 545–557.

(92) Holmgren, G. G. S. A Rapid Citrate-Dithionite Extractable Iron Procedure. *Soil Sci. Soc. Am. J.* **1967**, *31* (2), 210–211.

(93) Pinney, N.; Kubicki, J. D.; Middlemiss, D. S.; Grey, C. P.; Morgan, D. Density Functional Theory Study of Ferrihydrite and Related Fe-Oxyhydroxides. *Chem. Mater.* **2009**, *21* (24), 5727–5742.

(94) Wang, X.; Zhu, M.; Koopal, L. K.; Li, W.; Xu, W.; Liu, F.; Zhang, J.; Liu, Q.; Feng, X.; Sparks, D. L. Effects of Crystallite Size on the Structure and Magnetism of Ferrihydrite. *Environ. Sci. Nano* **2016**, *3* (1), 190–202.

(95) Tipping, E.; Somerville, C. J.; Luster, J. The C:N:P:S Stoichiometry of Soil Organic Matter. *Biogeochemistry* **2016**, *130* (1–2), 117–131.

(96) Regelink, I. C.; Weng, L.; Lair, G. J.; Comans, R. N. J. Adsorption of Phosphate and Organic Matter on Metal (Hydr)Oxides in Arable and Forest Soil: A Mechanistic Modelling Study. *Eur. J. Soil Sci.* **2015**, *66* (5), 867–875.

CHAPTER 8

Surface reactivity of the natural metal (hydr)oxide fraction for phosphate and organic matter interaction in weathered tropical soils

Juan C. Mendez[*], Elise van Eynde[*], Tjisse Hiemstra, Rob. N.J. Comans

To be submitted for publication

[*] These authors contributed equally to this chapter

Abstract

Assessing the surface reactivity of the natural metal (hydr)oxide fraction is essential for quantifying ion adsorption phenomena that control the availability of nutrients and pollutants in soils and is also important for studying the formation of organo-mineral associations. Despite the high natural abundance of Fe and Al (hydr)oxides in weathered tropical soils, the surface reactivity of the metal (hydr)oxide fraction has not been well-characterized for this type of soils. In this study, we assessed the reactive surface area (RSA) of the metal (hydr)oxide fraction for a set of tropical top-soils, using a novel probe-ion methodology and state-of-the-art surface complexation modeling. With this approach, insights into the reactivity of the metal (hydr)oxide fraction have been revealed, particularly in relation to adsorption of phosphate ions (PO_4) and to the interaction with soil organic matter (SOM). Our results show that ferrihydrite (Fh), rather than well-crystallized goethite, is a better proxy for describing the reactivity of the natural metal (hydr)oxide fraction in these tropical soils, despite the dominant presence of crystalline metal (hydr)oxides, expressed on a mass basis. Using Fh as a proxy, the RSA of these soils varied between ~2–40 $m^2\ g^{-1}$ soil. Scaling these RSA values to the amount of Fe and Al (hydr)oxides showed a large variation in the specific surface areas (SSA) of the reactive metal (hydr)oxide in soils, from ~400 to 1750 $m^2\ g^{-1}$ Fe+Al (hydr)oxides. A substantial fraction of the total PO_4 pool associated to the metal (hydr)oxide surfaces, on average ~60%, does not play any role in the solid-solution partitioning of PO_4, and instead, it might be occluded, present at the internal surfaces of crystalline metal (hydr)oxides. The SOM content strongly correlated with the amount of nanocrystalline Fe and Al (hydr)oxides, but not with the content of well-crystallized metal (hydr)oxides, indicating that organo-mineral associations are preferentially formed with nano-sized metal (hydr)oxide particles. With our results, we propose a structural model for describing the nano-scale interactions between metal (hydr)oxide particles and SOM, in which organo-mineral associations are formed by self-assembly of discrete SOM particles that coordinate a metal (hydr)oxide core. Overall, our results show the importance of the reactive metal (hydr)oxide fraction for the PO_4 speciation and organic carbon interactions in this set of weathered tropical soils.

8.1. Introduction

The bioavailability, mobility, and consequently the risk of deficiencies, toxicities, and leaching of ions in soils is strongly regulated by adsorption processes to the natural fraction of metal (hydr)oxides. This reactive (hydr)oxide fraction is particularly relevant for controlling the solid-solution partitioning of oxyanions such as phosphate (PO_4), arsenate (AsO_4), and selenite (SeO_3).[1–3] The natural metal (hydr)oxide fraction is also important for the adsorption of soil organic matter (SOM),[4,5] contributing to the long-term stabilization of organic carbon in soils, largely *via* formation of stable mineral-organic associations.[6,7] The natural metal (hydr)oxide fraction comprises a series of minerals with variable chemical composition and crystallinity, implying also different adsorption interactions with oxyanions and SOM. The dominant metal (hydr)oxide fraction varies across different environments.[8–10] For instance, soils from the (humid) tropics are often intensively weathered, resulting in a high abundance of Fe and Al (hydr)oxides, mainly present as crystalline metal (hydr)oxides.[11,12]

The adsorption of oxyanions to the natural fraction of metal (hydr)oxides in soils is a complex process that depends on the amount and properties of the mineral phases, the soil solution chemistry (*e.g.* pH, ionic strength, co-existing ions), and the competitive binding interaction of negatively charged soil organic matter (SOM).[13] Surface complexation models (SCMs) are helpful tools for describing how these multiple factors affect the overall adsorption behavior of oxyanions. A successful application of SCM to describe and predict the adsorption of oxyanions in soils requires a consistent characterization of the surface reactivity of the metal (hydr)oxide fraction. However, despite the naturally high content of Fe and Al (hydr)oxides in weathered tropical soils, the characterization of the natural metal (hydr)oxides for these soils is usually scarce, if not absent, in the literature.

The reactive surface area (RSA, in $m^2\ g^{-1}$ soil) of the metal (hydr)oxide fraction in soils has been reported to be a key factor determining the capacity of soils for adsorbing oxyanions and for interacting with SOM.[14–16] However, the consistent assessment of this important soil property is not trivial, and multiple challenges are faced when using traditional approaches. Gas adsorption analysis (*e.g.* N_2, Ar) and subsequent interpretation with the BET (Brunauer-Emmett-Teller) equation[17] is a classical methodology applied for assessing the surface area of soils and synthetic (hydr)oxides. This method has been applied in previous studies to measure the RSA of weathered tropical soils.[18–20] However, this approach has a number of disadvantages.[21] Drying and outgassing of samples lead to irreversible aggregation of colloidal nanoparticles, resulting in underestimations of the RSA.[16,22] Additionally, part of the (hydr)oxide surface area might not be measured because it is masked by the presence of natural organic matter (NOM).[23] Attempts to remove the NOM before BET analysis, for instance by oxidizing NOM,[18] may affect the surface properties of the metal (hydr)oxide particles, resulting in different RSA.[24]

An alternative method is the use of ethylene glycol monoethyl ether (EGME) as a probe molecule,[25] but this approach typically provides an estimation of the surface area related to clay minerals.[26] Another approach for estimating the RSA of soils is based on the amount of Fe and Al measured by selective dissolution extractions. Using the measured Fe and Al concentrations and assuming a set of "standard" values of molar mass and specific surface area (SSA) for the crystalline and nanocrystalline metal (hydr)oxides, the RSA of the soil is calculated.[27–30] However, the SSA of metal (hydr)oxides greatly varies across different soil samples.[24,31] In addition, inconsistencies are introduced as the molar mass, mass density, and surface curvature of metal (hydr)oxide nanoparticles are size dependent,[16] and this dependency needs to be accounted for in the interpretation and modeling of the adsorption data.

Recently, the use of native soil PO_4 as a probe-ion has been proposed to calculate the RSA of soils.[24] This probe-ion methodology is based on measuring the competitive adsorption interaction between CO_3

and PO_4 in a 0.5 M $NaHCO_3$ (pH = 8.5) solution. In this approach, a desorption curve is established by using a range of solution-to-solid ratios (SSR) in the soil extractions. The results are then interpreted with the charge-distribution (CD) model,[32] using a chosen metal (hydr)oxide material as reference for which the competitive adsorption isotherms of PO_4 have been well parameterized in synthetic systems in the presence of CO_3 ions. Recently, we have shown that the reactivity of the natural metal (hydr)oxide fraction of agricultural Dutch top-soils is better described when Fh, rather than well-crystallized goethite, is used as a reference oxide material in the CD model.[31]

In highly weathered soils from the humid tropics, crystalline Fe- and Al-(hydr)oxides (*e.g.* goethite, hematite and gibbsite) often dominate the (hydr)oxide fraction,[33,34] while the contribution of the nano-sized metal (hydr)oxides (*i.e.* Fh-like materials) may be relatively small on a mass basis. Nevertheless, it is still possible that these nano-sized materials greatly contribute to the overall reactivity of soils, even at low concentrations, because the specific surface area of these nanoparticles is relatively high. Therefore, the question that arises now is how to represent the behavior of the metal (hydr)oxide fractions of these tropical soils using synthetic (hydr)oxides as proxies. In this study, we attempt to answer this question.

In soils, PO_4 can be categorized in different pools: *i.e.* dissolved ions, reversibly adsorbed to surfaces, and occluded by minerals. Often, these pools are operationally defined by selective extraction methods.[35] The relative contribution of these different phosphorus pools may change according to the soil weathering stage,[35,36] and therefore, it can be very different for intensively weathered soils from the tropics, compared to the soils from temperate climates, studied previously.[31] The possible contribution of occluded PO_4 to the total pool of PO_4 associated to the metal (hydr)oxide minerals will be evaluated in the present study by measuring PO_4 in dithionite-citrate (DC) extracts of the highly-weathered tropical soils and comparing the results to the amount of reversibly bound phosphate (R-PO_4). The latter is calculated simultaneously with the RSA, by interpreting with the CD model the results of the probe-ion method.

The presence of SOM interacting with the surfaces of metal (hydr)oxides influences ion adsorption by occupying reactive sites and by introducing negative charge at the mineral-solution interface. For PO_4 and oxyanions in general, this competitive interaction with adsorbed SOM will lead to a decreased adsorption to the metal (hydr)oxide surfaces.[1,37,38] The interaction between SOM and metal (hydr)oxide nanoparticles is also important from the perspective of soil organic carbon (SOC) stabilization.[39–42] It has been proposed that metal (hydr)oxide nanoparticles in soils may be embedded in a matrix of organic molecules, forming relatively stable organo-mineral associations.[6,43,44] However, a clear structural view of these nano-scale associations is still missing in the literature.

The objective of the present study is to assess the surface reactivity of the natural metal (hydr)oxide fraction, applying the probe-ion method for a series of tropical top soils containing large amounts of Fe and Al-(hydr)oxide in comparison to the series of topsoils from a temperate climate, studied in our previous contribution.[31] The experimental PO_4 desorption data will be interpreted with the CD-model, using either Fh or goethite as reference metal (hydr)oxide material to establish which model oxide is a better proxy for the reactive fraction of metal (hydr)oxides in this set of weathered soils. In addition, by integrating our experimental and modeling results, important insights will be derived into the characteristics of the reactive metal (hydr)oxide fraction and its nano-scale interactions with SOM. The challenge is to formulate a conceptual model that describes the nanoscale structure of the organo-mineral associations of the highly weathered tropical soils.

8.2. Methodology

8.2.1. General soil characteristics

From a larger set of tropical soil samples, 18 samples were selected based on differences in pH, total SOC, acid ammonium oxalate (AO) extractable PO_4 and Fe and Al-(hydr)oxides content. The soils originate from Burundi (samples 1–15) and Kenya (samples 16–18). A set of general characteristics of the selected soil samples are shown in Table 8.1. These samples cover a wide range of soil characteristics such as pH (4.1–6.8), total SOC content (0.3–5 %), and clay content (2–71 %). According to the soil grids system,[45] based on the World Reference Base (WRB) soil classification system, the majority of the soils are classified as Acrisol and Ferralsol, which are typically highly weathered soils from the humid tropics, generally known for their low natural fertility and high P adsorption capacity.

8.2.2. Chemical analyses for samples characterization

Total SOC content in the soils was analyzed using a wet oxidation method according to the Kurmies procedure and measured with a spectrophotometer.[46] The clay content was measured by a laser-diffraction method. The volume percentage of the particle fraction smaller than 2 µm was re-calculated to the mass percentage of clay using a particle density of 2.6 g cm^{-3} and a bulk density of 1.3 g cm^{-3}. The equilibrium PO_4 concentration and pH were analyzed in 0.01 M $CaCl_2$ soil extracts, according to a standard procedure.[47] The colorimetric determination of PO_4 in the $CaCl_2$ extractions were done using a modified SFA instrument that increases the sensitivity of the analysis and reduces the detection limit of P-PO_4 to ~0.06 µM, as described recently by Koopmans et al.[48]

The nano-crystalline fraction of Fe and Al-(hydr)oxides of the soils was estimated using acid ammonium oxalate (AO). Dried soil samples were extracted with a solution (pH 3.0 ± 0.1) containing 0.1 M di-ammonium oxalate and 0.1 M oxalic acid at a solution-to-solid ratio (SSR) of 20 L kg^{-1}. Samples were equilibrated in the dark at a constant temperature of 20 °C and continuously shaken using an end-over-end shaker. After equilibration, samples were centrifuged at 2100*g* for 30 min and an aliquot of the supernatant was filtered over a 0.45 µm membrane filter. The filtrates were measured for Al (AO-Al), Fe (AO-Fe) and total P (AO-P_{tot}) using ICP-OES (Varian Vista Pro or Thermo Scientific iCAP6500). In a separate batch of AO extractions, the inorganic ortho-phosphate (AO-PO_4) was analyzed using a segmented flow analyzer (SFA), applying a colorimetric molybdenum-blue method.[49] For the AO-PO_4 analysis, the samples were diluted 100 times with demi-water to eliminate the interference of oxalate for the colorimetric reaction.[50,51] Preliminary tests showed no differences in the PO_4 concentration measured with either 10- or 100-times dilution of the AO soil extracts. Presently, we applied the ISO protocol for AO extractions which prescribes an extraction time of 4 h,[52] while this method was originally established using an extraction time of 2 h.[53] We assessed the effect of using either 4 or 2 h as extraction time on the measured concentrations of AO extractable P_{tot}, PO_4 Al and Fe. For PO_4 measurements, the concentration increased on average ~10 % when increasing the equilibration time from 2 to 4 h, while this increment was more for P_{tot} (22%), Fe_{AO} (40%) and Al_{AO} (27%). Since the AO-PO_4 data will be mainly used as an end point to validate our modeling results, we expect only slight effects of the choice of equilibration time for the discussion of the results.

To assess the crystalline metal (hydr)oxide fraction of the soils, dithionite-citrate (DC) extractions were done. The DC extractions were performed based on the ISO protocol.[54] Briefly, dried soil samples were extracted with a mixture of 0.3 M sodium acetate, 0.2 M trisodium citrate and 0.3 M sodium

dithionite, adjusted to pH 4.8 with sodium acetate, at a SSR of 20 L kg^{-1}. Samples were equilibrated for 3.5 h in a water bath at 60 °C. After equilibration, samples were centrifuged at 3000*g* for 30 min and an aliquot of the supernatant was filtered over a 0.45 µm membrane filter. The filtrates were subsequently analyzed for Fe (DC-Fe), Al (DC-Al) and total P (DC-P_{tot}) by ICP-OES and for inorganic ortho-PO_4 (DC-PO_4) by SFA using a colorimetric molybdenum-blue method.[49] For the soil samples 16 to 18, the DC-PO_4 pool was not analyzed. Similar to the AO extracts, the DC extracts were diluted (x100) with demi-water prior to the colorimetric analyses of PO_4. The crystalline fraction of Fe and Al-(hydr)oxides was estimated as the difference between the DC- and AO-extractable amounts of Fe and Al.

8.2.3. Equilibrium $NaHCO_3$ extractions

PO_4 desorption data were collected applying the probe-ion method proposed by Hiemstra et al.[24] In this method, soil extractions with a 0.5 M $NaHCO_3$ solution (pH 8.5) are performed to promote the PO_4 desorption from the soil mineral surfaces.[55] First, a fresh 0.5 M $NaHCO_3$ solution was prepared by dissolving 21.2 g of $NaHCO_3$ in 0.5 L of demi-water. The pH of the $NaHCO_3$ solution was then adjusted to pH 8.5 using a 2 M NaOH solution. Dried soil samples were extracted with the 0.5 M $NaHCO_3$ solution at six different SSR of 10, 20, 50, 80, 100 and 200 L kg^{-1}. For the three lowest SSRs, soils were extracted with 20 mL of the $NaHCO_3$ solution in 50 mL polyethylene tubes, whereas for the three highest SSRs, soils were extracted with 90 mL of $NaHCO_3$ in polyethylene 225 mL bottles. These conditions led to a constant gas-to-solution volume ratio of 1.5 L L^{-1} among all SSR.

In soils, the presence of SOM may affect the PO_4–CO_3 interaction due to competition with PO_4 for the binding sites at the soil surfaces. To suppress this possible effect during the $NaHCO_3$ extractions, an excess of powered activated carbon (AC) was added (0.40 g g^{-1} soil) to the soil suspensions. Because the AC might contain small amounts of PO_4, the AC was pre-cleaned with AO-solution.[48] An additional rising step with 0.5 M $NaHCO_3$ was included before drying the AC at 40 °C for 3 days. For each extraction batch, blank samples were included containing only AC and the $NaHCO_3$ solution. The PO_4 concentration in these blank samples ranged from 0.01 to 0.05 mg L^{-1}, which was relatively low compared to the PO_4 concentration measured in the supernatants of the soil samples (0.13 – 12.45 mg L^{-1} PO_4).

In a pre-experiment, we evaluated the kinetics of PO_4 desorption in the $NaHCO_3$ solution using three soil samples at two different SSR (10 and 100 L kg^{-1}). The samples were shaken for 24, 168, 336, 504 and 672 h in an end-over-end shaker at 30 cycles per min. Based on the kinetic experiment, a final equilibration time of 504 hours (21 days) was used for the main experiment. After equilibration, the pH was measured with a glass electrode and the samples were centrifuged at 3000*g* for 10 min and filtered over 0.45 µm membrane filters. Before measuring the PO_4 concentration using the colorimetric molybdenum-blue method,[49] the filtrate was diluted (3×) with a 0.3 M HCl solution to adjust the pH value to pH~2 and the excess CO_2 was removed from the filtrate by degassing these solutions in an ultrasonic bath for ~10 min.

Table 8.1. Chemical characteristics and modeling results of the soil samples selected for the present study.

												$CaCl_2$	*R*-PO_4		RSA	
Soil	**OC**	**<2 µm**	**AO-Fe** [a]	**AO-Al** [a]	**AO-P_{tot}** [a]	**AO-PO_4** [a]	**DC-Fe** [b]	**DC-Al** [b]	**DC-P_{tot}** [b]	**DC-PO_4** [b]	**pH** [c]	**PO_4** [c]	**Gt** [d]	**Fh** [e]	**Gt** [d]	**Fh** [e]
	%	%	---------- mmol kg^{-1} ----------									µM	--------- mmol kg^{-1}---------		---------	$m^2 g^{-1}$ --------
1	1.4	33	20.1	42.3	4.4	2.4	332.1	98.3	11.3	7.8	4.4	0.39	3.94 ± 0.10	2.09 ± 0.30	3.89 ± 0.08	8.24 ± 0.70
2	1.5	7	20.8	50.7	4.7	2.5	289.9	97.2	9.9	6.7	4.1	0.40	3.80 ± 0.07	1.94 ± 0.07	3.73 ± 0.07	6.62 ± 0.39
3	5	7	156.2	314.3	11.4	4.3	458.7	328.7	10.6	4.3	4.3	0.09	9.25 ± 0.125	2.96 ± 0.08	12.29 ± 0.07	15.50 ± 0.05
4	2	71	48.9	132.8	2.5	1.5	996.1	186.8	8.1	5.2	4.1	0.05	2.45 ± 0.09	1.26 ± 0.15	4.80 ± 0.19	23.04 ± 2.83
5	2.8	10	70.7	168.2	7.5	3.2	492.1	244.7	11.9	6.1	4.4	0.07	6.25 ± 0.07	2.71 ± 0.09	8.25 ± 0.12	16.88 ± 0.58
6	2.4	12	41.2	138.3	7.5	5.2	510.1	202.5	11.0	7.9	5.0	0.25	15.89 ± 0.13	7.22 ± 0.25	16.36 ± 0.07	24.74 ± 0.26
7	1.9	12	27.8	76.3	3.1	1.3	373.7	180.7	9.7	5.6	5.1	0.09	2.34 ± 0.02	1.38 ± 0.04	3.15 ± 0.02	12.54 ± 0.44
8	1.4	7	20.7	51.3	2.6	1.7	310.1	134.9	7.4	5.1	4.5	0.19	3.94 ± 0.14	2.01 ± 0.12	4.57 ± 0.10	11.24 ± 0.51
9	2.1	2	77.7	94.5	7.6	2.9	342.2	215.0	15.4	9.5	4.5	0.10	5.94 ± 0.064	2.98 ± 0.08	6.29 ± 0.06	12.09 ± 0.14
10	2.2	17	57.6	147.5	3.9	1.7	646.7	253.0	8.7	4.8	4.2	0.04	3.034 ± 0.08	1.59 ± 0.03	5.77 ± 0.18	27.83 ± 0.08
11	2.2	4	59.5	152.1	4.0	1.5	615.9	245.1	8.7	4.5	4.3	0.04	3.20 ± 0.07	1.54 ± 0.03	7.06 ± 0.13	39.13 ± 0.47
12	1.4	4	37.3	63.3	3.4	1.4	327.6	139.5	8.0	4.7	4.2	0.06	2.57 ± 0.02	1.15 ± 0.05	3.58 ± 0.02	11.072 ± 0.24
13	1.2	5	37.8	63.6	3.3	1.6	327.8	141.1	8.4	4.8	4.1	0.08	2.46 ± 0.02	1.32 ± 0.03	3.36 ± 0.02	12.59 ± 0.37
14	1.5	7	41.5	70.9	4.1	2.1	325.2	141.3	8.3	4.9	4.2	0.08	2.72 ± 0.04	1.54 ± 0.03	3.48 ± 0.03	12.99 ± 0.18
15	3.2	8	65.7	135.9	4.0	1.5	730.3	171.7	9.1	4.8	4.9	0.09	2.53 ± 0.05	1.20 ± 0.07	3.88 ± 0.08	10.34 ± 0.17
16	0.9	7	56.9	56.1	22.3	16.9	289.5	90.7	32.5	-	5.3	2.23	25.85 ± 0.18	14.25±0.22	15.14 ±0.05	9.69 ± 0.03
17	0.3	20	7.8	24.1	2.1	2.2	67.0	39.4	3.2	-	6.8	1.61	2.39 ± 0.05	1.57 ± 0.04	1.43 ± 0.05	1.70 ± 0.06
18	0.6	53	32.9	40.4	1.7	1.6	634.9	58.2	6.1	-	6.3	0.16	1.51± 0.13	0.92± 0.05	1.51± 0.14	3.47± 0.14

[a] Measured in an acid ammonium oxalate extraction (pH =3)[52]
[b] Measured in a dithionite citrate extraction[54]
[c] Measured in 0.01 M $CaCl_2$ (solution-to-solid ratio SSR = 10 L kg^{-1}, time = 2 h)[47]
[d] Pool of reversely bound PO_4 (*R*-PO_4) and reactive surface area (RSA) derived with the results of the probe-ion method, using goethite as reference oxide material in the CD modeling.
[e] Pool of reversely bound PO_4 (*R*-PO_4) and reactive surface area (RSA) derived with the results of the probe-ion method, using ferrihydrite as reference oxide material in the CD modeling.

8.2.4. Surface complexation modeling

The charge distribution (CD) model[32] was used to calculate the reactive surface area (RSA in m^2 g^{-1} soil) of each soil sample, based on the experimental PO_4 concentrations measured in the 0.5 M $NaHCO_3$ extraction solution at different SSRs. In this approach the amount of reactive PO_4 (R-PO_4 in mol kg^{-1}) that is reversibly adsorbed in soils is simultaneously calculated by modeling. A detailed modeling description is given by Hiemstra et al.[24] The RSA and R-PO_4 were calculated using two different Fe (hydr)oxides as proxy to represent the natural metal (hydr)oxide fraction, namely ferrihydrite (Fh) and goethite.

To identify which reference material (*i.e.* Fh or goethite) is a better proxy for the natural metal (hydr)oxide fraction in our set of soils, the amount of PO_4 extracted by the selective dissolution extractions (*i.e.* AO and DC) was compared to the R-PO_4 pool obtained by modeling the PO_4 desorption curves measured in 0.5 M $NaHCO_3$. In the modeling, the adsorption interaction between PO_4 and CO_3 is described using an internally consistent thermodynamic database calibrated previously in model systems with freshly prepared Fh nanoparticles[56] and well-crystallized goethite.[57] The CD model is combined with state-of-the-art multi-site ion complexation (MUSIC) models for the specific model (hydr)oxide considered.[32,58] The model calculations were done using ECOSAT program (version 4.9)[59] in combination with the FIT program (version 2.581)[60] for optimization of the RSA and R-PO_4 values.

8.3. Results and Discussion

8.3.1. Phosphate desorption in 0.5 M $NaHCO_3$ extractions

In a preliminary experiment, the PO_4 desorption kinetics were tested by measuring the concentration of PO_4 in the 0.5 M $NaHCO_3$ soil extracts for 3 samples at 2 different SSR (10 and 100 L kg^{-1}) and at 5 equilibration times (from 24 to 672 h). Based on these results, we considered an equilibration time of ~500 h (21 d) sufficient for reaching equilibrium concentrations of PO_4 in the 0.5 M $NaHCO_3$ soil extracts. This equilibration period was consequently used in the main experiment for measuring the PO_4 concentration at different SSR values.

In Figure 8.1, the equilibrium PO_4 concentration in the 0.5 M $NaHCO_3$ soil extracts as a function of the SSR is given for six selected soil samples. In general, our series of soil samples present a wide range of equilibrium PO_4 concentrations. At the lowest SSR, the lowest and highest PO_4 concentration differ by a factor of ~60 amongst all soil samples. For all SSRs, the measured PO_4 concentrations were considerably higher than our detection limit for measuring PO_4 colorimetrically in the 0.5 M $NaHCO_3$ soil extracts (dotted line in Figure 8.1). From a practical perspective, this observation is important because the probe-ion method was originally developed and tested for agricultural topsoils from the Netherlands, which usually have higher PO_4 concentrations in solution. The data in Figure 8.1 show that within the chosen SSR range, it is possible to measure accurately the equilibrium concentration of PO_4 in our set of tropical soils that have lower P levels.

As expected, the highest PO_4 concentrations in the soil extracts are found at the lowest SSR. At increasing the SSR (*i.e.* further dilution of the soil sample), the equilibrium PO_4 concentrations decrease but less than expected from the imposed dilution factor, because additional PO_4 is released from the soil surfaces. The PO_4 buffering capacity of the soil leads to non-linearity of the dilution curves. In Figure 8.1, the slope of the PO_4 dilution curves is therefore related to the soil buffer capacity of PO_4, which is

determined by the reactive surface area of the soil.[24] Soils with less steep dilution curves are expected to have a higher RSA. If the soil would not release any additional PO_4 upon soil sample dilution, the experimental PO_4 concentration would be expected to decrease linearly with the SSR (dashed line in Figure 8.1). As can be inferred from Figure 8.1, the PO_4 buffer capacity, and consequently the RSA, greatly differ among soil samples.

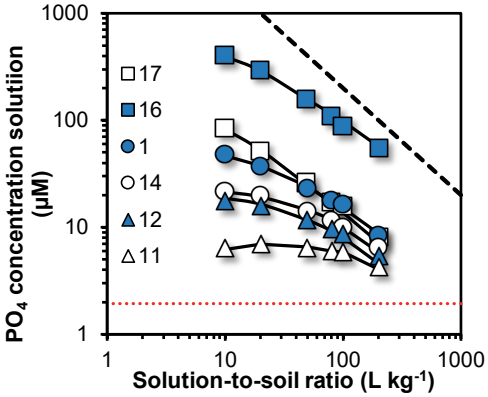

Figure 8.1. Phosphate (PO_4) concentrations in 0.5 M $NaHCO_3$ solution at a pH value near 8.5 as a function of the solution-to-solid ratios (SSR in L kg^{-1}) for six selected soil samples. The full lines are the CD model calculations using ferrihydrite as reference metal (hydr)oxide material and using RSA and *R*-PO_4 as the adjustable parameters of model. The adsorption interaction CO_3-PO_4 is described using the model parameters from Mendez and Hiemstra.[56] The dashed diagonal line represents a theoretical linear dilution curve, *i.e.* a 10 times decrease in SSR results in a 10 times lower PO_4 concentration in solution. The experimental data shows a lower slope than the linear dilution curve, which is due to release of PO_4 from the soil surfaces (*i.e.* PO_4 buffering) at a decreasing SSR. The red dotted horizontal line represents the lowest concentration in the 0.5 M $NaHCO_3$ solution measurable with our analytical procedure.

8.3.2. Reactive adsorbed phosphate pool

The pool of reactive PO_4 reversibly adsorbed to the soil surfaces (*R*-PO_4) can be revealed by interpreting with the CD model the results obtained with the probe-ion method. This *R*-PO_4 pool controls the solid-solution partitioning of PO_4 in the 0.5 M $NaHCO_3$ soil extractions at different SSRs. In the CD modeling, the calculated *R*-PO_4 pool size depends on the properties of the metal (hydr)oxide chosen as reference, in our study either goethite or Fh. In this section, we will compare the modeled *R*-PO_4 values with the amount of inorganic PO_4 that is removed with a soil extraction methodology that selectively dissolves the nano-(hydr)oxide fraction of soils. Our benchmark will be finding agreement between the experimental PO_4 pool and the *R*-PO_4 pool obtained by CD modeling of the results of the probe-ion method.

AO extractions are often applied to selectively dissolve and quantify the nanocrystalline fraction of Fe and Al (hydr)oxides in soils.[61–63] In the AO extractions, the total pool of P released (AO-P_{tot}) can also be conveniently analyzed by ICP-OES, simultaneously to the analysis of Fe and Al. The results are often used for assessing the degree of P saturation in soils.[64–66] Long-term experiments have shown that nearly all P that can be extracted with AO is potentially desorbable when the soil is exposed to an “infinite”

sink condition for P.[67] In line with these results, others have found that AO-P_{tot} was largely desorbable in a long-term P mining experiment.[64]

In the original probe-ion approach developed by Hiemstra et al.,[24] the calculated amount of reversibly bound PO_4 (*R*-PO_4) was compared with AO-P_{tot} measured by ICP-OES, rather than with inorganic ortho-PO_4 (AO-PO_4) measured using a colorimetric molybdenum-blue methodology.[49,51,68] However, the AO-P_{tot} pool may also include other P species different than inorganic ortho-PO_4, specially organic P,[69] whereas the probe-ion method is based on the measurement of the equilibrium concentration of ortho-PO_4 in the 0.5 M $NaHCO_3$ extracts. For instance, inositol phosphates, the most abundant organic P (P_{org}) form in soils, can be effectively extracted by AO solutions.[70] Therefore, we have used in the present study the experimental data of AO-PO_4, rather than AO-P_{tot}, as validation criterion in our evaluation of the *R*-PO_4 values obtained by CD modeling. For a series of Dutch top soils, we have recently shown that the experimental measurements of AO-PO_4 agree well with the *R*-PO_4 revealed by CD modeling of the desorption behavior of PO_4 in 0.5 M $NaHCO_3$, using Fh as a proxy.[31]

Figure 8.2a gives the amount of reversibly bound PO_4, calculated with the CD model using Fh as reference (hydr)oxide (colored spheres) in relation to the experimental AO-PO_4 pool. Both model and experimental PO_4 pools agree very well (1:1 line), while this is not the case when goethite is used as reference (hydr)oxide in the CD modeling (open squares). In the case of using goethite as proxy, the *R*-PO_4 values predicted by the model are ~ 2 times higher than the experimental AO-PO_4 pool. Therefore, using the AO-PO_4 data as validation criterion, we conclude that Fh is a better proxy for the reactive fraction of Fe and Al-(hydr)oxides of our soils.

In Figure 8.2a, we have used the amount of ortho-PO_4 measured in the AO extracts. If total P (AO-P_{tot}) is used instead, the 1:1 relationship with the *R*-PO_4 values found with Fh as reference (hydr)oxide is lost, which is due to the presence of organic P. Defining the amount of organic P in the AO extracts (P_{org}) as the difference between AO-P_{tot} and AO-PO_4, a positive relationship is found between P_{org} and the measured total SOC content ($R^2 = 0.80$, $p<0.05$), which suggests soil organic matter as an important source of P_{org} in the AO soil extracts. For our soils, the difference between the total amount of P (AO-P_{tot}) and ortho-PO_4 (AO-PO_4) is large and increases at increasing SOC content, reaching values of near 50%. On average, a value of 0.55 is found for the PO_4/P_{tot} ratio in the AO extracts of this set of weathered top-soil agricultural. This ratio agrees with the P_E /AO-P_{tot} fraction found in other SCM studies,[2,71] where P_E stands for the isotopically exchangeable PO_4, which was used to estimate the reversibly adsorbed fraction of PO_4 as an alternative to AO extraction method. In the latter studies, the use of AO-P_{tot} as a proxy for *R*-PO_4 in SCM led to overestimations of the P concentration in soil leachates[71] and soil extraction solutions.[2] However, the contribution of P_{org} to the AO-P_{tot} was not explicitly considered in these studies, whereas it can significantly contribute to the total pool of P measured in AO extractions, as we have shown here.

In addition to the AO extractions, soils are usually extracted with dithionite-citrate (DC) to assess the total content of Fe and Al (hydr)oxides, containing the fraction of nanocrystalline and crystalline metal (hydr)oxides.[72,73] Because our present set of tropical soils have a relatively high content of crystalline metal (hydr)oxides (Table 8.1), we have also measured the pool of inorganic PO_4 that can be extracted with the DC (DC-PO_4). The DC-PO_4 pool represents the total amount of PO_4 that is associated with natural metal (hydr)oxides in soils, but as shown in Figure 8.2b, there is no relationship between the experimental DC-PO_4 pool and the *R*-PO_4 values found by modeling, using either Fh or goethite as the reference metal (hydr)oxide. The experimental DC-PO_4 is considerably larger than the calculated *R*-PO_4, indicating that this PO_4 pool is an important contributor to the total PO_4 content in soils. However,

it does not contribute to the equilibration of PO_4 in the 0.5 M $NaHCO_3$ extractions, *i.e.* a significant fraction of PO_4 in these soils is irreversibly adsorbed. The DC-PO_4 measurements, together with our other model and experimental results, will provide information about the distribution of PO_4 within the nano and micro organo-mineral domains (Section 8.3.5).

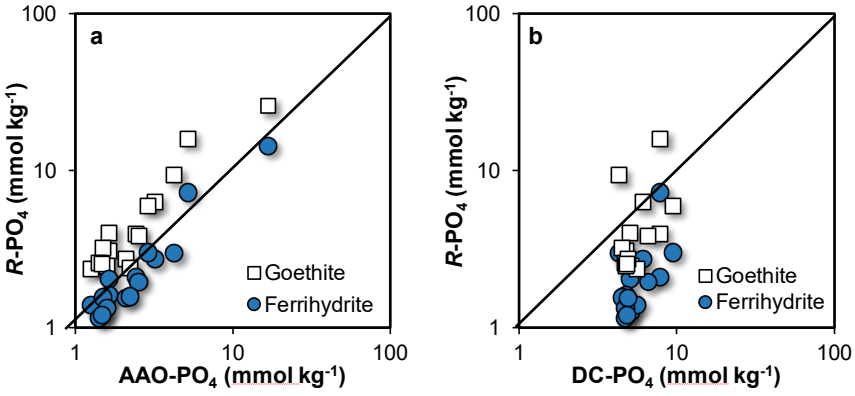

Figure 8.2. Comparison between the reversibly bound PO_4 (*R*-PO_4) calculated by the CD model using either goethite or Fh as reference metal (hydr)oxide and experimental measurements of PO_4 in (**a**) ammonium oxalate (AO) extractions or (**b**) in dithionite-citrate (DC) extractions. Both x-and y- axes are shown based on log_{10} scale. In panel b, no DC-PO_4 data are available for samples 16–18.

In Table 8.2, we summarize and compare the results of the selective dissolutions extraction as well as the modeling results of *R*-PO_4 and RSA for the tropical soils from this study and the Dutch top soils from our previous study.[31] The tropical soils have, on a molar basis, a larger contribution of crystalline metal (hydr)oxides, reflected in lower AO:DC ratio of Fe and Al. Interestingly, the reactivity of these tropical soils can be best described using Fh as reference metal (hydr)oxide. In this respect, these tropical top-soils do not differ from the temperate soils studied previously. A clear difference between both types of soils is the molar ratio PO_4 / (Fe+Al), measured in AO extracts. For the set of tropical soils, this molar ratio is on average 0.03, which is substantially lower than the average ratio (PO_4 / (Fe+Al) 0.13) found for the Dutch soils.[31] The difference might be due to the different origin and history of PO_4 fertilization, since the sum of Fe and Al in AO is similar between the two soil sets.

Table 8.2. Comparison of the experimental and modeling results between the tropical soils from this study and the set of topsoils from temperate regions, studied previously.[31] Fe and Al were measured in acid ammonium oxalate (AO) and dithionite-citrate (DC) extractions. P_{tot} and PO_4 were measured in the AO extracts by ICP-OES and a colorimetric blue method, respectively. Based on the probe-ion method described by Hiemstra et al.,[24] the reactive surface area (RSA) and reactive PO_4 pool (R-PO_4) were calculated using Fh as model (hydr)oxide.[31]

		AO		DC		AO:DC		AO	Probe-ion method	
		Fe	Al	Fe	Al	Fe	Al	PO_4/(Fe+Al)	R-PO_4	RSA
		----------mmol kg^{-1}----------				----------molar ratio----------			mmol kg^{-1}	m^2 g^{-1} soil
Tropical soils	mean	48.9	101.3	448.3	164.9	0.12	0.59	0.03	2.8	14.3
	min	7.8	24.1	67.0	39.4	0.05	0.38	0.01	0.9	1.7
	max	156.2	314.3	996.1	328.7	0.34	0.96	0.15	14.3	39.1
Temperate soils	mean	102.1	28.6	188.4	33.8	0.58	0.80	0.13	12.5	9.0
	min	10.5	3.0	16.0	6.0	0.28	0.50	0.03	3.2	2.1
	max	342.2	57.7	852.0	59.0	0.95	1.30*	0.48	27.9	19.5

* For the soil from the temperate regions, soils extractions with dithionite-citrate-bicarbonate (DCB) solution were performed, rather than the dithionite-citrate (DC) extraction used in the present study. Details of DCB extraction procedure are described in Hiemstra et al.[24]

** For one soil sample, the measured Al content in the AO soils extracts was higher than in the DCB extracts, which may be due to an experimental error in the measurement of either soil extracts.

8.3.3. Reactive and specific surface area

The reactive surface area (RSA) of our soils, calculated with Fh as a proxy, varies by a factor of ~20, over the range ~2–40 m^2 g^{-1} soil (Table 8.1). In case of using goethite as reference metal (hydr)oxide, the variation is less, over the range ~1.5–15 m^2 g^{-1} soil. The RSA values calculated with goethite as reference are generally lower than the values obtained by using Fh as reference (hydr)oxide. Remarkably, the opposite has been reported previously for a set of Dutch soils.[31] This difference can be understood from the difference in shape of the competitive PO_4 isotherm of goethite and Fh in 0.5 M $NaHCO_3$, relating the concentration (c) of PO_4 in solution to the surface PO_4 loading (Γ).

In 0.5 M $NaHCO_3$ solution (pH = 8.5), the high affinity character of PO_4 adsorption is much better preserved in goethite than in Fh systems. It implies that at low surface PO_4 loadings, the competitive PO_4 adsorption isotherm of goethite has larger variation in slope ($\Delta\Gamma_i/\Delta c_i$) than the corresponding PO_4 isotherm of Fh.[31,56] However, because of its higher affinity character, the competitive PO_4 isotherm of goethite flattens down sooner (*i.e.* at lower PO_4 concentrations) than the isotherm of Fh. Consequently, the slope ($\Delta\Gamma_I/\Delta c_i$) of the competitive PO_4 isotherm of goethite is steeper when the tropical soils are interpreted, as these soils have a relatively low PO_4 surface loading, while the isotherm of goethite is flatter in the range of interpretation of the probe-ion data of the Dutch soils, both relatively to the slopes of isotherms of Fh at the corresponding PO_4 levels. As the slope of the isotherms is leading in the outcome of the CD modeling,[31,56] using goethite as proxy results in RSA values that are underestimated for the tropical soils (*i.e.* with low PO_4 loadings) and overestimated in the Dutch soils (*i.e.* with high PO_4 loadings), both compared to the corresponding predictions using Fh as proxy.

In Section 8.3.2, based on the comparison between R-PO_4 and AO-PO_4, we have concluded that the reactivity of the natural metal (hydr)oxides with PO_4 in our set of tropical soils can be best described using Fh as reference metal (hydr)oxide in the CD modeling. Nevertheless, the question arises whether

the fraction of well-crystallized Fe and Al (hydr)oxides also contributes to the soil reactivity for PO_4. This will be discussed next.

Figure 8.3 shows that the calculated RSA of our tropical soils is positively correlated to the molar concentration of Fe and Al in the AO ($[Fe+Al]_{AO}$) and DC ($[Fe+Al]_{DC}$) soil extracts. The slope of the regression lines represents the mean specific surface area (SSA) of the metal (hydr)oxide fraction. Expressed per mole Fe+Al, it leads to a mean value of SSA = 110 ± 22 m^2 $mmol^{-1}$ when the RSA values are scaled to the content of $[Fe+Al]_{AO}$ and SSA = 23 ± 5 m^2 $mmol^{-1}$ in case of scaling to the content of $[Fe+Al]_{DC}$. This large difference is due to the significant contribution of well-crystallized Fe and Al (hydr)oxides ($[Fe+Al]_{Cryst}$) to the total Fe and Al measured in the DC soil extracts. The mean SSA value obtained at scaling RSA to $[Fe+Al]_{AO}$ is about two-fold higher for our tropical soils in comparison to the mean SSA (65 ± 22 m^2 $mmol^{-1}$) found for a series of Dutch agricultural topsoils.[31] The higher surface area per mole of $[Fe+Al]_{AO}$ of the tropical soils may be related to the much larger fraction of Al ions in the AO extracts of these soils (Table 8.2), as we will explain in Section 8.3.4.

The data in Figure 8.3 show a large scattering around the regression lines. It implies that the values for the SSA vary significantly amongst soils. Expressed in the more conventional unit of m^2 g^{-1}, the SSA varies between ~400 – 1750 m^2 g^{-1} at scaling of the RSA to the fraction of $[Fe+Al]_{AO}$ (see Section 8.3.4). This high variability implies that estimation of the RSA, based on the amount of Fe and Al extracted with AO and an assumed "standard" value for the SSA, is inadequate.

The difference between $[Fe+Al]_{DC}$ and $[Fe+Al]_{AO}$ represents the fraction of crystalline Fe and Al (hydr)oxides ($[Fe+Al]_{Cryst}$). On average, the molar ratio $[Fe+Al]_{AO}$ / $[Fe+Al]_{Cryst}$ is ~0.4 for the set of tropical soils, *i.e.* the crystalline fraction dominates. However, crystalline (hydr)oxides contribute generally much more in terms of mass than in terms of surface reactivity. The reason is the relatively large difference in SSA. Nanocrystalline (hydr)oxides typically have a ~10 times higher SSA than well-crystallized (hydr)oxides. Using this assumption, exploratory calculations show that the contribution of the nanocrystalline Fe and Al (hydr)oxides dominates the RSA, being on average ~75%. When doing a multiple regression analysis using $[Fe+Al]_{AO}$ and $[Fe+Al]_{Cryst}$ as two independent variables, only $[Fe+Al]_{AO}$ is found to be significant for explaining the modeled values of RSA (R^2= 0.87, with $p < 0.05$ for $[Fe+Al]_{AO}$ and $p > 0.5$ for$[Fe+Al]_{Cryst}$). This suggests that despite the large mass fraction of crystalline Fe and Al (hydr)oxides, the nanocrystalline (hydr)oxides are a major factor determining the reactivity of the metal (hydr)oxides in our set of highly weathered soils.

In our dataset, only soil 3 deviates from the relation between AO-extractable Fe and Al and RSA (open circle, Figure 8.3). This soil has almost no PO_4 associated to the crystalline (hydr)oxide fraction, *i.e.* AO-PO_4 ≈ DC-PO_4, and good agreement exists between AO-PO_4 and the model *R*-PO_4 (Figure 8.2a). Therefore, the observed deviation is likely due to a relatively high amount of AO extractable metal ions ($[Fe+Al]_{AO}$). This soil has the highest soil organic matter content (SOM = 5%) and its pH is low (~4.0), which in combination may lead to a contribution of Al^{3+} or Al polymers complexed by SOM, as AO solution is also able to extract such species.[74]

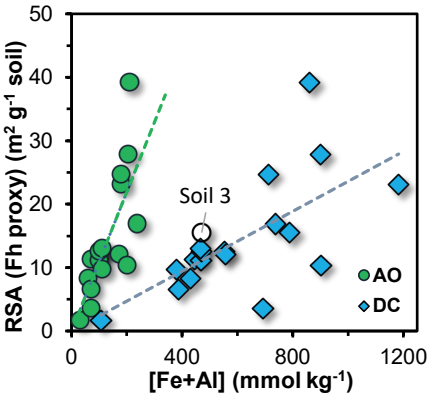

Figure 8.3. Relationship between the reactive surface area (RSA), calculated with the probe-ion method using Fh as reference (hydr)oxide in the CD model calculations, and the Fe+Al content measured either in the ammonium oxalate (AO) or in the dithionite-citrate (DC) soil extracts.

8.3.4. Mean particle size

As mentioned above, the slope of the regression lines in Figure 8.3 represents the mean SSA of the metal (hydr)oxide fraction expressed in m^2 $mmol^{-1}$. Expressing these SSAs in a more conventional unit of m^2 g^{-1} of metal (hydr)oxides requires information about the value of molar mass (M_{nano} in g (hydr)oxide mol^{-1} Fe or Al). In addition, the mass density value (ρ_{nano}) of the metal (hydr)oxide particles is needed for translating the SSA into an equivalent particle diameter. However, for metal (hydr)oxide nanoparticles, the values of SSA, M_{nano}, and ρ_{nano} are not constant but they are particle size-dependent, and therefore, they need to be calculated iteratively.

In the present contribution, we have used a recent approach for scaling, in a consistent and systematic manner, the modeled values of RSA to the amount Fe and Al extracted by AO.[31] In this approach, the chemical composition of the natural Fe and Al (hydr)oxides is represented by Fh ($FeO_{1.4}(OH)_{0.2}{\cdot}nH_2O$) and nano-particulate Al hydroxide ($Al(OH)_3{\cdot}nH_2O$), respectively. In both cases, nH_2O is the excess amount of water related to the presence of surface groups. The iterative calculations start by assuming an equal particle diameter (d) for both types of metal (hydr)oxides in a soil. Applying a set of mathematical relationships given by Hiemstra,[75] a consistent set of specific surface areas (A), M_{nano}, and ρ_{nano} can be calculated for each reactive fraction of Fe and Al (hydr)oxides. For calculating the total RSA, the values for the SSA of both Fe and Al (hydr)oxide particles are mass-weighted summed, based on the contents of Fe and Al measured in the AO-extractions. The calculations are repeated iteratively until the calculated RSA is equal to the RSA derived with the probe-ion method. The details of the calculations are described in Mendez et al.,[31] and the final results for each soil are given in Table S8.1.

For our tropical soils, we found an average particle diameter of the (hydr)oxides of d ~2.3 nm. This particle size is similar to the particle size of Fh, freshly prepared in the laboratory[76] having a SSA of A ~ 700 m^2 g^{-1}. For $Al(OH)_3.nH_2O$ nanoparticles with a mean size of d ~ 2.3, the SSA is A ~ 1200 m^2 g^{-1}, which is much larger than for Fh. The reason is the much lower mass density of the $Al(OH)_3.nH_2O$ nanoparticles as this material has light (Al) and very light (H) cations compensating the oxygen charge in the lattice, in contrast to Fh where most neutralizing cations are heavy (Fe).[31] The much lower mass density ρ_{nano} of the Al hydroxide fraction strongly changes the relation between SSA and spherical

particle diameter d according to SSA= 6/ (ρ_{nano} d). As the tropical soils have a high fraction of Al in the AO extracts (~ 67 ± 8 mass %), the mean SSA is close to A ~1000 m^2 g^{-1} at an equivalent particle mean diameter of d ~ 2.3 nm.

For the various tropical soils of this study, the representative spherical particle size is in the range of 1.4 – 5.5 nm. A similar range has been found for the topsoils from temperate regions studied previously, covering the range 1.5 – 5.1 nm.[31] In the tropical topsoils, the smallest particles would typically contain ~22 metal ions while for the temperate topsoils, the smallest size is equivalent to particles with ~50 metal ions. The difference might have various reasons. It can be related to the larger mean molar ratio Al/Fe of the nano oxide fraction, being for our tropical soils ~2.0 while it is just ~0.4 for the temperate soils. Moreover, if the Al rich particles have a slightly higher PO_4 affinity than Fh,[77] using the latter as proxy for the assessment of the RSA will lead to an overestimation of the surface area and consequently, a smaller particle size. This potential bias does not necessarily mean that the probe-ion is not suitable for application in this type of Al-rich soils. If the general adsorption behavior of both types of materials is similar, *i.e.* both have isotherms of similar shape,[77] a small systematic difference in affinity can be compensated by a slightly different RSA and then, nevertheless can be used in SCM of soils, for the time being.

An assumption in our approach of calculating the mean spherical size is that the Fe and Al are present in separate phases in soils, for which the corresponding size-dependent properties are calculated. However, in natural systems, it is often found that in metal (hydr)oxides Fe is substituted by Al, especially for highly weathered soils.[78] For natural goethite in highly weathered soils up to 30% of substitution of Fe with Al has been reported.[79] For the soils in this study, Al contributes on average 15 % to the total crystalline (hydr)oxide fraction but in the AO extract, the Al contribution is on average 68%. For the soils in this study, with relatively high molar contribution of the AO-extractable metal (hydr)oxide content, the formation of separate Al an Fe phases may be very likely.

8.3.5. Structural model for the metal (hydr)oxide fraction

8.3.5.1. *Crystalline fraction with occluded phosphate*

In Sections 8.3.2 to 8.3.4, we have shown that the nanocrystalline Fe and Al (hydr)oxides are the dominant reactive surfaces in our soils, controlling the solid-solution partitioning of PO_4 in the $NaHCO_3$ extractions. This observation seems remarkable considering that, on a mass basis, the crystalline Fe and Al (hydr)oxides are clearly the dominant fraction of metal (hydr)oxides in our set of tropical soil samples. In Figure 8.2, we also showed that the modeled values of R-PO_4, calculated with Fh as a proxy, correlates well (1:1 relationship) with the pool of AO-PO_4 but not with DC-PO_4. The latter PO_4 pool is significantly larger than the R-PO_4 values, indicating that an important fraction of DC-PO_4 is not desorbable and does not play a role in the solid-solution partition of PO_4 in the $NaHCO_3$ solutions. The difference between the PO_4 pools extractable with DC and AO can be attributed to the PO_4 pool associated to the crystalline (hydr)oxide fraction ($PO_{4,crys}$). This pool of $PO_{4,crys}$ does not take part in the surface equilibrium reactions and can be considered as occluded internally in the crystalline (hydr)oxide fraction. The possibility of occlusion is supported by observations in synthetic systems, showing that recrystallization of Fh to hematite and goethite in the presence of PO_4 may lead to a significant retention of this oxyanion in an non-desorbable (occluded) form.[80]

8.3.5.2. Organo-mineral associations

For our soils, a good correlation between SOC and $[Fe+Al]_{ox}$ (r = 0.93, p < 0.001) is observed whereas the correlation between SOC and $[Fe+Al]_{crys}$ is not statistically significant (r = 0.26, p = 0.28) (Figure S8.1). These experimental data suggest a preferential association of SOM with the nanocrystalline fraction of metal (hydr)oxides in agreement with previous observation based on selective dissolution extractions[41,42,81,82] and more recently confirmed with spectroscopy and electron microscopy techniques.[83,84] This suggests that in the tropical soils of this study, the AO extractable Fe and Al (hydr)oxides mainly determine the formation of organo-mineral associations, despite being less abundant than the crystalline Fe and Al (hydr)oxides.

Figure 8.4a shows the relationship between the experimentally derived RSA and SOC of our soils, suggesting that the SOC content tends to increase at increasing the RSA. However, statistically this relationship is poor (R^2 = 0.11, p < 0.01), and a large variation in SOC density (mg m^{-2}) is expected across soil samples. The relationship between RSA and SOC in the present set of soils is less clear than the corresponding relationship observed in the agricultural Dutch soils, studied previously[31] (see Figure 7.5 in Chapter 7). In the latter study, a distinct RSA-SOC relationship can be also distinguished in function of soil texture. For soils with a higher clay content (>= 20 %), the maximum surface loading of SOC is ~2 fold higher, suggesting than clay minerals might also contribute to the bulk SOC content. However, in the present set of tropical soils, such a distinction is not found neither (see blue squares *vs* green circles in Figure 8.4a), which may be due to the different type of dominant clay minerals present in both types of soils (1:1 clays in tropical soils *vs* 2:1 clays in Dutch soils).

The lack of a clear relationship in the data of Figure 8.4a indicates that apart from RSA, one or more other factors are involved in explaining the variation of SOC in these tropical soils. To elucidate this, the organo-mineral interaction will be interpreted structurally by considering a mineral core–surface layer model in which all SOM is accommodated in a layer with thickness L around the metal (hydr)oxide particles, as illustrated by the inset of Figure 8.4b. For each soil with a given diameter d for the metal oxide particles and RSA, the layer thickness L has been calculated by fitting it to the volume of SOM, assuming a generic carbon content of 58% of SOM and a mass density of ρ_{OM} = 1250 kg m^{-3}. A very good linear relationship is found between the calculated thickness L of organic matter layer and the mean particle diameter d size of the metal (hydr)oxide particles (R^2 = 0.87, p < 0.001). Counter-intuitively, one finds that larger particles are surrounded by thicker layers of SOM. The observed relationships of Figures 8.4a,b evidently indicate that the amount of SOC of the series of tropical soils cannot be only understood by the reactive surface area of the soil (RSA), but that the mean particle size (d) of the metal (hydr)oxide fraction play a crucial role. The latter parameter is directly related to the SSA and the metal (hydr)oxide content. In other words, with these basic data about the metal (hydr)oxide fraction, the SOC content can be very well explained.

The value of L varies between ~1 – 3 nm (Figure 8.4a), which is larger than the thickness of the compact of the double layer, being only ~0.7 nm.[85] The latter thickness is visualized in Figure 8.4b with a horizontal dashed line. Only in soils with the smallest metal (hydr)oxide particles and the lowest L, a significant fraction of the total SOC can be accommodated in the compact part of the double layer and is expected to be in direct contact with the metal (hydr)oxide surfaces.

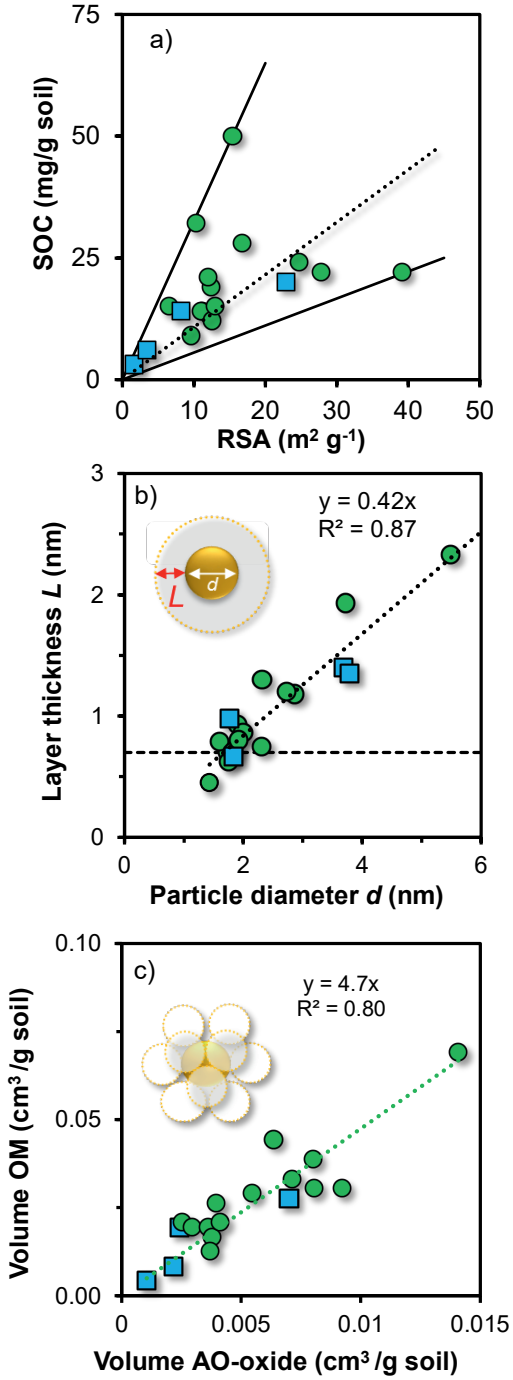

Figure 8.4. (**a**) Relationship between the bulk soil organic carbon (SOC) and the reactive surface area (RSA) for mineral soils with a low < 20 % (circles) and high clay content ≥ 20 % (squares). The slope of the dotted line represents the mean adsorption density of SOC (1.1 mg m^{-2}), whereas the full lines are for illustrating the wide range of variation of SOC adsorption density in the present data set. (**b**) Relationship between the layer thickness L of SOM according to a core-surface layer model (inset), showing that larger oxide particles are associated with more organic matter. The horizontal (dash) line represents the thickness of the compact part of the double layer, being ~0.7 nm.[85] (**c**) Relation between the volumes of SOM and the volumes of the Fe+Al nano-oxide fraction, extractable with AO, both in cm^3/g soil. If the volume ratio of $R_v = 5 \pm 1$ is interpreted as a coordination number, the arrangement of SOM particles around a metal (hydr)oxide core is about octahedral if SOM particles are not shared between metal (hydry)oxide cores. If SOM particles are shared, the coordination number may double, leading to a value typical for cub-octahedral coordination (CN = 12). The latter structure is shown in the inset.

In a temperate climate soil series, studied previously, the layer thickness also increases with the mean particle size. Similarly, the relationship passes through the origin (intercept = 0) and is linear. However, the slope of the relationship is steeper. This implies that at the same particle size (d), the SOM layer (L) is thicker. This difference in layer thickness between both types of soils may be due to a difference in climate and primary production creating another steady state in the organic matter dynamics. In the tropical topsoils, the layer thickness is on average ~2/3 of the layer thickness found for the topsoils of the temperate climate.

The above nano-scale organo-mineral interactions can also be interpreted with an alternative structural view, in which the associated material is considered as a collection of discrete particles of metal (hydr)oxide and soil organic matter. Remarkably, we found a significant linear relationship ($R^2 = 0.89$, $p < 0.001$) between the volumes of both types of primary particles (Figure 8.4c), yielding a volume ratio of $R_v \sim 5 \pm 1$. If the organo-mineral association in soils are due to self-assembly of SOM and metal (hydr)oxide nanoparticles, creating mineral cores surrounded by SOM particles, the volume ratio R_v can be interpreted as the mean coordination number (CN). In the tropical soils, this coordination number is considerably lower than the mean CN found in the temperate climate soils, where it is 10 ± 1. The latter CN is typical for a cubic or cub-octahedral coordination sphere. If these coordination spheres are interpreted with Pauling's first rule, the radii ratio of SOM and metal (hydr)oxide particles are respectively $r_r = 0.8$ and 1.0, indicating that both types of primary particles are of similar size. A similarly high radii ratio is also possible in tropical soils if the primary OM particles are shared between metal (hydr)oxide cores. It implies that a more condensed organo-mineral phase is formed in the tropical soils compared to the other soils. As mentioned above, this may be due to another steady state of the soil organic carbon dynamics in which agricultural productivity and climate are important factors.

In the above picture, the primary SOM and metal (hydr)oxide particles are thought to be organized by self-assembly at a level above the atomic ordering, leading to the formation of nano aggregates. At a higher organization hierarchy, *i.e.* formation of sub micrometer domains, these nano-scale organo-mineral associations may be attached to the surfaces of well-crystallized oxides or clay minerals,[86,87] jointly forming domains that contribute to the formation of bigger soil aggregates. Recently, direct evidence was found that nano-scale associations between poorly crystalline oxides and SOM act as major binding agents, favoring the adhesion of larger and less reactive mineral particles in submicron-sized aggregates in a volcanic soil.[83] The more stable and less reactive metal oxides have a reduced capacity to interact with SOM, as compared with the highly reactive nanocrystalline fraction of oxides. Increase in the degree of crystallinity of the metal (hydr)oxide fraction in such type of soils have been related to a decline in SOC content along two natural gradients of age (300 yr to 4100 kyr) and precipitation (180-3000 mm).[88]

The mass density of the formed organo-mineral association (ρ_{OMOX}) can be estimated using the volume (V_{OX}) and mass density of the metal (hydr)oxide particles (ρ_{OX}) of each soil, combined with the volume (V_{OM}) and mass density of soil organic matter ($\rho_{OM} = 1250$ kg m^{-3}). For the tropical soils, this leads to mean mass density of $\rho_{OMOX} = 1490 \pm 60$ kg m^{-3}, and for the soils from temperate climate, studied previously, this value is $\rho_{OMOX} = 1430 \pm 70$ kg m^{-3}. The calculated mass densities of the organo-metal (hydr)oxide association is typical for the "light" fraction of SOM, as often measured by mass density fractionation.[89,90] Using such experimental approaches, one may also obtain for soils a "heavy" SOM fraction, which has been interpreted as organic matter that is directly associated with minerals. To unify these observations with the mass densities obtained with our data analysis, one may assume that in part the organo-mineral associations are bound to the external surfaces of stacked clay plates, jointly

forming micro-aggregates. Moreover, the nano-scale organo-mineral associations may also attach to the external surfaces of crystalline metal (hydr)oxide domains and increase in that way the overall mass density the micro-aggregates. The organic matter present in these relatively robust and heavy micro-aggregates may be relatively stable against decomposition by microbes,[90] while the light fraction of SOC with organo-metal(hydr)oxide domains as dominant fraction may be more accessible to microorganisms.

The above structural picture for the metal (hydr)oxide fraction in our soils agrees with a recent conceptual model for the organo-mineral interactions, which proposes that in most soil environments, poorly crystalline materials are the first weathering products being formed from primary minerals and give rise to the formation of nano-sized organo-mineral associations.[91] In tropical soils, intensive weathering and relatively low surface PO_4 loadings will promote the transformation of nanocrystalline metal (hydr)oxides into more crystalline phases, which have a reduced capacity to stabilize SOM. In addition, this transformation leads to occlusion of PO_4 ,[36,92] as shown above in Section 3.5.1.

8.4. Conclusions

In this contribution, new insights have been elucidated into the properties of the reactive metal (hydr)oxide fraction and its nano-scale interactions with SOM in a series of weathered tropical soils. First, the effective reactive surface area (RSA) of the metal (hydr)oxide fraction in these soils was assessed by implementing a probe-ion methodology based on measuring the adsorption competition PO_4-CO_3 and succeeding CD model interpretation. The probe-ion methodology, initially developed and tested for P-rich top-soils from temperate climates, was effectively used in this set of low-P soils without major adaptations. Using the pool of AO-PO_4 as validation criterion, it has been concluded that Fh is a better proxy than goethite for the reactive fraction of Fe and Al-(hydr)oxides of the present set of soils. This result is remarkable, considering that in our weathered soils, the molar fraction of nanocrystalline metal (hydr)oxides is relatively small in comparison to the fraction of well-crystallized metal (hydr)oxides. A significant fraction of PO_4 associated to the metal (hydr)oxides (on average ~60%) does not take part in equilibrium reactions and can be considered as being occluded internally in the crystalline (hydr)oxide fraction. Scaling of the RSA to the AO extractable content of Fe and Al (hydr)oxides reveals the large variation in specific surface area (SSA) of the reactive metal (hydr)oxide fraction (SSA = ~ 400 – 1750 $m^2\ g^{-1}$). The corresponding mean particle size ranges between ~ 1.4 – 5.5 nm, indicating that nano-sized particles dominate the reactive fraction of metal (hydr)oxides in the present set of soils. Different from the series of top-soils from a temperate climate, studied previously, the relationship between RSA and SOC content is less clear. This apparent discrepancy can be reconciled by interpreting the organo-mineral interactions with a structural mineral core–surface layer model, in which SOM is accommodated in a layer with thickness *L* around the metal (hydr)oxide particles. In both cases, the layer thickness *L* of SOM increases linearly with increasing the mean particle size of the reactive metal (hydr)oxide fraction. The average *L* of the tropical soil is about ~2/3 of the average *L* value of the soils from temperate climate, which possibly results from a difference in the input and dynamics of SOM between the two types of soils. Alternatively, the nano-scale organo-mineral interactions can be interpreted as a collection of discrete particles of metal (hydr)oxide and soil organic matter that are organized by self-assembly. In this view, the volume ratio of SOM-to-metal (hydr)oxides particles can be interpreted as the mean coordination number (CN). In the tropical soils, this coordination number (5 ± 1) is significantly lower than the mean CN found in the temperate climate soils (10 ± 1), suggesting again, a different steady-state of the SOM dynamics between both types of soils.

Supplementary Information

Table S8.1. Size-dependent characteristics of the reactive metal (hydr)oxide fraction of the analyzed set of tropical soils.

Soil	d (nm)	M_{nano} (g mol^{-1}) [a]		ρ_{nano} (g cm^3) [a]		A (m^2 g^{-1}) [a]		SSA (m^2 g^{-1})
		Fe	Al	Fe	Al	Fe	Al	
1	1.8	105.9	94.4	3.36	2.25	1008	1509	1348
2	2.3	97.1	89.7	3.69	2.29	702	1133	1007
3	5.5	86.6	82.4	4.31	2.36	253	463	393
4	1.8	104.2	93.6	3.41	2.25	955	1447	1315
5	2.9	93.0	87.1	3.90	2.31	536	905	796
6	1.7	106.5	94.7	3.34	2.24	1027	1530	1415
7	1.9	102.8	92.9	3.46	2.26	907	1390	1261
8	1.6	111.3	96.9	3.20	2.23	1176	1691	1543
9	2.7	93.7	87.6	3.86	2.31	568	950	777
10	1.8	106.4	94.6	3.34	2.24	1024	1527	1386
11	1.4	119.1	99.9	3.03	2.20	1385	1901	1756
12	2.0	101.3	92.1	3.52	2.27	854	1327	1152
13	1.8	104.4	93.7	3.41	2.25	962	1455	1271
14	1.9	102.5	92.7	3.47	2.26	896	1378	1200
15	3.7	89.7	84.7	4.10	2.34	394	691	594
16	2.3	97.2	89.7	3.69	2.29	704	1136	918
17	3.7	89.7	84.8	4.09	2.34	396	695	622
18	3.8	89.5	84.6	4.11	2.34	385	677	546

[a] The reactive metal (hydr)oxide fraction is assumed to be composed by Fe and Al-(hydr)oxides, whose content is estimated from the amount of AO-extractable Fe and Al. The values of ρ_{nano} and M_{nano} are calculated iteratively, assuming a common equivalent particle diameter for the Fe and Al-(hydr)oxide nanoparticles (see for explanation the Supporting Information in Chapter 7).

[b] The SSA was calculated iteratively to account for the size dependency of ρ_{nano} and M_{nano}. It represents the overall SSA of the whole oxide fraction, which is mass-weighted based on the content Fe and Al extracted with AO.

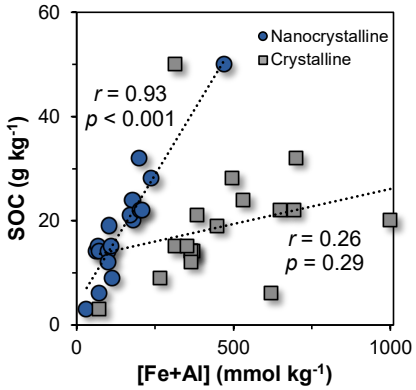

Figure S8.1. Correlation between bulk soil organic carbon (SOC) content and the amount of nanocrystalline (spheres) and crystalline (squares) Fe+Al (hydr)oxides. Both fractions are operationally defined as the amount of respectively, $[Fe+Al]_{AO}$ and $[Fe+Al]_{cryst} = [Fe+Al]_{DC} - [Fe+Al]_{AO}$.

References

(1) Hiemstra, T.; Antelo, J.; van Rotterdam, A. M. D.; van Riemsdijk, W. H. Nanoparticles in Natural Systems II: The Natural Oxide Fraction at Interaction with Natural Organic Matter and Phosphate. *Geochim. Cosmochim. Acta* **2010**, *74* (1), 59–69.

(2) Verbeeck, M.; Hiemstra, T.; Thiry, Y.; Smolders, E. Soil Organic Matter Reduces the Sorption of Arsenate and Phosphate: A Soil Profile Study and Geochemical Modelling. *Eur. J. Soil Sci.* **2017**, *68* (5), 678–688.

(3) Zhang, Y.; Wu, S.; Zheng, H.; Weng, L.; Hu, Y.; Ma, H. Modes of Selenium Occurrence and LCD Modeling of Selenite Desorption/Adsorption in Soils around the Selenium-Rich Core, Ziyang County, China. *Environ. Sci. Pollut. Res.* **2018**, *25* (15), 14521–14531.

(4) Kaiser, K.; Guggenberger, G. The Role of DOM Sorption to Mineral Surfaces in the Preservation of Organic Matter in Soils. In *Organic Geochemistry*; Pergamon, 2000; Vol. 31, pp 711–725.

(5) Wiseman, C. L. S.; Püttmann, W. Soil Organic Carbon and Its Sorptive Preservation in Central Germany. *Eur. J. Soil Sci.* **2005**, *56* (1), 65–76.

(6) Kleber, M.; Eusterhues, K.; Keiluweit, M.; Mikutta, C.; Mikutta, R.; Nico, P. S. Mineral-Organic Associations: Formation, Properties, and Relevance in Soil Environments. *Adv. Agron.* **2015**, *130*, 1–140.

(7) Lalonde, K.; Mucci, A.; Ouellet, A.; Gélinas, Y. Preservation of Organic Matter in Sediments Promoted by Iron. *Nature* **2012**, *483* (7388), 198–200.

(8) Chen, C.; Thompson, A. Ferrous Iron Oxidation under Varying PO2 Levels: The Effect of Fe(III)/Al(III) Oxide Minerals and Organic Matter. *Environ. Sci. Technol.* **2018**, *52* (2), 597–606.

(9) Perret, D.; Gaillard, J. F.; Dominik, J.; Atteia, O. The Diversity of Natural Hydrous Iron Oxides. *Environ. Sci. Technol.* **2000**, *34* (17), 3540–3546.

(10) van der Zee, C.; Roberts, D. R.; Rancourt, D. G.; Slomp, C. P. Nanogoethite Is the Dominant Reactive Oxyhydroxide Phase in Lake and Marine Sediments. *Geology* **2003**, *31* (11), 993–996.

(11) Basile-Doelsch, I.; Amundson, R.; Stone, W. E. E.; Masiello, C. A.; Bottero, J. Y.; Colin, F.; Masin, F.; Borschneck, D.; Meunier, J. D. Mineralogical Control of Organic Carbon Dynamics in a Volcanic Ash Soil on La Reunion. *Eur. J. Soil Sci.* **2005**, *0* (0), 050912034650042.

(12) Mikutta, R.; Schaumann, G. E.; Gildemeister, D.; Bonneville, S.; Kramer, M. G.; Chorover, J.; Chadwick, O. A.; Guggenberger, G. Biogeochemistry of Mineral-Organic Associations across a Long-Term Mineralogical Soil Gradient (0.3-4100 Kyr), Hawaiian Islands. *Geochim. Cosmochim. Acta* **2009**, *73* (7), 2034–2060.

(13) Weng, L.; Vega, F. A.; Van Riemsdijk, W. H. Competitive and Synergistic Effects in PH Dependent Phosphate Adsorption in Soils: LCD Modeling. *Environ. Sci. Technol.* **2011**, *45* (19), 8420–8428.

(14) Eusterhues, K.; Rumpel, C.; Kogel-Knabner, I.; Kögel-Knabner, I. Organo-Mineral Associations in Sandy Acid Forest Soils: Importance of Specific Surface Area, Iron Oxides and Micropores. *Eur. J. Soil Sci.* **2005**, *56* (6), 753–763.

(15) Mayer, L. M. Surface Area Control of Organic Carbon Accumulation in Continental Shelf Sediments. *Geochim. Cosmochim. Acta* **1994**, *58* (4), 1271–1284.

(16) Mendez, J. C.; Hiemstra, T. Surface Area of Ferrihydrite Consistently Related to Primary Surface Charge, Ion Pair Formation, and Specific Ion Adsorption. *Chem. Geol.* **2020**, *532*.

(17) Brunauer, S.; Emmett, P. H.; Teller, E. Adsorption of Gases in Multimolecular Layers. *J. Am. Chem. Soc.* **1938**, *60* (2), 309–319.

(18) Coward, E. K.; Thompson, A.; Plante, A. F. Contrasting Fe Speciation in Two Humid Forest Soils: Insight into Organomineral Associations in Redox-Active Environments. *Geochim. Cosmochim. Acta* **2018**, *238*, 68–84.

(19) Eisazadeh, A.; Kassim, K. A.; Nur, H. Morphology and BET Surface Area of Phosphoric Acid Stabilized Tropical Soils. *Eng. Geol.* **2013**, *154*, 36–41.

(20) Fontes, M. P. F.; Weed, S. B. *Phosphate Adsorption by Clays from Brazilian Oxisols: Relationships with Specific Surface Area and Mineralogy*; ELSEVIER, 1996; Vol. 72.

(21) Heister, K. The Measurement of the Specific Surface Area of Soils by Gas and Polar Liquid Adsorption Methods—Limitations and Potentials. *Geoderma* **2014**, *216*, 75–87.

(22) Dzombak, D. A.; Morel, F. F. M. M. *Surface Complexation Modeling: Hydrous Ferric Oxide*; John Wiley & Sons, 1990.

(23) Mödl, C.; Wörmann, H.; Amelung, W. Contrasting Effects of Different Types of Organic Material on Surface Area and Microaggregation of Goethite. *Geoderma* **2007**, *141* (3–4), 167–173.

(24) Hiemstra, T.; Antelo, J.; Rahnemaie, R.; van Riemsdijk, W. H. Nanoparticles in Natural Systems I: The Effective Reactive Surface Area of the Natural Oxide Fraction in Field Samples. *Geochim. Cosmochim. Acta* **2010**, *74* (1), 41–58.

(25) Cihacek, L. J.; Bremner, J. M. A Simplified Ethylene Glycol Monoethyl Ether Procedure for Assessment of Soil Surface Area1. *Soil Sci. Soc. Am. J.* **1979**, *43* (4), 821.

(26) Kennedy, M. J.; Pevear, D. R.; Hill, R. J. Mineral Surface Control of Organic Carbon in Black Shale. *Science (80-.).* **2002**, *295* (5555), 657–660.

(27) Dijkstra, J. J.; Meeussen, J. C. L.; Comans, R. N. J. Evaluation of a Generic Multisurface Sorption Model for Inorganic Soil Contaminants. *Environ. Sci. Technol.* **2009**, *43* (16), 6196–6201.

(28) Groenenberg, J. E.; Römkens, P. F. A. M.; Zomeren, A. Van; Rodrigues, S. M.; Comans, R. N. J. Evaluation of the Single Dilute (0.43 M) Nitric Acid Extraction to Determine Geochemically Reactive Elements in Soil. *Environ. Sci. Technol.* **2017**, *51* (4), 2246–2253.

(29) Tiberg, C.; Sjöstedt, C.; Gustafsson, J. P. Metal Sorption to Spodosol Bs Horizons: Organic Matter Complexes Predominate. *Chemosphere* **2018**, *196*, 556–565.

(30) Weng, L.; Temminghoff, E. J. M.; Van Riemsdijk, W. H. Contribution of Individual Sorbents to the Control of Heavy Metal Activity in Sandy Soil. *Environ. Sci. Technol.* **2001**, *35* (22), 4436–4443.

(31) Mendez, J. C.; Hiemstra, T.; Koopmans, G. F. Assessing the Reactive Surface Area of Soils with Ferrihydrite as Proxy for Natural Oxide Nanoparticles. *(Submitted)* **2020**.

(32) Hiemstra, T.; Van Riemsdijk, W. H. A Surface Structural Approach to Ion Adsorption: The Charge Distribution (CD) Model. *J. Colloid Interface Sci.* **1996**, *179* (2), 488–508.

(33) Kleber, M.; Schwendenmann, L.; Veldkamp, E.; Rößner, J.; Jahn, R. Halloysite versus Gibbsite: Silicon Cycling as a Pedogenetic Process in Two Lowland Neotropical Rain Forest Soils of La Selva, Costa Rica. *Geoderma* **2007**, *138* (1–2), 1–11.

(34) Xu, R. K.; Qafoku, N. P.; Van Ranst, E.; Li, J. Y.; Jiang, J. Adsorption Properties of Subtropical and Tropical Variable Charge Soils: Implications from Climate Change and Biochar Amendment. In *Advances in Agronomy*; 2016; Vol. 135, pp 1–58.

(35) Weihrauch, C.; Opp, C. Ecologically Relevant Phosphorus Pools in Soils and Their Dynamics: The Story so Far. *Geoderma* **2018**, *325* (August 2017), 183–194.

(36) Yang, X.; Post, W. M. Phosphorus Transformations as a Function of Pedogenesis: A Synthesis of Soil Phosphorus Data Using Hedley Fractionation Method. *Biogeosciences* **2011**, *8*, 2907–2916.

(37) Gustafsson, J. P. Arsenate Adsorption to Soils: Modelling the Competition from Humic Substances. *Geoderma* **2006**, *136* (1–2), 320–330.

(38) Regelink, I. C.; Weng, L.; Lair, G. J.; Comans, R. N. J. Adsorption of Phosphate and Organic Matter on Metal (Hydr)Oxides in Arable and Forest Soil: A Mechanistic Modelling Study. *Eur. J. Soil Sci.* **2015**, *66* (5), 867–875.

(39) Wagai, R.; Mayer, L. M. Sorptive Stabilization of Organic Matter in Soils by Hydrous Iron Oxides. *Geochim. Cosmochim. Acta* **2007**, *71* (1), 25–35.

(40) Mikutta, R.; Kleber, M.; Torn, M. S.; Jahn, R. Stabilization of Soil Organic Matter: Association with Minerals or Chemical Recalcitrance? *Biogeochemistry* **2006**, *77* (1), 25–56.

(41) Wiseman, C. L. S.; Püttmann, W. Interactions between Mineral Phases in the Preservation of Soil Organic Matter. *Geoderma* **2006**, *134* (1–2), 109–118.

(42) Kleber, M.; Mikutta, R.; Torn, M. S.; Jahn, R. Poorly Crystalline Mineral Phases Protect Organic Matter in Acid Subsoil Horizons. *Eur. J. Soil Sci.* **2005**, *56* (6), 717–725.

(43) Pédrot, M.; Boudec, A. Le; Davranche, M.; Dia, A.; Henin, O. How Does Organic Matter Constrain the Nature, Size and Availability of Fe Nanoparticles for Biological Reduction? *J. Colloid Interface Sci.* **2011**, *359* (1), 75–85.

(44) Hiemstra, T.; Antelo, J.; Rahnemaie, R.; van Riemsdijk, W. H. Nanoparticles in Natural Systems I: The Effective Reactive Surface Area of the Natural Oxide Fraction in Field Samples. *Geochim. Cosmochim. Acta* **2010**, *74* (1), 41–58.

(45) Hengl, T.; Mendes De Jesus, J.; Heuvelink, G. B. M.; Gonzalez, M. R.; Kilibarda, M.; Blagotí, A.; Shangguan, W.; Wright, M. N.; Geng, X.; Bauer-Marschallinger, B.; et al. SoilGrids250m: Global Gridded Soil Information Based on Machine Learning. *PLoS One* **2016**.

(46) Nelson, D. W.; Sommers, L. E. Total Carbon, Organic Carbon, and Organic Matter. In *Methods of soil analysis Part 3-Chemical Methoods*; 1996; pp 961–1010.

(47) Houba, V. J. G. J. G.; Temminghoff, E. J. M. J. M.; Gaikhorst, G. A. A.; van Vark, W. Soil Analysis Procedures Using 0.01 M Calcium Chloride as Extraction Reagent. *Commun. Soil Sci. Plant Anal.* **2000**, *31* (9–10), 1299–1396.

(48) Koopmans, G. F.; Hiemstra, T.; Vaseur, C.; Chardon, W. J.; Voegelin, A.; Groenenberg, J. E. Use of Iron Oxide Nanoparticles for Immobilizing Phosphorus In-Situ: Increase in Soil Reactive Surface Area and Effect on Soluble Phosphorus. *Sci. Total Environ.* **2020**, *711*, 135220.

(49) Murphy, J.; Riley, J. P. A Modified Single Solution Method for the Determination of Phosphate in Natural Waters. *Anal. Chim. Acta* **1962**, *27* (C), 31–36.

(50) Cui, Y.; Weng, L. Arsenate and Phosphate Adsorption in Relation to Oxides Composition in Soils: LCD Modeling. *Environ. Sci. Technol.* **2013**, *47* (13), 7269–7276.

(51) Hass, A.; Loeppert, R. H.; Messina, M. G.; Rogers, T. D. Determination of Phosphate in Selective Extractions for Soil

Iron Oxides by the Molybdenum Blue Method in an Automated Continuance Flow Injection System. *Commun. Soil Sci. Plant Anal.* **2011**, *42* (14), 1619–1635.

(52) ISO. *ISO 12782-3:2012 Soil Quality -- Parameters for Geochemical Modelling of Leaching and Speciation of Constituents in Soils and Materials -- Part 3: Extraction of Aluminium Oxides and Hydroxides with Ammonium Oxalate/Oxalic Acid*; 2012.

(53) Schwertmann, U. Differenzierung Der Eisenoxide Des Bodens Durch Extraktion Mit Ammoniumoxalat-Lösung. *Zeitschrift für Pflanzenernährung, Düngung, …* **1964**.

(54) ISO. *ISO 12782-2:2012 - Soil Quality -- Parameters for Geochemical Modelling of Leaching and Speciation of Constituents in Soils and Materials -- Part 2: Extraction of Crystalline Iron Oxides and Hydroxides with Dithionite*; 2012.

(55) Barrow, N. J.; Shaw, T. C. Sodium Bicarbonate as an Extractant for Soil Phosphate, II. Effect of Varying the Conditions of Extraction on the Amount of Phosphate Initially Displaced and on the Secondary Adsorption. *Geoderma* **1976**, *16* (2), 109–123.

(56) Mendez, J. C.; Hiemstra, T. Carbonate Adsorption to Ferrihydrite: Competitive Interaction with Phosphate for Use in Soil Systems. *ACS Earth Sp. Chem.* **2019**, *3* (1), 129–141.

(57) Rahnemaie, R.; Hiemstra, T.; van Riemsdijk, W. H. Carbonate Adsorption on Goethite in Competition with Phosphate. *J. Colloid Interface Sci.* **2007**, *315* (2), 415–425.

(58) Hiemstra, T.; Zhao, W. Reactivity of Ferrihydrite and Ferritin in Relation to Surface Structure, Size, and Nanoparticle Formation Studied for Phosphate and Arsenate. *Environ. Sci. Nano* **2016**, *3* (6), 1265–1279.

(59) Keizer, M. G.; Van Riemsdijk, W. H. *ECOSAT, a Computer Program for the Calculation of Chemical Speciation and Transport in Soil-Water Systems*; Wageningen, the Netherlands, the Netherlands, 1995.

(60) Kinniburgh, D. G. *FIT User Guide, Technical Report WD/93/23*; Keyworth, 1993.

(61) Borggaard, O. K. Dissolution of Poorly Crystalline Iron Oxides in Soils by EDTA and Oxalate. *Zeitschrift für Pflanzenernährung und Bodenkd.* **1992**, *155* (5), 431–436.

(62) Schwertmann, U. Use of Oxalate for the Fe Extraction from Soils. *Can. J. Soil Sci.* **1973**, *53* (2), 244–246.

(63) Schwertmann, U.; Schulze, D. G.; Murad, E. Identification of Ferrihydrite in Soils by Dissolution Kinetics, Differential X-Ray Diffraction, and Mössbauer Spectroscopy1. *Soil Sci. Soc. Am. J.* **1982**, *46* (4), 869–875.

(64) Koopmans, G. F.; Oenema, O.; Van Riemsdijk, W. H. Characterization, Desorption, and Mining of Phosphorus in Noncalcareous Sandy Soils, 2004.

(65) Maguire, R. O.; Foy, R. H.; Bailey, J. S.; Sims, J. T. Estimation of the Phosphorus Sorption Capacity of Acidic Soils in Ireland. *Eur. J. Soil Sci.* **2001**, *52* (3), 479–487.

(66) Van Der Zee, S. E. A. T. M.; Van Riemsdijk, W. H. Model for Long-Term Phosphate Reaction Kinetics in Soil. *J. Environ. Qual.* **1988**, *17* (1), 35–41.

(67) Lookman, R.; Freese, D.; Merckx, R.; Vlassak, K.; Van Riemsdijk, W. H. Long-Term Kinetics of Phosphate Release from Soil. *Environ. Sci. Technol.* **1995**, *29* (6), 1569–1575.

(68) Worsfold, P.; McKelvie, I.; Monbet, P. Determination of Phosphorus in Natural Waters: A Historical Review. *Analytica Chimica Acta*. Elsevier April 28, 2016, pp 8–20.

(69) Wolf, A. M.; Baker, D. E. Colorimetric Method for Phosphorus Measurement in Ammonium Oxalate Soil Extracts. *Commun. Soil Sci. Plant Anal.* **1990**, *21* (19–20), 2257–2263.

(70) Jørgensen, C.; Turner, B. L.; Reitzel, K. Identification of Inositol Hexakisphosphate Binding Sites in Soils by Selective Extraction and Solution ^{31}P NMR Spectroscopy. *Geoderma* **2015**, *257–258*, 22–28.

(71) Warrinnier, R.; Goossens, T.; Amery, F.; Vanden Nest, T.; Verbeeck, M.; Smolders, E. Investigation on the Control of Phosphate Leaching by Sorption and Colloidal Transport: Column Studies and Multi-Surface Complexation Modelling. *Appl. Geochemistry* **2019**, *100* (November 2018), 371–379.

(72) Aguilera, N. H.; Jackson, M. L. Iron Oxide Removal from Soils and Clays. *Soil Sci. Soc. Am. J.* **1953**, *17* (4), 359–364.

(73) Mehra, O. P.; Jackson, M. L. Iron Oxide Removal from Soils and Clays by a Dithionite-Citrate System Buffered with Sodium Bicarbonate. *Clays Clay Miner.* **1958**, *7* (1), 317–327.

(74) Jansen, B.; Tonneijck, F. H.; Verstraten, J. M. Selective Extraction Methods for Aluminium, Iron and Organic Carbon from Montane Volcanic Ash Soils. *Pedosphere* **2011**, *21* (5), 549–565.

(75) Hiemstra, T. Ferrihydrite Interaction with Silicate and Competing Oxyanions: Geometry and Hydrogen Bonding of Surface Species. *Geochim. Cosmochim. Acta* **2018**, *238*, 453–476.

(76) Hiemstra, T.; Mendez, J. C.; Li, J. Evolution of the Reactive Surface Area of Ferrihydrite: Time, PH, and Temperature Dependency of Growth by Ostwald Ripening. *Environ. Sci. Nano* **2019**, *6* (3), 820–833.

(77) Liu, Y. T.; Hesterberg, D. Phosphate Bonding on Noncrystalline Al/Fe-Hydroxide Coprecipitates. *Environ. Sci. Technol.* **2011**, *45* (15), 6283–6289.

(78) Lal, R.; Sanchez, P. A.; Schwertmann, U.; Herbillon, A. J. Some Aspects of Fertility Associated with the Mineralogy

of Highly Weathered Tropical Soils; 1992.

(79) Fitzpatrick, R. W.; Schwertmann, U. Al-Substituted Goethite-An Indicator of Pedogenic and Other Weathering Environments in South Africa. *Geoderma* **1982**, *27* (4), 335–347.

(80) Gálvez, N.; Barrón, V.; Torrent, J. Effect of Phosphate on the Crystallization of Hematite, Goethite, and Lepidocrocite from Ferrihydrite. *Clays Clay Miner.* **1999**, *47* (3), 304–311.

(81) Rasmussen, C.; Heckman, K.; Wieder, W. R.; Keiluweit, M.; Lawrence, C. R.; Berhe, A. A.; Blankinship, J. C.; Crow, S. E.; Druhan, J. L.; Hicks Pries, C. E.; et al. Beyond Clay: Towards an Improved Set of Variables for Predicting Soil Organic Matter Content. *Biogeochemistry* **2018**, *137* (3), 297–306.

(82) Souza, I. F.; Archanjo, B. S.; Hurtarte, L. C. C.; Oliveros, M. E.; Gouvea, C. P.; Lidizio, L. R.; Achete, C. A.; Schaefer, C. E. R.; Silva, I. R. Al-/Fe-(Hydr)Oxides–Organic Carbon Associations in Oxisols — From Ecosystems to Submicron Scales. *Catena* **2017**, *154*, 63–72.

(83) Asano, M.; Wagai, R.; Yamaguchi, N.; Takeichi, Y.; Maeda, M.; Suga, H.; Takahashi, Y. In Search of a Binding Agent: Nano-Scale Evidence of Preferential Carbon Associations with Poorly-Crystalline Mineral Phases in Physically-Stable, Clay-Sized Aggregates. *Soil Syst.* **2018**, *2* (2), 32.

(84) Vogel, C.; Mueller, C. W.; Höschen, C.; Buegger, F.; Heister, K.; Schulz, S.; Schloter, M.; Kögel-Knabner, I. Submicron Structures Provide Preferential Spots for Carbon and Nitrogen Sequestration in Soils. *Nat. Commun.* **2014**, *5*.

(85) Hiemstra, T.; Van Riemsdijk, W. H. On the Relationship between Charge Distribution, Surface Hydration, and the Structure of the Interface of Metal Hydroxides. *J. Colloid Interface Sci.* **2006**, *301* (1), 1–18.

(86) Singh, M.; Sarkar, B.; Sarkar, S.; Churchman, J.; Bolan, N.; Mandal, S.; Menon, M.; Purakayastha, T. J.; Beerling, D. J. Stabilization of Soil Organic Carbon as Influenced by Clay Mineralogy. In *Advances in Agronomy*; Academic Press, 2018; Vol. 148, pp 33–84.

(87) Pronk, G. J.; Heister, K.; Kögel-Knabner, I. Iron Oxides as Major Available Interface Component in Loamy Arable Topsoils. *Soil Sci. Soc. Am. J.* **2011**, *75* (6), 2158–2168.

(88) Torn, M. S.; Trumbore, S. E.; Chadwick, O. A.; Vitousek, P. M.; Hendricks, D. M. Mineral Control of Soil Organic Carbon Storage and Turnover. *Nature* **1997**, *389* (6647), 170–173.

(89) Golchin, A.; Oades, J. M.; Skjemstad, J. O.; Clarke, P. Soil Structure and Carbon Cycling. *Aust. J. Soil Res.* **1994**, *32* (5), 1043–1063.

(90) Poeplau, C.; Don, A.; Six, J.; Kaiser, M.; Benbi, D.; Chenu, C.; Cotrufo, M. F.; Derrien, D.; Gioacchini, P.; Grand, S.; et al. Isolating Organic Carbon Fractions with Varying Turnover Rates in Temperate Agricultural Soils – A Comprehensive Method Comparison. *Soil Biol. Biochem.* **2018**, *125*, 10–26.

(91) Basile-Doelsch, I.; Balesdent, J.; Rose, J. Are Interactions between Organic Compounds and Nanoscale Weathering Minerals the Key Drivers of Carbon Storage in Soils? *Environmental Science and Technology*. American Chemical Society April 7, 2015, pp 3997–3998.

(92) Jiang, Z.; Liu, Q.; Roberts, A. P.; Barrón, V.; Torrent, J.; Zhang, Q. A New Model for Transformation of Ferrihydrite to Hematite in Soils and Sediments. *Geology* **2018**, *46* (11), 987–990.

CHAPTER 9

Synthesis and Discussion

Juan C. Mendez

9.1. Introduction

9.1.1. Oxyanion adsorption in soils

Studying the reactivity of the natural metal (hydr)oxide fraction is essential for understanding the binding behavior of ions in the environment, in particular for oxyanions such as phosphate (PO_4^{3-}), arsenate (AsO_4^{3-}), chromate (CrO_4^{2-}), and antimonate ($Sb(OH)_6^-$). These oxyanions have a high binding affinity for the surfaces of metal (hydr)oxides,[1–5] which controls their bioavailability and mobility in the environment. In soils, the metal (hydr)oxide fraction comprises various mineral phases whose contribution to the total soil reactivity depends mostly on their specific surface area (SSA).[6,7] Goethite is one of the most abundant Fe (hydr)oxides in soils. Hematite may also be present, particularly in soils of (sub)tropical regions.[7] In the past, the reactivity of these materials towards oxyanions has been extensively studied.[8–11] However, these minerals have a relatively low specific surface area (SSA), which may limit their contribution to the overall reactivity of soils. Ferrihydrite (Fh) is a naturally occurring Fe (hydr)oxide nanoparticle which, thanks to its ultra-small particle size, has an extraordinarily high SSA. Therefore, even if present at low mass concentrations, Fh might greatly contribute to the total surface reactivity of soils. The present work contributes to improve our understanding of the crucial role of this omnipresent nanomineral in determining the reactivity of soils for binding oxyanions.

The adsorption behavior of oxyanions cannot be properly understood without analyzing the adsorption of major cations, and *vice versa*, as both types of ions interact at the mineral-solution interfaces in natural and engineered environments. For instance, the relatively abundant alkaline-earth metal ions interact with oxyanions, mutually enhancing their adsorption to metal (hydr)oxides.[12–14] This implies that information about the binding behavior of major cations is essential if the aim is understanding and predicting the adsorption of oxyanions under realistic environmental conditions. In addition, the interaction between oxyanions also needs to be considered, as the availability and mobility of one oxyanion can increase in the presence of another oxyanion that competes for the same binding sites at the surfaces of metal (hydr)oxides.[15–18] The principles of these cooperative and competitive interactions between ions have been also specific subjects of study in the present work.

9.1.1. Why studying phosphate adsorption matters?

Phosphate (hereinafter referred to as PO_4) is just one more of the many oxyanions that are important for environmental quality. However, in this thesis, the adsorption of PO_4 played a central role and its behavior has been extensively studied in model Fh systems and applied to soil samples. Phosphate was chosen as model oxyanion for studying the surface reactivity of Fh for multiple reasons. It is omnipresent in natural systems, where it takes part in the internal phosphorous (P) cycle. Phosphate is an essential nutrient for plant growth and food production. In the top-soils, the PO_4 surface loading is often high due to the high binding affinity of this oxyanion for the natural metal (hydr)oxides.[19] Paradoxically, the concentration of available PO_4 in the soil solution is generally too low to meet the plant growth requirements,[20] making this essential nutrient a major constraint on food production.

In human lifetimes, PO_4 is a non-renewable resource. This essential resource cannot be artificially manufactured and there is no substitute for it, both for plant growth and food production.[21] Good quality phosphate ores are only available in a few countries, making these ores a strategic and geopolitical resource. This situation puts at stake the independency of phosphate supply for many countries.[22] Although controversies have arisen about the origin of the current global P scarcity concerns,[23] there is

a general consensus that the present situation regarding inefficient management of PO_4, and its uneven geographical distribution, may compromise the access to this resource in the long-term.[21,24]

Phosphorus is intimately linked to a fragile nexus of water, energy and food security.[25] Part of the P paradox consists in overcoming shortages of available P to sustain food and biofuel production while addressing the issue of P surpluses entering aquatic systems, which threats water quality and security.[25] The local cycle of P in unmanaged ecosystems is rather closed; *i.e.* P transfers beyond the system boundary are small. However, various humans activities have altered the natural cycling of P converting it into a much more open cycle.[26] Transport of P resources from one place to another has important implications, not only for the environment, but also from an economic and societal perspective. In high-input agricultural systems of developed countries, there is often a P surplus due to massive imports of feed for livestock or to intensive P fertilizer applications. On a global scale, this implies the removal and transport of P resources from elsewhere, causing a series of environmental and societal problems such as soil degradation, lack of food and consequently, poverty, disintegration of communities, and migration of populations.

Therefore, there is a worldwide need for well-managing PO_4 in soils, particularly in a world with a still fast-growing population that needs to be fed. Changes in the habits of consumption of many emerging economies add additional pressure on the P resource.[21,26] Considering the above global context, the scientific, economic and societal relevance of studying the underlying processes affecting the availability of PO_4 is evident. As mentioned, the adsorption of PO_4 to the natural fraction of metal (hydr)oxides is one of these major processes controlling the environmental fate of this essential resource.

9.1.2. Thesis contribution

This thesis aimed to get insights into the surface reactivity of Fh, particularly in relation to the adsorption of PO_4 and its interfacial interactions with other ions that are relevant in the environment and from the perspective of soil chemical analysis (*i.e.* CO_3, Ca, Mg). To date, these interactions had not been systematically studied for well-characterized fresh Fh suspensions. The ultimate goal was to contribute to develop a consistent surface complexation modeling (SCM) approach for describing the adsorption behavior of PO_4 under environmentally relevant conditions and in the context of soil chemical analysis. The adsorption of Ca and Mg ions has been also studied extensively in single-ion systems due to their high abundance in the environment and their effect on the adsorption of other important ions, such as PO_4.

The developed modeling framework for Fh has allowed us to compile a self-consistent thermodynamic database, which was subsequently used for evaluating the surface reactivity of the natural fraction of metal (hydr)oxides in soils, in relation to the interaction with PO_4 ions and soil organic matter (SOM). The analysis was done for field soil samples with a very different pedogenesis and chemical properties (*e.g.* contrasting ratios of crystalline and nano-crystalline Fe and Al (hydr)oxides), showing that the modeling approach developed in this thesis for Fh can be applied for a wide range of soil conditions.

In general, this thesis contributes to better understanding the underlying chemical processes that determine the availability and mobility of PO_4 under a wide range of environmental and technological conditions. The insights gained in the present work are not only relevant for optimizing P use efficiency in agricultural ecosystems or for reducing the negative side-effects of PO_4 in the environment, but they are also relevant in the context of technological applications intended to improve P recovery and its recycling from water and waste treatments. Therefore, the subject addressed in this thesis has

implications for different disciplines, including soil and water chemistry, soil fertility and pollution, environmental technology, and chemical engineering.

In this final chapter, I will first recapitulate the major findings of my PhD thesis (Section 9.2). Then, I will discuss in more detail a selection of results and concepts, which in my opinion, deserve further analysis in the context of this thesis (Sections 9.3 – 9.5). When opportune, I will frame within a broader context the significance of the findings and I will propose future research opportunities, in light of the results obtained in this thesis.

9.2. Synthesis of the main findings

In this thesis, significant progress was made towards a better understanding of the surface reactivity of Fh (Chapters 2–3) and towards a consistent description of ion adsorption to this nanomaterial (Chapters 4–6). The CD-MUSIC model parametrized for Fh was then implemented to get insights into the properties of the nanometer sized fraction of metal (hydr)oxides in soil samples with contrasting chemical properties (Chapters 7–8). In the next sections, the main findings of my PhD thesis are summarized, according to the three major sections defined in the Introduction chapter, namely; *i*) basic insights into the surface reactivity of Fh, *ii*) parametrization of the ion adsorption model, and *iii*) application of the developed SCM to soils.

9.2.1. Insights into the surface reactivity of ferrihydrite

Interpretation of nearly all physical and chemical characteristics of Fh can be properly done only if information is available about its specific surface area (SSA) and the particle size, as Fh is a nano material *pur sang.* Therefore, a systematic approach has been developed for assessing the SSA of fresh Fh suspensions. This was done by interpreting the primary adsorption data of protons (H^+) with advanced surface complexation modeling (SCM) (Chapter 2). For Fh suspensions kept in the wet state, it has been shown that the scaling of the data cannot be done in a totally independent manner, as it is done for more traditional Fe (hydr)oxides using BET surface area (A_{BET}) as a reference. In my approach, the acid-base titration data of Fh were evaluated in a consistent manner accounting for the major differences between Fh and goethite, such as reactive site densities, molar masses, mass densities, and capacitances of the Stern layers. The basic assumption is that the electrical double layer (EDL) structure of both materials is the same, apart from surface curvature affecting particularly the compact part of the EDL of Fh. An additional assumption in my approach is that the ion pair formation constants ($\log K_{ip}$), of Na^+ and NO_3^- are the same for goethite and Fh. The latter assumption is reasonable, as the evaluation of the H^+ adsorption data of Fh in different background electrolyte solutions (*i.e.* NaCl, $NaNO_3$, and $NaClO_4$) showed a good correlation between the $\log K_{ip}$ values of Fh and goethite. The sensitivity analysis presented in Chapter 2 showed that omitting the difference in surface curvature between goethite and Fh, the estimated SSA of Fh increases by about ~20 %. Differences in site densities between both materials have little effect (~4%) on the estimated values of SSA.

Application of the developed approach for describing H^+ adsorption data reported in literature revealed a large variation in the SSA (~500–720 $m^2\ g^{-1}$) of fresh Fh suspensions, prepared and stored under different conditions. It shows that use of a "standard" SSA for Fh is not recommended because the methods of synthesis of this material usually differ. Moreover, my experience indicates that even with the same preparation protocol, reproducibility may sometimes fail as described with an example in

Chapter 2, advocating the use of a convenient method to assess the SSA of each batch of freshly prepared Fh.

From a practical perspective, the use of elaborate acid-base titrations is not recommended if the aim is to assess the SSA of Fh on a routine basis, for each Fh batch that is produced. Therefore, the use of another probe ion has been proposed. As shown in Chapter 2, PO_4 is an excellent choice, but other ions with a high binding affinity for Fh may work as well. A critical aspect is that the chosen probe ion must adsorb rapidly and suppress further particle growth during equilibration time. Moreover, its adsorption should not be sensitive to solution conditions that cannot be easily controlled. For instance, using a high affinity probe ion has the advantage of being less sensitive to possible interference of atmospheric CO_2, as I have shown in Chapter 6 for PO_4. Results showed that within an uncertainty of ~2%, the SSA of fresh Fh suspensions can be equally well assessed using either H^+ or PO_4. In general, collecting and interpreting PO_4 adsorption data is a more practical alternative to overcome the known limitations of the traditional BET technique for assessing the SSA of Fh nanoparticles kept in the wet state (Chapter 2). Therefore, PO_4 was implemented as the probe ion in all further work described in this thesis, allowing the development of an internally consistent thermodynamic database for describing the adsorption of several ions to Fh (Chapters 4–6).

Changes in the surface reactivity of Fh resulting from particle growth processes (*i.e.* aging) were effectively quantified by probing the surface of this material with PO_4 (Chapter 3). With the collected data, a dynamic model was developed that describes the pH-, temperature-, and time-dependency of the growth of Fh particles by Ostwald ripening. The rate of growth of Fh is proportional to the square of the solution super saturation, $R \propto (Q_{so}/K_{so})$.[2] This result was interpreted as a growth process of Fh by the dual attachment of Fe atoms, limited by the size-dependent solubility of Fh. The dynamic model also provided insights into the size ($d \sim 1.68$ nm) and surface area ($A \sim 1100$ m^2 g^{-1}) of the initial Fh nanoparticles, *i.e.* non-aged particles. The presence of weakly bound organic molecules strongly reduced the rate of Fh growth, especially at low pH conditions, suggesting that in the environment the presence of natural organic matter would contribute to the kinetic stability of Fh. The insights obtained in Chapter 3 can help to optimize the synthesis and aging conditions of Fh suspensions, leading to improved control and quality of ion adsorption experiments.

The experiments of Chapter 3 underlined the importance of pH in the process of aging of Fh suspensions. Based on my experience and results, the use of a relatively low pH (*e.g.* pH 6) in the synthesis is recommended in combination with a longer time of aging, *i.e.* more than the conventional 4 h aging. These conditions help to create Fh materials that are less prone to changes in SSA during the adsorption experiments. Moreover, aging at relatively low pH for at least 48 hours facilitated the removal of CO_2(g) by N_2(g) purging. This is important to perform adsorption experiments with ions that are sensitive to interference by atmospheric CO_2. Because the objective of this thesis was to compile, as consistently as possible, a thermodynamic database with intrinsic adsorption parameters, the use of different preparation protocols of Fh has not been tested for ion adsorption experiments. In future research, such types of experiments may help to analyze whether variations in the synthesis protocol of Fh ultimately lead to slight differences in the surface structure of Fh, and changes in for instance the number of high affinity sites, affecting the ion adsorption even if scaled properly to the SSA.

9.2.2. Parametrization of the ion adsorption model

In Chapter 2, the relative variation in ion-pair constants ($\log K_{ip}$) of common electrolyte anions was measured using a stock Fh suspension with a unique reference state. The charging behavior of Fh in

$NaNO_3$ solutions was taken as a reference, assuming for Fh the same $\log K_{Na}$ and $\log K_{NO3}$ values as determined for well-crystallized goethite. The $\log K_{ip}$ values of electrolyte anions decreases in the order of $Cl^- > NO_3^- > ClO_4^-$ for Fh, following the same trend as for goethite. Extrapolating the results to other ions, not evaluated yet experimentally, the $\log K_{ip}$ values of electrolyte cations decreases in the order of $Li^+ > Na^+ > K^+$. The electrolyte pair Na^+–NO_3^- is the most symmetrical in relation to the interaction with the surface groups of Fh, allowing a better approximation of the point of zero charge (pH_{PZC}) from the pH of the common intersection point (pH_{CIP}) found in potentiometric titration curves performed at different $NaNO_3$ levels. For $\log K_{Na} = \log K_{NO3}$, consequently the pH_{CIP} corresponds to the pristine point of zero charge (pH_{PZZC}) of the material, which for Fh is ~ 8.1. Higher pH_{PZC} values have been reported in literature for Fh. In Chapter 2, it was shown that these values can be well understood from the asymmetrical interaction of electrolytes with the reactive surface groups, due to the use of for instance KCl, KNO_3, or NaCl as background solutions, rather than $NaNO_3$. These variations in pH_{PZC} were well-predicted by the parametrized CD-MUSIC model.

The adsorption of Ca and Mg ions (jointly referred to as M^{2+}) was extensively analyzed in single-ion systems with freshly precipitated Fh (Chapter 4). The trend in the pH-dependent adsorption of both ions is rather similar, however, under the same solution conditions, Ca interacts stronger than Mg with the surface groups of Fh. As argued in Chapter 4, both cations form predominantly inner-sphere bidentate surface complexes ($\equiv(FeOH)_2^{\Delta z0}M^{\Delta z1}$) with singly coordinated groups at the surfaces of Fh, most likely in a binuclear double corner (^2C) configuration. This binding mechanism is supported by the joint interpretation of the optimized geometries obtained with molecular orbital (MO) calculations, applying density functional theory (DFT), and spectroscopy data reported in literature for other cations (*i.e.* Sr^{2+} and Cd^{2+}). Formation of bidentate complexes is thermodynamically consistent with macroscopic data such as the H^+/Ca^{2+} exchange and the marked pH-dependency of the M^{2+} adsorption observed in my own data. Moreover, formation of bidentate complexes was required for consistently describing the adsorption interaction of M^{2+} and PO_4 in binary Fh systems (Chapter 5). However, direct spectroscopic evidence is not available yet for the surface complexes of Ca and Mg ions present on Fh surfaces.

The insights gained from the analysis of the Ca and Mg adsorption to Fh have been extended for interpreting the binding of the full series of alkaline-earth ions, which revealed important physical-chemical insights into the adsorption behavior of this entire series of ions (Chapter 4). For Fh, the binding affinity increases with increasing ionic radius of these cations, *i.e.* $Be^{2+} < Mg^{2+} < Ca^{2+} \approx Sr^{2+} < Ba^{2+} < Ra^{2+}$. This affinity trend is opposite to the trend observed for other Fe (hydr)oxides (*e.g.* hematite, goethite), which can be attributed to differences in the Gibbs free energy released by exchange of interfacial water occurring upon M^{2+} binding. If the energy contribution related to the exchange of interfacial water is low, a decrease in affinity is expected when the ionic size increases, while the opposite is expected if this energy contribution is large. The results suggest that physisorbed water is more strongly structured near the surfaces of Fh, in comparison to goethite and hematite. If true, it may affect the capacitance value of the Stern layers, whereas this was assumed to be the same for Fh and goethite in Chapter 2. In future research, molecular dynamic simulations may provide further insights into this issue.

An important aspect of cation adsorption to Fh is the claim of surface site heterogeneity (*i.e.* presence of sites with low and high affinity). Surface site heterogeneity was implemented in the CD-MUSIC model for describing adequately the data collected in this thesis and reported in the literature for the adsorption of the alkaline-earth metal ions to Fh (Chapter 4). For my Fh suspensions, only a relatively small fraction (~10%) of reactive sites available for forming ^2C bidentate complexes (*i.e.* $\equiv FeOH^{-0.5}(b)$) show a high affinity character toward M^{2+}. Nevertheless, this fraction of high affinity sites dominates

the M^{2+}adsorption at low ion loadings, particularly at low pH values. For other Fh materials evaluated in Chapter 4, lower values have been derived for the density of high affinity sites. When translated into a mean number of sites per particle, about 1–3 ions per particle are bound to these high affinity sites. In Section 9.4.1, further discussion about this phenomenon will be presented, making an emphasis on the analysis of Ca adsorption data.

As no physic-chemical explanation for the high affinity phenomenon is presently available in literature, an attempt has been made in this thesis to rationalize this phenomenon, which is based on a detailed analysis of the surface structure of Fh. Briefly, the high affinity sites may originate from a charge redistribution within specific pairs of Fe1 octahedra at the surfaces of Fh, causing a high charge undersaturation of surface –OH ligands. This leads to an increase in the binding affinity of M^{2+} to compensate this charge undersaturation. However, with the current knowledge, it is difficult to indisputably attribute a specific structural configuration to this adsorption phenomenon. Nevertheless, the proposed mechanism explains the number of high affinity sites found by modeling the adsorption data and offers a rationale for the presence of these sites. If undersaturation of the bond valence charge of the surface –OH ligands plays an important role, it may affect the CD values of the complexes adsorbed to the high affinity site, compared to those adsorbed to the low affinity sites. This is a point of concern, as the CD value was calculated using a standard template in the MO/DFT optimizations and it was assumed to be the same for both the high and low affinity sites. If the latter is true, then the log*K*s fitted for ion adsorption to the high affinity sites may vary slightly. Increasing the complexity of the Fe template used in the MO/DFT calculations to represent better the structure of proposed high affinity moiety could help to evaluate the above-mentioned concern. However, this approach may be rather complex in terms of computations time and interpretation.

The interfacial interactions of PO_4 with Ca and Mg ions (M^{2+}) were evaluated in binary PO_4-M^{2+} systems with freshly prepared Fh (Chapter 5). The adsorption of M^{2+} ions to Fh was enhanced in the presence of PO_4, and *vice versa*. This synergistic binding could not be understood only on the basis of electrostatic interactions, as found previously for goethite. Instead, formation of anion-bridged (*i.e.* ≡Fe–PO_4–M^{2+}) ternary complexes is the main mechanism explaining the cooperative binding between PO_4 and M^{2+}. Anion-bridged (*i.e.* ≡Fe–PO_4–M^{2+}) ternary complexes are favored over of cation-bridge complexes (*i.e.* ≡Fe–M^{2+}–PO_4) because the affinity of PO_4 for the surface of Fh is significantly higher than the affinity of M^{2+}. For the Ca-PO_4 systems, the formation of two anion-bridged ternary complexes, *i.e.*, ≡$(FeO)_2PO_2Ca$ and ≡$FeOPO_3Ca$ was resolved, whereas for Mg-PO_4 systems only the formation of the ternary ≡$FeOPO_3Mg$ complex could be resolved. CD model calculations indicate that Ca interacts stronger than Mg with the PO_4 ions adsorbed at the surface of Fh. The pH-dependency of PO_4 adsorption in Ca solutions differs between Fh and goethite, which was explained by the difference in the mechanism (*i.e.* ternary complex formation *vs* electrostatic interactions) ruling the synergistic Ca-PO_4 interaction in both Fe (hydr)oxides. This issue will be more critically discussed in Section 9.4.2.

In Chapter 6, the competitive adsorption interaction CO_3-PO_4 was analyzed in Fh systems for a wide range of solution conditions (*i.e.* pH, total CO_3, and PO_4 concentrations) that are relevant for environmental systems, such as groundwaters, or applied in laboratory systems for soil chemical analysis (*e.g.* equilibrium 0.5 M $NaHCO_3$ soil extractions). For a given pH, the adsorption of PO_4 to Fh decreases at increasing the total concentration of added CO_3, which is due to the direct competition between both oxyanions for the same binding sites at the Fh surface. However, the relative affinity of PO_4 for these sites is significantly larger than the affinity of CO_3, meaning that PO_4 is substantially removed from the surface of Fh only at high total CO_3/PO_4 molar ratios. A remarkable difference is found for the shape of the PO_4 adsorption isotherm of Fh and goethite in 0.5 M $NaHCO_3$ solution. This

may be related to differences in the surface speciation of CO_3 between both minerals. The measured difference in the CO_3-PO_4 competition between both Fe (hydr)oxides has important implications for the assessment of the reactive surface area of soils if probed in PO_4-CO_3 systems (as discussed further in Section 9.2.3).

The surface speciation of CO_3 in Fh systems was derived by measuring the competitive effect of CO_3 on the adsorption of PO_4, followed by interpreting the data with the CD model (Chapter 6). The CO_3 adsorption was not measured directly. According to the data analysis, CO_3 adsorbs to Fh mainly *via* formation of inner-sphere bidentate complexes, either $(\equiv FeO)_2CO$ or $(\equiv FeO)_2CO\cdot\cdot Na^+$. To verify the validity of the CD model parameters derived from the competition CO_3-PO_4 system, the adsorption of CO_3 was also measured in a few single-ion systems with concentrations of total added CO_3 that were significantly lower than the ones used in the competition experiments. Good agreement was found between experimental and modeled CO_3 adsorption data, showing that the model parameters of CO_3 derived from the competition experiments with PO_4 can effectively describe the adsorption behavior of CO_3 over a broader range of conditions, in the absence of PO_4

9.2.3. Application of the developed SCM to soils

A meaningful application of SCM in soils is only possible if one has insight into the effective reactive surface area (RSA, $m^2\ g^{-1}$ soil) of the soils. Therefore, this was studied extensively in this thesis. The RSA of a series of agricultural Dutch top-soils (Chapter 7) and weathered tropical top-soils (Chapter 8) was assessed using the CD model for interpreting the competitive CO_3-PO_4 interaction measured in series of PO_4 extractions of soils, using 0.5 M $NaHCO_3$ solutions. Originally, this probe-ion method was used for P-rich soils but was successfully applied without major changes to the set of weathered soils with a low P status. Despite the contrasting differences between the two soil series in the ratios of crystalline and nano-crystalline Fe and Al (hydr)oxides, in both cases, Fh was a better proxy for the natural fraction of reactive metal (hydr)oxides, than well-crystallized goethite. This result seems remarkable considering that the molar contribution of nanocrystalline oxides represents, on average, only ~25% of the total metal (hydr)oxide content in the tropical soils. For the Dutch top-soils, this contribution is on average ~60%. Scaling the RSA derived by CD modelling to the content of ammonium oxalate (AO) extractable Fe and Al (hydr)oxides, using a consistent approach presented in Chapter 7, revealed a range of specific surface area (SSA) values of ~350–1700 $m^2\ g^{-1}$ Fe+Al (hydr)oxide. This result showed that the SSA of the reactive oxide fraction is highly variable and cannot be represented by a single "standard" value, as commonly done in many SCM studies. These SSA values are equivalent to mean particle diameters of d ~1.5–5.5 nm, indicating that the reactive metal (hydr)oxide fraction in these soils is dominated by nano-sized particles.

Using the results of the above probe-ion methodology, the interaction between metal (hydr)oxide nanoparticles and SOC was evaluated. This analysis provided novel insights into the nanometer scaled arrangement of the organo-mineral associations in soils. For both the Dutch (Chapter 7) and tropical (Chapter 8) soils, the surface SOC loading is highly variable but this variability can be explained by the large differences in mean particle size of the reactive metal (hydr)oxide fraction. The SOC data of our soils can be interpreted with a mineral core–surface layer model, in which the oxide nanoparticles with a mean diameter d are seen as mineral cores coated by a SOM layer of thickness L. In this view, the layer thickness L and particle diameter d are linearly and positively correlated in the range of oxide particles size of ~1.5–5.5 nm found for the studied soil samples, indicating that larger metal (hydr)oxide nanoparticles store comparatively more SOC than the smaller ones. This is found for both soil types. The organo-mineral associations were also interpreted as self-assembled entities in which a collection

of discrete SOM particles surround a central metal (hydr)oxide nanoparticle. If the metal (hydr)oxide and SOC particles are of similar size, the SOC particles are shared between metal oxide particles in soils with a relatively low SOC content (P-poor tropical soils), while this direct sharing is substantially less in soils with a relatively high SOC content (P-rich temperate soils). This structural view of the organo-mineral associations will be further discussed in Section 9.5.4.

9.3. On the reactivity of ferrihydrite

9.3.1. Assessment of the surface area of ferrihydrite in suspension

The assessment of the specific surface area (SSA) of Fh was a key topic addressed in this thesis. It was an essential aspect for the consistent interpretation and modeling of the ion adsorption data collected in this thesis. Due to its importance and because of the multiple challenges for its consistent evaluation, the assessment of the SSA of fresh Fh suspensions will be further discussed in this section.

9.3.1.1. Problems related to surface area assessment for ferrihydrite

The analysis of N_2(g) adsorption, implementing the BET equation, is by far the most used methodology for assessing the SSA (A_{BET}) of well-crystallized metal (hydr)oxides. Its successful and widespread application have made this method a practical tool for distinguishing between goethite preparations with different surface areas.[9,11] However, concerns have been raised since long ago about the suitability of the BET approach for assessing the SSA of nanocrystalline metal (hydr)oxides, such as Fh.[27–30] Despite such concerns, the BET approach is still used for characterizing the SSA of Fh in recent studies.[31–33] In Chapter 2, I provided further quantitative evidence confirming that the BET approach is not suitable for assessing the SSA of Fh.

For non-dried Fh suspensions,[31,34] the reported A_{BET} values are ~50% lower than the surface areas found by CD modelling of the reported H^+ adsorption data (A_H). The A_{BET} values may also be compared with surface area values (A_{TEM}) estimated from Transmission Electron Microscopy (TEM) data, as shown in Figure 9.1 for a dataset collected by Michel et al.[35] The values of A_{BET} and A_{TEM} are similar only for the largest particles ($d \sim > 5.5$ nm) with corresponding SSA of ~ 250 $m^2\ g^{-1}$. For smaller particles ($d < \sim 5.5$ nm) with corresponding higher A values, the s A_{BET} value are substantially lower than the estimated A_{TEM} values, suggesting a significant reduction of A_{BET} due to aggregation of primary particles. Anschutz and Penn[36] found a good agreement between A_{BET} (~ 235 ± 0.5 $m^2\ g^{-1}$) and A_{TEM} (~ 270 ± 50 $m^2\ g^{-1}$) values for a 6L-Fh material with a particle diameter of ~ 6 nm. However, for a Fh material with a particle size of ~ 4 nm and corresponding A_{TEM} of ~ 400 ± 74 $m^2\ g^{-1}$, the measured A_{BET} was unrealistically high (~ 1500 $m^2\ g^{-1}$), for which the authors could not explicitly offer an explanation. This kind of inconsistency confirms the lack of reliability of the A_{BET} measurements for Fh.

TEM data can been used to obtain a first approximation of the SSA of Fh in agreement with the mean particle size.[37,38] However, as noticed from the above data by Anschutz and Penn,[36] a large uncertainty is reported for A_{TEM} measurements as TEM data analysis is often associated with methodological artefacts and statistical-related problems.[39] Moreover, conventional TEM analysis does not consider aspects such as particle porosity and surface roughness, making the A_{TEM} values even more uncertain. Nevertheless, if A_{TEM} values are to be employed for comparing SSA obtained by other approaches, then size-dependent values for mass density (ρ_{nano}) should be applied for translating the mean particle diameter of Fh into a value of surface area. This was done here for the TEM data presented in Figure 9.1. Ignoring this correction would lead to ~ 20% deviation in the A_{TEM} calculated for a mean particle

diameter of ~ 2.5 nm in comparison to using a "standard" mass density value, *e.g.* as found for the mineral core of Fh.

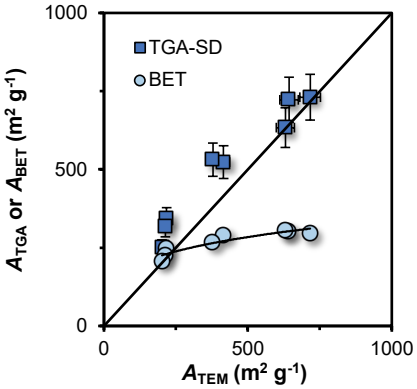

Figure 9.1. Relationship between the specific surface area (SSA) of ferrihydrite derived from TEM data (A_{TEM}) and the SSA derived either from thermogravimetric analysis data (A_{TGA}) or gas adsorption (A_{BET}). Data are from Michel et al.[35] The A_{TEM} values were calculated from the reported mean particle size obtained by TEM analysis, using size-dependent values of mass density (ρ_{nano}). The A_{TGA} values were calculated by interpreting the experimental data of chemisorbed water (> 125 °C) according to the surface depletion model (SD).[40] Figure is taken from the Supplementary Information of Chapter 2.

In theory, an alternative approach for assessing the surface area of Fh is measuring its water content. The size-dependent chemical composition of Fh can be given as $FeO_{1.4}(OH)_{0.2}{\cdot}nH_2O{\cdot}mH_2O$, where nH_2O is the amount of chemisorbed water and mH_2O is the physiosorbed water. These types of water can be experimentally determined by thermogravimetric analysis (TGA),[35,41] and the results can be interpreted with the surface depletion (SD) model[40] to calculate A_{TGA} (Chapter 2). In general, a good relationship is observed in Figure 9.1 between the values of A_{TEM} and A_{TGA}. A critical aspect in this approach is the accurate distinction between the different fractions of water. A small variation in the temperature chosen as a reference for distinguishing physiosorbed and chemisorbed water (*e.g.* 125 °C) may lead to large deviations in the estimated A_{TGA} value. This approach has not been well explored yet in literature; therefore, more research is needed to better test its validity.

Because of the aforementioned drawbacks for assessing accurately and independently the SSA of Fh, ion adsorption studies often use fixed "standard" values for the SSA of Fh (*e.g.* 600 m^2 g^{-1}).[29,42] However, as shown in Chapters 2 and 3 and also in earlier studies,[7,43,44] the SSA of fresh Fh suspensions largely varies according to the preparation protocol and aging conditions. Therefore, ion adsorption data reported in different studies cannot be objectively compared if results are scaled to fixed SSA values. As an alternative, the SSA could be treated as an additional adjustable parameter in the model interpretations. However, this approach is disputable because the SSA is often correlated to other model parameters such as log*K* and capacitance values.[10,45–47] Bompoti et al.[47] have suggested that treating capacitance as an adjustable parameter would account for most of the uncertainty related to the SSA. However, fitting log*K* values simultaneously with capacitance and/or SSA may result in multiple combinations of "optimized" parameters that provide a reasonably good description of a specific dataset. Recently, an optimization approach was developed to find statistically the "best" set of optimized parameters, based on the search of a global optimum that is defined as the minimum mean squared error (MSE) value.[47,48] However, without a critical evaluation, the optimum fit in terms of MSE may yield

solutions with unrealistic values of SSA or capacitance.[47] Considering the above drawbacks, there is a clear need for a robust approach that allows the assessment of the SSA of Fh suspensions in a practical and consistent manner. For this, the use of ions that specifically adsorb to Fh appears as a good alternative, which I will discuss in the next section for PO_4.

9.3.1.2. Surface probing with ions: Consistency between H^+ and PO_4 adsorption

In this thesis, I implemented a probe-ion methodology that allowed calibrating the SSA and other size-dependent properties of Fh, including the Stern layer capacitance(s), in a practical and self-consistent manner. This method is a good alternative to overcome the above limitations of the traditional BET method. In this probe-ion approach, the SSA of Fh (A_{PO4}) is calculated by interpreting the experimental data of PO_4 adsorption with the CD model, using the parameters set given by Hiemstra and Zhao.[49] These parameters were calibrated from the scaling of the primary adsorption data (mol PO_4 mol^{-1} Fe) to a best guess of the SSA (m^2 g^{-1} Fh) and molar mass (g mol^{-1} Fe) of the used Fh suspension.[49] This best guess SSA was based on the preliminary analysis[50] of the charging behavior of "average" fresh Fh suspensions reported in literature.[29,34] However, until now, the consistency between this best guess SSA and the description of surface charge had not been explicitly tested for the same Fh material. Therefore, in Chapter 2, I measured in parallel experiments the adsorption of H^+ and PO_4 for a same Fh suspension, at different ageing times. Interpreting both datasets using a common modelling framework yielded values of A_H and A_{PO4} that are consistent within a precision of ~2%. This result is important because it shows that probing the surface of Fh with PO_4 yields SSA values that are internally consistent with the description of a fundamental surface property of this material, *i.e.* the primary charging behavior.

As mentioned previously, in the interpretation of H^+ adsorption to Fh, values of Stern layer capacitance and $\log K_{ip}$ of Na^+ and NO_3^- determined previously for goethite[51] were used as reference, which have been calibrated based on A_{BET}. The reason for this assumption was the impossibility to parametrize the charging behavior of fresh Fh in a fully independent way, as it can be typically done for crystalline oxides using externally collected information, *i.e.* the measured A_{BET}. Thus, after accounting for differences in surface site density between both materials, the calculated A_H values for Fh are ultimately related to the A_{BET} of the reference goethite material. In the data interpretation, additional correction was needed to account for the size-dependent values of molar mass, mass density, and surface curvature. The latter is used to account for the size dependency of the capacitance values, which is based on electrical double layer theory.[50] The proposed approach has the advantage of incorporating consistency, based on theoretical considerations, in the relationship between SSA and capacitance,[50] rather than treating these properties as fitting parameters or as fixed "standard" values,[47] while being variable.

It is important to note that even though, the inferred probe-ion methodology yields precise and reproducible results, its accuracy remains unknown. In order words, the SSA values derived with this approach do not represent absolute values but are relative to the goethite material used as reference in the calibration. Nevertheless, after the above mentioned corrections, the calculated SSAs correspond to Fh particles with mean particle sizes that resemble those obtained from the analysis of TEM images.[35] It remains a challenge to test in the future, for a same reference Fh material, the consistency in the results obtained by the ion-probing methodology and other independent approaches, *e.g.* high resolution TEM and TGA.

9.3.1.3. Applications and implications for future studies

Probing the surface of all Fh suspensions used in the ion adsorption data collection has enabled the development of a self-consistent database with intrinsic CD model parameters, which can be used for applications of SCM. In this thesis, the focus was to parametrize the adsorption interactions between an important anion (PO_4) and a cation (Ca) to develop a methodology of study that can be applied in future to more types of anions and cations. Phosphate and calcium were chosen to open the way to build a consistent modeling approach. As outlined in section 9.1, these ions are omnipresent in nature and are highly relevant from the perspective of environment quality, (agro)ecology, soil fertility, as well as for soil chemical analysis. In future research, this database can be extended by parametrizing the adsorption interaction of other ions. For instance, as part of the PhD project of Elise van Eynde, ongoing research in our department is analyzing now the adsorption interactions of PO_4 with important microelements in agriculture such as boron (B) and zinc (Zn), following the same consistent approach developed here for freshly prepared Fh materials. The ultimate goal is to create a robust database that allows the use of Fh as reference material for CD model applications in a wide set of geochemical conditions. This objective promises intensive work for the upcoming research, especially if the aim is also to incorporate into the model approach a realistic physical-chemical description of the adsorption interactions between cat- and anions. My thesis work has shown that quantifying surface speciation in single ion systems alone can be sufficient if ions interact only *via* site competition and electrostatic interactions (*e.g.* CO_3–PO_4), but it certainly fails if ions have additional interactions such as ternary complex formation (*e.g.* Ca/Mg–PO_4).

From a more fundamental perspective, assessing the surface area of Fh with the probe-ion approach would enable the study of important interfacial processes, other than adsorption, for which the scaling of the collected data to the value of SSA is essential, *e.g.* size-dependent dissolution, complexation, and redox reactions occurring at Fh surfaces. One example of the application of this approach is presented in Chapter 3, where tracing the dynamic changes of SSA by probing with PO_4 the surface of Fh permitted to gain important insights into the mechanism and rate of growth of this nanomaterial, which otherwise would have been difficult to measure accurately with other methods (*e.g.* TEM data).

9.3.2. Freeze-dried *vs* freshly-prepared ferrihydrite

9.3.2.1. Rationale

As discussed above and in Chapter 2, convincing evidence shows that drying the Fh materials leads to a significant reduction of the SSA. The degree of this SSA reduction is variable and would depend on the specific drying conditions and the initial properties of the primary Fh particles. Drying procedures may also provoke changes in the crystal morphology and phase transformation of Fh,[52] changing consequently the surface reactivity of Fh for ion adsorption. These issues make the using of freeze-dried Fh materials questionable for parametrizing consistently ion adsorption data and for studying, in a reproducible manner, fundamental properties of Fh. For this reason, all data collection in this thesis has been done using fresh Fh materials kept in the wet state, rather than using freeze-dried materials. An additional problem is that the A_{BET} of freeze-dried material cannot be used *a priori* for scaling the adsorption data, as my analysis of such type of materials suggests (Chapter 2).

Moreover, fresh Fh materials may represent better than freeze-dried Fh the formation conditions of Fe (hydr)oxide nanoparticles in most soils and sediments. In nature, Fh particles may precipitate without extensive aggregation if formed in the presence of natural organic matter (NOM). This contributes to the thermodynamic stabilization of Fh and prevents its transformation into more crystalline phases.

Certainly, many physicochemical properties of naturally formed nanoparticles would differ from those of their synthetic counterparts.[7] For instance, the nanocrystalline structure and particle size distribution of Fh is affected when it precipitates in the presence of organic matter.[53–56] Furthermore, Al substituted and Si-rich Fh materials can be found in nature. These materials present structural changes affecting a series of microscopic properties.[57–60] For instance, changes in surface speciation[61] and interaction energy[62] of various oxyanions have been reported at increasing levels of Al substitution in Fh.

Nevertheless, despite the molecular-scale differences found in the binding of PO_4 to synthetic Al and Fe coprecipitates[2] and mixtures,[18] the macroscopic adsorption of PO_4 was indistinguishable from that of pure Fh at molar ratios of Al/(Al+Fe) lower than 0.50.[2] This observation is in line with the results obtained in Chapters 7 and 8, where it was shown than the macroscopic adsorption behavior of PO_4 in the 0.5 M $NaHCO_3$ soils extracts can be well-represented for the time being using only freshly-prepared Fh as a proxy.

9.3.2.2. *Prospective studies*

In the aforementioned 0.5 M $NaHCO_3$ soil extractions, the interference of NOM on the adsorption interaction CO_3-PO_4 is suppressed by adding an excess of activated carbon (AC) to the soil extracts. However, for other soil extractions (see for instance Section 9.5.2) and/or under field conditions, the presence of NOM will play a key role in determining the adsorption behavior of PO_4 and oxyanions in general. Therefore, for future studies, using Fh materials *in-situ* precipitated in the presence of NOM (*i.e.* Fh-NOM coprecipitates) is a good alternative for analyzing in more realistic manner the ion adsorption mechanisms in natural systems. Conventionally, adsorption experiments with NOM are performed using mineral-organic complexes formed by NOM adsorption to existing (*ex-situ* formed) Fe oxide particles. However, the adsorption properties of those complexes differ from these of the *in-situ* Fh-NOM coprecipitates. For instance, higher C/Fe molar ratios have been reported in Fh-NOM coprecipitates than in Fh-NOM complexes formed by adsorption.[53] In addition, less NOM desorption has been measured in the *in-situ* complexes than in the *ex-situ* formed Fh-NOM associations,[53] indicating a higher stability of the former complexes. Differences in the preparation procedure of the Fh-NOM complexes (*i.e.* coprecipitation *vs* adsorption) also affects the interaction between NOM and oxyanions for adsorption to Fh, as shown recently for AsO_4.[56] To the best of my knowledge, the competitive NOM-PO_4 interaction has not been tested yet in literature in systems with *in-situ* Fh-NOM coprecipitates.

Preliminary adsorption experiments performed in our department with *in-situ* and *ex-situ* produced Fh-NOM indeed suggest important differences in their adsorption behavior of PO_4. To make progress, the challenge will be to unravel the major factors that may contribute to these differences, *i.e.* created differences in particle size and/or difference in NOM-PO_4 competition. Scaling of adsorption data to the mineral surface area is a major challenge of studying ion adsorption to Fh-NOM coprecipitates, which currently impedes a consistent parameterization of SCM for this type of materials. However, the probe-ion method proposed in this thesis cannot yet be applied to Fh-NOM coprecipitates straightforwardly as the approach was calibrated and tested only for pure Fh systems. Our ongoing research has taken first steps to solve this constraint by linearly extrapolating to a C/Fe = 0 condition the PO_4 adsorption results obtained in a series of Fh-NOM systems with different C/Fe ratios, and estimating by CD modeling the corresponding SSA at such C/Fe = 0 conditions.

9.4. Insights from the model ferrihydrite systems

In this section, I will discuss two of the major insights obtained from the CD model interpretation of the collected ion adsorption data, namely *i*) surface sites heterogeneity and *ii*) formation of ternary Fe-PO_4-M^{2+} complexes. These insights make evident that fundamental differences exist in the surface reactivity of Fh and goethite. Understanding these differences is important in the context of SCM applications to soils, because choosing either Fh or goethite as reference oxide material will have implications in the outcome of the model predictions.

9.4.1. Surface site heterogeneity for metal ion binding

Surface site heterogeneity is a concept suggested since long ago for explaining the non-proportional behavior of the adsorption isotherms of metal ions, which cannot be explained only by changes in the electrostatic adsorption energy.[42,63,64] In Chapter 4, the heterogeneous adsorption phenomenon seems evident for the series of alkaline-earth metal ions. In this section, I will discuss only the heterogeneous binding of Ca because the adsorption of this ion was analyzed more extensively in this thesis and in a previous study.[65] As mentioned before, formation of double corner (^{2}C) bidentate complexes is the most probable binding mechanism of Ca to Fh, based on the interpretations of MO/DFT optimized geometries and EXAFS data reported for the adsorption of other divalent cations to Fe (hydr)oxides.[13,66–69] According to the MUSIC approach for Fh,[49] ^{2}C bidentate complexes are formed only with a subset of singly coordinated surface groups, *i.e.*≡FeOH(b) surface groups.

Using ^{2}C bidentate complexes as the main binding mode, surface site heterogeneity was required in the modelling for describing the Ca adsorption data. Excluding site heterogeneity from the modelling led to unacceptable deviations in the model predictions, particularly in systems with a high Ca loading. Considering alternative binding mechanisms for Ca did neither provide an accurate description of the experimental adsorption data. For instance, with the option of inner-sphere monodentate complexes as the main binding mode, the model failed in describing simultaneously my own collected data and the data from Kinniburgh and Jackson,[65] collected for a wider range of Ca/Fe molar ratios. In addition, the description of Ca-PO_4 interaction in the binary systems (Chapter 5) was also inconsistent with the formation of monodentate complexes. Including additionally the formation of hydrolyzed and/or outer-sphere complexes did neither provide a satisfactory description of the Ca adsorption data. This experience with extensive modeling strongly suggests that, within the implemented modeling framework, the presence of a fraction of surface sites with a higher affinity for Ca cannot be explained by alternative binding mechanisms.

Model interpretation of Ca adsorption data indicates that the surface density of high affinity sites is in the order of ~0.30 ± 0.02 sites nm^{-2} for my Fh material and the Fh material used by Kinniburgh and Jackson.[65] This density represents only ~10% of the total ≡FeOH(b) groups available for binding Ca as a double corner complex. For other Fh materials evaluated in the present thesis (Chapter 4), the site density was lower (~0.1 – 0.2 nm^{-2}). These numbers fall within the range reported for high affinity sites available for adsorption of divalent cations to Fh.[42,64,67] The intrinsic affinity of the ions may play a role in the determination of the site density of the high affinity sites, as suggested by a preliminary CD model interpretation of the Zn adsorption data reported by Kinniburgh and Jackson,[65] pointing to a surface density of ~0.10 ± 0.01 nm^{-2} for high affinity sites, which is clearly lower than the site density found by fitting the Ca adsorption data for the same type of Fh material.

In the thesis, I have presented plausible surface configurations that can rationalize the presence of high affinity sites. Details of this rationale were described in Chapter 4 and a possible structure was

shown in Figure 4.7. Briefly, in the attempt, high affinity sites are related to a charge redistribution occurring within specific pairs of Fe1 octahedra at the surface of Fh leading to stronger ≡FeOH-M^{2+} bond formation to satisfy the charge undersaturation of the surface -OH ligands of this moiety. A structural analysis of various constructed Fh particles indicates that, depending on the particle, only ~1–3 of such moieties can be identified on a single particle, which is equivalent to a site density that is in the same order as found by modeling. Despite explaining the number of high affinity sites and a structural rationale for their presence, the current analysis represents the first attempt to link a macroscopic phenomenon to a specific molecular scaled configuration in the Fh surface. More information about the fitted site density as a function of the type of ion involved, as well as the synthesis and aging of the particles may contribute to convincingly unravelling any underlying structural reason for the heterogeneous binding of metal ions.

9.4.2. Ternary surface complexes

As mentioned above, the adsorption data collected for the binary Fh systems with PO_4 and Ca or Mg ions (M^{2+}) cannot be described with the CD model using only the parameters derived for single-ion systems (Chapter 5). Including ternary surface complexes Fe-PO_4-M^{2+} was required in the CD model for describing the measured experimental data. This result represents a remarkable difference with respect to the M^{2+}-PO_4 interaction described previously for goethite. In the latter system, the synergistic binding interactions between M^{2+} and PO_4 can be understood only on the basis of electrostatics.[12,70]

For the Ca-PO_4 systems, the CD model interpretation and the MO/DFT optimized geometries suggested the formation of two anion-bridged ternary complexes, in which a mononuclear monodentate ≡$FeOPO_3$ and a binuclear bidentate ≡$(FeO)_2PO_2$ complex interact with Ca^{2+} by forming a P-O-Ca bond. For the Mg-PO_4 systems, only the former type of complex was revealed. Presently, there is no direct spectroscopic evidence for the formation of these types of complexes at the surfaces of Fh. Further research might help to confirm the identity of the ternary complexes proposed here for Fh. Nevertheless, the type of ternary complexes resolved are in line with the notion that the dominant ternary complexes (*i.e.* anion-bridged *vs* cation-bridged) depend on the relative affinity of the co-adsorbing ions for the Fe-(hydr)oxide surfaces.[71] In this case, PO_4 ions have a much higher affinity than the M^{2+} ions for the binding sites of Fh. Formation of Fe-PO_4-Ca complexes is also supported by data collected following Fe-PO_4 co-precipitation in the presence of Ca, showing direct complexation of PO_4 to Fe(III) polymers, where these units form larger networks interconnected by Ca ions.[72,73] Formation of PO_4-bridged ternary complexes with Ca were also found using spectroscopy techniques in systems with hydrous zirconium oxide[74] and titanium dioxide (TiO_2).[75]

The modeling results of Chapter 5 suggest that in the ternary complexes a significant part of the Ca charge is allocated in the 2-plane of the Electrical Double Layer (EDL). The fitted Δz_2 values for the $(FeO)_2PO_2$-Ca and ≡$FeOPO_3$-Ca complexes are respectively +1.46 ± 0.17 and +1.06 ± 0.06 v.u. If sufficient Ca is bound, as a consequence, a positive electrostatic potential (ψ) develops in the 2-plane of the EDL, whereas in the 1-plane the ψ value can be negative due to the presence of negatively charged outer –O ligands of the adsorbed PO_4 ions. As an example, Figure 9.2 sketches the ψ profile of the EDL for a Fh particle in 0.01 M $CaCl_2$ solution, at a given surface PO_4 loading of 2 μmol m^{-2} and pH 7. For comparison, the corresponding ψ profile is also shown for goethite under the same conditions. As mentioned, formation of ternary complexes has not been found by modeling for goethite in binary Ca-PO_4 systems.[12,70] Ca adsorption to goethite occurs mainly *via* formation of inner-sphere monodentate complexes.[12,76] With this binding mechanism, most of the positive charge of Ca is allocated at the 1-

plane ($\Delta z_1 = +1.69$)[76] where it counteracts the negative charge of the outer -O ligands of PO_4. For the example in Figure 9.2, the electrostatic potential in the 1-plane of goethite is nearly ~0 mV.

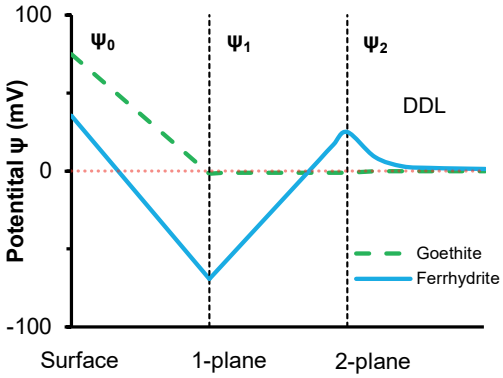

Figure 9.2. Sketch of the electrostatic potential (ψ) profile for the Electrical Double Layer (EDL) at the interface of Fh and goethite. The sketch is for systems in 0.01 M $CaCl_2$ solution with a surface PO_4 loading of ~2 µmol m^{-2} at pH 7. Lines are drawn based on CD model calculations. For Fh, the formation of ternary Fe-PO_4-Ca complexes leads to a positive electrostatic potential in the 2-plane, due to the charge attribution of Ca to this plane. This is not the case for goethite, where the synergistic binding between Ca and PO_4 is only based on electrostatic interactions. The depicted differences between Fh and goethite have important implications for the pH-dependent PO_4 adsorption in Ca solutions (see Chapter 5).

For Fh, the sketched profile of Figure 9.2 is based on CD model calculations, using the parameter set derived in Chapter 5. Complementary experimental data, such as zeta potential measurements, may be used to confirm that the potential of the particles as a whole is near zero at these conditions. In a wider context, the relevance of this finding goes beyond an accurate description of the Ca-PO_4 interactions at interface of Fh. In soil systems, Ca ions play an important role in the colloidal stabilization of negatively charged metal (hydr)oxide particles that carry adsorbed oxyanions. Formation of ternary ≡Fe-PO_4-Ca complexes, as described above, would create externally a layer of divalent cations that enable metal ion bridges between metal (hydr)oxide nanoparticles carrying PO_4 and negatively charged functional groups of SOC (*e.g.* $RCOO^-$), which may contribute to stabilizing organic carbon in soils and the formation of organo-mineral micro-aggregates.[77,78]

Moreover, the aforementioned differences between Fh and goethite have important implications for the pH-dependent adsorption of PO_4 in Ca solutions. As explained in Chapter 5, the intrinsic pH dependency of PO_4 adsorption (*i.e.* in the absence of Ca) is much higher in Fh than in goethite systems. However, this difference is largely compensated by the binding of Ca. The increase in PO_4 adsorption due to the formation of ternary Fe-complexes in Fh is less important than the increase in the PO_4 adsorption on goethite due to strong electrostatic interactions between the large fraction of Ca^{2+} charge present in the 1-plane and the –O ligands of PO_4. This electrostatic interaction increases at higher pH values, which might even reverse the trend of the pH-dependent PO_4 adsorption to goethite, as shown previously.[79] Therefore, it is obvious that choosing either Fh or goethite as reference material will have important implications for the application of surface complexation modeling in natural systems, for instance, for interpreting the results of routine soil extractions with 0.01 M $CaCl_2$ solutions. A concrete assessment of this implication in relation to PO_4 extractability is part of our ongoing research (See Section 9.5.2). An unanswered question in this thesis is the rationale behind this difference in surface

reactivity between Fh and goethite. This can also be said for the differences in binding mechanism of *e.g.* CO_3 ions as shown in Chapter 6. Differences in the density of reactive $\equiv FeOH^{-0.5}$ groups between the dominant crystallographic faces of nearly spherical Fh nanoparticles and the main crystallographic planes of goethite might be an aspect to consider in future research.

9.5. From synthetic to natural systems: insights into soil chemical processes

9.5.1. Implications for assessing reactive surface area of soils

The reactive surface area (RSA) of a series of agricultural Dutch top-soils (Chapter 7) and weathered tropical top-soils (Chapter 8) was assessed with the probe-ion method proposed by Hiemstra et al.[76] The thermodynamic database developed in this thesis for Fh was used for CD model interpretation of the data collected with the probe-ion method. A hypothesis in this thesis was that Fh is a better proxy than goethite for the natural fraction of metal (hydr)oxides in these series of soils. The results of Chapters 7 and 8 clearly showed that the calculated values of RSA and pool of reactive PO_4 reversibly bound to the mineral surfaces (R-PO_4) depend on the selection of either Fh or goethite as proxy. The reason for this difference is related to the different shape of the competitive adsorption isotherm of PO_4 in 0.5 M $NaHCO_3$ solutions, as was comprehensively discussed in Chapters 6 and 7.

For testing which Fe (hydr)oxide material is the better proxy for the natural oxide fraction, modeled (R-PO_4) and experimental pools of reversibly adsorbed PO_4 were compared. The latter pool has been assessed by measuring the amount of ammonium oxalate extractable PO_4 (AO-PO_4). The rationale for using AO-PO_4 as validation criterion was given in Chapters 7 and 8 and is based on experimental evidence indicating that nearly all AO extractable P was desorbable in long-term experiments.[80,81] Alternatively, the pool of isotopically exchangeable PO_4 has been used as a proxy for R-PO_4 in other SCM studies.[82,83] For both sets of soil samples, the modelled R-PO_4 values using goethite as proxy were clearly higher than the measured amounts of AO-PO_4. This indicates that the adsorption behavior of PO_4 in the 0.5 M $NaHCO_3$ soil extracts cannot be represented adequately by goethite. On the other hand, when Fh was used as a reference oxide material, in general a good agreement (close to 1:1 line) was found between modelled R-PO_4 values and measured AO-PO_4, supporting the initial hypothesis that Fh is a better proxy for assessing the reactivity of the natural fraction of metal (hydr)oxides in the sets of soils studied.

The fact that Fh, rather than goethite, describes better the reactivity of the natural oxide fraction in both data sets (Dutch and tropical soils) is remarkable, considering that these types of soils have contrasting chemical properties, including the ratio of crystalline and nano-crystalline metal (hydr)oxides as well as the Fe to Al ratio in the AO extracts. For the weathered tropical soils, the crystalline Fe- and Al-(hydr)oxides dominate the oxide fraction, while the contribution of the nano-sized metal (hydr)oxides (*i.e.* Fh-like materials) to the total metal (hydr)oxide fraction is relatively small on a molar basis, being on average only ~25 ± 10%. Nevertheless, due to their high specific surface area, these nano-sized materials still dominate the surface reactivity of the natural fraction of metal (hydr)oxides, even at low molar concentrations. For the Dutch soils, the molar contribution of nano-crystalline (hydr)oxides to the total metal (hydr)oxide fraction is on average ~60 ± 15%.

In the present approach, the effective RSA of soils is approximated by only using Fh as a proxy. In case of the tropical soils, the nanocrystalline fraction of Al (hydr)oxides plays a dominant role in determining the surface reactivity of soil. This may have implications for the value of the RSA derived

with the probe-ion method. However, there may be differences in PO_4 affinity between Fe and Al (hydr)oxides, which may lead to systematic bias in the estimation of the surface area. For this reason, the term effective reactive surface area should be used rather than the surface area. In future research, the difference in reactivity of Al and Fe natural nanocrystalline oxides can be studied using for instance a probe-ion methodology, if it can be shown *a priori* that the chosen ion has a different affinity for both types of materials. This would allow distinguishing between both metal (hydr)oxide fractions in soils if important differences in their binding properties exist.

9.5.2. Interpretation of soil extractions: effect of calcium on PO_4 equilibration

The model outputs of RSA and *R*-PO_4 obtained with the probe-ion method can be used to get insights into the mechanisms affecting the equilibration of PO_4 in soil chemical extraction procedures. Soil P status is routinely assessed using a variety of soil chemical analyses that are based on different mechanisms of extraction.[84–86] The practical significance of these analyses often relies on empirical correlations between the amount of PO_4 extracted and, for instance, the measured P uptake by plants and crops. These correlations often show a large unexplained variability, which may be attributed to a poor mechanistic understanding of the chemical processes affecting the amount of PO_4 extracted.[87] This evidences the importance of improving our understanding of the underlying chemical processes that affect the extractability of PO_4 in soil chemical analyses. For soil extractions that ultimately lead to equilibration, changes in the Ca concentration, ionic strength, solution pH, and the soil-to-solution ratio (SSR, kg L^{-1}) result in different amounts of extracted PO_4. These conditions may greatly vary between different routine soil extraction methods, *e.g.* standard soil extraction with 0.01 M $CaCl_2$ solution (SSR 1:10 [w/v]) *vs* extraction with demi-water (SSR 1:2 [w/v]).[88,89]

The CD model is a promising yet insufficiently explored tool for improving the interpretation of routine soil chemical analyses. Figure 9.3 shows an example of the applicability of the CD model, parametrized in this thesis for Fh, for describing the effect of Ca concentration in the extracting solution on the equilibration concentration of PO_4. The range of Ca levels explored is relevant for various soil extractions as well as for field conditions.[88,89] The preliminary results are part of my ongoing research with the aim to contribute to more mechanistic interpretations of the outcome of different PO_4 extraction methods.

The insights obtained in Chapter 5 for synthetic Fh systems have been applied here in Figure 9.3 for describing the experimental Ca-PO_4 relationship in a number of agricultural Dutch top-soils. The RSA and *R*-PO_4, derived for these soils in Chapter 7 were used as independent input in the CD modeling. As shown in Figure 9.3, the pH of the extracting solution tends to decrease at increasing Ca^{2+} activity (see data labels). The simultaneous changes in these two variables affect the adsorption of PO_4 to metal (hydr)oxides,[79] and affect consequently the measured equilibrium PO_4 concentrations. The CD model effectively accounts for the simultaneous change in pH and Ca^{2+} activity. In addition, the mechanistic CD model accounts for any change in surface PO_4 loading resulting from PO_4 release into solution, which is particularly relevant for soils with a low PO_4 buffer capacity, *i.e.* with a low RSA.

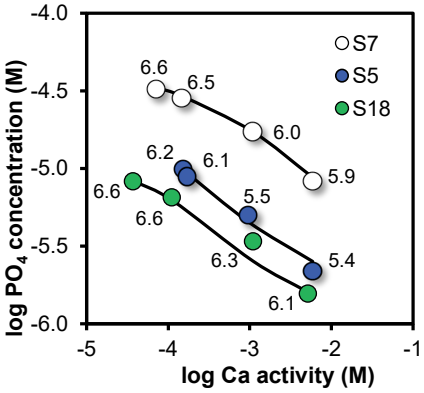

Figure 9.3. Relationship between $\log_{10}$ of the Ca^{2+} activity and the $\log_{10}$ of the equilibrium PO_4 concentration in 1:60 [v/v] soil extracts for three of the agricultural Dutch soils studied in Chapter 7. The different Ca levels were adjusted by adding $CaCl_2$ solutions, except for the lowest Ca level, which was determined by the released of native Ca of each soil upon addition of demi-water. The Ca^{2+} activity was measured with an ion-selective electrode, and the PO_4 concentration was analyzed colorimetrically using segmented flow analysis (SFA). The data label of each point gives the measured pH at equilibrium. The lines are CD model calculations using Fh as proxy. For each soil, the values of reactive surface area (RSA) and reversibly adsorbed PO_4 (R-PO_4), determined in Chapter 7, were used as independently determined model input. The surface PO_4 loading (Γ_{PO4}) of these selected soils, calculated as Γ_{PO4} = RSA / R-PO_4, varied from 1.3 to 2.3 µmol m^{-2}. The synergistic adsorption interaction between Ca and PO_4 in soils can be well understood with the CD model, defining the effective surface NOM density as the only adjustable parameter.[90] The data correspond to preliminary experiments performed by the author of this thesis.

In the modeling, the competitive effect of NOM has been included for predicting accurately the equilibrium concentrations of PO_4 in solution. Ignoring the adsorption competition between NOM and PO_4 results in lower predictions of the PO_4 concentration in solution.[91–93] Preliminary, this competition effect of NOM has been described here using the approach given by Hiemstra et al.[91] More recently, the approach was adapted to give credits to the difference in binding mechanism of functional groups of NOM, *i.e.* inner-sphere *vs* outer-sphere complexation, as well as protonation at low pH.[90] The latter approach was calibrated by describing the pH-dependent adsorption of PO_4 in goethite systems and soils. For consistency, this approach still needs to be revaluated using Fh as model (hydr)oxide because the pH-dependent adsorption interaction Ca-PO_4 is quite different for Fh in comparison to goethite (Chapter 5). This will potentially affect the pH dependency of the relationship between NOM and PO_4 in $CaCl_2$ solutions. A fully consistent description of the PO_4-NOM relationship is part of the pending challenges. Nevertheless, in Figure 9.3, the change in PO_4 concentration as a function of Ca activity in solution is well described by the CD model, assuming a constant NOM surface loading (≡FeNOM).

Similarly, for the tropical soils studied in Chapter 8, higher PO_4 concentrations (~two-fold) were measured in soil extractions with 10^{-3} M $CaCl_2$ than in the standard extractions with 10^{-2} M $CaCl_2$ (data not presented). These differences can also be described with the CD model, parametrized in this thesis for Fh. The NOM loading was fitted based on the PO_4 concentration measured in the standard 10^{-2} M $CaCl_2$ extraction. This fitted ≡FeNOM values provide reasonably good description of PO_4 concentration measured in 10^{-3} M $CaCl_2$ extracts. This suggests that the differences in PO_4 concentration between both $CaCl_2$ extractions are mainly controlled by the synergistic binding interaction Ca-PO_4, rather than by changes in the NOM competition at varying Ca levels.

As mentioned above, the SSR (kg L^{-1}) also differs amongst soil P extractions. At decreasing SSRs, *i.e.* increasing dilution of the soil sample with extraction solution, larger amounts of PO_4 (in mol kg^{-1} soil) are released into the liquid phase. Depending on the degree of dilution, the surface PO_4 loading may change significantly, which will affect in turn the interaction of NOM and PO_4 at the soil surfaces. Preliminary results (not shown) suggest that, upon strong changes in SSR, the assumption of a constant ≡FeNOM loading is no longer valid. It indicates that changes in ≡FeNOM loading are required for effectively describing with SCM the PO_4 extractability at varying SSRs. The question that arises is whether the change in NOM loading upon strong dissolution of a soil sample can be linked to an experimentally observable variable (*e.g.* DOC concentration). If so, a related challenge is how this link can be implemented in the CD model calculations. This issue is not solved yet, and it is part of the challenges faced in the search for an "all-inclusive" SCM for soils.

From the above insights, it is clear that the measured concentration of PO_4 in equilibrium solution is largely affected by both the characteristics of the extraction method and the intrinsic chemical properties of the soil sample. This makes it difficult to relate straightforwardly, *e.g.* using empirical relationships, the outcome of routine soil extraction methods to the PO_4 concentrations that are representative of *in-situ* field conditions. Being able to effectively quantify with SCM the major factors determining the extractability of PO_4 in specific equilibrium extractions might enable this possibility. However, under field conditions, kinetic desorption limitations might decrease the PO_4 availability that would be estimated from PO_4 concentrations measured in equilibrium conditions. Continuous removal of PO_4 and/or NOM from the soil surfaces, due to for instance plant uptake and/or leaching, may lead to electrostatic changes on the oxide surfaces that can affect the further desorption of PO_4. Therefore, an additional future challenge will be to develop a dynamic model for describing the kinetics of PO_4 release, based on the same electrostatic principles as used in the equilibrium CD model.

9.5.3. Characterizing the nano-sized metal (hydr)oxide fraction

For both Dutch and tropical soils, the content of AO-extractable Fe and Al ($[Fe+Al]_{AO}$, mmol kg^{-1}) is positively correlated to the RSA derived with the probe-ion method (Figures 7.3 and 8.3). For the Dutch soils, the mean value of specific surface area (SSA) is 65 m^2 $mmol^{-1}$ $[Fe+Al]_{AO}$, whereas for the tropical soil the mean SSA is nearly twice as high, namely 110 m^2 $mmol^{-1}$ $[Fe+Al]_{AO}$. The variation around the mean values can be relatively high. The highest and lowest value differ by a factor of more than ~4, which indicates that SSA of the reactive metal (hydr)oxides in these soils is highly variable. Therefore, using fixed SSA values for the nanocrystalline fraction of Fe and Al-(hydr)oxides, as is often done in SCM studies,[83,94] may lead to substantial deviations in the estimated amount of available reactive sites for ion adsorption. For the tropical soils, scaling the RSA values to the total content of Fe and Al (hydr)oxides (*i.e.* extracted with dithionite-citrate) yields a significantly lower mean SSA, ~23 ± 12 m^2 $mmol^{-1}$ $[Fe+Al]_{DC}$, which is due to the important mass contribution of crystalline metal (hydr)oxides in these soils. However, the results of Chapter 8 showed that in these soils the nanocrystalline fraction of metal (hydr)oxides dominates in terms of surface reactivity. Therefore, a possible explanation for the higher SSA of the tropical soils may be related to the larger fraction of Al in the AO extracts of these soils, in comparison with the Dutch soils. As explained earlier, if the Al (hydr)oxides have a different affinity than Fh for binding PO_4, it may lead to a systematic difference in the calculated RSA.

In Chapter 7, I showed that for spherical particles with the same diameter, the SSA of $Al(OH)_3$ is considerably larger than the SSA of Fh. The reason is that $Al(OH)_3$ nanoparticles have a much lower mass density than Fh, which changes the relationship between particle size and surface area. This could explain the reported higher PO_4 adsorption capacity of Al-(hydr)oxides compared to Fe-(hydr)oxides,

when expressed as mol PO_4 per mol Al/Fe.[2] Similarly, higher adsorption of PO_4 and AsO_4 per mol of metal ion has been recently found for nanocrystalline Al (hydr)oxide than for Fh.[18] The results were attributed to possible differences in the surface sites density between the two materials.

Scaling the calculated RSA to the $[Fe+Al]_{AO}$ content shows that the reactive fraction of metal (hydr)oxides, in both Dutch and tropical soils, is dominated by nano-sized particles with mean diameters ranging between ~1.5–5.5 nm. This result is in line with previous studies that have found evidence for the presence of nanoparticles as the dominant reactive fraction of metal (hydr)oxide in soils,[95–97] particularly for soils from temperate climates. For soils from tropical regions, however, less information is available about the properties of the reactive metal (hydr)oxide fraction. For the scaling of RSA values to the content of metal(hydr)oxides, a self-consistent approach has been developed (Chapter 7) that considers the size dependency of the molar mass and mass density of the metal (hydr)oxide nanoparticles. In this approach, Fh and $Al(OH)_3$ nanoparticles are used as reference for the natural Fe and Al (hydr)oxides, respectively. An assumption of this approach is that Fe and Al (hydr)oxides form separated solid phases with the same mean particle diameter, regardless the Al/Fe molar ratio in the AO extracts. Fe (hydr)oxides with different degree of Al-substitution are also found in nature.[98] At coprecipitation of Fe and Al in the laboratory, substitution of up to ~20–30 mol% with Al has been found for Fh before precipitation of secondary Al-(hydr)oxide phases occurs.[99,100] This implies that the formation of separate solid phases of nanocrystalline Fe and Al (hydr)oxide is more plausible for the tropical soils, which have higher Al/Fe ratios in the AO extracts (on average ~2.0) than the Dutch soils (on average ~0.4). In the assessment of the effective RSA with the probe-ion method, the implications of having two distinct oxide phases with a possible difference in PO_4 affinity have been discussed in Section 9.5.1. At scaling the calculated RSA values to the content of Fe and Al (hydr)oxides, the distinction between two solid Fe and Al phases with distinct size-dependent values of molar mass (M_{nano}) and mass density (ρ_{nano}) is particularly relevant for soils with high Al/Fe ratios. Neglecting this, and assuming instead fixed and equal M_{nano} and ρ_{nano} for both oxide phases, as the Fh core for instance, would lead to smaller mean particle sizes and corresponding higher values of SSA.

9.5.4. Organo-mineral interactions: Size matters for soil carbon stabilization

The interaction of soil organic matter (SOM) with natural metal (hydr)oxide nanoparticles is one of the main processes determining the capacity of soils to store SOC.[101–105] Different pathways have been proposed for the formation of organo-mineral associations, *e.g.* sorption of microbial byproducts[106] or direct sorption of plant derived SOM.[107] It is recognized that metal (hydr)oxide nanoparticles may be embedded in a matrix of organic molecules when they precipitate in the presence of SOM.[76,108,109] However, a clear structural view of these nanoscale associations is still missing in the literature. In Chapters 7 and 8, a model has been proposed for the structural arrangement of organo-mineral associations at the ultra-small nanometer scale.

In Figure 7.5a, a clear positive linear relationship between the calculated RSA values and the SOC content was shown for the series of Dutch top-soils. However, for the tropical soils, this relationship is less clear (Figure 8.4a), suggesting a large variation in the SOC surface density (mg m^{-2}) across soil samples. This seeming discrepancy can be reconciled if the effect of particle size of the metal (hydr)oxides is considered. In the proposed mineral core–surface layer model, the organo-metal (hydr)oxide nanoparticles are seen as a collection of mineral cores with a mean diameter d coated by a SOM layer with a thickness L (see Figure 9.4a). For each soil, the value of L was fitted iteratively (see Chapter 7 for details). Remarkably, for both series of soils, an excellent relationship is found between the mean size (d) of the metal (hydr)oxide particles in a sample and the thickness L of the SOM layer

surrounding these particles (Figure 9.4a). For most soils, the value of L is considerably larger than the thickness of the compact part of the double layer (*i.e.* ~0.7 nm),[51] indicating that only a fraction of the total SOC is allocated in the closed proximity of the mineral surfaces. In general, the thickness of the SOM layer in tropical soils is about 2/3 of the thickness found in soils from the Netherlands. These differences may result from differences in the steady-state of SOM input and output for both types of soils, due to for instance contrasting climate conditions influencing SOM decomposition and differences in the nutrient status affecting the primary biomass production, and subsequently the SOM inputs.

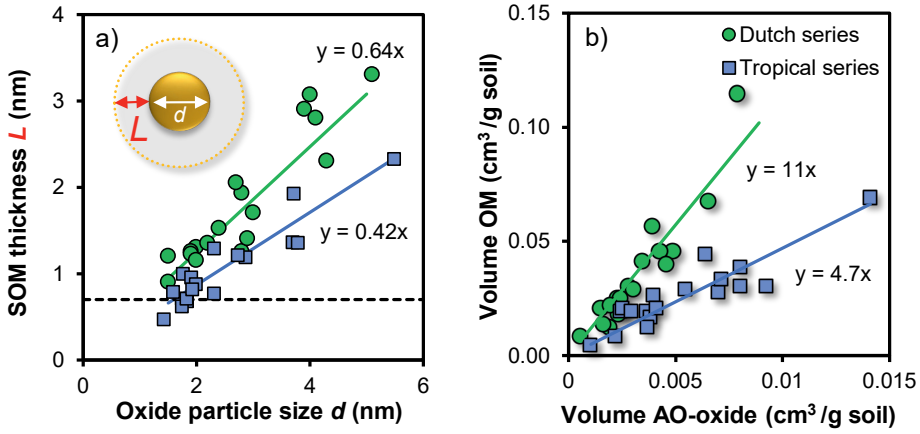

Figure 9.4. a) Relationship between the layer thickness L of soil organic matter and the mean size d of the metal (hydr)oxide nanoparticles for a set of Dutch soil (green circles) and tropical soils (blue squares). The horizontal line represents the approximated thickness of the Stern layer at the interface of Fe (hydr)oxides.[51] In the calculation of L the mass density of SOM has been set to 1250 kg m^{-3}. **b)** Relationship between the volume of SOM and the volume of metal (hydr)oxide nanoparticles, both expressed in cm^3 g^{-1}, for the same data series described in panel a. NB = for the series of Dutch soils, samples 3 and 11 have been excluded from the relationships, because these soils present extremely high contents of oxides and SOM, respectively in relation to the rest of soils of this data series (see Chapter 7). The relationships present for the series of Dutch soils varies slightly from those presented in Chapter 7, where the relationships were categorized according to the clay content of soils.

The interaction of metal (hydr)oxides and SOM can also be interpreted using another structural view in which the organo-mineral associations are seen as a collection of spherical entities organized by self-assembly. Using atomic force microscopy (AFM), it was shown that globular, rather than linear, OM molecules are preferentially associated to the surfaces of porous goethite.[110] For both sets of soils, the SOM volume is remarkably well correlated to the calculated volume of metal (hydr)oxide nanoparticles, both expressed in cm^3 g^{-1} soil (Figure 9.4b). From these relationships, the mean volumetric ratio of SOM-to-oxides (R_V) can be derived, being on average ~11 for the Dutch soils and ~5 for the tropical soils. The R_V can be interpreted structurally as the average number of SOM particles coordinating to a central metal (hydr)oxide core. According to Pauling's first rule, a coordination number (CN) in crystals is determined by the ratio of radii of the interacting particles. In case of 10–12, the ratio of particle radii is ~0.73–1.0, a similar size for the SOM and metal (hydr)oxide particles. For the tropical soils, the volume ratio of just 5 could be interpreted as a significantly lower ratio of radii, typically ~0.4, *i.e.* the SOM particles are then substantially smaller than the central oxide particle. However, for the tropical soils, it might also be possible to find a similar CN similar as for the Dutch soils (*i.e.* 10-12) if the SOM particles are shared between various metal (hydr)oxide cores in a 3D arrangement, having a ratio of particle radii

close to ~1.0. If that is the case, it would imply that more condensed organo-mineral associations are formed in the tropical soils than in the Dutch soils.

The above structural view for the nano-scale organo-mineral interactions, using the common self-assembly framework is novel. It is remarkable that for both types of soils with very contrasting properties the same relationships are found, suggesting that the proposed concept for the nano-scale association of metal (hydr)oxides and SOM might be universally applicable. However, at higher organization hierarchy, *i.e.* formation of sub-micrometer domains, the structural organization of the tropical and the Dutch top-soils may differ. The reason is the significant contribution of crystalline oxides in the former soils. These crystalline oxide phases with reduced capacity to react with SOM[111] may be present mainly within internal regions of sub micrometer scale domains. The above organo-mineral associations organized at the nano-scale can act as binding agents that favor the adhesion of larger and less reactive mineral particles (*e.g.* crystalline oxides and clays), leading to formation of micrometer-sized aggregates.[112,113] Exposure of "new" metal (hydr)oxide surfaces has been reported after selectively removing the fraction of poorly crystalline oxides in soils,[114,115] which suggests the existence of more crystalline oxide phases coated by the nanocrystalline oxides, probably in association with SOM as follows from our interpretations.

The structural model for the organo-mineral associations proposed in Chapters 7 and 8 may open a new debate about the way in which metal (hydr)oxides and SOM interact at the nanometer scale. From a wider perspective, this topic is relevant for better understanding the mechanisms and capacity of soils for stabilizing SOM. Soil is the largest reservoir of organic carbon in terrestrial systems, and therefore, it is an important component of the global C-cycle with a great potential to mitigate the effects of climate change. The results presented in this thesis suggest that both the amount and size of the metal (hydr)oxide nanoparticles play a central role in the potential of soils for storing SOC. This advocates the need to pay more attention to the metal (hydr)oxide-SOM interactions in global models intended to predict the potential of soils for sequestering SOC. Presently, biogeochemical models mainly focused their attention on the interaction between SOM and clay minerals, whereas this relationship has little explanatory power for predicting SOM stabilization.[116]

The presented view on the organo-mineral association might be also useful for understanding the release of ions from soil surfaces. For instance, organo-mineral associations probably lead to the formation of nano- and micro-aggregates that may influence the dynamics of exchange of adsorbed ions. Rate limitation of ion release due to intra-aggregate diffusion may affect the outcome of soil chemical extractions depending on the micro-aggregate size. This may play a role in soil chemical extraction methodologies that are based on the principle of adding an "infinite sink", such as the Fe oxide paper methodology[117] or the Dutch P water (P_w) extraction method.[118] Such a rate limitation of desorption by diffusion may also influence the rate of PO_4 uptake by plants. In other words, organo-mineral association and micro-aggregate formation may be a relevant factor in soil fertility too, which pledges further study of these association mechanisms also from that perspective.

9.6. Concluding remarks

In line with the objectives that I formulated in the Introduction chapter, the results of this thesis are organized into three main focal areas, namely *i*) basic insights into the surface reactivity of Fh, *ii*) parametrization of the ion adsorption model, and *iii*) application of the developed SCM to soils. Overall, the results presented in this thesis contribute to improve our understanding of the surface reactivity of ferrihydrite. The detailed and consistent study of ion adsorption phenomena to this nanomaterial will

also allow better predictions of the chemical behavior of nutrients and pollutants in natural as well as in engineered environments. In this particular case, significant progress has been added to understanding the mechanisms of the interfacial interactions of PO_4 ions. Across all the chapters, I have addressed a series of concepts that cover a wide range of scientific aspects, from fundamentals of surface chemistry to applications in soil and water chemistry. As such, the results discussed in this thesis might be relevant for a range of scientific disciplines, including soil and environmental science, geochemistry, colloid and interface science, material and surface science, as well as soil- and water chemistry. Overall, in this thesis a major leap forward has been made towards a more accurate description of ion adsorption to natural oxides in field samples, using an internally consistent SCM as a tool. Nevertheless, a number of challenges still remain in the development of a fully consistent SCM approach for soil samples, for which I have indicated a number of specific suggestions in this discussion chapter. These challenges will require intensive, yet promising, research in the upcoming years.

References

(1) Dixit, S.; Hering, J. G. Comparison of Arsenic(V) and Arsenic(III) Sorption onto Iron Oxide Minerals: Implications for Arsenic Mobility. *Environ. Sci. Technol.* **2003**, *37* (18), 4182–4189.

(2) Liu, Y. T.; Hesterberg, D. Phosphate Bonding on Noncrystalline Al/Fe-Hydroxide Coprecipitates. *Environ. Sci. Technol.* **2011**, *45* (15), 6283–6289.

(3) Cui, Y.; Weng, L. Arsenate and Phosphate Adsorption in Relation to Oxides Composition in Soils: LCD Modeling. *Environ. Sci. Technol.* **2013**, *47* (13), 7269–7276.

(4) Johnston, C. P.; Chrysochoou, M. Mechanisms of Chromate Adsorption on Hematite. *Geochim. Cosmochim. Acta* **2014**, *138*, 146–157.

(5) Verbeeck, M.; Warrinnier, R.; Gustafsson, J. P.; Thiry, Y.; Smolders, E. Soil Organic Matter Increases Antimonate Mobility in Soil: An Sb(OH)6 Sorption and Modelling Study. *Appl. Geochemistry* **2019**, *104*, 33–41.

(6) Guo, H.; Barnard, A. S. Naturally Occurring Iron Oxide Nanoparticles: Morphology, Surface Chemistry and Environmental Stability. *J. Mater. Chem. A* **2013**, *1* (1), 27–42.

(7) Cornell, R. M.; Schwertmann, U. *The Iron Oxides: Structure, Properties, Reactions, Ocurrence and Uses*, Second Edi.; WILEY-VCH, Germany, 2003.

(8) Arai, Y.; Sparks, D. L.; Davis, J. A. Effects of Dissolved Carbonate on Arsenate Adsorption and Surface Speciation at the Hematite−Water Interface. *Environ. Sci. Technol.* **2004**, *38* (3), 817–824.

(9) Hiemstra, T.; Van Riemsdijk, W. H. A Surface Structural Approach to Ion Adsorption: The Charge Distribution (CD) Model. *J. Colloid Interface Sci.* **1996**, *179* (2), 488–508.

(10) Salazar-Camacho, C.; Villalobos, M. Goethite Surface Reactivity: III. Unifying Arsenate Adsorption Behavior through a Variable Crystal Face - Site Density Model. *Geochim. Cosmochim. Acta* **2010**, *74* (8), 2257–2280.

(11) Villalobos, M.; Pérez-Gallegos, A. Goethite Surface Reactivity: A Macroscopic Investigation Unifying Proton, Chromate, Carbonate, and Lead(II) Adsorption. *J. Colloid Interface Sci.* **2008**, *326* (2), 307–323.

(12) Rietra, R. P. J. J.; Hiemstra, T.; van Riemsdijk, W. H. Interaction between Calcium and Phosphate Adsorption on Goethite. *Environ. Sci. Technol.* **2001**, *35* (16), 3369–3374.

(13) Nie, Z.; Finck, N.; Heberling, F.; Pruessmann, T.; Liu, C.; Lützenkirchen, J. Adsorption of Selenium and Strontium on Goethite: EXAFS Study and Surface Complexation Modeling of the Ternary Systems. *Environ. Sci. Technol.* **2017**, *51* (7), 3751–3758.

(14) Antelo, J.; Arce, F.; Fiol, S. Arsenate and Phosphate Adsorption on Ferrihydrite Nanoparticles. Synergetic Interaction with Calcium Ions. *Chem. Geol.* **2015**, *410*, 53–62.

(15) Gao, Y.; Mucci, A. Individual and Competitive Adsorption of Phosphate and Arsenate on Goethite in Artificial Seawater. *Chem. Geol.* **2003**, *199* (1–2), 91–109.

(16) Gustafsson, J. P. Modelling Competitive Anion Adsorption on Oxide Minerals and an Allophane-Containing Soil. *Eur. J. Soil Sci.* **2001**, *52* (4), 639–653.

(17) Stachowicz, M.; Hiemstra, T.; Van Riemsdijk, W. H. Arsenic-Bicarbonate Interaction on Goethite Particles. *Environ. Sci. Technol.* **2007**, *41* (16), 5620–5625.

(18) Tiberg, C.; Sjöstedt, C.; Eriksson, A. K.; Klysubun, W.; Gustafsson, J. P. Phosphate Competition with Arsenate on Poorly Crystalline Iron and Aluminum (Hydr)Oxide Mixtures. *Chemosphere* **2020**, *255*, 126937.

(19) Frossard, E.; Condron, L. M.; Oberson, A.; Sinaj, S.; Fardeau, J. C. Processes Governing Phosphorus Availability in

Temperate Soils. *J. Environ. Qual.* **2000**, *29* (1), 15.

(20) Kruse, J.; Abraham, M.; Amelung, W.; Baum, C.; Bol, R.; Kühn, O.; Lewandowski, H.; Niederberger, J.; Oelmann, Y.; Rüger, C.; et al. Innovative Methods in Soil Phosphorus Research: A Review. *J. Plant Nutr. Soil Sci.* **2015**, *178* (1), 43–88.

(21) Cordell, D.; White, S. Peak Phosphorus: Clarifying the Key Issues of a Vigorous Debate about Long-Term Phosphorus Security. *Sustainability* . 2011.

(22) Cooper, J.; Lombardi, R.; Boardman, D.; Carliell-Marquet, C. The Future Distribution and Production of Global Phosphate Rock Reserves. *Resour. Conserv. Recycl.* **2011**, *57*, 78–86.

(23) Ulrich, A. E.; Frossard, E. On the History of a Reoccurring Concept: Phosphorus Scarcity. *Sci. Total Environ.* **2014**, *490*, 694–707.

(24) Withers, P. J. A.; van Dijk, K. C.; Neset, T.-S. S.; Nesme, T.; Oenema, O.; Rubæk, G. H.; Schoumans, O. F.; Smit, B.; Pellerin, S. Stewardship to Tackle Global Phosphorus Inefficiency: The Case of Europe. *Ambio* **2015**, *44* (2), 193–206.

(25) Jarvie, H. P.; Sharpley, A. N.; Flaten, D.; Kleinman, P. J. A.; Jenkins, A.; Simmons, T. The Pivotal Role of Phosphorus in a Resilient Water–Energy–Food Security Nexus. *J. Environ. Qual.* **2015**, *44* (4), 1049–1062.

(26) Yuan, Z.; Jiang, S.; Sheng, H.; Liu, X.; Hua, H.; Liu, X.; Zhang, Y. Human Perturbation of the Global Phosphorus Cycle: Changes and Consequences. *Environ. Sci. Technol.* **2018**, *52* (5), 2438–2450.

(27) van der Giessen, A. A. The Structure of Iron (III) Oxide-Hydrate Gels. *J. Inorg. Nucl. Chem.* **1966**, *28* (10), 2155–2159.

(28) Yates, D. E.; Grieser, F.; Cooper, R.; Healy, T. W. Tritium Exchange Studies on Metal Oxide Colloidal Dispersions. *Aust. J. Chem.* **1977**, *30* (8), 1655–1660.

(29) Davis, J. A.; Leckie, J. O. Surface Ionization and Complexation at the Oxide/Water Interface II. Surface Properties of Amorphous Iron Oxyhydroxide and Adsorption of Metal Ions. *J. Colloid Interface Sci.* **1978**, *67* (1), 90–107.

(30) Weidler, P. G. BET Sample Pretreatment of Synthetic Ferrihydrite and Its Influence on the Determination of Surface Area and Porosity. *J. Porous Mater.* **1997**, *4* (3), 165–169.

(31) Moon, E. M.; Peacock, C. L. Modelling Cu(II) Adsorption to Ferrihydrite and Ferrihydrite-Bacteria Composites: Deviation from Additive Adsorption in the Composite Sorption System. *Geochim. Cosmochim. Acta* **2013**, *104*, 148–164.

(32) Wang, X.; Li, W.; Harrington, R.; Liu, F.; Parise, J. B.; Feng, X.; Sparks, D. L. Effect of Ferrihydrite Crystallite Size on Phosphate Adsorption Reactivity. *Environ. Sci. Technol.* **2013**, *47* (18), 10322–10331.

(33) Sowers, T. D.; Stuckey, J. W.; Sparks, D. L. The Synergistic Effect of Calcium on Organic Carbon Sequestration to Ferrihydrite. *Geochem. Trans.* **2018**, *19* (1), 4.

(34) Hsi, C. D.; Langmuir, D. Adsorption of Uranyl onto Ferric Oxyhydroxides: Application of the Surface Complexation Site-Binding Model. *Geochim. Cosmochim. Acta* **1985**, *49* (9), 1931–1941.

(35) Michel, F. M.; Barron, V.; Torrent, J.; Morales, M. P.; Serna, C. J.; Boily, J.-F.; Liu, Q.; Ambrosini, A.; Cismasu, A. C.; Brown, G. E. Ordered Ferrimagnetic Form of Ferrihydrite Reveals Links among Structure, Composition, and Magnetism. *Proc. Natl. Acad. Sci.* **2010**, *107* (7), 2787–2792.

(36) Anschutz, A. J.; Penn, R. L. Reduction of Crystalline Iron(III) Oxyhydroxides Using Hydroquinone: Influence of Phase and Particle Size. *Geochem. Trans.* **2005**, *6* (3), 60.

(37) Burleson, D. J.; Penn, R. L. Two-Step Growth of Goethite from Ferrihydrite. *Langmuir* **2006**, *22* (1), 402–409.

(38) Strehlau, J. H.; Toner, B. M.; Arnold, W. A.; Penn, R. L. Accessible Reactive Surface Area and Abiotic Redox Reactivity of Iron Oxyhydroxides in Acidic Brines. *Geochim. Cosmochim. Acta* **2017**, *197*, 345–355.

(39) Michen, B.; Geers, C.; Vanhecke, D.; Endes, C.; Rothen-Rutishauser, B.; Balog, S.; Petri-Fink, A. Avoiding Drying-Artifacts in Transmission Electron Microscopy: Characterizing the Size and Colloidal State of Nanoparticles. *Sci. Rep.* **2015**, *5* (1), 9793.

(40) Hiemstra, T. Surface and Mineral Structure of Ferrihydrite. *Geochim. Cosmochim. Acta* **2013**, *105*, 316–325.

(41) Xu, W.; Hausner, D. B.; Harrington, R.; Lee, P. L.; Strongin, D. R.; Parise, J. B. Structural Water in Ferrihydrite and Constraints This Provides on Possible Structure Models. *Am. Mineral.* **2011**, *96* (4), 513–520.

(42) Dzombak, D. A.; Morel, F. M. M. *Surface Complexation Modeling: Hydrous Ferric Oxide*; John Wiley & Sons, Inc.: New York, 1990.

(43) Hiemstra, T. Ferrihydrite Interaction with Silicate and Competing Oxyanions: Geometry and Hydrogen Bonding of Surface Species. *Geochim. Cosmochim. Acta* **2018**, *238*, 453–476.

(44) Bompoti, N.; Chrysochoou, M.; Machesky, M. Surface Structure of Ferrihydrite: Insights from Modeling Surface Charge. *Chem. Geol.* **2017**, *464*, 34–45.

(45) Boily, J. F.; Lützenkirchen, J.; Balmès, O.; Beattie, J.; Sjöberg, S. Modeling Proton Binding at the Goethite (α-FeOOH)-Water Interface. *Colloids Surfaces A Physicochem. Eng. Asp.* **2001**, *179* (1), 11–27.

(46) Lützenkirchen, J.; Boily, J. F.; Gunneriusson, L.; Lövgren, L.; Sjöberg, S. Protonation of Different Goethite Surfaces-

Unified Models for NaNO3 and NaCl Media. *J. Colloid Interface Sci.* **2008**, *317* (1), 155–165.

(47) Bompoti, N. M.; Chrysochoou, M.; Machesky, M. L. Assessment of Modeling Uncertainties Using a Multistart Optimization Tool for Surface Complexation Equilibrium Parameters (MUSE). *ACS Earth and Space Chemistry*. American Chemical Society January 10, 2019, p acsearthspacechem.8b00125.

(48) Bompoti, N. M.; Chrysochoou, M.; Machesky, M. L. A Unified Surface Complexation Modeling Approach for Chromate Adsorption on Iron Oxides. *Environ. Sci. Technol.* **2019**, *53* (11), 6352–6361.

(49) Hiemstra, T.; Zhao, W. Reactivity of Ferrihydrite and Ferritin in Relation to Surface Structure, Size, and Nanoparticle Formation Studied for Phosphate and Arsenate. *Environ. Sci. Nano* **2016**, *3*, 1265–1279.

(50) Hiemstra, T.; Van Riemsdijk, W. H. A Surface Structural Model for Ferrihydrite I: Sites Related to Primary Charge, Molar Mass, and Mass Density. *Geochim. Cosmochim. Acta* **2009**, *73* (15), 4423–4436.

(51) Hiemstra, T.; Van Riemsdijk, W. H. On the Relationship between Charge Distribution, Surface Hydration, and the Structure of the Interface of Metal Hydroxides. *J. Colloid Interface Sci.* **2006**, *301* (1), 1–18.

(52) Greffié, C.; Amouric, M.; Parron, C. HRTEM Study of Freeze-Dried and Untreated Synthetic Ferrihydrites: Consequences of Sample Processing. *Clay Miner.* **2001**, *36* (3), 381–387.

(53) Chen, C.; Dynes, J. J.; Wang, J.; Sparks, D. L. Properties of Fe-Organic Matter Associations via Coprecipitation versus Adsorption. *Environ. Sci. Technol.* **2014**, *48* (23), 13751–13759.

(54) Chen, K. Y.; Chen, T. Y.; Chan, Y. T.; Cheng, C. Y.; Tzou, Y. M.; Liu, Y. T.; Teah, H. Y. Stabilization of Natural Organic Matter by Short-Range-Order Iron Hydroxides. *Environ. Sci. Technol.* **2016**, *50* (23), 12612–12620.

(55) Eusterhues, K.; Wagner, F. E.; Häusler, W.; Hanzlik, M.; Knicker, H.; Totsche, K. U.; Kögel-Knabner, I.; Schwertmann, U. Characterization of Ferrihydrite-Soil Organic Matter Coprecipitates by X-Ray Diffraction and Mössbauer Spectroscopy. *Environ. Sci. Technol.* **2008**, *42* (21), 7891–7897.

(56) Mikutta, R.; Lorenz, D.; Guggenberger, G.; Haumaier, L.; Freund, A. Properties and Reactivity of Fe-Organic Matter Associations Formed by Coprecipitation versus Adsorption: Clues from Arsenate Batch Adsorption. *Geochim. Cosmochim. Acta* **2014**, *144*, 258–276.

(57) Cismasu, A. C.; Levard, C.; Michel, F. M.; Brown, G. E. Properties of Impurity-Bearing Ferrihydrite II: Insights into the Surface Structure and Composition of Pure, Al- and Si-Bearing Ferrihydrite from Zn(II) Sorption Experiments and Zn K-Edge X-Ray Absorption Spectroscopy. *Geochim. Cosmochim. Acta* **2013**, *119*, 46–60.

(58) Cismasu, A. C.; Michel, F. M.; Tcaciuc, A. P.; Brown, G. E. Properties of Impurity-Bearing Ferrihydrite III. Effects of Si on the Structure of 2-Line Ferrihydrite. *Geochim. Cosmochim. Acta* **2014**, *133*, 168–185.

(59) Lee, S.; Xu, H. One-Step Route Synthesis of Siliceous Six-Line Ferrihydrite: Implication for the Formation of Natural Ferrihydrite. *ACS Earth Sp. Chem.* **2019**, *3* (4), 503–509.

(60) Hofmann, A.; Vantelon, D.; Montargès-Pelletier, E.; Villain, F.; Gardoll, O.; Razafitianamaharavo, A.; Ghanbaja, J. Interaction of Fe(III) and Al(III) during Hydroxylation by Forced Hydrolysis: The Nature of Al-Fe Oxyhydroxy Co-Precipitates. *J. Colloid Interface Sci.* **2013**, *407*, 76–88.

(61) Johnston, C. P.; Chrysochoou, M. Mechanisms of Chromate, Selenate, and Sulfate Adsorption on Al-Substituted Ferrihydrite: Implications for Ferrihydrite Surface Structure and Reactivity. *Environ. Sci. Technol.* **2016**, *50* (7), 3589–3596.

(62) Namayandeh, A.; Kabengi, N. Calorimetric Study of the Influence of Aluminum Substitution in Ferrihydrite on Sulfate Adsorption and Reversibility. *J. Colloid Interface Sci.* **2019**, *540*, 20–29.

(63) Benjamin, M. M.; Leckie, J. O. Multiple-Site Adsorption of Cd, Cu, Zn, and Pb on Amorphous Iron Oxyhydroxide. *J. Colloid Interface Sci.* **1981**, *79* (1), 209–221.

(64) Kinniburgh, D. G.; Barker, J. A.; Whitfield, M. A Comparison of Some Simple Adsorption Isotherms for Describing Divalent Cation Adsorption by Ferrihydrite. *J. Colloid Interface Sci.* **1983**, *95* (2), 370–384.

(65) Kinniburgh, D. G.; Jackson, M. L. Concentration and PH Dependence of Calcium and Zinc Adsorption by Iron Hydrous Oxide Gel. *Soil Sci. Soc. Am. J.* **1982**, *46* (1), 56–61.

(66) Axe, L.; Bunker, G. B.; Anderson, P. R.; Tyson, T. A. An XAFS Analysis of Strontium at the Hydrous Ferric Oxide Surface. *J. Colloid Interface Sci.* **1998**, *199* (1), 44–52.

(67) Tiberg, C.; Gustafsson, J. P. Phosphate Effects on Cadmium(II) Sorption to Ferrihydrite. *J. Colloid Interface Sci.* **2016**, *471*, 103–111.

(68) Collins, C. R.; Sherman, D. M.; Vala Ragnarsdóttir, K. The Adsorption Mechanism of Sr2+ on the Surface of Goethite. *Radiochim. Acta* **1998**, *81* (4), 201–206.

(69) Fuller, A. J.; Shaw, S.; Peacock, C. L.; Trivedi, D.; Burke, I. T. EXAFS Study of Sr Sorption to Illite, Goethite, Chlorite, and Mixed Sediment under Hyperalkaline Conditions. *Langmuir* **2016**, *32* (12), 2937–2946.

(70) Talebi, M.; Rahnemaie, R.; Goli Kalanpa, E.; Davoodi, M. H. Competitive Adsorption of Magnesium and Calcium with Phosphate at the Goethite Water Interface: Kinetics, Equilibrium and CD-MUSIC Modeling. *Chem. Geol.* **2016**, *437*, 19–29.

(71) Elzinga, E. J.; Kretzschmar, R. In Situ ATR-FTIR Spectroscopic Analysis of the Co-Adsorption of Orthophosphate

and Cd(II) onto Hematite. *Geochim. Cosmochim. Acta* **2013**, *117*, 53–64.

(72) van Genuchten, C. M.; Gadgil, A. J.; Peña, J. Fe(III) Nucleation in the Presence of Bivalent Cations and Oxyanions Leads to Subnanoscale 7 Å Polymers. *Environ. Sci. Technol.* **2014**, *48* (20), 11828–11836.

(73) Voegelin, A.; Kaegi, R.; Frommer, J.; Vantelon, D.; Hug, S. J. Effect of Phosphate, Silicate, and Ca on Fe(III)-Precipitates Formed in Aerated Fe(II)- and As(III)-Containing Water Studied by X-Ray Absorption Spectroscopy. *Geochim. Cosmochim. Acta* **2010**, *74* (1), 164–186.

(74) Lin, J.; Zhan, Y.; Wang, H.; Chu, M.; Wang, C.; He, Y.; Wang, X. Effect of Calcium Ion on Phosphate Adsorption onto Hydrous Zirconium Oxide. *Chem. Eng. J.* **2017**, *309*, 118–129.

(75) Ronson, T. K.; McQuillan, A. J. Infrared Spectroscopic Study of Calcium and Phosphate Ion Coadsorption and of Brushite Crystallization on TiO2. *Langmuir* **2002**, *18* (12), 5019–5022.

(76) Hiemstra, T.; Antelo, J.; Rahnemaie, R.; van Riemsdijk, W. H. Nanoparticles in Natural Systems I: The Effective Reactive Surface Area of the Natural Oxide Fraction in Field Samples. *Geochim. Cosmochim. Acta* **2010**, *74* (1), 41–58.

(77) Sowers, T. D.; Adhikari, D.; Wang, J.; Yang, Y.; Sparks, D. L. Spatial Associations and Chemical Composition of Organic Carbon Sequestered in Fe, Ca, and Organic Carbon Ternary Systems. *Environ. Sci. Technol.* **2018**, *52* (12), 6936–6944.

(78) Mikutta, R.; Mikutta, C.; Kalbitz, K.; Scheel, T.; Kaiser, K.; Jahn, R. Biodegradation of Forest Floor Organic Matter Bound to Minerals via Different Binding Mechanisms. *Geochim. Cosmochim. Acta* **2007**, *71* (10), 2569–2590.

(79) Weng, L.; van Riemsdijk, W. H.; Hiemstra, T. Factors Controlling Phosphate Interaction with Iron Oxides. *J. Environ. Qual.* **2012**, *41* (3), 628–635.

(80) Koopmans, G. F.; Chardon, W. J.; Ehlert, P. A. I.; Dolfing, J.; Suurs, R. A. A.; Oenema, O.; van Riemsdijk, W. H. Phosphorus Availability for Plant Uptake in a Phosphorus-Enriched Noncalcareous Sandy Soil. *J. Environ. Qual.* **2004**, *33* (3), 965–975.

(81) Lookman, R.; Freese, D.; Merckx, R.; Vlassak, K.; van Riemsdijk, W. H. Long-Term Kinetics of Phosphate Release from Soil. *Environ. Sci. Technol.* **1995**, *29* (6), 1569–1575.

(82) Warrinnier, R.; Goossens, T.; Amery, F.; Vanden Nest, T.; Verbeeck, M.; Smolders, E. Investigation on the Control of Phosphate Leaching by Sorption and Colloidal Transport: Column Studies and Multi-Surface Complexation Modelling. *Appl. Geochemistry* **2019**, *100* (November 2018), 371–379.

(83) Verbeeck, M.; Hiemstra, T.; Thiry, Y.; Smolders, E. Soil Organic Matter Reduces the Sorption of Arsenate and Phosphate: A Soil Profile Study and Geochemical Modelling. *Eur. J. Soil Sci.* **2017**, *68* (5), 678–688.

(84) Sánchez-Alcalá, I.; del Campillo, M. C.; Torrent, J. Critical Olsen P and CaCl 2 -P Levels as Related to Soil Properties: Results from Micropot Experiments. *Soil Use Manag.* **2015**, *31* (2), 233–240.

(85) McDowell, R. .; Sharpley, A. . Phosphorus Solubility and Release Kinetics as a Function of Soil Test P Concentration. *Geoderma* **2003**, *112* (1–2), 143–154.

(86) van Rotterdam, A. M. D.; Bussink, D. W.; Temminghoff, E. J. M.; van Riemsdijk, W. H. Predicting the Potential of Soils to Supply Phosphorus by Integrating Soil Chemical Processes and Standard Soil Tests. *Geoderma* **2012**, *189–190*, 617–626.

(87) Morel, C.; Tunney, H.; Plénet, D.; Pellerin, S. Transfer of Phosphate Ions between Soil and Solution: Perspectives in Soil Testing. In *Journal of Environmental Quality*; American Soc of Agronomy Inc, 2000; Vol. 29, pp 50–59.

(88) Houba, V. J. G.; Temminghoff, E. J. M.; Gaikhorst, G. A.; van Vark, W. Soil Analysis Procedures Using 0.01 M Calcium Chloride as Extraction Reagent. *Commun. Soil Sci. Plant Anal.* **2000**, *31* (9–10), 1299–1396.

(89) Koopmans, G. F.; Chardon, W. J.; Dekker, P. H. M.; Römkens, P. F. A. M.; Schoumans, O. F. Comparing Different Extraction Methods for Estimating Phosphorus Solubility in Various Soil Types. *Soil Sci.* **2006**, *171* (2), 103–116.

(90) Hiemstra, T.; Mia, S.; Duhaut, P.-B.; Molleman, B. Natural and Pyrogenic Humic Acids at Goethite and Natural Oxide Surfaces Interacting with Phosphate. *Environ. Sci. Technol.* **2013**, *47* (16), 9182–9189.

(91) Hiemstra, T.; Antelo, J.; van Rotterdam, A. M. D.; van Riemsdijk, W. H. Nanoparticles in Natural Systems II: The Natural Oxide Fraction at Interaction with Natural Organic Matter and Phosphate. *Geochim. Cosmochim. Acta* **2010**, *74* (1), 59–69.

(92) Gustafsson, J. P. Arsenate Adsorption to Soils: Modelling the Competition from Humic Substances. *Geoderma* **2006**, *136* (1–2), 320–330.

(93) Regelink, I. C.; Weng, L.; Lair, G. J.; Comans, R. N. J. Adsorption of Phosphate and Organic Matter on Metal (Hydr)Oxides in Arable and Forest Soil: A Mechanistic Modelling Study. *Eur. J. Soil Sci.* **2015**, *66* (5), 867–875.

(94) Bonten, L. T. C.; Groenenberg, J. E.; Weng, L.; van Riemsdijk, W. H. Use of Speciation and Complexation Models to Estimate Heavy Metal Sorption in Soils. *Geoderma* **2008**, *146* (1), 303–310.

(95) Eusterhues, K.; Rumpel, C.; Kögel-Knabner, I. Organo-Mineral Associations in Sandy Acid Forest Soils: Importance of Specific Surface Area, Iron Oxides and Micropores. *Eur. J. Soil Sci.* **2005**, *56* (6), 753–763.

(96) Kiem, R.; Kögel-Knabner, I. Refractory Organic Carbon in Particle-Size Fractions of Arable Soils II: Organic Carbon

in Relation to Mineral Surface Area and Iron Oxides in Fractions < 6 Mm. *Org. Geochem.* **2002**, *33* (12), 1699–1713.

(97) Regelink, I. C.; Weng, L.; Koopmans, G. F.; van Riemsdijk, W. H. Asymmetric Flow Field-Flow Fractionation as a New Approach to Analyse Iron-(Hydr)Oxide Nanoparticles in Soil Extracts. *Geoderma* **2013**, *202–203*, 134–141.

(98) Cornell, R. M.; Schwertmann, U. The Iron Oxides. In *Iron Oxides in the Laboratary*; Wiley-VCH Verlag GmbH & Co. KGaA: Weinheim, FRG, 2007; pp 5–18.

(99) Adra, A.; Morin, G.; Ona-Nguema, G.; Menguy, N.; Maillot, F.; Casiot, C.; Bruneel, O.; Lebrun, S.; Juillot, F.; Brest, J. Arsenic Scavenging by Aluminum-Substituted Ferrihydrites in a Circumneutral PH River Impacted by Acid Mine Drainage. *Environ. Sci. Technol.* **2013**, *47* (22), 12784–12792.

(100) Cismasu, A. C.; Michel, F. M.; Stebbins, J. F.; Levard, C.; Brown, G. E. Properties of Impurity-Bearing Ferrihydrite I. Effects of Al Content and Precipitation Rate on the Structure of 2-Line Ferrihydrite. *Geochim. Cosmochim. Acta* **2012**, *92*, 275–291.

(101) Wagai, R.; Mayer, L. M. Sorptive Stabilization of Organic Matter in Soils by Hydrous Iron Oxides. *Geochim. Cosmochim. Acta* **2007**, *71* (1), 25–35.

(102) Mikutta, R.; Kleber, M.; Torn, M. S.; Jahn, R. Stabilization of Soil Organic Matter: Association with Minerals or Chemical Recalcitrance? *Biogeochemistry* **2006**, *77* (1), 25–56.

(103) Wiesmeier, M.; Urbanski, L.; Hobley, E.; Lang, B.; von Lützow, M.; Marin-Spiotta, E.; van Wesemael, B.; Rabot, E.; Ließ, M.; Garcia-Franco, N.; et al. Soil Organic Carbon Storage as a Key Function of Soils - A Review of Drivers and Indicators at Various Scales. *Geoderma*. Elsevier B.V. January 1, 2019, pp 149–162.

(104) Wiseman, C. L. S.; Püttmann, W. Interactions between Mineral Phases in the Preservation of Soil Organic Matter. *Geoderma* **2006**, *134* (1–2), 109–118.

(105) Kleber, M.; Mikutta, R.; Torn, M. S.; Jahn, R. Poorly Crystalline Mineral Phases Protect Organic Matter in Acid Subsoil Horizons. *Eur. J. Soil Sci.* **2005**, *56* (6), 717–725.

(106) Cotrufo, M. F.; Wallenstein, M. D.; Boot, C. M.; Denef, K.; Paul, E. The Microbial Efficiency-Matrix Stabilization (MEMS) Framework Integrates Plant Litter Decomposition with Soil Organic Matter Stabilization: Do Labile Plant Inputs Form Stable Soil Organic Matter? *Glob. Chang. Biol.* **2013**, *19* (4), 988–995.

(107) Mikutta, R.; Turner, S.; Schippers, A.; Gentsch, N.; Meyer-Stüve, S.; Condron, L. M.; Peltzer, D. A.; Richardson, S. J.; Eger, A.; Hempel, G.; et al. Microbial and Abiotic Controls on Mineral-Associated Organic Matter in Soil Profiles along an Ecosystem Gradient. *Sci. Rep.* **2019**, *9* (1), 10294.

(108) Pédrot, M.; Boudec, A. Le; Davranche, M.; Dia, A.; Henin, O. How Does Organic Matter Constrain the Nature, Size and Availability of Fe Nanoparticles for Biological Reduction? *J. Colloid Interface Sci.* **2011**, *359* (1), 75–85.

(109) Kleber, M.; Eusterhues, K.; Keiluweit, M.; Mikutta, C.; Mikutta, R.; Nico, P. S. Mineral-Organic Associations: Formation, Properties, and Relevance in Soil Environments. *Adv. Agron.* **2015**, *130*, 1–140.

(110) Kaiser, K.; Guggenberger, G. Sorptive Stabilization of Organic Matter by Microporous Goethite: Sorption into Small Pores vs. Surface Complexation. *Eur. J. Soil Sci.* **2007**, *58* (1), 45–59.

(111) Torn, M. S.; Trumbore, S. E.; Chadwick, O. A.; Vitousek, P. M.; Hendricks, D. M. Mineral Control of Soil Organic Carbon Storage and Turnover. *Nature* **1997**, *389* (6647), 170–173.

(112) Asano, M.; Wagai, R.; Yamaguchi, N.; Takeichi, Y.; Maeda, M.; Suga, H.; Takahashi, Y. In Search of a Binding Agent: Nano-Scale Evidence of Preferential Carbon Associations with Poorly-Crystalline Mineral Phases in Physically-Stable, Clay-Sized Aggregates. *Soil Syst.* **2018**, *2* (2), 32.

(113) Singh, M.; Sarkar, B.; Sarkar, S.; Churchman, J.; Bolan, N.; Mandal, S.; Menon, M.; Purakayastha, T. J.; Beerling, D. J. Stabilization of Soil Organic Carbon as Influenced by Clay Mineralogy. In *Advances in Agronomy*; Academic Press, 2018; Vol. 148, pp 33–84.

(114) Borggaard, O. K. The Influence of Iron Oxides on the Surface Area of Soil. *J. Soil Sci.* **1982**, *33* (3), 443–449.

(115) Pronk, G. J.; Heister, K.; Kögel-Knabner, I. Iron Oxides as Major Available Interface Component in Loamy Arable Topsoils. *Soil Sci. Soc. Am. J.* **2011**, *75* (6), 2158–2168.

(116) Rasmussen, C.; Heckman, K.; Wieder, W. R.; Keiluweit, M.; Lawrence, C. R.; Berhe, A. A.; Blankinship, J. C.; Crow, S. E.; Druhan, J. L.; Hicks Pries, C. E.; et al. Beyond Clay: Towards an Improved Set of Variables for Predicting Soil Organic Matter Content. *Biogeochemistry* **2018**, *137* (3), 297–306.

(117) van der Zee, S. E. A. T. M.; Fokkink, L. G. J.; van Riemsdijk, W. H. A New Technique for Assessment of Reversibly Adsorbed Phosphate1. *Soil Sci. Soc. Am. J.* **1987**, *51* (3), 599.

(118) Sissingh, H. A. Analytical Technique of the Pw Method, Used for the Assessment of the Phosphate Status of Arable Soils in the Netherlands. *Plant Soil* **1971**, *34* (1), 483–486.

Summary

Ferrihydrite (Fh) is an important iron (hydr)oxide nanoparticle present in most natural environments and in many engineered systems. Due to the ultra-small size of the primary particles, typically ~2–4 nm, Fh has an extraordinarily large surface reactivity. For this reason, even if present at low mass concentrations, Fh can largely control the availability of nutrients and contaminants in soils *via* adsorption processes. Ferrihydrite also forms chemically stable organo-mineral associations with soil organic matter (SOM), contributing to the long-term stabilization of organic carbon. This nanomineral is also a promising material for applications in environmental engineering and remediation technologies. In the context of Surface Complexation Modeling (SCM), studying the surface reactivity of Fh is important because this nanomaterial is envisioned as a good proxy for describing, using SCM, ion adsorption phenomena at the reactive surfaces of metal (hydr)oxides in soils. Despite the importance of Fh as a highly reactive material, several aspects of its surface reactivity remain poorly understood.

Oxyanions such as phosphate (PO_4), arsenate (AsO_4), and chromate (CrO_4) have a remarkable high affinity for binding to the surfaces of Fh. This property makes these oxyanions good candidates for probing the surface reactivity of Fh. In this thesis, PO_4 has been chosen as a model oxyanion to probe the surface of Fh for multiple reasons. Phosphate is omnipresent in natural environments, and due to its high binding affinity for the metal (hydr)oxide surfaces, it naturally accumulates in an adsorbed form in top-soils. Moreover, PO_4 is an essential nutrient for plant growth and food production. However, its concentration in the soil solution is often too low to meet the requirements for optimum crop yields. On the other hand, intensive and repetitive applications of P fertilizers (organic or inorganic) may lead to PO_4 surpluses entering aquatic systems, compromising water quality and safety. The soil phosphorus (P) status in field samples is commonly assessed using a variety of chemical extraction procedures. However, there is generally a poor mechanistic understanding of the processes affecting the release of PO_4 from the soil surfaces during these routine analytical procedures. This may lead to inaccurate interpretations about the actual soil P status. Considering all the above, it is clear that studying the underlying mechanisms controlling PO_4 adsorption to metal (hydr)oxides is highly relevant from a scientific, environmental, economic and societal perspective.

This PhD thesis aims to gain new insights into the surface reactivity of Fh nanoparticles, given emphasis to the analysis of the PO_4 adsorption mechanisms and to the development of a SCM approach for consistently describing the adsorption of this oxyanion under a wide range of solution conditions. In this work, the cooperative adsorption interaction between PO_4 and the metal ions Ca^{2+} and Mg^{2+}, as well as the competitive adsorption interaction PO_4-CO_3, have been extensively studied. A consistent analysis of these interactions is crucial if the objective is to understand the adsorption behavior of PO_4 in complex media, *e.g.* in natural environments and in the extraction solutions of common soil tests for P. In addition, the adsorption of Ca^{2+} and Mg^{2+} to Fh has been studied extensively in single-ion systems due to the large abundance of these ions in the environment and their effect on the adsorption behavior of other important ions. The ultimate goal is to contribute to the development of a self-consistent SCM approach for describing simultaneously, in a realistic physical-chemical manner, the adsorption of a whole suite of relevant cat- and anions to Fh.

The approaches implemented in this thesis comprise adsorption experiments with freshly-prepared Fh nanoparticles, determination of its specific surface area using a novel developed methodology, as well as data interpretation using an advanced SCM (*i.e.* CD-MUSIC model) and molecular orbital (MO) calculations to derive independently the charge distribution (CD) coefficients for all the adsorbing

complexes considered in the modeling. The combination of these approaches allowed the compilation of an internally consistent thermodynamic database for describing ion adsorption to Fh. Subsequently, this database has been applied for evaluating the reactive surface area (RSA) of the metal (hydr)oxides in actual soil samples.

In line with the objectives formulated in the Introduction chapter (**Chapter 1**), the experimental and modeling chapters of this thesis are organized, according to their main subject, into three sections: *i*) basic insights into the surface reactivity of Fh (Chapters 2–3), *ii*) parametrization of the ion adsorption model (Chapters 4–6), and *iii*) application of the developed SCM to soils (Chapters 7–8).

For Fh and nanoparticles in general, many physical and chemical properties change drastically as a function of the particle size. Therefore, having reliable information about the mean particle size and corresponding specific surface area (SSA, $m^2\ g^{-1}$ Fh) of Fh is essential for consistently interpreting ion adsorption data collected for this nanomaterial. In the first section of this thesis, I derived a systematic approach for assessing the SSA of Fh preparations kept in the wet state, using H^+ as a probe ion (**Chapter 2**). The H^+ adsorption to Fh was measured in solutions with different types of electrolyte ions. For data interpretation and modeling, the capacitance(s) of the Stern layer(s) of well-crystallized goethite was used as a reference and translated into the capacitance of Fh, using a consistent set of values for the molar mass (M_{nano}), mass density (ρ_{nano}), and the surface curvature. The results showed full consistency between the values of SSA of Fh derived with the present H^+ probing methodology and an alternative proposed approach that uses PO_4 as probe ion. However, the use of PO_4 as probe-ion is a more practical alternative to overcome the known limitations of more traditional techniques (*e.g.* BET) for assessing the SSA of Fh kept in the wet state. In addition, PO_4 adsorption measurements are less sensitive to possible interference of atmospheric CO_2. Therefore, PO_4 was used as a probe ion to assess the SSA of Fh in all ion adsorption experiments performed subsequently in this thesis, allowing the development of an internally consistent thermodynamic database for describing the adsorption of several ions to Fh (Chapters 4–6). Applying the approach for interpreting H^+ adsorption data reported in literature revealed a large variation in the SSA (A_H ~500–720 $m^2\ g^{-1}$) of fresh Fh suspensions, indicating that the use of a "standard" SSA for freshly-prepared Fh is not recommended.

In **Chapter 3**, the probe-ion method with PO_4 was used to quantify changes in the surface reactivity of Fh resulting from the particle growth processes. This enabled the study of the major factors (*i.e.* time, pH, temperature, and organic molecules) controlling the change in surface reactivity of Fh. The data collected with the probe-ion approach provided insights into the mechanism and rate of growth of Fh particles in suspension. In addition, a dynamic model was developed for describing changes in SSA of Fh as a result of ageing, which also provided insights into the size (d ~ 1.68 nm) and SSA (A ~ 1100 $m^2\ g^{-1}$) of the initial (*i.e.* non-aged) Fh nanoparticles. These results are relevant for a tunable synthesis of Fh suspensions with well-targeted surface reactivity and for a suitable scaling of ion adsorption data.

In the second section of this thesis, I parametrized with the CD-MUSIC model the complete set of ion adsorption data collected presently for systems with fresh Fh suspensions. In **Chapter 4**, the adsorption of the metal ions Ca^{2+} and Mg^{2+} (jointly referred to as M^{2+}) was extensively studied in single-ion Fh systems. Both ions adsorbed to Fh most probably forming inner-sphere bidentate complexes ($\equiv(FeOH)_2^{\Delta z0}M^{\Delta z1}$). Surface site heterogeneity (*i.e.* presence of sites with low and high affinity) is a particular aspect of the adsorption of M^{2+} to Fh. In this thesis, the MUSIC model for Fh, initially developed for describing the adsorption of oxyanions, was extended by including surface site heterogeneity for describing the binding of metal ions to Fh. The results showed that only a small fraction (~10%) of the available surface sites that react with M^{2+} has a high affinity character for these

cations. Nevertheless, this fraction of high affinity sites controls the binding of M^{2+} at low surface loadings and particularly at low pH values. Additionally, in this thesis, a first attempt was made to identify plausible surface configurations that may be related to the observed surface site heterogeneity, using for the first-time state-of-the-art insights into the surface structure of Fh. Additionally, in **Chapter 4**, the insights gained for Ca and Mg have been generalized for describing in a self-consistent manner the binding of the entire series of alkaline-earth ions. For Fh, the binding affinity increases with increasing the ionic radius of these cations, *i.e.* $Be^{2+} < Mg^{2+} < Ca^{2+} \approx Sr^{2+} < Ba^{2+} < Ra^{2+}$. Interestingly, this affinity trend is opposite to trend observed for other Fe-(hydr)oxides (*i.e.* hematite, goethite). The possible reasons for this difference in affinity trend have been discussed.

In **Chapter 5**, the adsorption interaction of PO_4 with Ca^{2+} and Mg^{2+} ions (M^{2+}) was evaluated in binary PO_4-M^{2+} systems with freshly prepared Fh. The adsorption of M^{2+} to Fh is enhanced in the presence of PO_4, and *vice versa*. This synergistic binding cannot be understood only on the basis of electrostatic interactions, as found previously for goethite. Instead, formation of anion-bridged (*i.e.* ≡Fe–PO_4–M^{2+}) ternary surface complexes is the main mechanism explaining the cooperative binding between PO_4 and M^{2+} in Fh systems. For the Ca-PO_4 systems, two types of anion-bridged ternary complexes, *i.e.* ≡$(FeO)_2PO_2Ca$ and ≡$FeOPO_3Ca$ were resolved, whereas for the Mg-PO_4 systems only the formation of ≡$FeOPO_3Mg$ was resolved. The structural configuration of these complexes was derived based on the interpretation of adsorption data with CD-MUSIC model and by MO/DFT geometries optimization. Further research with *in-situ* spectroscopic techniques might help to confirm the configuration of these ternary complexes derived by modeling. The pH-dependency of the PO_4 adsorption is quite different for Fh and goethite in Ca solutions. This was explained by the difference in the mechanism (*i.e.* ternary complex formation *vs* electrostatic interactions) ruling the synergistic Ca-PO_4 interaction in both Fe (hydr)oxides. This implies that choosing either Fh or goethite as reference material will have important implications for the application of SCM in natural systems, *e.g.* for interpreting the results of routine soil extractions with 0.01 M $CaCl_2$ solutions.

In Chapter 6, the competitive adsorption interaction CO_3-PO_4 was analyzed in Fh systems in a range of solution conditions (*i.e.* pH, total CO_3 and PO_4 concentration) that are relevant for environmental systems (*e.g.* groundwater) and from the perspective of soil chemical analysis (*e.g.* equilibrium 0.5 M $NaHCO_3$ soil extractions). For a given pH, the adsorption of PO_4 to Fh decreases at increasing the total concentration of added CO_3, which is due to the direct competition between both oxyanions for the same binding sites at the surface of Fh. However, the relative affinity of PO_4 for these sites is significantly larger than the affinity of CO_3. The binding modes of CO_3 to Fh and the affinity constants of the corresponding adsorption reactions have been derived by only measuring the competitive effect of this ion on the adsorption of PO_4. According to the data interpretation with the CD-MUSIC model, CO_3 adsorbs to Fh forming mainly inner-sphere bidentate complexes, either ≡$(FeO)_2CO$ or ≡$(FeO)_2CO\cdot\cdot Na^+$. The latter is electrostatically promoted at high PO_4 loadings and high pH values. The thus-calibrated CD-MUSIC model for CO_3 described very well the adsorption of this ion to Fh in single-ion systems, showing the validity of the model for describing the adsorption of CO_3 over a wider range of conditions, in the absence of PO_4. A remarkable difference was found in the shape of the PO_4 adsorption isotherm of Fh and goethite in 0.5 M $NaHCO_3$ solution. This different CO_3-PO_4 competition between both Fe (hydr)oxides has important implications for the assessment of the reactive surface area (RSA) of soils if probed in 0.5 M $NaHCO_3$ systems, as shown in Chapter 7 and 8.

A meaningful application of SCM in soils is only possible if one has insight into the effective RSA of the soils. This was studied in the third section of my thesis for soils with different pedogenesis and chemical properties. The RSA of a series of agricultural Dutch top-soils (**Chapter 7**) and weathered

tropical top-soils (**Chapter 8**) was assessed using the CD model for interpreting the competitive CO_3-PO_4 interaction measured in series of soil extractions with 0.5 M $NaHCO_3$ solution. The thermodynamic database developed in this thesis (Chapters 4-6) was used for modeling interpretation. Despite the contrasting differences in the ratios of crystalline and nano-crystalline metal (hydr)oxides between the two soil series, in both cases, Fh was a better proxy for the natural fraction of reactive metal (hydr)oxides, rather than well-crystallized goethite. The results also showed that the natural fraction of (hydr)oxides in these top-soils is dominated by nano-sized particles (d ~1.5–5.0 nm), with a highly variable SSA of ~350–1700 $m^2\ g^{-1}$. Combining modeling and experimental data, the interaction between metal (hydr)oxide nanoparticles and SOM was evaluated, which provided novel insights into the nanometer scaled arrangement of the organo-mineral associations in soils. The results obtained for both types of soils shows that soil samples with larger metal (hydr)oxide particles store comparatively more SOC than samples with smaller metal (hydr)oxide particles. A structural model was proposed for interpreting these results in which the organo-mineral associations are seen as a collection of discrete SOM and metal (hydr)oxide nanoparticles organized by self-assembly. This structural model may open a new debate about the way in which the nanoscale organo-mineral associations are understood.

Finally, in **Chapter 9**, I summarize and integrate the major findings obtained in my PhD thesis. Further discussion is elaborated for a selected number of topics, which from my perspective, are of great relevance in the context of this thesis. In addition, yet unanswered questions, challenges, and prospective research opportunities are discussed in light of the results obtained in this thesis.

Overall, this thesis integrates a series of concepts and approaches that cover a wide range of scientific aspects, from fundamentals of surface chemistry to applications in soil and water chemistry. Therefore, the present contribution can be of interest to various scientific disciplines, including environmental science, geochemistry, colloid and interface science, material and surface science, as well as soil- and water chemistry. The insights obtained in synthetic systems with freshly prepared Fh contribute to improve our understanding of ion adsorption processes occurring at the molecular scale, which are important to enable accurate predictions of the behavior and availability of ions at the macroscopic level, studied at the laboratory and field scale. From a broader perspective, the results of this work can be relevant for optimizing management practices intended to improve P use efficiency in agricultural systems or to reduce the negative side-effects of P in the environment. The results can also be relevant in the context of technological applications for improving P recovery from water and waste treatments. In relation to SCM development, a major step forward has been taken towards a more accurate description of ion adsorption to the natural metal (hydr)oxides in field samples. Nevertheless, several challenges remain in the search of a fully consistent SCM approach for soil samples.

Resumen

Ferrihidrita (Fh) es una nanopartícula de (hidr)óxido de hierro presente en la mayoría de los ambientes naturales, así como en muchos sistemas industriales (*e.g.* desechos de minería). Ferrihidrita tiene una gran reactividad superficial debido al tamaño extremadamente pequeño de las partículas primarias, usualmente ~2–4 nm. Por tal motivo, aun presente en bajas concentraciones (en términos de masa), Fh controla en gran medida la disponibilidad de nutrimentos y contaminantes en los suelos, principalmente mediante procesos de adsorción. Ferrihidrita forma, en conjunto con la materia orgánica del suelo (MOS), complejos organo-minerales de gran estabilidad química los cuales contribuyen a la estabilización a largo plazo del carbono orgánico en los suelos. Ferrihidrita también es un material promisorio para aplicaciones en ingeniería y tecnologías de remediación ambiental. En el contexto de modelización de adsorción de iones en superficies minerales (*i.e. Surface Complexation Modelling*, SCM), estudiar la reactividad superficial de Fh es importante ya que este nanomineral se vislumbra como un excelente material de referencia para describir, usando SCM, los procesos de adsorción de iones que ocurren en la superficie de óxidos metálicos presentes en el suelo. A pesar de su importancia como material altamente reactivo, muchos aspectos relacionados con la reactividad de la superficie de Fh son poco conocidos.

Ferrihidrita tiene una afinidad particularmente alta para adsorber en sus superficies oxoaniones tales como fosfato (PO_4), arsenato (AsO_4), y cromato (CrO_4). Por tal motivo, estos oxoaniones son buenos candidatos para evaluar la reactividad de la superficie de Fh. En el presente trabajo, PO_4 ha sido elegido como oxoanión modelo debido a varias razones. El ion PO_4 está omnipresente en ambientes naturales, y debido a su gran afinidad por las superficies de (hidr)óxidos de hierro y aluminio, el PO_4 tiende a acumularse naturalmente en los horizontes superficiales del suelo en forma de especies químicas adsorbidas. Además, PO_4 es un nutrimento esencial para el crecimiento vegetal y la producción de alimentos. No obstante, la concentración de PO_4 en la solución del suelo se encuentra usualmente por debajo del nivel óptimo requerido para garantizar un adecuado rendimiento de los cultivos. Por otro lado, el uso intensivo y repetitivo de fertilizantes con fósforo (P), tanto orgánicos como inorgánicos, puede conllevar a un exceso de PO_4 en sistemas acuáticos, comprometiendo la calidad del agua y su seguridad. La disponibilidad de P en los suelos de sistemas naturales y agrícolas es evaluada convencionalmente por medio de una serie de análisis de rutina basados en extracciones químicas. Sin embargo, a nivel general prevalece un entendimiento deficiente de los mecanismos y procesos que afectan la liberación de PO_4 de las superficies del suelo durante dichos análisis de rutina. Esto puede conducir a interpretaciones imprecisas acerca del estado real de disponibilidad de P en los suelos. Considerando todo lo anterior, resulta claro que el estudio de los mecanismos fundamentales que controlan la adsorción de PO_4 en las superficies de (hidr)óxidos metálicos es relevante desde un punto de vista científico, ambiental, económico y social.

El objetivo de esta tesis es generar nuevos conocimientos acerca de la reactividad superficial de nanopartículas de Fh, dando énfasis al análisis de los mecanismos de adsorción de PO_4, y al desarrollo de un esquema de modelización para describir consistentemente la adsorción de PO_4 en un amplio rango de condiciones. En este trabajo, la interacción cooperativa de adsorción entre PO_4 y los cationes Ca^{2+} y Mg^{2+}, así como la interacción competitiva entre los oxoaniones PO_4 y CO_3, has sido analizadas en detalle. Un análisis consistente de estas interacciones es esencial si el objetivo es comprender el comportamiento de adsorción de PO_4 en sistemas complejos, *e.g.* ambientes naturales y soluciones extractoras en análisis rutinarios de suelos. La adsorción de Ca^{2+} y Mg^{2+} en Fh ha sido también analizada exhaustivamente en sistemas mono-componente (*i.e.* adsorción especifica de un único ion) debido a la

gran abundancia de estos cationes en el ambiente y a su efecto en el comportamiento de adsorción de otros iones de gran relevancia ambiental. El objetivo final es contribuir al desarrollo de un enfoque de modelización que permita describir realísticamente, desde un punto de vista fisicoquímico, la adsorción simultanea de una serie de cationes y aniones en nanopartículas de Fh.

Los métodos utilizados en esta tesis comprenden experimentos de adsorción con nanopartículas de Fh recién sintetizadas en el laboratorio, así como interpretación de los datos experimentales usando un modelo avanzado de adsorción de iones (*i.e.* CD-MUSIC) y cálculos de orbitales moleculares (OM) para estimar de manera independiente los coeficientes de distribución de carga (CD) de todas las especies químicas adsorbidas, utilizadas en el modelo desarrollado. La combinación de estos métodos ha permitido compilar una base de datos con parámetros termodinámicos para describir consistentemente la adsorción de iones en Fh. Dicha base de datos has sido utilizada posteriormente para evaluar el área superficial reactiva (ASR) de la fracción natural de (hidr)óxidos metálicos en muestras de suelos.

De acuerdo con los objetivos formulados en el capítulo de Introducción (Capítulo 1), los capítulos experimentales y de modelización de esta tesis han sido organizados, según su tema principal, en tres secciones: *i*) aspectos fundamentales de la reactividad de la superficie de Fh (Capítulos 2-3), *ii*) parametrización del modelo de adsorción de iones (Capítulos 4-6), y *iii*) aplicación del modelo desarrollado en muestras de suelos (Capítulos 7-8).

Muchas de las propiedades fisicoquímicas de Fh y de nanopartículas en general, cambian drásticamente en función del tamaño de partícula. Por lo tanto, una interpretación coherente de los datos de adsorción de iones colectados para Fh requiere de información precisa acerca del tamaño promedio de partícula y de la respectiva área superficial específica (ASE, $m^2\ g^{-1}$ Fh) de este nanomineral. En la primera sección de esta tesis se ha desarrollado un protocolo para evaluar el ASE de Fh en suspensión, el cual se basa en la medición e interpretación de adsorción de protones (H^+) (**Capítulo 2**). Para la interpretación y modelización de los datos, la capacitancia de la doble capa eléctrica (*i.e.* capa de Stern) de goethita (*i.e.* un óxido de hierro cristalino) ha sido utilizada como referencia y convertida en valores de capacitancia para Fh, usando valores consistentes de masa molar (M_{nano}), densidad de masa (ρ_{nano}) y curvatura de superficie. Los resultados muestran total consistencia entre los valores de ASE obtenidos con la presente metodología (H^+-método) y con un método alternativo que utiliza datos de adsorción de PO_4 (PO_4-método). Sin embargo, el PO_4-método es una alternativa más práctica para superar las conocidas limitaciones de técnicas tradicionales (*e.g.* BET) para evaluar el ASE de nanopartículas de Fh en suspensión. Además, la medición de la adsorción de PO_4 es poco sensible a posibles interferencias de CO_2 atmosférico. Por lo tanto, el PO_4-método ha sido utilizado para evaluar el ASE de Fh en todos los experimentos de adsorción realizados en esta tesis. Esto permitió el desarrollo de una base de datos termodinámica para describir la adsorción de varios iones de importancia ambiental en Fh (Capítulos 4-6). La interpretación de datos de adsorción de H^+ reportados en la literatura revela una gran variación en el ASE para suspensiones de Fh ($A_H \sim 500–720\ m^2\ g^{-1}$), lo cual indica que el uso de un valor estándar de ASE no recomendado para suspensiones de Fh recién preparadas.

En el **Capítulo 3**, el PO_4-método ha sido usado para cuantificar los cambios en la reactividad de la superficie de Fh, los cuales son el resultado del proceso de crecimiento de partículas. Lo anterior permitió analizar los principales factores (*i.e.* tiempo, pH, temperatura, presencia de moléculas orgánicas) que controlan el cambio en reactividad de Fh. Los datos colectados con el PO_4-método proporcionaron información fundamental acerca de los mecanismos y tasa de crecimiento de nanopartículas de Fh en suspensión. Además, se desarrolló un modelo dinámico que describe los

cambios en ASE de Fh, y que además revela el tamaño (d ~ 1.68 nm) y ASE (A ~ 1100 m^2 g^{-1}) inicial de las nanopartículas de Fh, previos al proceso de crecimiento. Estos resultados son relevantes al momento de sintetizar nanopartículas de Fh con tamaño y reactividad definidos, así como para interpretar consistentemente datos de adsorción de iones en este nanomaterial.

En la segunda sección de esta tesis, el modelo CD-MUSIC ha sido parametrizado con el fin de describir los datos de adsorción obtenidos en sistemas con nanopartículas de Fh. En el **Capítulo 4**, la adsorción de los iones Ca^{2+} y Mg^{2+} (referidos conjuntamente como M^{2+}) ha sido estudiada en detalle en sistemas mono-componente con Fh. Ambos cationes son adsorbidos en las superficies de Fh formando principalmente complejos bidentados de esfera interna ($\equiv(FeOH)_2^{\Delta z0}M^{\Delta z1}$). La heterogeneidad de los grupos reactivos en la superficie (*i.e.* presencia de grupos superficiales de baja y alta afinidad) es un aspecto particular de la adsorción de M^{2+} en Fh. En esta tesis, el modelo MUSIC, inicialmente desarrollado para describir la adsorción de oxoaniones, ha sido extendido con el concepto de heterogeneidad superficial con el fin de describir simultáneamente la adsorción de iones metálicos en Fh. Los resultados muestran que solo una pequeña fracción (~10%) de los sitios reactivos disponibles que reaccionan con M^{2+} presentan un carácter de alta afinidad por estos cationes. No obstante, estos grupos superficiales de alta afinidad controlan la adsorción de M^{2+} en condiciones de baja densidad de adsorción y bajos valores de pH. Adicionalmente en esta tesis, se intentó identificar las posibles configuraciones en la superficie de Fh que son responsables por el fenómeno de heterogeneidad superficial, utilizando por primera vez información avanzada de la estructura superficial de Fh. Adicionalmente, en el **Capítulo 4**, los conocimientos fundamentales obtenidos con respecto a la adsorción de Ca y Mg han sido generalizados para describir de manera consistente la adsorción de toda la serie de cationes alcalinotérreos. En sistemas con Fh, la afinidad de adsorción aumenta con el incremento del radio iónico de esta serie de cationes, *i.e.* $Be^{2+} < Mg^{2+} < Ca^{2+} \approx Sr^{2+} < Ba^{2+} < Ra^{2+}$. Esta tendencia en afinidad es opuesta a la tendencia observada en otros (hidr)óxidos de Fe (*i.e.* hematita, goethita). Las posibles causas de esta diferencia han sido analizadas en este trabajo.

En el **Capítulo 5**, la interacción entre PO_4 y los cationes Ca^{2+} y Mg^{2+} ha sido evaluada en sistemas binarios PO_4-M^{2+} con nanopartículas de Fh. La adsorción de M^{2+} en las superficies de Fh incrementa en presencia de PO_4, y viceversa. Esta sinergia no es explicada únicamente por el incremento de las interacciones electrostáticas anion-cation, a diferencia de lo reportado previamente en sistemas con goethita. En cambio, la formación de compuestos ternarios de puente aniónico (*i.e.* $\equiv Fe–PO_4–M^{2+}$) en las superficies de Fh es el principal mecanismo responsable por la adsorción cooperativa entre PO_4 y M^{2+}. En los sistemas binarios Ca-PO_4, dos tipos de compuestos ternarios han sido revelados, *i.e.* $\equiv(FeO)_2PO_2Ca$ y $\equiv FeOPO_3Ca$, mientras que en los sistemas Mg-PO_4 únicamente el compuesto $\equiv FeOPO_3Mg$ ha sido resuelto. Las configuraciones de estos compuestos ternarios fueron derivadas con base en la interpretación de datos de adsorción usando el modelo CD-MUSIC, así como por medio de la optimización de las geometrías de dichos compuestos, usando cálculos de orbitales moleculares (OM). La configuración de estos compuestos ternarios deberá ser confirmada en investigaciones futuras usando por ejemplo técnicas espectroscópicas *in-situ*. En presencia de Ca, la relación entre la adsorción de PO_4 y el pH de la solución difiere sustancialmente entre sistemas con Fh y goethita. Lo anterior se debe a la diferencia en el mecanismo principal (*i.e.* interacciones electrostáticas *versus* formación de complejos ternarios) que controla la interacción sinérgica entre Ca y PO_4 en las superficies de Fh y goethita. Esto implica que la elección de Fh o goethita como material de referencia tendrá implicaciones importantes en la modelización de adsorción de iones en sistemas naturales, *e.g.* en la interpretación de los resultados de análisis rutinarios de suelo utilizando soluciones de 0.01 M $CaCl_2$.

En el **Capítulo 6**, la interacción competitiva entre PO_4 y CO_3 por la adsorción en Fh ha sido analizada en un amplio rango de condiciones (*i.e.* pH, concentración total de CO_3 y PO_4), las cuales son relevantes en sistemas ambientales (*e.g.* aguas subterráneas) y desde el punto de vista de análisis químico de suelos (*e.g.* extracciones con 0.5 M $NaHCO_3$). Para un determinado pH en solución, la adsorción de PO_4 en Fh disminuye con el incremento de la concentración total de CO_3 añadido en el sistema, lo cual resulta debido a la competencia directa entre ambos oxoaniones por los mismos sitios de adsorción en las superficies de Fh. Sin embargo, la afinidad de PO_4 por dichos sitios de adsorción es significativamente mayor que la afinidad de CO_3. Los mecanismos de adsorción de CO_3 en Fh, así como las constantes de afinidad de las correspondientes reacciones de adsorción, han sido derivadas analizando únicamente el efecto competitivo de CO_3 sobre la adsorción de PO_4. Según la interpretación de datos experimentales con el modelo CD-MUSIC, CO_3 forma predominantemente complejos bidentados de esfera interna en las superficies de Fh, ya sea $(\equiv FeO)_2CO$ or $(\equiv FeO)_2CO\cdot\cdot Na^+$. La formación del segundo complejo es favorecida electrostáticamente en condiciones de altas densidades de adsorción de PO_4 y altos valores de pH. El modelo CD-MUSIC, calibrado en sistemas binarios CO_3-PO_4, es capaz de describir razonablemente bien la adsorción de CO_3 en Fh en sistemas mono-componente, lo cual confirmar la validez de este modelo para describir la adsorción de CO_3 bajo un amplio rango de condiciones, en ausencia de PO_4. Se encontró una diferencia sobresaliente en la forma de la isoterma de adsorción de PO_4 entre sistemas con Fh y goethita en solución de 0.5 M $NaHCO_3$. Esta diferencia entre ambos (hidr)óxidos de Fe tiene implicaciones importantes en la evaluación del área superficial reactiva (ASR) de suelos, cuando esta propiedad es evaluada con base en los resultados de extracciones de suelo con 0.5 M $NaHCO_3$, tal y como se demostró en los Capítulos 7 y 8.

La aplicabilidad de SCM en muestras de suelo es de utilidad únicamente si se cuenta con información válida acerca del ASR del suelo. Lo anterior ha sido estudiado en la tercera sección de esta tesis en muestras de suelos con diferente pedogénesis y propiedades químicas. El ASR de una serie de suelos agrícolas holandeses (**Capítulo 7**) y suelos tropicales meteorizados (**Capítulo 8**) ha sido evaluada interpretando con el modelo CD-MUSIC la interacción CO_3-PO_4. Dicha interacción fue analizada en una serie de extracciones de suelo con 0.5 M $NaHCO_3$. La base de datos termodinámica desarrollada en esta tesis (Capítulos 4–6) ha sido utilizada en los cálculos de modelización. A pesar de las diferencias contrastantes en la proporción de (hydr)óxidos metálicos cristalinos y nanocristalinos entre ambas series de suelos, en ambos casos Fh fue identificada como mejor material de referencia que goethita para describir la reactividad de la fracción natural de (hydr)óxidos metálicos. Los resultados muestran que la fracción reactiva de (hydr)óxidos metálicos en estos suelos está compuesta dominantemente por nanopartículas (d ~1.5–5.0 nm), con un área superficial específica altamente variable de ~350–1700 m^2 g^{-1}. La interacción entre las nanopartículas de (hydr)óxidos metálicos y la materia orgánica del suelo (MOS) fue evaluada en los **Capítulos 7 y 8**, suministrando nueva información acerca de la configuración nanométrica de los complejos organo-minerales en los suelos. Los resultados obtenidos en ambos tipos de suelos indican que las muestras con partículas de (hydr)óxidos metálicos de mayor tamaño almacenan comparativamente más MOS que las muestras con partículas de (hydr)óxidos metálicos de menor tamaño. Para interpretar estos resultados, se propuso un modelo estructural en el cual las asociaciones organo-minerales son percibidas como una colección de nanopartículas discretas de MOS y (hydr)óxidos metálicos organizadas por un mecanismo de auto ensamblaje. Se espera que este modelo estructural abra las puertas a un nuevo debate acerca del modo en que visualiza los complejos organo-minerales a escala nanométrica.

Finalmente, en el **Capítulo 9**, se recapitula e integra los resultados más relevantes obtenidos en mi tesis de doctorado y se elabora una discusión más detallada acerca de un selecto número de temas los

cuales, desde mi perspectiva, son de mayor relevancia en el contexto de esta tesis. Además, preguntas aún sin responder, desafíos y posibles oportunidades de investigación se discuten a la luz de los resultados obtenidos en esta tesis.

En general, esta tesis integra una serie de conceptos y enfoques afines a un amplio espectro de aspectos científicos, los cuales van desde fundamentos de química de superficies hasta aplicaciones en química de suelos. Por lo tanto, el presente trabajo es de interés para diversas disciplinas científicas, incluyendo ciencias ambientales, geoquímica, ciencia de coloides e interfases, ciencia de materiales y superficies, así como química de suelo y agua. Los conocimientos adquiridos en sistemas sintéticos con nanopartículas de Fh contribuyen a mejorar nuestro entendimiento de los procesos de adsorción de iones que ocurren a nivel molecular, lo cual es de gran relevancia para elaborar predicciones más precisas acerca del comportamiento y disponibilidad de iones a escala macroscópica, *e.g.* en laboratorio o en condiciones de campo. Desde una perspectiva más amplia, los resultados de este trabajo son relevantes para optimizar prácticas de gestión que pretenden mejorar la eficiencia del uso de P en sistemas agrícolas, o bien para reducir efectos negativos de P en el medio ambiente. Los resultados también pueden ser relevantes en el contexto de aplicaciones tecnológicas para mejorar la recuperación de P en aguas residuales. En relación con el desarrollo de SCM, en esta tesis se ha dado un avance importante hacia una descripción más precisa de la adsorción de iones en la fracción natural de (hidr)óxidos metálicos presentes en suelos, usando técnicas avanzadas de modelización. No obstante, varios desafíos persisten en la búsqueda de un enfoque de modelización que sea completamente consistente y aplicable a muestras de suelo.

Acknowledgments

It has been a little more than six years since I arrived in the Netherlands, first to follow a MSc program and then to pursue the present PhD project. For me, this has been a journey full of fulfilling experiences, learnings, and challenges. Undoubtedly, the time I have spent in Wageningen will shape in a large extent my years to come, both personally and professionally. Of course, this whole experience, and particularly the successful completion of this PhD project, would not have been possible without the help and support of many people, to whom I want to express my gratitude.

My deepest gratitude goes to my supervisor Dr. Tjisse Hiemstra. Tjisse, I feel honored to have had the opportunity to work with you during the last years. I did really learn from this experience and I did truly enjoy it. I believe that, for a successful completion of a PhD, a motivated supervisor is just as important as a motivated student. Thank you for your motivation and for helping me to stay motivated. Thank you also for challenging me and for pushing me in several opportunities to go beyond what I thought it was my limit. Your constant search for answers, your self-criticism, and overall, your passion for science are lessons that will undoubtedly persist for the rest of my professional career. To me, this makes the difference between a supervisor and a mentor. Thank you for your mentoring!

I also want to thank Prof. Rob Comans for the opportunity to work at the Soil Chemistry Group. I still remember when I walked into your office for the first time, more than 5 years ago, and I told you that, after finishing my MSc program, I would like to continue with a PhD at the Soil Chemistry group and work on a project related to phosphorous adsorption to oxides, because this is a “big problem” in the soils of my home country. Today, thanks to the work performed at the Soil Chemistry group, this project could be done. Moreover, I also want to thank all the staff members of the Soil Chemistry group that in one or another way have contributed to this project. Particularly, I would like to thank Dr. Gerwin Koopmans for his valuable input in the preparation of the research proposal and as a co-author of one of the chapters of this thesis.

I would like to acknowledge the work of all the staff members of the Soil Chemistry Laboratory (CBLB), in particular I thank Gerlinde Vink, Peter Nobels, and Johan Uijtenbroek for their readiness to help in the laboratory and their enthusiasm to solve various analytical challenges. Your dedicated work has been essential to guarantee the quality of the results presented in this thesis. I also want to thank Marnella, Esther, and Priskila for their always opportune help when I needed it most.

During my time as a PhD student, I had the opportunity to share experiences with many fellow PhD candidates, interns, and post-doc researchers at the former Soil Quality Department. To all these colleagues with whom I had the pleasure to share a coffee, a drink, or a conversation, I also want to say thanks. In particular, I want to thank those people with whom I shared the most, and who made my days at work (and after work!) happier. Anupol, it was nice to coincide with you in the group for some time, I hope we will meet again, either in Thailand or in Costa Rica (yes, you are welcome to go back!). A special thanks to the SOC-girls Elise, Hui, Yilina, and Rima (a chemist at heart ;)). Elise, it has been a pleasure to share with you during this time and to have the opportunity to work together. I hope you enjoyed as much as I did all our conversations and discussions about several topics, going from ferrihydrite-related issues to cats ;). Hui, it is time for the “office boy” to leave our “box of shame”, but I will keep all the nice memories in our office. Thanks for all the good moments also outside the office (including hot-pot and noodles of course!). Yilina, I enjoyed sharing time with you in the SOC group,

attending to courses and conferences with you made these experiences more fun and somehow epic. Rima, thank you for being there to support and for always making livelier even the less lively days. Also, thank you for forbearing my annoyances, like when I insistently tried to make sense of my limited Dutch vocabulary (*geniet van…*, *apart betalen*, *speciale situatie*).

I would also like to thank to all the MSc and BSc students that contributed to this project: Jelle, Frank, Imtiaz, Koen, Zoë, Jurrian, and Thomas.

A special thanks to my paranymphs Elise Van Einde (thanks again) and Andrés Hernández for your support and for being part of this important day.

Muchas gracias a Alice, Alberto, Daniela y Diana por todos los buenos momentos compartidos durante el periodo de maestría y una buena parte del doctorado. Mi tiempo en Wageningen no hubiese sido lo mismo de no haber tenido la oportunidad de compartir con ustedes. Pura vida.

Quiero expresar mi agradecimiento a las personas en la Universidad de Costa Rica quienes me apoyaron desde el inicio, y quienes me impulsaron para llegar hasta aquí el día de hoy. En ese sentido agradezco particularmente el apoyo de Carlos Henríquez, Eric Guevara y Rafael Salas. También, mi más profunda gratitud a Floria Bertsch, cuyas enseñanzas trascienden mucho más allá de su pasión y dedicación por las ciencias del suelo.

Por supuesto, mi más profundo agradecimiento a mi familia porque de una u otra manera todos ustedes han contribuido a lo largo de los años para que yo pudiera llegar hasta aquí el día de hoy. El esfuerzo ha sido de todos. A mis padres Yamileth y Juan Carlos, gracias por apoyar mis decisiones, por su esfuerzo, y por creer en mi desde siempre. A mis hermanos Carmen, Javier, Jacob y Dahiana: gracias porque las mejores lecciones en esta vida las he aprendido al lado de ustedes, y eso determina en gran medida la persona que soy hoy en día. A Juan Pablo, quien llegó hace poco tiempo a la familia a traer alegría y esperanza, espero que algún día podas leer orgulloso este mensaje de tu tío.

Por último, quiero expresar mi más profundo agradecimiento a la persona que ha estado conmigo desde el inicio de este viaje, y quien sabe mejor que nadie lo que significa para mí llegar hasta aquí el día de hoy. María, gracias por todas las experiencias que vivimos durante este tiempo, en ambos lados del océano. Gracias por apoyar mis decisiones, por estar presente para compartir alegrías, pero sobre todo por tu apoyo y compañía en los momentos de incertidumbre. Gracias por hacerme recordar las cosas que son realmente importantes en la vida. Cerramos ya esta etapa del viaje, el cual continua ahora con la ilusión de nuevos retos y metas por cumplir. Ahora es tiempo de ir a casa :).

About the author

Juan Carlos Méndez Fernández was born on November 25th, 1988 in Cartago, Costa Rica. He studied Agronomy at the University of Costa Rica (2006–2011) and in his major thesis he compiled and analyzed an extensive database of soil chemical analyses to identify the major constraints to soil fertility in agricultural soils of Costa Rica. After graduating (with honors), he worked as a research assistant (2012-2013) at the Agronomic Research Center (Centro de Investigaciones Agronómicas, CIA) of the University of Costa Rica (UCR). In 2014, he arrived in the Netherlands to study a MSc program in Environmental Science at Wageningen University with a specialization in Soil Chemistry. His MSc thesis aimed to analyze the main chemical factor affecting the release of phosphate from the soil surfaces during chemical soil extraction procedures. During this period, under the supervision of Dr. Tjisse Hiemstra, he developed a great interest for studying the fundamental processes that occur at the mineral-solution interfaces and that affect the chemical behavior of phosphate in soils. As part of this MSc program, Juan Carlos also conducted an internship at the Department of Soil Science of Temperate Ecosystems in Göttingen University, Germany, where he participated in a research project focused on studying the availability of phosphorous in European forest soils. Upon completion of his MSc degree in 2016, he started a PhD program at the Soil Chemistry Group of Wageningen University, where he continued working under the supervision of Tjisse Hiemstra. His PhD research focused on studying the surface reactivity of ferrihydrite, an important nanoparticle in the environment, and on developing a modeling approach for describing ion adsorption phenomena to this nanomaterial. The results of his PhD project are presented in this thesis. After finishing his PhD, Juan Carlos will return to Costa Rica where he will take a research and education position at CIA, UCR.

Email contact: juancarlos.mendez@ucr.ac.cr

Netherlands Research School for the
Socio-Economic and Natural Sciences of the Environment

D I P L O M A

for specialised PhD training

The Netherlands research school for the
Socio-Economic and Natural Sciences of the Environment
(SENSE) declares that

Juan Carlos Mendez Fernandez

born on 25 November 1988 in Cartago, Costa Rica

has successfully fulfilled all requirements of the
educational PhD programme of SENSE.

Wageningen, 27 August 2020

Chair of the SENSE board

Prof. dr. Martin Wassen

The SENSE Director

Prof. Philipp Pattberg

The SENSE Research School has been accredited by the Royal Netherlands Academy of Arts and Sciences (KNAW)

303

KONINKLIJKE NEDERLANDSE
AKADEMIE VAN WETENSCHAPPEN

The SENSE Research School declares that **Juan Carlos Mendez Fernandez** has successfully fulfilled all requirements of the educational PhD programme of SENSE with a work load of 41.6 EC, including the following activities:

SENSE PhD Courses

- Environmental research in context (2016)
- Speciation and bioavailability of metals, organics and nanoparticles (2017)
- Research in context activity: 'Writing research proposal: Interaction of natural iron-oxide nanoparticles with soil organic matter' (2020)

Other PhD and Advanced MSc Courses

- Reviewing scientific papers , Wageningen Graduate Schools (2017)
- PhD summer school: "Sustainable land use: Decrease the environmental footprint – Increase the economic and social output", Climate-KIC, Hungary-Spain (2017)
- Scientific writing, Wageningen Graduate Schools (2017)
- Coupled processes in Physics, Chemistry and Biology, Wageningen University (2017)
- Teaching and supervising thesis students, Wageningen Graduate Schools (2018)
- The art of modelling, PE&RC and WIMEK (2019)
- Writing grant proposal, Wageningen Graduate Schools (2019)

Didactic Skills Training

- Supervising four BSc students with thesis (2017-2019)
- Supervising three MSc students with thesis (2017-2019)
- Teaching assistant in the BSc/MSc course: 'Chemical processes in Soil-Water-Atmosphere' (2016-2019)

Oral Presentation

- *Competitive adsorption of phosphate and carbonate: from model systems with ferrihydrite nanoparticles to field soil samples*, Soil Science Society of America International Soil Conference, 6-9 January 2019, San Diego, United States of America

SENSE coordinator PhD education

Dr. ir. Peter Vermeulen

The research presented in this thesis was performed at the Soil Chemistry and Chemical Soil Quality Group, Wageningen University & Research, the Netherlands.

The grant provided by the University of Costa Rica to the author of this thesis is gratefully acknowledged.

The financial support of Wageningen University and the University of Costa Rica for printing this thesis is gratefully acknowledged.

Cover design by Bregje Jaspers
Lay-out by Juan C. Mendez
Printed by Proefschiftmaken

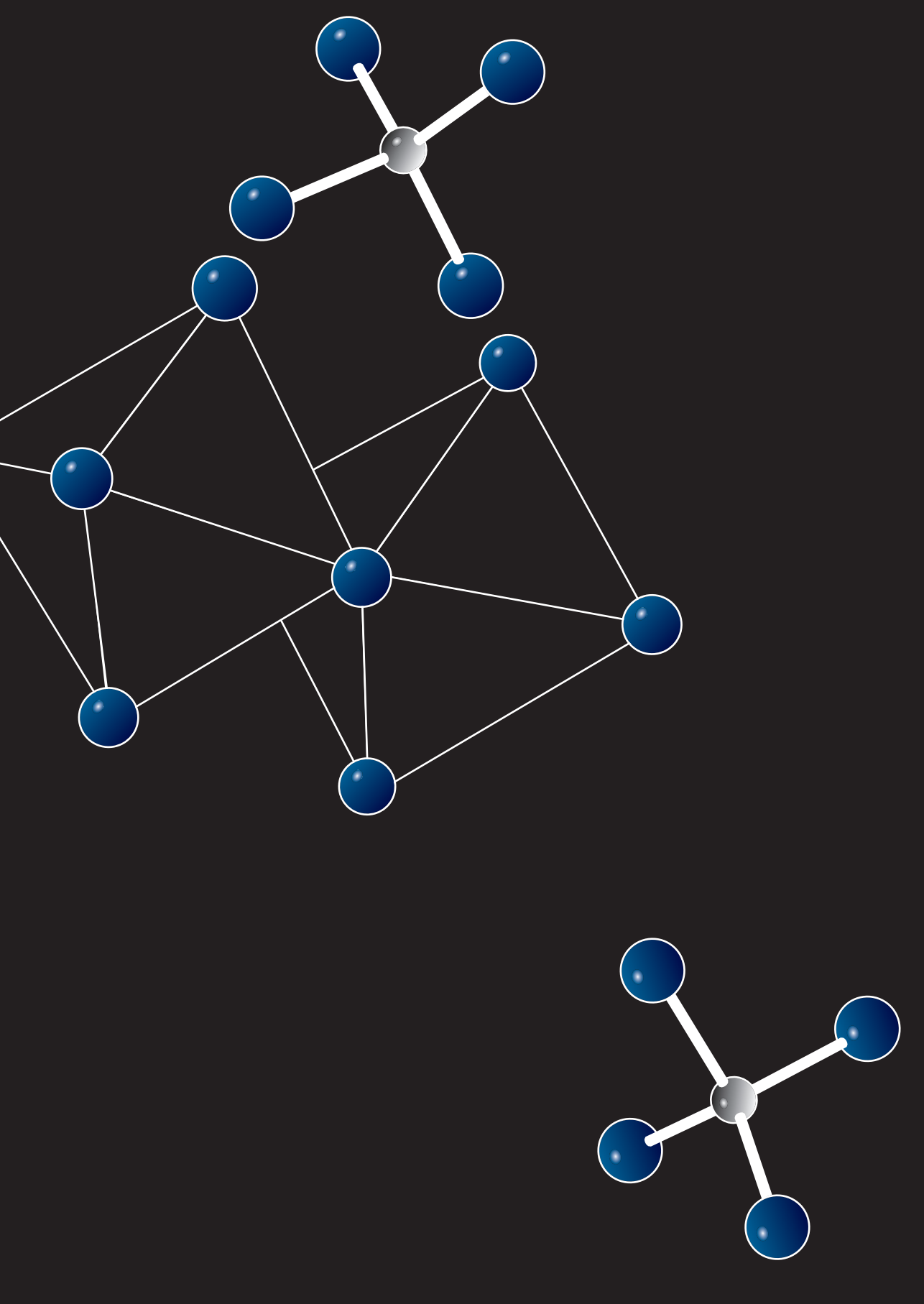

Propositions

1. Due to the intrinsic nature of ferrihydrite as a nanoparticle, surface complexation modelling for this material is only meaningful if its specific surface area can be assessed consistently. (this thesis)

2. The interaction of phosphate and the reactive metal (hydr)oxides in tropical soils can be described effectively with surface complexation modelling using ferrihydrite as a proxy for these natural reactive surfaces. (this thesis)

3. In global geochemical models for carbon sequestration, the contribution of clay minerals in protectively binding soil organic carbon is overrated. (Rasmussen et al. 2018. *Biogeochemistry 137:297-306*)

4. Present concerns about global scarcity of P resources are primarily based on a legacy of past discourses on depletion, rather than on factual available data. (Ulrich and Frossard. 2014. *Science of the Total Environment, 490:694-707*).

5. Commodification of education and research activities puts on stake the long-term stability of the global society.

6. The unprecedented increase in the accessibility and amount of information to the general public is, paradoxically, a risk for the well-functioning of science and democracy.

Propositions belonging to the thesis, entitled:

Ion complexation modelling of ferrihydrite: From fundamentals of metal (hydr)oxide nanoparticles to applications in soils systems

Juan Carlos Mendez Fernandez

Wageningen, 27 August 2020